The Design, Synthesis and Applications of Copper Paddle-Wheel Based Metal-Organic Framework Nanosheets

David James Ashworth

160121328

A thesis submitted to the University of Sheffield in partial fulfilment
of the requirements for the Degree of Doctor of Philosophy

November 2019

Department of Chemistry, University of Sheffield

A thesis submitted to the University of Sheffield in
partial fulfilment of the requirements for the award of a
Degree of *Philosophiae doctor* (Doctor of Philosophy - Ph.D.) in Chemistry.

Abstract

Metal-organic framework nanosheets (MONs) are an exciting new class of modular two-dimensional (2D) nanomaterial. They are formed from organic linker ligands that link metal ions or clusters in two dimensions. These 2D materials combine the tunability of metal-organic structures with properties of other 2D materials, such as large external surface area, nanoscopic dimensions and high aspect ratio. This has led to increasingly widespread utilisation of MONs in applications as diverse as catalysis, sensing, gas separation, water purification, optoelectronics and energy conversion.

Top-down exfoliative methods can be used to produce MONs from layered metal-organic frameworks (MOFs). Factors that govern this process are poorly understood. MON design remains in its infancy, with most current MONs utilising well-known, relatively simple building blocks, such as benzene-1,4-dicarboxylate (BDC). In this thesis, new isoreticular series of layered MOFs were synthesised utilising different functionalised BDC (fu-BDC) ligands to link copper paddle-wheel (PW) secondary building units in two dimensions. These were exfoliated using liquid ultrasonic exfoliation to form MONs and characterised using a diverse range of techniques in order to understand the effect of different functional groups on the structure, dimensions and properties of the MONs formed.

In **Chapter 3**, functionalisation with relatively hydrophilic or hydrophobic moieties influenced the concentration, morphology and size of MONs when exfoliated in a wide range of solvents. Generally, MONs formed using the relatively hydrophilic ligand were observed in higher concentration in polar solvents. Clear differences in the binding properties of small aromatic heterocycles were observed, and DFT calculations indicated potential intramolecular coordination of the relatively hydrophilic moiety upon removal of DMF from axial coordination sites of the PW.

Functionalisation with a series of different length alkoxy chains enabled synthesis of an isoreticular MOF series in **Chapter 4**. Pawley and Rietveld refinements of PXRD data allowed structure determination, which indicated that increasing the chain length increased the interlayer spacing. This corresponded to an increase in CO_2 adsorption. Statistical particle size analyses showed that increasing the chain length resulted in MONs of decreasing height but larger lateral dimensions.

Chapter 5 and **Chapter 6** demonstrated that multiple different fu-BDC ligands could be blended within the layered MOF structure to form mixed-ligand multivariate-(MTV-)MOFs. Liquid ultrasonic exfoliation resulted in mixed-ligand MTV-MONs for the first time. Blending of relatively hydrophilic and hydrophobic fu-BDC resulted in MONs with which had intermediary properties compared to the single-ligand parent MONs. Blending different fu-BDC ligands with different length alkoxy chains demonstrated tuneable MON composition. In **Chapter 6**, a different series of fu-BDC ligands (fu= $(H)_2$, NH_2, $(Cl)_2$, $(Br)_2$ and NO_2) was used to synthesise a series of isoreticular layered MOFs and exfoliation formed MONs down to monolayer thickness. Eleven MTV-MOFs were then synthesised using combinations of fu-BDC, in which generally a larger number of different ligands produced nanosheets with a decreased average height.

Overall, this thesis demonstrates the utility of liquid ultrasonic exfoliation as a top-down exfoliative method for the production of MONs from layered, PW-based MOFs. MONs are a modular class of nanomaterial that fall at the interface of 2D and metal-organic chemistry. The isoreticular approach to their design demonstrates tunability of the materials' chemistry. MONs therefore have significant potential as 2D nanomaterials with controllable, tuneable surface chemistry.

Author's declaration

This research has been performed between the months of October 2016 and October 2019, within the Department of Chemistry at the University of Sheffield, under the supervision of Dr Jonathan Foster.

1st referee   Dr Robert Dawson, The University of Sheffield

2nd referee, external   Prof. Neil Champness, The University of Nottingham

Declaration

The work described herein has been performed and written independently and without unauthorised aid. It is the original work of the author, except where specifically acknowledged in text. Contributions from other authors within the presented work are described in the "author contributions" prior to each chapter. Where applicable, all relevant sources of information or quotation have been referenced as completely as possible.

This thesis has not been submitted in whole or in part, or in any similar form, to any other academic establishment. Additionally, I declare I have not unsuccessfully attempted to obtain a doctorate from any alternate establishment prior to this submission.

What are sun, stars, chemistry, geology, mathematics but pages of a book whose author is God? I want to know the meaning of this book, to penetrate the spirit of this author!

John Tyndall, FRS. 1820 – 1893

September 1848, lecturing to students at Queenwood College, Hampshire.[*]

Image credits: Philip Dolby, Sheffield, 05 Nov 2017

Acknowledgements

A day without a friend is like a pot without a single drop of honey left inside.

Winnie-the-Pooh (24 December 1925 - timeless), A. A. Milne (18 January 1882 – 31 January 1956), a widely celebrated author and playwright.

The best and most beautiful things in the world cannot be seen or even touched –they must be felt with the heart.

Anne Sullivan, teaching Helen Keller (27 Jun 1880 – 01 Jun 1968), an author, activist and academic.

An investment in knowledge always pass the best interest.

Benjamin Franklin, FRS (17 Jan 1706 – 17 Apr 1790), a polymath and US Founding Father in, "The Way to Wealth," 1758.

He who can no longer pause to wonder and stand rapt in awe, is as good as dead; his eyes are closed.

Albert Einstein Ph.D. (14 March 1879 – 18 April 1955), a theoretical physicist and Nobel Prize winner in Physics 1921, in Living Philosophies, Simon and Schuster, New York, 1931.

When a PhD takes its toll, it can be very easy to lose perspective on your work. Friends and family have been an interesting mix of constantly bewildered and bewondered at my work, but my befuddled attempts to explain a nanoscale game of 52-card pickup never ceased to interest them – at least for the first 52 seconds. Thank you to you all who have supported, laughed with and laughed at me over the last 3 years. In particular: **Mum**, **Dad**, **Nicky**, **Andy** and **Will** – you mean more than you can ever know.

My **Jenny**, life is a billion times as colourful with you by my side. Thank you for who you are and all you are, to me and to everyone you encounter. You are forever my inspiration to be all I can, my greatest cheerleader, and my love. I love you.

For the **Lord**, through whom all things are possible.

List of publications

Published manuscripts

1. Metal-organic nanosheets (MONs): a new dimension in materials chemistry
   David J. Ashworth and Jonathan A. Foster,
   J. Mater. Chem. A, 2018, **6**, 16292-16307 (review article)
   DOI: 10.1039/c8ta03159b

2. Ultrasonic exfoliation of hydrophobic and hydrophilic metal-organic frameworks to form nanosheets
   David J. Ashworth, Adam Cooper, Mollie Trueman, Rasha W. M. Al-Saedi, Liam D. Smith, Anthony J. H. M. Meijer and Jonathan A. Foster,
   Chem. Eur. J., 2018, **24**, 17986-17996 (full paper)
   DOI: 10.1002/chem.201803221

3. Increasing alkyl chain length in a series of layered metal-organic frameworks aids ultrasonic exfoliation to form nanosheets
   David J. Ashworth, Thomas M. Roseveare, Andreas Schneemann, Max Flint, Irene Dominguez Bernáldes, Pia Vervoorts, Roland A. Fischer, Lee Brammer and Jonathan A. Foster
   Inorg. Chem., 2019, **58**, 10837-20845 (full paper)
   DOI: 10.1021/acs.inorgchem.9b01128

Manuscripts in preparation

1. Blending functionalised ligands to form multivariate metal-organic framework nanosheets (MTV-MONs) with tuneable surface chemistry
   David J. Ashworth and Jonathan A. Foster

2. Tuning the surface chemistry of mixed ligand multivariate metal-organic framework nanosheets (MTV-MONs)
   David J. Ashworth and Jonathan A. Foster

Contribution to other projects

1. A theoretical study into benzoic acid and di-acid formation from irradiated benzene and carbon dioxide ice
   E. C. S. Slate, R. James, D. J. Ashworth, A. Dawes, N. Mason and A. J. H. M. Meijer,
   manuscript in preparation

List of conference presentations

Oral presentations

1. "Metal-Organic Nanosheets: Sensing and Catalysis in Two Dimensions,"
   Nanomaterials: from Theory to Application, Young Researchers Symposium, Manchester
   16 May **2017**

2. "Exploring the World of 2D Paddlewheel-Based Metal-Organic Nanosheets (MONs),"
   Dalton North Regional Meeting, York
   13 June **2019**

Poster presentations

1. D. J. Ashworth and Dr J. A. Foster, "Programmable 2D Materials for Sensors, Catalysts and Composites," Dalton Northern Regional Meeting, Sheffield, 29 Jun **2017**

2. David J. Ashworth, A. Cooper, M. Flint and Dr J. A. Foster, "Metal-Organic Nanosheets: Catalysis and Sensing in Two Dimensions," 12th International Symposium on Macrocyclic and Supramolecular Chemistry (ISMSC), Cambridge, 2-6 Jul **2017**

3. David J. Ashworth, J. Nicks, K. Sasitharan, C. M. Kiker and Dr J. A. Foster, "Metal-Organic Nanosheets: Programmable 2D Nanomaterials," STEM for Britain 2018, Houses of Parliament, Westminster, 12 March **2018**

4. David J. Ashworth, J. Nicks, K. Sasitharan, C. M. Kiker and Dr J. A. Foster, "Metal-Organic Nanosheets: Sensing and Catalysis in Two Dimensions," Dalton Northern Regional Meeting, Leeds, 29 Jun **2018**

5. David J. Ashworth, J. Nicks, K. Sasitharan, C. M. Kiker and Dr J. A. Foster, "Metal-Organic Nanosheets: Sensing and Catalysis in Two Dimensions," 2nd Macrocyclic and Supramolecular Chemistry (MASC) Early Career Researcher meeting, Manchester, 27 Jul **2018**

6. David J. Ashworth, J. Nicks, K. Sasitharan, C. M. Kiker and Dr J. A. Foster, "Metal-Organic Nanosheets: Sensing and Catalysis in Two Dimensions," Jilin University Chemistry Delegation Celebratory Symposium, Sheffield, 26 October **2018**

7. David J. Ashworth and Jonathan A. Foster, "Design and Applications of Paddle-wheel based Metal-Organic Nanosheets," 9th Chemical Nanoscience Symposium, Newcastle, 4 April **2019** – RSC Poster Prize

Contents

Chapter 1

A♠

Metal-organic framework nanosheets (MONs): a new dimension in materials chemistry

Chapter 2

2♦

Aims and objectives

Chapter 3

3♣

Ultrasonic Exfoliation of Hydrophobic and Hydrophilic Metal–Organic Frameworks To Form Nanosheets

Chapter 4

4♥

Increasing Alkyl Chain Length in a Series of Layered Metal–Organic Frameworks Aids Ultrasonic Exfoliation to Form Nanosheets

Common abbreviations

1D	one dimensional
2D	two dimensional
3D	three dimensional
AFM	atomic force microscope/y
ATR	attenuated total reflectance
(H$_2$)BDC	benzene dicarboxylic acid
BET	Brunauer–Emmett–Teller (surface area)
(H)bim	benzimidazole
CP	coordination polymer
COF	covalent organic framework
CON	covalent organic nanosheet
CSD	Cambridge structural database
DFT	density functional theory
DLS	dynamic light scattering
DMA	*N,N*-dimethylacetamide
DMF	*N,N*-dimethylformamide
DMSO	dimethylsulfoxide
EA	elemental analysis/es
Et$_2$O	diethylether
EtOH	ethanol
FTIR	Fourier-transform infrared (spectroscopy)
G	guest
H	height
H	host
HG	host-guest
h-BN	hexagonal boron nitride
H-bonds	hydrogen bonds
LCC	liquid cascade centrifugation
LD	lateral dimension
MeCN	acetonitrile
MeOH	methanol
MOF	metal-organic framework
MON	metal-organic framework nanosheet
MS	mass spectrometry
NMP	*N*-methyl-2-pyrrolidone
NMR	nuclear magnetic resonance
PVP	polyvinylpyrrolidone
PW	paddle-wheel
PXRD	powder x-ray diffraction
rpm	rotations per minute
SBU	secondary building unit
SCXRD	single crystal x-ray diffraction
SD	standard deviation
SEM	scanning electron microscope/y
TCPP	tetrakis(4-carboxy-phenyl)porphyrin
TEM	transmission electron microscope/y
TGA	thermogravimetric analysis
TMD	transition metal dichalcogenide

TMT	transition metal trichalcogenide
UV-Vis	Ultraviolet-visible (spectroscopy)
VdW	Van der Waals
vis	visible
ZIF	zeolitic imidazolate framework

Diacid ligand precursor abbreviations

Chapter 3

H_2BDC	benzene-1,4-dicarboxylic acid
H_2**A**	2,5-bis(3-methoxypropoxy)-benzene-1,4-dicarboxylic acid
H_2**B**	2,5-bis(pentoxy)-benzene-1,4-dicarboxylic acid

Chapter 4

H_2**1**	2,5-bis(methoxy)-benzene-1,4-dicarboxylic acid
H_2**2**	2,5-bis(ethoxy)-benzene-1,4-dicarboxylic acid
H_2**3**	2,5-bis(propoxy)-benzene-1,4-dicarboxylic acid
H_2**4**	2,5-bis(butoxy)-benzene-1,4-dicarboxylic acid
H_2**5**	2,5-bis(pentoxy)-benzene-1,4-dicarboxylic acid

Chapter 5

H_2**1**	2,5-bis(methoxy)-benzene-1,4-dicarboxylic acid
H_2**2**	2,5-bis(ethoxy)-benzene-1,4-dicarboxylic acid
H_2**3**	2,5-bis(propoxy)-benzene-1,4-dicarboxylic acid
H_2**4**	2,5-bis(butoxy)-benzene-1,4-dicarboxylic acid
H_2**5**	2,5-bis(pentoxy)-benzene-1,4-dicarboxylic acid
H_2**5***	2,5-bis(3-methoxypropoxy)-benzene-1,4-dicarboxylic acid

Chapter 6

H_2BDC	benzene-1,4-dicarboxylic acid
fu-H_2BDC	functionalised-benzene-1,4-dicarboxylic acid
$(Br)_2$-H_2BDC	2,5-dibromobenzene-1,4-dicarboxylic acid
$(Cl)_2$-H_2BDC	2,5-dichloro-benzene-1,4-dicarboxylic acid
NH_2-H_2BDC	2-amino-benzene-1,4-dicarboxylic acid
NO_2-H_2BDC	2-nitro-benzene-1,4-dicarboxylic acid

List of corrections

Preliminary

Page iii, para 1, line 2	removed ")" after "clusters" in paragraph 1 line 2.

Contents page updated to reflect inclusion of list of corrections

List of corrections inserted

Chapter 1

Page 1	Chapter title corrected: "A" changed to "a"
Page 2	Chapter title corrected: "A" changed to "a"

Chapter 2

Page 22, para 2, line 7	deleted repeated "in"
Page 24, para 1, line 7	deleted "2-" charge on BDC
Page 26, para 1, line 2	comma after "form" removed
Page 26, para 3, line 3	inserted space after "Table 1," and "There is" corrected to "there are"
Page 37, references 45	spacing corrected

Chapter 3

This chapter has already been published, however the following corrections are acknowledged.

ESI page 2, para 2	"1H" and "13C" should be "^{1}H" and "^{13}C" respectively, however no ^{13}C NMR analysis was reported, so ^{13}C references should not have been included in the experimental
ESI page 3, para 2	Molecular formula in the elemental analysis should read "$C_{18}H_{26}O_6$," not "$C_{18}H_{26}O6$"
ESI page 17, Tables S6 and S7	Ligand **1** should be emboldened in both table titles
ESI page 39, Figure S46	"^{1}H" NMR should be specified in the caption, and ligand **2** should be emboldened in the formula unit
ESI page 44, reference 1 and 2	"*J Am Chem Soc*" should read "*J. Am. Chem. Soc.*"
ESI page 44, reference 3	"*Chemical Communications*" should be abbreviated to "*Chem. Comm.*"

Chapter 4

This chapter has already been published, however the following corrections are acknowledged.

ESI page 14, Figure S21 — Ligands **3**-**5** should be emboldened in the figure caption

Chapter 5

Top and bottom margins removed

Page 5, references to Table 2 — Corrected line break in reference to Table 2 (x2)

Page 5, Table 2 — Ligands **1**-**5** emboldened in the table caption

Page 6, Table 3 — Hydrodynamic diameters for **3**, **4**, **5**, **5*** inserted, with reference to previous chapters

ESI page S2 — Ligands emboldened throughout the contents page

ESI page S16, Figure S18 — Positioning of arrow indicating change in Absorbance upon increasing titres corrected

ESI page S30, para 1, line 2 — "saving experimenter time" removed as this is inferred by "much faster"

Chapter 6

Top and bottom margins removed

Subscripts of "$_2$" checked throughout

Page 2, column 1, para 2, line 8 — Corrected "]" to ")" in "(H)"

Page 3, column 1, para 2, line 7 — Yellow highlight of NO_2 removed

Page 3, column 2, line 8 — "pka" corrected to "pk$_a$"

ESI page S3, Table S1 — "2" corrected to "H$_2$" in "H$_2$BDC" and "Fu-H$_2$BDC"

ESI page S7-S9, Figures S4-S7 — "^{1}H-NMR" corrected to "^{1}H NMR"

Chapter 7

Figure 1b — Updated to reflect possibility of R,R'-difunctionalised-BDC inclusion

Page 233, para 2, line 6 — Space removed between "MONs, [12-15]"

Page 233 — New sentences included describing the potential of R,R'-difunctionalised-BDC inclusion on the structure and properties of potential "Janus" MONs formed. Additional reference added.

Page 234 — "Outlook" section included. Concluding sentence added.

Take a deck of cards and throw them in the air,

Cards will separate, with more surface to share.

Face to face no longer, the cards are now free –

They are two-dimensional materials, analogously.

A ♠

Metal-organic framework nanosheets (MONs): a new dimension in materials chemistry
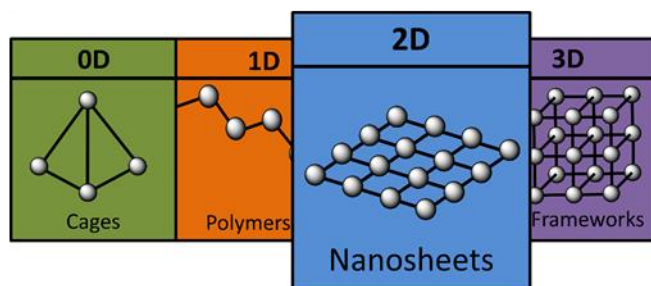
Chapter 1

Metal-organic framework nanosheets (MONs): a new dimension in materials chemistry

David J. Ashworth and Jonathan A. Foster

Author Contributions

David J. Ashworth	Confirmation review provided starting point and main contents for the review. Drafted Sections 1, 3 and 5. Drafted the abstract and conclusions. Prepared Figures 3, 4 and 8. Redrafts and rewrites of all sections were completed with JAF.
Jonathan A. Foster	Drafted Sections 2 and 4. Prepared Figures 1, 2, 5, 6 and 7.

REVIEW

Check for updates
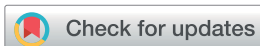
Metal–organic framework nanosheets (MONs): a new dimension in materials chemistry

David J. Ashworth [ID] and Jonathan A. Foster [ID] *

Metal–organic framework nanosheets (MONs) are emerging as a novel class of two-dimensional materials with a distinct set of design principles, synthetic approaches, characterisation techniques and applications. MONs are free standing, nominally two-dimensional materials formed by the co-ordination of organic ligands to metal ions or clusters. In comparison to other metal–organic and two-dimensional materials, the principles behind their design and synthesis are only just beginning to be understood. Here we seek to bring together recent highlights from this rapidly growing field and attempt to draw out common principles and strategies which we hope will aid the development of this exciting new class of materials. We consider the range of chemistries and different synthetic strategies used to fabricate MONs, the methods employed to characterise them and the applications that have so far been investigated.

1. Introduction

Two-dimensional materials offer a distinct set of mechanical, electronic, optical and magnetic properties compared to their bulk, layered forms. Graphene is the archetypal two-dimensional material and consists of a single layer of sp^2 hybridised carbon atoms giving it exceptional conductivity, tensile strength, flexibility and transparency.[1] A wide variety of other elemental and inorganic two-dimensional materials with complimentary properties have also been investigated including boron nitride,[2] black phosphorus,[3] metal-oxides,[4] double layer metal hydroxides,[5] transition metal dichalcogenides,[6] clays and zeolites.[7] However, despite the remarkable properties shown by many of these materials, their simple composition means that it is often challenging to modify or systematically tune their structures in order to optimise these properties for particular applications.

Department of Chemistry, The University of Sheffield, Dainton Building, Sheffield, S3 7HF, UK. E-mail: jona.foster@sheffield.ac.uk

Dave Ashworth was awarded his MChem, with study in industry, degree in 2016 from the University of Sheffield, under the tutorship of Prof. Lee Brammer and Dr Jonathan Foster. He is currently studying for his PhD at the same institution, under the supervision of Dr Foster. His research centres around the development and chemical understanding of novel two-dimensional metal–organic framework nanosheets and their potential applications.

Dr Jonathan Foster graduated with an MChem from the University of Durham in 2008 where he also completed a PhD in the groups of Prof. Jonathan Steed and Prof. Judith Howard CBE FRS. He undertook post-doctoral positions at the University of Cambridge in the groups of Prof. Jonathan Nitschke and Prof. Anthony Cheetham FRS. In 2015 he was awarded a Ramsay Memorial Trust Fellowship and the position of Vice Chancellors Fellow which he holds in the department of Chemistry at the University of Sheffield. Jonathan has experience working with a wide range of nano-structured supramolecular materials including gels, polymers, cages and frameworks. His current research is focussed on realising the potential of metal–organic framework nanosheets for use in creating novel sensors, catalysts, composite materials and devices.

16292 | *J. Mater. Chem. A*, 2018, **6**, 16292–16307

This journal is © The Royal Society of Chemistry 2018

Metal–organic materials combine the diversity of organic ligands with the unique properties of metal ions to produce robust materials with well-defined and readily tuneable structures. This approach has been used to create a variety of different metal–organic architectures ranging from discrete complexes, cages, grids, helicates and knots to extended polymers, gels, liquids and liquid crystals.[8–12] In particular, there are over 70 000 thousand metal–organic frameworks (MOFs) reported in the Cambridge structural database (CSD), many of which have a layered structure.[13] A number of well-established coordination motifs exist allowing for a high degree of predictability over the topology of the structures that will form. The modular nature of these materials often allows them to be systematically tuned and modified through reticular substitution of different ligands and metal ions and through postsynthetic modifications. The versatility of metal–organic materials means they have been exploited for applications as diverse as gas-storage,[14] water purification,[15] catalysis,[16] drug-delivery,[17] sensing,[18] imaging[19] and electronics.[20]

Two-dimensional metal–organic framework nanosheets (MONs) have emerged as the most recent form-factor for metal–organic materials. MONs have been variously described in the literature as metal–organic framework nanosheets,[21] two-dimensional MOFs,[22] metal–organic layers (MOLs),[23] metal–organic graphene analogues (MOGs),[24] metal–organic surfaces,[25] single-layered MOF based materials (MOFenes),[26] metal–organic flakes,[27] two-dimensional coordination polymers,[28] coordination nanosheets (CONASH),[29] organometallic sheets,[30,31] and hybrid organic–inorganic nanosheets.[32] Whilst there are meaningful distinctions between some of the terms used in these descriptions, in an effort to draw out the commonality in the underlying chemistry, approaches to synthesis, techniques for characterisation and applications envisaged we group them here under a common name.

The term "nanosheet" has been used extensively in the MOF literature and whilst a large number of layered MOFs exist or have been grown on surfaces, in most cases the individual layers will not be stable or cannot be isolated using a given method. However, as with other two-dimensional materials, the ideals of a uniform crystalline material with single unit thickness extended infinitely in the other two dimensions is not often achieved in practice. Here we employ a broad definition which encompasses materials which clearly display 'nanosheet'-like structure and properties and that, with iterative development, could form free standing single-layers. More specifically, MONs consist of: [1] organic ligands coordinated to metal ions or clusters with continuous connectivity in two-dimensions but only non-covalent interactions in the third dimension; [2] highly anisotropic materials with one dimension approaching monolayer thickness and the others being at least an order of magnitude larger and approximately equal in size; [3] materials which can be isolated in a form with the dimensions outlined above as free standing sheets, not attached to a surface or other scaffold or as layers in a bulk material.

In this critical review we shall describe recent progress in this rapidly developing area and seek to highlight the breadth of approaches taken and draw out informative examples of good practice and recent innovations. We begin in Section 2 by discussing the diverse range of chemistries used to synthesise MONs and attempt to draw-out common design principles. In Section 3 we present different approaches for synthesising MONs, either directly or from their parent layered frameworks. We will then discuss the range of characterisation techniques that have developed for analysing the molecular, nanoscopic and macroscopic structure and properties of MONs in Section 4. In Section 5 we consider the distinct opportunities offered by MONs for use in a wide range of applications before summarising and providing our own perspective on the future of this field in Section 6.

2.   The anatomy of MONs

The basic principle behind the structure of two-dimensional nanosheets is to design materials with strong, directional interactions within a plane, but weak interactions between the layers in the bulk material. This is exemplified by graphene in which strong covalent carbon–carbon bonds form a hexagonal lattice, layers of which are held together by relatively weak dispersion interactions.[33] Connectivity within the layers of MONs can be achieved either through organic ligands which bridge isolated metal ions or clusters or through connected inorganic clusters, or a mixture of the two.[34] Any connectivity in the third dimension is typically a mixture of dispersive, hydrogen bonding and ionic interactions which allows for the individual layers to be separated out and isolated. Here we seek to capture the diversity of structures investigated so far by bringing together examples of MONs which share common ligands and structural motifs.

2.1   Carboxylate based MONs

As with MOFs, the most popular organic ligands for the synthesis of MONs are polycarboxylates thanks to their strong, directional coordination chemistry and the wide variety of ligands commercially available. The paddlewheel (PW) motif is an ideal secondary building unit (SBU) for creating MONs as it consists of four carboxylate ligands organised in a plane around two metal cations capped with axial ligands (Fig. 1a). The archetypal MOF-2 was amongst the first layered MOFs to be exfoliated to form MONs and consists of layers of 1,4-benzene dicarboxylate (BDC) coordinated via Zn paddlewheels with water molecules occupying the axial positions of the paddlewheel.[35] Isostructural MONs have since been formed using a variety of metal ions (Cu, Zn, Co) and 1,4-BDC[36–38] and 1,3-BDC derivatives,[39–41] as well as longer linear diacid chains.[42] In our own work, we functionalised 1,4-BDC with weakly interacting alkyl-ether chains designed to weaken interlayer interactions and aid exfoliation into solvent (Fig. 1c).[43] Several MONs based on tetrakis(4-carboxy-phenyl)porphyrin (TCPP) structure have been synthesised (Fig. 1d) in combination with a variety of metal-PW's (Zn, Cu, Cd, Co).[44–55] This motif also allows for the formation of bimetallic MONs by using different metal ions coordinated at the PW and porphyrin sites.[45,52] The high degree of connectivity and preorganisation afforded by the porphyrin units makes them particularly well suited to the formation of MONs.

This journal is © The Royal Society of Chemistry 2018

J. Mater. Chem. A, 2018, 6, 16292–16307 | 16293
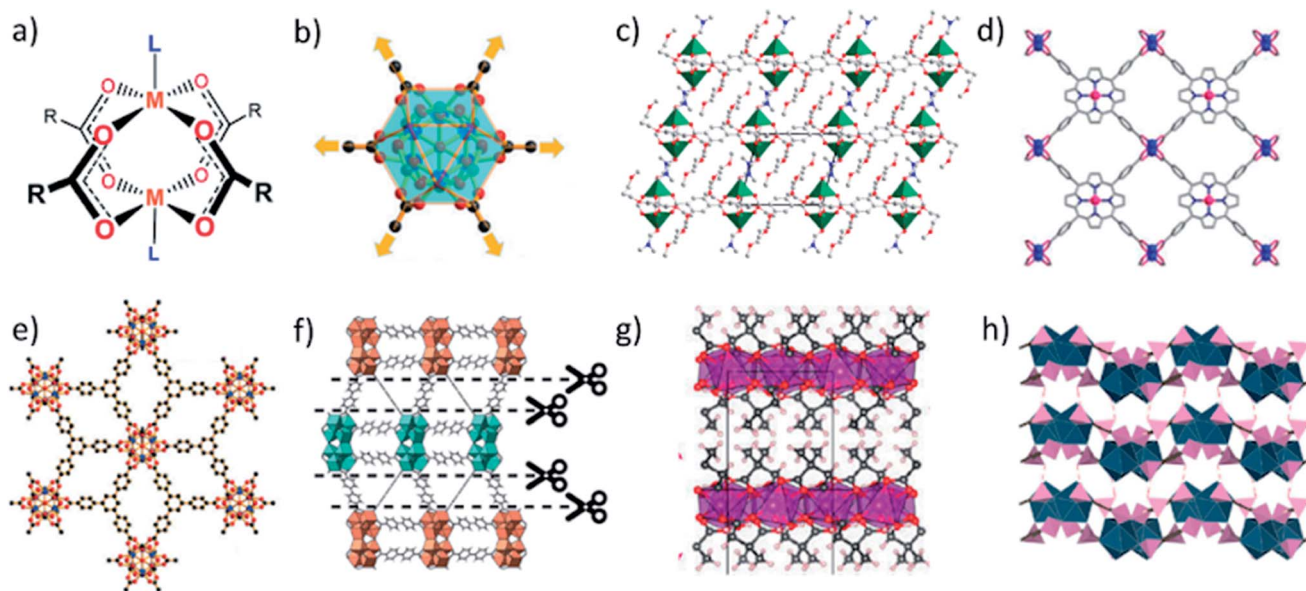
Fig. 1 Schemes showing (a) paddlewheel and (b) M_6L_6 secondary building units. (c–h) example crystal structures showing diversity of carboxylic acid based linkers and secondary building units used in the synthesis of MONs. Specifically, (c) $Zn_2(BDC-x_2)(DMF)_2$, where x = $O(CH_2)_3OMe$; (d) M(TCPP) where M = Zn, Cu, Cd, Co; (e) $[Hf_6(\mu_3-O)_4(\mu_3-OH)_4(carboxylate)_{12}]$; (f) hcp UiO-67; (g) $Mn(DMS)(H_2O)$; (h) lanthanum 1,3,5-benzene-triphosphonate (LBP-II). Adapted with permission from ref. 56, 43, 52, 56, 60, 32 and 65 for images (b–h) respectively.

Zr and Hf carboxylate clusters have proved popular SBU's for creating robust 3D MOFs but have only recently be used to create 2D MONs. Cao *et al.* synthesised a series of MONs by combining 3-connected carboxylate ligands, initially benzene-1,3,5-tribenzoate (BTB) moieties, with the Hf^{4+} cluster $[Hf_6(\mu_3-O)_4(\mu_3-OH)_4(carboxylate)_{12}]$ to create an infinite 3,6-connected 2D network with kagome dual (kgd) topology (Fig. 1e).[56] The 12-connectivity of the Hf_6 cluster violates the geometric requirement of a 2D layer so they used formate to cap six of the connection sites on the cluster, leaving the remaining six in the same plane to connect to the BTB ligands (Fig. 1b). Zhao and coworkers produced analogous layered structures based on BTB with both Hf and Zr $M_6O_4(OH)_4$ clusters synthesised using a modulated hydrothermal approach,[57] and Wang *et al.* recently demonstrated a continuous flow reaction in order to synthesise the Zr analogue.[58] The same Zr_6 cluster but with different sites capped was used to create MONs with tetraphenylethylene-based tetracarboxylate (TCBPE),[23] as well as TCPP ligands.[59] A Hf_{12} cluster was used by Cliffe *et al.* who used 4,4-biphenyldi-carboxylate ($bpdc^{2-}$) to form a 3D framework containing a "double cluster" $(Hf_{12}O_8(OH)_{14})$ which they were able to exfoliate through selective scission of the interlayer ligands (Fig. 1f).[60] A related double-decker Hf_{12} clusters has also been used as an SBU with extended tritopic carboxylates.[61]

Inorganic (I) corner sharing octahedra have also been used alongside coordination bonds (O) to create two-dimensional layers. In the nomenclature defined by Cheetham, Rao and Fuller, superscript numbers are used to define the types of connectivity in different dimensions.[34] Cheetham and coworkers combined 2,2-dimethylsuccinate (DMS) and its isomers with different metal ions to produce a series of layered frameworks which they exfoliated to form nanosheets.[32,62,63] Fig. 1g shows the archetypal I^1O^1 network for the Mn-DMS network in which

distorted MnO_6 octahedra form corner-sharing chains along the *b*-axis which are bridged *via* DMS ligands to form 2D layers.[32,64] The methyl groups of the ligands protrude between the layers providing weakly interacting hydrophobic caps. Other closely related systems had either inorganic (I^2O^0) or organic connectivity in two dimensions (I^0O^2) highlighting the challenges associated with predicting structure when using less preorganised ligands. Phosphonic acids can also be used to create inorganic layers. Araki *et al.* exploit the high coordination numbers of lanthanide ions by coordinating 1,3,5-benzene-triphosphonate to lanthanum ions to form layered MOFs with either (I^1O^1) or (I^2O^0) connectivity (Fig. 1h).[65]

2.2 N-Donor based MONs

Zeolitic imidazolate frameworks (ZIFs) are a highly successful class of MOF due to their relatively high stability, diversity and structural similarity to zeolites.[66] However, the topology of imidazole-zinc coordination does not automatically lend itself to the formation of layered structures. Lotsch and coworkers used the lamellar surfactant CTAB to template benzimidazole (bim) and Zn to form a ZIF with the composition Zn(bim)(OAc).[67] The layers are composed of $Zn(bim)_{2/2}$ chains and $Zn(OAc)_{2/2}$ chains connected by Zn^{2+} tetrahedra which stack together through weak van der Waals interactions (Fig. 2a). Peng *et al.* successfully exfoliated large nanosheets from a different layered ZIF with the composition $Zn_2(bim)_4$. Here the layers are formed by Zn atoms coordinated to four bim ligands in a distorted tetrahedral geometry, and each bim ligand bridges two Zn atoms *via* a bis-monodentate linkage (Fig. 2b).[68,69] It should also be noted that the reaction of 2-methylimidazole (Hmim) with zinc nitrate in water at room temperature produces highly anisotropic leaf shaped crystals of
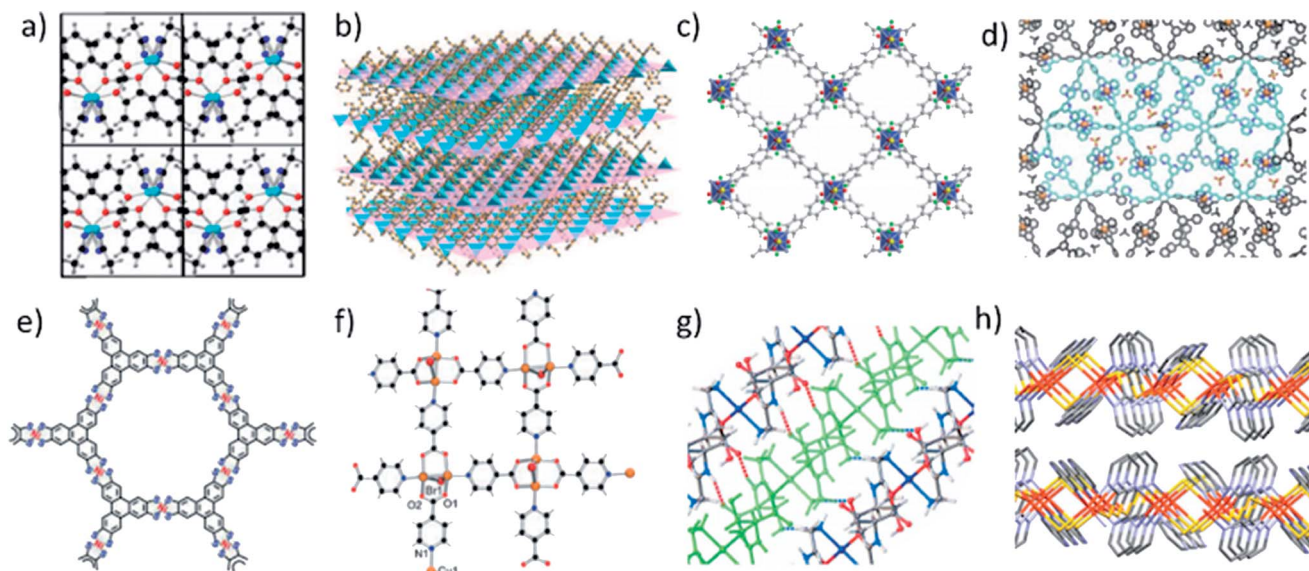
Fig. 2 Example structures of nitrogen (a–d), sulfur (e) and mixed linkers (f–h) used in the synthesis of MONs. Specific repeat structural units are: (a) Zn(bim)(OAc); (b) $Zn_2(bim)_4$; (c) $Cu(bpy)_2(OTf)_2$, (d) S1(M^{2+}), where M = Zn, Fe, Co, Pd and S1-see reference; (e) Ni_3(bis(dithiolene))$_2$; (f) $[Cu_2Br(IN)_2]$ where IN = isonicotinate; (g) $[Zn(Gly-Thr)_2]·CH_3OH$; (h) $[Fe(Py_2th)_2]$. Adapted with permission from ref. 67, 68, 74, 76, 80–83 for images (a–h) respectively.

ZIF-L $(Zn(mim)_2·(Hmim)_{1/2}·(H_2O)_{3/2})$ with thicknesses as low as ~100 nm. Several studies exploiting the sheet like properties of these materials for gas separation,[70] templation[71] and catalysis[72] have been reported, although sheets approaching monolayer thickness are, to our knowledge, yet to be reported. However, nanosheets of the closely related ZIF-67, $Co(mim)_2$, formed using a salt templated synthesis have recently been reported.[73]

The neutral N-donor systems, 4,4-bipyridine (bpy), was used to create a layered framework with the formula $Cu(bpy)_2(OTf)_2$ in which the trifluoromethanesulfonate (OTf) counterions capped weakly interacting layers (Fig. 2c).[74] Atomic force microscopy (AFM) and transmission electron microscopy (TEM) indicate that single and few layer nanosheets are formed which show crumpling and rolling to form nanoscrolls highlighting the flexibility of these systems. A variety of tri- and hexa-dentate terpyridine (tpy) building blocks have also been used to form monolayers through self-assembly at interfaces through coordination to M(II) ions (Zn, Co, Ru, Pb, Ni and Fe) (Fig. 2d).[30,52,75–77] These multidentate building blocks provide a high degree of connectivity and robust coordination interactions through their multidentate binding. The often single layered nanosheets which were formed through interfacial assembly can be up to several cm in lateral dimensions and mechanically strong enough to be spanned over 20 × 20 μm sized holes, however the degree of crystallinity can be low.[76] A structurally related series of MONs have also been synthesised using tri- or tetra-dipyrinato ligands coordinating to tetrahedral zinc ions.[78,79]

2.3 Diamine/dithiolene based MONs

A series of MONs assembled from square-planar metal ions and aromatic bis(dithiolenes) have received considerable attention thanks to their remarkable electronic properties.

Benzenehexathiol (BHT) for example was reacted with d^8 metal ions including Ni(II)[84] and Pd(II)[85] to create 2D planar nanosheets with six-fold symmetry via the formation of the nickel bis(dithiolene) motif (Fig. 2e). These complexes exhibit strong charge delocalization across the three metalladithiolene units through the phenylene linker in mixed-valent states. Expanded versions of these systems have been synthesised using triphenylene hexathiolate with nickel[80] and cobalt.[25] The amino analogues of these materials have also been investigated. The interfacial reaction of hexaminobenzene with $Ni^{2+}/Cu^{2+}/Co^{2+}$ acetylacetonate produced flakes several microns wide and approximately 10 nm thick which were shown to be mildly conducting. Expanded analogues of these layered materials have been formed by reacting hexaminotriphenylene with Ni and Cu ions to create semi-conducting frameworks, although individual flakes of these materials have not yet been isolated.[24,86,87] Mixed amine/thiolene MONs have also been formed with related structures using mixtures of triphenylene hexathiolate and hexaminotriphenylene with Ni or Co[22] and Ni(1,3,5-triaminobenzene-2,4,6-trithiol).[88]

2.4 MONs based on other ligand systems

A number of other MONs have been investigated which are not readily grouped into the classes of MON described above. Notable examples include the earliest example of a single layer thick MON, reported by Zamora and coworkers in 2010. The framework is based on pairs of copper atoms which are bridged by the carboxylate end of two isonicotinato ligands and a bromine ligand and capped by the nitrogen of two further isonicotinato ligands to produce layers (Fig. 2f).[81] This is an interesting example of a MON with a mixed-valent state and the authors investigate their electrical and magnetic properties.

This journal is © The Royal Society of Chemistry 2018

J. Mater. Chem. A, 2018, **6**, 16292–16307 | **16295**

Rosseinsky and coworkers investigated a peptide based layered MOF [Zn(Gly-Thr)$_2$]·CH$_3$OH which formed single layered nanosheets following exfoliation with ultrasound (Fig. 2g).[82] Other examples of MONs incorporating multiple coordination motifs within a single framework include a lamellar iron(II)-pyrimidine-2-thiolate coordination polymer [Fe(Py2th)$_2$]$_n$ (Fig. 2h),[83] large single layer thick flakes of [Cu(μ-pym$_2$S$_2$)(μ-Cl)]$_n$ (pymS2 = dipyrimidindisulfide)[27] and lanthanide based MONs formed by the coordination of 2,2-thiodiacetic acid.[89] Examples of de-symmetrised MONs with different bonding motifs running in different directions include work by Gao *et al.* created a zinc based MON with a layered structure consisting of perpendicular chains of carboxylate coordinated ibuprofen and 1,2-bis(4-pyridyl)ethane.[90] Another interesting de-symmetrised case is a two-dimensional coordination polymer consisting of Cu$_2$I$_2$ chains linked by 2-aminopyrazine.[91]

3.   Synthetic approaches

There are two distinct approaches to the syntheses of MONs: "bottom-up" methodologies in which the nanosheets are synthesised directly as discreet entities through various methods of arresting the crystallisation process, and "top-down" approaches in which the nanosheets are isolated from bulk layered materials. The coordination bonding present within the layers of MONs is much more dynamic than those of graphene and most other inorganic materials. This opens up opportunities for processing MONs from solution and removes some of the challenges associated with irreversible bond formation. However, it also means milder processes may be required and the structures have the potential to rearrange. Here we discuss various iterations of the two main approaches focussing on examples which have yielded promising nanosheets. A general scheme outlining different approaches is given in Fig. 3 and examples of nanosheets produced by each method are given in Fig. 4.

3.1   Arresting crystallisation

The "bottom-up" synthesis of MONs can be seen as an arrested crystallisation in which growth occurs preferentially in two-dimensions. The use of ligands and SBUs with a predisposition to crystallise preferentially in two-dimensions may result in the formation of nanosheets without the need for further modification. For example, Kitagawa and coworkers showed that Cu(TCPP) MONs of average thickness of ~15 nm, which corresponds to 33 layers, could be synthesised in this manner through a solvothermal synthesis in DMF and EtOH (3 : 1 v/v) (Fig. 4a).[47]

Surfactants have been used to modify crystal habit by binding to the surface of the growing nanosheets, inhibiting growth and preventing stacking of the layers. The surfactant species can also decrease the surface energy and so total energy of the system, which favours the formation of the 2D morphology.[92] Zhang and coworkers used polyvinylpyrrolidone (PVP) in the synthesis of Zn(TCPP).[49] Addition of PVP to the reactant mixture resulted in MONs of 1.2 ± 0.4 μm × 7.6 ± 2.6 nm, corresponding to 8 ± 3 layers thick (Fig. 4c). FTIR investigations of PVP interacting with Zn^{2+} ions showed a strong interaction of the PVP C=O group with Zn^{2+} ions, suggesting that PVP could attach onto the surface of the nanosheet after nucleation, leading to highly anisotropic growth to form MONs. The generality of this method was demonstrated through the additional synthesis of Cu/Co/Cd(TCPP), in which nanosheets of <10 nm thickness were obtained for all but Co(TCPP). These MONs have been further used for various applications.[50–52,55] PVP has also been used within the synthesis of Cu(HBTC) (where BTC = 1,3,5-benzene tricarboxylate) in a reaction which occurred at room temperature and pressure to produce nanosheets between 30–55 nm thick.[95] The cationic surfactant CTAB has been suggested to adsorb to specific crystal planes. The hydrophobic tail adsorbing to the crystal surface could aid in MON stabilisation and dispersion in particular solvents. This
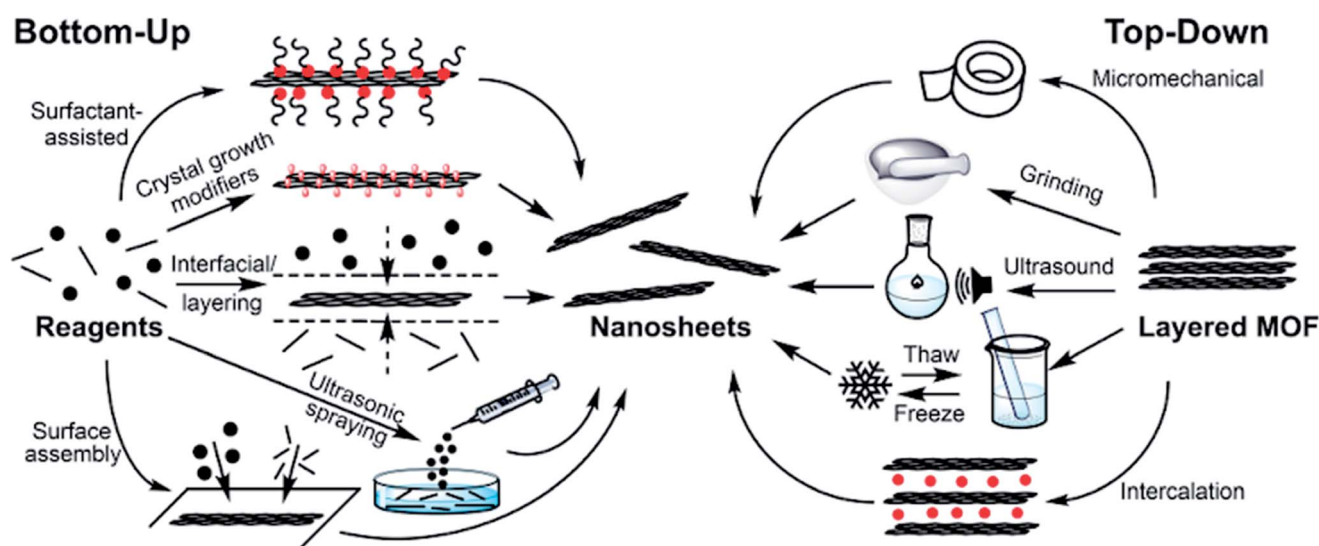
Fig. 3   Scheme showing different bottom-up and top-down methodologies used to produce MONs.
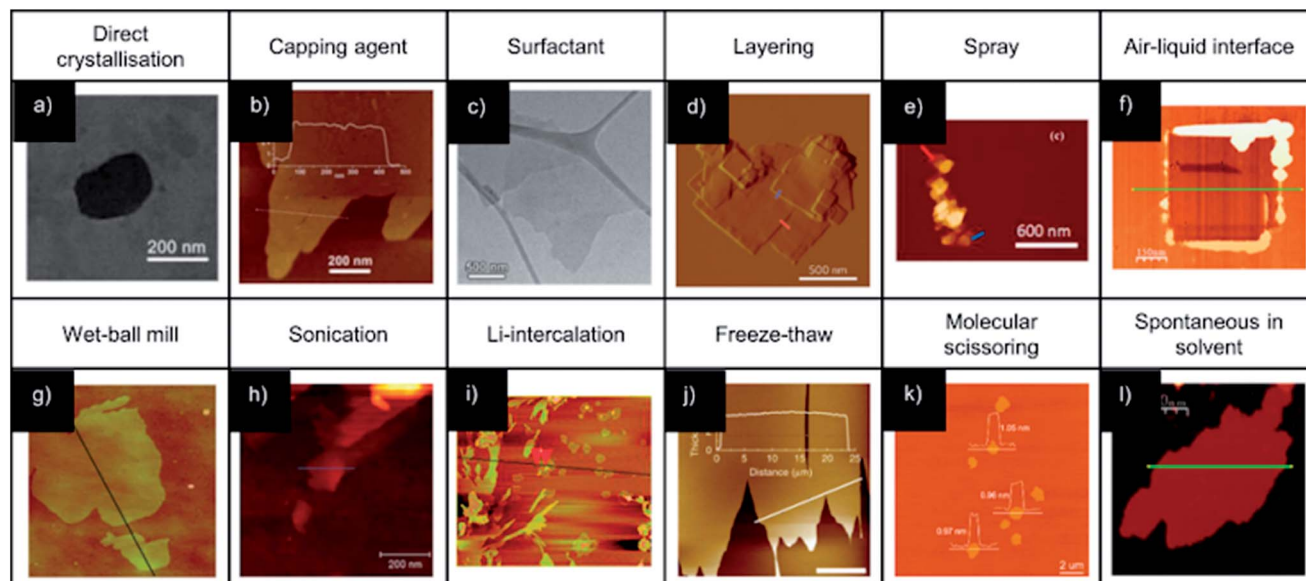
Fig. 4 Example AFM (b, d–l) and TEM (a, c) images illustrating MONs synthesized using various bottom-up (a–f) and top-down (g–l) methodologies. Heights of nanosheets across the indicated vectors are approximately: (b) – 3 nm; (d) – 6 and 8 nm (red and blue, respectively), (e) – both 5 nm, (f) – 0.8 nm, (g) – 1.1 nm, (h) – 1.9 nm, (i) – 2 nm, (j) – 4 nm and (l) – 2 nm. Image (g) is 3 µm square, the indicated vector in (i) is 5 µm and the scale bar in (j) is 10 µm. Images adapted with permission from ref. 47, 93, 49, 36, 37, 30, 68, 43, 89, 40, 53 and 94, for images (a–l) respectively.

approach has been used to directly produce Zn(bim)(OAc) MONs down to 7 nm thickness.[67,96]

Small molecule crystal growth modifiers that bind preferentially to a particular facet of a growing crystal can modify the resulting crystal habit. A classic example of this is the addition of pyridine to the synthesis of the pillared MOF $[Cu_2(NDC)_2(DABCO)]$ (where NDC = 1,4-naphthalene dicarboxylate and DABCO = 1,4-diazabicyclo[2.2.2]octane) which resulted in the formation of large nanosheets up to 500 nm^2 as a result of competition with the pillaring ligands.[97] PVP has been used to similar effect to produce highly anisotropic nanosheets of the pillared MOF Co(TCPP)(BiPY).[50] It should be noted that these nanosheets are connected in three-dimensions through coordination bonds and therefore do not fulfill our definition of a MON. However, in principle this approach could be used to produce single layers or pillared bilayers which would then have two-dimensional connectivity.

Small molecule addictives can also become incorporated into growing MOFs resulting in the formation of layered structures. Zhao and coworkers exploited acetic acid as a modulator to prevent the formation of interpenetrated networks. This lead to the formation of MONs of 10–20 nm thickness which exhibit stability superior to the analogous 3D MOF (Fig. 4b).[93] Lin and coworkers found that the 12-connectivity of Zr_6 and Hf_6 SBUs could be modified by incorporating six formate ions into the SBU to produce nanosheets with thickness of <4 nm and lateral dimensions >10 µm, with nanosheets observed down to monolayer thickness.[23,29,50,61]

Wang and coworkers demonstrated a "pseudoassembly disassembly" strategy for the formation of Zr_6-(NiTCPP) MONs in high yield (85%) and high dimensional uniformity of around 200 × 1.5 nm.[59] Incorporation of controlled concentrations of small monoacid (formic, acetic, lauric and oleic acid) ligands as a modulator into the reaction mixture lead to layered MOFs, within which the monoacids occupied the interlayer coordination sites of the Zr cluster (confirmed by quantitative NMR and SAXRD) which lead to destabilisation and "disassembly" to MONs. Stacking of produced MONs was observed under TEM with lengthening of the aliphatic chain. Rodenas *et al.* were able to produce a series of nanosheets of 5–25 nm thickness and up to 4 µm square using a "layered synthesis" method (Fig. 4d).[36] The ligands and metal ions were dissolved in different ratios of DMF and acetonitrile to produce solutions of different densities which were layered on top of each other, with a buffer layer in between. Slow diffusion of the ligand and metal ions into the buffer layer produced preferential growth in two-dimensions to produce nanosheets, which then sank as a result of gravity into a metal ion deficient layer preventing further growth (Fig. 4e). Inspired by this work, Fu and coworkers developed a spray technique which used ultrasonic atomisation to spray a solution of metal salt onto a reservoir of the ligand solution. This approach reduces the disturbance caused by contact between the layers, providing a steady interface for anisotropic crystal growth. The nanosheets produced through this method were <500 nm and >5 nm thick (Fig. 4e).

An alternative method for directing crystal growth into two-dimensions is the use of phase interfaces such as air–liquid (Fig. 4f, for example)[30,45,48,75,76,78,80,98] or liquid–liquid.[22,77–79,85,99,100] These methods also generally proceed under ambient conditions. Liquid–gas interfacial growth has been demonstrated using Langmuir–Blodgett troughs, in which a solution of ligand in a volatile solvent is applied on top of the aqueous phase containing metal ions.[46,48,75,80,98,101,102] Surface compression can result in large extended nanosheets of potentially infinite size,

with domains demonstrated up to sub-mm scale, although questions remain about the crystallinity of these large sheets. Additionally, MON films can also be built up by layer-by-layer deposition of these large MONs. More detailed methodology and examples of nanosheets produced in these ways can be found in a recent review by Nishihara and coworkers.[29,103,104]

Additionally, there have been multiple demonstrations since 2003 of the growth of MOF layers at solid–liquid interfaces. These materials have been recently reviewed elsewhere,[105,106] and the difficulties associated with removing these materials from the surfaces mean we will not cover these approaches in detail here. Another interesting approach that has been explored is the growth of MOFs on other two-dimensional materials such as graphene oxide, although in most cases the MOFs are not themselves two-dimensional.[107] Rare examples of the formation of MOF thin films at the vacuum–solid interface by chemical-vapour deposition (CVD) have also been reported,[108] but again are outside the focus of this review.

3.2 Exfoliating layered MOFs

Just as layers of graphite can be separated to form nanosheets of graphene, crystals of layered MOFs can similarly be exfoliated to form MONs. This approach relies on being able to preferentially break apart weak interactions between the layers, without disrupting strong bonding interactions between them.

Abher´e *et al.* mimicked the famous "Scotch tape" method, originally used to isolate graphene nanosheets, to produce MONs with heights down to 2 nm from a layered cationic framework.[109] Exfoliation can also be achieved mechanically, either through grinding by hand or with the use of a ball mill. For example, UiO-67 was exfoliated from the bulk MOF to form sheets of ~10 nm thickness (Fig. 4g).[60] This approach produced a relatively broad distribution of particle sizes, in terms of both lateral dimensionality and thickness. Grinding can also cleave chemical bonds, which was utilised by Cliffe *et al.* to create sheet-like particulates from non-layered MOFs to form nanosheets with a relatively broad distribution of layer thicknesses.[60] Wet-ball-milling has been additionally demonstrated in a solvent mixture of MeOH/^{n}PrOH.[68] The authors suggest that methanol penetrates into the galleries of the layered MOF, which is facilitated by the ball-milling process, and the ^{n}PrOH acts to stabilize the exfoliated nanosheets through adsorbing onto the surface through the alkane tails, fulfilling a similar role as surfactants previously described.

Liquid exfoliation through sonication has perhaps been the most widely adopted method of MOF exfoliation over the past decade. The energy input provided by the ultrasonicator (typically 20–80 kHz, with powers of 80–750 W) can overcome the inter-layer interactions, facilitating solvent penetration, and serve as a stimulus for layer separation. As yet, there has not been a universal set of conditions demonstrated to produce the highest quality and quantity of nanosheets. Various authors have used sonication times from 20 minutes to 24 hours, and although exfoliation through sonication has been shown to achieve better results at lower temperature,[110] the temperature of sonication is rarely controlled. Systematically varying

centrifugation rates used to collect MONs from suspension can be used to select for different sizes of nanosheet.[110] The sonication process breaks bonds within the layers as well as between them resulting in smaller crystallite fragments, and subsequently broader particle size distribution and smaller MON size than bottom-up methodology. This is due to the low elastic modulus (3–7 GPa)[27,32] of these crystalline materials, compared to other 2D systems such as monolayer graphene and graphene oxide (1000 ± 100 GPa and 207.6 ± 23.4 GPa respectively).[70,72] However, mono- and few-layer nanosheets have been found to be produced through this methodology (Fig. 4h), with lateral dimensions that are comparable to mono/few-layer graphene nanosheets produced from liquid phase graphite exfoliations through sonication, which typically produces nanosheets of below 1 μm size.[111,112]

Liquid exfoliation has additionally been achieved by simply stirring,[113] or shaking a MOF in a solvent (in the presence of surfactant in order to prevent restacking).[67] Junggeburth *et al.* note the effect of shaking in differing solvent systems. Their use of a hydrophobic MOF showed decreasing exfoliation in THF > tol > CHCl$_3$, and poor exfoliation observed when using the polar solvents DMF and H$_2$O. This was suggested to result from an inability of these solvents to efficiently penetrate between the hydrophobic interlayer space. In contrast, Moorthy and coworkers showed that hydrogen bonds between layers of MOF could be overcome by hydrogen-bond-accepting solvents, resulting in spontaneous exfoliation.[114] This shows that the selection of an appropriate solvent system for exfoliation may be of paramount importance. A solvent system that works well for one MOF is not generalizable to others as each MOF has widely varying properties depending on its makeup of metal and ligands. Lower energy-input liquid exfoliation techniques may generally be preferred, as these are less likely to fragment the produced nanosheets.

The intercalation of molecular/ionic species between MOF layers in order to increase interlayer distance and induce exfoliation has been demonstrated for the production of MONs. Lithium-ions were intercalated into various layered frameworks by Wang *et al.* which were shown to undergo complete exfoliation following sonication in water (Fig. 4i). The forced hydration of the lithium ions is thought to push the layers of MOF apart to such an extent that the interlayer interactions are negated.[64,89] A freeze–thaw method has been demonstrated by Zhou and coworkers, in which a hexane dispersion of MOF was repeatedly frozen in liquid nitrogen and then thawed at elevated temperature with a temperature differential of 256 °C.[40] The authors suggest that a shear force was exerted on the MOF crystals as a result of the volumetric change to the hexane upon gas–liquid phase transition. Bilayer thick nanosheets with a broad distribution of lateral dimensions (10.7 ± 4.8 μm) were produced in 95% yield (Fig. 4j).

The exfoliative techniques discussed so far all rely on the pre-ordered layered 2D structure of MOF, in order to separate layers. However, there is also the potential for chemical modification of the system in order to promote exfoliation. Zhou and coworkers intercalated a pillaring dipyridyl ligand which contained a disulphide bond between layers of a pre-designed

16298 | *J. Mater. Chem. A*, 2018, **6**, 16292–16307

This journal is © The Royal Society of Chemistry 2018

layered MOF.[53] This increased the interplanar distance from 9.8 to 22.6 Å. Scissoring of the ligand through chemical reduction of the disulphide bond resulted in spontaneous exfoliation upon stirring the reaction media, which resulted in single layer nanosheets with lateral dimensions up to several micrometres (Fig. 4k). An element of control upon the produced nanosheet size was additionally demonstrated through varying the reaction conditions for the disulphide scissor. Huang *et al.* demonstrated an electrochemical exfoliation of a MOF through oxidation of pillaring 2,3-dihydroxybenzene dicarboxylic acid ligands to cyclopenta-2,4-dienone. This allowed for facile removal of the pillars due to weakened coordination ability from both structural strain and electronic differences between the ligands and reported nanosheets with lateral dimensions 100–200 nm and as little as 2 nm in height.[41]

In addition, there has been exciting recent work demonstrating solvent induced structural transformations resulting in the formation of nanosheets. Banerjee and coworkers demonstrated a transformative hydrolytic process from metal–organic polyhedra to layered MOF, which resulted in a spontaneous exfoliation to nanosheets of 6–8 layers thick upon addition of larger relative amounts of water.[39] Similarly, Gallego *et al.* found that exposure of bulk layered crystals to excess water induced layer separation down to monolayer thickness, without any additional energetic input (Fig. 4l).[94] This is suggested to be due to incorporation of additional solvent molecules within the cavities present in the starting framework.

4. Characterisation

MONs are complex, hierarchical nanomaterials whose structure and properties must be probed using a wide variety of techniques drawn from the solid state, surface, nanomaterials, solution and colloidal characterisation communities. Here we focus on the core-set of methods that have emerged for the characterisation of MONs whilst highlighting innovative use of advanced techniques.

4.1 Structure and composition

The prolific success of MOFs has to a large extent been thanks to developments in single-crystal X-ray diffraction (SC-XRD) allowing for atomic resolution of these complex structures. The reduced dimensions of MONs mean the crystals are too small for SC-XRD. The high surface area and often labile structures of metal–organic materials mean that they have a high potential to undergo structural and compositional rearrangements during exfoliation or through subsequent drying or heating of the MONs.[36,43] However, where the structure of the parent layered MOF or that of a closely related structure is known, comparison or refinement of the X-ray powder diffraction (XRPD) patterns of MONs against the known structure can allow, the structure of the nanosheets to be determined. The powder patterns of MONs measured in reflection or transmission may show systematic loss of peaks corresponding to out of plane reflections in the parent MOF. This may be due to peak broadening resulting from the reduced dimensions of the

nanosheet as well as preferred orientation of crystallites. This effect is well illustrated in the work of Gascon and coworkers who were able to assign peaks in the XRPD pattern of their nanosheets to reflections corresponding to the layers which stack along the $[\bar{2}01]$ direction (Fig. 5a).[36] However, broadening of peaks is not always observed which may indicate re-aggregation of nanosheets or larger particles dominating powder patterns. Grazing incidence (GIXRD) can be used to enhance detection of in-plane peaks in thin-films.[46,48,101,104]

A diverse range of other techniques have also been used to provide additional information about the structure and composition of the MONs. Solid state nuclear magnetic resonance (NMR) spectroscopy, pair distribution function (PDF) data, thermal gravimetric analysis (TGA), infrared spectroscopy and elemental analysis have been widely used to provide evidence of the composition of MONs, as well as NMR analysis of digested samples.[23,60,117] Surface analysis techniques such as X-ray photo spectroscopy (XPS), X-ray fluorescence (XRF) and Ultraviolet Photoelectron Spectroscopy (UPS) also been used to give information about the elemental composition and oxidation states of the nanosheets (Fig. 5c–f).[24,79,89,94,116] Density functional theory modelling has also been used alongside experimental data to calculate likely MON structures.[60]

4.2 Nanoscopic dimensions

In addition to understanding the molecular structure of MONs, their nanoscopic dimensions must also be probed. AFM represents the gold standard for determining the thickness of nanosheets with angstrom level resolution (Fig. 4 and 6a). In many cases the height of the nanosheets observed match those predicted from the crystal structures. However, the height of multilayer nanosheets may not match those of a single layer

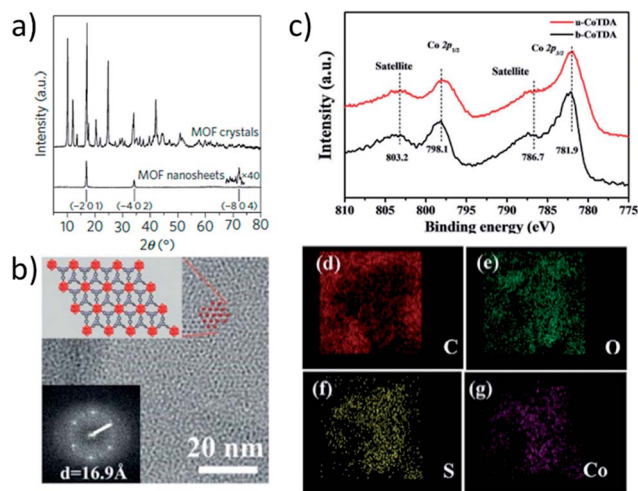**Fig. 5** (a) XRPD patterns comparing nanosheets with parent MOF showing systematic loss of out of plane reflections; (b) STEM-HAADF image of nanosheet showing lattice spacing and corresponding structural model; (c) XPS data providing evidence on elemental composition of a MON; (d–g) EDXS mapping distribution of elements (C, O, S and Co) within a MON. Images reprinted with permission from ref. 36 (a), ref. 115 (b) and ref. 116 (c–g).
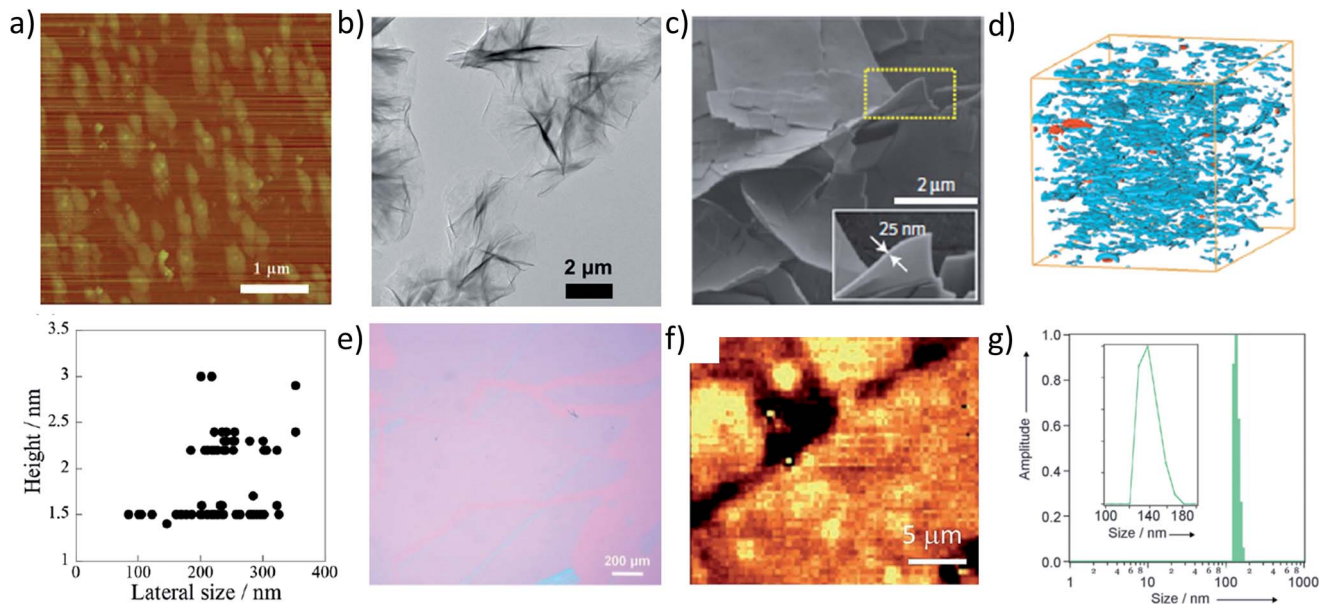
Fig. 6 (a) AFM images of nanosheets and (below) plot of corresponding size profiles; (b) TEM images of crinkled nanosheets; (c) SEM image of nanosheets grown by layering method and associated (d) FEB-SEM of nanosheets dispersed in a polymer membrane; (e) Brewster angle optical microscopy of nanosheets formed at the liquid–gas interface using Langmuir–Blodgett method; (f) Raman microscopy images of MONs; (g) DLS data showing lateral size distribution of nanosheets in suspension. Images reprinted with permission from ref. 74, 56, 36, 30, 27 and 82 respectively.

exactly due to interpenetration of components within layers, as well as instrumental set-up.[118] The presence of surface water or solvent molecules and counter ions may also lead to nanosheets appearing thicker than expected.[68,119] MONs have been imaged using a variety of substrates including silica, mica and HOP graphene and different nanosheets will stick to different surfaces to different degrees. Key to imaging the MONs is getting the concentration low enough to see isolated nanosheets. Nanosheets can also aggregate during drying and heating the substrate to speed up drying has been shown to help with imaging other nanosheets.[110]

Scanning electron microscopy (SEM) and TEM can provide high resolution images of the nanosheets, giving information about their dimensions and rigidity. The non-conductive and labile nature of most MONs mean they readily suffer electron damage and charging which can make imaging challenging, although many systems have been successfully imaged with high resolution (Fig. 6b and c). A wide variety of advanced electron microscopy techniques have been used to provide additional information about the underlying structure of the MONs. For example, Lin and coworkers used fast Fourier transform and rotation electron diffraction to determine the reciprocal lattice of sub-micron sized nanosheets as well as high resolution TEM and scanning TEM high angle annular dark-field (STEM-HAADF) images to corroborate their structural model (Fig. 5b).[23] Selected area electron diffraction (SAED) has also been used to confirm unit-cell measurements.[29,32] Energy-dispersive X-ray spectroscopy (EDX) and electron energy-loss spectroscopy (EELS) have been used to map the elemental distribution of the nanosheets.[59,67,116] These powerful techniques provide an important route to understanding the nature and position of defects, functional groups and active sites which are often essential to their performance in a range of applications.

SEM can also achieve good resolution and can be useful for characterising the layers of parent material and getting an overview of the particle size distribution. For example, Rodenas *et al.* used focused ion beam SEM (FIB-SEM) to image the distribution of MONs within their composite membranes (Fig. 6d).[36] SEM microscopes can also be coupled to elemental characterisation techniques such as EDX. Brewster angle optical microscopy can be used to image nanosheets at interfaces such as those shown in Fig. 6d,[30] as can Raman microscopy (Fig. 6e).[27]

Often only selected images of nanosheets are shown which may not be representative of the bulk sample. Some groups have attempted to quantify the size distribution by imaging a large number of nanosheets and tallying their thickness against their largest lateral dimension, as shown in Fig. 6a taken from the research of Maeda and coworkers.[74] Although time consuming, this provides a more reliable account of the range of particles observed and must be considered good practice. Dynamic light scattering (DLS) has been used to measure the lateral size distribution of nanosheets. Lin and coworkers observed hydrodynamic diameters of 600–800 nm which corresponds with wrinkled nanosheets of ∼0.5 × 1 μm observed by TEM,[61] whilst Rosseinsky and coworkers produced a narrow distribution of lateral sizes between 120–180 nm consistent with those observed by AFM (Fig. 6f).[82]

4.3 Macroscopic characterisation

The ability to disperse MONs in solution allows them to be used and processed as suspensions making them available to interact as sensors and catalysts with molecules in solution. The

16300 | *J. Mater. Chem. A*, 2018, **6**, 16292–16307

This journal is © The Royal Society of Chemistry 2018

presence of Tyndall scattering when a laser is shone through a sample is indicative of the presence of nanosheets in suspension (Fig. 7a).[32] It should be noted that other shapes of nanoparticle create the same effect and the morphology of the particles in suspension should be evaluated using a suitable imaging technique. The concentration of material that can form a stable suspension is often very low, typically less than 0.1 mg mL^{-1}. However, careful choice of solvent, the presence of surfactants and the incorporation of functional groups can all enhance the concentration of material in suspension.[43] The concentration of material in suspension can be evaluated by accurately measuring the mass of material left over following careful drying or filtration of a suspension. Alternatively, an estimate can be obtained from UV-vis data by creating a calibration curve from samples of known concentration.[43] Recently, Moorthy and coworkers were able to compare the degree of exfoliation achieved in different solvents using fluorescence spectroscopy due to quenching of emission upon aggregation or stacking of layers (Fig. 7b).[114] Elder et al. probed the surface interactions of water and ethanol molecules to Cu-BDC nanosheets using temperature-programmed desorption (TPD) and were able to extract kinetic parameters for desorption from edge, pore and external surface sites.[38]

As with MOFs, many of the applications of MONs take advantage of their porous structure and high surface area in the solid state. Gas adsorption measurements have relatively routinely been used to characterise the accessible volumes of MONs (Fig. 7c).[68,121,122] The Brunauer–Emmett–Teller BET surface area of the nanosheets is typically lower than that of the

parent bulk porous material due to inefficient packing of the small crystallites,[120] however other properties such as permeability may be significantly enhanced, which is discussed further in Section 5.1.

Understanding the mechanical properties of MONs is also essential for optimising their use in applications such as in membranes for gas separation and in forming composites. The group of Cheetham used a spherical-tip diamond indentor to compare the mechanical properties of different faces of a bulk layered MOF.[32] They were able to determine the critical resolved shear stress needed for the micromechanical delamination of individual layers to be relatively small at ≤0.4 GPa. AFM can also be used to undertake nanoindentation experiments of nanosheets positioned over wells of different diameters. Gomez-Herrero, Zamora and coworkers calculated the Young's modulus and breaking strength of their frameworks to be 5 GPa and 0.12 N m^{-1} (Fig. 7d).[27] This is 200 and 150 times lower than the values reported for pristine graphene, but the MONs were still strong enough for free standing sheets to be suspended over micron sized holes.

5. Applications

Other metal–organic materials have been developed extensively for a wide variety of applications ranging from 'smart' materials and sensors, to light harvesting, gas storage and drug delivery. MONs share many of the advantages of other metal–organic materials, such as the ease with which their structures can be varied and new properties introduced, allowing them to be tuned for a wide variety of applications. However, their distinct 2D structure, vast external surface area and colloidal nature mean they present a range of opportunities for use in a variety of applications. Here, we seek to illustrate the main bodies of research and recent highlights within the MON literature.

5.1 Molecular separation

As with MOFs, MONs can have an open structure creating regular arrays of 1D channels large enough to allow solvent and other molecules to pass through. The tuneable length, sterics and chemistry of the organic linker means that pore size can be controlled to selectively allow certain molecules to pass through, whilst excluding others. The two-dimensional structure of MONs makes them ideal for use in membranes due to the shorter diffusional pathway required as compared to MOFs. Tailoring of the properties of the pore gives opportunities to increase the permeance without a corresponding decrease in specificity. Peng et al. used 1 μm × 1 nm ZIF-based MONs as building blocks for a molecular sieving membrane.[68,121] They achieved a selectivity ratio over 200 for H$_2$ over CO$_2$ (Fig. 8b). Additionally they showed these membranes to be stable over 400 hours of use at room temperature, and for 120 hours at 150 °C with 4 mol% steam. Rodenas et al. found up to an 8-fold increase in the selectivity of membranes for CO$_2$ over CH$_4$ of upon incorporation of MONs compared with the parent layered MOF.[36] They attribute this large difference to better packing of the highly anisotropic nanosheets within the membranes, key
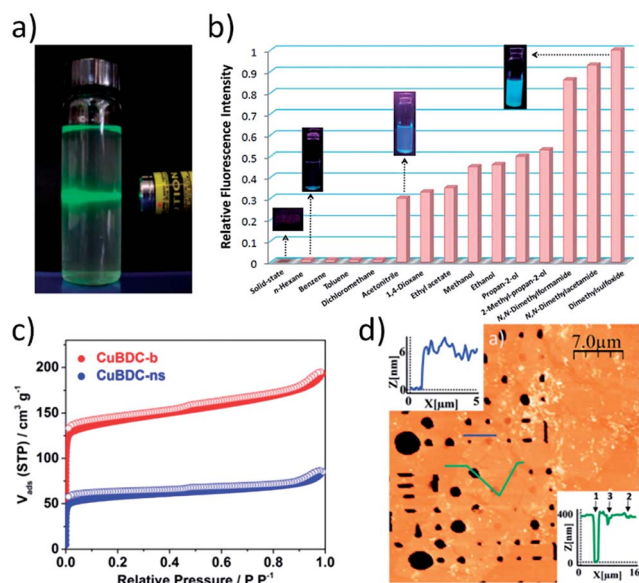
Fig. 7 (a) Photo showing typical Tyndall scattering resulting from a suspension of MONs. (b) Fluorescence emission profiles (λ_{ex} = 330 nm) of Cd MONs in different solvents. (c) Gas adsorption isotherm comparing N$_2$ uptake for Cu(BDC) bulk MOF (red) and MONs (blue). (d) AFM topographic image of Cu-based nanosheets suspended over micron-sized wells (400 nm depth) within a Si/SiO$_2$ substrate. Images reprinted with permission from ref. 32, 114, 120 and 27, for images (a–d) respectively.

This journal is © The Royal Society of Chemistry 2018

J. Mater. Chem. A, 2018, 6, 16292–16307 | 16301

Fig. 8 (a) Schematic illustration of selectively permeable MON composite membrane (left), and permeance as a function of the energy consumption for the 2D M-TCP(Fe)-based membranes, compared with additional advanced membranes. (b) N_2 adsorption–desorption isotherms (77 K) on pristine $Zn_2(bim)_4$ and $Zn_2(bim)_4$ nanosheets, with inset photographs of material used for analyses. (c) Schematic of catalytic activity of Fe-TPY MONs. (d) Absorbance of juglone ($\lambda = 419$ nm) as a function of reaction time with different catalysts (right) and catalytic reaction scheme (left). (e) UV-Vis titration of pyridine into an aqueous suspension of Cu-MONs, with an inset of absorbance *vs.* concentration, used to calculate the binding constant. (f) Operation of the dual-electrochromic MON device. (g) Confocal fluorescence image of a single cell, showing two-colour sensing of DNA and small molecules with La-MONs. (h) TEM image of CuS nanoparticle-MON composite (left), and schematic illustration of the used photoelectrochemical cell (right). (i) Charge–discharge profile (black) and specific capacitance (red) at a current density of 2 A g^{-1} of the Co-MOF electrode. (j) Variable-temperature van der Pauw conductivity measurement on a ~500 nm thick MON film on quartz. Images reprinted with permission. Images reprinted with permission from ref. 123, 68, 56, 53, 43, 100, 89, 51, 125 and 24 for images (a–j) respectively.

for the occupation of gas permeation pathways. Further steps in CO_2/CH_4 separation have been made by Zhao and coworkers, where a CO_2 permeance of 407 GPU was maintained over 100 h.[120] Interestingly, the same authors have also identified the first reversed thermoswitchable membranes, where H_2 permeance decreases at elevated temperatures.[40] This property is attributed to the flexibility of the 2D framework leading to blocking of the apertures at elevated temperatures.

Recently, MONs have been used for water purification through high-performance nanofiltration (NF).[123] Membranes showed permeance about two orders of magnitude higher than a commercial NF membrane, while exhibiting high rejection rates of over 90% for organic dye molecules with sizes larger than 0.8×1.1 nm (Fig. 8a). The large body of research on the use of MOFs in gas storage and separation, coupled with the inherent advantages of MON morphology in enhancing the performance of membranes, means this area is likely to see considerable future investment.

5.2 Catalysis
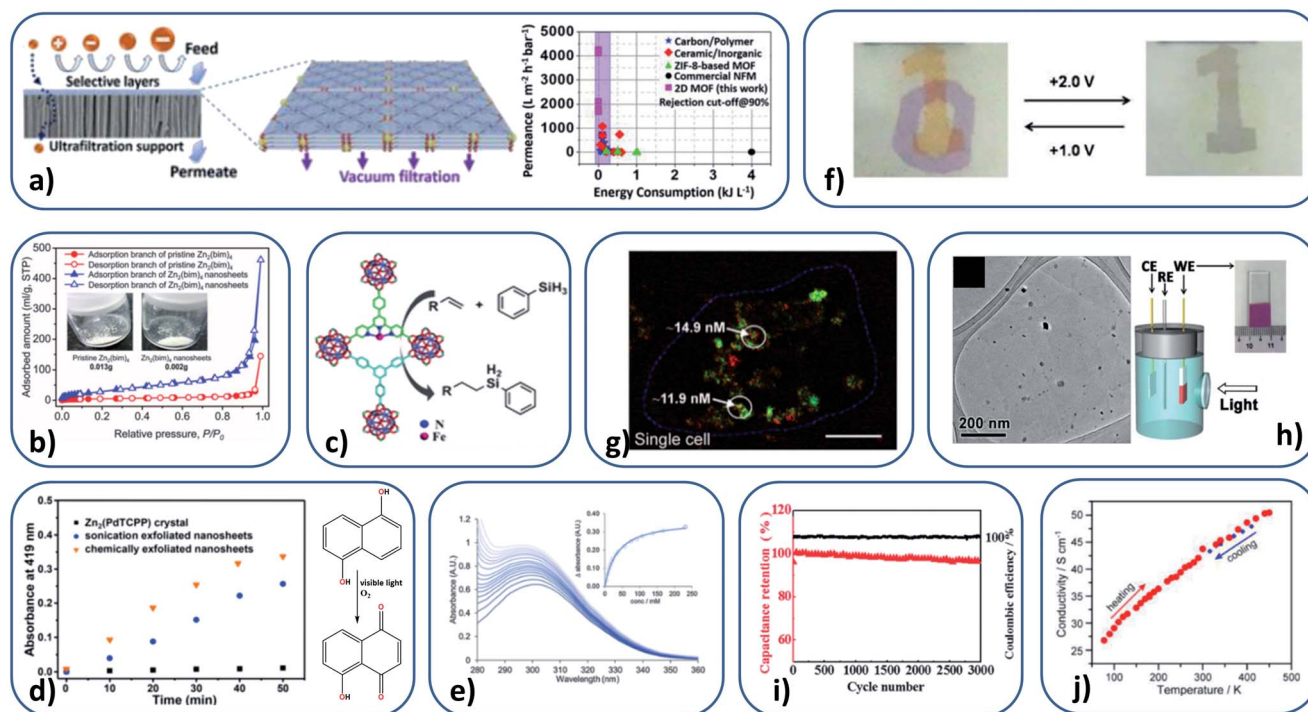
The large external surface area of MONs compared to bulk materials makes them ideal candidates as catalysts. They have well-defined structures but can readily be separated from

reaction mixtures, combining many of the advantages of homogeneous and heterogeneous catalysts. In MOFs, the majority of active sites are buried within the bulk of the material and reagents must diffuse to the active site. This also limits the size of reagents that may be used and the products that can be formed. The increased on- or near-surface active site presentation of MONs negates these limitations. Various authors have demonstrated that MONs show increased catalytic activity relative to the corresponding 3D MOF, including: hydrosilylation of terminal olefins (Fig. 8c),[56] H_2O_2 reduction (used as biomimetic enzymes for real-time tracking of live cell H_2O_2 secretion),[52,54] and Lewis acid activity for the oxidation of thioanisoles.[37] The cycloaddition of CO_2 with epoxides has also been demonstrated.[37]

MONs have also been used as photocatalysts and in electrochemical reactions. Ding *et al.* demonstrated Zn(Pd-TCPP) MONs perform better in singlet oxygen generation that the unexfoliated MOF, leading to increased rate of photooxidation of 1,5-dihydroxynaphthalene to juglone (Fig. 8d).[53] The same photocatalytic reaction has been demonstrated using a Zr_6-cluster-linked (NiTCPP) MON.[59] Similarly, Zn-(ZnTCPP) MONs were used as a semiconductor photosensitizer along with ZIF-67 as a cocatalyst for the photochemical reduction of CO_2 and exhibited enhanced photocatalytic efficiency compared to the

16302 | *J. Mater. Chem. A*, 2018, **6**, 16292–16307

This journal is © The Royal Society of Chemistry 2018

bulk MOF.[55] Multiple authors have incorporated MONs into electrodes for use within the electrochemical catalytic splitting of water, for H_2 generation.[22,25,41,57,80] Recent efforts outperform standard IrO_2-based catalysts and comparing favourably with state-of-the-art transition-metal-based catalysts.[57]

5.3 Sensing

The high external surface area and diverse chemistry of the nanosheets also makes them ideally suited for creating sensors. The binding of analytes to free coordination sites of metal ions, such as the axial position of PW based MONs, can result in changes in the MONs photophysical properties. This allows detection and quantification of binding interactions (Fig. 8d, for example).[43,92,124] Similarly, Dincă and coworkers were able to sense ammonia down to <5 ppm by recording the change in electrical response of the MONs upon substrate coordination.[86]

An alternative approach has been to use MONs to quench the fluorescence of adsorbed, dye-labelled DNA and mRNA,[49,64] of which detection limits have been found as low as 20×10^{-12} M,[49] and 1 pM (after hybridisation chain reaction amplification).[64] Similarly, background flourescence quenching enabled a signal-to-noise ratio increase of 7.5× that when using 2D graphene oxide, and enabled a detection limit down to 0.9 pM (0.3 pg mL^{-1}) of chloramphenical, a model antibiotic,[126] and luminescent quenching of nanosheet photoluminescence has been used to detect Fe^{3+} to a detection limit of 0.45 μM, amongst additional metal ions,[127] and 0.054 μM (compared with 0.11 μM for bulk MOF).[128]

He *et al.* have developed MONs within a biosensor for the protein MUC1, with a detection limit of 0.12 ng mL^{-1}.[129] The cancer marker protein was detected from human serum, which points towards MON application within medicinal biosensing and diagnoses. Wang *et al.* have additionally demonstrated a lanthanide-based MON, useful as a two-colour sensing platform for intracellular DNA and small molecules (Fig. 8g).[89] For further information on the preparation of MONs for chemical and biosensing and examples within this area, see Yang *et al.*'s recent review.[130]

5.4 Electronics

Perhaps the greatest excitement surrounding graphene has been the possibility of harnessing its electronic properties to create a new generation of ultrathin electronic devices. Graphene can potentially be combined with other 2D materials with insulating or semiconducting properties in order to form ultrathin electronic devices. In 2013, Nishihara and coworkers demonstrated a planer π-conjugated MON which was shown to be semiconducting, opening up research into MONs within molecular electronics.[99] Since then, multiple authors have found MONs to be semiconducting,[24,84,86,88,99,131,132] with Dincă and coworkers setting a record in 2014 for conductivity of metal–organic materials, at 40 S cm^{-1} (Fig. 8i).[24] Zeng and coworkers have suggested from theoretical calculations that it may be possible to tune semiconducting MONs to metals through alteration of the metal ions used.[87] Additional work fabricating MONs into electrochemical devices has suggested

MONs may be useful within devices such as colour displays and electronic paper, due to their rapid electrochemical response rate (Fig. 8f).[100,132]

Recent work has been directed towards the incorporation of MONs into supercapacitor electrodes.[50,125,133] The groups of Jia and Wei have utilised MONs as electrode materials. Jia and coworkers found an 80.2% retention rate after 500 charge–discharge cycles,[133] and more recently the group of Wei set records for both capacitance (2564 F g^{-1}) and retention (95.8% after 3000 cycles) for MO materials (Fig. 8i).[125]

5.5 Photofunctional nanomaterials

As with other new materials, researchers seek novel, inventive uses for them to further the body of research and excitement surrounding them. Lin and coworkers have recently demonstrated that fluorescence of few-layer MONs can be used in white light emitting diodes (WLEDs), which exhibit a switching speed of at least three times as fast as current commercial WLEDs, due to the shorter fluorescence lifetime of MONs. This makes them useful for visible-light communications, used within wireless information transmission applications.[23] The group of Nishihara have demonstrated an avenue into development of MONs into photofunctional devices.[77] They found photoluminescent colour could be modified through alteration of both the metal ions and ligands used, as well as almost quantitative exciton transmission to bound guest dyes. This opens up possibilities of further development for novel photofunctional nanomaterials.

5.6 Other applications

MONs have been used as a surface in order to grow *in situ* M–S nanoparticles (M = Cu, Cd, Co), using the metal sites presented on the nanosheet surface to stimulate growth (Fig. 8h).[51] This led to the CuS-nanosheet composite performing with notably increased photocurrent within a photoelectrochemical cell, compared to the nanosheet alone. This is due to the improved exciton separation and charge carrier transport from the CuS nanoparticles. Zhang and coworkers suggest these types of composite MON materials may have applications within solar cells and photochromism, for example.

Liu *et al.* have utilised MONs as a clean-background matrix for MALDI-TOF mass spectrometry analysis of small biomolecules.[69] Biomarkers are normally below the scope of this technique as interference from conventional matrices normally limits the size of molecules that can be seen to ∼700 Da. The superior background provided by the nanosheet composite allowed detection of glutamic acid (147 Da) amongst other small molecules and biomarkers. The same group also demonstrate MON inhibition of enzyme activity, allowing activity modulation.[113]

6. Conclusions and outlook

The extensive body of research on MOFs has provided an important starting point for identifying promising layered compounds and SBUs for the construction of MONs. A diverse

This journal is © The Royal Society of Chemistry 2018

J. Mater. Chem. A, 2018, **6**, 16292–16307 | **16303**

range of MOF SBUs and ligands readily provide the strong, directional interactions within two-dimensions required to form MONs and innovation has already occurred in adapting well known SBUs to give two-dimensional connectivity. Other key MOF concepts such as reticular substitution and post-synthetic modification are also already beginning to be used in MONs with great effect. However, the design principles behind creating the porous, three-dimensional structures which have been the focus of the MOF community may be quite distinct from those required to create effective two-dimensional MONs. For example, in MOFs neutral frameworks have generally been favoured as counterions tend to occupy pore space. However, in MONs counterions can sit above or below the nanosheets and aid formation of nanosheets through solvation. Structural rearrangements may occur in nanosheets which do not occur in bulk structures due to the high surface area and MONs may form higher order structures such as rolling into "nanoscrolls." We anticipate that as research into MONs develops, new SBUs and design features not found in MOF chemistry will emerge to address the distinct requirements and opportunities faced in forming nanosheets from metal–organic building blocks.

Intensive research over the last decade into the synthesis of two-dimensional materials and the exfoliation of layered materials into nanosheets similarly provides an important starting point for research into MONs. The use of ultrasound, solvation, intercalants, surfactants and crystal-growth modifiers all have parallels in the formation of nanosheets from other materials. There has been considerable innovation over the last year in new 'softer forms' of exfoliation and new ways to direct crystal growth, but it is not yet clear how broadly applicable these approaches will be. As with other nanosheets, the preferred method of synthesis is likely to depend on the properties of nanosheets required. In general, bottom-up methods have tended to produce larger nanosheets with narrower size distributions whilst top-down exfoliations have tended to give smaller, thinner sheets. However, the diversity of MON chemistry means it is difficult to generalise and compare different studies, and in most cases the synthesis or exfoliation will not have been optimised. More detailed and systematic studies are therefore required to understand the effect of different parameters on the dimensions of nanosheets produced to allow more targeted synthesis.

A diverse range of solid, solution, colloidal and surface analysis techniques must be combined to provide insights into different levels of their structure. The complex molecular structure of MONs, their relatively fragile and non-conducting composition and the spread of sizes and thicknesses of nanosheets produced makes them particularly challenging to characterise. Greater understanding of the mechanical, opto-electronic and porosity of nanosheets and how this compares with the parent, layered materials will be important for identifying new applications. There is also little general acceptance of what constitutes a "nanosheet" in terms of the number of layers, size distribution and crystallinity of the materials formed. Setting the bar too high at this early stage has the potential to stifle innovation. Setting it too low will dilute the field with compounds without the potential to form free-standing, crystalline, single-layered materials.

The success of MONs as a distinct class of nanomaterials is likely to rest on their utility. The billions of dollars invested by industry and funding councils in other two-dimensional and metal–organic materials demonstrates both the potential demand for these type of materials and the challenges in bringing them to market. The chemical diversity, modular structure and tunability of MONs offers obvious advantages over simple inorganic nanosheets and the inherent reversibility of coordination bonds and unique properties of metal ions offers distinct opportunities compared to covalent–organic framework (COF) nanosheets. The high external surface area and tuneable structure of MONs make them obvious candidates for a wide range of sensing, separation and catalytic applications and there are already promising examples of MONs out-performing bulk MOFs when used as membranes for gas-separation and as catalysts. The tuneable electronic, optical and magnetic properties of MONs also potentially allow them to be used as layers in diverse range of devices including displays, solar-cells and batteries. The wide range of inexpensive and abundant ligands and metal ions that can be used to construct MONs and the ability to synthesise them from solution and process them as suspensions offers further environmental and economic advantages.

In conclusion, MONs represent a rich new class of materials requiring distinct approaches in their design, synthesis and characterisation and offering a novel combination of properties that can be harnessed for a wide range of applications. This is an emerging field whose boundaries, techniques, rules and potential are only just beginning to be explored. Here we have tried to highlight both the breadth of different approaches that have so far been taken and draw out common threads between the different studies. We hope that this review will further stimulate this exciting area of research and look forward to contributing further to its development.

Conflicts of interest

There are no conflicts to declare.

Acknowledgements

References

1 T. Torres, *Chem. Soc. Rev.*, 2017, **46**, 4385–4386.
2 J. Wang, F. Ma and M. Sun, *RSC Adv.*, 2017, **7**, 16801–16822.
3 Y. Zhou, M. Zhang, Z. Guo, L. Miao, S.-T. Han, Z. Wang, X. Zhang, H. Zhang and Z. Peng, *Mater. Horiz.*, 2017, **4**, 997–1019.
4 H. T. Tan, W. P. Sun, L. B. Wang and Q. Y. Yan, *ChemNanoMat*, 2016, **2**, 562–577.
5 H. Yin and Z. Tang, *Chem. Soc. Rev.*, 2016, **45**, 4873–4891.

16304 | *J. Mater. Chem. A*, 2018, **6**, 16292–16307

This journal is © The Royal Society of Chemistry 2018

6 R. Lv, J. A. Robinson, R. E. Schaak, D. Sun, Y. F. Sun, T. E. Mallouk and M. Terrones, *Accounts Chem. Res.*, 2015, **48**, 56–64.

7 L. Xu and J. Sun, *Adv. Energy Mater.*, 2016, **6**, 1600441.

8 M. Pan, Z. W. Wei, Y. W. Xu and C. Y. Su, *Prog. Chem.*, 2017, **29**, 47–74.

9 J. Y. Zhang and C. Y. Su, *Coord. Chem. Rev.*, 2013, **257**, 1373–1408.

10 R. Gaillac, P. Pullumbi, K. A. Beyer, K. W. Chapman, D. A. Keen, T. D. Bennett and F. X. Coudert, *Nat. Mater.*, 2017, **16**, 1149–1154.

11 J. L. Serrano and T. Sierra, *Coord. Chem. Rev.*, 2003, **242**, 73–85.

12 A. Winter and U. S. Schubert, *Chem. Soc. Rev.*, 2016, **45**, 5311–5357.

13 P. Z. Moghadam, A. Li, S. B. Wiggin, A. Tao, A. G. P. Maloney, P. A. Wood, S. C. Ward and D. Fairen-Jimenez, *Chem. Mater.*, 2017, **29**, 2618–2625.

14 B. Li, H. M. Wen, W. Zhou and B. Chen, *J. Phys. Chem. Lett.*, 2014, **5**, 3468–3479.

15 E. M. Dias and C. Petit, *J. Mater. Chem. A*, 2015, **3**, 22484–22506.

16 M. Ranocchiari and J. A. van Bokhoven, *Phys. Chem. Chem. Phys.*, 2011, **13**, 6388–6396.

17 X. L. Jiang, H. H. Wu, S. J. Chang, R. Si, S. Miao, W. X. Huang, Y. H. Li, G. X. Wang and X. H. Bao, *J. Mater. Chem. A*, 2017, **5**, 19371–19377.

18 L. E. Kreno, K. Leong, O. K. Farha, M. Allendorf, R. P. Van Duyne and J. T. Hupp, *Chem. Rev.*, 2012, **112**, 1105–1125.

19 H. S. Wang, *Coord. Chem. Rev.*, 2017, **349**, 139–155.

20 I. Stassen, N. Burtch, A. Talin, P. Falcaro, M. Allendorf and R. Ameloot, *Chem. Soc. Rev.*, 2017, **46**, 3185–3241.

21 M. Zhao, Q. Lu, Q. Ma and H. Zhang, *Small Methods*, 2016, **1**, 1600030.

22 R. Dong, Z. Zheng, D. C. Tranca, J. Zhang, N. Chandrasekhar, S. Liu, X. Zhuang, G. Seifert and X. Feng, *Chem.–Eur. J.*, 2017, **23**, 2255–2260.

23 X. Hu, Z. Wang, B. Lin, C. Zhang, L. Cao, T. Wang, J. Zhang, C. Wang and W. Lin, *Chem.–Eur. J.*, 2017, **23**, 8390–8394.

24 D. Sheberla, L. Sun, M. A. Blood-Forsythe, S. Er, C. R. Wade, C. K. Brozek, A. Aspuru-Guzik and M. Dincă, *J. Am. Chem. Soc.*, 2014, **136**, 8859–8862.

25 A. J. Clough, J. W. Yoo, M. H. Mecklenburg and S. C. Marinescu, *J. Am. Chem. Soc.*, 2015, **137**, 118–121.

26 C. Kutzscher, A. Gelbert, S. Ehrling, C. Schenk, I. Senkovska and S. Kaskel, *Dalton Trans.*, 2017, **46**, 16480–16484.

27 C. Hermosa, B. R. Horrocks, J. I. Martinez, F. Liscio, J. Gomez-Herrero and F. Zamora, *Chem. Sci.*, 2015, **6**, 2553–2558.

28 D. Rodriguez-San-Miguel, P. Amo-Ochoa and F. Zamora, *Chem. Commun.*, 2016, **52**, 4113–4127.

29 R. Sakamoto, K. Takada, T. Pal, H. Maeda, T. Kambe and H. Nishihara, *Chem. Commun.*, 2017, **53**, 5781–5801.

30 T. Bauer, Z. Zheng, A. Renn, R. Enning, A. Stemmer, J. Sakamoto and A. D. Schlüter, *Angew. Chem., Int. Ed.*, 2011, **50**, 7879–7884.

31 G. Z. Zhu and Q. Sun, *Comp. Mater. Sci.*, 2016, **112**, 492–502.

32 J.-C. Tan, P. J. Saines, E. G. Bithell and A. K. Cheetham, *ACS Nano*, 2012, **6**, 615–621.

33 C. Lee, X. Wei, J. W. Kysar and J. Hone, *Science*, 2008, **321**, 385–388.

34 A. K. Cheetham, C. N. R. Rao and R. K. Feller, *Chem. Commun.*, 2006, **46**, 4780–4795.

35 P. Z. Li, Y. Maeda and Q. Xu, *Chem. Commun.*, 2011, **47**, 8436–8438.

36 T. Rodenas, I. Luz, G. Prieto, B. Seoane, H. Miro, A. Corma, F. Kapteijn, F. X. Llabrés, i. Xamena and J. Gascon, *Nat. Mater.*, 2015, **14**, 48–55.

37 Y.-N. Li, S. Wang, Y. Zhou, X.-J. Bai, G.-S. Song, X.-Y. Zhao, T.-Q. Wang, X. Qi, X.-M. Zhang and Y. Fu, *Langmuir*, 2017, **33**, 1060–1065.

38 A. C. Elder, A. B. Aleksandrov, S. Nair and T. M. Orlando, *Langmuir*, 2017, **33**, 10153–10160.

39 B. Garai, A. Mallick, A. Das, R. Mukherjee and R. Banerjee, *Chem.–Eur. J.*, 2017, **23**, 7361–7366.

40 X. Wang, C. Chi, K. Zhang, Y. Qian, K. M. Gupta, Z. Kang, J. Jiang and D. Zhao, *Nat. Commun.*, 2017, **8**, 14460.

41 J. Huang, Y. Li, R. K. Huang, C. T. He, L. Gong, Q. Hu, L. Wang, Y. T. Xu, X. Y. Tian, S. Y. Liu, Z. M. Ye, F. Wang, D. D. Zhou, W. X. Zhang and J. P. Zhang, *Angew. Chem., Int. Ed.*, 2018, **57**, 4632–4636.

42 Y. Hou, L. Liu, S. Qiu, X. Zhou, Z. Gui and Y. Hu, *ACS Appl. Mater. Interfaces*, 2018, **10**, 8274–8286.

43 J. A. Foster, S. Henke, A. Schneemann, R. A. Fischer and A. K. Cheetham, *Chem. Commun.*, 2016, **52**, 10474–10477.

44 R. Makiura, S. Motoyama, Y. Umemura, H. Yamanaka, O. Sakata and H. Kitagawa, *Nat. Mater.*, 2010, **9**, 565–571.

45 R. Makiura, K. Tsuchiyama and O. Sakata, *CrystEngComm*, 2011, **13**, 5538–5541.

46 S. Motoyama, R. Makiura, O. Sakata and H. Kitagawa, *J. Am. Chem. Soc.*, 2011, **133**, 5640–5643.

47 G. Xu, T. Yamada, K. Otsubo, S. Sakaida and H. Kitagawa, *J. Am. Chem. Soc.*, 2012, **134**, 16524–16527.

48 R. Makiura, R. Usui, Y. Sakai, A. Nomoto, A. Ogawa, O. Sakata and A. Fujiwara, *ChemPlusChem*, 2014, **79**, 1352–1360.

49 M. Zhao, Y. Wang, Q. Ma, Y. Huang, X. Zhang, J. Ping, Z. Zhang, Q. Lu, Y. Yu, H. Xu, Y. Zhao and H. Zhang, *Adv. Mater.*, 2015, **27**, 7372–7378.

50 F. Cao, M. Zhao, Y. Yu, B. Chen, Y. Huang, J. Yang, X. Cao, Q. Lu, X. Zhang, Z. Zhang, C. Tan and H. Zhang, *J. Am. Chem. Soc.*, 2016, **138**, 6924–6927.

51 Q. Lu, M. T. Zhao, J. Z. Chen, B. Chen, C. Tan, X. Zhang, Y. Huang, J. Yang, F. Cao, Y. Yu, J. Ping, Z. Zhang, X.-J. Wu and H. Zhang, *Small*, 2016, **12**, 4669–4674.

52 Y. Wang, M. Zhao, J. Ping, B. Chen, X. Cao, Y. Huang, C. Tan, Q. Ma, S. Wu, Y. Yu, Q. Lu, J. Chen, W. Zhao, Y. Ying and H. Zhang, *Adv. Mater.*, 2016, **28**, 4149–4155.

53 Y. Ding, Y. P. Chen, X. Zhang, L. Chen, Z. Dong, H. L. Jiang, H. Xu and H. C. Zhou, *J. Am. Chem. Soc.*, 2017, **139**, 9136–9139.

54 Y. Huang, M. T. Zhao, S. K. Han, Z. C. Lai, J. Yang, C. L. Tan, Q. L. Ma, Q. P. Lu, J. Z. Chen, X. Zhang, Z. C. Zhang, B. Li, B. Chen, Y. Zong and H. Zhang, *Adv. Mater.*, 2017, **29**, 1700102.

This journal is © The Royal Society of Chemistry 2018

J. Mater. Chem. A, 2018, **6**, 16292–16307 | **16305**

55 L. Ye, Y. Gao, S. Cao, H. Chen, Y. Yao, J. Hou and L. Sun, *Appl. Catal., B*, 2018, **227**, 54–60.

56 L. Cao, Z. Lin, F. Peng, W. Wang, R. Huang, C. Wang, J. Yan, J. Liang, Z. Zhang, T. Zhang, L. Long, J. Sun and W. Lin, *Angew. Chem., Int. Ed.*, 2016, **128**, 5046–5050.

57 L. Zhao, B. Dong, S. Li, L. Zhou, L. Lai, Z. Wang, S. Zhao, M. Han, K. Gao, M. Lu, X. Xie, B. Chen, Z. Liu, X. Wang, H. Zhang, H. Li, J. Liu, H. Zhang, X. Huang and W. Huang, *ACS Nano*, 2017, **11**, 5800–5807.

58 Y. Wang, L. Li, L. Yan, X. Gu, P. Dai, D. Liu, J. G. Bell, G. Zhao, X. Zhao and K. M. Thomas, *Chem. Mater.*, 2018, **30**, 3048–3059.

59 T. He, B. Ni, S. Zhang, Y. Gong, H. Wang, L. Gu, J. Zhuang, W. Hu and X. Wang, *Small*, 2018, **14**(16), 1703929.

60 M. J. Cliffe, E. Castillo-Martinez, Y. Wu, J. Lee, A. C. Forse, F. C. N. Firth, P. Z. Moghadam, D. Fairen-Jimenez, M. W. Gaultois, J. A. Hill, O. V. Magdysyuk, B. Slater, A. L. Goodwin and C. P. Grey, *J. Am. Chem. Soc.*, 2017, **139**, 5397–5404.

61 L. Cao, Z. Lin, W. Shi, Z. Wang, C. Zhang, X. Hu, C. Wang and W. Lin, *J. Am. Chem. Soc.*, 2017, **139**, 7020–7029.

62 P. J. Saines, J.-C. Tan, H. H. M. Yeung, P. T. Barton and A. K. Cheetham, *Dalton Trans.*, 2012, **41**, 8585–8593.

63 P. J. Saines, M. Steinmann, J.-C. Tan, H. H. M. Yeung, W. Li, P. T. Barton and A. K. Cheetham, *Inorg. Chem.*, 2012, **51**, 11198–11209.

64 W.-J. Song, *Talanta*, 2017, **170**, 74–80.

65 T. Araki, A. Kondo and K. Maeda, *Chem. Commun.*, 2013, **49**, 552–554.

66 R. Chen, J. Yao, Q. Gu, S. Smeets, C. Baerlocher, H. Gu, D. Zhu, W. Morris, O. M. Yaghi and H. Wang, *Chem. Commun.*, 2013, **49**, 9500–9502.

67 S. C. Junggeburth, L. Diehl, S. Werner, V. Duppel, W. Sigle and B. V. Lotsch, *J. Am. Chem. Soc.*, 2013, **135**, 6157–6164.

68 Y. Peng, Y. Li, Y. Ban, H. Jin, W. Jiao, X. Liu and W. Yang, *Science*, 2014, **346**, 1356–1359.

69 H. L. Liu, Y. J. Chang, T. Fan and Z. Y. Gu, *Chem. Commun.*, 2016, **52**, 12984–12987.

70 Y. Lo and D. Y. Kang, *J. Mater. Chem. A*, 2016, **4**, 4172–4179.

71 Q. Liu, Z. X. Low, Y. Feng, S. Leong, Z. X. Zhong, J. F. Yao, K. Hapgood and H. T. Wang, *Microporous Mesoporous Mater.*, 2014, **194**, 1–7.

72 H. Jiang, S. L. Xue, Y. F. Liu, W. H. Xing and R. Z. Chen, *Microporous Mesoporous Mater.*, 2017, **243**, 16–21.

73 L. Huang, X. P. Zhang, Y. J. Han, Q. Q. Wang, Y. X. Fang and S. J. Dong, *J. Mater. Chem. A*, 2017, **5**, 18610–18617.

74 A. Kondo, C. C. Tiew, F. Moriguchi and K. Maeda, *Dalton Trans.*, 2013, **42**, 15267–15270.

75 Z. Zheng, C. S. Ruiz-Vargas, T. Bauer, A. Rossi, P. Payamyar, A. Schuetz, A. Stemmer, J. Sakamoto and A. D. Schlueter, *Macromol. Rapid Commun.*, 2013, **34**, 1670–1680.

76 Z. Zheng, L. Opilik, F. Schiffmann, W. Liu, G. Bergamini, P. Ceroni, L.-T. Lee, A. Schuetz, J. Sakamoto, R. Zenobi, J. VandeVondele and A. D. Schlueter, *J. Am. Chem. Soc.*, 2014, **136**, 6103–6110.

77 T. Tsukamoto, K. Takada, R. Sakamoto, R. Matsuoka, R. Toyoda, H. Maeda, T. Yagi, M. Nishikawa, N. Shinjo, S. Amano, T. Iokawa, N. Ishibashi, T. Oi, K. Kanayama, R. Kinugawa, Y. Koda, T. Komura, S. Nakajima, R. Fukuyama, N. Fuse, M. Mizui, M. Miyasaki, Y. Yamashita, K. Yamada, W. Zhang, R. Han, W. Liu, T. Tsubomura and H. Nishihara, *J. Am. Chem. Soc.*, 2017, **139**, 5359–5366.

78 R. Sakamoto, K. Hoshiko, Q. Liu, T. Yagi, T. Nagayama, S. Kusaka, M. Tsuchiya, Y. Kitagawa, W.-Y. Wong and H. Nishihara, *Nat. Commun.*, 2015, **6**, 6713.

79 R. Sakamoto, T. Yagi, K. Hoshiko, S. Kusaka, R. Matsuoka, H. Maeda, Z. Liu, Q. Liu, W.-Y. Wong and H. Nishihara, *Angew. Chem., Int. Ed.*, 2017, **56**, 3526–3530.

80 R. Dong, M. Pfeffermann, H. Liang, Z. Zheng, X. Zhu, J. Zhang and X. Feng, *Angew. Chem., Int. Ed.*, 2015, **54**, 12058–12063.

81 P. Amo-Ochoa, L. Welte, R. Gonzalez-Prieto, P. J. Sanz Miguel, C. J. Gomez-Garcia, E. Mateo-Marti, S. Delgado, J. Gomez-Herrero and F. Zamora, *Chem. Commun.*, 2010, **46**, 3262–3264.

82 C. Marti-Gastaldo, J. E. Warren, K. C. Stylianou, N. L. O. Flack and M. J. Rosseinsky, *Angew. Chem., Int. Ed.*, 2012, **51**, 11044–11048.

83 P. J. Beldon, S. Tominaka, P. Singh, T. S. Dasgupta, E. G. Bithell and A. K. Cheetham, *Chem. Commun.*, 2014, **50**, 3955–3957.

84 K. Hoshiko, T. Kambe, R. Sakamoto, K. Takada and H. Nishihara, *Chem. Lett.*, 2014, **43**, 252–253.

85 T. Pal, T. Kambe, T. Kusamoto, M. L. Foo, R. Matsuoka, R. Sakamoto and H. Nishihara, *ChemPlusChem*, 2015, **80**, 1255–1258.

86 M. G. Campbell, D. Sheberla, S. F. Liu, T. M. Swager and M. Dinca, *Angew. Chem., Int. Ed.*, 2015, **54**, 4349–4352.

87 S. Chen, J. Dai and X. C. Zeng, *Phys. Chem. Chem. Phys.*, 2015, **17**, 5954–5958.

88 X. Sun, K.-H. Wu, R. Sakamoto, T. Kusamoto, H. Maeda and H. Nishihara, *Chem. Lett.*, 2017, **46**, 1072–1075.

89 H.-S. Wang, J. Li, J.-Y. Li, K. Wang, Y. Ding and X.-H. Xia, *NPG Asia Mater.*, 2017, **9**, e354.

90 X. Gao, R. Cui, M. Zhang and Z. Liu, *Mater. Lett.*, 2017, **197**, 217–220.

91 J. Conesa-Egea, J. Gallardo-Martinez, S. Delgado, J. I. Martinez, J. Gonzalez-Platas, V. Fernandez-Moreira, U. R. Rodriguez-Mendoza, P. Ocon, F. Zamora and P. Amo-Ochoa, *Small*, 2017, **13**, 1700965.

92 Y. P. Yuan, W. Wang, L. G. Qiu, F. M. Peng, X. Jiang, A. J. Xie, Y. H. Shen, X. Y. Tian and L. D. Zhang, *Mater. Chem. Phys.*, 2011, **131**, 358–361.

93 Z. Hu, E. M. Mahdi, Y. Peng, Y. Qian, B. Zhang, N. Yan, D. Yuan, J.-C. Tan and D. Zhao, *J. Mater. Chem. A*, 2017, **5**, 8954–8963.

94 A. Gallego, C. Hermosa, O. Castillo, I. Berlanga, C. J. Gomez-Garcia, E. Mateo-Marti, J. I. Martinez, F. Flores, C. Gomez-Navarro, J. Gomez-Herrero, S. Delgado and F. Zamora, *Adv. Mater.*, 2013, **25**, 2141–2146.

95 G. Zhan and H. C. Zeng, *Adv. Funct. Mater.*, 2016, **26**, 3268–3281.

96 F. Xue, P. Kumar, W. Xu, K. A. Mkhoyan and M. Tsapatsis, *Chem. Mater.*, 2017, **30**, 69–73.

16306 | *J. Mater. Chem. A*, 2018, **6**, 16292–16307

This journal is © The Royal Society of Chemistry 2018

97 M.-H. Pham, G.-T. Vuong, F.-G. Fontaine and T.-O. Do, *Cryst. Growth Des.*, 2012, **12**, 3091–3095.

98 R. Makiura and O. Konovalov, *Dalton Trans.*, 2013, **42**, 15931–15936.

99 T. Kambe, R. Sakamoto, K. Hoshiko, K. Takada, M. Miyachi, J.-H. Ryu, S. Sasaki, J. Kim, K. Nakazato, M. Takata and H. Nishihara, *J. Am. Chem. Soc.*, 2013, **135**, 2462–2465.

100 K. Takada, R. Sakamoto, S.-T. Yi, S. Katagiri, T. Kambe and H. Nishihara, *J. Am. Chem. Soc.*, 2015, **137**, 4681–4689.

101 R. Makiura and O. Konovalov, *Sci. Rep.*, 2013, **3**, 2506.

102 G. Xu, K. Otsubo, T. Yamada, S. Sakaida and H. Kitagawa, *J. Am. Chem. Soc.*, 2013, **135**, 7438–7441.

103 R. Sakamoto, K. Takada, X. Sun, T. Pal, T. Tsukamoto, E. J. H. Phua, A. Rapakousiou, K. Hoshiko and H. Nishihara, *Coord. Chem. Rev.*, 2016, **320**, 118–128.

104 H. Maeda, R. Sakamoto and H. Nishihara, *Langmuir*, 2016, **32**, 2527–2538.

105 J. X. Liu and C. Woll, *Chem. Soc. Rev.*, 2017, **46**, 5730–5770.

106 V. Rubio-Gimenez, M. Galbiati, J. Castells-Gil, N. Almora-Barrios, J. Navarro-Sanchez, G. Escorcia-Ariza, M. Mattera, T. Arnold, J. Rawle, S. Tatay, E. Coronado and C. Marti-Gastaldo, *Adv. Mater.*, 2018, **30**, 8.

107 S. Li, K. Yang, C. Tan, X. Huang, W. Huang and H. Zhang, *Chem. Commun.*, 2016, **52**, 1555–1562.

108 K. Sakata, S. Kashiyama, G. Matsuo, S. Uemura, N. Kimizuka and M. Kunitake, *ChemNanoMat*, 2015, **1**, 259–263.

109 A. Abhervé, S. Manas-Valero, M. Clemente-Leon and E. Coronado, *Chem. Sci.*, 2015, **6**, 4665–4673.

110 C. Backes, T. M. Higgins, A. Kelly, C. Boland, A. Harvey, D. Hanlon and J. N. Coleman, *Chem. Mater.*, 2017, **29**, 243–255.

111 A. O'Neill, U. Khan, P. N. Nirmalraj, J. Boland and J. N. Coleman, *J. Phys. Chem. C*, 2011, **115**, 5422–5428.

112 A. Ciesielski and P. Samori, *Chem. Soc. Rev.*, 2014, **43**, 381–398.

113 M. Xu, S. Yuan, X. Y. Chen, Y. J. Chang, G. Day, Z. Y. Gu and H. C. Zhou, *J. Am. Chem. Soc.*, 2017, **139**, 8312–8319.

114 P. Chandrasekhar, A. Mukhopadhyay, G. Savitha and J. N. Moorthy, *J. Mater. Chem. A*, 2017, **5**, 5402–5412.

115 W. Shi, L. Cao, H. Zhang, X. Zhou, B. An, Z. Lin, R. Dai, J. Li, C. Wang and W. Lin, *Angew. Chem., Int. Ed.*, 2017, **56**, 9704–9709.

116 Y. Ning, X. Lou, C. Li, X. Hu and B. Hu, *Chem.–Eur. J.*, 2017, **23**, 15984–15990.

117 H. S. Quah, L. T. Ng, B. Donnadieu, G. K. Tan and J. J. Vittal, *Inorg. Chem.*, 2016, **55**, 10851–10854.

118 C. J. Shearer, A. D. Slattery, A. J. Stapleton, J. G. Shapter and C. T. Gibson, *Nanotechnology*, 2016, **27**, 125704.

119 P. Nemes-Incze, Z. Osváth, K. Kamarás and L. P. Biró, *Carbon*, 2008, **46**, 1435–1442.

120 Y. D. Cheng, X. R. Wang, C. K. Jia, Y. X. Wang, L. Z. Zhai, Q. Wang and D. Zhao, *J. Membr. Sci.*, 2017, **539**, 213–223.

121 Y. Peng, Y. Li, Y. Ban and W. Yang, *Angew. Chem., Int. Ed.*, 2017, **56**, 9757–9761.

122 Z. Kang, Y. Peng, Z. Hu, Y. Qian, C. Chi, L. Y. Yeo, L. Tee and D. Zhao, *J. Mater. Chem. A*, 2015, **3**, 20801–20810.

123 H. X. Ang and L. Hong, *ACS Appl. Mater. Interfaces*, 2017, **9**, 28079–28088.

124 Z.-Q. Li, L.-G. Qiu, W. Wang, T. Xu, Y. Wu and X. Jiang, *Inorg. Chem. Commun.*, 2008, **11**, 1375–1377.

125 J. Yang, Z. Ma, W. Gao and M. Wei, *Chem.–Eur. J.*, 2017, **23**, 631–636.

126 Q. Yang, L. Zhou, Y.-X. Wu, K. Zhang, Y. Cao, Y. Zhou, D. Wu, F. Hu and N. Gan, *Anal. Chim. Acta*, 2018, **1020**, 1–8.

127 H. Xu, J. Gao, X. Qian, J. Wang, H. He, Y. Cui, Y. Yang, Z. Wang and G. Qian, *J. Mater. Chem. A*, 2016, **4**, 10900–10905.

128 L. J. Han, D. Zheng, S. G. Chen, H. G. Zheng and J. Ma, *Small*, 2018, **14**(17), e1703873.

129 L. He, F. Duan, Y. Song, C. Guo, H. Zhao, J.-Y. Tian, Z. Zhang, C.-S. Liu, X. Zhang, P. Wang, M. Du and S.-M. Fang, *2D Mater.*, 2017, **4**, 025098.

130 T. Yang, Y. N. Cui, H. Y. Chen and W. H. Li, *Acta Chim. Sin.*, 2017, **75**, 339–350.

131 S. Benmansour, A. Abherve, P. Gomez-Claramunt, C. Valles-Garcia and C. J. Gomez-Garcia, *ACS Appl. Mater. Interfaces*, 2017, **9**, 26210–26218.

132 N. Lahiri, N. Lotfizadeh, R. Tsuchikawa, V. V. Deshpande and J. Louie, *J. Am. Chem. Soc.*, 2017, **139**, 19–22.

133 Z. P. Sun, L. Hui, W. S. Ran, Y. Lu and D. Z. Jia, *New J. Chem.*, 2016, **40**, 1100–1103.

2 ♦

Aims and objectives

1 ....
2 ....
3 ....
a ....
b ....
c ....

Motivation

Metal-organic framework nanosheets (MONs) occupy an exciting junction in materials chemistry, at the interface between two-dimensional (2D) nanomaterials and metal-organic (MO) materials.[1] They benefit from a combination of properties shared with other 2D materials such as high aspect ratio and vast accessible surface area, whilst combining this with the possibilities offered from metal-organic materials: tunability and the unique chemistry of metal ions.

Controlling the surface properties of 2D materials is key to their performance but is often difficult to achieve. For example, graphene surfaces can be altered through the introduction of a relatively small number of functional groups (hydroxyl, aldehyde, carboxylic acid, for example), however this often occurs in a poorly defined way with limited control over position and quantity,[2] leading to disorder as well as defects within the 2D structure.[3] Surface functionalisation also disturbs the conjugated backbone which gives rise to the remarkable electronic and mechanical properties of graphene.[4] For example, the oxidation of graphene to graphene oxide results in a change from electrical conductor to insulator, and results in much lower thermal stability.[5]

MONs provide an exciting opportunity to establish a new class of 2D nanomaterials with controllable, tuneable surfaces. As outlined in **Chapter 1**, MONs are formed from inorganic nodes consisting of metal ions or clusters, known as secondary building units (SBUs), which are linked in two dimensions with multitopic organic ligands. The rich variety of organic linker ligands accessible through synthetic routes, a wide range of which are commercially available, combined with the properties offered from incorporation of different metals (such as magnetic, catalytic and electronic) mean that these materials are well-placed to occupy this vacant niche within materials chemistry.

At the onset of this project in 2016, the field of MONs was in its infancy, with a literature base of less than 60 papers which had been published gradually over the previous decade. Over the last three years, the literature on MONs has grown exponentially to now consist of more than 200 papers (Figure 1). Several reviews of the topic also appeared, initially in regards to structure and approaches to synthesis,[6–9] including applied uses,[1,10–15] and now specific applications.[16–20] This body of research sits within the wider context of 2D nanosheet development, which has accelerated rapidly since the discovery of graphene (Figure 2). It also takes inspiration from the rapidly developing field of three dimensional metal-organic frameworks (MOFs), of which there are now over 80,000 crystal structures within the Cambridge Crystallographic Data Centre (CCDC).[21]
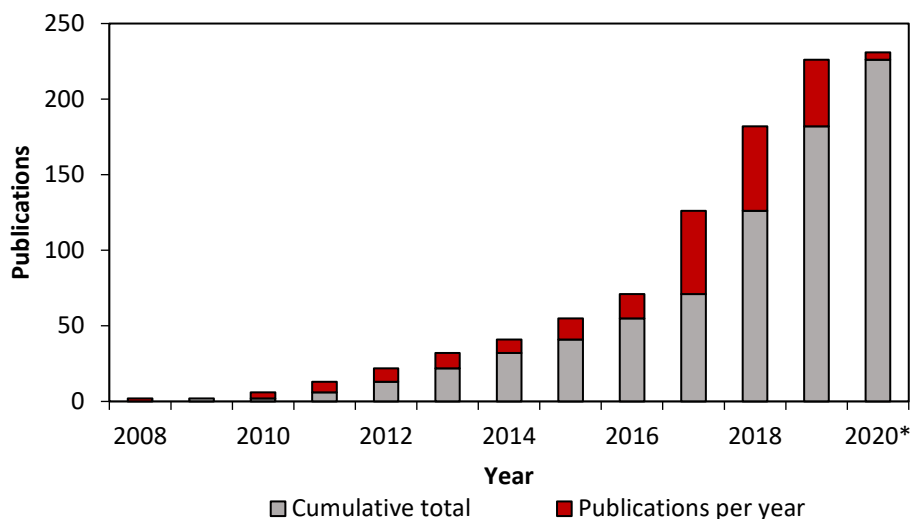
*Figure 1. Publications in which the main materials of study are MONs. Sourced from our in-house library. *Publication year is represented by articles' references, rather than articles' acceptance dates.*
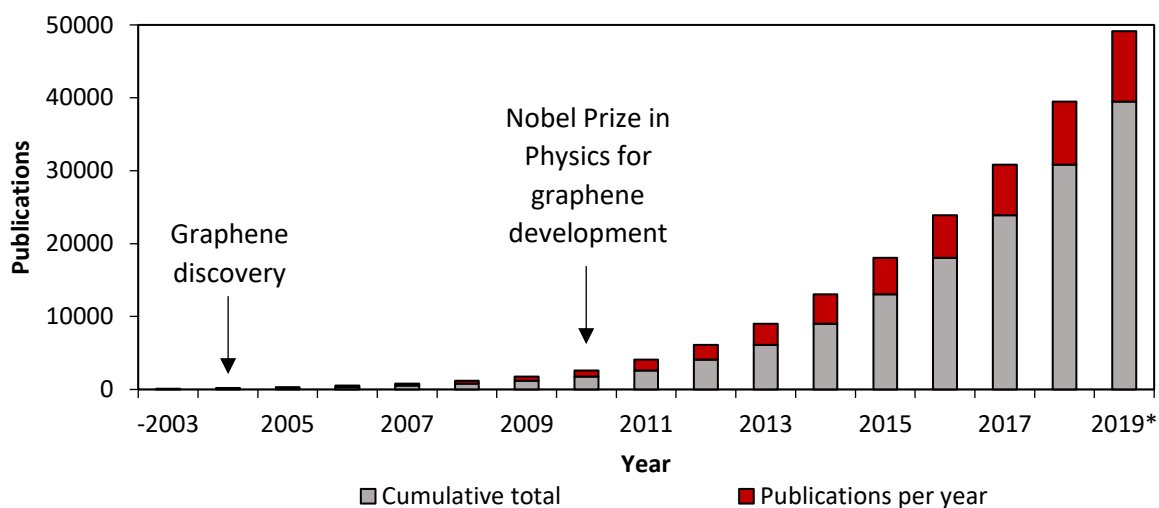

*Figure 2. Publications containing "nanosheets."[22] *01 Nov 2019. Scifinder, search term: containing "nanosheets," refined by document type to include journal and review, then refined by publication year.*

Research background

The research in this thesis builds on the work of Foster and Cheetham *et al.* who in 2016 presented a seminal example of a 2D MOF which incorporated ligands purposefully designed to aid exfoliation and affect the properties of the MONs formed.[23] In this work, layered MOFs were synthesised which used the dimetallic paddle-wheel (PW) SBU, linked with benzene-1,4-dicarboxylate (BDC) ligands, which had been difunctionalised in the 2- and 5-positions with methoxy propoxy- chains. The PW motif is formed of a dinuclear metal cluster in which the two metal ions are μ_2-bridged by four carboxylate ligands, giving a formula $M_2(O_2C\text{-})_4$.[24] PWs can be connected by using dicarboxylates such as BDC, to build up a 2D grid network, as typified by one of the early archetypal MOFs, MOF-2 - $[Zn(BDC)(H_2O).DMF]$.[25]

A single crystal structure obtained for $[Zn(fu\text{-}BDC)(DMF)]_n$, (fu=2,5-bis(3-methoxypropoxy)) revealed an in-plane structure of Zn(BDC), which formed a 2D **sql** grid network, similar to that of MOF-2. However, the methoxy-propoxy chains projected above/below the layer plane (Figure 3), which expanded layer separation from 5.3 Å in MOF-2 to 9.4 Å in this compound. The copper analogue was found to adopt an isostructural form with very similar unit cell parameters. These layered MOFs were then exfoliated using liquid ultrasonication to form MONs, and could be observed down to monolayer thickness (~1.4 nm) in the case of $[Cu(fu\text{-}BDC)(DMF)]_n$ when exfoliated in water. The copper analogue was used for further studies as syntheses using zinc produced a mixed phase consisting of the desired layered MOF as well as a functionalised derivative of the well-known MOF-5.[26]
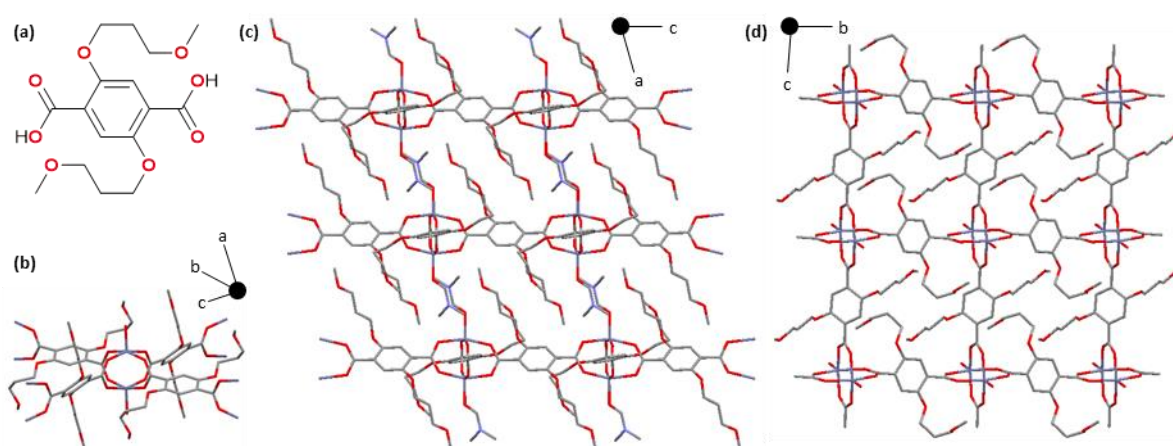

Figure 3. (a) fu-H₂BDC, fu= 2,5-bis(3-methoxypropoxy). Crystal structure of $[Zn(fu\text{-}BDC)(DMF)]_n$, illustrating the paddle-wheel motif (b) and viewed down the b-axis (c) and a-axis (d). Hydrogen atoms are omitted for clarity. DMF molecules are omitted in (b) and (d), other than the coordinating oxygen atoms. Zinc, carbon, oxygen and nitrogen atoms are in light blue, grey, red and dark blue, respectively. Crystal structure ref. no. 1460747, Cambridge Crystallographic Data Centre (CCDC).

Exfoliation in a range of solvents showed that the axial coordination site was relatively labile. DMF was replaced by H_2O when $[Cu(fu\text{-}BDC)(DMF)]_n$ was exfoliated in water, and was removed entirely when exfoliating in acetonitrile, acetone or ethanol. In each case, Pawley refinement of PXRD patterns showed that the layered form had been maintained. The lability of the axial site was then exploited for sensing pyridine in aqueous suspension (Figure 4).
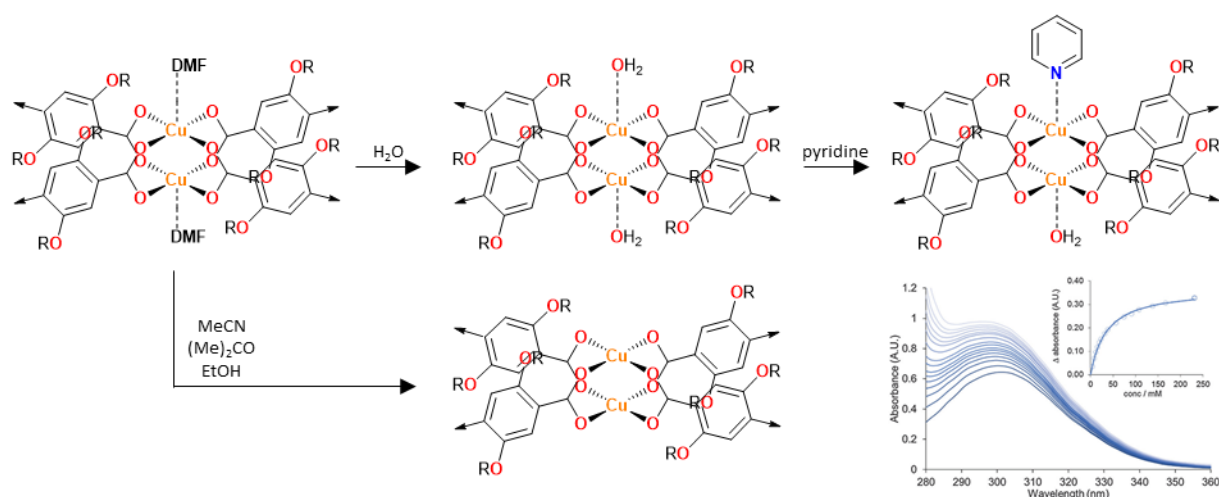
Figure 4. Ligand exchange/removal from the axial PW sites upon exfoliation in different solvents and sensing of pyridine from aqueous solution. R=$(CH_2)_3OCH_3$. Adapted with permission from reference [23]. Copyright 2016, Royal Society of Chemistry.

The work of Foster *et al.*, introduced different key aspects that are also utilised throughout this thesis. Building on the general introduction provided in **Chapter 1**, the following sections provide further background to topics which will be central to the work described within this thesis. In particular: [1] the structure of layered Cu_2-PW-based MOFs, [2] the chemical functionalisation of 2D MO materials and [3] liquid ultrasonic exfoliation of layered MOFs to form MONs.

Layered Cu₂-PW-based MOFs

The PW motif is adopted by a variety of simple metal salts, for example copper acetate monohydrate.[27] The PW was one of the first SBUs to be used within MOF syntheses.[25] Yaghi and co-workers reported "MOF-2" in 1998, which had a 2D **sql** grid network in which Zn_2-PWs were linked by BDC ligands. Water molecules were coordinated to the axial sites and there was additional DMF in the pores of the framework, yielding a structure of $[Zn(BDC)(H_2O).DMF]_n$. Carson *et al.* reported a structure similar to MOF-2 in 2009, in which zinc atoms were replaced by copper. The MOF synthesis proceeded in DMF, which was coordinated to the axial PW sites within the crystal structure, and there was no additional free solvent, *i.e.* $[Cu(BDC)(DMF)]_n$ (Figure 5).[28] Numerous different metals have been found to adopt the PW SBU, including first-row transition metals chromium, manganese, iron, cobalt, nickel, copper and zinc, as well as heavier metals such as ruthenium and tungsten, amongst others, as well as combinations of these within the same structure.[29]
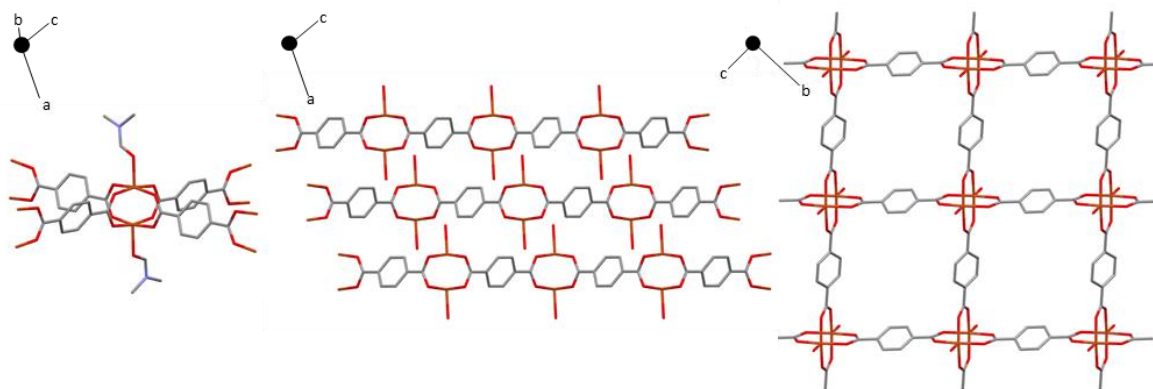
Figure 5. Crystal structure of Cu(BDC)(DMF) illustrating the paddle-wheel motif (left) and viewed down the b-axis (centre) and a-axis (right). Copper, carbon, oxygen and nitrogen atoms are portrayed in orange, grey, red and blue respectively. Hydrogen atoms are omitted for clarity. In the centre and right images, DMF molecules are hidden, apart from the coordinating oxygen. Crystal structure ref. no. 687690, Cambridge Crystallographic Data Centre (CCDC).

$[Cu(BDC)(DMF)]_n$ is a relatively robust MOF, thermally stable up to 160 °C, after which the labile DMF is lost and the structure rearranges to a non-layered form where the axial coordination sites of the PW are filled by an oxygen from a BDC ligand in the layer above and below.[28,30] This is in contrast to what Foster *et al*. observed for $[Cu(fu-BDC)(DMF)]_n$ (fu=methoxy-propoxy-), where the layered form is maintained after exfoliation, despite desolvation.[23] This is attributed to the increased sterics of the fu-BDC, relative to just BDC. The chains extend out of the layer plane and prevent the layer "slipping" and coming within the close proximity of the neighbouring layer above/below and so prevents this rearrangement.

The controlled synthesis of 2D layered materials such as these falls within the area of reticular chemistry, "*linking molecular building blocks by strong bonds to make crystalline open frameworks*."[31–33] The PW SBU coupled with linear dicarboxylates, such as BDC, allows prediction of 2D directional coordination connectivity. According to the principles of reticular chemistry, BDC can be replaced by functionalised derivatives to form isoreticular versions of the same framework. The concept of "isoreticular" chemistry was first demonstrated for MOF-5,[26] also known as IRMOF-1 (IR=isoreticular). BDC was substituted for longer or functionalised derivatives, but the same overall structure of $Zn_4O(O_2C-)_6$ SBUs linked in all three dimensions with fu-BDC remained.[34] In principle, the same idea can be used to build up a library of 2D layered MOFs with the in-plane **sql** network structure of M(fu-BDC). In 2D, this is somewhat complicated by the fact that fu-BDC derivatives will have an influence over the packing and layer stacking, and therefore produce different unit cells. For example, the isoreticular $[Cu(BDC)(DMF)]_n$[28] and $[Cu(2,5-dihydroxyBDC)(DMF)]_n$[35] crystallise in different space groups (C2/m and I2/m, respectively) and have similar but subtly different unit cells. This results in differences in interlayer spacing (5.22 Å and 5.27 Å, respectively).

Numerous authors have presented copper-based MOF structures that adopt the 2D layered PW-based **sql** structure, using mono, di or tetra fu-BDC (Figure 6), which could potentially be exfoliated to form fu-MONs. These are summarised in Table 1. There are also a significant number of examples of the desired 2D network being "pillared" by bidentate N-donor ligands (also see Table 1). Substitution of the pillaring ligand with monodentate ligands[36] could be used to isolate the desired 2D structure, or MOF syntheses could be altered to target the 2D layered structure directly.
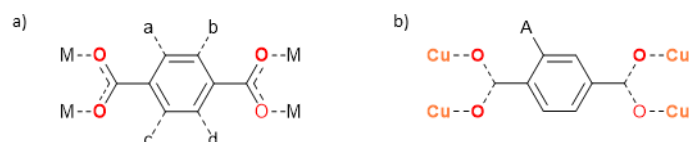
26

Figure 6. a) Sites of potential functionalisation (a-d) in benzene-1,4-dicarboxylate MONs, and b) structure used in CCDC search. A= "any non-H atom" and dashed bonds are type: any.

Table 1. Summary of benzene-1,4-dicarboxylate layered copper paddle-wheel based MOFs in the CCDC.

Ligand	CCDC number	Axial molecule	Uncoordinated molecules	Ref.
BDC	687690	DMF	-	[28]
1,4-NDC	744618	MeOH	MeOH	[37]
	744619	H_2O	H_2O	[37]
benzene-1,2,4,5-tetracarboxylate	640755	DMF	-	[38]
	669082	DMF	-	[39]
2-hydroxy-BDC	768340	H_2O	DEF	[40]
2-carboxy-BDC	235624	4,4'-bipyridine	-	[41]
2,5-dichloro-BDC	179115	DMF	DMF	[42]
2,5-dihydroxy-BDC	1860730	DMF	-	[35]
2,5-dimethoxy-BDC	898032	H_2O	EtOH	[43]
2,5-dicarboxy-BDC	891353	DMF	DMF	[44]
2,5-dipentoxy-BDC	1910582	DMF	-	Herein[45]
2,5-dibenzoyl-BDC and 4,6-dibenzoyl-1,3-dicarboxylate	796814	H_2O	-	[46]
2,3,5,6-tetrafluoro-BDC	235831	MeOH	-	[47]
	667992	DMF	DMF	[48]

Ligand	CCDC number	Pillaring ligand	Uncoordinated molecules	Ref.
1,4-NDC	260861	DABCO	-	[49]
2,3-difluoro-BDC	260860	DABCO	-	[50]
2,3-dimethoxy-BDC	260862	DABCO	-	[50]
2,3,5,6-tetrafluoro-BDC	236931	DABCO	-	[47]
1,4-NDC	930205	see ref	1,4-NDC, H_2O	[51]
	1053074	see ref	-	[52]
	1517721	see ref	-	[53]
9,10-anthracene dicarboxylate	1047271*	see ref	-	[54]

*This structure has a PW based 2D net, pillared with a long chain N-donor ligand. The structure is sufficiently large that it exists in a doubly interpenetrated form. Acronyms: BDC=benzene-1,4-dicarboxylate, 1,4-NDC= naphthalene-1,4-dicarboxylate, MeOH=methanol, EtOH=ethanol, DMF=*N,N*-dimethylformamide, DEF=*N,N*-diethylformamide, DABCO=1,4-diazobicyclo[2.2.2]octane.

In most cases of these 2D layered MOFs, the reaction solvent (H_2O or DMF) is coordinated at the axial PW positions. There are also a number of related materials in which M(fu-BDC) layers are pillared with DABCO, a commonly-used pillaring agent within MOF syntheses. It is worth highlighting that much of the focus around MOF design has been centred around gas storage applications,[55] making use of large pore spaces to capture atoms or gases. This means that the majority of frameworks are rigid 3D systems through design, although flexible systems are not uncommon.[56] PW-based layers are commonly pillared to form 3D MOFs as these provide rigid, defined pore spaces. Making use of fu-BDC can functionalise these frameworks to aid specific gas adsorption. As such, there is a significant body of literature surrounding these PW-fu-BDC layers, using metals including zinc, copper and cobalt, among others. Only the relevant examples of copper-based pillared PW-based MOFs are illustrated here in Table 1.

Most of the fu-BDC derivatives exemplified here incorporate only a limited range of functional groups. The Fischer group have designed series of fu-BDC linkers and studied the structure and gas adsorption properties of MOFs formed using Zn-PWs linked with fu-BDC and pillared with 4,4'-bipyridine or DABCO.[57–60] More complex functionalities, for example fu= 2,5-bis(^{i}propoxy), 2,5-bis(pentoxy) and 2,5-bis(prop-2-ynyloxy), allowed tuning of the network dynamics and responsiveness to gas uptake.[57] The introduction of more complex functionalities within 2D systems could have significant impact on their surface chemistry.

Surface functionalisation of MONs

MONs intrinsically have complex, non-uniform surface chemistries as they typically combine charged metal ions, electronegative atoms such as oxygen and nitrogen and aromatic organic linkers. However, at the onset of this project in 2016 there were no examples of intentional surface functionalisation, either pre- or post-synthetically, with intent to influence the surface chemistry and subsequent properties, or examples of isoreticular series designed to investigate the effects of specific functionalities. Since then, there have been numerous examples and strategies presented to influence surface chemistry through addition of functional groups, examples of which are discussed in the following section.

PW-based MONs

Gascon and coworkers presented a novel layered synthesis method for the bottom-up synthesis of $[Cu(BDC)(DMF)]_n$ MONs in 2015.[61] As well as demonstrating the utility of the approach by synthesising isostructural Co or Zn analogues, they showed that isoreticular MONs using 1,4- and 2,6-naphthalene dicarboxylate could be formed. In 2018, the same synthetic method was used to synthesise $[Cu(ABDC)(DMF)]_n$ MONs (ABDC = 2-amino-benzene-1,4-dicarboxylate).[62]

Recently, in an adaption of the polymer-assisted bottom-up synthetic methodology (see **Chapter 1**),[1,13] Zhang *et al.* demonstrated a pre-synthetic functionalisation of ABDC with polyvinylpyrrolidone (PVP).[63] A bottom-up synthesis of $[Ni(PVP-ABDC)(DMF)]_n$ directly crystallised monolayer MONs, as the surface PVP prevented epitaxial layer growth. Conversely, Nicks and Foster *et al.*, recently demonstrated the post-synthetic functionalisation of $[Cu(ABDC)(DMF)]_n$ by reacting 1,3-propanesultone with the projecting amine groups (Figure 7).[64] This resulted in improved exfoliation down to monolayer MONs, which was hypothesised to result from the introduction of charge and subsequent layer repulsion, meanwhile additionally imparted the MONs with multiple different active catalytic sites (acidic and basic) which were exploited for tandem catalysis.
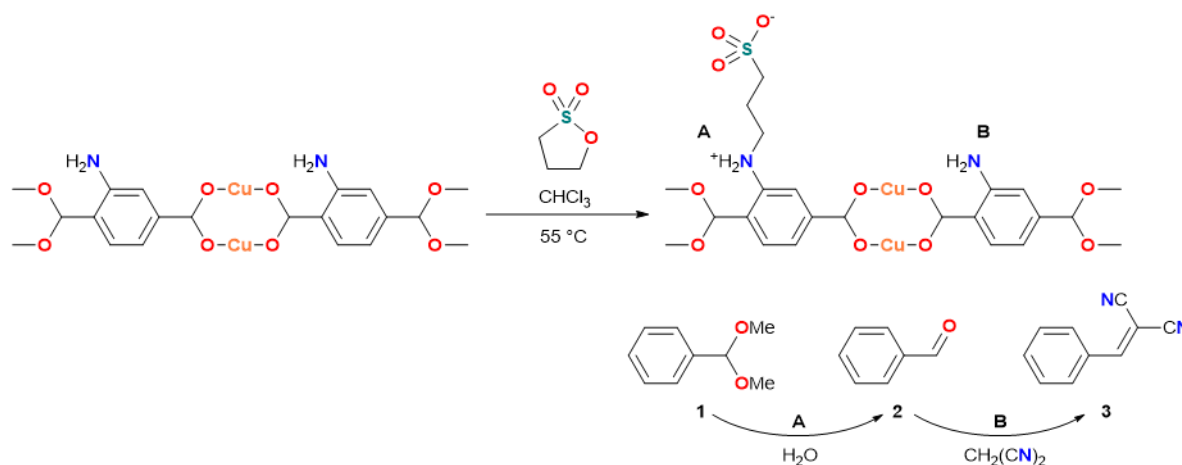

Figure 7. PSF of $[Cu(ABDC)(DMF)]n$ with 1,3-propanesultone, and subsequent tandem acid-base catalysis of benzaldehyde dimethyl acetal (1) to form benzaldehyde (2) then benzylidene malononitrile (3).[64]

Banerjee and coworkers presented one of the first systematic studies into the effect of different functional groups on the exfoliation of MOFs to MONs in 2017.[65] fu-benzene-1,3-dicarboxylates (fu=OMe, OEt or O^{n}Pr) linked Cu_2-PWs to first make crystals of discrete metal-organic polyhedra (Figure 8). These polyhedra then underwent a transformation to layered MOFs upon addition of a

certain amount of water. Further exposure to excess water resulted in spontaneous exfoliation to form thin few-layer MONs. The MOP-MOF transformation was through an amorphous intermediate, which the authors suggest was due to the action of the hydrophobic alkoxy functionalitiess. MOP units "unfold" upon contact with water due to a combination of hydrophobic repulsion and hydration pressure. With limited water content this process was controlled, and unfolded MOP units join to form crystals of extended 2D MOF. However, with higher water content the full layer stacking was prevented, which resulted in MON formation. Although not applied to anything, this demonstrates the use of functionalised BDC ligands driving the creation of hydrophobic surfaces. However, there was no observable trend on the extent of exfoliation across the series. Average heights of observed MONs were 15.3±1.2, 17.2±1.1, and 11.8±0.6 nm for -OMe, -OEt and -O^{n}Pr respectively, corresponding to 6-8 layers. Au *et al*. incorporated 5-methylthioisophthalate ligands into a similar structure in which the methylthio-groups projected above/below the layer plane.[66] Immersion of layered crystals in THF resulted in spontaneous exfoliation to monolayers. Numerous other solvents were used for structure expansion (which lead to auto-exfoliation) and authors found the best correlation of expansion with surface tension of the solvent, suggesting this may have an important role in how well a layered MOF exfoliates to form MONs.
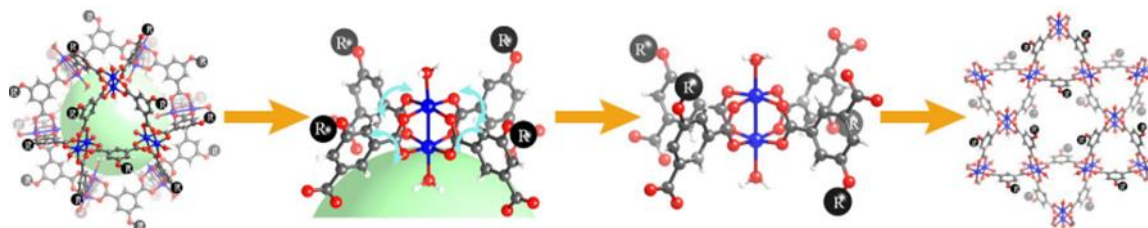

Figure 8. The mechanism for the conversion of alkyloxy-decorated MOPs into layered MOFs. Adapted with permission from reference [65]. Copyright 2017, Wiley-VCH.

Non PW-based MONs

Cheetham and co-workers demonstrated in a series of papers the exfoliation of several dimethylsuccinate based MOFs to form MONs, in which the methyl groups are directed out of the layer plane, which creates hydrophobic surfaces.[67–69] Zhou and coworkers demonstrated that monolayer MONs could be formed through ligand exchange of methylated pyridines for pillaring 4,4'-bipyridine (Figure 9), which resulted in MONs with hydrophobic surfaces that were exploited for oil/water separations.[36]
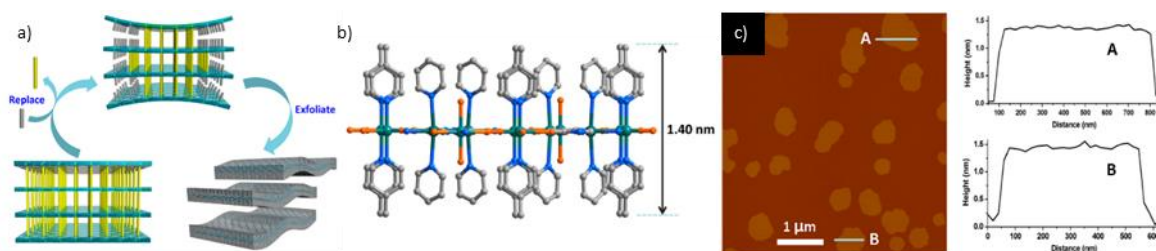

Figure 9. a) Schematic showing production of MONs through ligand exchange. b) Monolayer structure of the MON. c) AFM topographical image of MONs deposited on mica, with height plots of the vectors A and B indicated. Adapted with permission from reference [36]. Copyright 2019, American Chemical Society.

Functionalisation of MONs with metal nanoparticles has been shown to be an effective way to introduce new functionality. The Zhang and Lu groups have adopted different approaches to incorporating Au nanoparticles within MONs.[70,71] Zhang's group grew Au nanoparticles with glucose oxidase-like activity on Cu-TCPP(M) MONs (TCPP= tetrakis(4-carboxyphenyl)porphyrin, M = Fe, Co) with peroxidase-like activity, producing hybrid MONs that could be used for a biomimetic artificial enzymatic cascade reaction, as well as biomolecular detection.[70] Lu and coworkers loaded MONs with Au precursor $HAuCl_4$ which was then reduced, immobilizing ultra-small 1 nm diameter Au nanoparticles within the MON, forming nanocomposites.[71] These were used as highly active catalysts towards the reduction of 4-nitrophenol with $NaBH_4$ in H_2O, with excellent recyclability. Quan and coworkers anchored Fe_3O_4 and Au nanoparticles onto the surface of MONs which improved catalytic ability, and demonstrated their potential as colorimetric sensors and biocompatible H_2O_2 sensors with promise to use as biological diagnostics.[72]

Notably, the Lin research group have demonstrated post-synthetic functionalisation (PSF) through metalation of MONs to introduce various functionalities.[73–75] The incorporation of ligands within the MON structure with additional potentially coordinating sites (Figure 10) allowed PSF with $CoCl_2$ or $FeBr_2$, $Ir(ppy)_2^+$ (ppy= 2-phenylpyridine), and $Re/Mn(CO)_3(X)$ (X=Cl or Br), for improved benzylic C–H borylation and C_{sp3}–H amination catalysis,[73] photopolymerisation,[74] and photocatalytic CO_2 reduction,[75] respectively.
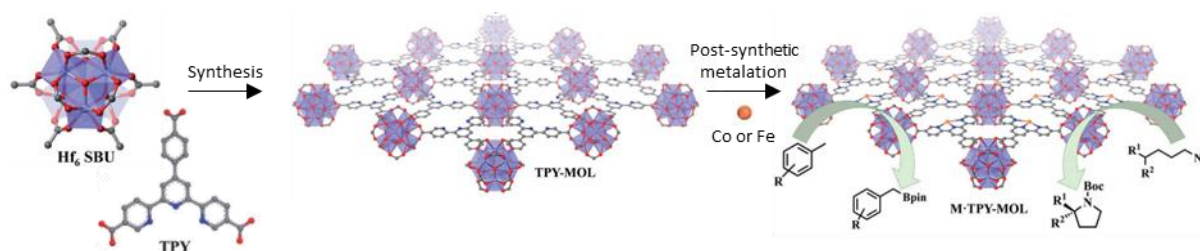

Figure 10. Schematic of M(TPY) (M= Hf$_6$ SBU, TPY= 4'-(4-carboxyphenyl)-[2,2':6',2''-terpyridine]-5,5''-dicarboxylate) MON synthesis and post-synthetic metalation with Co or Fe for benzylic C–H borylation and intramolecular sp^3 C–H amination reactions, respectively. Adapted with permission from reference [73]. Copyright 2017, Royal Society of Chemistry.

The recent work of López-Cabrelles *et al*. demonstrated a series of isoreticular layered MOFs with the structure [Fe(fu-BIM)$_2$]$_n$, where fu-BIM= functionalised benzimidazole, which was functionalised in the 5-position with H, Cl, Br, CH_3, or NH_2 (Figure 11).[76] Each material is isostructural, and fu-moieties project above and below the layer plane. MOFs were exfoliated using the micromechanical Scotch-tape method down to monolayer thickness. The differing functionalities afforded the MONs with different surface properties, exemplified by the difference in hydrophilicity portrayed through contact angle measurements (Figure 11). Additionally, the magnetic properties of the MONs remained constant despite the introduced functionalities. This is an important demonstration of controllable surface modification, as it demonstrates that selection of appropriate ligand functionalisations can affect MON surface chemistry, and paves the way for increased chemical control of surface properties.
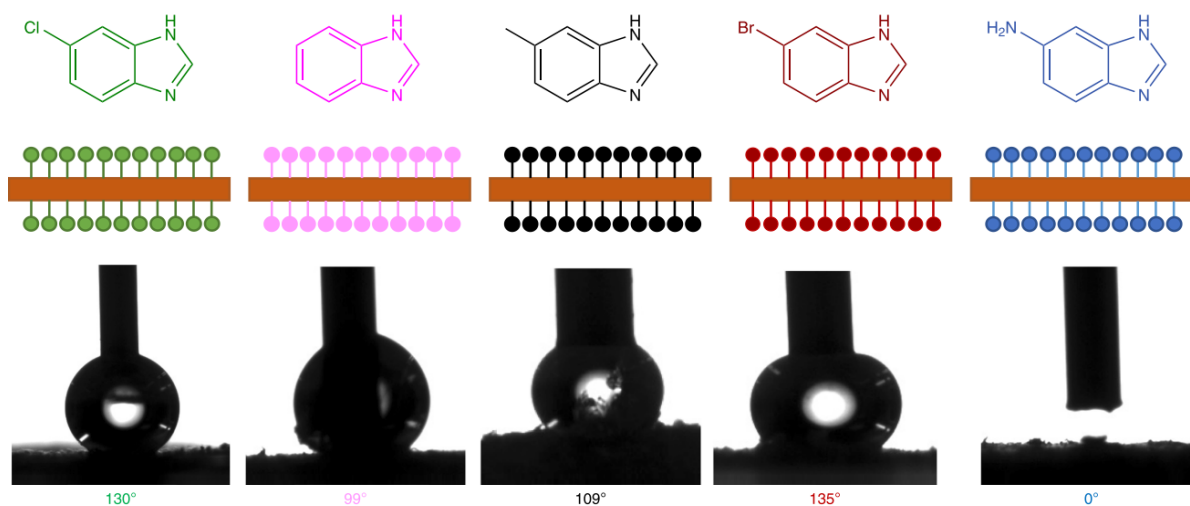
Figure 11. top) The different fu-benzimidazole derivative ligands used within the series of isoreticular 2D frameworks, with middle) schematic of individual functionalised layers. bottom) Water droplets in contact with a surface of deposited MONs, used for contact angle measurements. Reproduced with permission from reference [76]. Copyright 2018, Springer Nature.

Liquid ultrasonic exfoliation to form MONs

Synthetic methods of MON production can be split into two approaches: bottom-up and top-down methodologies (Figure 12a, and Figure 3 in **Chapter 1**).[1] These methods have been presented extensively previously in this thesis,[13] as well as elsewhere since.[1,14,15,19,77,78] Broadly speaking, bottom-up methodologies target the direct synthesis of MONs from constituent metal atoms and organic linker ligands, producing high quality, ultrathin nanosheets in small quantities, often with long or relatively complex synthetic procedures. Top-down methods isolate MONs from layered MOFs, through various delaminative processes which are generally termed "exfoliations."[79, a] This is conceptually analogous to separating individual cards from a deck. These methods commonly produce large distributions of particle sizes, both in terms of lateral dimensions as well as heights. Typically, these methods are more scalable, as MOF syntheses can be straightforward and in large scale, and exfoliating methods can be designed with potential scalability in mind.

Liquid ultrasonic exfoliation is a widely used exfoliative technique that has been applied to exfoliate other layered materials such as graphite, hexagonal boron-nitride, metal oxides and chalcogenides to form nanosheets.[79,80] Ultrasonication of layered MOFs in solvents has been widely used for MON synthesis, and is a potentially scalable method of exfoliation, through parallel operation for high volume production.
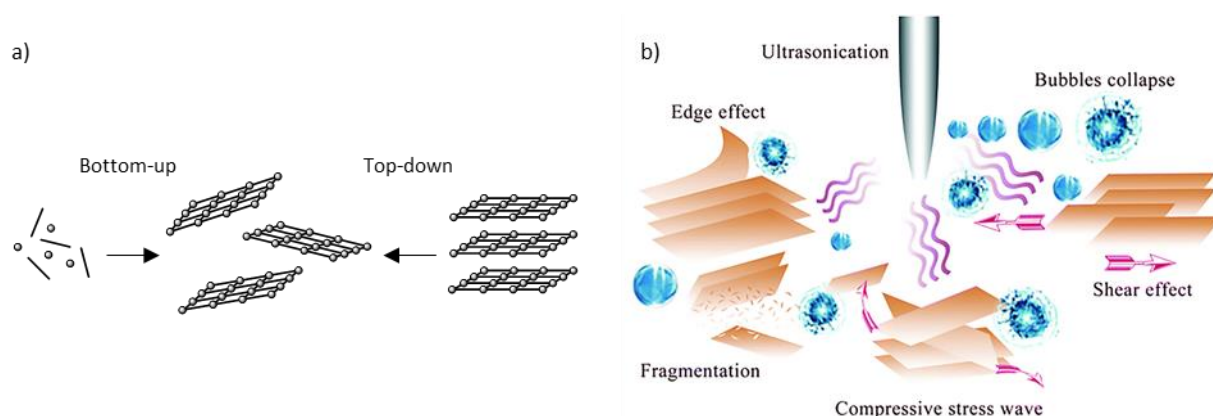

Figure 12. a) Schematic of MON synthesis approaches. b) Modes of exfoliation through ultrasonication. Adapted with permission from reference [81]. *Copyright 2017, Royal Society of Chemistry.*

To produce MONs through liquid ultrasonic exfoliation, shear forces are exerted on MOF particles, which originate from acoustic cavitations resulting from microbubble collapse.[82] This produces instantaneous temperatures up to 5000 K, localised pressures up to 20 MPa and heating/cooling rates up to 10^9 K s^{-1}. The modes of exfoliation from these effects are summarised in Figure 12b.[81] However, the process of exfoliation and factors that govern or affect how "well" it proceeds are not well understood. The process has not previously been optimised for the exfoliation of MOFs to MONs, with numerous authors using ultrasonic probes or baths with various powers, for varying lengths of time, at various temperatures. This clearly is not conducive to comparing the relative successes of exfoliation across different systems.

---

[a] The Oxford Dictionary defines "exfoliate" as *verb*, (of a material) be shed from a surface in scales or layers.

Factors that affect exfoliation of MOFs to MONs are not well understood. Peng *et al*. reported a mixture of methanol and propanol as best exfoliating $[Zn(bim)_2]_n$.[83] They hypothesised that the small methanol molecules were able to penetrate into layers, whilst propanol adsorbed onto the surface of the nanosheets through its hydrophobic tail, which also helped to stabilise the MONs in suspension. Junggeburth *et al*. noted that the hydrophobic layered MOF $[Zn(bim)(OAc)]_n$ showed decreasing exfoliation in THF>toluene>CHCl$_3$, and that exfoliation in polar solvents H$_2$O and DMF were unsuccessful, due to apparent inefficient penetration of the framework.[84] Moorthy *et al*., found a correlation between the Gutmann's hydrogen-bond-accepting parameter of the solvent used as the liquid media, and the concentration of MON (which used a ligand with both hydrogen bond donating and accepting positions) following exfoliation.[85] As discussed in Section 2.2, Au *et al*. recently found a correlation between solvent surface tension and auto-exfoliation of $[Cu(SMe-ip)(H_2O)]_n$ (ip=isophthalate) (i.e. no sonication was required).[66] Clearly, the factors that govern exfoliation of layered MOFs to form MONs are complex, and there may not be a single factor which determines how well a layered MOF may exfoliate.

As sonication is a non-chemical top-down method, it can be consistently applied to many different systems, with the same expected general effect of exfoliation to form MONs. This makes it a good method to use for the investigations presented herein, which will involve multiple systems as well as different solvent systems used as the liquid medium for exfoliation.

Aims

This thesis aims to introduce MONs as 2D materials with controllable properties and tuneable surface chemistry. The Cu_2-PW based system (Figure 13) provides an opportunity for systematically varying the functionalisation of the BDC ligands in order to affect exfoliation as well as influence MON properties. Specifically, series of isoreticular MOFs based on the 2D layer structure of Cu_2-PWs linked with fu-BDC ligands will be synthesised with the aim to use liquid ultrasonic exfoliation to produce MONs. The nanoscopic, molecular and macroscopic structure of MONs will then be characterised.
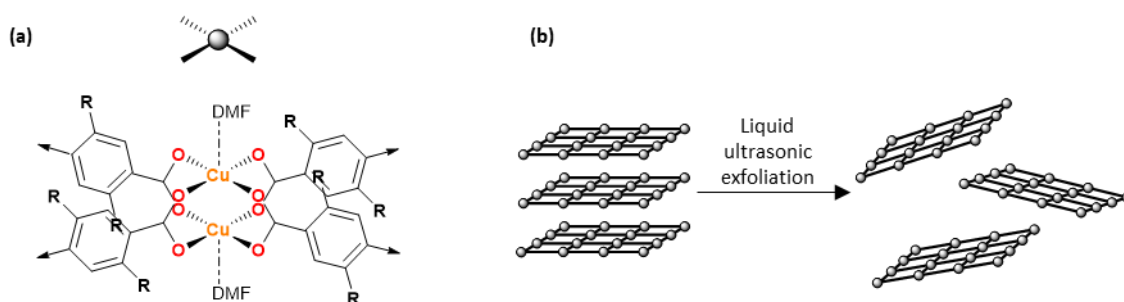

Figure 13. (a) Schematic of the Cu_2-PW SBU using fu-BDC ligands. (b) Schematic of liquid ultrasonic exfoliation of layered MOFs to form MONs.

This thesis is structured around four papers that test hypotheses on the effects of different functionalised BDC derivatives on the exfoliation of layered MOFs to form MONs, and the properties of MONs formed:

1) How does changing the hydrophobicity of BDC functionalised with either alkoxy or alkylether chains influence MON production? (**Chapter 3**)

2) How does altering the length of alkoxy chain functionalisation affect MONs formed? (**Chapter 4**)

3) Can multiple different BDC ligands functionalised with chains be incorporated into a layered MOF, and how does this affect the exfoliation and MONs formed? (**Chapter 5**)

4) Can other small functional moieties (e.g. NH_2, Cl_2, Br_2, NO_2) be introduced and how does this affect MON formation? Can these ligands be used in combination within a system, and what affect does this have? (**Chapter 6**)

In order to understand the effects of the changes in ligand structure on the exfoliation of MOFs and MONs, several underpinning methods must first be developed.

i. Develop a standard operating procedure for the liquid ultrasonic exfoliation of layered MOF which can be followed to allow comparison between exfoliation studies across different solvents and MOF systems.

ii. Develop techniques to capture and present information of the height, lateral size, aspect ratio and concentration of MONs produced through liquid ultrasonic exfoliation in a quantitative manner.

References

1   M. Zhao, Y. Huang, Y. Peng, Z. Huang, Q. Ma and H. Zhang, *Chem. Soc. Rev.*, 2018, **47**, 6267–6295.

2   G. Bottari, M. Ángeles Herranz, L. Wibmer, M. Volland, L. Rodríguez-Pérez, D. M. Guldi, A. Hirsch, N. Martín, F. D'Souza and T. Torres, *Chem. Soc. Rev.*, 2017, **46**, 4464–4500.

3   A. Lerf, H. He, M. Forster and J. Klinowski, *J. Phys. Chem. B*, 1998, **102**, 4477–4482.

4   L. Yan, Y. B. Zheng, F. Zhao, S. Li, X. Gao, B. Xu, P. S. Weiss and Y. Zhao, *Chem. Soc. Rev.*, 2012, **41**, 97–114.

5   D. R. Dreyer, S. Park, C. W. Bielawski and R. S. Ruoff, *Chem. Soc. Rev.*, 2010, **39**, 228–240.

6   H. Maeda, R. Sakamoto and H. Nishihara, *Langmuir*, 2016, **32**, 2527–2538.

7   D. Rodríguez-San-Miguel, P. Amo-Ochoa and F. Zamora, *Chem. Commun.*, 2016, **52**, 4113–4127.

8   R. Sakamoto, K. Takada, X. Sun, T. Pal, T. Tsukamoto, E. J. H. Phua, A. Rapakousiou, K. Hoshiko and H. Nishihara, *Coord. Chem. Rev.*, 2016, **320**–**321**, 118–128.

9   M. Zhao, Q. Lu, Q. Ma and H. Zhang, *Small Methods*, 2017, **1**, 1600030.

10   R. Sakamoto, K. Takada, T. Pal, H. Maeda, T. Kambe and H. Nishihara, *Chem. Commun.*, 2017, **53**, 5781–5801.

11   C. Tan, X. Cao, X. J. Wu, Q. He, J. Yang, X. Zhang, J. Chen, W. Zhao, S. Han, G. H. Nam, M. Sindoro and H. Zhang, *Chem. Rev.*, 2017, **117**, 6225–6331.

12   M. Xu, S. S. Yang and Z.-Y. Gu, *Chem. - A Eur. J.*, 2018, 15131–15142.

13   D. J. Ashworth and J. A. Foster, *J. Mater. Chem. A*, 2018, **6**, 16292–16307.

14   J. Liu, H. Yu, L. Wang, Z. Deng, K. ur R. Naveed, A. Nazir and F. Haq, *Inorganica Chim. Acta*, 2018, **483**, 550–564.

15   J. Duan, Y. Li, Y. Pan, N. Behera and W. Jin, *Coord. Chem. Rev.*, 2019, **395**, 25–45.

16   T. Yang, Y. Cui, H. Chen and W. Li, *Acta Chim. Sin.*, 2017, **75**, 339.

17   S. Kim, H. Wang and Y. M. Lee, *Angew. Chemie Int. Ed.*, , DOI:10.1002/anie.201814349.

18   A. Dhakshinamoorthy, A. M. Asiri and H. Garcia, *Adv. Mater.*, 2019, **31**, 1900617.

19   T. Hyun, J. Jeong, A. Chae, Y. K. Kim and D.-Y. Koh, *BMC Chem. Eng.*, 2019, **1**, 1–26.

20   W. Zhao, J. Peng, W. Wang, S. Liu, Q. Zhao and W. Huang, *Coord. Chem. Rev.*, 2018, **377**, 44–63.

21   P. Z. Moghadam, A. Li, S. B. Wiggin, A. Tao, A. G. P. Maloney, P. A. Wood, S. C. Ward and D. Fairen-Jimenez, *Chem. Mater.*, 2017, **29**, 2618–2625.

22   SciFinder, Chemical Abstracts Service, http://www.cas.org/products/scifinder, (accessed 26 September 2019).

23   J. A. Foster, S. Henke, A. Schneemann, R. A. Fischer and A. K. Cheetham, *Chem. Commun.*, 2016, **52**, 10474–10477.

24   M. Eddaoudi, D. B. Moler, H. Li, B. Chen, T. M. Reineke, M. O'Keeffe and O. M. Yaghi, *Acc. Chem.*

Res., 2001, **34**, 319–330.

25 H. Li, M. Eddaoudi, T. L. Groy and O. M. Yaghi, *J. Am. Chem. Soc.*, 1998, **120**, 8571–8572.

26 H. Li, M. Eddaoudi, M. O'Keeffe and O. M. Yaghi, *Nature*, 1999, **402**, 276–279.

27 G. M. Brown and R. Chidambaram, *Acta Crystallogr.*, 1973, **B29**, 2393–2403.

28 C. G. Carson, K. Hardcastle, J. Schwartz, X. Liu, C. Hoffmann, R. A. Gerhardt and R. Tannenbaum, *Eur. J. Inorg. Chem.*, 2009, **16**, 2338–2343.

29 D. J. Tranchemontagne, J. L. Mendoza-Cortés, M. O'Keeffe and O. M. Yaghi, *Chem. Soc. Rev.*, 2009, **38**, 1257–1283.

30 C. G. Carson, G. Brunnello, S. G. Lee, S. S. Jang, R. A. Gerhardt and R. Tannenbaum, *Eur. J. Inorg. Chem.*, 2014, 2140–2145.

31 O. M. Yaghi, M. O'Keeffe, N. W. Ockwig, H. K. Chae, M. Eddaoudi and J. Kim, *Nature*, 2003, **423**, 705–714.

32 O. M. Yaghi, *J. Am. Chem. Soc.*, 2016, **138**, 15507–15509.

33 O. M. Yaghi, *ACS Cent. Sci.*, 2019, **5**, 1295–1300.

34 M. Eddaoudi, J. Kim, N. Rosi, D. Vodak, J. Wachter, M. O'Keeffe and O. M. Yaghi, *Science*, 2002, **295**, 469–472.

35 L. Asgharnejad, A. Abbasi, M. Najafi and J. Janczak, *J. Solid State Chem.*, 2019, **277**, 187–194.

36 J.-H. Deng, Y.-Q. Wen, J. Willman, W.-J. Liu, Y.-N. Gong, D.-C. Zhong, T.-B. Lu and H.-C. Zhou, *Inorg. Chem.*, 2019, **58**, 11020–11027.

37 P. Kanoo, K. L. Gurunatha and T. K. Maji, *J. Mater. Chem.*, 2010, **20**, 1322–1331.

38 H. K. Zhao, B. Ding, E. C. Yang, X. G. Wang and X. J. Zhao, *Z. Anorg. Allg. Chem*, 2007, **633**, 1735–1738.

39 A. F. J. Æ. X. L. Æ., M. R. Hassan, Æ. G. M. G. Hossain, A. F. Jalbout, X. H. Li, M. R. Hassan and G. M. Golzar Hossain, *Transit. Met. Chem.*, 2008, **33**, 597–603.

40 Z. Chen, S. Xiang, H. D. Arman, P. Li, S. Tidrow, D. Zhao and B. Chen, *Eur. J. Inorg. Chem.*, 2010, 3745–3749.

41 L. Wang, M. Yang, Z. Shi, Y. Chen and S. Feng, *J. Solid State Chem.*, 2005, **178**, 3359–3365.

42 M. Eddaoudi, J. Kim, D. Vodak, A. Sudik, J. Wachter, M. O'Keeffe and O. M. Yaghi, *Proc. Natl. Acad. Sci. U. S. A.*, 2002, **99**, 4900–4904.

43 Z. Guo, M. V. Reddy, B. M. Goh, A. K. P. San, Q. Bao and K. P. Loh, *RSC Adv.*, 2013, **3**, 19051–19056.

44 C. Yuste-Vivas, M. Ramos Silva, P. Martín-Ramos, L. C. J. Pereira, J. Ferrando-Soria, P. Amorós and M. Julve, *Polyhedron*, 2015, **87**, 220–225.

45 D. J. Ashworth, T. M. Roseveare, A. Schneemann, M. Flint, I. Dominguez Bernáldes, P. Vervoorts, R. A. Fischer, L. Brammer and J. A. Foster, *Inorg. Chem.*, 2019, **58**, 10837–10845.

46 Y. Pang, D. Tian, Y. Luo, X. Zhu and H. Zhang, *J. Coord. Chem.*, 2011, **64**, 2002–2009.

47 R. Kitaura, F. Iwahori, R. Matsuda, S. Kitagawa, Y. Kubota, M. Takata and T. C. Kobayashi, *Inorg. Chem.*, 2004, **43**, 6522–6524.

48   E.-J. Zhu, Q. Liu, Q. Chen, M.-Y. He, S.-C. Chen, H.-X. Huang and Q. Yang, *Chinese J. Inorg. Chem.*, 2008, **24**, 1428.

49   S. Furukawa, K. Hirai, K. Nakagawa, Y. Takashima, R. Matsuda, T. Tsuruoka, M. Kondo, R. Haruki, D. Tanaka, H. Sakamoto, S. Shimomura, O. Sakata and S. Kitagawa, *Angew. Chemie - Int. Ed.*, 2009, **48**, 1766–1770.

50   R. Matsuda, W. Kosaka, R. Kitaura, Y. Kubota, M. Takata and S. Kitagawa, *Microporous Mesoporous Mater.*, 2014, **189**, 83–90.

51   X. L. Wang, J. Luan, H. Y. Lin, Q. L. Lu, M. Le and G. C. Liu, *J. Mol. Struct.*, 2014, **1074**, 441–448.

52   L. Yang, C. Qin, B. Q. Song, X. Li, C. G. Wang and Z. M. Su, *CrystEngComm*, 2015, **17**, 4517–4524.

53   L. Yang, X. Li, C. Y. Sun, H. Wu, C. G. Wang and Z. M. Su, *New J. Chem.*, 2017, **41**, 3661–3666.

54   H. Y. Lin, X. Z. Zhao, L. Zeng, Q. L. Wang, X. L. Wang and G. C. Liu, *Aust. J. Chem.*, 2015, **68**, 1550–1561.

55   M. Ding, R. W. Flaig, H. L. Jiang and O. M. Yaghi, *Chem. Soc. Rev.*, 2019, **48**, 2783–2828.

56   Z. Chang, D. H. Yang, J. Xu, T. L. Hu and X. H. Bu, *Adv. Mater.*, 2015, **27**, 5432–5441.

57   S. Henke, A. Schneemann, A. Wütscher and R. A. Fischer, *J. Am. Chem. Soc.*, 2012, **134**, 9464–9474.

58   J. M. Chem, S. Henke, A. Schneemann, S. Kapoor, R. A. Fischer, R. Winter and R. A. Fischer, *J. Mater. Chem.*, 2012, **22**, 909–918.

59   S. Henke, A. Schneemann, S. Kapoor, R. Winter and R. A. Fischer, *J. Mater. Chem.*, 2012, **22**, 909–918.

60   S. Henke and R. A. Fischer, *J. Am. Chem. Soc.*, 2011, **133**, 2064–2067.

61   T. Rodenas, I. Luz, G. Prieto, B. Seoane, H. Miro, A. Corma, F. Kapteijn, F. X. Llabrés i Xamena and J. Gascon, *Nat. Mater.*, 2015, **14**, 48–55.

62   S. Hu, J. Yan, X. Huang, L. Guo, Z. Lin, F. Luo, B. Qiu, K. Y. Wong and G. Chen, *Sensors Actuators B Chem.*, 2018, **267**, 312–319.

63   X. Zhang, L. Chang, Z. Yang, Y. Shi, C. Long, J. Han, B. Zhang, X. Qiu, G. Li and Z. Tang, *Nano Res.*, 2019, **12**, 437–440.

64   J. Nicks, J. Zhang and J. A. Foster, *Chem. Commun.*, 2019, **55**, 8788–8791.

65   B. Garai, A. Mallick, A. Das, R. Mukherjee and R. Banerjee, *Chem. - A Eur. J.*, 2017, **23**, 7361–7366.

66   V. K. M. Au, K. Nakayashiki, H. Huang, S. Suginome, H. Sato and T. Aida, *J. Am. Chem. Soc.*, 2019, **141**, 53–57.

67   P. J. Saines, M. Steinmann, J. C. Tan, H. H. M. Yeung, W. Li, P. T. Barton and A. K. Cheetham, *Inorg. Chem.*, 2012, **51**, 11198–11209.

68   J. C. Tan, P. J. Saines, E. G. Bithell and A. K. Cheetham, *ACS Nano*, 2012, **6**, 615–621.

69   P. J. Saines, J. C. Tan, H. H. M. Yeung, P. T. Barton and A. K. Cheetham, *Dalt. Trans.*, 2012, **41**, 8585–8593.

70   Y. Huang, M. Zhao, S. Han, Z. Lai, J. Yang, C. Tan, Q. Ma, Q. Lu, J. Chen, X. Zhang, Z. Zhang, B. Li,

B. Chen, Y. Zong and H. Zhang, *Adv. Mater.*, 2017, **29**, 1–5.

71   R. Yan, Y. Zhao, H. Yang, X. J. Kang, C. Wang, L. L. Wen and Z. Da Lu, *Adv. Funct. Mater.*, 2018, **28**, 1–8.

72   B. Tan, H. Zhao, W. Wu, X. Liu, Y. Zhang and X. Quan, *Nanoscale*, 2017, **9**, 18699–18710.

73   Z. Lin, N. C. Thacker, T. Sawano, T. Drake, P. Ji, G. Lan, L. Cao, S. Liu, C. Wang and W. Lin, *Chem. Sci.*, 2017, **9**, 143–151.

74   R. Xu, Z. Cai, G. Lan and W. Lin, *Inorg. Chem.*, 2018, **57**, 10489–10493.

75   G. Lan, Z. Li, S. S. Veroneau, Y.-Y. Zhu, Z. Xu, C. Wang and W. Lin, *J. Am. Chem. Soc.*, 2018, **140**, 12369–12373.

76   J. López-Cabrelles, S. Mañas-Valero, I. J. Vitórica-Yrezábal, P. J. Bereciartua, J. A. Rodríguez-Velamazán, J. C. Waerenborgh, B. J. C. Vieira, D. Davidovikj, P. G. Steeneken, H. S. J. van der Zant, G. Mínguez Espallargas and E. Coronado, *Nat. Chem.*, 2018, **10**, 1001–1007.

77   L. Cao, T. Wang and C. Wang, *Chinese J. Chem.*, 2018, **36**, 754–764.

78   M. A. Solomos, F. J. Claire and T. J. Kempa, *J. Mater. Chem. A*, 2019, **7**, 23537–23562.

79   C. Backes, T. M. Higgins, A. Kelly, C. Boland, A. Harvey, D. Hanlon and J. N. Coleman, *Chem. Mater.*, 2017, **29**, 243–255.

80   J. N. Coleman, M. Lotya, A. O'Neill, S. D. Bergin, P. J. King, U. Khan, K. Young, A. Gaucher, S. De, R. J. Smith, I. V. Shvets, S. K. Arora, G. Stanton, H.-Y. Kim, K. Lee, G. T. Kim, G. S. Duesberg, T. Hallam, J. J. Boland, J. J. Wang, J. F. Donegan, J. C. Grunlan, G. Moriarty, A. Shmeliov, R. J. Nicholls, J. M. Perkins, E. M. Grieveson, K. Theuwissen, D. W. McComb, P. D. Nellist and V. Nicolosi, *Science*, 2011, **331**, 568–571.

81   H. Tao, Y. Zhang, Y. Gao, Z. Sun, C. Yan and J. Texter, *Phys. Chem. Chem. Phys.*, 2017, 19, 921–960.

82   K. S. Suslick, D. A. Hammerton and R. E. Cline, *J. Am. Chem. Soc.*, 1986, **108**, 5641–5642.

83   Y. Peng, Y. Li, Y. Ban, H. Jin, W. Jiao, X. Liu and W. Yang, *Science*, 2014, **346**, 1356–1359.

84   S. C. Junggeburth, L. Diehl, S. Werner, V. Duppel, W. Sigle and B. V Lotsch, *J. Am. Chem. Soc.*, 2013, **135**, 6157–6164.

85   P. Chandrasekhar, A. Mukhopadhyay, G. Savitha and J. N. Moorthy, *J. Mater. Chem. A*, 2017, **5**, 5402–5412.

3 ♣

Ultrasonic Exfoliation of Hydrophobic and Hydrophilic Metal–Organic Frameworks To Form Nanosheets
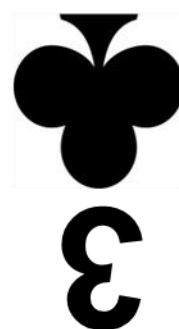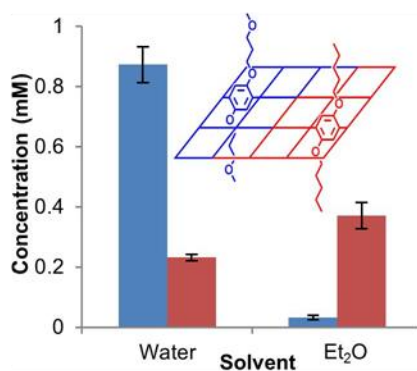
Chapter 3

Ultrasonic exfoliation of hydrophobic and hydrophilic metal-organic frameworks to form nanosheets

Chem. Eur. J., 2018, 24, 17986-17996 (full paper)

https://onlinelibrary.wiley.com/doi/full/10.1002/chem.201803221

David J. Ashworth, Adam Cooper, Mollie Trueman, Rasha W. M. Al-Saedi, Liam D. Smith, Anthony J. H. M. Meijer and Jonathan A. Foster

Author Contributions

David J. Ashworth	Supervised AC and MT. Supervised ligand precursor and MOF syntheses and exfoliation process development. Performed solid-state characterisation of MOFs and MONs. Performed all MON imaging, sizing analyses and sensing studies. Collated all data, drafted manuscript and ESI and created all figures. Assisted in redrafting and editing the manuscript.
Adam Cooper	An MChem student supervised by DJA and JAF. Developed the experimental set-up for exfoliations. Synthesised ligand precursors $H_2\mathbf{n}$ and MOFs Cu(**n**)(DMF) (**n** = **1**,**2**). Calculated extinction coefficients in solvents and performed 30 minute exfoliations in a range of solvents to calculate MON concentrations.
Mollie Trueman	A summer placement student working under the supervision of DJA and JAF. Performed 12 hr exfoliations of [Cu(**n**)DMF)]$_n$ (**n** = **1**, **2**) in a range of solvents and assisted in the solid-state characterisation of recollected unexfoliated MOF.
Rasha W. M. Al-Saedi	Performed all DFT modelling and theoretical calculations.
Liam D. Smith	SURE summer student. Initially synthesised [Cu(BDC)(DMF)]$_n$ and explored the ultrasonic exfoliation.
Anthony J. H. M. Meijer	Supervised and coordinated RWMA-S work.
Jonathan A. Foster	Supervised DJA, AC, MT and LDS and coordinated this body of work. Assisted in redrafting and editing the manuscript.

▌Nanomaterials

Ultrasonic Exfoliation of Hydrophobic and Hydrophilic Metal–Organic Frameworks To Form Nanosheets

David J. Ashworth, Adam Cooper, Mollie Trueman, Rasha W. M. Al-Saedi, Liam D. Smith, Anthony J. H. M. Meijer, and Jonathan A. Foster*[a]

Abstract: The modular structure of metal–organic framework nanosheets (MONs) provides a convenient route to creating two-dimensional materials with readily tuneable surface properties. Here, the liquid exfoliation of two closely related layered metal–organic frameworks functionalised with either methoxy-propyl (**1**) or pentyl (**2**) pendent groups intended to bestow either hydrophilic or hydrophobic character to the resulting nanosheets is reported. Exfoliation of the two materials in a range of different solvents highlighted significant differences in their dispersion properties, as well as their molecular and nanoscopic structures. Exchange or loss of solvent was found to occur at the labile axial position of the paddle-wheel based MONs and DFT calculations indicated that intramolecular coordination by the oxygen of the methoxy-propyl pendant groups may take place. The nanoscopic dimensions of the MONs were further tuned by varying the exfoliation conditions and through "liquid cascade centrifugation". Aqueous suspensions of the nanosheets were used as sensors to detect aromatic heterocycles with clear differences in binding behaviour observed and quantified.

Introduction

Metal–organic framework nanosheets (MONs) are free-standing, nominally two-dimensional materials formed by the co-ordination of organic ligands to metal ions or clusters.[1] A key advantage of MONs over inorganic nanosheets such as graphene, boron nitride and molybdenum disulfide is that their modular structure allows for ready tuning of their properties. This tunability, combined with their large external surface area and high aspect ratio, makes MONs ideal for a diverse range of applications including separation,[2] sensing,[3] templation,[4] electronics[5] and catalysis.[6] As with other nanosheets, understanding how to form concentrated suspensions of high aspect ratio nanosheets is an important technological challenge.[7] The modular structure of MONs potentially provides advantages over simple inorganic nanosheets in allowing easy modification of surface functionalities to enable nanosheets to be designed for use in particular solvents. However, their porosity, flexibility, lability and potential for structural rearrangements also present additional challenges in undertaking this type of study.

Liquid exfoliation provides an attractive, simple and scalable, top-down approach to producing ultrathin nanosheets from layered materials.[8] In some cases, immersion of layered MOFs in solvent has been shown to result in spontaneous exfoliation of the materials into nanosheets.[9] In most cases however, additional energy is required to overcome interlayer interactions in order for exfoliation to occur. A variety of different methods for the liquid exfoliation of MONs have been investigated including ball milling,[2b,10] freeze–thaw[11] and intercalation,[6c,12] with sonication[2b,10,13] being the most widely employed approach. In most cases these processes produce a broad distribution of particle sizes. Samples are therefore left to sediment or centrifuged in order to separate out bulk material from the nanosheets. Top-down approaches are particularly attractive for the study of new systems as the bulk layered materials are typically easier to characterize which aids determining the structure of the nanosheets.

The effect of parameters such as solvent, sonication time and centrifugation time for the liquid exfoliation of other layered materials have been extensively studied and optimized.[8a–c] To date, most studies on the liquid exfoliation of MONs have focused on investigating a single framework in a single solvent. Polar solvents such as acetone and alcohols have most commonly been employed. Peng et al. reported a mixture of methanol and propanol as being optimal for exfoliation of a layered ZIF.[2b] They hypothesize that the small methanol molecules are able to penetrate into layers whilst propanol adsorbs onto the surface of the nanosheets through its hydrophobic tail helping to stabilize the exfoliated nanosheets in suspen-

[a] D. J. Ashworth, A. Cooper, M. Trueman, R. W. M. Al-Saedi, L. D. Smith,
Prof. A. J. H. M. Meijer, Dr. J. A. Foster
Department of Chemistry, University of Sheffield
Sheffield, S3 7HF (UK)
E-mail: jona.foster@sheffiled.ac.uk

sion. Junggeburth et al. note that their hydrophobic layered MOF showed decreasing exfoliation in THF > toluene > CHCl$_3$.[14] Poor exfoliation was observed when using the polar solvents DMF and H$_2$O which was attributed to an inability of the solvents to efficiently penetrate between the hydrophobic interlayer space. In contrast, Moorthy and co-workers investigated exfoliation of a layered MOF in which there was hydrogen bonding between the layers.[15] They found a correlation between the Gutmann's hydrogen-bond-accepting parameter of the solvent used and the intensity of fluorescence of nanosheets formed following exfoliation. These studies highlight the different roles that different solvent molecules can play in aiding exfoliation of different layered MOFs and stabilizing the resulting nanosheets.

In our work we seek to design new layered MOFs which incorporate features intended to enhance their exfoliation and stabilize the resulting MONs in suspension. We recently communicated a study reporting the liquid exfoliation of Cu(1)(DMF), a layered MOF incorporating weakly interacting methoxy-propyl chains designed to aid exfoliation of the layers into nanosheets.[13g] The nanosheets are based on the popular metal-paddlewheel secondary building unit (SBU) which has a labile, Lewis acidic axial coordination site which makes it ideal for a wide range of sensing, catalytic, electronic, separation and storage applications.[2c, 3b, 6b, c, e] We hypothesized that liquid exfoliation of layered metal–organic frameworks functionalized with either hydrophobic or hydrophilic functionalities would produce nanosheets with different concentrations, stabilities and thicknesses in different solvents. To investigate this, we compared the liquid exfoliation of the relatively hydrophilic methoxy-propyl functionalized MOF with an isostructural MOF incorporating a more hydrophobic pentyl-chain in a wide range of different solvents. We then investigated the molecular and nanoscopic structure of the resulting nanosheets in selected solvents under different conditions in order to understand and optimize the exfoliation process.

Results and Discussion

Synthesis of layered MOFs

Compounds H$_2$(1) and H$_2$(2) (see Figure 1) were synthesized via Williamson etherification of dimethyl 2,5-dihydroxy-1,4-benze-nedicarboxylic acid with 1-bromo-3-methoxypropane and 1-bromopentane, respectively. The difference in polarity of the ligands was evident during deprotection of the ligands. Compound H$_2$1 was readily obtained from the corresponding methyl ester by heating under reflux in aqueous NaOH solution.[13g] Under the same condition only partial deprotection of 2 occurred due to poor solubility so an alternative method involving 1:1 THF/5% KOH(aq) was employed.[16] Both compounds were achieved in good yields and the purity of the compounds was established by NMR, mass spectrometry, and elemental analysis.

Heating of H$_2$(1) or H$_2$(2) with copper nitrate in DMF in a sealed reaction vial at 110 °C for 18 h resulted in the formation of green microcrystalline powders. Attempts to grow single crystals of these materials were unsuccessful. However, XRPD analysis of the microcrystalline powders indicates these structures are isostructural with the single crystal structure that we have previously reported for Zn(1)(DMF).[13g] In this structure four carboxylate linkers are coordinated to the M$_2$-paddlewheel (PW) while DMF coordinates to the axial sites of the PWs. Importantly, in this form the weakly interacting 3-methoxypropoxy groups or pentyl chains are positioned between the layers whilst there is strong metal-carboxylate bonding within the layers. Small differences in the unit cell parameters (Table S1 in the Supporting Information) for the copper complexes are ascribed to the different ligand field effects and different ionic radii of Zn^{2+} and Cu^{2+} and to substitution of the oxygen for a methylene in case of 2. Elemental analysis is consistent with the proposed formulas and IR and TGA analysis confirms the presence of coordinated DMF in these structures.

Liquid exfoliation

Exfoliation experiments were undertaken using a bath sonicator. We undertook preliminary experiments investigating the effect of different variables on the degree of exfoliation using DMF and isopropanol as model solvents. Different powers (320 W at 30% and 100%), frequencies (37 kHz, 80 kHz) and temperature of sonication were investigated. It was found that high power produced higher concentrations of material in suspension and high frequency increased concentration and avoided dissolution of the nanosheets (Figure S4). Sonication was applied using a sweep mode and samples were rotated
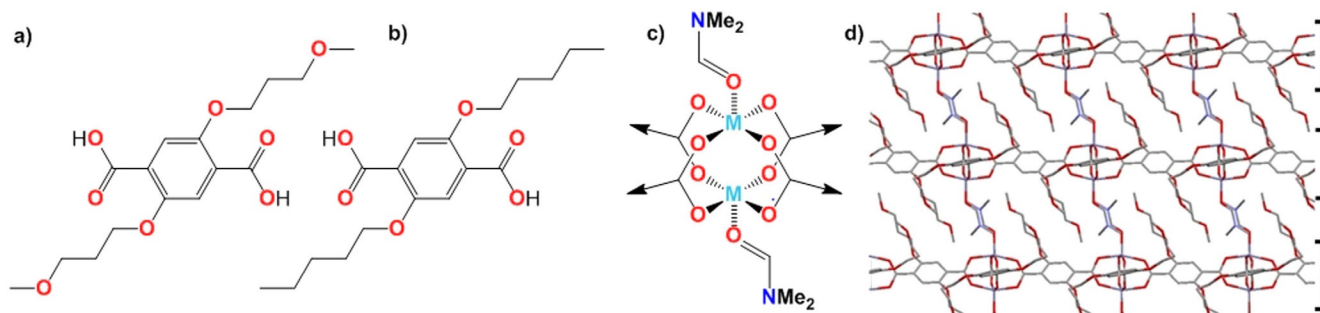

Figure 1. Structure of ligands H$_2$1 (a) and H$_2$2 (b). c) Paddlewheel SBU, with DMF coordinated in the axial positions. d) X-ray crystal structure showing layered structure of Zn(1)(DMF).

through the bath using an overhead stirrer in order to ensure samples were irradiated evenly. Sonication is known to be more effective at lower temperature[17] and the temperature was maintained over the course of the experiment using a cooling coil giving a temperature of around 16 °C. The set-up for exfoliation is shown in Figure S2 in the Supporting Information.

The following protocol was therefore established for the exfoliation of the MOFs which was used unless stated otherwise. The layered MOFs were weighed into glass vials to which solvent was added (5 mg in 6 mL) and then exfoliated in a sonicator bath at a frequency of 80 kHz for 30 minutes at a temperature of < 20 °C. The samples were then centrifuged at 1500 rpm for 10 minutes to remove larger particles and care was taken to avoid redispersion of the sediment during transport. UV/Vis spectra were measured using the top 3 mL of suspension and highly absorbing samples diluted as required using further solvent.

The solvent that the nanosheets are exfoliated into was expected to have a large effect on the degree of exfoliation and the stability of the resulting suspension. An initial screen of 23 different solvents was undertaken. However, some solvents had to be excluded due to their UV/Vis cut-off points preventing analysis or their high viscosity resulting in poor dispersion and centrifugation (Table S2 in the Supporting Information). A selection of the 11 solvents representing a diverse range of polarities and chemical functionalities were selected for further investigation: water, dimethylsulfoxide (DMSO), N-Methyl-2-pyrrolidone (NMP), dimethylacetamide (DMA), dimethylformamide (DMF), acetonitrile (MeCN), isopropanol (IPA), tetrahydrofuran (THF), diethylether (Et$_2$O), cyclohexane and hexane.

Both compounds typically show a single major absorption band the λ_{max} of which ranged between 271–303 nm depending on the solvent used (Figure S5 in the Supporting Information). Absorption bands were generally broader and less well defined for Cu(1)(DMF), particularly in poorly coordinating solvents such as diethylether, THF and acetonitrile. In acetonitrile, a second local maximum was observed at 361 nm and 304 nm for Cu(1)(DMF) and Cu(2)(DMF) respectively. The MLCT band was typically too weak and broad to be distinguished so the major peak attributed to the dicarboxylate ligand was used in all subsequent analysis. Neither compound was able to form stable dispersions in either cyclohexane or hexane, nominal values of zero are therefore used for these solvents in the subsequent analysis.

The extinction coefficient for the compounds in each solvent was estimated by dilution of a suspension containing a known mass of each compound. Values ranged from 1892–6693 mol^{-1} dm^3 cm^{-1} for Cu(1)(DMF) to 2467–4489 mol^{-1} dm^3 cm^{-1} for Cu(2)(DMF). These differences in spectra are attributed to exchange of the coordinated DMF, variations in ligand geometry in the different solvents and differences in particle size which are discussed in detail later in this article.

Clear differences were observed in the concentration of exfoliated material in suspension following sonication and centrifugation of Cu(1 or 2)(DMF) in different solvents. Figure 2

shows a plot of the concentration in mM of Cu(1)(DMF) [blue] or Cu(2)(DMF) [red] suspended in different solvents listed in order of increasing polarity (left to right) as measured by UV/Vis spectroscopy. Data shown are the average of four repeats.

At either extreme, the more hydrophilic Cu(1)(DMF) showed a significantly higher degree of dispersion in water than Cu(2)(DMF) whilst the opposite is true in diethyl ether where the more hydrophobic Cu(2)(DMF) is present at significantly higher concentrations. Higher concentrations are observed for Cu(1)(DMF) in all solvents except diethyl ether and DMA. DMSO and NMP give the highest concentrations of both materials and significantly higher than DMA and DMF which have very similar polarities. Samples of both compounds exfoliated into cyclohexane and hexane showed negligible absorbance following centrifugation whilst only Cu(2)(DMF) showed any absorbance following exfoliation into toluene.

In studies of other nanosheets formed by liquid exfoliation, a wide range of solubility parameters have been put forward as being important for determining the concentration of exfoliated material in suspension.[8b,c] We plotted the concentration of material in suspension against a range of parameters including polarity, surface tension and Hansen solubility parameters (Figure 2c–e) as well as Kamlet–Taft, Gutman, Swain, Reichardt's polarity parameters and viscosity (see Section 3.3 in the Supporting Information). The data in these plots is normalized relative to the highest concentration solvent in order to allow easier visual comparison.

In line with similar studies of other nanomaterials, no single parameter by itself was a reliable determinant of the concentration of material left in suspension following exfoliation for either material.[8b] In many cases, solvents with similar solubility parameters to the best performing solvents showed low concentrations of dispersed materials. For example, the concentration of Cu(2)(DMF) exfoliated in DMA is only 20 % of that in NMP even though they have similar surface tensions (γ_L) 36.70 and 40.21 mNm^{-1} respectively. Conversely, water and isopropanol have very different polar Hansen solubility parameters (δp), 16 and 6.1 respectively, but suspensions of Cu(2)(DMF) with very similar concentrations are formed. It should be highlighted that the fact that exfoliation of the pentyl functionalized MOF produces stable suspension in water at all, albeit at a lower concentration than the methoxy-propyl functionalized MOF indicate that they are only "relatively" hydrophobic and hydrophilic. It should also be noted that this experiment provides a comparison of the concentration of material in suspension following exfoliation in different solvents, not necessarily the suitability of the solvents to form nanosheets. A detailed discussion of the nanoscopic dimensions of the materials produced following exfoliation in different solvents is presented in the section entitled nanoscopic analysis later in the paper. First, the differences in UV/Vis spectrum observed for the materials in different solvents also led us to question the composition of the exfoliated material which we discuss in the following section.
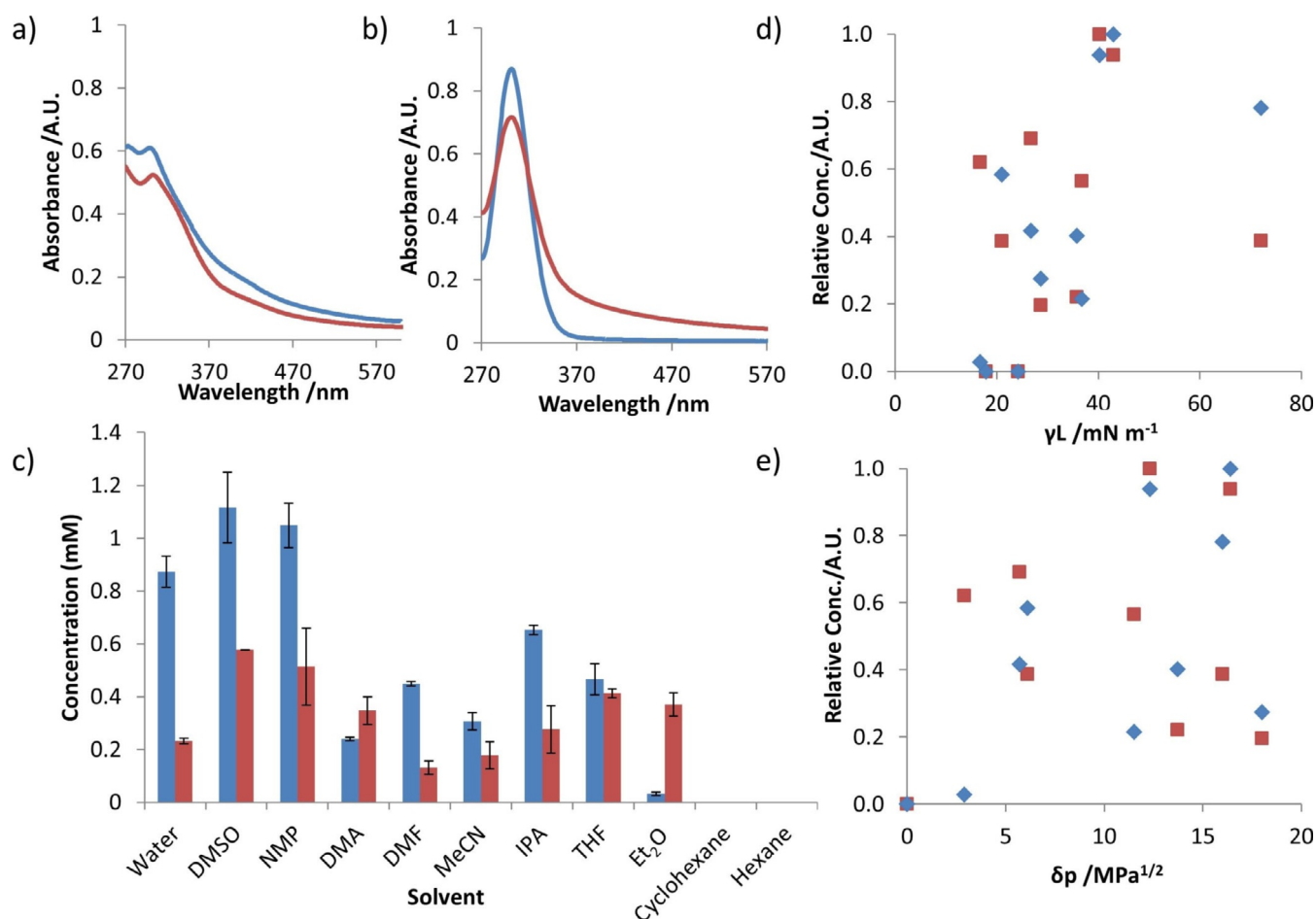
Figure 2. Cu(**1**)(DMF) and Cu(**2**)(DMF) are represented with blue and red data, respectively. a, b) UV/Vis spectral traces of MONs in suspension following exfoliation in DMF (a) and water (b). c) plots of concentrations of nanosheets in suspension, following exfoliation and centrifugation; d, e) normalized concentrations of MON suspensions plotted against the solvent's surface tension (d) and Hansen solubility parameter of energy from dipolar intermolecular force (e).

Structural analysis

The relatively labile nature of coordination bonds and the high surface area of the nanosheets mean that it cannot be assumed that the MOF structure is unchanged following liquid exfoliation. In particular, the axial site on the copper paddlewheel is known to be highly labile, allowing for the possibility of loss or exchange of the coordinated DMF molecules with those of the exfoliation solvent. We previously observed differences in the XRPD patterns of Cu(**1**)(DMF) following exfoliation in different solvents.[13g] Here we undertake a more detailed study to probe the structure of nanosheets of Cu(**1**)(DMF) and Cu(**2**)(DMF) following exfoliation in selected solvents (water, DMF, acetonitrile, NMP and diethylether) representing a range of polarities. The as-synthesised MOF (5 mg in 6 mL of solvent) was sonicated for 12 h at 80 kHz before centrifugation at 1500 rpm for 1 h and the resulting sediment collected for analysis by using XRPD, IR, TGA and NMR spectroscopy.

The XRPD pattern for Cu(**1**)(DMF) following exfoliation into DMF matches the as-synthesised compound indicating no structural change occurred. In contrast to this, material analysed following exfoliation in water showed a distinct, new XRPD pattern. For this sample, no nitrogen was observed by

elemental analysis while TGA showed a 1.4% mass loss at 66–94 °C.

Furthermore, the IR pattern shows a loss of the DMF carbonyl peak at 1670 cm^{-1} and a small new peak at 3604 cm^{-1}. All these results are consistent with substitution of the axial DMF for H$_2$O, giving Cu(**1**)(H$_2$O). Material exfoliated in acetonitrile, diethyl ether and NMP all showed correlating peaks in their XRPD patterns corresponding to a third, new phase. In the diethyl ether samples this was accompanied by coincidences with the pattern assigned to Cu(**1**)(H$_2$O) indicating a mixture of the desolvated and hydrated phases. In acetonitrile and diethyl ether, negligible weight loss was observed in TGA below the decomposition temperature around 300 °C and elemental analysis showed no nitrogen was present. The same analysis on Cu(**1**)(DMF) exfoliated in NMP shows a mass loss of 4.2% at 83–205 °C, and small quantities of nitrogen (0.72 wt%) indicating a small amount of non-coordinated solvent is present. We suggest this new material (formed in acetonitrile, diethyl ether and NMP) is caused by the loss of axial DMF to give a desolvated phase with the structure Cu(**1**). This matches previous findings following exfoliation in acetone and methanol.[13g]

Samples of Cu(**2**)(DMF) exfoliated into DMF generated XRPD data correlating with the pattern produced from the parent
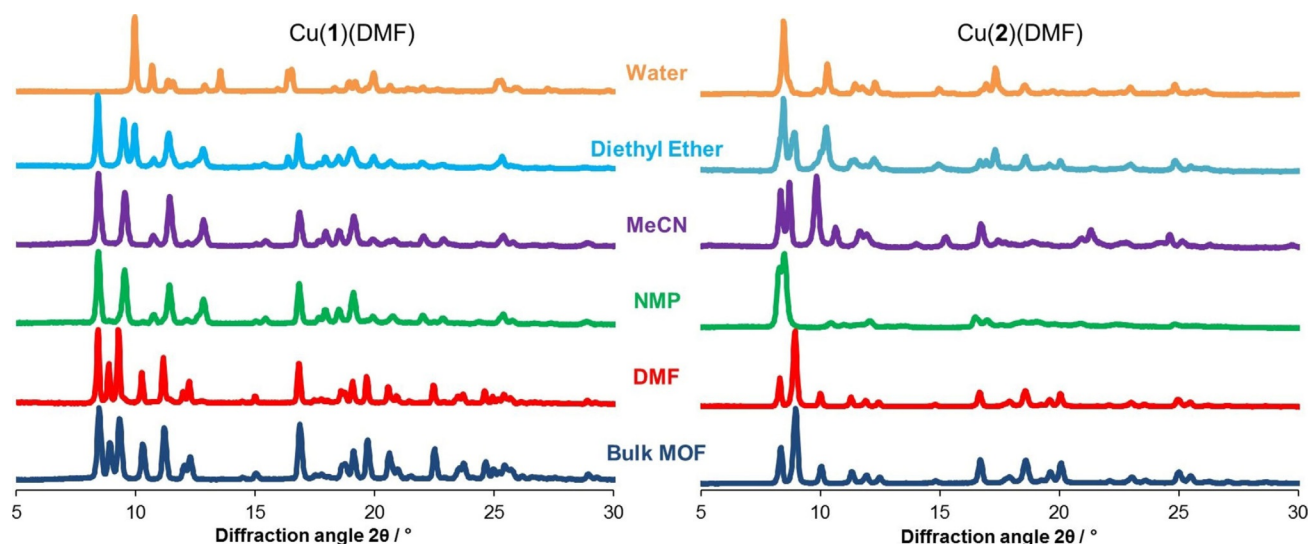
Figure 3. Experimental powder diffraction patterns of Cu(**1**)(DMF) and Cu(**2**)(DMF) as-synthesised (dark blue), and of post-exfoliation solids recollected through centrifugation for 1 h at 1500 rpm, in DMF, NMP, MeCN, diethyl ether and water.

MOF. Exfoliation in water produced a powder pattern corresponding to a distinct phase. This fact, along with the absence of nitrogen in the elemental analysis and mass loss of 4.6% at 23–107 °C shown by TGA, is consistent with the formation of Cu(**2**)(H$_2$O). In a divergence from the behaviour shown by Cu(**1**)(DMF), exfoliation of Cu(**2**)(DMF) into diethyl ether, acetonitrile and NMP gave materials which showed weak correlation in peak positions between the resulting XRPD patterns (Figure 3). Exfoliation into diethyl ether gave rise to a pattern in which each peak could be assigned to either Cu(**2**)(DMF), or to the phase assigned to Cu(**2**)(H$_2$O). Elemental analysis concluded a value of 0.59 wt% nitrogen (in comparison to 2.99 wt% calculated for Cu(**2**)(DMF), which is consistent with incomplete removal of DMF and partial substitution by trace quantities of water. In contrast to this, elemental analysis of the sample produced through exfoliation in acetonitrile showed no detectable nitrogen and TGA showed no mass loss. We therefore assign this powder pattern as corresponding to that of the desolvated materials. Elemental analysis of the Cu(**2**)(DMF) exfoliated into NMP indicates significant levels of nitrogen present (2.21%) and a decrease in mass at around 105 °C consistent with loss of co-ordinated solvent, on heating the sample. Proton NMR of the digested samples confirmed the presence of residual DMF, and ruled out substitution by NMP. The two large, but poorly resolved peaks around 8° in the powder pattern are consistent with the formation of the sql topology and the distortions are presumed to be due to partial desolvation.

DFT modelling

In order to gain further insights into the structure of the different phases, we undertook DFT modelling to visualize the structure of the MONs and confirm the phase assignments. Structures of **1** and **2** were initially modelled using a single PW formed using model monocarboxylate ligands functionalized with only a single methoxy propyl- or pentyl- chain to speed up the calculation (**1*** and **2***). Previous studies by us of PW MOFs have shown that using isolated unit-cells produces very comparable results to calculations performed on extended structures.[18] Coordinates from the known crystal structure of Zn(**1**)(DMF) were used to generate starting coordinates. The structure was then modified, replacing DMF with water and acetonitrile. The fourth iteration removed any solvent from the axial position. In this final iteration we manipulated the arms, so that the ether functionality could conceivably coordinate in the axial position. For **2** the same procedure was followed. The functional used was B3LYP[19] with dispersion-corrections due to Grimme (GD3-BJ). Structures of **1*** were subsequently re-modelled with both methoxy-propyl chains (**1****) resulting in slight improvements in the correlation between the calculated and experimental data, but showed no substantive differences. For further details, please see the supporting information.

Figure 4 a–c shows images of the relaxed structures for the three different phases obtained with **1**** in which DMF, water and no-solvent are coordinated at the axial position, respectively. Similar images are shown for the other derivatives in Figure S54 in the Supporting Information. The corresponding calculated IR patterns for these structures were compared with the experimental patterns (Figures S55–57). Whilst there are some significant shifts in peak position and intensity between the calculated and experimental patterns particularly in the fingerprint region, the presence or absence of characteristic solvent peaks could be used to assign the phases. In particular, characteristic peaks corresponding to the carbonyl of the coordinated DMF molecules at 1706 cm^{-1} and of water around 3500 cm^{-1} were observed in the corresponding calculated and experimental patterns for material exfoliated in DMF and water, respectively. Experimental patterns for material exfoliated in acetonitrile lacked the calculated peaks for acetonitrile at 2200 cm^{-1} as well as those for water and DMF and provided closer matches to the calculated structure with no solvent co-
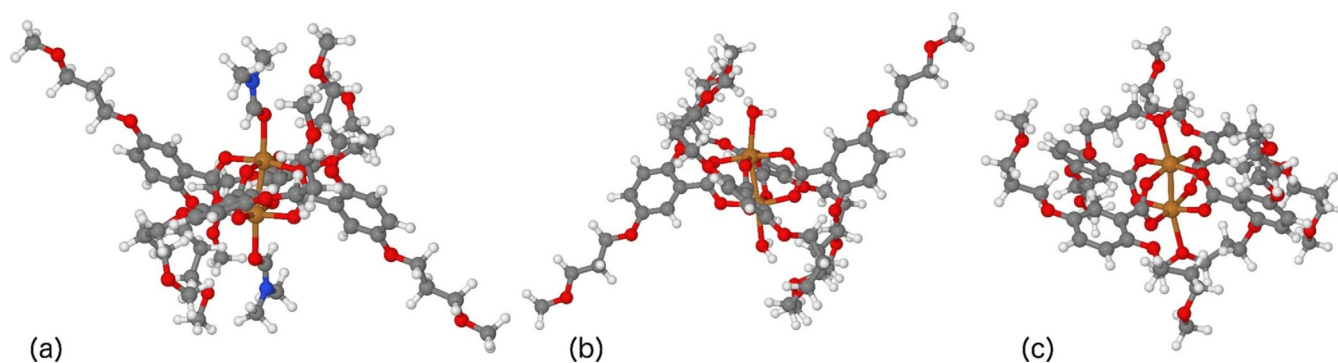
Figure 4. DFT calculations showing optimised structures for (a) $Cu_2(1^{**})_4(DMF)_2$, (b) $Cu_2(1^{**})_4(H_2O)_2$, (c) $Cu_2(1^{**})_4$ where 1^{**} is 2,5-Bis(3-methoxypropoxy)benzoate.

ordinated. This data therefore supports the assignments given in the previous section.

Coordination of two acetonitrile, ethanol, acetone, DMF and water molecules to Cu(1^{**}) have binding energies of 58, 66, 72, 87 and 119 kJ mol^{-1}, respectively, relative to three infinitely separated molecules. This broadly corroborates what is observed experimentally in that more weakly bound solvents such as acetonitrile are lost whilst more strongly coordinating solvents such as DMF and water are retained. However, it should be noted that these values are based on gas phase calculations and so do not take into account solvent–solvent interactions. This may account for discrepancies such as our previous observation that Cu(**1**)(DMF) is the observed structure in 10% DMF in water mixtures.

It is interesting to note that in the calculated structures obtained for Cu(1^{**}), methoxy propyl chains on either side of the PW are bent over to allow the lone pair of the oxygen to coordinate intramolecularly to the axial positions of the complex. This is not observed in the structure for Cu(**2***) where the oxygen is replaced with a methylene group. The binding energy for a single arm coordinating to Cu(1^{**}) (as calculated through the difference between the energies of structures with one coordinated or uncoordinated arm) is 30 kJ mol^{-1}. In our calculations coordination of the second arm only has a binding energy of 7 kJ mol^{-1}. It should be noted that these calculations are highly dependent on the confirmation around the paddle wheel and a full conformational search would be required to provide a better estimate of the true value for the intramolecular binding which is beyond the scope of this study.

We therefore suggest that this ability of the methoxy-propyl chains, but not the propyl chains, to intramolecularly coordinate to this axial position with values comparable to those of some solvent molecules may provide at least a partial explanation for some of the differences observed between the nanosheets. For example, the co-ordinated methoxy-propyl chains make the surface of the Cu(**1**) structures less polar resulting in high concentrations of nanosheets in apolar solvents than might otherwise be expected. Similarly, the flexibility of the frameworks might reduce the impact of the hydrophobic pentyl chains in polar solvents. These structural insights high-

light the challenges of predicting and understanding the effects of even small changes in molecular structure on the macroscopic properties of the nanosheets.

Nanoscopic analysis

In addition to understanding the effect of solvent on the molecular structure of the nanosheets, we sought to examine the influence of solvent on the nanoscopic structure of the resulting material. Exfoliation protocols for other layered materials have varied significantly, with sonication times ranging from 20 min to several days. Here, we first investigated the exfoliation of the hydrophilic Cu(**1**)(DMF) and hydrophobic Cu(**2**)(DMF) in water and diethyl ether, using two exfoliation time periods: 30 min and 12 h. It was hypothesized that longer exfoliation times would lead to thinner nanosheets being pro-
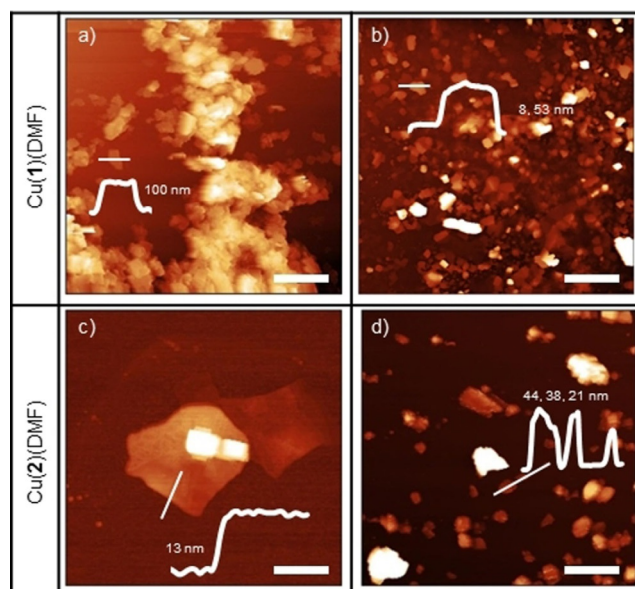

Figure 5. AFM images of Cu(**1**)(DMF) exfoliated in water for different time periods: a) 30 min, b) 12 h. AFM images of Cu(**2**)(DMF) exfoliated in different solvents: c) water and d) diethyl ether (c and d, respectively) for 12 h. Scale bars are 2, 2, 2 and 1 μm, and height scales are 1000, 200, 50 and 150 nm for a–d, respectively.

duced, and anticipated that the Cu(**1**)(DMF) would exfoliate better in H_2O than diethyl ether, and the reverse true for Cu(**2**)(DMF). After exfoliation, centrifugation at 1500 rpm for 10 min removed large, unexfoliated material, and AFM was used to assess nanosheets produced (see Figure 5.)

Both exfoliation procedures resulted in nanosheets with varying size distributions. In general, more nanosheets with smaller heights were observed from 12 h exfoliation than 30 min, suggesting that longer exposure to ultrasonic waves results in increased exfoliation. For example, Cu(**2**)(DMF) in diethyl ether exfoliated for 30 min and 12 h resulted in nanosheets with thicknesses of 20–100 and 20–50 nm, respectively. Selected examples of nanosheets observed using AFM can be found in Figure 5, and additional figures found in the Supporting Information (Figures S13–19). There are noticeably large agglomerates and sheet-like particles with heights over 100 nm in many of these images, suggesting that 10 min centrifugation at 1500 rpm is not effective at removing all larger particles from the post-sonication suspension.

In order to compare the effect of solvent on the nanoscopic dimensions of the nanosheets formed, Cu(**1**)(DMF) and Cu(**2**)(DMF) were exfoliated for 12 hrs in water, DMF, NMP, acetonitrile and diethyl ether. Samples were centrifuged at 1500 rpm for 1 h as longer/ faster centrifugation times resulted in insufficient material for analysis in some solvents. Typical AFM images of observed nanosheets can be found in Figures S27–36.

In general, exfoliation in DMF and NMP resulted in nanosheets of low quality—lateral dimensions and aspect ratios were low, with observed particles having relatively large heights of >40 nm. Particles appeared to be rounded in nature, rather than lamellar, particularly in NMP. This could suggest that the energetic input upon prolonged exposure times to ultrasound facilities MON breakdown and dissolution of ligand and Cu into solution—both H_2**1** and H_2**2** are soluble at these low concentrations in DMF and NMP.

We investigated the stability of the nanosheets in DMF over 5 days by UV/Vis spectroscopy and found broadening of the ligand absorption band which was attributed to the formation of a new peak corresponding to the neutral ligand (Figure S13a,b in the Supporting Information). In contrast, material exfoliated in water and diethylether showed no shift in absorbance maximum over time. Furthermore, the intensity of these bands remained constant over 5 days indicating that stable suspensions had been formed (Figure S13c).

Nanosheets of Cu(**2**)(DMF) exfoliated in water were angular and typically <1 µm laterally with heights 10–30 nm. Some examples of ultrathin flakes of 5 µm × 2 nm were observed (Figure 6). Nanosheets of Cu(**1**)(DMF) exfoliated in H_2O were more irregularly shaped and typically 10–40 nm in height, with lateral dimensions up to 1.5 µm, consistent with our previous report.[13g] Exfoliation of Cu(**1**)(DMF) in diethyl ether produced low concentrations of materials in suspension and the nanosheets observed have relatively low aspect ratios, typically 50–100 nm in height and <600 nm laterally. In contrast, Cu(**2**)(DMF) exfoliated in diethyl ether produces nanosheets which were typically <40 nm with examples observed below 10 nm thickness and with lateral dimensions up to 2 µm (Figure S37 in the Supporting Information).

It is interesting to note the more hydrophobic ligand **2** produced nanosheets with higher aspect ratios and more regular shapes than those of the hydrophilic ligand **1** in both water and diethylether. This is contrary to our expectation that closer matching of the solvent and nanosheet properties would lead to thinner nanosheets. An alternative explanation might be that the thinner nanosheets formed from Cu(**2**)(DMF) are the result of weaker interlayer interactions between the pentyl chains compared to the methoxy-propyl chains aiding exfolia-
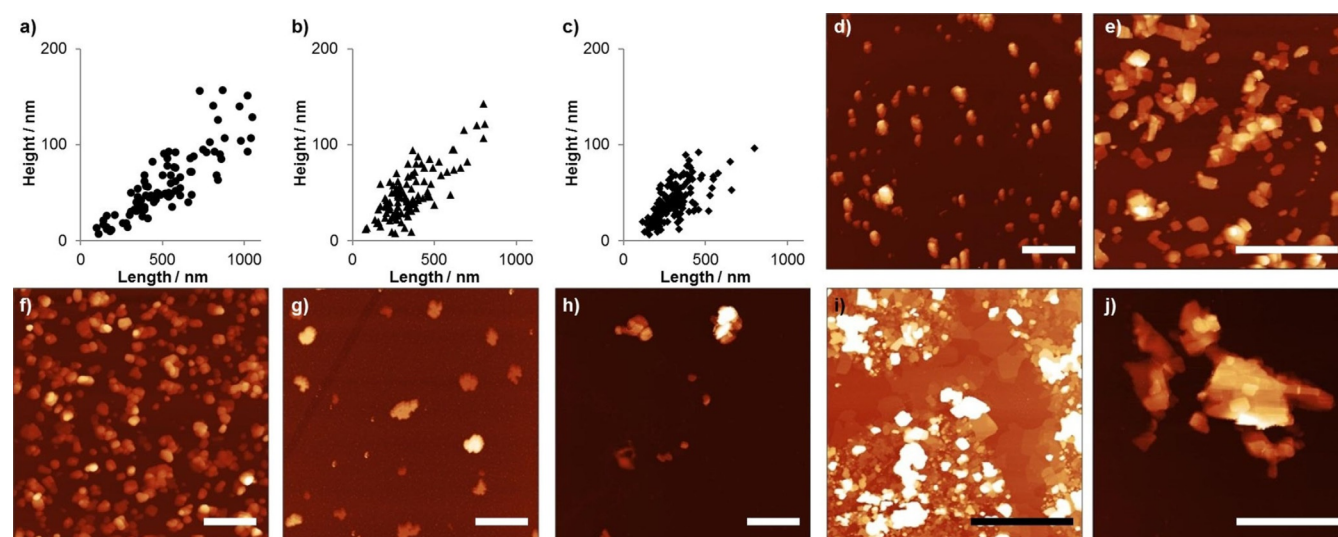

Figure 6. Scatter plots of height and lateral dimensions of Cu(**1**)(DMF) nanosheets observed from exfoliation in MeCN and cascade centrifuged for 1 h at 1500 rpm (a), then 30 min at 4500 rpm (b), then 4 hrs at 4500 rpm (c). Topographical AFM images of Cu(**1**)(DMF) (d) and Cu(**2**)(DMF) (e) exfoliated for 12 hrs, and Cu(**2**)(DMF) exfoliated for 30 min (f) and centrifuged at 4500 rpm for 4 hrs. AFM images of Cu(**1**)(DMF) exfoliated in water (g) and diethyl ether (h), and Cu(**2**)(DMF) exfoliated in water (i) and diethyl ether (j). AFM scale bars are 2 µm, and height scales are 150 nm (d, e, j), 80 nm (f), 40 nm (g), 200 nm (h), and 50 nm (i).

tion during sonication. Another factor to consider is that poorer interactions between the nanosheets and solvent may result in more of the thicker nanosheets produced during sonication being removed from suspension during centrifugation. This would mean that on average thinner nanosheets are observed when there is a mismatch in solvent and nanosheet properties. Optimising nanosheet design must therefore balance minimizing inter-layer interactions with complimenting solvent properties to form stable dispersions of nanosheets and developing centrifugation protocols that ensure removal of larger particles.

In order to investigate nanosheet size control, Cu(**1**)(DMF) was selected as a test system, and exfoliated in acetonitrile for 12 h. Acetonitrile was chosen as we observed good particle separation and minimal agglomeration upon deposition for AFM analysis using this solvent, which enabled more accurate sizing of nanosheets. Liquid cascade centrifugation (LCC) is a versatile strategy that uses multiple sequential centrifugation steps of increasing rate or time period, using the supernatant of the previous step as the suspension for the next, in order to remove particles of various size from suspension.[20] We employed LCC using steps of 1500 rpm for 1 h, 4500 rpm for 30 min then 4500 rpm for 4 h. The particle size distribution of the resulting nanosheets as determined through a statistical analysis ($n = 94$–161) can be seen in Figure 6 a–c and the mean ($\bar{x}$) and standard deviation (SD) in particle size are summarized in Table 1. AFM images used for these analyses can be found in the Supporting Information (Figures S20–22).

The results of the statistical analyses show that the average nanosheet thickness and length of Cu(**1**)(DMF) decrease sequentially from 59×512 nm to 41×307 nm between the first and last steps due to the removal of larger particles. This correlates with a decrease in the concentration of material in suspension from 0.33 mM to 0.09 mM. The smallest nanosheets observed in each case are of a similar size at 6–8 nm. The concentration of Cu(**2**)(DMF) in suspension following the final centrifugation step is lower than for Cu(**1**)(DMF), however the nanosheets are significantly thinner and larger than Cu(**1**)(DMF) with minimum thicknesses of 4 nm and average dimensions of 19×367 nm following the final step.

DLS data were also collected for both systems after each of the three steps of LCC (Figures S28–S29 in the Supporting Information). The trend observed by DLS is consistent with that observed by AFM in that LCC lowers the average particle diameter of the MONs by reducing the number of larger particles remaining in the supernatant. However, the diameters determined by DLS are consistently lower (Table S9) than those obtained in the AFM analysis. For example, the mean LD for Cu(**1**)(DMF) exfoliated in acetonitrile for 12 h followed by the three steps of LCC is measured as 106 nm by DLS and 307 nm by AFM. Obtaining accurate particle size measurements from high aspect ratio nanosheets using DLS is known to be problematic as the Stokes-Einstein equation assumes spherical particles[21] and previous comparisons have also shown DLS produces lower average particle sizes than AFM.[22]

Exfoliation by sonication is recognized to be an effective delaminative technique. For MONs, long exfoliation times at low temperatures produce more, thinner nanosheets. Solvent choice is important in determining the thickness and morphology of the nanosheets obtained and avoiding dissolution over time. Small differences in ligand too can have a significant impact on the strength of interlayer interactions. Complimentary solvents may play a role at weakening interlayer interactions and aiding exfoliation. However, poor matching of solvent-nanosheet interactions may also result in thinner nanosheets being observed as thicker nanosheets are removed from solution by centrifugation. The wide distributions of particle sizes that result from prolonged exposure of the bulk MOF to ultrasonic waves can be narrowed through LCC and the average particle size reduced. Controlling the centrifugation rate enables nanosheet size distribution to be optimized for particular applications. In some applications having a narrow distribution of ultrathin nanosheets will be essential, for others having a broader distribution of thicker nanosheets at a higher concentration could be more important.

Sensing

We have previously reported the sensing of the small aromatic heterocycle pyridine from aqueous solution, using aqueous suspension of Cu(**1**)(H$_2$O) nanosheets. Titration of pyridine was found to bind to the axial position of the Cu$_2$-paddlewheel, with a K_a of 30±8 M^{-1}. When this experiment was replicated, instead using Cu(**2**)(H$_2$O), a drop-off in absorbance at λ_{max} was observed, as well as the suspension of nanosheets visibly turning cloudy upon addition of pyridine. This could be attributed

Table 1. Statistics calculated from nanosheets produced from the 12 h exfoliation of Cu(**1**)(DMF) and Cu(**2**)(DMF) in acetonitrile, and cascade centrifuged.

Sample	Cu(**1**)(DMF)			Cu(**2**)(DMF)	
Centrifugation Cycle	1500 rpm, 1 h	4500 rpm, 30 min	4500 rpm, 4 h	1500 rpm, 1 h	4500 rpm, 4.5 h
n	95	111	161	94	134
Conc. [mM]	0.33	0.12	0.09	0.12	0.04
$\bar{x}$ LD ± SD [nm]	512±234	347±154	307±108	348±202	367±155
$\bar{x}$ H ± SD [nm]	59±35	49±26	41±19	20±12	19±9
H range [nm]	7–157	8–143	6–96	5–64	4–58
LD range [nm]	100–1050	80–810	120–800	80–830	120–820

n = number of analysed nanosheets, conc. = concentration, determined through UV/Vis spectroscopy, $\bar{x}$ = mean, SD = standard deviation, LD = lateral dimension (recorded as the largest lateral vector across a nanosheet), H = height. See the Supporting Information for AFM images used.

to agglomeration of nanosheets upon addition of pyridine, which displaces coordinated H_2O. This would render the MON surface increasingly hydrophobic, which may cause agglomeration.

In order to be able to compare the binding strength of Cu(**1**) and Cu(**2**) MONs, imidazole was selected as a more hydrophilic binding substrate to prevent agglomeration. Cu(**1**)(DMF) and Cu(**2**)(DMF) were exfoliated in water for 12 h and centrifuged at 1500 rpm for 1 h to give suspensions with concentrations of 0.65 and 0.2 mM respectively. The samples were diluted with water and aliquots of the guest substrate (73 mM and 43 mM for Cu(**1**)(H_2O) and Cu(**2**)(H_2O), respectively) in aqueous host suspension (0.13 mM Cu(**1**)(H_2O) and 0.08 mM (Cu(**2**)(H_2O)) were titrated into host suspension and monitored using UV/Vis spectroscopy. Addition of imidazole in both cases resulted in bathochromic shifts of λ_{max} from 301-297 nm and 42% and 36% increases, respectively, in the absorption intensity (Figures S48 and S51 in the Supporting Information). These changes are consistent with expected substitution of water molecules for imidazole at the axial positions of the Cu_2-paddlewheel, which would result in changes to the absorption band of the coordinated dicarboxylate ligands **1** and **2**. It is most likely that imidazole binds to the Cu atoms through the sp^2-hybridised N electron pair donation.

This data was used to calculate binding constants of $K_a = 1370 \pm 180$ and 1950 ± 140 M^{-1} for imidazole to Cu(**1**)(H_2O) and Cu(**2**)(H_2O) respectively. The 43% increase of K_a observed between Cu(**1**) and Cu(**2**) is consistent with the hypothesis of the terminal methoxy oxygen of the ligand alkyl-ether arm in **1** being able to bind to the axial Cu sites, as this would provide an extra competing species for substrate coordination in Cu(**1**)(H_2O) which is not present in Cu(**2**)(H_2O), which could explain why imidazole binds more strongly to Cu(**2**)(H_2O).

Conclusions

MONs are an emerging class of two dimensional materials with significant potential for use in a wide range of applications thanks to their tuneable structure, high surface area and nanoscopic dimensions.[1e] Liquid exfoliation using ultrasound is an appealing route to generating nanosheets from layered MOFs thanks to its broad applicability to different systems, the wide availability of ultrasonic baths and scalability of the approach. However, there have so far been few studies investigating the impact of ligand design, solvent choice and exfoliation conditions on the molecular and nanoscopic structures of the nanosheets formed and their stability in suspension.

We investigated two layered Cu-PW based MOFs formed using dicarboxylic acid ligands functionalised with either methoxy-propyl or pentyl pendant groups intended to bestow hydrophilic and hydrophobic character, respectively. Exfoliation of Cu(**1**)(DMF) using an ultrasonic bath produced higher concentrations of material suspended in water than diethylether whilst the opposite trend was observed for Cu(**2**)(DMF). Cu(**1**)(DMF) typically showed higher dispersed concentrations than Cu(**2**)(DMF) and NMP and DMSO gave the highest overall concentrations for both compounds. Exfoliation in a wide

range of other solvents showed significant differences in the degree of exfoliation between the two compounds, however this was not found to correlate with any single solvent parameter.

The lack of simple correlation was partially explained by solid state analysis which showed that whilst the two-dimensional connectivity of the layered MOFs is maintained following exfoliation, the presence of a labile axial site on the Cu-PW SBUs mean that the surface functionalization of the nanosheets can vary depending on the exfoliation solvent. This effect is not typically observed in simple inorganic nanosheets but is likely to be common amongst MONs with exchangeable metal sites. DFT analysis indicated that the oxygen of the methoxy-propyl ligand **1** is able to coordinate intramolecularly to the axial position of the copper paddlewheels. This may further explain the complex dispersion behaviour of the MONs.

The nanoscopic dimensions of the exfoliated material were investigated using AFM and nanosheets with thickness as low as 2 and 10 nm were observed. Cu(**2**)(DMF) typically formed nanosheets which were thinner, had higher aspect ratios and were more angular than those of Cu(**1**)(DMF) in both water, diethylether and acetonitrile. This is hypothesized to be the result of the apolar pentyl chains resulting in weaker interlayer interactions than those of the methoxy-propyl chains aiding exfoliation during sonication. However, as with the dispersion study, a complex balance of sometimes competing factors will determine the profile of the nanosheets generated. Longer exfoliation times typically produced higher concentrations of thinner nanosheets whilst liquid cascade centrifugation could be used to remove larger particles and narrow the size distribution.

The ability of the axial position to exchange solvent molecules and the photophysical properties of the nanosheets were exploited for use as sensors. Addition of pyridine resulted in aggregation of Cu(**2**) but not Cu(**1**) whilst imidazole was shown to bind significantly stronger to Cu(**2**) than Cu(**1**). We note that the weaker binding seen for Cu(**1**) may be in part due to competition from intramolecular binding by the oxygen of the methoxy-propyl chain.

Overall, this study demonstrates the potential of the modular structure of MONs in allowing systematic tuning of their surface properties through isoreticular substitutions. It also highlights the subtle interplay between ligand, metal cluster, solvents and exfoliation conditions in determining the molecular, nanoscopic and macroscopic structure and properties of nanosheets. Only by better understanding these structure–property relationships will we be able to harness the potential of MONs for use as sensors, catalysts and for processing into composite materials for separation and electronics applications.

Experimental Section

Synthesis

Commercial solvents and reagents were used without further purification. Synthesis of organic ligands was carried out in dry glass-

ware with a nitrogen overpressure. Solvothermal synthesis of MOFs was undertaken using borosilicate vials with Teflon faced rubber lined caps.

Dimethyl 2,5-dihydroxyterephthalate and 2,5-Bis(3-methoxypropoxy)-1,4-benzenedicarboxylate (**1**) were synthesised according to previously reported procedures.[23] 2,5-Bis(pentoxy)-1,4-benzenedicarboxylate was similarly synthesised, however the hydrolysis of the protected acid groups was achieved instead through refluxing in THF with aq. KOH (5%). See Section 1.1 in the Supporting Information for details and full materials characterisation.

Cu(**1**)(DMF) was synthesised according to our previous method.[13g] Cu(**2**)(DMF) was similarly synthesised. Specifically, $Cu(NO_3)_2.6H_2O$ and ligand H_2**1** or H_2**2** were dissolved in DMF and sealed into reaction vials, and heated to 110°C for 18 hrs, then slow-cooled, resulting in a 77% yield of green, microcrystalline Cu(**2**)(DMF). Synthetic details and characterisation including elemental analysis, FTIR, TGA and PXRD can be found in the Supporting Information.

Exfoliation

MOF and solvent were added to 10 mL reaction vials in the quantities stated in-text. These were rotated using an adapted Heidolph RZR 2020 overhead stirrer with a multi sample holder, in a Fisher brand Elmasonic P 30H ultrasonic bath (2.75 L, 380/350 W, UNSPSC 42281712) filled with water. The ultrasonic bath was operated at 100% power, at 80 kHz, and was fitted with a cooling coil so as to prevent bath heating upon prolonged exfoliation times.

Characterisation

NMR spectra were recorded on a Bruker Advance DPX 400 spectrometer. ¹H and ¹³C chemical shifts are reported in ppm on the δ scale and were referenced to the residual solvent peak. All coupling constants are reported in Hz. Mass spectra were collected using an Agilent 6530 QTOF LC-MS in positive ionization mode. Elemental analyses were obtained on an Elementar vario MICRO cube. X-Ray powder diffraction patterns were collected using a Bruker D8 Advance powder diffractometer equipped with a copper k_α source ($\lambda = 1.5418$ Å) operating at 40 kV and 40 mA. The instrument was fitted with an energy-dispersive LYNXEYE detector. IR spectroscopy was performed on a PerkinElmer ATR-FTIR Spectrum 2. Thermogravimetric analyses were collected using a PerkinElmer Pyris 1 TGA from 30–600°C at 10°C min⁻¹, under a 10 cm³ min⁻¹ flow of nitrogen. UV/Vis absorption spectra were obtained on a Varian Cary 50 UV or Varian Cary 5000 UV/Vis-NIR spectrophotometer, using standard 1 cm width quartz cells and PerkinElmer Spectrum One software. The nanoscopic morphology of the samples was investigated using a Bruker Multimode 5 AFM with an equipped Nokia 10x visualising lens, operating in soft tapping-mode using Bruker OTESPA-R3 cantilever. Samples were prepared by dropping 10 μL (sample dependant) of suspension onto a freshly cleaved mica substrate. Images were processed using standard techniques with Gwyddion software. DLS data were collected using a Malvern Zetasizer Nano Series particle size analyser equipped with a He-Ne laser at 633 nm, operating in backscatter mode (173 °).

DFT modelling

All calculations were performed using Gaussian 09, version D.01.[24] The functional used was B3LYP.[19] For all atoms the 6–311G** basis set was used[25] apart from Cu, for which we used the SDD pseudo-potential [SDD]. All calculations were run with ultrafine integrals ignoring any potential symmetry in the calculations. All optimiza-

tions were performed with the standard parameters as implemented in G09. All systems were assumed to be dry, so that no additional solvent field was included. For all optimized structures, frequencies were calculated in the harmonic approximation. In a few cases a small (between 0 and −10 cm⁻¹) imaginary frequency was found, which was subsequently ignored, following standard practice, since these are usually caused by quadrature errors. For all comparisons between theory and experiment presented below, a scaling factor of 0.973 was used for values below 2000 cm⁻¹, while for values above 2000 cm⁻¹ a scaling factor of 0.95 was used. It is noted that in previous work it was found that using a single PW to describe a 2D structure resulted in a reasonable agreement between theory and experiment.[26] The computational part of the Supporting Information was created using in-house developed software based on the OpenEye toolkit.

Conflict of interest

The authors declare no conflict of interest.

[1] a) R. Sakamoto, K. Takada, T. Pal, H. Maeda, T. Kambe, H. Nishihara, *Chem. Commun.* **2017**, *53*, 5781–5801; b) D. Rodríguez-San-Miguel, P. Amo-Ochoa, F. Zamora, *Chem. Commun.* **2016**, *52*, 4113–4127; c) M. Zhao, Q. Lu, Q. Ma, H. Zhang, *Small Methods* **2017**, *1*, 1600030; d) R. Sakamoto, K. Takada, X. Sun, T. Pal, T. Tsukamoto, E. J. H. Phua, A. Rapakousiou, K. Hoshiko, H. Nishihara, *Coord. Chem. Rev.* **2016**, *320*, 118–128; e) D. J. Ashworth, J. A. Foster, *J. Mater. Chem. A* **2018**, *6*, 16292–16307.

[2] a) C. Martí-Gastaldo, J. E. Warren, K. C. Stylianou, N. L. O. Flack, M. J. Rosseinsky, *Angew. Chem. Int. Ed.* **2012**, *51*, 11044–11048; *Angew. Chem.* **2012**, *124*, 11206–11210; b) Y. Peng, Y. Li, Y. Ban, H. Jin, W. Jiao, X. Liu, W. Yang, *Science* **2014**, *346*, 1356–1359; c) T. Rodenas, I. Luz, G. Prieto, B. Seoane, H. Miro, A. Corma, F. Kapteijn, F. X. Llabrés i Xamena, J. Gascon, *Nat. Mater.* **2015**, *14*, 48–55.

[3] a) Z.-Q. Li, L.-G. Qiu, W. Wang, T. Xu, Y. Wu, X. Jiang, *Inorg. Chem. Commun.* **2008**, *11*, 1375–1377; b) P. Z. Li, Y. Maeda, Q. Xu, *Chem. Commun.* **2011**, *47*, 8436–8438; c) Y. P. Yuan, W. Wang, L. G. Qiu, F. M. Peng, X. Jiang, A. J. Xie, Y. H. Shen, X. Y. Tian, L. D. Zhang, *Mater. Chem. Phys.* **2011**, *131*, 358–361; d) T. Araki, A. Kondo, K. Maeda, *Chem. Commun.* **2013**, *49*, 552–554; e) M. G. Campbell, D. Sheberla, S. F. Liu, T. M. Swager, M. Dinca, *Angew. Chem. Int. Ed.* **2015**, *54*, 4349–4352; *Angew. Chem.* **2015**, *127*, 4423–4426; f) H.-Q. Zhao, G.-H. Qiu, Z. Liang, M.-M. Li, B. Sun, L. Qin, S.-P. Yang, W.-H. Chen, J.-X. Chen, *Anal. Chim. Acta* **2016**, *922*, 55–63.

[4] a) Q. Liu, Z. X. Low, Y. Feng, S. Leong, Z. X. Zhong, J. F. Yao, K. Hapgood, H. T. Wang, *Microporous Mesoporous Mater.* **2014**, *194*, 1–7; b) Q. Lu, M. T. Zhao, J. Z. Chen, B. Chen, C. Tan, X. Zhang, Y. Huang, J. Yang, F. Cao, Y. Yu, J. Ping, Z. Zhang, X.-J. Wu, H. Zhang, *Small* **2016**, *12*, 4669–

4674; c) Z. P. Sun, L. Hui, W. S. Ran, Y. Lu, D. Z. Jia, *New J. Chem.* **2016**, *40*, 1100 – 1103.

[5] a) X. Sun, K.-H. Wu, R. Sakamoto, T. Kusamoto, H. Maeda, H. Nishihara, *Chem. Lett.* **2017**, *46*, 1072 – 1075; b) R. Sakamoto, T. Yagi, K. Hoshiko, S. Kusaka, R. Matsuoka, H. Maeda, Z. Liu, Q. Liu, W.-Y. Wong, H. Nishihara, *Angew. Chem. Int. Ed.* **2017**, *56*, 3526 – 3530; *Angew. Chem.* **2017**, *129*, 3580 – 3584; c) J. Yang, Z. Ma, W. Gao, M. Wei, *Chem. Eur. J.* **2017**, *23*, 631 – 636; d) N. Lahiri, N. Lotfizadeh, R. Tsuchikawa, V. V. Deshpande, J. Louie, *J. Am. Chem. Soc.* **2017**, *139*, 19 – 22; e) L. Cao, Z. Lin, W. Shi, Z. Wang, C. Zhang, X. Hu, C. Wang, W. Lin, *J. Am. Chem. Soc.* **2017**, *139*, 7020 – 7029.

[6] a) L. Cao, Z. Lin, F. Peng, W. Wang, R. Huang, C. Wang, J. Yan, J. Liang, Z. Zhang, T. Zhang, L. Long, J. Sun, W. Lin, *Angew. Chem. Int. Ed.* **2016**, *55*, 14952 – 14957; *Angew. Chem.* **2016**, *128*, 15176 – 15181; b) Y. Wang, M. Zhao, J. Ping, B. Chen, X. Cao, Y. Huang, C. Tan, Q. Ma, S. Wu, Y. Yu, Q. Lu, J. Chen, W. Zhao, Y. Ying, H. Zhang, *Adv. Mater.* **2016**, *28*, 4149 – 4155; c) Y. Ding, Y. P. Chen, X. Zhang, L. Chen, Z. Dong, H. L. Jiang, H. Xu, H. C. Zhou, *J. Am. Chem. Soc.* **2017**, *139*, 9136 – 9139; d) L. Zhao, B. Dong, S. Li, L. Zhou, L. Lai, Z. Wang, S. Zhao, M. Han, K. Gao, M. Lu, X. Xie, B. Chen, Z. Liu, X. Wang, H. Zhang, H. Li, J. Liu, H. Zhang, X. Huang, W. Huang, *ACS Nano* **2017**, *11*, 5800 – 5807; e) Y.-N. Li, S. Wang, Y. Zhou, X.-J. Bai, G.-S. Song, X.-Y. Zhao, T.-Q. Wang, X. Qi, X.-M. Zhang, Y. Fu, *Langmuir* **2017**, *33*, 1060 – 1065; f) W. Shi, L. Cao, H. Zhang, X. Zhou, B. An, Z. Lin, R. Dai, J. Li, C. Wang, C. Lin, *Angew. Chem. Int. Ed.* **2017**, *56*, 9704 – 9709; *Angew. Chem.* **2017**, *129*, 9836 – 9841.

[7] F. Bonaccorso, A. Bartolotta, J. N. Coleman, C. Backes, *Adv. Mater.* **2016**, *28*, 6136 – 6166.

[8] a) M. Yi, Z. Shen, *J. Mater. Chem. A* **2015**, *3*, 11700 – 11715; b) J. N. Coleman, M. Lotya, A. O'Neill, S. D. Bergin, P. J. King, U. Khan, K. Young, A. Gaucher, S. De, R. J. Smith, I. V. Shvets, S. K. Arora, G. Stanton, H.-Y. Kim, K. Lee, G. T. Kim, G. S. Duesberg, T. Hallam, J. J. Boland, J. J. Wang, J. F. Donegan, J. C. Grunlan, G. Moriarty, A. Shmeliov, R. J. Nicholls, J. M. Perkins, E. M. Grieveson, K. Theuwissen, D. W. McComb, P. D. Nellist, V. Nicolosi, *Science* **2011**, *331*, 568 – 571; c) C. Backes, T. M. Higgins, A. Kelly, C. Boland, A. Harvey, D. Hanlon, J. N. Coleman, *Chem. Mater.* **2017**, *29*, 243 – 255; d) V. Nicolosi, M. Chhowalla, M. G. Kanatzidis, M. S. Strano, J. N. Coleman, *Science* **2013**, *340*, 1226419; e) H. Tao, Y. Zhang, Y. Gao, Z. Sun, C. Yan, J. Texter, *Phys. Chem. Chem. Phys.* **2017**, *19*, 921 – 960.

[9] a) A. Gallego, C. Hermosa, O. Castillo, I. Berlanga, C. J. Gomez-Garcia, E. Mateo-Marti, J. I. Martinez, F. Flores, C. Gomez-Navarro, J. Gomez-Herrero, S. Delgado, F. Zamora, *Adv. Mater.* **2013**, *25*, 2141 – 2146; b) B. Garai, A. Mallick, A. Das, R. Mukherjee, R. Banerjee, *Chem. Eur. J.* **2017**, *23*, 7361 – 7366.

[10] M. J. Cliffe, E. Castillo-Martinez, Y. Wu, J. Lee, A. C. Forse, F. C. N. Firth, P. Z. Moghadam, D. Fairen-Jimenez, M. W. Gaultois, J. A. Hill, O. V. Magdysyuk, B. Slater, A. L. Goodwin, C. P. Grey, *J. Am. Chem. Soc.* **2017**, *139*, 5397 – 5404.

[11] X. Wang, C. Chi, K. Zhang, Y. Qian, K. M. Gupta, Z. Kang, J. Jiang, D. Zhao, *Nat. Commun.* **2017**, *8*, 14460.

[12] a) W.-J. Song, *Talanta* **2017**, *170*, 74 – 80; b) H.-S. Wang, J. Li, J.-Y. Li, K. Wang, Y. Ding, X.-H. Xia, *NPG Asia Mater.* **2017**, *9*, e354.

[13] a) P. Amo-Ochoa, L. Welte, R. Gonzalez-Prieto, P. J. Sanz Miguel, C. J. Gomez-Garcia, E. Mateo-Marti, S. Delgado, J. Gomez-Herrero, F. Zamora, *Chem. Commun.* **2010**, *46*, 3262 – 3264; b) J.-C. Tan, P. J. Saines, E. G. Bithell, A. K. Cheetham, *Acs Nano* **2012**, *6*, 615 – 621; c) A. Kondo, C. C. Tiew, F. Moriguchi, K. Maeda, *Dalton Trans.* **2013**, *42*, 15267 – 15270;

d) P. J. Beldon, S. Tominaka, P. Singh, T. S. Dasgupta, E. G. Bithell, A. K. Cheetham, *Chem. Commun.* **2014**, *50*, 3955 – 3957; e) C. Hermosa, B. R. Horrocks, J. I. Martinez, F. Liscio, J. Gomez-Herrero, F. Zamora, *Chem. Sci.* **2015**, *6*, 2553 – 2558; f) H. Xu, J. Gao, X. Qian, J. Wang, H. He, Y. Cui, Y. Yang, Z. Wang, G. Qian, *J. Mater. Chem. A* **2016**, *4*, 10900 – 10905; g) J. A. Foster, S. Henke, A. Schneemann, R. A. Fischer, A. K. Cheetham, *Chem. Commun.* **2016**, *52*, 10474 – 10477.

[14] S. C. Junggeburth, L. Diehl, S. Werner, V. Duppel, W. Sigle, B. V. Lotsch, *J. Am. Chem. Soc.* **2013**, *135*, 6157 – 6164.

[15] P. Chandrasekhar, A. Mukhopadhyay, G. Savitha, J. N. Moorthy, *J. Mater. Chem. A* **2017**, *5*, 5402 – 5412.

[16] K. K. Tanabe, C. A. Allen, S. M. Cohen, *Angew. Chem. Int. Ed.* **2010**, *49*, 9730 – 9733; *Angew. Chem.* **2010**, *122*, 9924 – 9927.

[17] T. Y. Wu, N. Guo, C. Y. Teh, J. X. W. Hay, 2013 ed., Springer, Dordrecht, **2013**, pp. 5 – 11.

[18] J. R. Loader, University of Sheffield (Sheffield), **2013**.

[19] A. D. Becke, *J. Chem. Phys.* **1993**, *98*, 5648 – 5652.

[20] C. Backes, B. M. Szydłowska, A. Harvey, S. Yuan, V. Vega-Mayoral, B. R. Davies, P.-l. Zhao, D. Hanlon, E. J. G. Santos, M. I. Katsnelson, W. J. Blau, C. Gadermaier, J. N. Coleman, *ACS Nano* **2016**, *10*, 1589 – 1601.

[21] M. Lotya, A. Rakovich, J. F. Donegan, J. N. Coleman, *Nanotechnology* **2013**, *24*, 265703.

[22] a) A. Liscio, K. Kouroupis-Agalou, X. D. Betriu, A. Kovtun, E. Treossi, N. M. Pugno, G. De Luca, L. Giorgini, V. Palermo, *2D Mater.* **2017**, *4*, 025017; b) A. Mukhopadhyay, V. K. Maka, G. Savitha, J. N. Moorthy, *Chem.* **2018**, *4*, 1059 – 1079.

[23] a) S. Henke, R. A. Fischer, *J. Am. Chem. Soc.* **2011**, *133*, 2064 – 2067; b) S. Henke, A. Schneemann, A. Wutscher, R. A. Fischer, *J. Am. Chem. Soc.* **2012**, *134*, 9464 – 9474.

[24] Gaussian 09, Revision D.01, M. J. Frisch, G. W. Trucks, H. B. Schlegel, M. A. Robb, J. R. Cheeseman, G. Scalmani, V. Barone, G. A. Petersson, H. Nakatsuji, X. Li, M. Caricato, A. Marenich, J. Bloino, B. G. Janesko, R. Gomperts, B. Mennucci, H. P. Hratchian, J. V. Ortiz, A. F. Izmaylov, J. L. Sonnenberg, D. Williams-Young, F. Ding, F. Lipparini, F. Egidi, J. Goings, B. Peng, A. Petrone, T. Henderson, D. Ranasinghe, V. G. Zakrzewski, J. Gao, N. Rega, G. Zheng, W. Liang, M. Hada, M. Ehara, K. Toyota, R. Fukuda, J. Hasegawa, M. Ishida, T. Nakajima, Y. Honda, O. Kitao, H. Nakai, T. Vreven, K. Throssell, J. A. Montgomery, Jr., J. E. Peralta, F. Ogliaro, M. Bearpark, J. J. Heyd, E. Brothers, K. N. Kudin, V. N. Staroverov, T. Keith, R. Kobayashi, J. Normand, K. Raghavachari, A. Rendell, J. C. Burant, S. S. Iyengar, J. Tomasi, M. Cossi, J. M. Millam, M. Klene, C. Adamo, R. Cammi, J. W. Ochterski, R. L. Martin, K. Morokuma, O. Farkas, J. B. Foresman, D. J. Fox, Gaussian, Inc., Wallingford, CT, **2016**.

[25] a) R. Krishnan, J. S. Binkley, R. Seeger, J. A. Pople, *J. Chem. Phys.* **1980**, *72*, 650 – 654; b) A. D. McLean, G. S. Chandler, *J. Chem. Phys.* **1980**, *72*, 5639 – 5648; c) U. H.-u. D. Andrae, M. Dolg, H. Stoll, H. Preuss, *Theor. Chim. Acta* **1990**, *77*, 123 – 141.

[26] P. Smart, C. A. Mason, J. R. Loader, A. J. H. M. Meijer, A. J. Florence, K. Shankland, A. J. Fletcher, S. P. Thompson, M. Brunelli, A. H. Hill, L. Brammer, *Chem. Eur. J.* **2013**, *19*, 3552 – 3557.

CHEMISTRY
A European Journal

Supporting Information

Ultrasonic Exfoliation of Hydrophobic and Hydrophilic Metal–Organic Frameworks To Form Nanosheets

David J. Ashworth, Adam Cooper, Mollie Trueman, Rasha W. M. Al-Saedi, Liam D. Smith, Anthony J. H. M. Meijer, and Jonathan A. Foster*[a]

chem_201803221_sm_miscellaneous_information.pdf

Contents

2. General Experimental

Commercial solvents and reagents were used without further purification, solvents used for UV-vis studies were HPLC or spectroscopic grade. Synthesis of organic ligands was carried out in dry glassware with a nitrogen overpressure. Solvothermal synthesis of metal-organic frameworks was undertaken using borosilicate vials with Teflon faced rubber lined caps.

NMR spectra were recorded on a Bruker Advance DPX 400 spectrometer. Chemical shifts for 1H and 13C are reported in ppm on the δ scale; 1H and 13C chemical shifts were referenced to the residual solvent peak. All coupling constants are reported in Hz. Mass spectra were collected using an Agilent 6530 QTOF LC-MS in positive ionization mode.

Elemental analyses were obtained on an Elementar vario MICRO cube CHNS analyser equipped with a thermal conductivity detector. X-Ray powder diffraction patterns were collected using a Bruker D8 Advance powder diffractometer equipped with a copper k_{α} source (λ=1.5418 Å) operating at 40 kV and 40 mA. The instrument was fitted with an energy-dispersive LYNXEYE detector. Measurements were conducted using a rotatable capillary goniometer stage or a fixed goniometer stage with a rotating flat plate sample holders. IR spectroscopy was performed on a Perkin Elmer ATR-FTIR Spectrum 2. Thermogravimetric analysis was collected using a Perkin Elmer Pyris 1 TGA from 30-600 ºC at 10 ºC min^{-1}, under a 20 mL min^{-1} N$_2$ flow.

UV-vis absorption spectra were collected on a Cary 5000 UV-vis-NIR instrument, using a 1 cm internal length quartz cuvette and Cary WinUV (version 3.00) software in absorbance mode, with a resolution of 1 nm^{-1}. Calculation of absorption coefficients were undertaken with Excel software.

Nanoscopic characterisation was performed using a Bruker Multimode 5 AFM, operating in soft tapping mode under ambient conditions. Bruker OTESPA-R3 cantilever were used, with a drive amplitude and nominal resonance frequency of 20.4 mV and 290 kHz, respectively. Images were processed using standard techniques with free Gwyddion (version 2.47) software.

DLS data were collected using a Malvern Zetasizer Nano Series particle size analyser, using a He-Ne laser at 633 nm, operating in backscatter mode (173 °). Samples were equilibrated at 298 K for 60 s prior to analysis.

3. MOF Syntheses and Characterisation

Synthesis of ligand H$_2$**1**
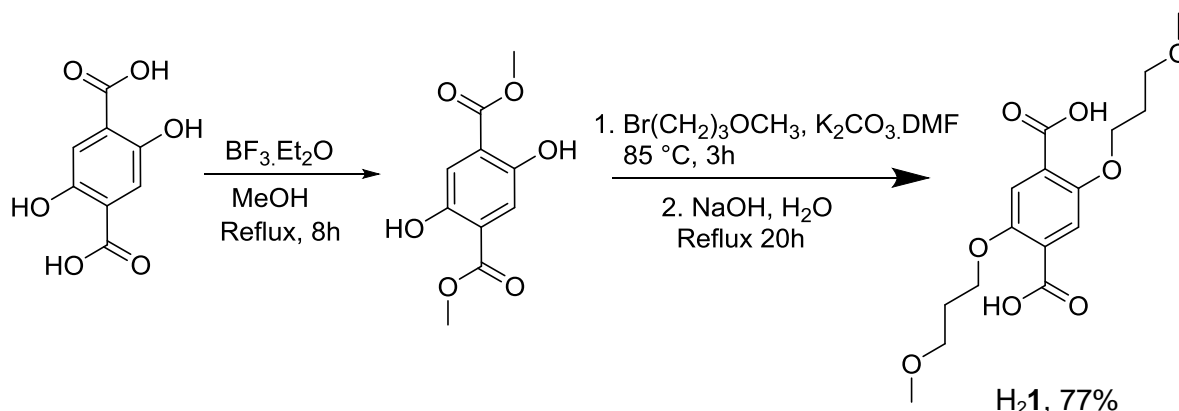
Scheme S1. Synthetic pathway for the synthesis of 2,5-Bis(3-methoxypropoxy)-1,4-benzenedicarboxylate

Dimethyl 2,5-dihydroxyterephthalate,[1] ligand H$_2$**1** synthesised were synthesised according to a previously reported method summarised in scheme S1.[2,3] This method had to be adapted for the synthesis of H$_2$**2** in order to improve the solubility of the more hydrophobic ligand during the final deprotection step.

Synthesis of ligand H$_2$**2**
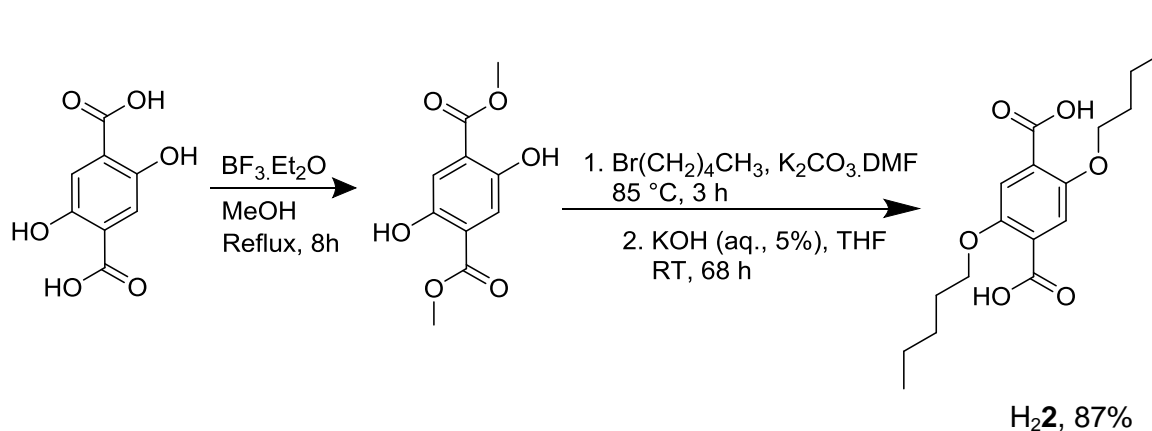
Scheme S2. Synthetic pathway for the synthesis of 2,5-Bis(pentoxy)-1,4-benzenedicarboxylate

Dimethyl 2,5-dihydroxyterephtalate (2.089 g) and K$_2$CO$_3$ (5.228 g) were suspended in DMF (70 mL). 1-bromopentane (3.4 ml) was then added and the mixture heated at 85°C for 3 h. The mixture was then allowed to cool to RT overnight. The mixture was filtered and the filtrate collected. The solvent was removed under reduced pressure to yield a brown oil. This was refluxed in THF (70 mL) with aq. KOH (5%, 70 mL) for 68 h. The THF was removed under reduced pressure and the remaining mixture was acidified with aq. HCl (10%) then filtered to yield H$_2$**2** (2.714 g, 87%) as a white solid. ^{1}H NMR (400 MHz, CDCl$_3$) δ/ppm 11.34 (2H, s, COO*H*), 7.88 (2H, s, Ar-*H*), 4.40 (4H, t, *J*=5.68, Ar-OC*H$_2$*), 3.63 (4H, t, *J*=5.32, CH$_3$OC*H$_2$*), 3.40 (6H, s, OC*H$_3$*), 2.19 (4H, q, *J*=5.44, 5.64, OCH$_2$C*H$_2$*). ESI-MS (CH$_3$Cl): m/z 321.2 ([M-H$_2$O]$^+$), 339.2 ([MH]$^+$), 361.2 ([M+Na]$^+$). Elemental Analysis, calculated for C$_{18}$H$_{26}$O6: Expected: C, 63.89; H, 7.74. Found: C, 63.70; H, 7.46.

3

Synthesis of Cu(**1**)(DMF)

Cu(NO$_3$)$_2$.3H$_2$O (0.1208 g, 0.5 mmol) and H$_2$**1** (0.1712 g, 0.5 mmol) were dissolved in DMF (10 mL) and sealed in a 10 mL reaction vial. The vial was heated at 110°C for 18 h then cooled to room temperature at 0.1 °C min^{-1}. The precipitate was filtered then washed with DMF (3x5 mL) and DCM (1x5 mL) to yield Cu(**1**)(DMF) (0.1625 g, 68%) as a light green powder. Elemental Analysis, calculated for C$_{19}$H$_{27}$CuNO$_9$: Expected: C, 47.83; H, 5.43; N, 2.94 %. Found: C, 45.95; H, 5.43; N, 2.78 %.

Synthesis of Cu(**2**)(DMF)

Cu(NO$_3$)$_2$.3H$_2$O (0.1358 g, 0.56 mmol) and H$_2$**2** (0.1685 g, 0.5 mmol) were dissolved in DMF (10 mL) and sealed in a 10 mL reaction vial. The vial was heated at 110°C for 18 h then cooled to room temperature. The precipitate was filtered and washed with DMF (3x5 mL) and DCM (1x5 mL) to yield Cu(**2**)(DMF) (0.1825 g, 77%) as a light green powder. Elemental Analysis, calculated for C$_{21}$H$_{31}$CuNO$_7$: Expected: C, 53.30; H, 6.61; N, 2.96 %. Found: C, 51.11; H, 6.38; N, 2.96 %.
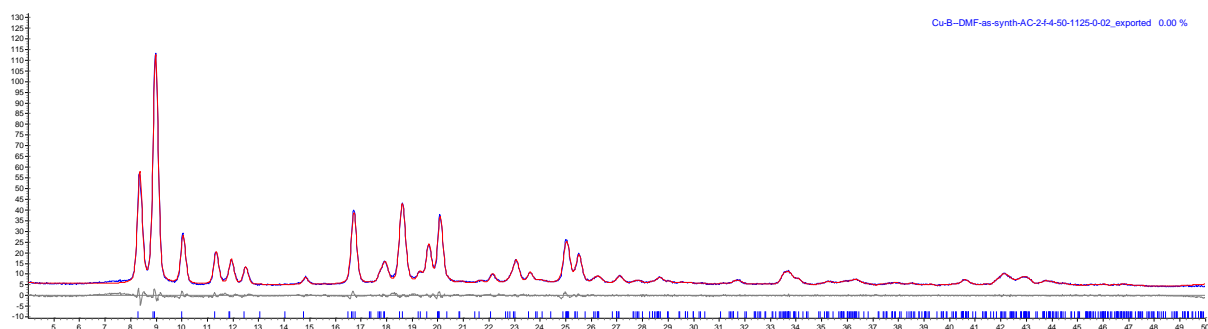
Figure S1. Pawley fit to the X-ray diffraction pattern of Cu(**2**)(DMF). The blue lines, red lines, and black lines represent the experimental, calculated, and difference profiles respectively. The blue tick marks indicate the positions of allowed Bragg reflections in the space group P-1. Experimental data was collected with the diffractometer operating in flat plate mode.

The corresponding Pawley fit for Cu(**1**)(DMF) can be found in reference S3.

Table S1. Crystallographic data of the Cu(X)(DMF) materials determined by Pawley refinement of XRPD data, where X is **1** or **2**.

Sample	Zn(**1**)(DMF)[a]	Cu(**1**)(DMF)[b]	Cu(**2**)(DMF)
Space Group	*P*-1	*P*-1	*P*-1
a / Å	10.4273(6)	10.5245(6)	10.825(3)
b / Å	10.8211(5)	10.7624(6)	10.795(2)
c / Å	10.8805(3)	10.8072(6)	10.835(3)
a / °	85.208(3)	85.293(8)	83.81(1)
b / °	74.992(3)	77.110(5)	79.95(2)

g / °	67.508(5)	68.264(4)	67.55(2)
V / Å^3	1095.45(9)	1108.43(12)	1151.0(6)
R_{wp}		2.898	4.353
R_{exp}		1.081	2.105

[a] Reference single crystal data collected at 100 K (CCDC 1460747).[3] [b] Data previously reported in [3].

4. UV-Vis Studies

Liquid Exfoliation method

The Cu(**1**)(DMF) or Cu(**2**)(DMF) powders were lightly ground to ensure homogeneity and 5 mg was added to a 10 mL glass vial along with 6 mL of the desired solvent. The sample was mixed in a vortex mixer for 30 seconds to disperse the sediment. The samples were sonicated using a Fisherbrand Elmasonic P 30H ultrasonic bath (2.75 L, 380/350 W, UNSPSC 42281712) filled with water. Samples were sonicated for 30 min at a frequency of 80 kHz with 100% power and the temperature was thermostatically maintained at 16-20°C using a steel cooling coil. Sonication was applied using a sweep mode and samples were rotated through the water using an overhead stirrer to minimise variation due to ultrasound "hot-spots". The set-up for exfoliation is shown in **Figure S2**. Following sonication, the vials were transferred to centrifuge tubes and centrifuged at 1500 RPM for 10 minutes and care was taken to avoid redispersing the samples on removal. All analysis was conducted on the top 3 mL of suspension.

Figure S2. Experimental set-up for exfoliation using ultrasonication.
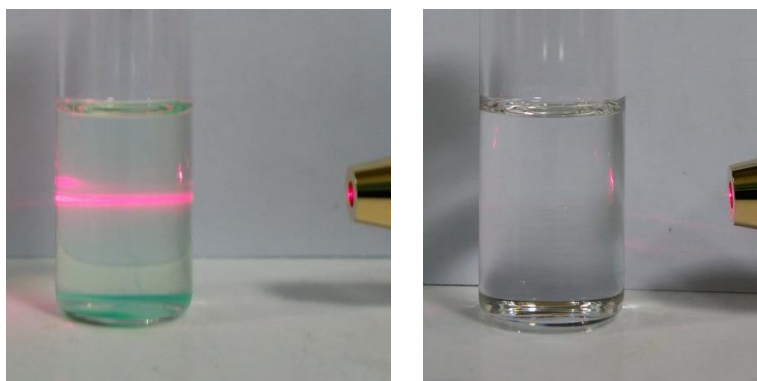
Figure S3. Images showing the presence of Tyndall scattering following the exfoliation of Cu(**1**)(DMF) in DMF (left) which is absent in the reference solution of DMF (right).
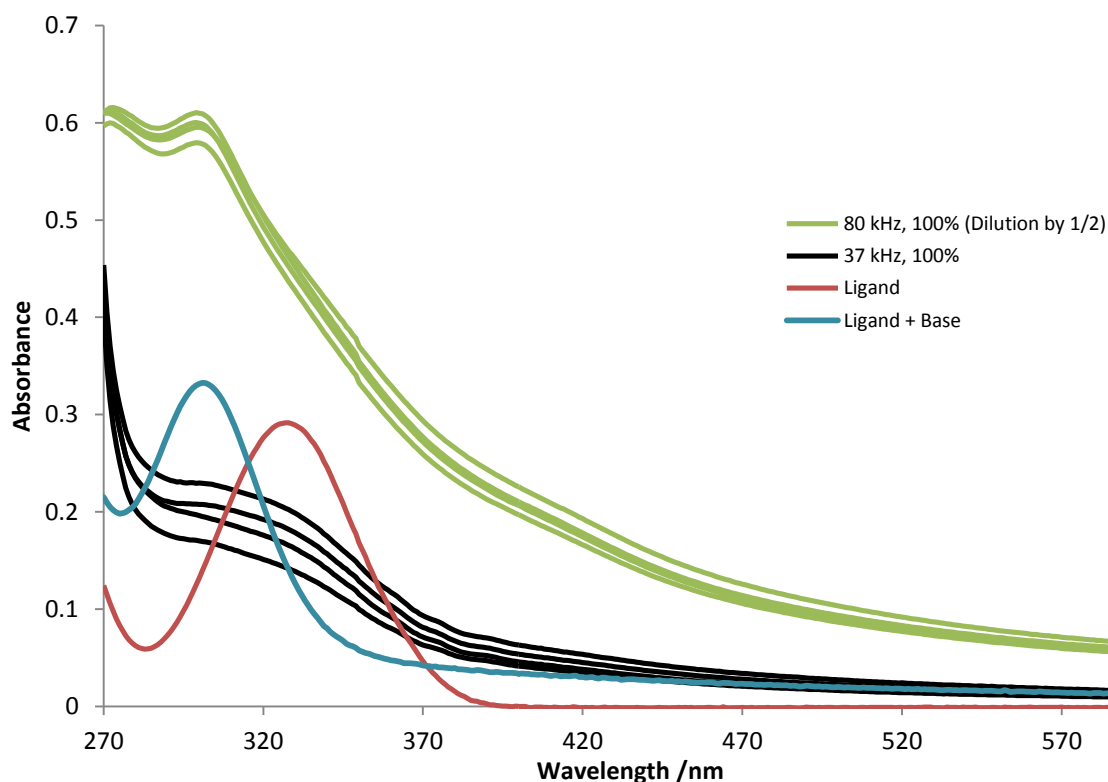
Figure S4 Preliminary data showing UV-vis spectra of suspension following liquid exfoliation of Cu(**1**)(DMF) for <u>30 mins</u> in DMF at 80 KHz (green) and 37 KHz (black) as well as for **1** in DMF (red) and **1** + 2 eq. NaOH. It should be noted that the temperature was not regulated during this experiment.

UV-vis Method

A background was taken of a quartz cuvette with 1 cm internal path length filled with the relevant solvent. The cuvette was then loaded with 3 mL of sample taken from the top of a freshly prepared suspension and loaded into the spectrophotometer. Spectra were recorded in absorbance mode with a scan range of 200-800 nm and a resolution of 1 nm^{-1}. Highly absorbing samples were diluted with additional solvent.
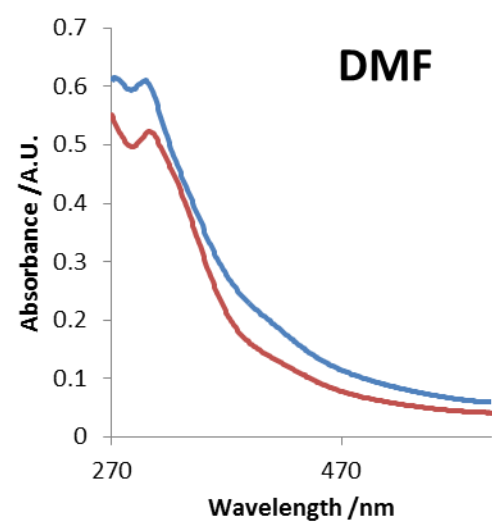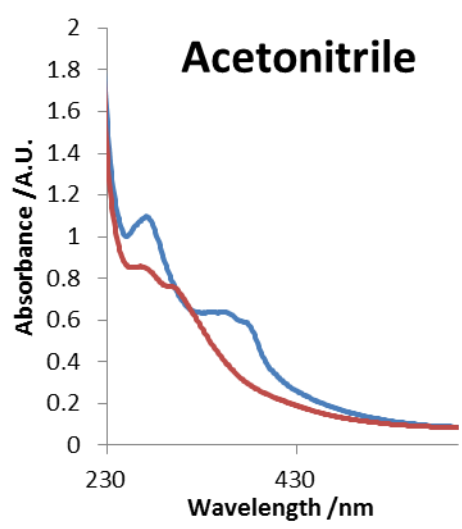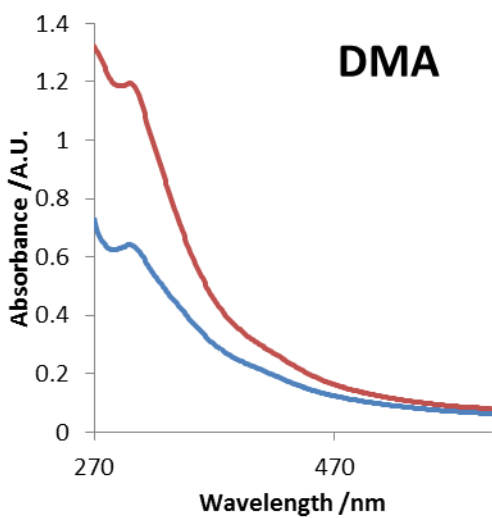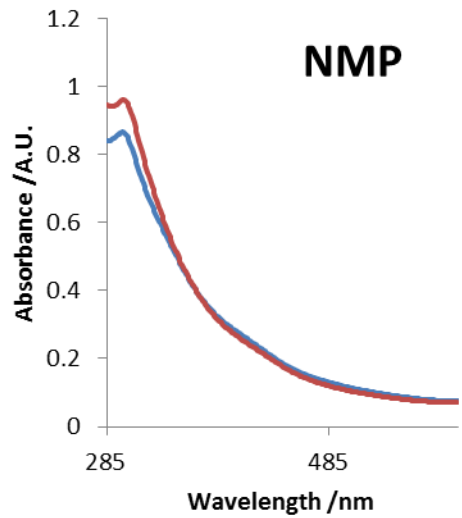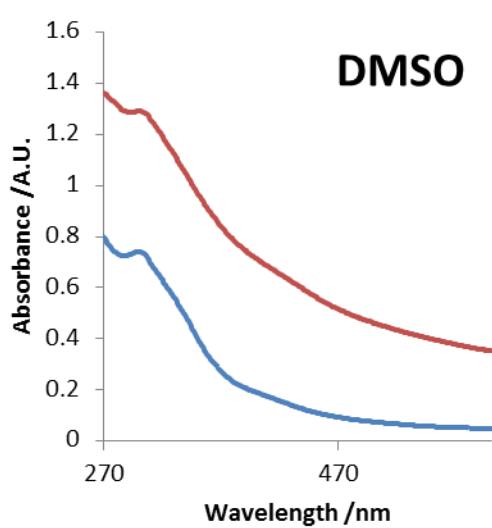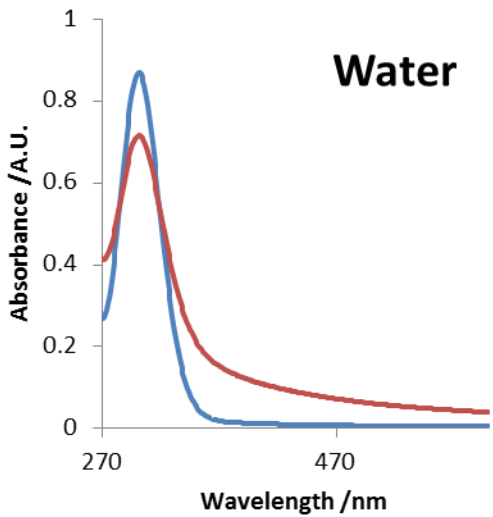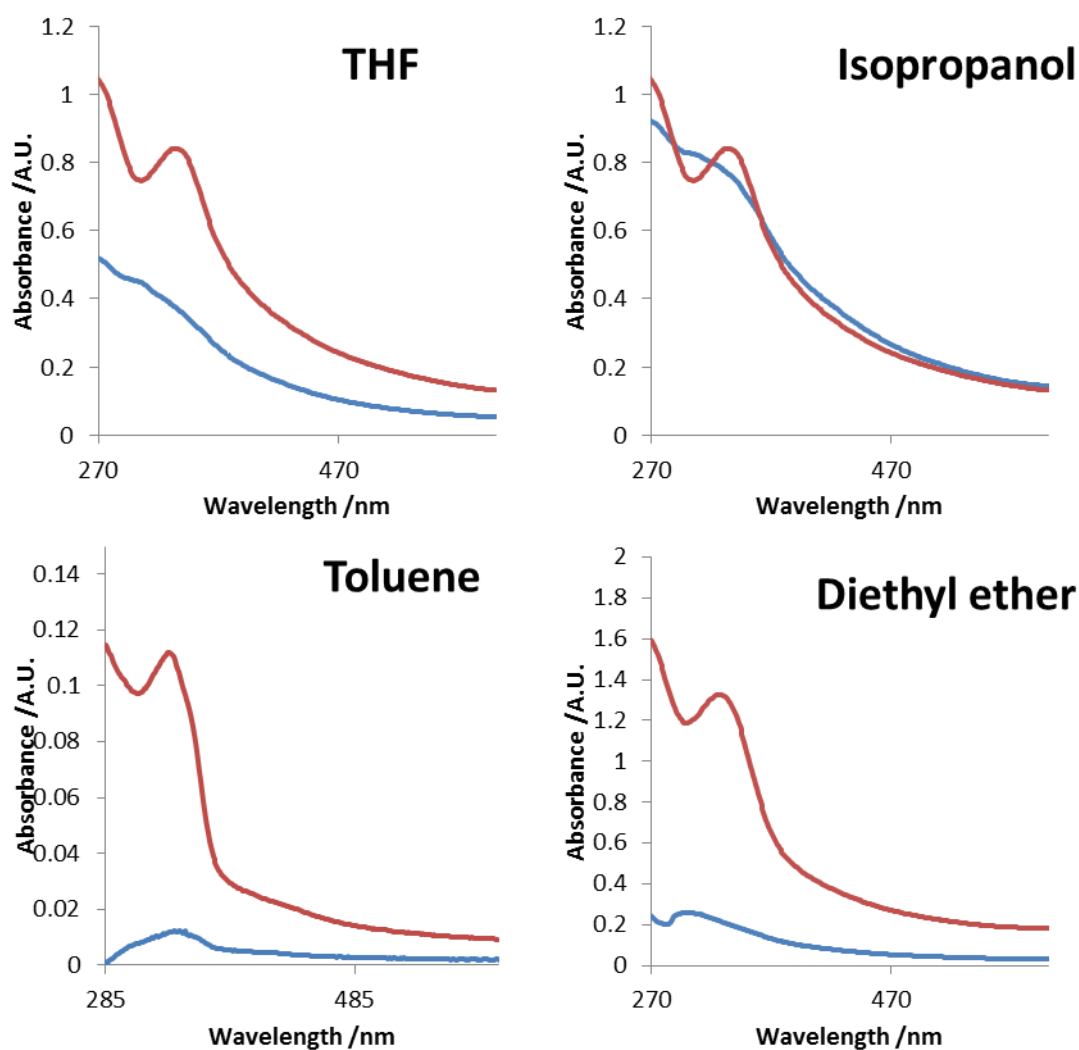
Figure S5. Representative spectra for the exfoliation of Cu(**1**)(DMF) [blue] and Cu(**2**)(DMF) [red] in a range of solvents.

Table S2. List of solvents initially investigated but excluded from further analysis

Excluded solvents	Reason
Acetone	UV/Vis cut off too high (330 nm).
Benzonitrile	UV/Vis cut off too high (330 nm). No absorption maximum in 300-305 nm region.
Benzyl alcohol	Hygroscopic. Handling recommended under inert atmosphere.
tert-Butanol	Solid at ambient temperature.
Carbon disulfide	UV/Vis cut-off too high (380 nm).
Ethanol	No absorption maximum in 300-305 nm region.
Ethyl acetate	No absorption maximum in 300-305 nm region.
Ethylene glycol	Viscosity too high.

Glycerol	Viscosity too high.
Methanol	No absorption maximum in 300-305 nm region.
Methyl isobutyl ketone	UV/Vis cut-off too high (335 nm).

4.2 Molar Extinction Coefficients

A known mass of MOF (approximately 8 mg) was added to a 10 mL volumetric flask which was then made up with the relevant solvent. The flask was sonicated at 80 kHz until all solid material was dispersed in solution i.e. no sediment remained on the bottom of the flask and large particles could not be seen in solution. This solution was then diluted accordingly and analysed by UV/Vis spectrometry. The absorbance values at λ_{max} of the spectra obtained was plotted against MOF concentration. This yielded a linear plot to which the gradient corresponds to the molar extinction coefficient for the MOF in that specific solvent.

Note, it was not possible to calculate extinction coefficients for samples dispersed in cyclohexane or hexane due to the low degree of dispersion.

Table S3. Molar extinction coefficients for Cu(**1**)(DMF) exfoliated in the selected solvents.

Solvent	λ_{max} /nm	Molar extinction coefficient / mol^{-1} dm^3 cm^{-1}	%Standard Error
Acetonitrile	276	3466	8
DCM	274	3274	7
Diethyl ether	299	6693	13
DMA	300	2732	5
DMF	302	2644	4
DMSO	299	1892	6
IPA	271	5104	10
NMP	299	2705	6
THF	304	2404	6
Water	302	2827	5

Table S4. Molar extinction coefficients for Cu(**2**)(DMF) exfoliated in the selected solvents.

Solvent	λ_{max} /nm	Molar extinction coefficient / mol^{-1} dm^3 cm^{-1}	%Standard Error
Acetonitrile	304	4208	1
DCM	271	2467	10
Diethyl ether	334	3519	6
DMA	303	3423	2
DMF	303	3976	2

IPA	338	4339		4	
NMP	301	3731		3	
THF	331	4489		3	
Water	303	3088		3	

Table S5. List of solvent properties used for analysis

	Polarity index	∂_t	∂_d	∂_p	∂_h	γ_L @25 C /(mN/m)
Acetonitrile	5.8	24.4	15.3	18.0	6.1	28.66
DMSO	7.2	26.7	18.4	16.4	10.2	42.92
Water	9	47.8	15.6	16	42.3	71.99
DMF	6.4	24.8	17.4	13.7	11.3	35.74
NMP	6.7	22.9	18	12.3	7.2	40.21
DMA	6.5	22.7	16.8	11.5	10.2	36.70
Isopropanol	3.9	23.5	15.8	6.1	16.4	20.93
Tetrahydrofuran	4	19.4	16.8	5.7	8.0	26.70
Diethyl ether	2.8	15.8	14.5	2.9	5.1	16.65
Cyclohexane	0.2	16.8	16.8	0.0	0.2	24.16
n-Hexane	0.1	14.9	14.9	0.0	0.0	17.89

4.3 Dispersed Concentration vs Solvent Parameter Plots
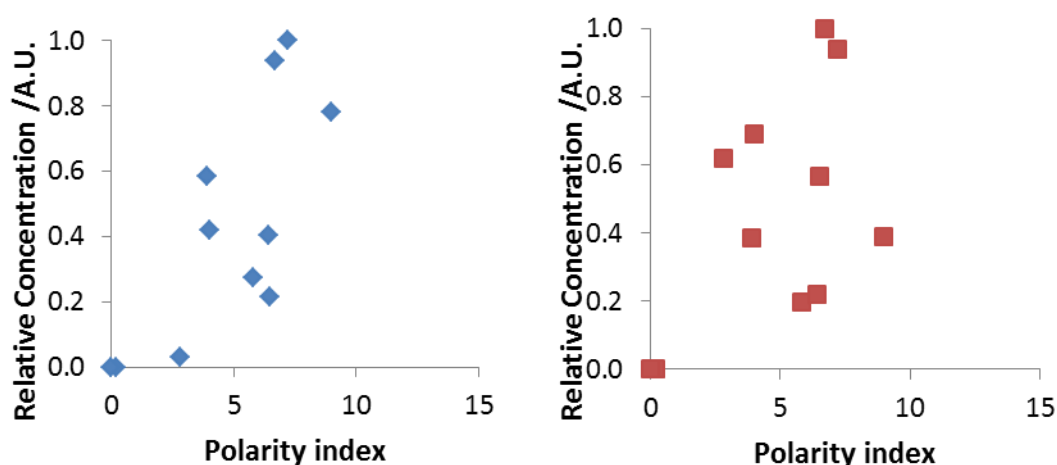
Figure S6. Plots showing the concentration Cu(**1**)(DMF) (left/blue) and Cu(**2**)(DMF) (right/red) normalised relative to the highest value against polarity index of the exfoliation solvent.
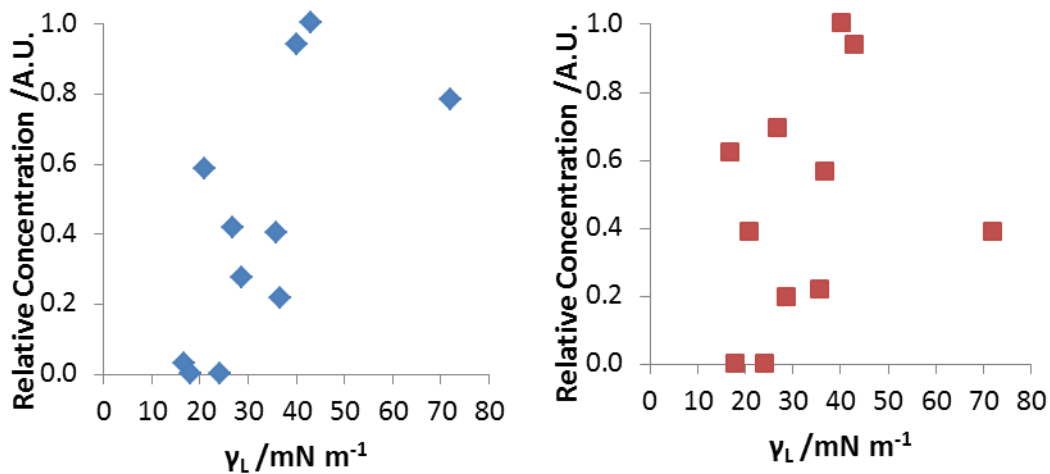
Figure S7. Plots showing the concentration Cu(**1**)(DMF) (left/blue) and Cu(**2**)(DMF) (right/red) normalised relative to the highest value against the surface tension γ_L of the exfoliation solvent.
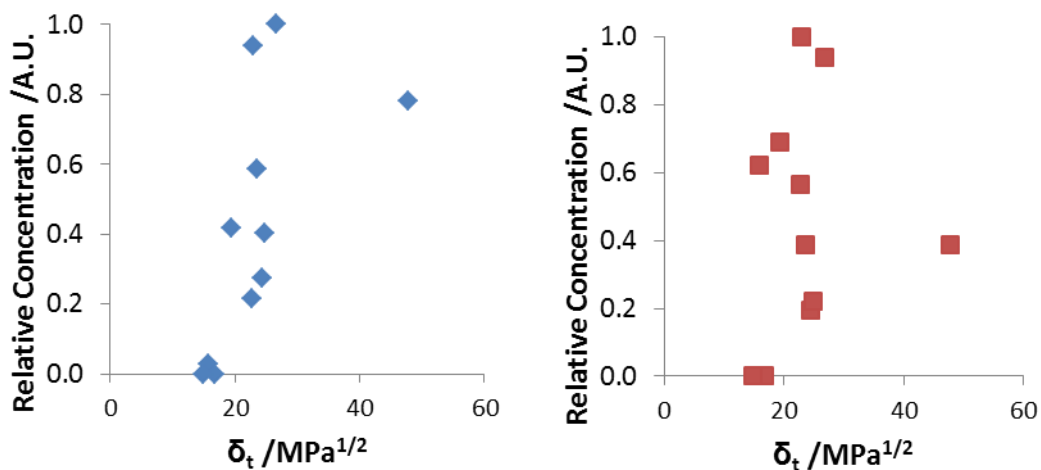
Figure S8. Plots showing the concentration Cu(**1**)(DMF) (left/blue) and Cu(**2**)(DMF) (right/red) normalised relative to the highest value against the total Hansen Solubility parameter (δ_t) of the exfoliation solvent.
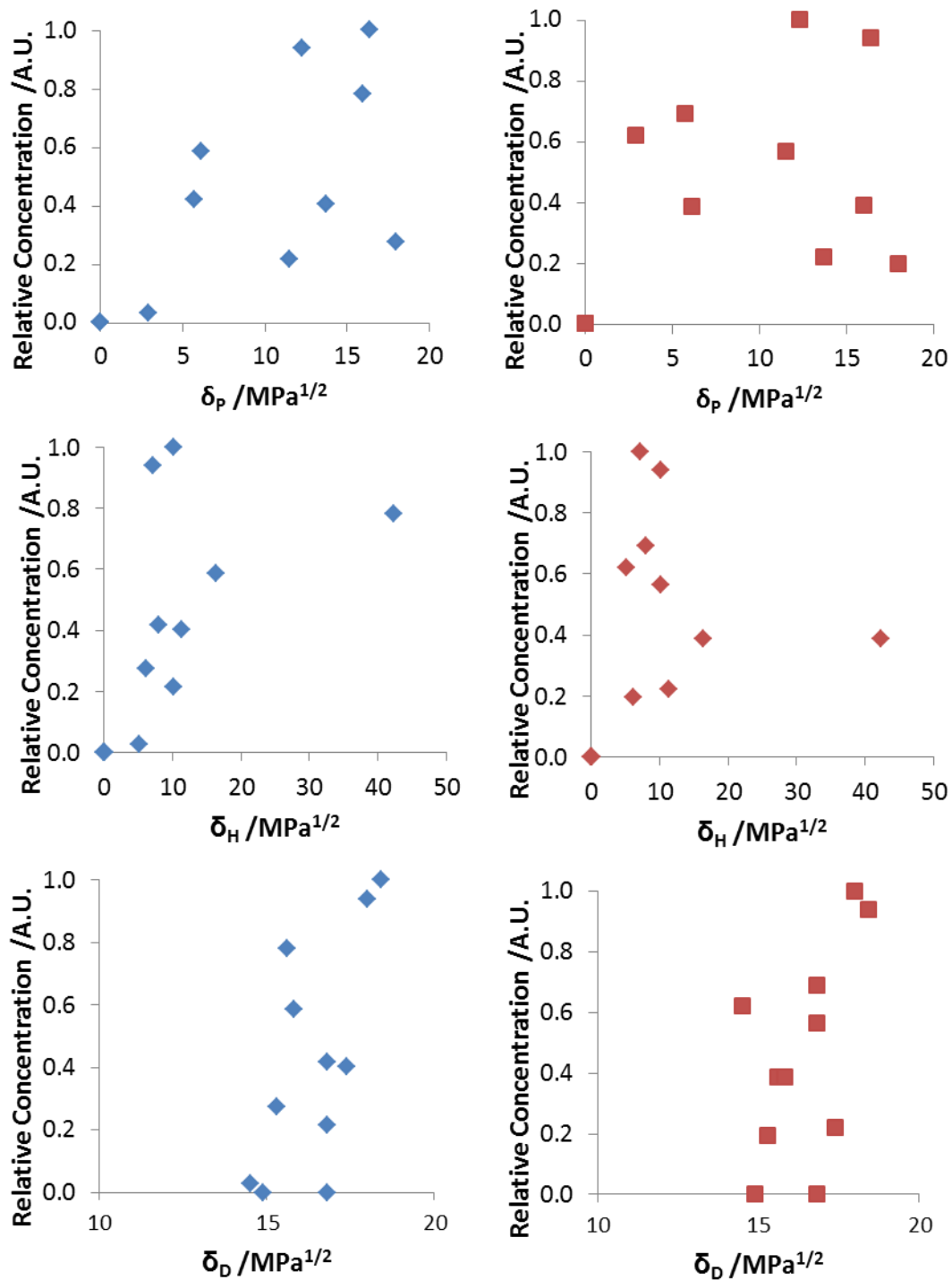
Figure S9. Plots showing the concentration Cu(**1**)(DMF) (left/blue) and Cu(**2**)(DMF) (right/red) normalised relative to the highest value against (top to bottom) the polar (δ_p), hydrogen bonding (δ_d) and dispersive (δ_d) Hansen Solubility parameters of the exfoliation solvent.

12
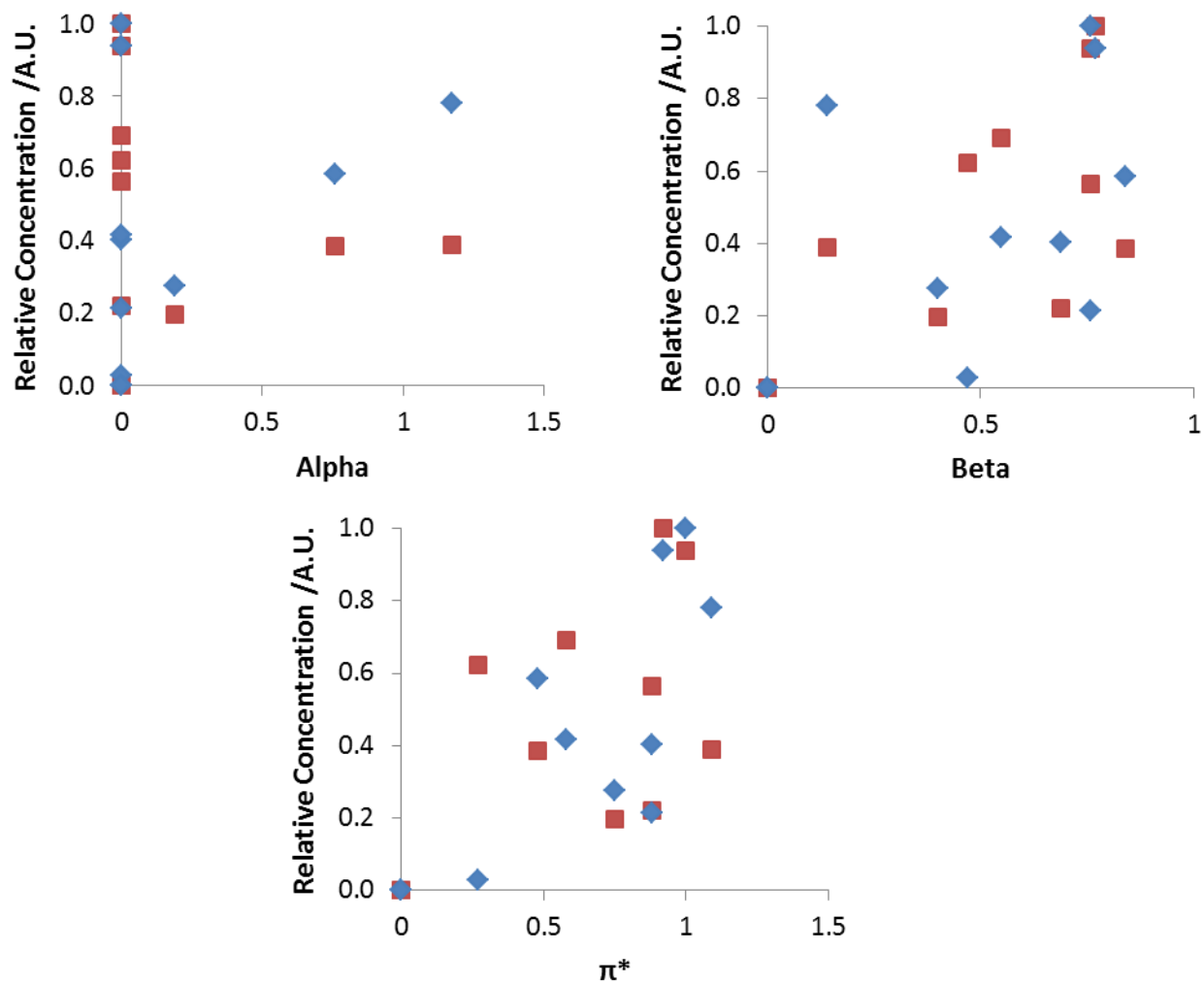
Figure S10. Plots showing the concentration Cu(**1**)(DMF) (blue) and Cu(**2**)(DMF) (red) normalised relative to the highest value against hydrogen bond donor (alpha), hydrogen bond acceptor (beta) and dipolarity/polarizability (π*) Kamlet-Taft parameters of the exfoliation solvent.
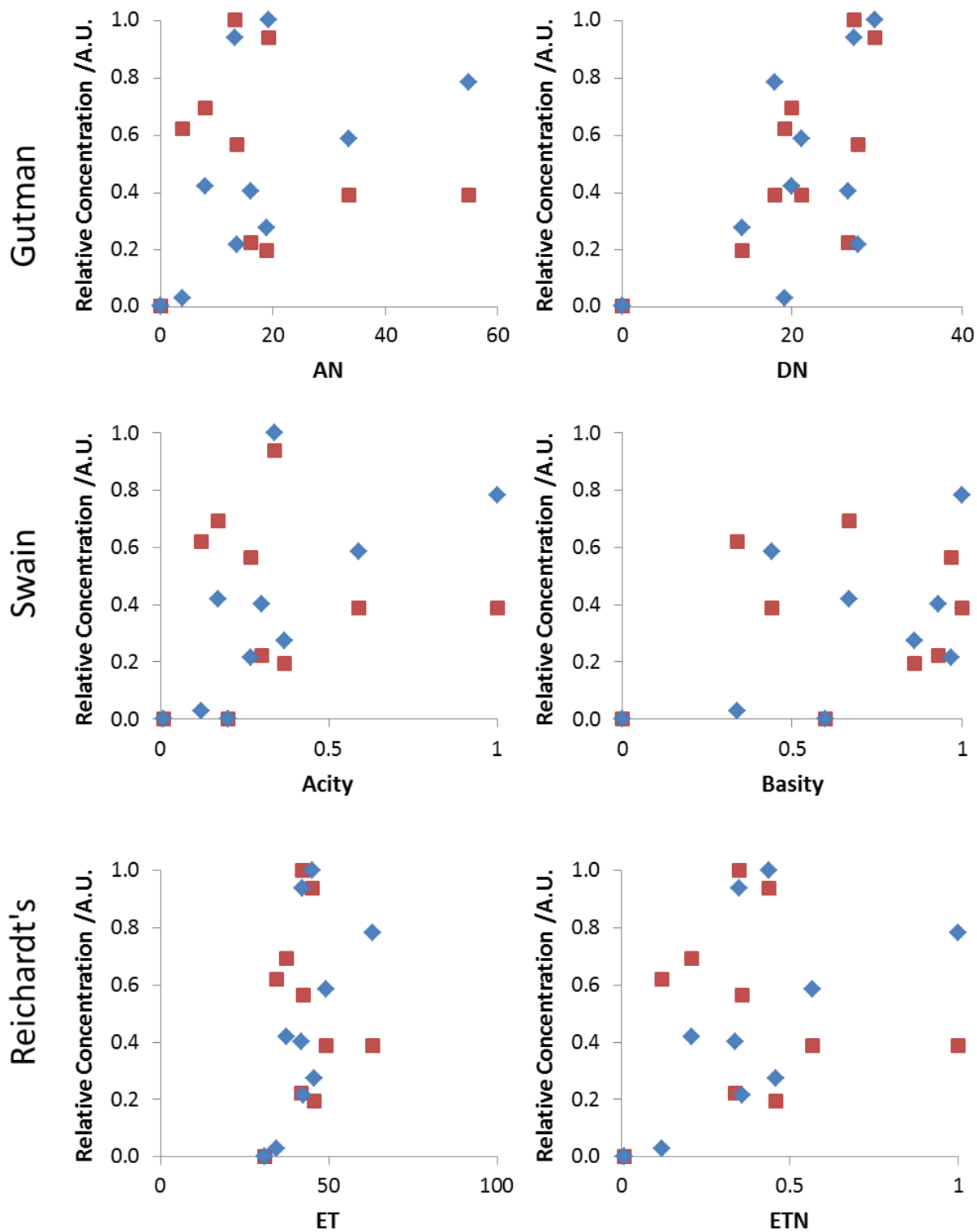
Figure S11. Plots showing the concentration Cu(**1**)(DMF) (blue) and Cu(**2**)(DMF) (red) normalised relative to the highest value against (top to bottom) the Gutman, Swain and Reichardt's solubility parameters of the exfoliation solvent.
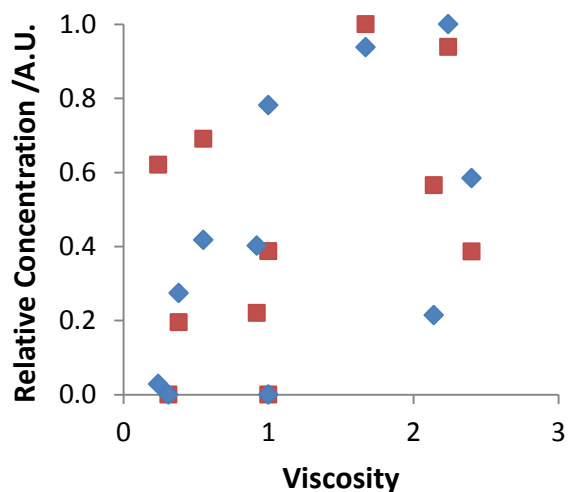
Figure S12. Plots showing the concentration Cu(1)(DMF) (blue) and Cu(2)(DMF) (red) normalised relative to the highest value against the viscosity of the exfoliation solvent.

4.4 Stability Tests

a)
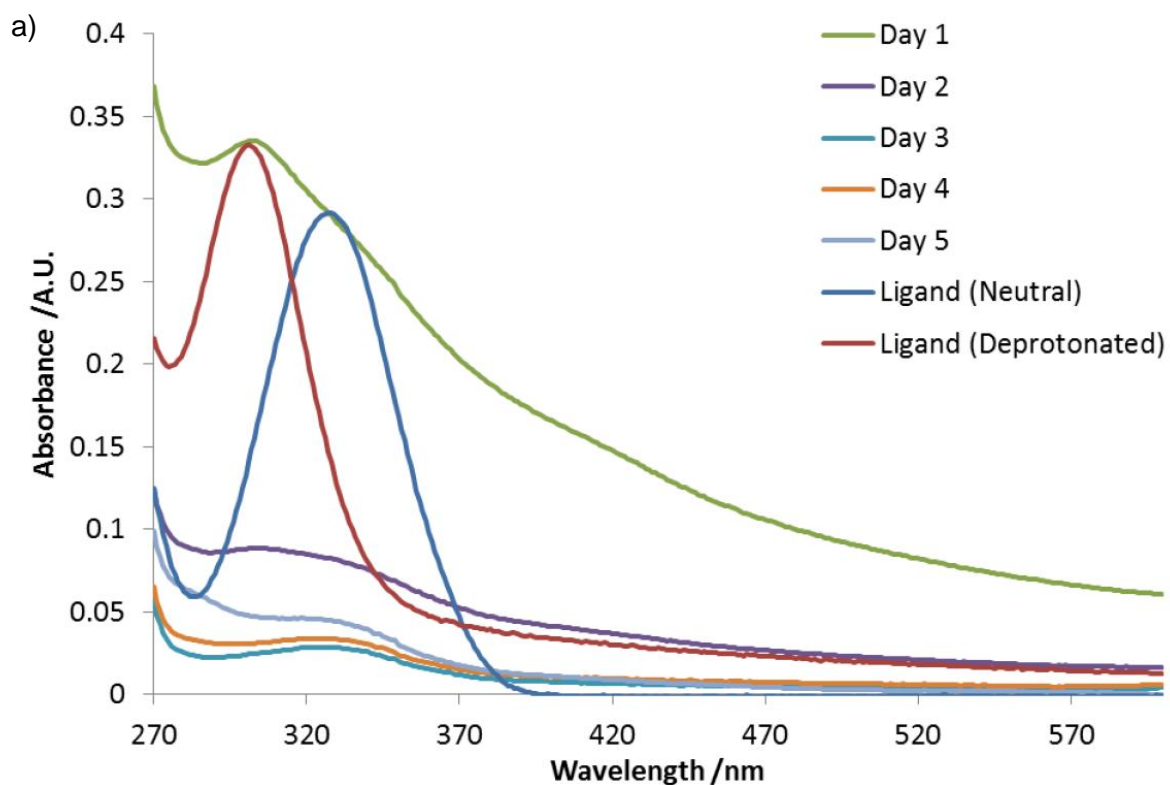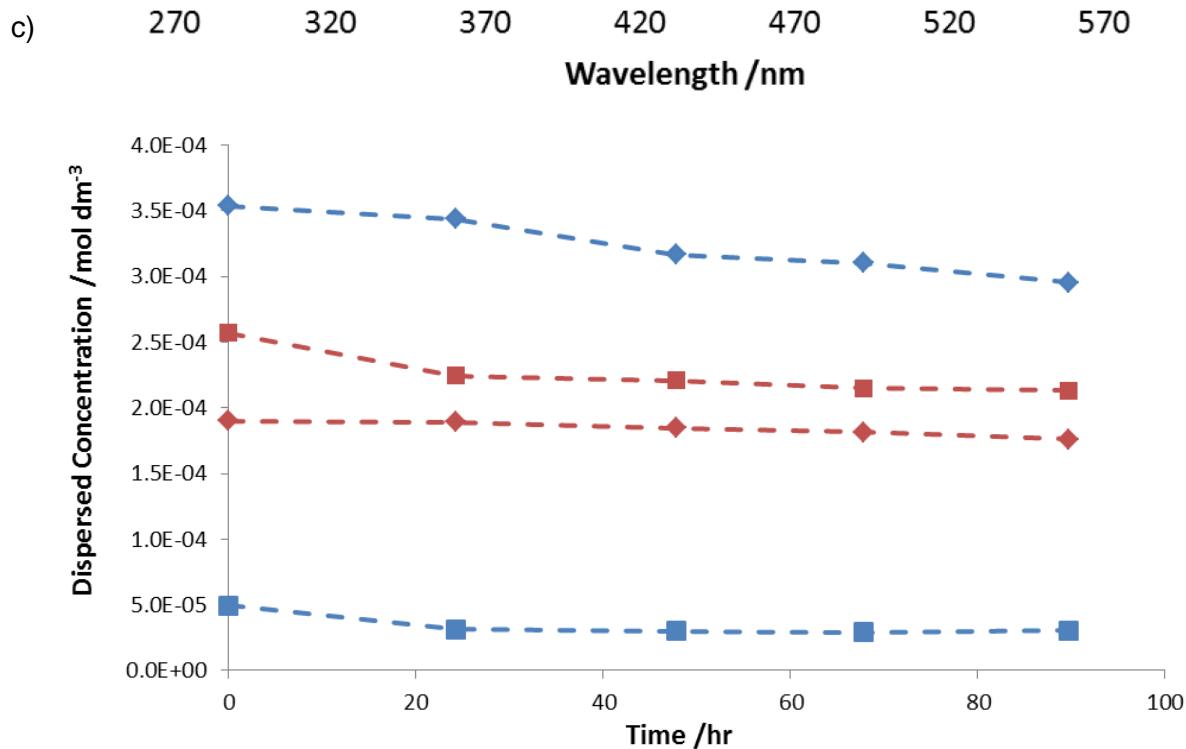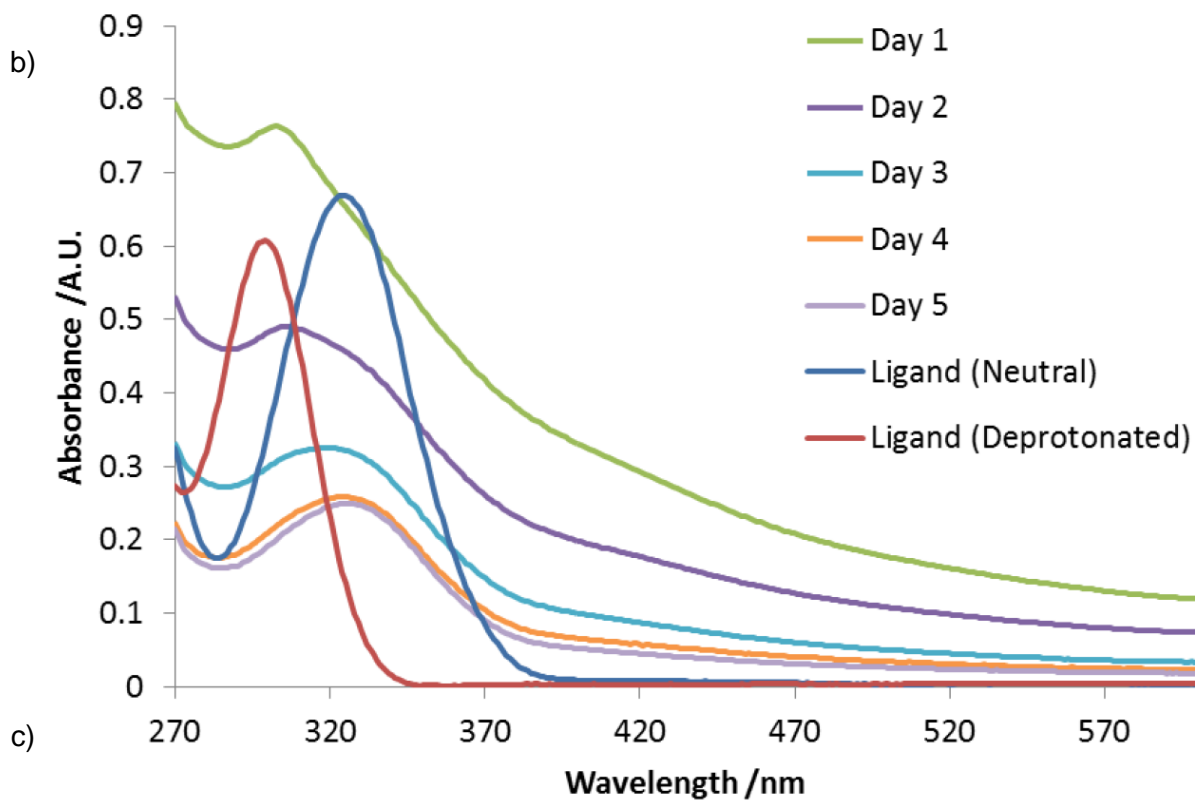
Figure S13. a) Change in absorption spectra over 5 days for Cu(**1**)(DMF) exfoliated in DMF. **b)** Change in absorption spectra over 5 days for Cu(2)(DMF) exfoliated in DMF. c) Dispersed concentration of Cu(**1**)(DMF) [blue] and Cu(**2**)(DMF) [red] exfoliated in water [diamonds] and diethyl ether [squares] over time.

5. Atomic Force Microscopy

5.1 Method Development

Samples for AFM analysis were prepared by pipetting 5x5 μl of suspension onto a freshly cleaved mica substrate heated to 80°C. AFM images were captured in soft tapping mode under ambient conditions using a Bruker Multimode 5 Atomic Force Microscope. Bruker OTESPA-R3 cantilevers were used with a drive amplitude and resonance frequency of approximately 20.4 mV and 290 kHz, respectively. Captured images were processed using Gwyddion (version 2.47) software.

Table S6. Table summarising AFM images obtained following sonication of Cu(1)(DMF)

Solvent	Sonication Time (h)	Thickness	Lateral Dimension	Notes
Water	0.5	Typically 100-200 nm. Thinnest ~30 nm	Discrete sheets usually 0.5-1 μm	-
	12	Typically 400 nm. Stepped edges of 15 nm observed	0.5-2 μm	-
Et$_2$O	0.5	100-300 nm	Broad distribution. Between 0.1-4 μm	Spherical and not "sheet-like"
	12	100-150 nm	1.5 μm	-

Table S7. Table summarising AFM images obtained following sonication of Cu(1)(DMF)

Solvent	Sonication Time	Thickness	Lateral Dimensions	Notes
Water	30 minutes	Typically 400 nm, Thinnest 15-60 nm.	0.5-2 μm	-
	12 hours	Range 9-600 nm, Typically ~100 nm	0.5-1.5 μm	Single large flake, 9 nm thick and almost 2 μm square
Et$_2$O	30 minutes	Thinnest 13 nm, Typically 20-100 nm	0.5-1 μm	Significant amount of aggregates
	12 hours	20-50 nm	0.5-1.5 μm	Large proportion of sheet-like material
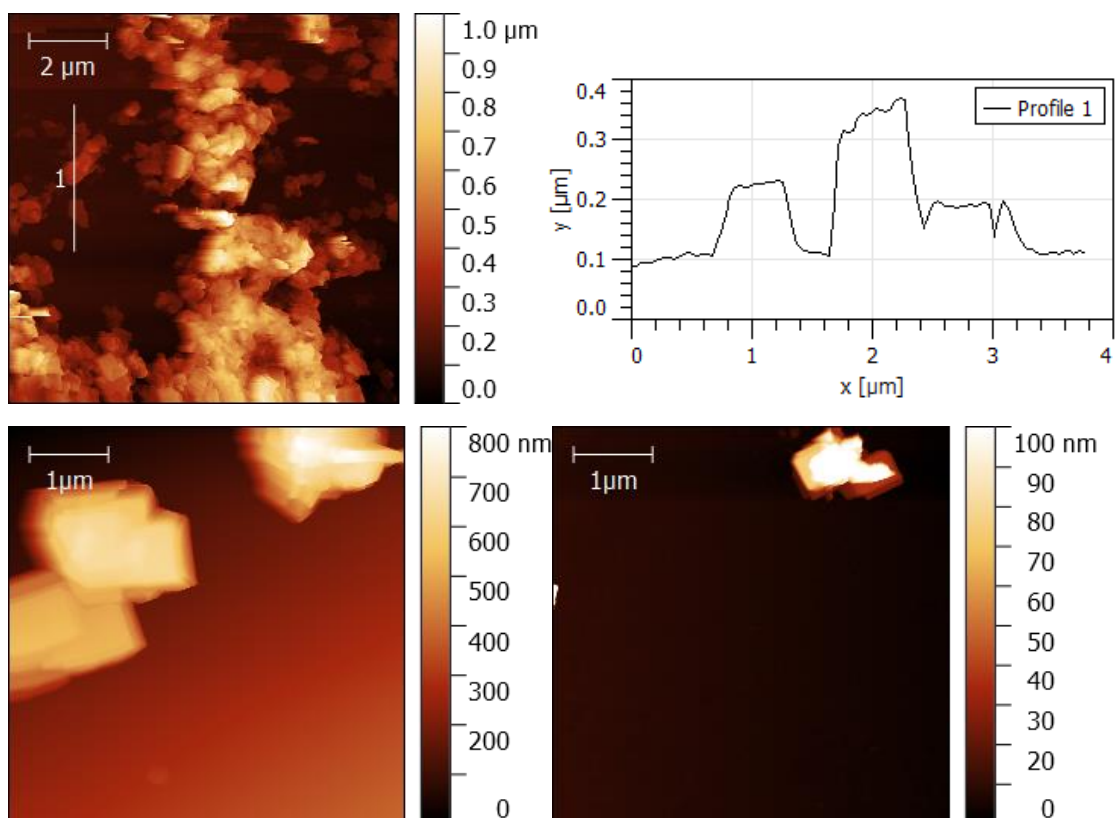
Figure S14. AFM image and height profile of Cu(**1**)(DMF) exfoliated for 30 minutes in water.
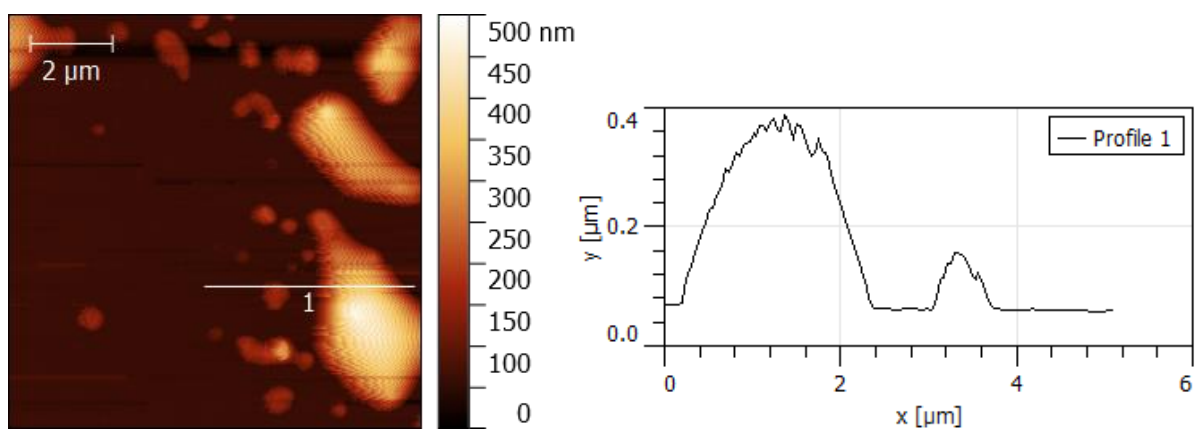
Figure S15. AFM image and height profile for Cu(**1**)(DMF) exfoliated for 30 minutes in diethyl ether.
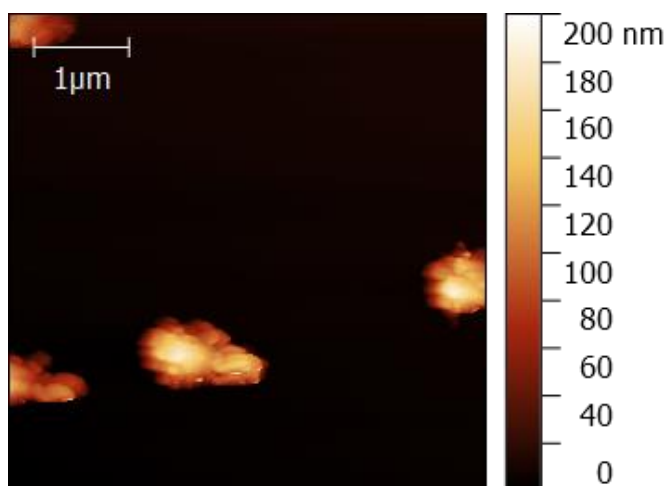
Figure S16. AFM image of Cu(**1**)(DMF) exfoliated in diethyl ether for 12 hours.
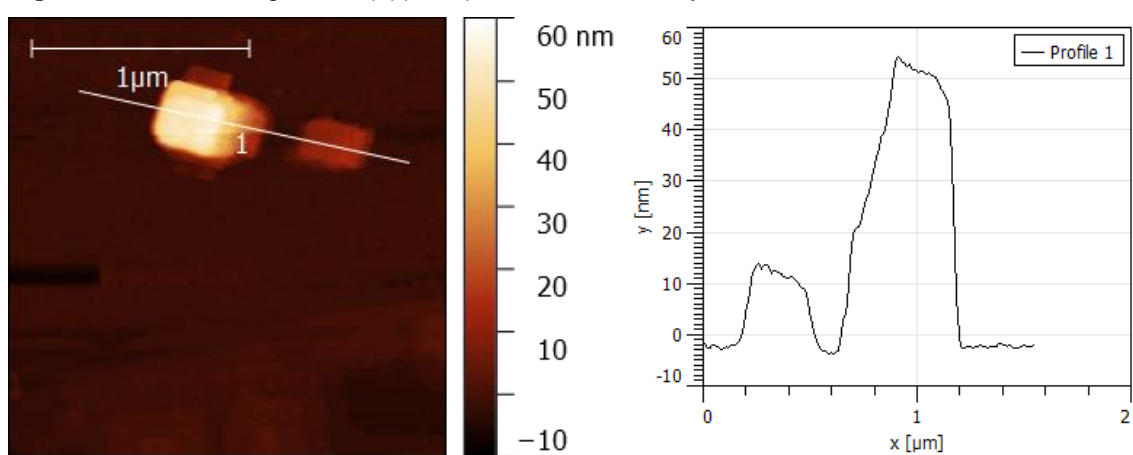
Figure S17. AFM image and height profile of Cu(**2**)(DMF) exfoliated for 30 minutes in water.
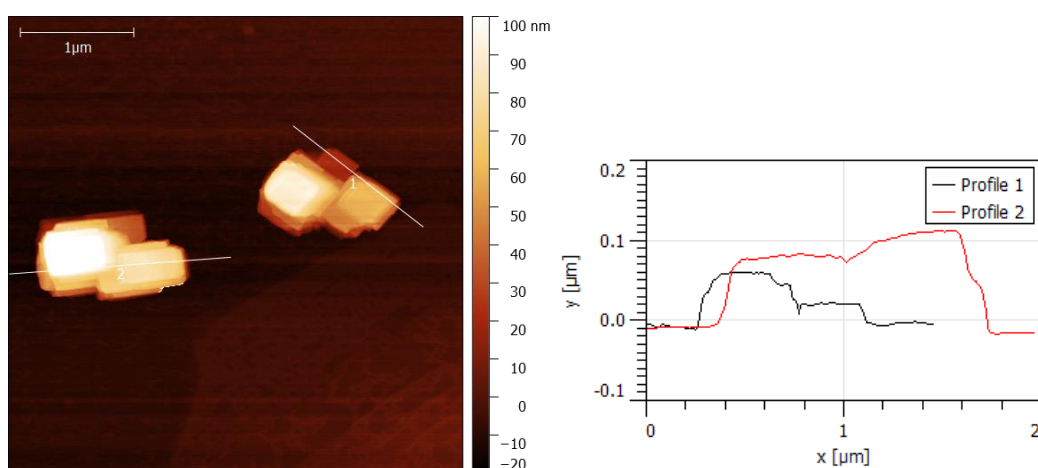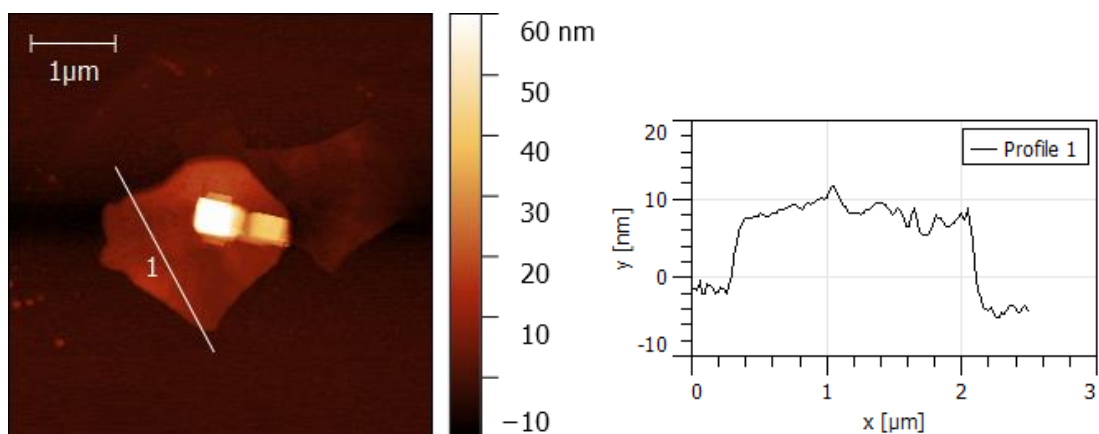
Figure S18. AFM images and height profiles for Cu(**2**)(DMF) exfoliated for 12 hours in diethyl ether.
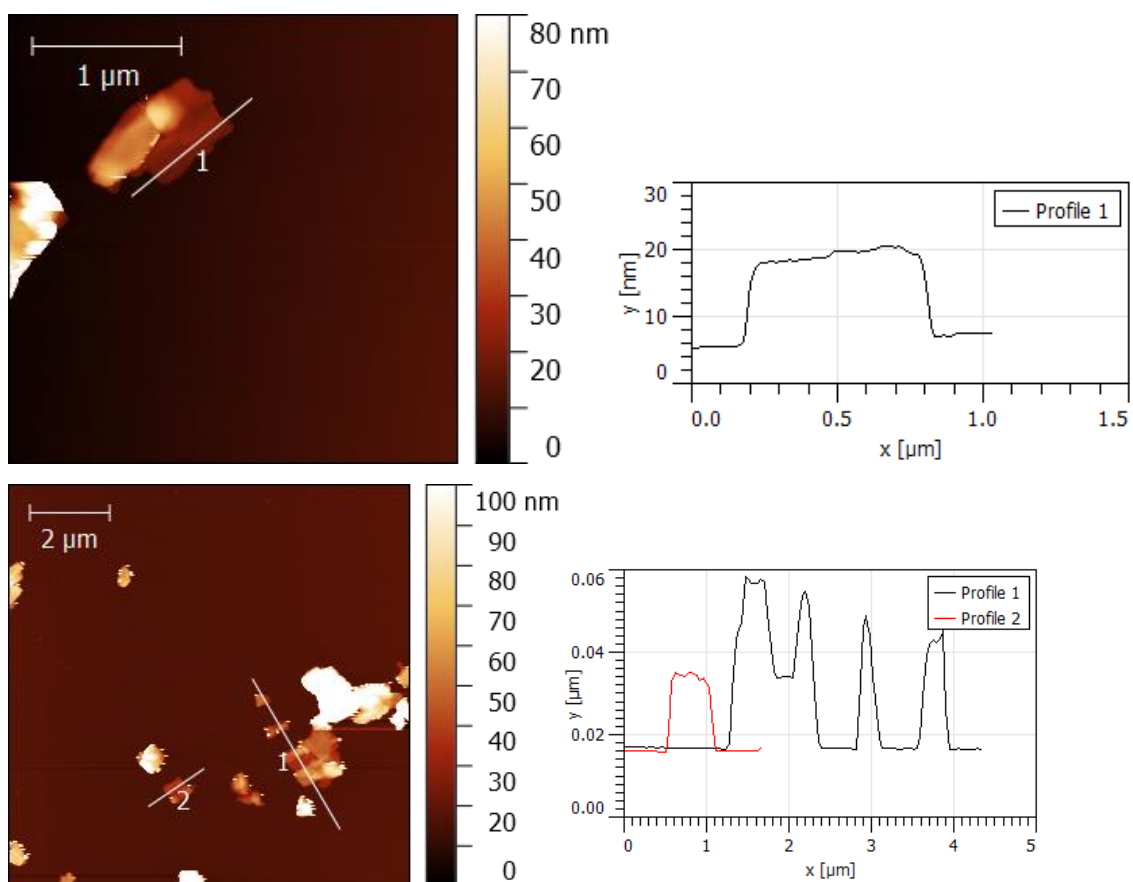
Figure S19. AFM images and height profiles for Cu(**2**)(DMF) exfoliated for 30 minutes in diethyl ether. For the bottom image, the height profile of line 1 and 2 are shown in black and red, respectively.
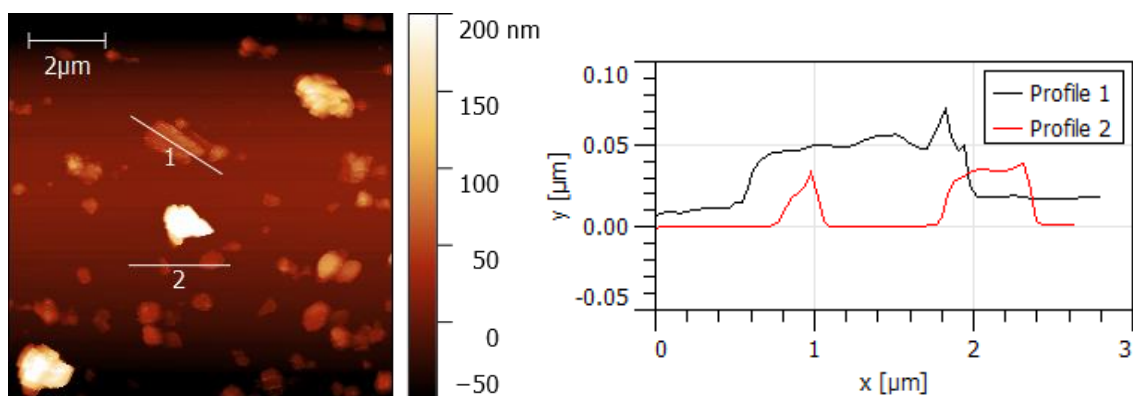
Figure S20. AFM image and height profile for Cu(**2**)(DMF) exfoliated in 12 hours in diethyl ether. The height profile of line 1 and 2 are shown in black and red, respectively.

5.2 Particle Sizing Studies

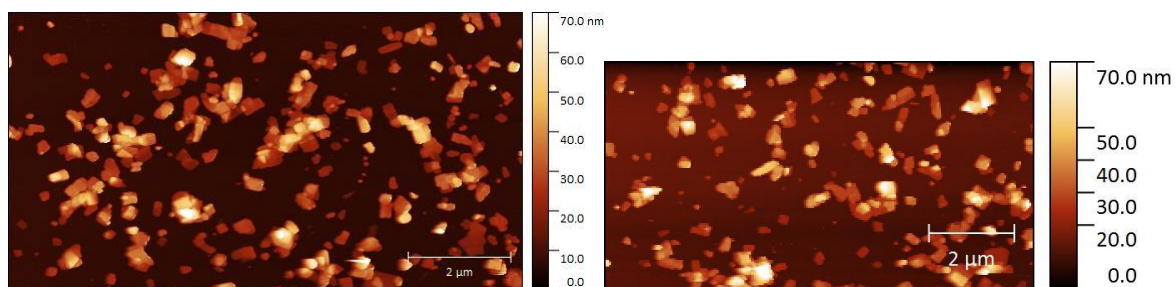**Cu(1)(DMF) exfoliated in MeCN for 12 hrs, sequential centrifugation steps.**
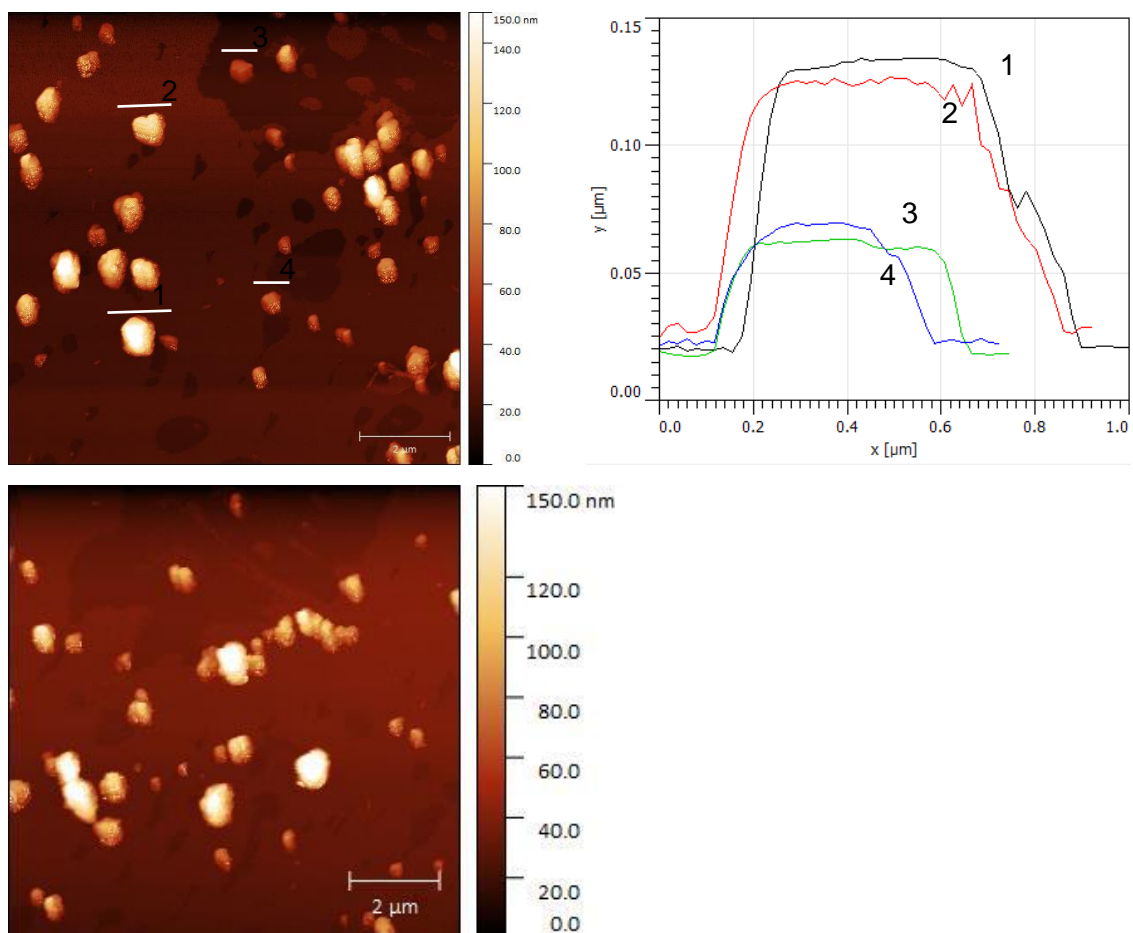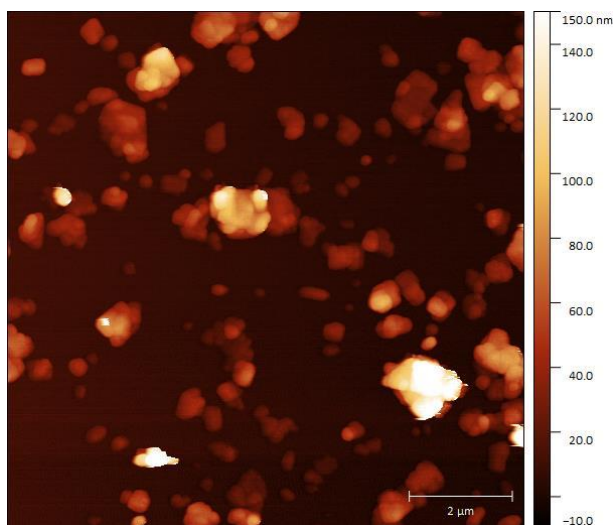

Figure S21. AFM images and example height plot used for the particle sizing of Cu(**1**)(DMF) exfoliated for 12 hrs and centrifuged at 1500 rpm for 1 hr.
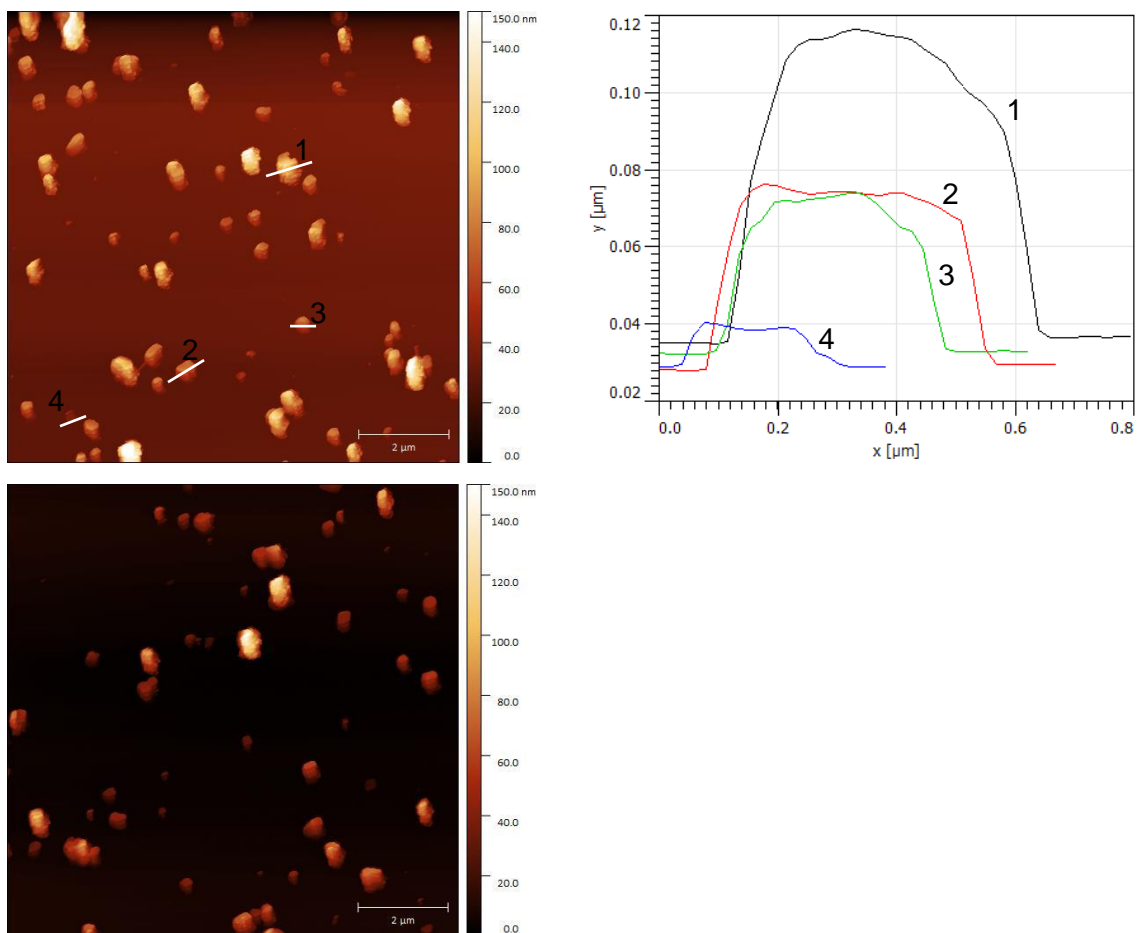
Figure S22. AFM images and example height plot used for the particle sizing of Cu(**1**)(DMF) exfoliated for 12 hrs and centrifuged at 4500 rpm for 30 mins.
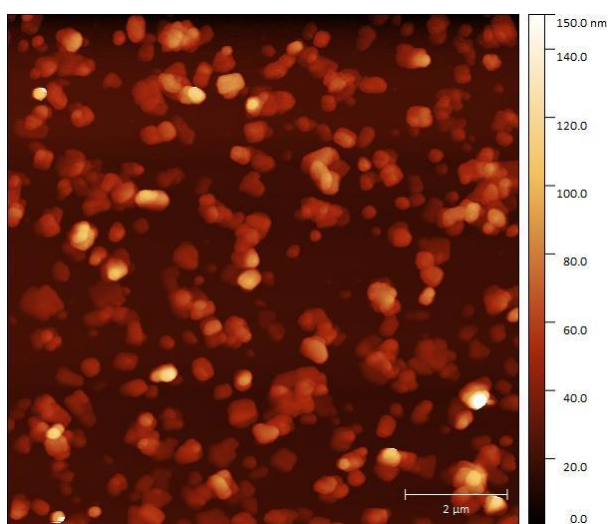

22
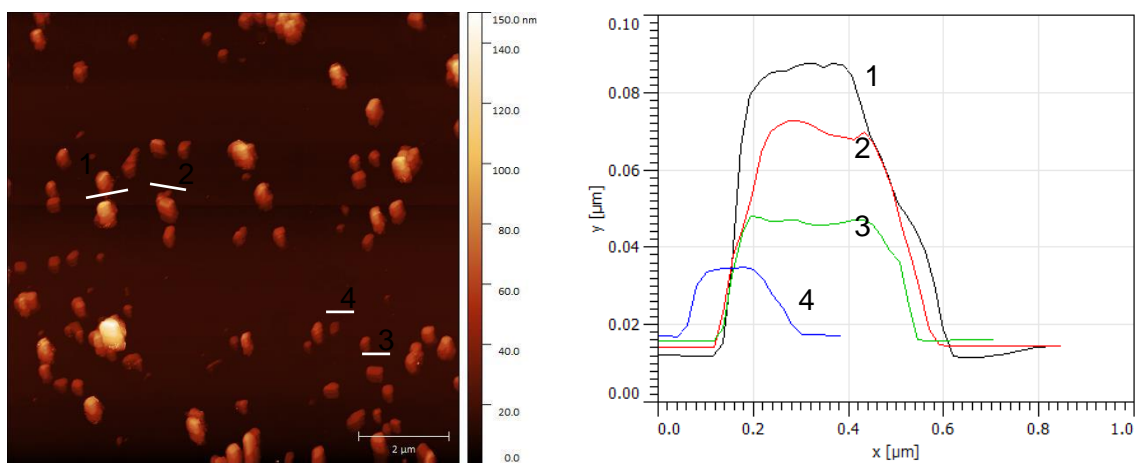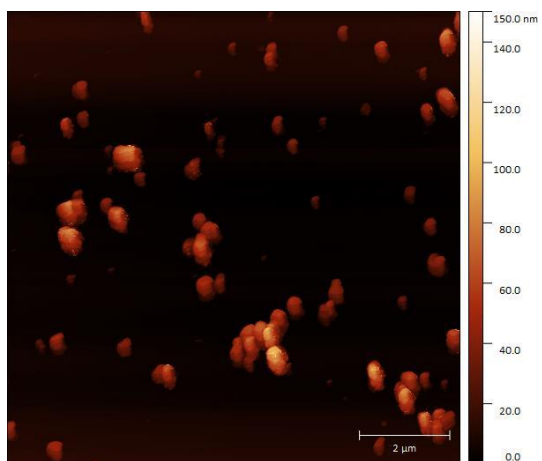
Figure S23. AFM images and example height plot used for the particle sizing of Cu(**1**)(DMF) exfoliated for 12 hrs and centrifuged at 4500 rpm for 4 hrs.

Cu(2)(DMF) exfoliated in MeCN for 12 hrs with sequential centrifugation
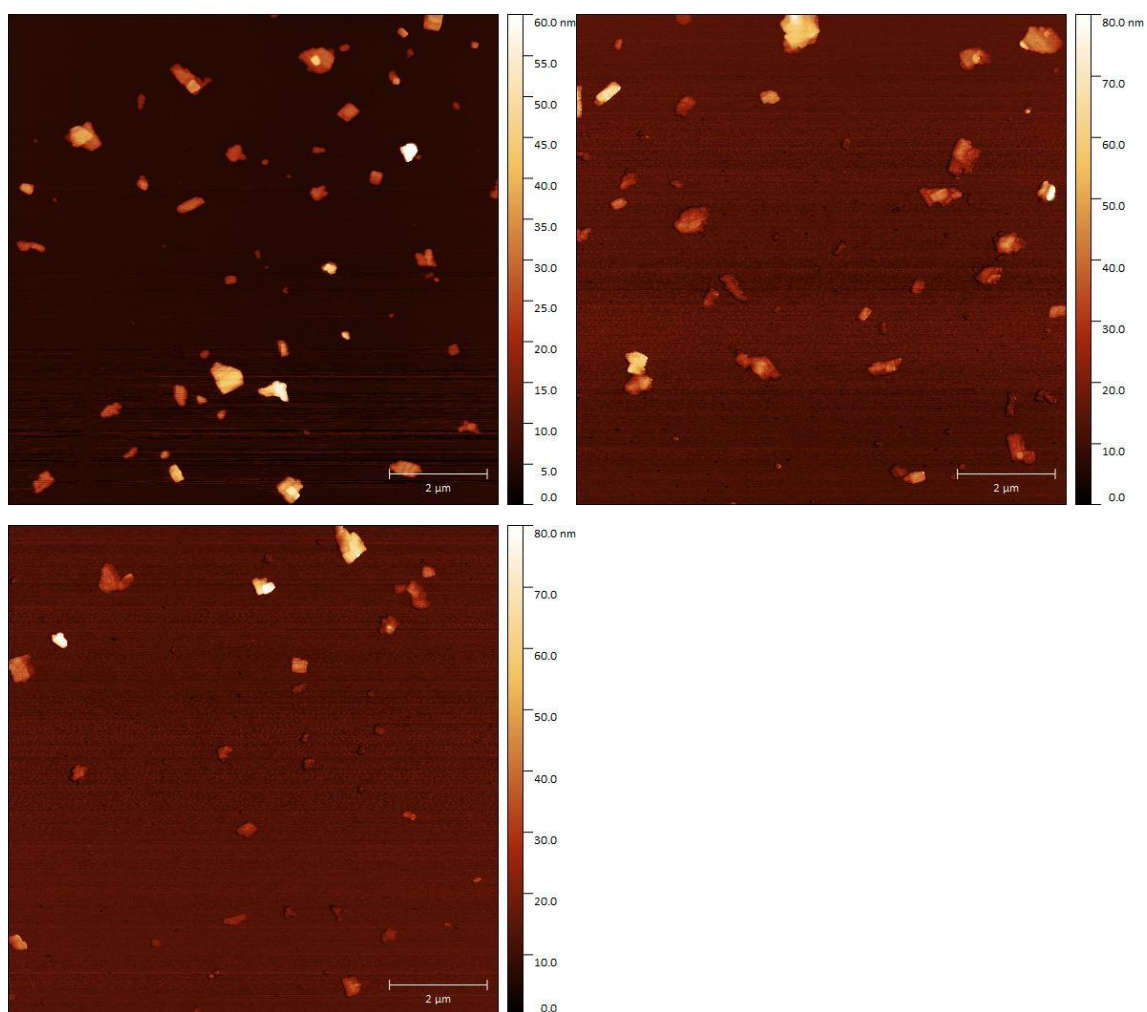
Figure S24. AFM images and example height plot used for the particle sizing of Cu(**2**)(DMF) exfoliated for 12 hrs and centrifuged at 1500 rpm for 30 mins.

Figure S25. AFM images and example height plot used for the particle sizing of Cu(**2**)(DMF) exfoliated for 12 hrs and centrifuged at 4500 rpm for 4 hrs. N.B. scanning down the image on the left, the cantilever disengaged from the mica substrate. The tip was re-engaged and scanning continued, producing the image on the right. N.B Particle sizing analysis was carried out on the right hand image, as this gave n=138 nanosheets.

Cu(2)(DMF) exfoliated in MeCN for 30 mins with sequential centrifugation

Figure S 26. AFM images and example height plot used for the particle sizing of Cu(**2**)(DMF) exfoliated for 30 mins and centrifuged at 1500 rpm for 30 mins.

Figure S 27. AFM images and example height plot used for the particle sizing of Cu(**2**)(DMF) exfoliated for 30 mins and centrifuged at 4500 rpm for 4 hrs.

Table S 8. Size distribution statistics of the samples portrayed above. All lengths are in nm.

Sample	Cu(**1**)(DMF)			Cu(**2**)(DMF)			
Exfoliation Time	12 hr			12 hr		30 min	
Centrifugation	1500 rpm, 1 hr	4500 rpm, 30 mins	4500 rpm, 4 hrs	1500 rpm, 1 hr	4500 rpm, 4 hrs	1500 rpm, 1 hr	4500 rpm, 4 hrs
# Nanosheets	95	111	161	94	138	117	223
Mean lateral dimension*	512	347	307	348	367	468	413
SD lateral dimension*+	234	153	108	202	155	206	132
Mean height	59	49	41	20	19	28	26
SD height+	35	26	19	12	10	18	15
% > 600 nm lateral	30	9	2	14	11	24	8
% < 400 nm lateral	37	73	83	63	61	42	50
% < 40 nm height	32	41	57	93	97	83	86
% < 30 nm height	18	30	44	83	90	69	73
% > aspect ratio of 10$	42	23	39	83	92	90	90

* Lateral dimension was recorded as the largest edge-to-edge distance across the nanosheet, to the nearest 10 nm. + SD = standard deviation. $ Aspect ratio calculated as recorded lateral dimension divided by the average height of a nanosheet.

5.4 DLS Studies
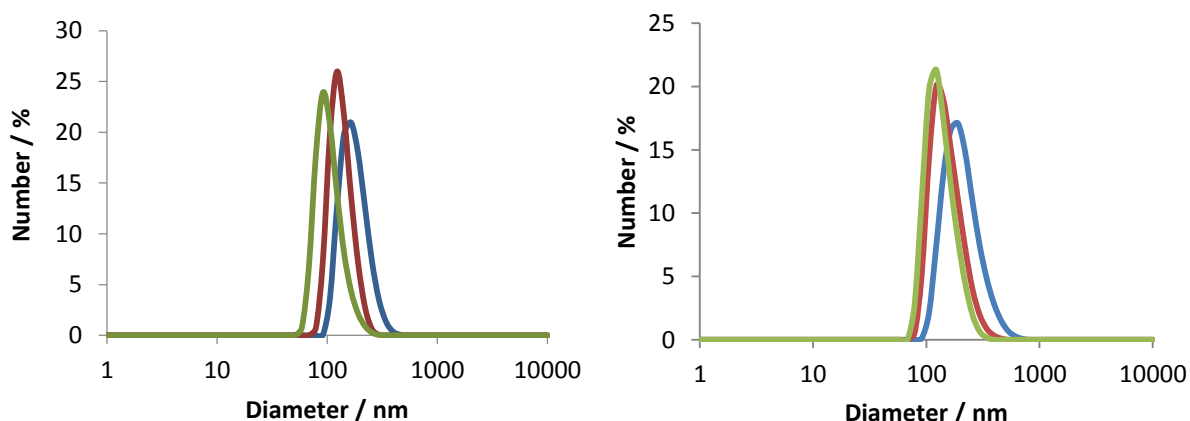
Figure S 28. Number average of three repeat collections of DLS data. Cu(**1**)(DMF) (left) and Cu(**2**)(DMF) (right) exfoliated for 12 hrs in MeCN then cascade centrifuged at 1500 rpm for 1 hr (blue), then 4500 rpm for 30 mins (red), then 4500 rpm for 4 hrs (green).

Table S 9. DLS data: average determined diameter of MONs using Z-average, intensity average and number average, and polydispersity index (PdI)

Sample	Cu(**1**)(DMF)			Cu(**2**)(DMF)		
Centrifugation	1500 rpm, 1 hr	4500 rpm, 30 mins	4500 rpm, 4 hrs	1500 rpm, 1 hr	4500 rpm, 30 mins	4500 rpm, 4 hrs
Z-average (diameter) / nm	204	153	135	276	195	168
Intensity average (diameter) / nm	220	159	146	320	213	181
Number average (diameter) / nm	179	135	106	213	155	137
PdI	0.075	0.0183	0.068	0.163	0.118	0.064

It should be noted that size averages determined through these DLS measurements do not match exactly with those determined through statistical analysis of topographical AFM images. DLS measurements are based on a translational diffusion coefficient, which is converted to a hydrodynamic diameter using the Stokes-Einstein equation. This equation is valid for spherical particles. It is widely known that diffusion of 2D nanosheets with high aspect ratios is not well characterised by DLS, and the presence of periodic porosity within the MON structures may complicate the diffusion behaviour further. As such, information is provided on the relative size of the MONs in dispersion; however absolute values should not be taken from this analysis.
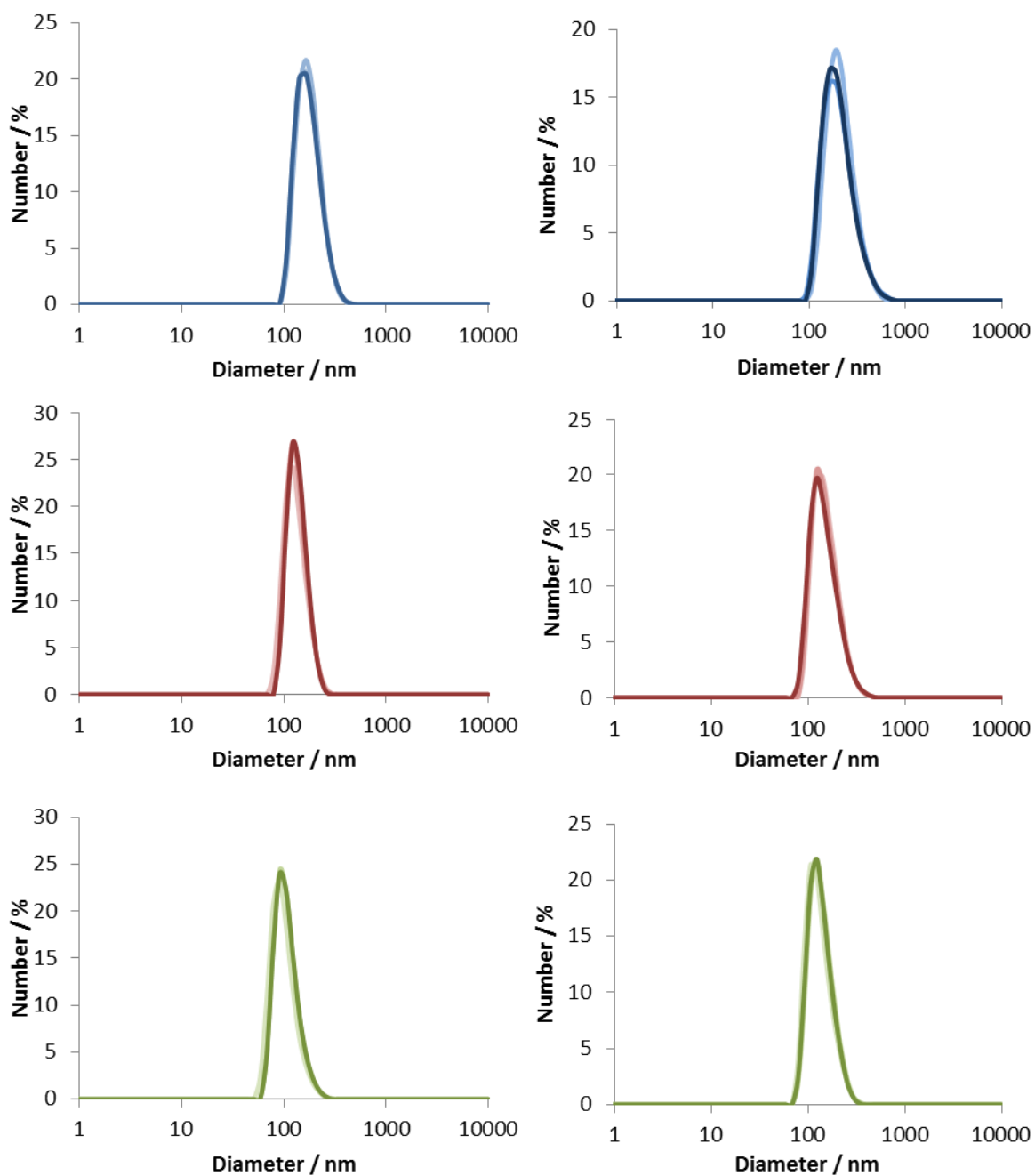
Figure S 29. DLS data from three runs for each respective sample. Cu(**1**)(DMF) (left) and Cu(**2**)(DMF) (right) exfoliated in MeCN for 12 hrs and then cascade centrifuged at 1500 rpm for 1 hr (blue), then 4500 rpm for 30 mins (red), then 4500 rpm for 4 hrs (green). Each run is an average of between 10-18 analyses (number computationally selected in an automated data collection optimisation).

5.5 Exfoliation Studies in Various Solvents

6 mL of solvent was added to 5 mg of Cu(**1**)(DMF) or Cu(**2**)(DMF). These were exfoliated for 12 hrs, and then the resulting mixtures were centrifuged at 1500 rpm for 1 hr. 5 mL of supernatant was removed, and this suspension of nanosheets in solvent was used for AFM analysis. Typically, 10 µL of suspension was drop cast onto a freshly-cleaved mica substrate, which was held at a temperature around the boiling point of the solvent used in order to aid the evaporation of solvent, which has been previously suggested to aid in nanosheet characterisation, as this may prevent nanosheet aggregation throughout a slow evaporative process. Representative AFM images of deposited material from these suspensions, using the solvents DMF, NMP, water, diethyl ether and acetonitrile, can be found below.

DMF
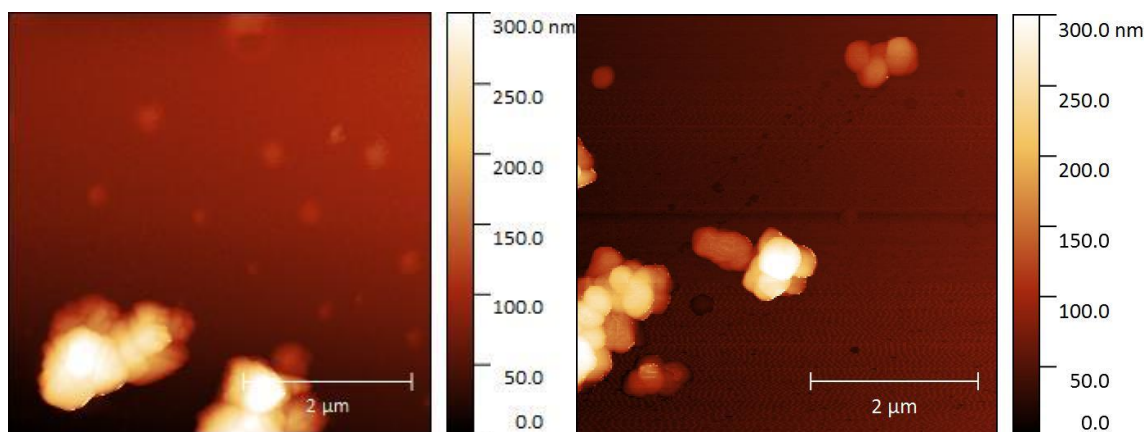
Figure S30. AFM images of Cu(**1**)(DMF) exfoliated in DMF.
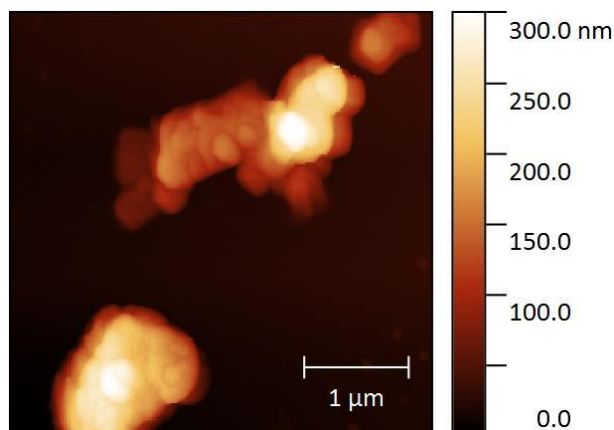
Figure S31. AFM image of Cu(**2**)(DMF) exfoliated in DMF.

NMP
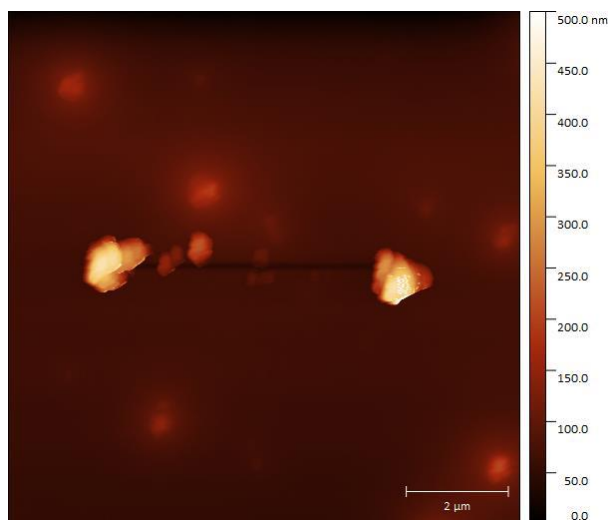
Figure S32. AFM images of Cu(**1**)(DMF) exfoliated in NMP.
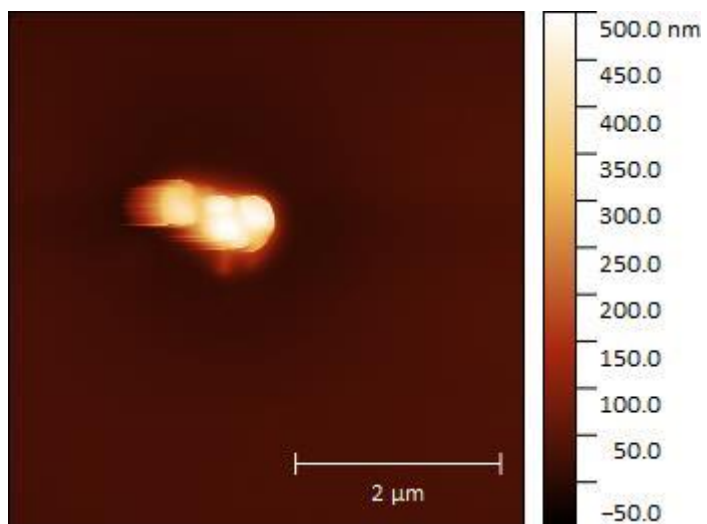

Figure S33. AFM images of Cu(**2**)(DMF) exfoliated in NMP. N.B. Very little was observed under AFM, however attached light microscope showed what appear to be a large number of particles across the substrate surface, potentially indicating a high level of nanosheet/particle agglomeration.
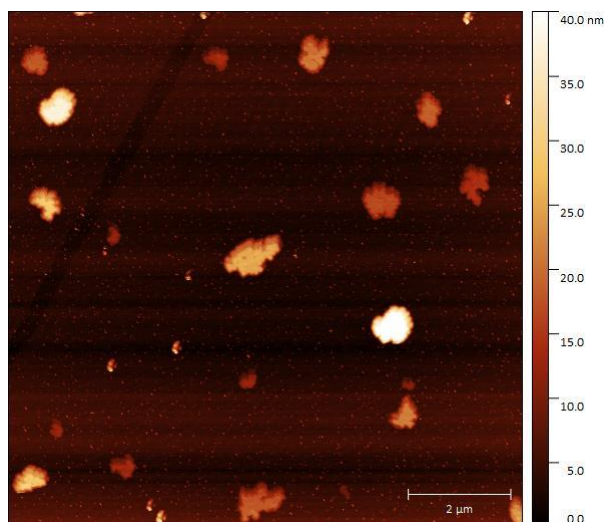
Water
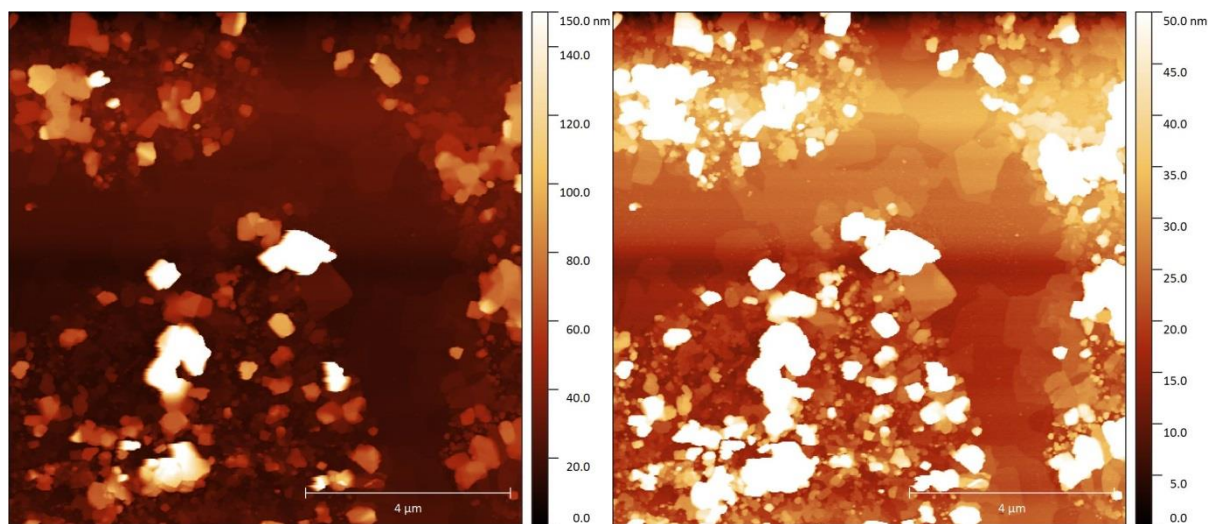

Figure S34. AFM images of Cu(**1**)(DMF) exfoliated in water.

Figure S35. AFM images of Cu(**2**)(DMF) exfoliated in water. Both images are identical, with different height scales, to illustrate both larger and thinner nanosheets.
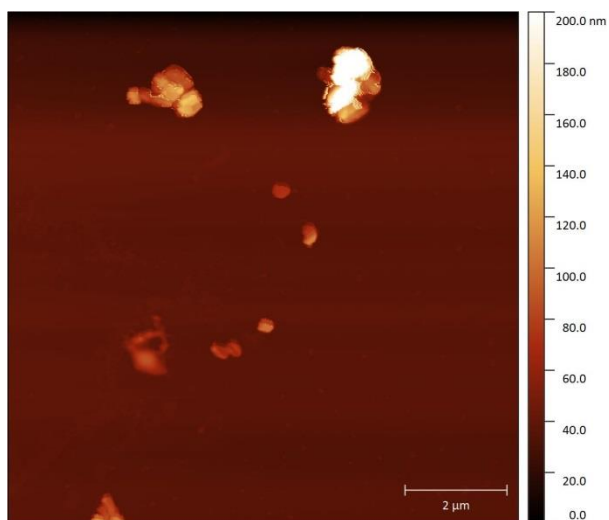
Diethyl ether

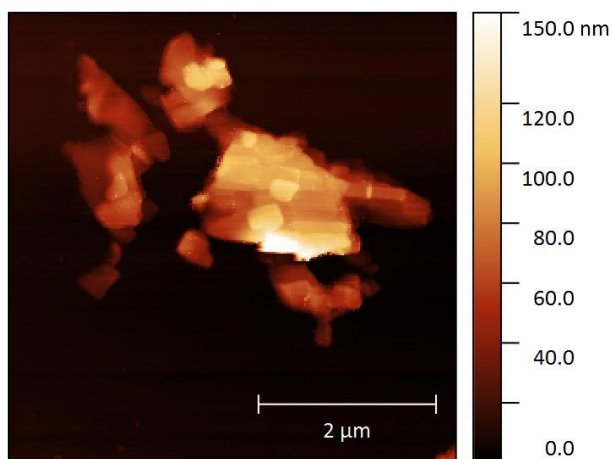**Figure S36.** AFM images of Cu(**1**)(DMF) exfoliated in diethyl ether.

Figure S37. AFM images of Cu(**2**)(DMF) exfoliated in diethyl ether.
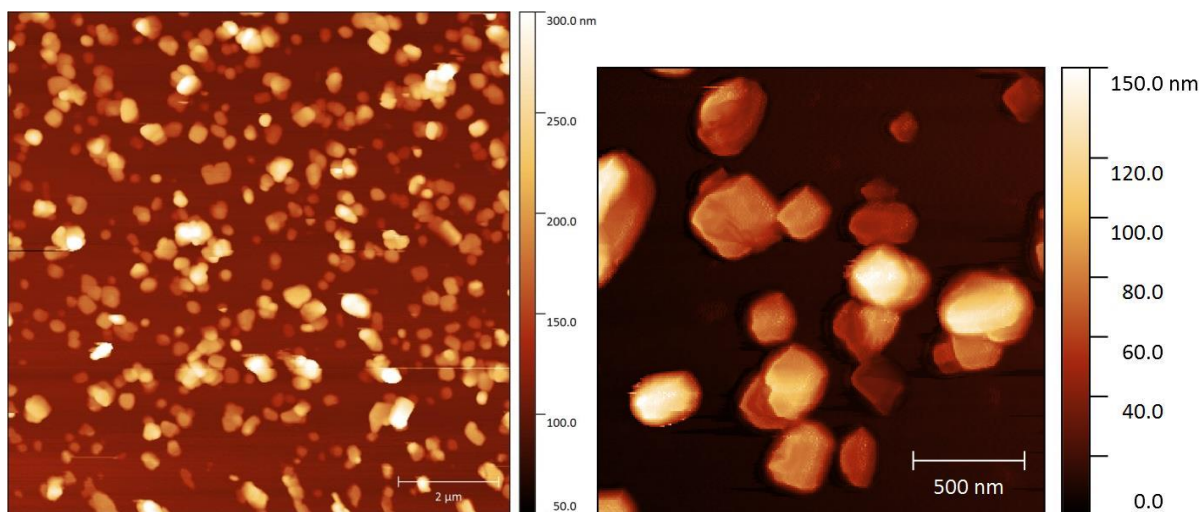
Acetonitrile

Figure S38. AFM images of Cu(**1**)(DMF) exfoliated in acetonitrile.
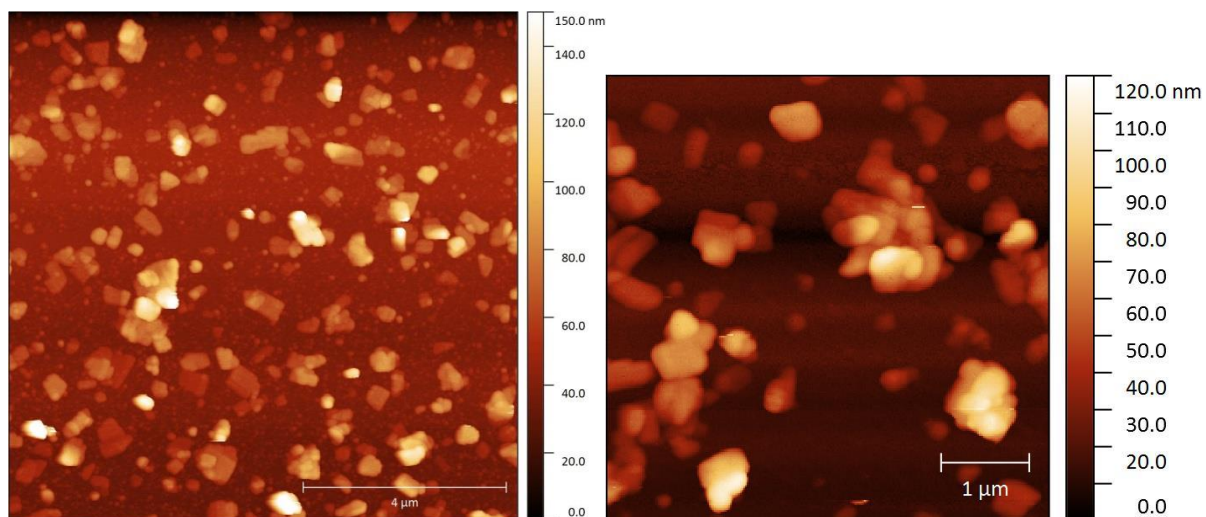
Figure S39. AFM images of Cu(**2**)(DMF) exfoliated in acetonitrile.

6. Structural Analysis
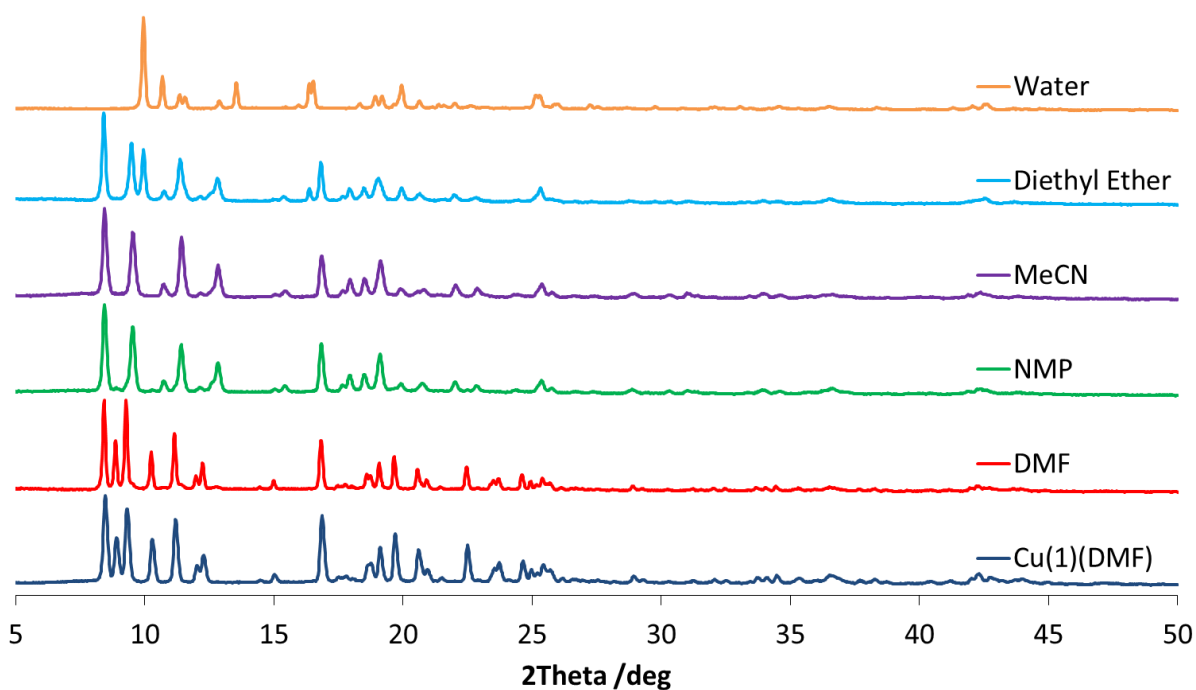
5.1 Powder X-Ray Diffraction

Figure S40. XRPD patterns for parent Cu(**1**)(DMF) as synthesised and following exfoliation in named solvents
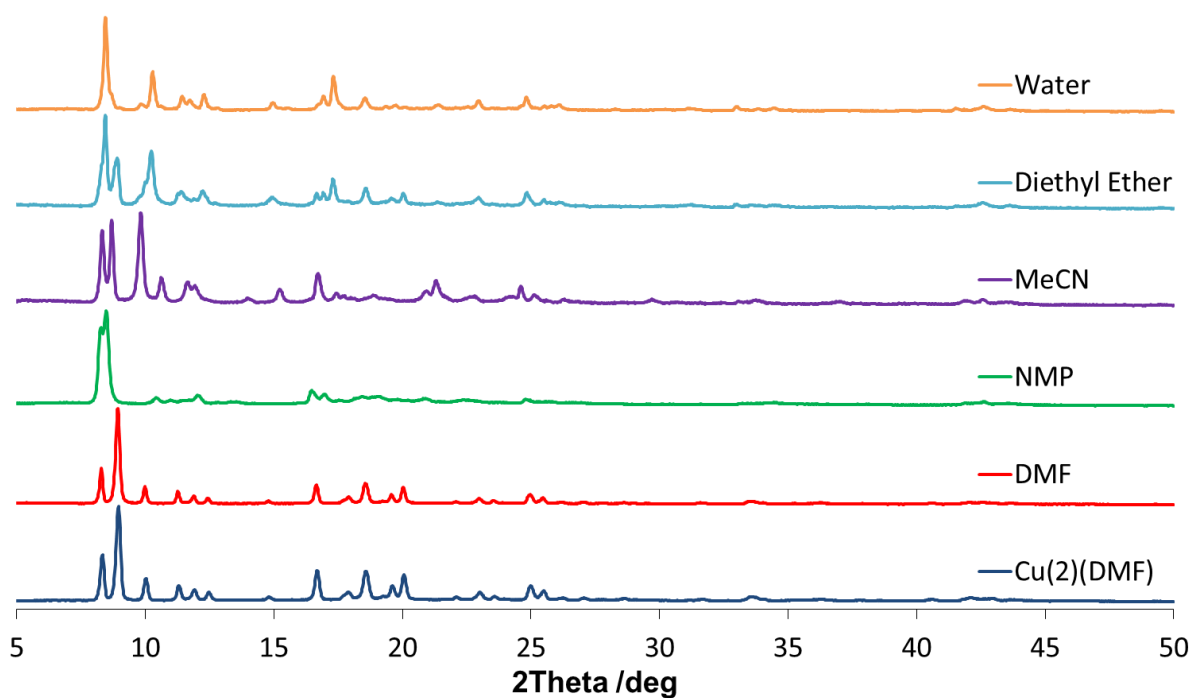

Figure S41. XRPD patterns for parent Cu(**2**)(DMF) as synthesised and following exfoliation in named solvents

6.2 Fourier Transform Infrared Spectroscopy

FTIR spectra were recorded using a Perkin-Elmer Spectrum Two FTIR spectrometer equipped with a diamond UATR (universal attenuated total reflectance) accessory. A background of air was taken. A spatula tip of sample was then loaded onto the stage and pressure was applied. Spectra were recorded in reflectance mode with a scan range of 4000-500 cm^{-1}, a resolution of 1 cm^{-1}, with 8 scans recorded.

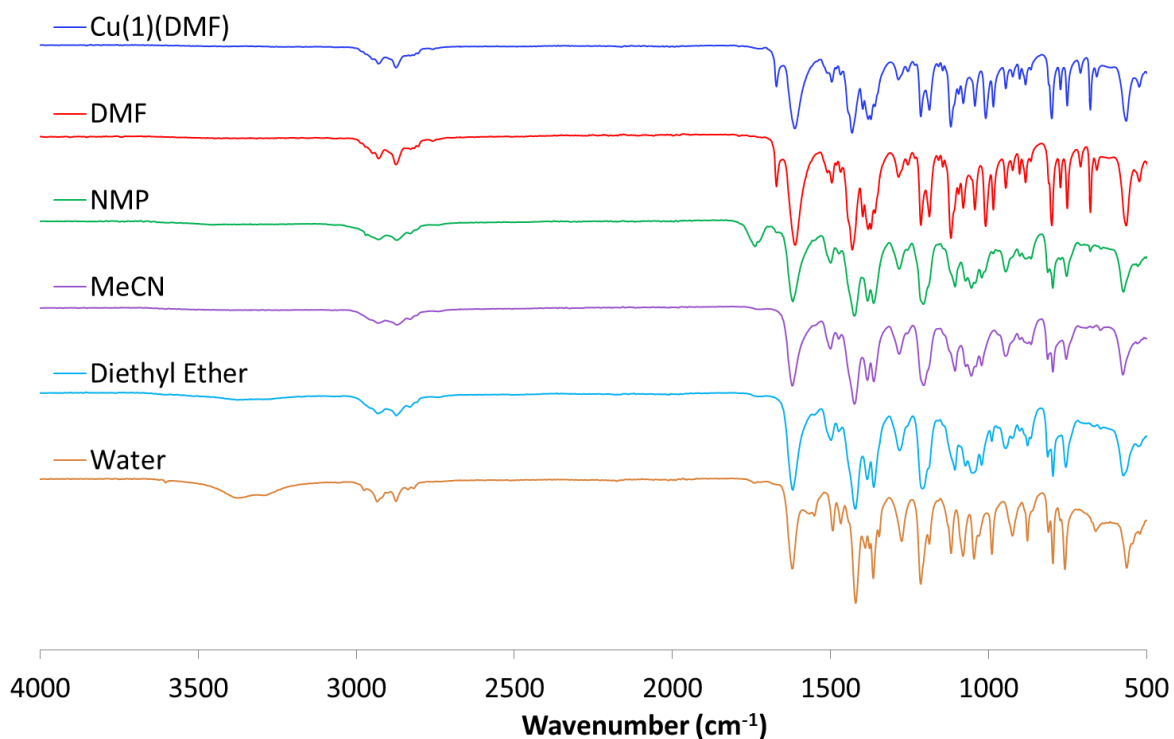**Figure S42.** IR spectra for parent Cu(**1**)(DMF) as synthesised and following exfoliation in named solvents.
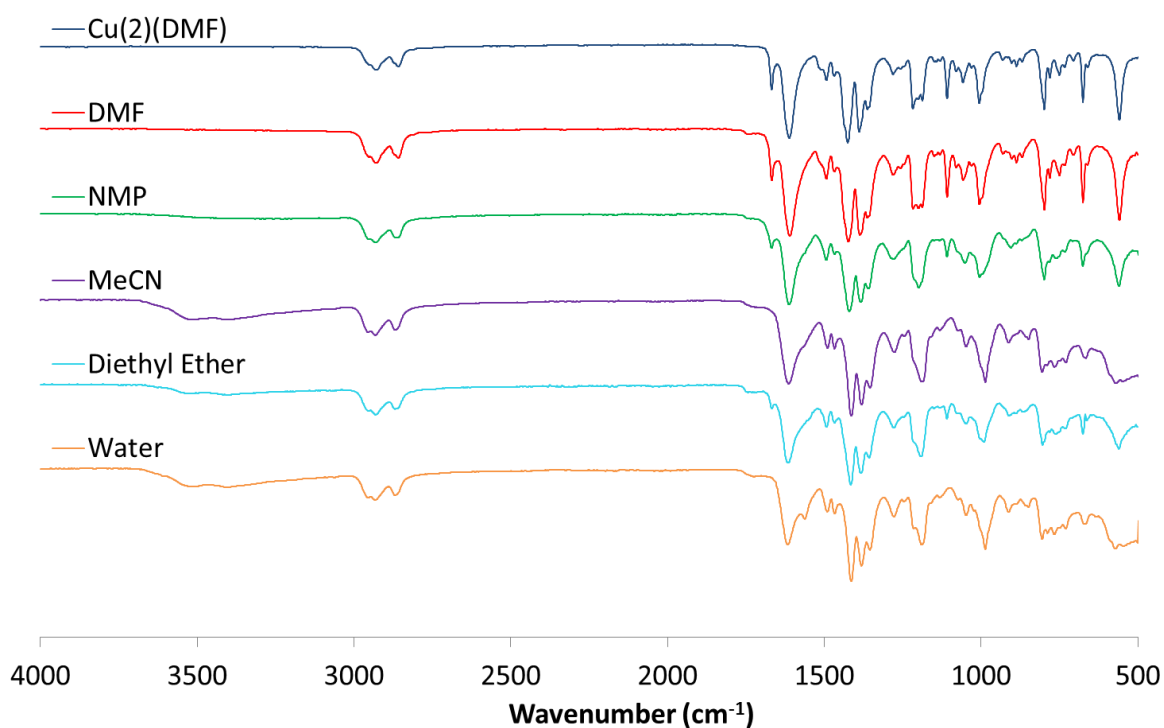
Figure S43. IR spectra for parent Cu(**2**)(DMF) as synthesised and following exfoliation in named solvents.

6.3 Thermogravimetric Analysis

Thermogravimetric analyses were performed using a Perkin-Elmer Pyris 1 TGA instrument. 4 – 6 mg was accurately weighed into a ceramic TGA pan and loaded into the instrument. Sample was held under a constant 20 mL min^{-1} N$_2$ flow. An initial equilibration period of 10 mins at 30 °C was used, and then sample was heated at a continuous rate of 10 °C min^{-1} to the end temperature.
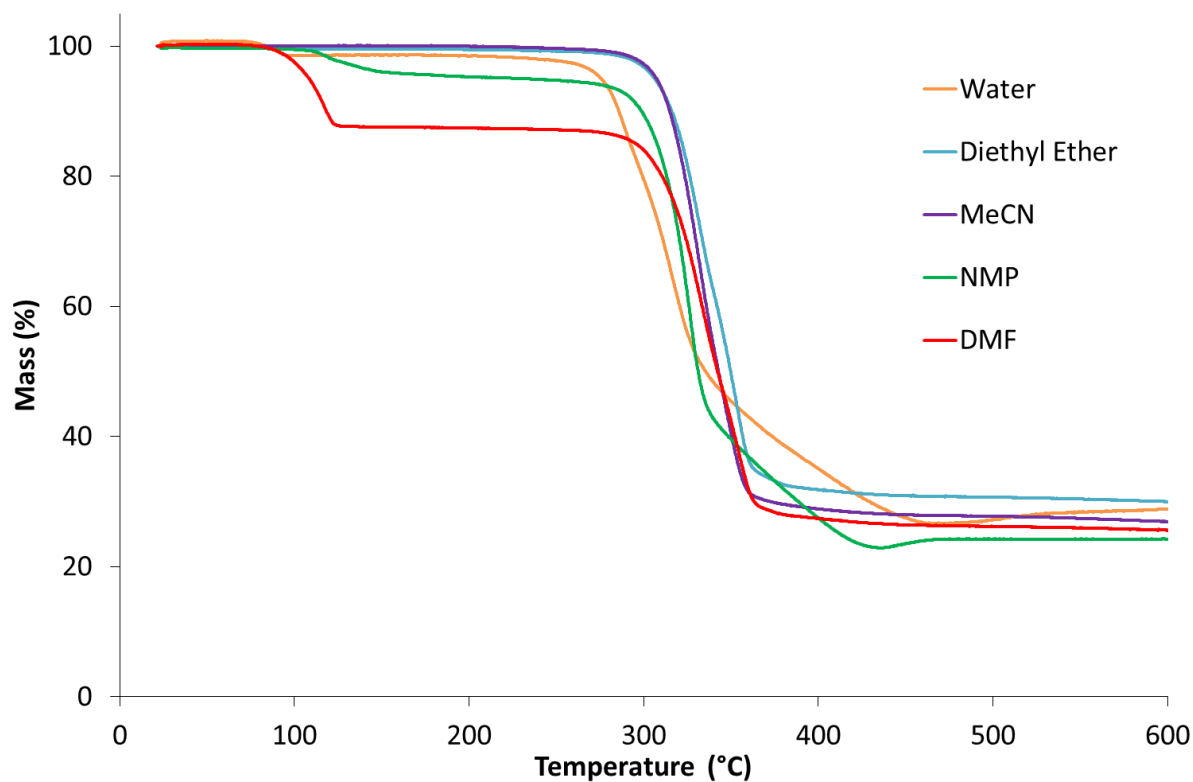
Figure S44. TGA thermograms for parent Cu(**1**)(DMF) following exfoliation in named solvents.

Table S10. Summary of TGA thermogram data below 250°C for bulk Cu(**1**)(DMF) and following exfoliation in different solvents.

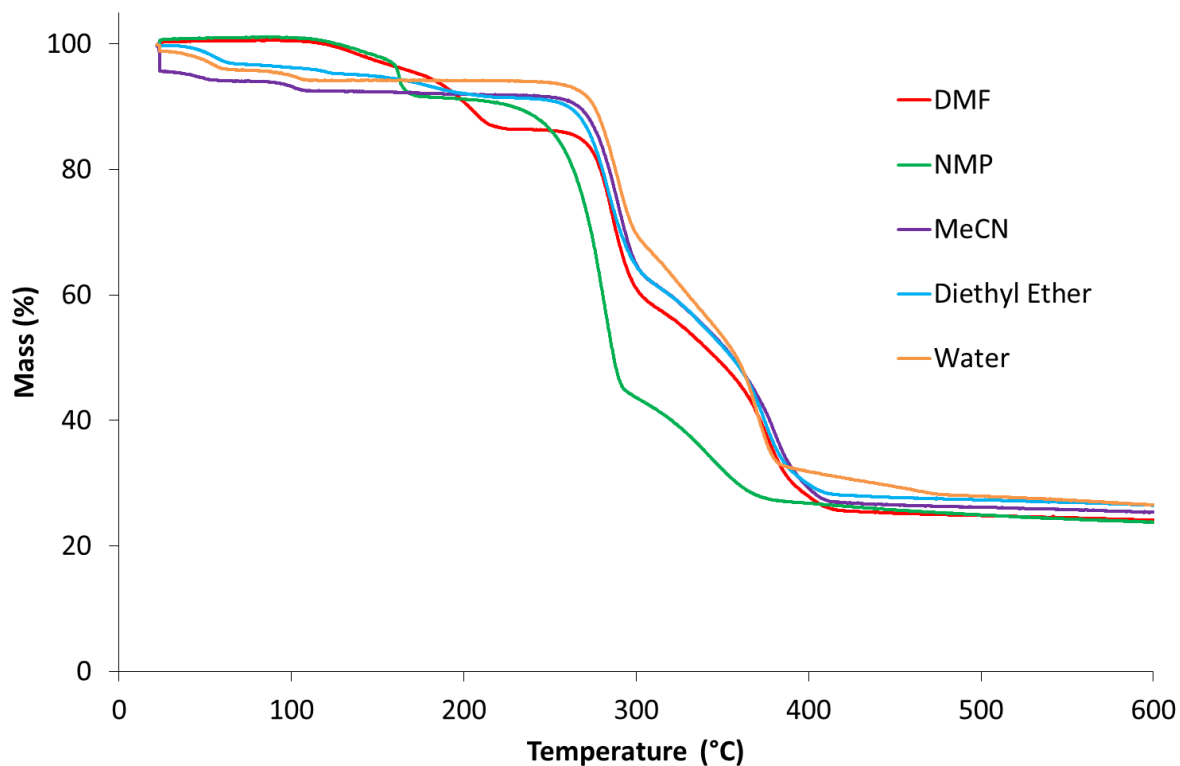| Sample	Suggested Solvent Lost	Event Temperature / °C	Difference %
Cu(**1**)(DMF)	DMF	65-123	13.5
DMF	DMF	68-135	12.3
NMP	NMP	83-205	4.2
MeCN	MeCN	No solvent loss	
Diethyl Ether	Et$_2$O	66-86	0.5
Water	H$_2$O	66-94	1.4

Figure S45. TGA thermograms for parent Cu(**2**)(DMF) following exfoliation in named solvents.

Table S11. Summary of TGA thermogram data below 250°C for bulk Cu(**2**)(DMF) and following exfoliation in different solvents.

Sample	Suggested Solvent Lost	Event Temperature / °C	Difference %
Cu(**2**)(DMF)	DMF	65-123	13.6
DMF	DMF	103-223	13.4
NMP	H_2O/NMP	94-178	8.6
MeCN	MeCN/H_2O	56-115	3.1
Diethyl Ether	H_2O	66-127	4.7
Water	H_2O	71-107	4.6

6.4 Elemental Analysis

Table S12. Calculated and experimental elemental analysis data for Cu(**1**)(DMF) derivatives

Calculated Structure	Calculated / wt%			Exfoliation Solvent	Experimental / wt%		
	C	H	N		C	H	N
Cu(**1**)	47.58	4.99	0				
Cu(**1**)(DMF)	47.85	5.71	2.94	DMF	44.00	5.26	2.45
Cu(**1**)(NMP)	50.14	5.81	2.78	NMP	43.38	4.84	0.72
Cu(**1**)(MeCN)	47.39	4.91	3.25	MeCN	44.35	4.76	0
Cu(**1**)(Et$_2$O)	50.26	6.33	0	Diethyl ether	41.27	4.43	0
Cu(**1**)(H$_2$O)	45.55	5.26	0	Water	39.83	5.15	0

Table S13. Calculated and experimental elemental analysis data for Cu(**2**)(DMF) derivatives

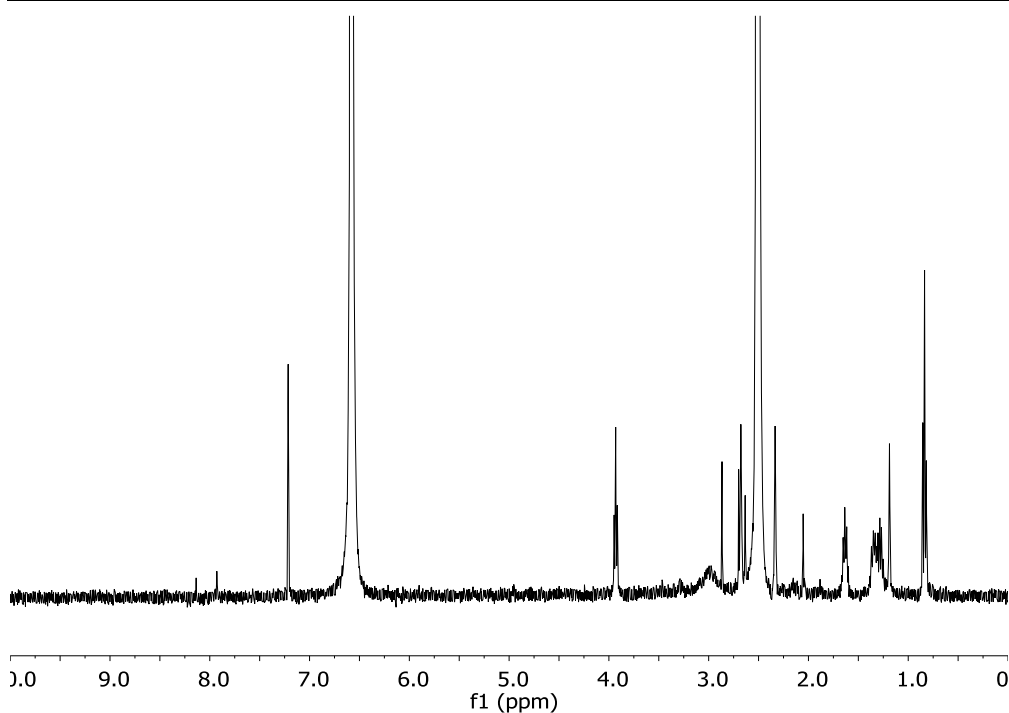| Calculated Structure	Calculated / wt%			Exfoliation Solvent	Experimental / wt%		
	C	H	N		C	H	N
Cu(**2**)	54.06	6.05	0				
Cu(**2**)(DMF)	58.59	7.52	2.99	DMF	51.1	6.15	2.76
Cu(**2**)(NMP)	55.35	6.67	2.81	NMP	51.5	6.14	2.21
Cu(**2**)(MeCN)	53.45	5.90	3.28	MeCN	45.98	6.13	0
Cu(**2**)(Et$_2$O)	55..74	7.23	0	Diethyl ether	47.79	6.23	0.59
Cu(**2**)(H$_2$O)	51.73	6.27	0	Water	45.64	5.96	0

Figure S46. NMR showing Cu(2)(DMF) following exfoliation in NMP, digested in DCl(aq)/DMSO.

7. Binding Studies

7.1 Estimation of Nanosheet Concentration in Suspension

Compounds Cu(**1**)(DMF) or Cu(**2**)(DMF) (5 mg) were suspended in H_2O (6 mL) and sonicated for 12 hrs, using 80 kHz, 100 % power, 21 °C. The resulting suspensions of Cu(**1**)(H_2O) and Cu(**2**)(H_2O) were centrifuged at 1500 rpm for 1 hr in order to collect larger unexfoliated particles from suspension, giving MON suspensions of 0.65 mM and 0.20 mM respectively. Cu(**1**)(H_2O) was diluted in water (1 in 5) to give a suspension with an absorption maximum at 0.37 AU. Using the extinction coefficient determined in section 1.2.2, this indicates a concentration of 0.13 mM. Cu(**2**)(H2O) suspension was diluted in water (1 in 2.5), giving an absorption maxima of 0.25 AU, indicating a concentration of 0.08 mM. These were used as host suspensions.
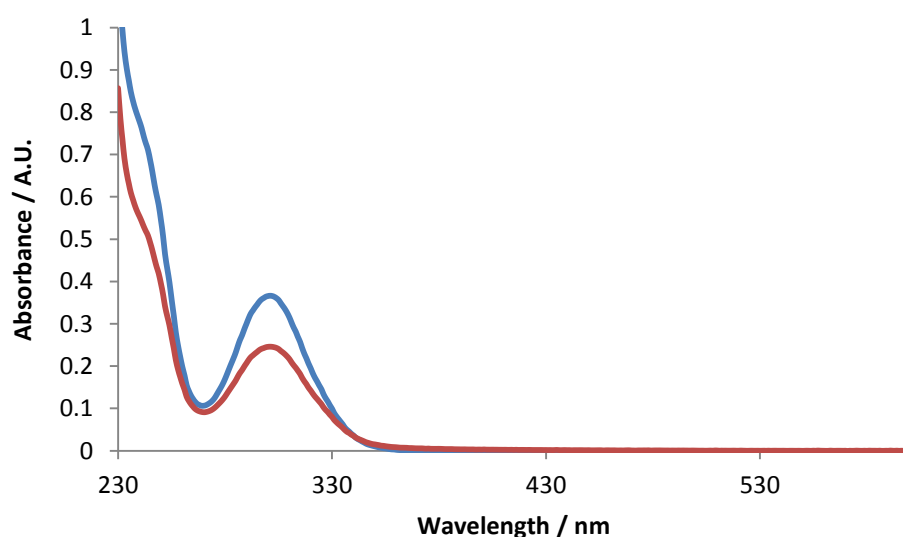

Figure S47. UV-vis spectra of suspensions of Cu(**1**)(H_2O) (0.13 mM) (blue) and Cu(**2**)(H_2O) (0.08 mM) (red) in water.

7.2 Binding Studies

Imidazole (10 mg and 6 mg), respectively was dissolved in 2 mL of the Cu(**1**)(H_2O) and Cu(**2**)(H_2O) suspensions, giving 43 mM and 73 mM aqueous solutions, respectively. These were used as the guest solutions. UV titration bidning experiments were performed three separate times in each case. Binding constants were calculated by fitting the experimental data to a binding isotherm using 14Allmaster, a macro based excel fitting programme written by Prof. Christopher A. Hunter (University of Cambridge). Values are reported as the global average of the three repeat measurements, with the error quoted as two standard deviations from the mean. Tyndall scattering confirmed the presence of nanosheets following addition of imidazole.
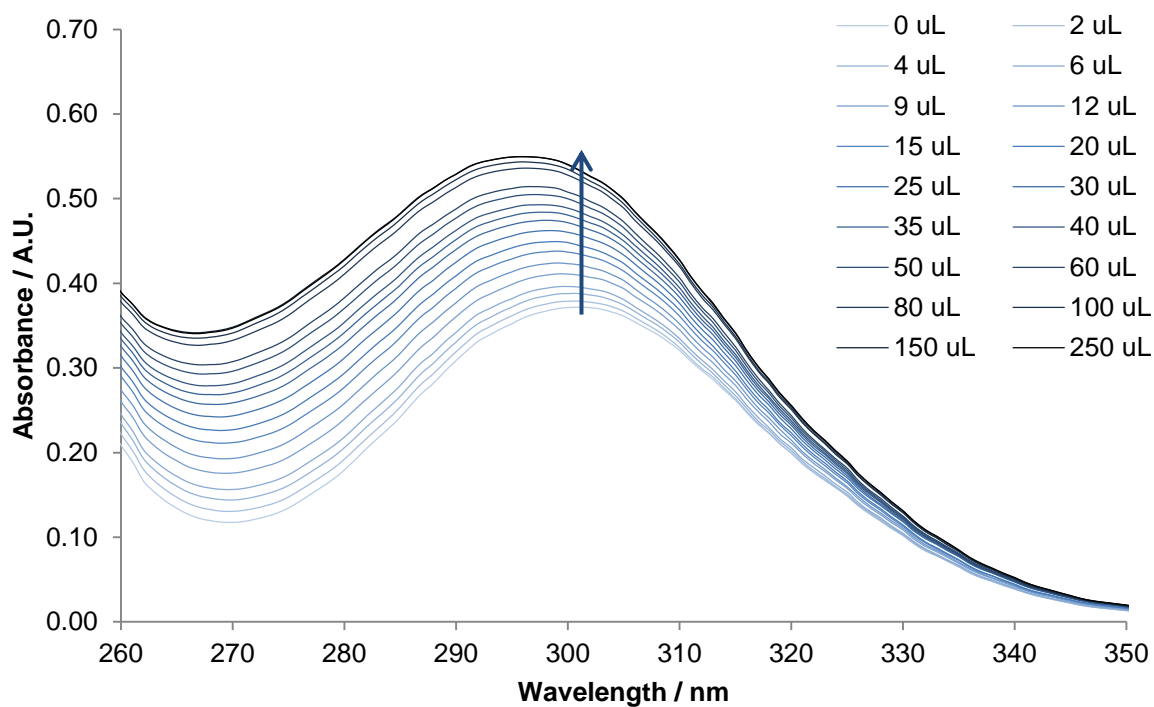
Figure S48. UV-vis plot showing the addition of aliquots of X uL imidazole solution (73 mM in water) to 2.5 mL of aqueous suspension of Cu(**1**)(H$_2$O) (0.13 mM). Aliquots of volume 0, 2, 6, 9, 12, 15, 20, 25, 30, 35, 40, 50, 60, 80, 100, 150 and 250 uL were used.
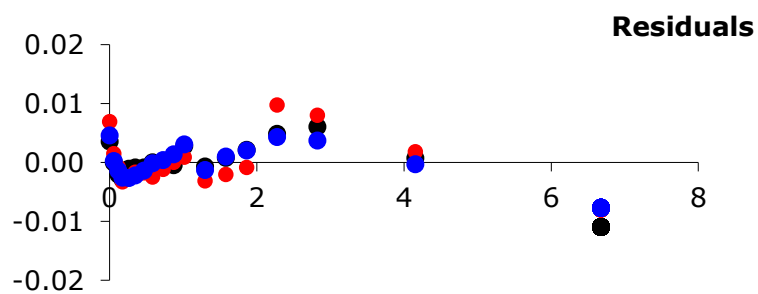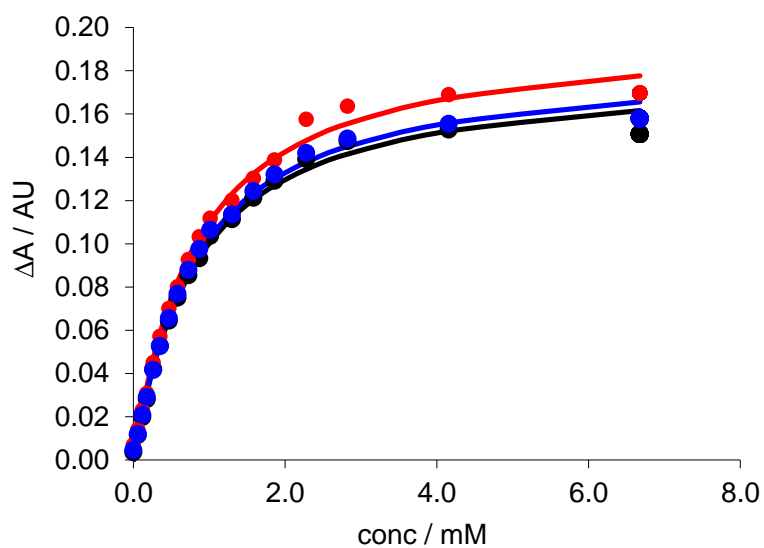
Figure S49. UV-vis binding titration showing the change in absorbance at λmax = 301 nm for Cu(**1**)(H$_2$O) with increasing concentration of imidazole. The three experiments were repeated three times, with individual experiments shown in red, black and blue. Residuals for the fits are shown below.

Figure S50. Speciation plot showing formation of HG complex upon addition of imidazole (G) to a suspension of Cu(**1**)(H$_2$O) nanosheets (H).
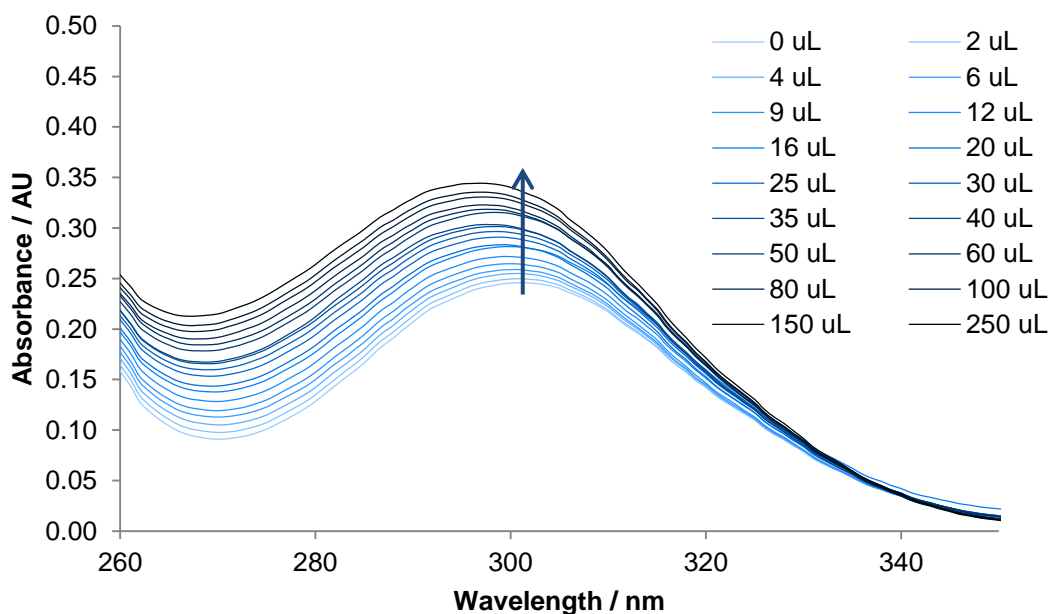
Figure S51. UV-vis plot showing the addition of aliquots of X uL imidazole solution (43 mM in water) to 2.5 mL of aqueous suspension of Cu(**2**)(H$_2$O) (0.08 mM). Aliquots of volume 0, 2, 4, 6, 9, 12, 15, 20, 25, 30, 35, 40, 50, 60, 80, 100, 150 and 250 uL were used.
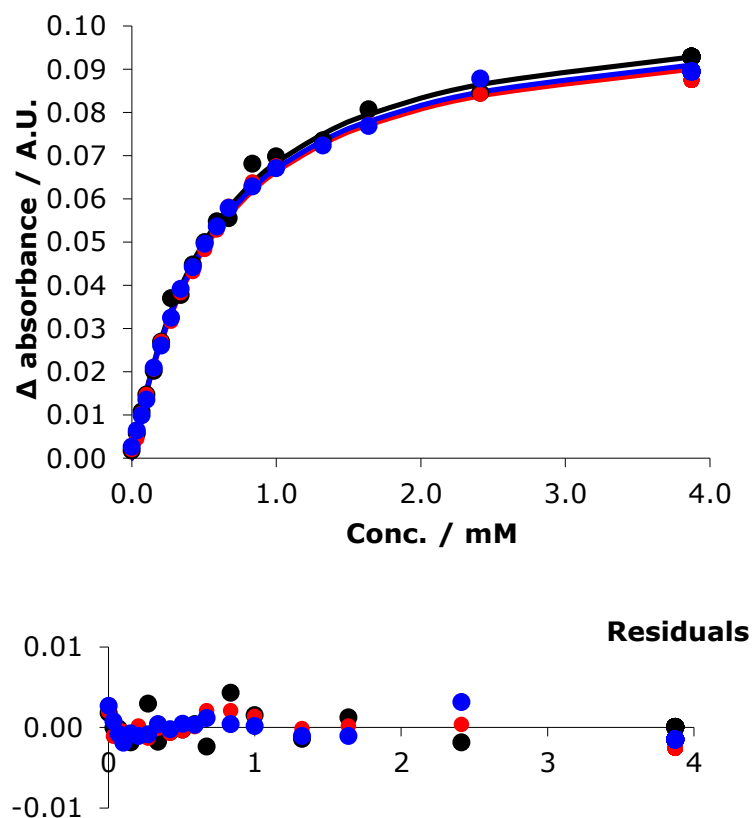
Figure S52. UV-vis binding titration showing the change in absorbance at λmax = 301 nm for Cu(**2**)(H$_2$O) with increasing concentration of imidazole. The three experiments were repeated three times, with individual experiments shown in red, black and blue. Residuals for the fits are shown below.
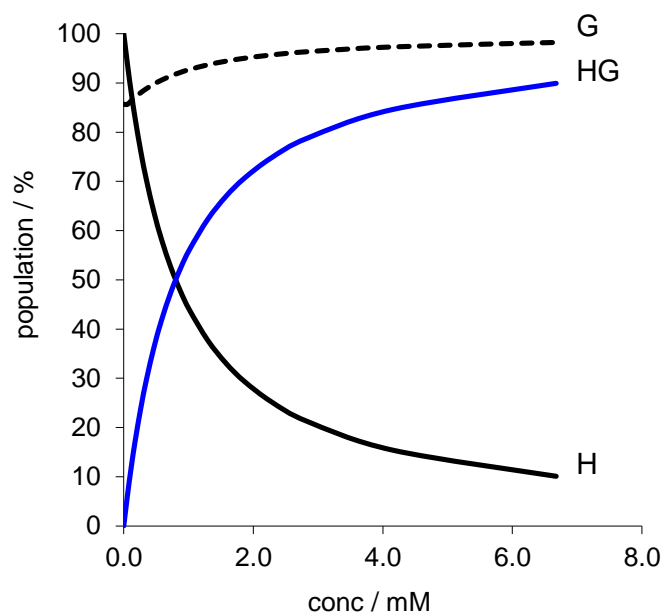

Figure S 53. Speciation plot showing formation of HG complex upon addition of imidazole (G) to a suspension of Cu(**2**)(H$_2$O) nanosheets (H).

Detection limit and sensitivity

The sensitivity of imidazole sensing depends on both the [host] and [guest] and the response curve is steepest following addition of the first aliquot of imidazole solution. The concentration of host was maintained at 0.13 mM and 0.08 mM for $Cu(\mathbf{1})(H_2O)$ and $Cu(\mathbf{2})(H_2O)$ respectivel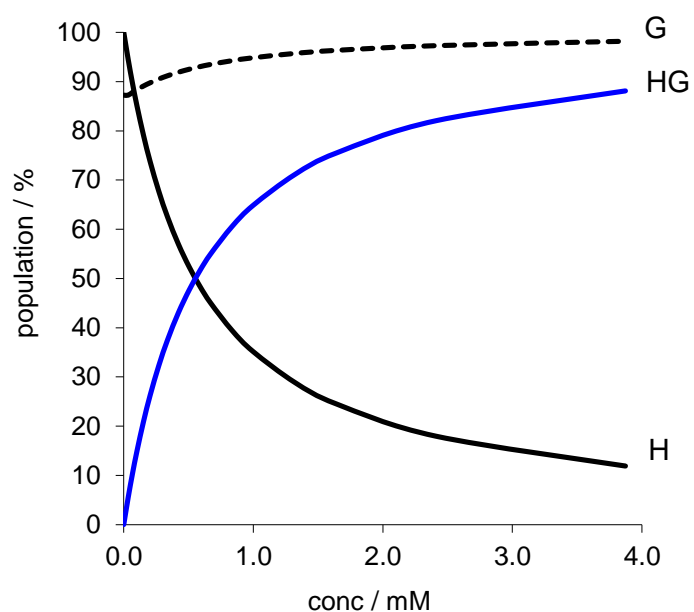y and the concentration of the guest in solution following addition of the first aliquot was 59 µM and 34 µM. This resulted in a positive Δ(absorbance) at λ_{max} in the UV spectra of +0.0075 and +0.0034 A.U. for $Cu(\mathbf{1})(H_2O)$ and $Cu(\mathbf{2})(H_2O)$. The standard deviation in absorbance of the three blank host runs was 0.0026 and 0.0008 respectively – both lower than the average Δ(absorbance). The detection limit of $Cu(\mathbf{1})(H_2O)$ and $Cu(\mathbf{2})(H_2O)$ for imidazole is therefore below 59 µM and 34 µM respectively."

8. References

1. S. Henke, A. Schneemann, A. Wutscher and R. A. Fischer, *J Am Chem Soc*, 2012, **134**, 9464-9474.

2. S. Henke and R. A. Fischer, *J Am Chem Soc*, 2011, **133**, 2064-2067.

3. J. A. Foster, S. Henke, A. Schneemann, R. A. Fischer and A. K. Cheetham, *Chemical Communications*, 2016, **52**, 10474-10477.

Further supplementary data can be found at:

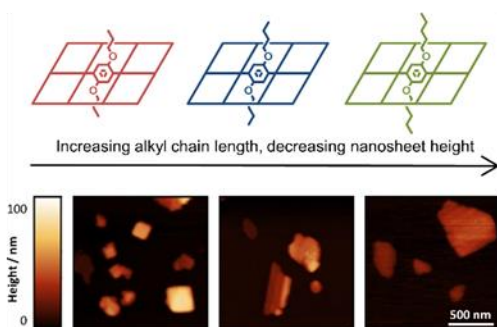https://onlinelibrary.wiley.com/doi/full/10.1002/chem.201803221

This contains details of DFT calculations performed by Dr Rasha W. M. Al-Saedi and Prof. Anthony J. H. M. Meijer, which is supplementary to the work presented in this thesis.

4 ♥

Increasing Alkyl Chain Length in a Series of Layered Metal–Organic Frameworks Aids Ultrasonic Exfoliation to Form Nanosheets

Increasing alkyl chain length in a series of layered metal-organic frameworks aids ultrasonic exfoliation to form nanosheets

David J. Ashworth, Thomas M. Roseveare, Andreas Schneemann, Max Flint, Irene Dominguez Bernáldes, Pia Vervoorts, Roland A. Fischer, Lee Brammer and Jonathan A. Foster

Author Contributions

David J. Ashworth	Performed MOF synthesis and solid-state characterisation. Assisted PXRD data collection at Diamond Light Source. Explored MOF desolvation and characterised desolvated MOFs. Performed all exfoliation studies, solid-state characterisation, suspension analyses and nanoscopic imaging. Collated data, drafted manuscript and ESI and prepared all figures other than ESI Figures S11-20. Assisted in redrafting and editing the manuscript. Supervised MF.
Thomas M. Roseveare	Lead PXRD data collection at Diamond Light Source. Performed all Rietveld and Pawley refinements. Prepared ESI Figures S11-20.
Andreas Schneemann	Synthesised ligand precursors H$_2$**n** (**n**= **1** – **4**) and lead gas adsorption studies.
Max Flint	An MChem student directly supervised by DJA within the Foster group. Developed the syntheses of H$_2$**5**, and first synthesised MOFs Cu(**n**)(DMF) (**n**= **1,2,4,5**).
Irene Dominguez Bernáldes	An MSc student supervised by JAF. Assisted in preliminary syntheses and explorations of long-chain ligands (n > **5**) and MOF syntheses.
Pia Vervoorts	Assisted AS with gas adsorption studies.
Roland A. Fischer	Supervised AS and PV.
Lee Brammer	Assisted data collection at Diamond Light Source. Assisted with PXRD data refinements. Supervised TMR.
Jonathan A. Foster	Supervised DJA, MF and IDB and coordinated this body of work. Assisted in redrafting and editing the manuscript.

Inorganic Chemistry

Article

pubs.acs.org/IC

Increasing Alkyl Chain Length in a Series of Layered Metal−Organic Frameworks Aids Ultrasonic Exfoliation to Form Nanosheets

David J. Ashworth,[†] Thomas M. Roseveare,[†] Andreas Schneemann,[‡,§] Max Flint,[†]
Irene Dominguez Bernáldes,[†] Pia Vervoorts,[‡,§] Roland A. Fischer,[‡,§] Lee Brammer,[†]
and Jonathan A. Foster*,[†]

[†]Department of Chemistry, University of Sheffield, Brook Hill, Sheffield S3 7HF, U.K.
[‡]Department of Chemistry, Technische Universität München, Lichtenbergstraße 4, 85748 Garching, Germany
[§]Catalysis Research Centre, Technische Universität München, Ernst-Otto-Fischer Straße 1, 85748 Garching, Germany

S *Supporting Information*

ABSTRACT: Metal−organic framework nanosheets (MONs) are attracting increasing attention as a diverse class of two-dimensional materials derived from metal−organic frameworks (MOFs). The principles behind the design of layered MOFs that can readily be exfoliated to form nanosheets, however, remain poorly understood. Here we systematically investigate an isoreticular series of layered MOFs functionalized with alkoxy substituents in order to understand the effect of substituent alkyl chain length on the structure and properties of the resulting nanosheets. A series of 2,5-alkoxybenzene-1,4-dicarboxylate ligands ($O_2CC_6H_2(OR)_2CO_2$, R = methyl−pentyl, **1−5**, respectively) was used to synthesize copper paddle-wheel MOFs. Rietveld and Pawley fitting of powder diffraction patterns for compounds Cu(**3−5**)(DMF) showed they adopt an isoreticular series with two-dimensional connectivity in which the interlayer distance increases from 8.68 Å (R = propyl) to 10.03 Å (R = pentyl). Adsorption of CO_2 by the MOFs was found to increase from 27.2 to 40.2 cm^3 g^{-1} with increasing chain length, which we attribute to the increasing accessible volume associated with increasing unit-cell volume. Ultrasound was used to exfoliate the layered MOFs to form MONs, with shorter alkyl chains resulting in higher concentrations of exfoliated material in suspension. The average height of MONs was investigated by AFM and found to decrease from 35 ± 26 to 20 ± 12 nm with increasing chain length, with the thinnest MONs observed being only 5 nm, corresponding to five framework layers. These results indicate that careful choice of ligand functionalities can be used to tune nanosheet structure and properties, enabling optimization for a variety of applications.
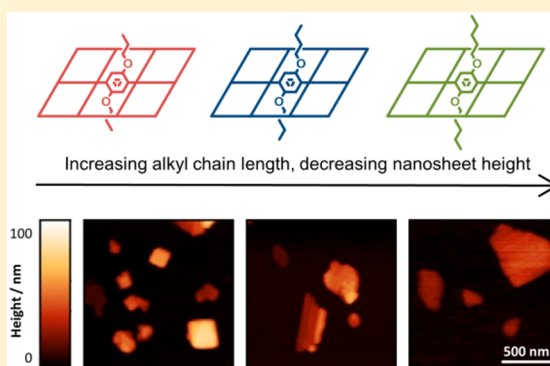
1. INTRODUCTION

Metal−organic framework nanosheets (MONs) are free-standing, nominally two-dimensional materials formed by the coordination of organic ligands to metal ions or clusters.[1−4] MONs share many of the advantages of other metal−organic materials, such as the ease with which their structures can be varied and new properties introduced. However, they also benefit from the high aspect ratio, vast external surface area, and nanoscopic dimensions of other two-dimensional materials such as graphene, boron nitride, and molybdenum disulfide. These properties have already enabled MONs to outperform their bulk counterparts in a variety of applications, including gas separation,[5] water purification,[6] sensing,[7−12] catalysis,[13−20] and optoelectronics.[21−26]

The development of metal−organic frameworks (MOFs) over the past two decades has been focused on understanding how to design and tune the properties of open porous three-dimensional structures, for applications including gas storage,[27] catalysis,[28] and sensing.[29−31] During this time, a large number

of layered MOFs have been reported. It is these MOFs that provide a platform for the development of MONs. Two distinct approaches have emerged to convert layered MOFs into MONs: (1) "bottom-up" self-assembly of subcomponents in the presence of a directing interface[5,32] or chemical species[33,34] and (2) "top-down" exfoliation from layered MOFs. For the latter approach, a wide variety of methods have been developed including freeze−thaw,[35] ball-milling,[36,37] intercalation,[38,39] and ultrasonication.[7,36,40−49] Among these, liquid exfoliation using ultrasound is one of the most widely applicable and readily scalable methods, which has been widely applied in the exfoliation of other two-dimensional (2D) materials.[50−53] The vast majority of MONs reported to date are based on known MOF structures being repurposed to form nanosheets. Understanding how to optimize the design of layered MOFs to facilitate exfoliation into free-standing

nanosheets is therefore an important and necessary new crystal engineering challenge.

Functionalization of 2,5-dihydroxybenzene-1,4-dicarboxylic acid (H$_2$DHBDC) with pendant flexible substituents has proved useful for understanding the structure−property relationships of three-dimensional MOFs, particularly regarding their gas adsorption properties, as well as their framework flexibility, introducing new behaviors and optimizing their design for the adsorption of specific gases.[54,55] In most of these systems, the pendant chains sit within the pores of the MOF and do not affect the overall structure, although they can influence the architecture that is formed.[54] We have recently developed this approach further in a series of layered MOFs designed to incorporate short alkyl-ether chains between the layers intended to aid exfoliation by weakening interlayer interactions and increasing interactions with solvent molecules.[47] In a related study, two layered MOFs functionalized with either −O(CH$_2$)$_4$CH$_3$ or −O(CH$_2$)$_3$OCH$_3$ chains which bestowed hydrophobic or hydrophilic character, respectively, were exfoliated in a wide range of solvents.[56] The more hydrophobic system formed thinner, more well-defined nanosheets comprising fewer framework layers. Optimization and control of the exfoliation process by framework design, however, remain key challenges, which we seek to address in the current study.

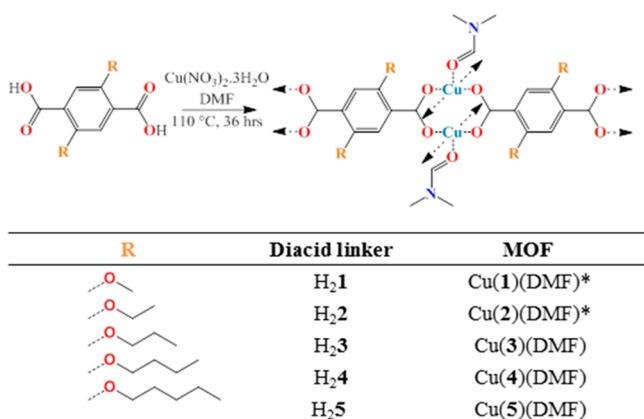Here, we report a series of layered MOFs (Figure 1) formed using DHBDC$^{2−}$ ligands functionalized with alkyl chains

R	Diacid linker	MOF
⋯O─	H$_2$1	Cu(1)(DMF)*
⋯O╱╲	H$_2$2	Cu(2)(DMF)*
⋯O╱╲╱	H$_2$3	Cu(3)(DMF)
⋯O╱╲╱╲	H$_2$4	Cu(4)(DMF)
⋯O╱╲╱╲╱	H$_2$5	Cu(5)(DMF)

Figure 1. General reaction scheme for the targeted syntheses of MOFs [Cu(**n**)(DMF)]$_n$, where **n** = 1−5. R groups in dicarboxylic acid ligands precursors H$_2$1 to H$_2$5 are defined, and the terminology used throughout this Article is provided. [*When using H$_2$1 and H$_2$2, the anticipated MOF structures were not formed (see text)].

(methyl to pentyl). We show that increasing chain length improves exfoliation to yield MONs of improved aspect ratio. We suggest that increasing chain length weakens the interlayer interactions and improves interactions of the framework layers with solvent molecules, leading to the enhanced exfoliation. The study is underpinned by a detailed characterization of the MOF series in their solvated and unsolvated forms, enabling the effect of alkyl chain length on their structure to be understood. We also report on the CO$_2$/N$_2$ adsorption behavior of the MOFs, which can be related to the trend in their unit-cell dimensions.

2. RESULTS AND DISCUSSION

2.1. MOF Syntheses and Characterization. Dicarboxylic acids H$_2$1−H$_2$4[54] and H$_2$5[56] were synthesized via Williamson etherification of dimethoxy-2,5-dihydroxybenzenedicarboxylate with iodomethane or 1-bromoalkane (where alkane = ethane-pentane) following previously reported protocols. High yields (83−91%) of 2,5-bis(alkoxy)-1,4-benzenedicarboxylic acid (alkoxy = methoxy-pentoxy) were obtained, and compound purity was confirmed through ^{1}H NMR spectroscopy (Figures S1−S5). MOFs were formed by the solvothermal reaction of H$_2$1−H$_2$5 (10 mol % excess) and copper nitrate in DMF at 110 °C for 36 h. Green microcrystalline powders were obtained following slow cooling of the mixtures to room temperature and were then analyzed by powder X-ray diffraction (PXRD), Fourier-transform infrared (FTIR) spectroscopy, thermogravimetric analysis (TGA), and elemental analysis to understand their structure.

In line with our previous study, H$_2$5 was found to give a compound with the formula Cu(5)(DMF). TGA shows a 15.2% mass loss in the region 110−230 °C (theoretical 15.5% mass loss, Figure S7); FTIR shows the C = O stretch of coordinated DMF at 1668 cm$^{−1}$ (Figure S6), shifted from the expected wavenumber of 1676 cm$^{−1}$ for free DMF,[57] and elemental analysis shows good agreement for the empirical formula CuC$_{21}$H$_{31}$NO$_7$ (Table S1).

For the first time, we were also able to determine the structure of Cu(5)(DMF) (Figure 2b) from a high-resolution PXRD pattern collected at Diamond Light Source, beamline I11, and refine the structural model by Rietveld methods (see Figures S15 and S16; CCDC 1910582). Carboxylate groups of four ligands of 5 coordinate to Cu$_2$ dimers in a bidentate bridging manner, forming the paddle-wheel (PW) secondary building unit (SBU) (Figure 1). DMF is coordinated at the axial positions to form a distorted square-pyramidal coordination environment around the Cu$_2$ atoms, which are separated by a distance of 3.16 Å. Ligand 5 connects adjacent PWs, which form a square-net topology within a layer (Figure 2c). The pentoxy chains and DMF molecules extend out of the layer interdigitating with those in adjacent layers, holding them together through van der Waals forces (Figure 2b). This layered structure is isoreticular with that of MOF-2[58] and our previously reported single-crystal structure for Zn(**X**)(DMF) where **X** is 2,5-bis(3-methoxypropoxy)-1,4-benzene-dicarboxylate (i.e., R = O(CH$_2$)$_3$OCH$_3$).[47]

Dicarboxylic acids H$_2$**n** (**n** = 3, 4) form MOFs Cu(**n**)-(DMF), with structures closely related to Cu(5)(DMF). Mass losses corresponding to the loss of coordinated DMF were observed by TGA over the temperature range of 90−240 °C; FTIR showed the C=O stretch around 1665 cm$^{−1}$ of coordinated DMF; elemental analysis was consistent with the anticipated formula unit (Table S1). Pawley refinements of synchrotron PXRD data indicated unit cell parameters similar to Cu(5)(DMF) (Table 1 and Figures S11−S13), which suggests that they adopt the same square-grid topology. There is an increase in the volume of the unit cell with increasing alkyl chain length (3−5) from 1009 to 1155 Å^3. However, it is difficult to attribute this to expansion along a single axis because of the triclinic lattice symmetry. The flexibility of the alkyl chains, potential of the aromatic rings to rotate, and interplay with coordinated solvent molecules and pores mean that the effect of each additional methylene unit is likely to be more subtle than simply moving the layers apart.
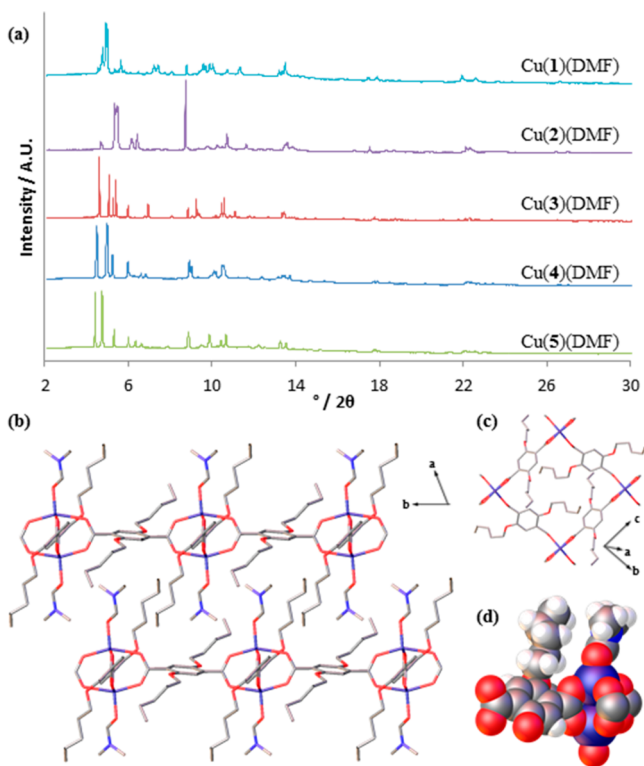
Figure 2. (a) PXRD patterns of microcrystalline powders resulting from the syntheses of Cu(1−5)(DMF), collected at Diamond Light Source, beamline I11 (λ = 0.826015 Å). (b) Crystal structure of Cu(5)(DMF) as refined through Rietveld methods, viewed down the c-axis. H atoms are omitted for clarity. (c) Square net structure of Cu(5)(DMF), viewed down the Cu-PW Cu−Cu axis. H atoms and coordinated DMF molecules omitted for clarity. (d) Space-filling view of Cu(5)(DMF) showing −O(CH₂)₄CH₃ chain and axial DMF packing. Copper, carbon, hydrogen, nitrogen, and oxygen atoms are depicted in purple, gray, white, blue, and red, respectively.

Rietveld refinements were attempted on high-resolution synchrotron PXRD patterns of Cu(n)(DMF) (n = 3, 4) but it was not possible to solve the structures or to obtain models suitable for Rietveld refinement. However, Cu sites could be located from electron density maps. Cu₂ units are situated with their centroids at the inversion centers within the structures (Table S5). Locating the Cu atoms allowed calculation of the

2D directional connectivity within layers (based on distances between Cu−Cu centroids and length of a coordinating BDC ligand) and confirmed the anticipated square-grid network structure. This enabled calculation of the interlayer distance, which was found to increase 8.37 < 9.42 < 9.91 Å from Cu(3)(DMF) to Cu(5)(DMF), correlating with increasing alkyl chain length (Figure S14). Particle morphologies of Cu(3−5)(DMF) were visualized using scanning electron microscopy (SEM). Platelets were observed with lateral dimensions in the range of 1−10 μm (Figure S22).

Microcrystalline powders resulting from the reactions using H₂n (n = 1, 2) were similarly assessed. Elemental analyses (Table S1) were not consistent with the anticipated Cu(n)-(DMF) (n = 1, 2) formula. Indexing and Pawley refinement indicated a mixture of phases present. Guo et al. reported a structurally similar Cu-PW MOF using 1, which has water capping the axial positions of the PW. Although TGA indicated that water may be present (4.5% mass loss between 50 and 110 °C), this phase was not observed in our synthesis (Figure S9).[59] There are no examples of layered MOFs using 2 as the linker, to the best of our knowledge. Attempts to grow larger crystals of these materials were unsuccessful. Analogous syntheses using zinc and H₂1 or H₂2, attempting to grow single crystals, resulted in cubic crystals of MOFs isoreticular with the 3D MOF-5,[60] in which 1,4-benzenedicarboxylate ligands (BDC) were replaced by 1 or 2, respectively. These materials were therefore excluded from further studies. Similar crystallizations using zinc and H₂3−5 also resulted in the 3D MOF-5 structure.

2.2. MOF Desolvation. We have previously observed that desolvation of this class of layered PW-MOFs can take place during ultrasonic exfoliation in noncoordinating solvents, for instance with acetonitrile (MeCN) for Cu(5)(DMF).[56] Desolvation is also anticipated to occur during gas adsorption measurements where frameworks are typically first activated through heating under dynamic vacuum (in our work, 160 °C for 10 h), in order to remove any solvent coordinated or present from the pores. Before moving on to discuss the results of exfoliation or gas sorption studies, we therefore first sought to characterize the structures of the desolvated MOFs. This is particularly important for these systems as the parent, nonfunctionalized Cu(BDC)(DMF) undergoes a structural rearrangement upon desolvation, in which the carboxylate groups coordinate to the vacated axial position of the Cu₂

Table 1. Unit Cell Parameters Determined through Pawley Refinements of PXRD Data (298 K) for Cu(3−5)(DMF) and Cu(3−5) and Rietveld Refinement of Cu(5)(DMF)[a]

MOF	refinement	space group	a (Å)	b (Å)	c (Å)	α (deg)	β (deg)	γ (deg)	vol (Å³)	R_{wp}[b]	R_{wp}'[c]
Cu(X)(DMF)[47]	N/A	P-1	10.42	10.82	10.88	85.21	74.99	67.51	1095	N/A	N/A
Cu(3)(DMF)	Pawley	P-1	10.60	10.62	10.81	71.12	79.91	61.22	1009	0.0224	0.0894
Cu(4)(DMF)	Pawley	P-1	10.62	10.80	10.94	76.01	62.54	81.99	1080	0.0377	0.1539
Cu(5)(DMF)	Pawley	P-1	10.84	10.81	10.86	83.79	79.74	67.34	1155	0.0256	0.1129
Cu(5)(DMF)	Rietveld	P-1	10.84	10.80	10.85	83.82	79.82	67.44	1154	0.0517	0.2455
Cu(3)	Pawley	P-1	10.81	10.69	11.00	71.51	77.35	63.35	1072	0.0655	0.1278
Cu(4)	Pawley	P-1	10.42	10.72	11.03	77.27	64.11	82.87	1081	0.0474	0.0942
Cu(5)	Pawley	P-1	10.86	11.04	10.87	84.04	76.89	70.65	1197	0.0593	0.1101

[a]All unit cell parameters are rounded to two decimal places; more accurate values and associated errors are provided in the Supporting Information (Table S3). X = 2,5-bis(3-methoxypropoxy)-1,4-benzenedicarboxylate (i.e., R = O(CH₂)₃OCH₃). [b]$R_{wp} = \sqrt{\sum [w(Y_{obs} - Y_{calc})^2]/\sum [wY_{obs}{}^2]}$ and [c]$R_{wp}' = \sqrt{\sum [w(Y_{obs} - Y_{calc})^2]/\sum [w(Y_{obs} - bkgr)^2]}$, where y_{obs} is the observed intensity, y_{calc} the calculated intensity, w the weight, and bkgr the background.

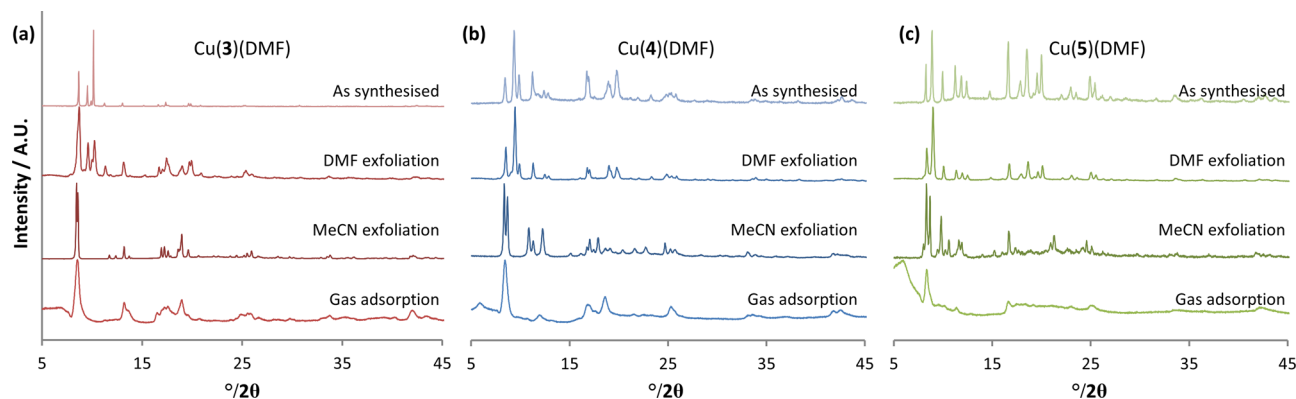**Figure 3.** PXRD patterns (λ = 1.5406 Å) of (a) Cu(**3**)(DMF), (b) Cu(**4**)(DMF), and (c) Cu(**5**)(DMF) MOFs after gas adsorption analyses and after exfoliation in DMF and MeCN, compared with as-synthesized MOFs.

dimer of neighboring layers to form a porous nonlayered 3D MOF, Cu(BDC).[61,62]

Figure 3 shows PXRD patterns of Cu(**3–5**)(DMF) after gas adsorption analyses and after sonication in DMF or MeCN, compared with the as-synthesized MOFs. A distinct new PXRD pattern was observed for each of the MOFs following gas adsorption measurements or exfoliation in MeCN. Gas adsorption resulted in peak broadening and poorly defined patterns; however, peak positions broadly match those observed from exfoliating in MeCN, indicating a similar phase has been formed in both cases. Sonication in MeCN gave sharper diffraction patterns. These samples were then digested using DCl/D$_2$O in d_6-DMSO for ^{1}H NMR spectroscopy. No DMF or MeCN was observed in any of the digested Cu(**3–5**) samples (Figures S23–S25), indicating that exfoliation in MeCN results in complete removal of DMF from compounds Cu(**3–5**)(DMF), and there is no coordination by MeCN.

Pawley fitting of the PXRD patterns after exfoliation in MeCN indicated crystal phases distinct from the solvated MOFs, which were assigned as the desolvated phases Cu(**3**), Cu(**4**), and Cu(**5**) (Table 1). There are slight increases in unit cell volume compared to the solvated structures. Without a full structure solution, it is difficult to explain this. Locating the Cu atoms (Table S5) again allowed calculation of the interlayer distances in the same manner as for Cu(**3–5**)(DMF). These increased with the trend 8.68 < 9.37 < 10.03 Å from Cu(**3**) to Cu(**5**), with the only notable increase upon desolvation being for Cu(**3**)(DMF) to Cu(**3**) (8.37–8.68 Å). It is worth noting that these structures do not undergo the equivalent rearrangement upon desolvation of Cu(BDC)(DMF), instead maintaining their layered structure. We suggest this difference is due to the increased interlayer distance of Cu(*n*)(DMF) compared to Cu(BDC)(DMF) (5.2 Å); sterics of the alkoxy arms may prevent the slipping of the layers and the close proximity needed to establish 3D coordination.

The diffraction patterns for all three frameworks following sonication in DMF were found to match those of the as-synthesized material, indicating no substantial structural changes had occurred. Some broadening of the PXRD peaks was observed, most prominently in the case of Cu(**3**)(DMF), consistent with decreases in crystallite size during sonication.

2.3. Gas Adsorption. Figure 4 shows the N$_2$ adsorption isotherms (77 K) for Cu(**3–5**). The BET surface areas were determined as 8.6, 9.0, and 5.4 m^2 g^{-1}, respectively. The type III adsorption isotherms,[63] observed with negligible N$_2$ uptake
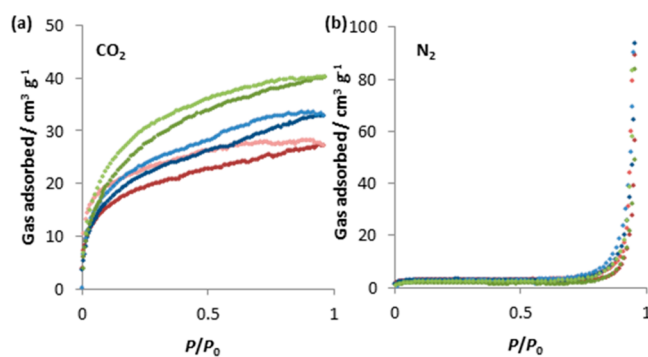

Figure 4. (a) CO$_2$ and (b) N$_2$ isotherms of Cu(**3–5**), recorded at 195 and 77 K, respectively. Gas adsorption is represented by darker shades, and desorption by lighter shades. Isotherms for Cu(**3**), Cu(**4**), and Cu(**5**) are red, blue, and green, respectively.

below 0.7 P/P_0, are consistent with related alkoxy functionalized MOFs, where the pore space is not accessible for nonpolar gases.[64] CO$_2$ adsorption (195 K) follows a type Ib isotherm, with a moderate type H1 hysteresis loop. CO$_2$ uptake increases from 27.2, to 32.9, to 40.2 cm^3 g^{-1}, from Cu(**3**) to Cu(**5**). This relatively large uptake, compared to N$_2$, could be due to increased penetration of the framework layers by CO$_2$, which has a higher binding affinity for the Cu sites. The unit cell volume increases by 11% (1072 to 1197 Å^3, Table 1) from Cu(**3**) to Cu(**5**), which could account for the increasing uptake of CO$_2$, also bearing in mind that the DMF has been removed, leaving coordinatively unsaturated Cu sites. If the unit cell volume remained constant across the series, it could be anticipated that the CO$_2$ uptake would decrease with an increase in alkyl chain length, because of the increased packing density of the chains between the 2D framework layers, but this is presumably compensated by the observed unit cell expansion.

2.4. Ultrasonic Exfoliation To Form MONs. In order to exfoliate the MOFs, 5 mg of Cu(**3–5**)(DMF) was suspended in 6 mL of DMF or MeCN and sonicated for 12 h in a water bath. Samples were rotated in the bath to ensure even exposure, and the bath was fitted with a water coil to maintain temperature, which equilibrated at 21 °C.[56] The samples were then centrifuged for either 1 h at 1500 rpm or 4.5 h at 4500 rpm to remove the larger unexfoliated MOF crystallites. A calibration curve, obtained by serial dilution of a suspension containing a known mass of Cu(**3–5**)(DMF), was used to

estimate the concentration of the nanosheets in suspension (Table 2 and Figures S26–S35).

Table 2. Concentration (mg mL^{-1}) of MONs Remaining in Suspension Following Different Centrifugation Protocols

solvent	rate[a]	time (h)	Cu(3) (DMF)	Cu(4) (DMF)	Cu(5) (DMF)
DMF	1500	1	0.23	0.22	0.13
	4500	4.5	0.13	0.07	0.05
MeCN	1500	1	0.40	0.24	0.11
	4500	4.5	0.11	0.06	0.04

[a]Rate is in revolutions per minute (rpm).

As expected, the concentration of MONs in suspension decreased in all cases as the centrifugation rate increased from 1500 to 4500 rpm (Table 2). No visible sedimentation was observed in any of the samples after a week. Interestingly, shorter alkyl chains resulted in higher concentrations of material in suspension after exfoliation in both DMF and MeCN, from both centrifugation protocols. The concentration of material in suspension for Cu(3–5)(DMF) was higher following exfoliation in DMF than in MeCN following the faster (and longer) centrifugation protocol. From the slower (and shorter) centrifugation protocol, Cu(3-4)(DMF) had a higher concentration in MeCN, but Cu(5)(DMF) had a higher concentration in DMF. These results demonstrate the importance of solvent–surface interactions in optimizing exfoliation and the effect that even small changes in the surface functionalities can have.

To assess the effect that chain length has on MON particle sizes following ultrasonic exfoliation in MeCN, suspensions following centrifugation (1500 rpm, 1 h) were deposited onto freshly cleaved mica and analyzed by AFM. A statistical analysis of the nanosheet dimensions was undertaken from resulting AFM images (Figures 5 and S36–S38). As the alkyl chain length increases from Cu(3) to Cu(5), the average thickness of the observed nanosheets decreased from 35 nm,
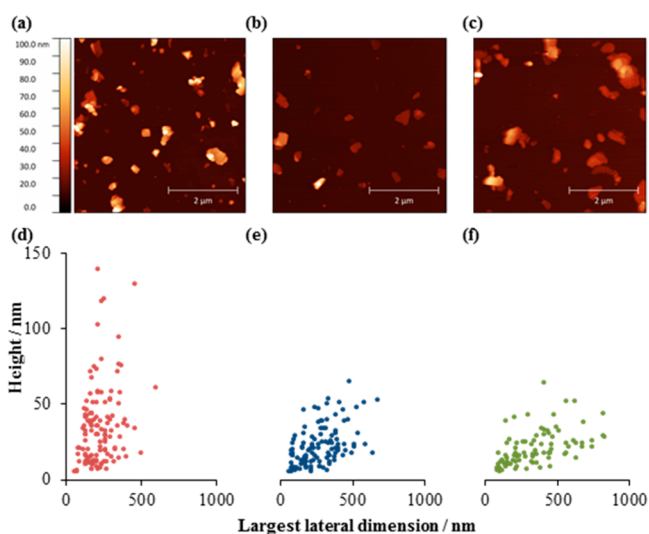

Figure 5. Topographic AFM images of nanosheets of Cu(3), Cu(4), and Cu(5) (a–c) observed after ultrasonic exfoliation of Cu(3–5)(DMF) in MeCN, centrifugation (1500 rpm for 1 h), and deposition onto mica. Associated scatter plots of MON dimensions (d–f).

through 22 nm, to 20 nm. Objects with heights of only 5 nm were observed in all three samples, corresponding to just five layers of framework. There is also an increase in lateral dimensions, from 222 to 348 nm across the series. These averages sit within a broad particle size distribution, with particles ranging between 50 and 900 nm. However, the observed differences in lateral dimensions between Cu(3)–Cu(4) and Cu(4)–Cu(5) are statistically significant (unpaired t test at 99% confidence level), and differences in both lateral dimensions and height are significant between Cu(3) and Cu(5) (unpaired t test, 99% confidence level). Additionally, the general trends are corroborated through dynamic light scattering (DLS) measurements (Figure S42 and Table S6), which confirmed the mean hydrodynamic diameter increased 185 < 213 < 247 nm (Table 3). As noted elsewhere, DLS underestimates nanosheet lateral dimensions with respect to AFM,[65,66] in part because of the Stokes–Einstein equation assumption of spherical particles.[67]

Table 3. Summary of Statistical Size Data from Cu(3–5) MONs Observed after Exfoliation of MOFs Cu(3–5)(DMF) in MeCN[a]

	Cu(3)	Cu(4)	Cu(5)[56]
n	129	114	94
$\bar{x}$ LD ± SD	222 ± 95	275 ± 148	348 ± 202
$\bar{x}$ H ± SD	35 ± 26	22 ± 13	20 ± 12
$\bar{x}$ aspect ratio ± SD[b]	10 ± 7	15 ± 9	19 ± 10
diameter[c]	185	213	247

[a]LD = largest lateral dimension (nm). H = height (nm) and SD= standard deviation (nm). [b]Mean aspect ratio determined for individual particles. [c]Hydrodynamic diameter (nm) according to number-averaged DLS data.

Overall, it is remarkable that increasing the alkyl chain length by just two methylene units almost doubles the aspect ratio of the nanosheets formed, from 10 to 19. The opposite trend might be expected as each extra methylene unit will contribute additional van der Waals interactions. However, the longer alkyl chains also increase the interlayer distance, reducing other interlayer interactions and potentially making the layers easier to shear apart during sonication. Solvent is also expected to play a key role in offsetting the energy penalty for creating new interfaces during exfoliation.[68,69] Contact angle measurements revealed complete surface wetting (0°) upon addition of either DMF or MeCN to thin films of Cu(3–5)(DMF) MONs on mica compared to angles of 11° and 14°, respectively, for uncoated mica surfaces. The decrease in concentration of material in suspension with increasing alkyl chain length indicates less favorable solvent–MON interactions. This could also result in more of the larger particles sedimenting out of suspension during centrifugation, resulting in a lower average particle size distribution for the MONs with longer alkyl chains. However, given the larger lateral dimensions of the nanosheets of Cu(5) compared to Cu(3), we suggest that weaker interlayer interactions are the major driver for the thinner nanosheets observed in this case.

In contrast to exfoliation in MeCN, AFM analyses of the samples resulting from exfoliation in DMF showed only a small number of MONs with heights <50 nm across all samples. Cu(3)(DMF) heights ranged from 50 to 200 nm, Cu(4)-(DMF) 40–150 nm and Cu(5)(DMF) 40–350 nm (Figures S39–41) with a broad lateral size distribution comparable to

those observed in MeCN. A key difference between exfoliation in DMF compared to MeCN is that DMF remains coordinated to the axial position of the Cu-PW throughout the exfoliation process when carried out in DMF, indicated by no change to the diffraction pattern post sonication in DMF (Figure 3). Considering Cu(**5**)(DMF), the alkyl chains and DMF from adjacent layers interdigitate, contributing to the interlayer interactions (see Figure 2). If DMF is removed, the interactions between the remaining alkyl chains are likely to be weaker, potentially accounting for the thinner MONs observed following exfoliation in MeCN.

3. CONCLUSIONS

We have developed a series of layered MOFs incorporating ligands with alkyl side-chains of different length which are situated between the layers, in order to understand how this affects the nanosheets formed through liquid ultrasonic exfoliation of these MOFs. Ligands **1**−**5**, which are 2,5-bis(alkoxy)benzene-1,4-dicarboxylates with alkoxy chains ranging from methoxy to pentoxy, were used to generate a series of Cu PW-based layered MOFs. Pawley and Rietveld refinements of synchrotron PXRD data revealed that three of the compounds, Cu(**3**−**5**)(DMF), formed an isoreticular series of layered PW MOFs with the square-grid topology. The fully desolvated structures Cu(**3**−**5**) were also characterized by Pawley refinement, and both series of compounds showed an increase in unit cell volume with increasing alkyl chain length. CO_2 uptake in the relatively dense layered frameworks increases by nearly 50% from 27.2 to 40.2 cm^3 g^{-1} with an increase in chain length across the series Cu(**3**−**5**), whereas negligible N_2 uptake was observed in all cases.

Liquid exfoliation in an ultrasonic bath produced suspensions of MONs in DMF and MeCN with shorter alkyl chains found to result in higher concentrations of material in suspension for both solvents. Although higher concentrations of material were typically observed in DMF, this was found to correspond to thick sheets >50 nm in height. AFM revealed the formation of nanosheets in MeCN with thicknesses as low as 5 nm, corresponding to just five layers of the framework. The difference in behavior between the two solvents was attributed to removal of the apical DMF from the Cu PWs in MeCN, weakening interlayer interactions. We observed a decrease in the mean height of the MONs in MeCN from 35 nm > 22 nm > 20 nm for Cu(**3**)−Cu(**4**)−Cu(**5**), respectively. This trend of thinner nanosheets with increasing chain length was attributed to reducing the interlayer interactions and increasing the interlayer distance.

Together, these results demonstrate that an isoreticular series of MONs enables systematic studies to elucidate the rules governing the exfoliation of layered materials to form nanosheets. These insights will help in the design of new MOFs that are more readily exfoliated to form high concentrations of high-aspect-ratio nanosheets. The ability of MONs to be systematically tuned and optimized in this way provides them an advantage over other two-dimensional materials that are not modular in construction and will enable MONs to make an important contribution to sensing, catalysis, separation, electronics, and composite materials applications.

4. EXPERIMENTAL SECTION

Materials and reagents were obtained from multiple different commercial suppliers and used without further purification, specifically: dimethoxy-2,5-dihydroxybenzenedicarboxylate (Sigma-

Aldrich, 99+%), methyl iodide (Alfa Aesar, 99%, stabilized with copper), ethyl bromide (Sigma-Aldrich, 98%), propyl bromide (Sigma-Aldrich, 99%), butyl bromide (Acros, 99%), pentyl bromide (Alfa Aesar, 99%), copper nitrate trihydrate (SLS, 98%), acetonitrile (Fisher, ≥ 99.9%) and *n,n*-dimethylformamide (Fisher, ≥99%).

4.1. Ligand Precursor Syntheses. Ligand precursors H_2**1** to H_2**4** were synthesized in close accordance with previously reported methodologies.[54] Generally, dimethoxy-2,5-dihydroxybenzenedicarboxylate (1 g, 4.42 mmol) and K_2CO_3 (1.83 g, 13.28 mmol) were placed in a Schlenk flask and suspended in 30 mL of *N,N*-dimethylformamide (DMF). The corresponding alkyl halide was added under stirring via syringe (13.26 mmol of methyl iodide, ethyl bromide, propyl bromide, butyl bromide, or pentyl bromide, respectively). The reaction mixture was stirred overnight at 85 °C and transferred into a round-bottom flask, and the DMF was removed under reduced pressure. A NaOH solution (100 mL H_2O, 400 mg NaOH) was added, and the product was refluxed overnight. After the mixture was allowed to cool to room temperature, aqueous HCl (10%) was added to precipitate the products as off-white powders. Yields: H_2**1**, 91% (0.91 g, 4.02 mmol); H_2**2**, 90% (0.91 g, 4.02 mmol); H_2**3**, 83% (1.0 g, 3.55 mmol); H_2**4**, 86% (1.2 g, 3.88 mmol).

The method was adapted for H_2**5**.[47] A 2.089 g (9.24 mmol) sample of dimethoxy-2,5-dihydroxybenzenedicarboxylate was used, and other reagents were scaled accordingly. Instead of refluxing in NaOH(aq), the functionalized ester was refluxed in a 1:1 (v:v) mixture of THF and KOH(aq) (5%), before HCl workup in the same way to precipitate a white powder. Yield: H_2**5**, 87% (2.714 g, 8.02 mmol).

4.2. MOF Syntheses. Typically, $Cu(NO_3)_2$·$3H_2O$ (100 mg, 0.414 mmol) and H_2(**1**−**5**) (0.455 mmol, 10% excess) were dissolved in 10 mL of DMF and sealed into 12 mL reaction vials with Teflon-lined lids. These were heated to 110 °C, held for 36 h, and then cooled at 0.1 °C min^{-1} to 25 °C. Green solids were isolated through centrifugation and washed with DMF (3 × 5 mL) and diethyl ether (2 × 5 mL). The resulting green microcrystalline powders were air-dried prior to characterization. Yields: Cu(**1**)(DMF), 82%; Cu(**2**)-(DMF), 97%; Cu(**3**)(DMF), 93%; Cu(**4**)(DMF), 82%; Cu(**5**)-(DMF), 89%. All yields are based on the anticipated structural formula [Cu(**1**−**5**)(DMF)]$_n$ and calculated based on Cu.

4.3. Ultrasonic Exfoliation. Five mg of the respective MOFs were suspended in 6 mL of solvent (DMF or MeCN). Mixtures were vortexed for 30 s before being placed in a Fisher brand Elmasonic P 30H ultrasonic bath (2.75 L, 380/350 W, UNSPSC 42281712) filled with water. Samples were held and rotated around the bath at 40 rpm using an adapted Heidolph RZR 2020 overhead stirrer with a multisample holder. The ultrasonic bath was operated at 100% and 80 kHz, and samples were sonicated for 12 h. A cooling water coil was equipped to prevent bath heating upon prolonged use, with the bath temperature equilibrating at 21 °C.

4.4. Characterization. TGA was performed using a PerkinElmer Pyris 1 TGA from 30 to 600 °C at 10 °C min^{-1}, under a 20 mL min^{-1} N_2 flow. FTIR specta were recorded using a PerkinElmer Spectrum One spectrometer equipped with a diamond ATR accessory. Data were collected from 500 to 4000 cm^{-1} using a resolution of 1 cm^{-1} and 16 scans. Elemental analyses were performed using a Elementar vario MICRO cube. Samples for SEM analysis were loaded onto a carbon sticky tab on an aluminum sample stub and coated with approximately 20 nm of gold using an Edwards S150B sputter coater. SEM micrographs were collected using a TESCAN VEGA3 LMU SEM instrument, operating at 15 keV and using the secondary electron detector. N_2 and CO_2 adsorption isotherms were measured using a Micromeritics 3 Flex volumetric gas adsorption instrument. Prior to dosing, samples were activated on the Micromeritics Smart Vac Prep Sample preparation station at 160 °C and 10^{-3} mbar for 10 h. Approximately 50 mg of solid, dried sample was used in each case. CO_2 and N_2 gases used had purity grades of 99.5 and 99.999%, respectively. N_2 adsorption isotherms were recorded at 77 K using a liquid nitrogen bath for cooling of the sample cell, and CO_2 adsorption isotherms were conducted at 195 K using a dry ice/isopropanol slurry for cooling of the sample cell. The Brunauer−Emmett−Teller equation was used to calculate the specific surface

area from adsorption data obtained at $0.05 \leq P/P_0 \leq 0.3$. ^1H NMR spectroscopy was performed on a Bruker Avance IIIHD 400 MHz spectrometer. ^1H chemical shifts are reported in parts per million on the δ scale and referenced to the residual proton resonance of the solvent. UV–vis spectra were recorded with a Varian Cary 50 UV spectrophotometer using a resolution of 1 nm and scan speed of 600 nm min^{-1}, controlled with PerkinElmer Spectrum One software. Measurements were made using 10 mm path length quartz cuvettes. AFM images were obtained using a Bruker Multimode 5 AFM equipped with a Nokia 10× visualizing lens, operating in soft tapping-mode using Bruker OTESPA-R3 cantilevers. Samples were prepared by dropping 10 μL (sample dependent) of suspension onto a freshly cleaved mica substrate. Images were processed using standard techniques with Gwyddion software.[70] DLS data were collected using a Malvern Zetasizer Nano Series particle size analyzer equipped with a He–Ne laser at 633 nm, operating in backscatter mode (173°). Contact angle measurements were made using a Ramé-Hart goniometer.

4.5. Powder X-ray Diffraction Data. PXRD data were recorded at the University of Sheffield on a Bruker D8 ADVANCE powder X-ray diffractometer or using synchrotron radiation at beamline I11 at Diamond Light Source.[71−73] Unit cell dimensions for samples Cu(**3**−**5**)(DMF) were determined by indexing of synchrotron PXRD patterns in the range $3° \leq 2\theta \leq 40°$ and fitting by Pawley refinement,[74] using TOPAS software.[75,76] A structural model for Cu(**5**)(DMF), adapted from a previously published single-crystal structure,[47] was subsequently fitted to the PXRD pattern by Rietveld refinement[77] using TOPAS. Pawley and Rietveld refinement details are provided in the Supporting Information (Tables S3 and S4 and Figures S11−S20).

ASSOCIATED CONTENT

Ⓢ Supporting Information

The Supporting Information is available free of charge on the ACS Publications website at DOI: 10.1021/acs.inorgchem.9b01128.

> Material syntheses and characterization, PXRD refinement procedures, gas adsorption isotherms, UV data, AFM data, and statistical analyses (PDF)

Accession Codes

CCDC 1910582 contains the supplementary crystallographic data for this paper. These data can be obtained free of charge via www.ccdc.cam.ac.uk/data_request/cif, or by emailing data_request@ccdc.cam.ac.uk, or by contacting The Cambridge Crystallographic Data Centre, 12 Union Road, Cambridge CB2 1EZ, UK; fax: +44 1223 336033.

AUTHOR INFORMATION

Corresponding Author
*E-mail: jona.foster@sheffield.ac.uk (J.A.F.).
ORCID Ⓘ
Andreas Schneemann: 0000-0001-6801-2735
Roland A. Fischer: 0000-0002-7532-5286
Lee Brammer: 0000-0001-6435-7197
Jonathan A. Foster: 0000-0002-0588-2474
Notes
The authors declare no competing financial interest.

ACKNOWLEDGMENTS

REFERENCES

(1) Ashworth, D. J.; Foster, J. A. Metal-Organic Framework Nanosheets (MONs): A New Dimension in Materials Chemistry. *J. Mater. Chem. A* **2018**, *6* (34), 16292−16307.

(2) Zhao, M.; Huang, Y.; Peng, Y.; Huang, Z.; Ma, Q.; Zhang, H. Two-Dimensional Metal-Organic Framework Nanosheets: Synthesis and Applications. *Chem. Soc. Rev.* **2018**, *47* (16), 6267−6295.

(3) Zhao, W.; Peng, J.; Wang, W.; Liu, S.; Zhao, Q.; Huang, W. Ultrathin Two-Dimensional Metal-Organic Framework Nanosheets for Functional Electronic Devices. *Coord. Chem. Rev.* **2018**, *377*, 44−63.

(4) Xu, M.; Yang, S. S.; Gu, Z.-Y. Two-Dimensional Metal-Organic Framework Nanosheets: A Rapidly Growing Class of Versatile Nanomaterials for Gas Separation, MALDI-TOF Matrix and Biomimetic Applications. *Chem. - Eur. J.* **2018**, *24*, 15131−15142.

(5) Rodenas, T.; Luz, I.; Prieto, G.; Seoane, B.; Miro, H.; Corma, A.; Kapteijn, F.; Llabrés I Xamena, F. X.; Gascon, J. Metal-Organic Framework Nanosheets in Polymer Composite Materials for Gas Separation. *Nat. Mater.* **2015**, *14* (1), 48−55.

(6) Ang, H.; Hong, L. Polycationic Polymer-Regulated Assembling of 2D MOF Nanosheets for High-Performance Nanofiltration. *ACS Appl. Mater. Interfaces* **2017**, *9* (33), 28079−28088.

(7) Li, Z. Q.; Qiu, L. G.; Wang, W.; Xu, T.; Wu, Y.; Jiang, X. Fabrication of Nanosheets of a Fluorescent Metal-Organic Framework [Zn(BDC)(H2O)]n (BDC = 1,4-Benzenedicarboxylate): Ultrasonic Synthesis and Sensing of Ethylamine. *Inorg. Chem. Commun.* **2008**, *11* (11), 1375−1377.

(8) Xu, H.; Gao, J.; Qian, X.; Wang, J.; He, H.; Cui, Y.; Yang, Y.; Wang, Z.; Qian, G. Metal-Organic Framework Nanosheets for Fast-Response and Highly Sensitive Luminescent Sensing of Fe3+. *J. Mater. Chem. A* **2016**, *4* (28), 10900−10905.

(9) He, L.; Duan, F.; Song, Y.; Guo, C.; Zhao, H.; Tian, J.-Y.; Zhang, Z.; Liu, C.-S.; Zhang, X.; Wang, P.; et al. 2D Zirconium-Based Metal-Organic Framework Nanosheets for Highly Sensitive Detection of Mucin 1: Consistency between Electrochemical and Surface Plasmon Resonance Methods. *2D Mater.* **2017**, *4* (2), 025098.

(10) Yang, Q.; Zhou, L.; Wu, Y. X.; Zhang, K.; Cao, Y.; Zhou, Y.; Wu, D.; Hu, F.; Gan, N. A Two Dimensional Metal-Organic Framework Nanosheets-Based Fluorescence Resonance Energy Transfer Aptasensor with Circular Strand-Replacement DNA Polymerization Target-Triggered Amplification Strategy for Homogenous Detection of Antibiotics. *Anal. Chim. Acta* **2018**, *1020*, 1−8.

(11) Chen, J.; Shu, Y.; Li, H.; Xu, Q.; Hu, X. Nickel Metal-Organic Framework 2D Nanosheets with Enhanced Peroxidase Nanozyme Activity for Colorimetric Detection of H2O2. *Talanta* **2018**, *189* (March), 254−261.

(12) Hu, S.; Yan, J.; Huang, X.; Guo, L.; Lin, Z.; Luo, F.; Qiu, B.; Wong, K. Y.; Chen, G. A Sensing Platform for Hypoxanthine Detection Based on Amino-Functionalized Metal Organic Framework Nanosheet with Peroxidase Mimic and Fluorescence Properties. *Sens. Actuators, B* **2018**, *267*, 312−319.

(13) Zhan, G.; Zeng, H. C. Synthesis and Functionalization of Oriented Metal-Organic-Framework Nanosheets: Toward a Series of 2D Catalysts. *Adv. Funct. Mater.* **2016**, *26* (19), 3268−3281.

(14) Cao, L.; Lin, Z.; Peng, F.; Wang, W.; Huang, R.; Wang, C.; Yan, J.; Liang, J.; Zhang, Z.; Zhang, T.; et al. Self-Supporting Metal-Organic Layers as Single-Site Solid Catalysts. *Angew. Chem., Int. Ed.* **2016**, *55* (16), 4962−4966.

(15) Huang, Y.; Zhao, M.; Han, S.; Lai, Z.; Yang, J.; Tan, C.; Ma, Q.; Lu, Q.; Chen, J.; Zhang, X.; et al. Growth of Au Nanoparticles on 2D Metalloporphyrinic Metal-Organic Framework Nanosheets Used as Biomimetic Catalysts for Cascade Reactions. *Adv. Mater.* **2017**, *29* (32), 1700102.

(16) Dong, R.; Zheng, Z.; Tranca, D. C.; Zhang, J.; Chandrasekhar, N.; Liu, S.; Zhuang, X.; Seifert, G.; Feng, X. Immobilizing Molecular Metal Dithiolene-Diamine Complexes on 2D Metal-Organic Frameworks for Electrocatalytic H2Production. *Chem. - Eur. J.* **2017**, *23* (10), 2255−2260.

(17) Ling, P.; Qian, C.; Gao, F.; Lei, J. Enzyme-Immobilized Metal-Organic Framework Nanosheets as Tandem Catalysts for the Generation of Nitric Oxide. *Chem. Commun.* **2018**, *54* (79), 11176−11179.

(18) Lan, G.; Li, Z.; Veroneau, S. S.; Zhu, Y.-Y.; Xu, Z.; Wang, C.; Lin, W. Photosensitizing Metal-Organic Layers for Efficient Sunlight-Driven Carbon Dioxide Reduction. *J. Am. Chem. Soc.* **2018**, *140* (39), 12369−12373.

(19) He, T.; Ni, B.; Zhang, S.; Gong, Y.; Wang, H.; Gu, L.; Zhuang, J.; Hu, W.; Wang, X. Ultrathin 2D Zirconium Metal-Organic Framework Nanosheets: Preparation and Application in Photocatalysis. *Small* **2018**, *14* (16), 1703929.

(20) Huang, J.; Li, Y.; Huang, R. K.; He, C. T.; Gong, L.; Hu, Q.; Wang, L.; Xu, Y. T.; Tian, X. Y.; Liu, S. Y.; et al. Electrochemical Exfoliation of Pillared-Layer Metal-Organic Framework to Boost the Oxygen Evolution Reaction. *Angew. Chem., Int. Ed.* **2018**, *57* (17), 4632−4636.

(21) Saines, P. J.; Tan, J. C.; Yeung, H. H. M.; Barton, P. T.; Cheetham, A. K. Layered Inorganic-Organic Frameworks Based on the 2,2-Dimethylsuccinate Ligand: Structural Diversity and Its Effect on Nanosheet Exfoliation and Magnetic Properties. *Dalt. Trans.* **2012**, *41* (28), 8585−8593.

(22) Sun, Z.; Hui, L.; Ran, W.; Lu, Y.; Jia, D. Facile Synthesis of Two-Dimensional (2D) Nanoporous NiO Nanosheets from Metal-Organic Frameworks with Superior Capacitive Properties. *New J. Chem.* **2016**, *40* (2), 1100−1103.

(23) Benmansour, S.; Abhervé, A.; Gómez-Claramunt, P.; Vallés-García, C.; Gómez-García, C. J. Nanosheets of Two-Dimensional Magnetic and Conducting Fe(II)/Fe(III) Mixed-Valence Metal-Organic Frameworks. *ACS Appl. Mater. Interfaces* **2017**, *9* (31), 26210−26218.

(24) Hu, X.; Wang, Z.; Lin, B.; Zhang, C.; Cao, L.; Wang, T.; Zhang, J.; Wang, C.; Lin, W. Two-Dimensional Metal-Organic Layers as a Bright and Processable Phosphor for Fast White-Light Communication. *Chem. - Eur. J.* **2017**, *23* (35), 8390−8394.

(25) Xing, W.; Ye, P.; Lu, J.; Wu, X.; Chen, Y.; Zhu, T.; Peng, A.; Huang, H. Tellurophene-Based Metal-Organic Framework Nanosheets for High-Performance Organic Solar Cells. *J. Power Sources* **2018**, *401* (August), 13−19.

(26) Jayaramulu, K.; Masa, J.; Morales, D. M.; Tomanec, O.; Ranc, V.; Petr, M.; Wilde, P.; Chen, Y. T.; Zboril, R.; Schuhmann, W.; et al. Ultrathin 2D Cobalt Zeolite-Imidazole Framework Nanosheets for Electrocatalytic Oxygen Evolution. *Adv. Sci.* **2018**, *5* (11), 1801029.

(27) Li, J.-R.; Kuppler, R. J.; Zhou, H.-C. Selective Gas Adsorption and Separation in Metal-Organic Frameworks. *Chem. Soc. Rev.* **2009**, *38* (5), 1477.

(28) Huang, Y. B.; Liang, J.; Wang, X. S.; Cao, R. Multifunctional Metal-Organic Framework Catalysts: Synergistic Catalysis and Tandem Reactions. *Chem. Soc. Rev.* **2017**, *46* (1), 126−157.

(29) Morris, R. E.; Brammer, L. Coordination Change, Lability and Hemilability in Metal-Organic Frameworks. *Chem. Soc. Rev.* **2017**, *46* (17), 5444−5462.

(30) Evans, J. D.; Garai, B.; Reinsch, H.; Li, W.; Dissegna, S.; Bon, V.; Senkovska, I.; Fischer, R. A.; Kaskel, S.; Janiak, C.; et al. Metal-Organic Frameworks in Germany: From Synthesis to Function. *Coord. Chem. Rev.* **2019**, *380*, 378−418.

(31) Grigoropoulos, A.; McKay, A. I.; Katsoulidis, A. P.; Davies, R. P.; Haynes, A.; Brammer, L.; Xiao, J.; Weller, A. S.; Rosseinsky, M. J. Encapsulation of Crabtree's Catalyst in Sulfonated MIL-101(Cr): Enhancement of Stability and Selectivity between Competing Reaction Pathways by the MOF Chemical Microenvironment. *Angew. Chem., Int. Ed.* **2018**, *57* (17), 4532−4537.

(32) Xu, G.; Otsubo, K.; Yamada, T.; Sakaida, S.; Kitagawa, H. Superprotonic Conductivity in a Highly Oriented Crystalline Metal-Organic Framework Nanofil. *J. Am. Chem. Soc.* **2013**, *135* (20), 7438−7441.

(33) Pustovarenko, A.; Goesten, M. G.; Sachdeva, S.; Shan, M.; Amghouz, Z.; Belmabkhout, Y.; Dikhtiarenko, A.; Rodenas, T.; Keskin, D.; Voets, I. K.; et al. Nanosheets of Nonlayered Aluminum Metal-Organic Frameworks through a Surfactant-Assisted Method. *Adv. Mater.* **2018**, *30* (26), 1707234.

(34) Lan, G.; Li, Z.; Veroneau, S. S.; Zhu, Y.-Y.; Xu, Z.; Wang, C.; Lin, W. Photosensitizing Metal-Organic Layers for Efficient Sunlight-Driven Carbon Dioxide Reduction. *J. Am. Chem. Soc.* **2018**, *140*, 12369.

(35) Wang, X.; Chi, C.; Zhang, K.; Qian, Y.; Gupta, K. M.; Kang, Z.; Jiang, J.; Zhao, D. Reversed Thermo-Switchable Molecular Sieving Membranes Composed of Two-Dimensional Metal-Organic Nanosheets for Gas Separation. *Nat. Commun.* **2017**, *8*, 14460.

(36) Peng, Y.; Li, Y.; Ban, Y.; Yang, W. Two-Dimensional Metal-Organic Framework Nanosheets for Membrane-Based Gas Separation. *Angew. Chem., Int. Ed.* **2017**, *56* (33), 9757−9761.

(37) Peng, Y.; Li, Y.; Ban, Y.; Jin, H.; Jiao, W.; Liu, X.; Yang, W. Metal-Organic Framework Nanosheets as Building Blocks for Molecular Sieving Membranes. *Science (Washington, DC, U. S.)* **2014**, *346* (6215), 1356.

(38) Ding, Y.; Chen, Y. P.; Zhang, X.; Chen, L.; Dong, Z.; Jiang, H. L.; Xu, H.; Zhou, H. C. Controlled Intercalation and Chemical Exfoliation of Layered Metal-Organic Frameworks Using a Chemically Labile Intercalating Agent. *J. Am. Chem. Soc.* **2017**, *139* (27), 9136−9139.

(39) Song, W.-J. J. Intracellular DNA and MicroRNA Sensing Based on Metal-Organic Framework Nanosheets with Enzyme-Free Signal Amplification. *Talanta* **2017**, *170* (February), 74−80.

(40) Chandrasekhar, P.; Mukhopadhyay, A.; Savitha, G.; Moorthy, J. N. Orthogonal Self-Assembly of a Trigonal Triptycene Triacid: Signaling of Exfoliation of Porous 2D Metal-Organic Layers by Fluorescence and Selective CO2capture by the Hydrogen-Bonded MOF. *J. Mater. Chem. A* **2017**, *5* (11), 5402−5412.

(41) Ashworth, D. J.; Cooper, A.; Trueman, M.; Al-Saedi, R. W. M.; Smith, L. D.; Meijer, A. J.; Foster, J. A. Ultrasonic Exfoliation of Hydrophobic and Hydrophilic Metal-Organic Frameworks to Form Nanosheets. *Chem. - Eur. J.* **2018**, *24* (68), 17986−17996.

(42) Li, P.-Z.; Maeda, Y.; Xu, Q. Top-down Fabrication of Crystalline Metal-Organic Framework Nanosheets. *Chem. Commun.* **2011**, *47* (29), 8436−8438.

(43) Xu, G.; Yamada, T.; Otsubo, K.; Sakaida, S.; Kitagawa, H. Facile "Modular Assembly" for Fast Construction of a Highly Oriented Crystalline MOF Nanofilm. *J. Am. Chem. Soc.* **2012**, *134* (40), 16524−16527.

(44) Tan, J. C.; Saines, P. J.; Bithell, E. G.; Cheetham, A. K. Hybrid Nanosheets of an Inorganic-Organic Framework Material: Facile Synthesis, Structure, and Elastic Properties. *ACS Nano* **2012**, *6* (1), 615−621.

(45) Junggeburth, S. C.; Diehl, L.; Werner, S.; Duppel, V.; Sigle, W.; Lotsch, B. V. Ultrathin 2D Coordination Polymer Nanosheets by Surfactant-Mediated Synthesis. *J. Am. Chem. Soc.* **2013**, *135*, 6157−6164.

(46) Beldon, P. J.; Tominaka, S.; Singh, P.; Saha Dasgupta, T.; Bithell, E. G.; Cheetham, A. K. Layered Structures and Nanosheets of Pyrimidinethiolate Coordination Polymers. *Chem. Commun.* **2014**, *50* (31), 3955−3957.

(47) Foster, J. A.; Henke, S.; Schneemann, A.; Fischer, R. A.; Cheetham, A. K. Liquid Exfoliation of Alkyl-Ether Functionalised Layered Metal-Organic Frameworks to Nanosheets. *Chem. Commun.* **2016**, *52* (69), 10474−10477.

(48) Liu, H.-L.; Chang, Y.-J.; Fan, T.; Gu, Z.-Y. Two-Dimensional Metal-Organic Framework Nanosheets as a Matrix for Laser

Desorption/Ionization of Small Molecules and Monitoring Enzymatic Reactions at High Salt Concentrations. *Chem. Commun.* **2016**, *52* (88), 12984−12987.

(49) Cliffe, M. J.; Castillo-Martínez, E.; Wu, Y.; Lee, J.; Forse, A. C.; Firth, F. C. N.; Moghadam, P. Z.; Fairen-Jimenez, D.; Gaultois, M. W.; Hill, J. A.; et al. Metal-Organic Nanosheets Formed via Defect-Mediated Transformation of a Hafnium Metal-Organic Framework. *J. Am. Chem. Soc.* **2017**, *139* (15), 5397−5404.

(50) Peng, Y.; Huang, Y.; Zhu, Y.; Chen, B.; Wang, L.; Lai, Z.; Zhang, Z.; Zhao, M.; Tan, C.; Yang, N.; et al. Ultrathin Two-Dimensional Covalent Organic Framework Nanosheets: Preparation and Application in Highly Sensitive and Selective DNA Detection. *J. Am. Chem. Soc.* **2017**, *139* (25), 8698−8704.

(51) Fan, Z.; Nomura, K.; Zhu, M.; Li, X.; Xue, J.; Majima, T.; Osakada, Y. Synthesis and Photocatalytic Activity of Ultrathin Two-Dimensional Porphyrin Nanodisks via Covalent Organic Framework Exfoliation. *Commun. Chem.* **2019**, *2* (1), 1−8.

(52) Kim, J.; Kwon, S.; Cho, D. H.; Kang, B.; Kwon, H.; Kim, Y.; Park, S. O.; Jung, G. Y.; Shin, E.; Kim, W. G.; et al. Direct Exfoliation and Dispersion of Two-Dimensional Materials in Pure Water via Temperature Control. *Nat. Commun.* **2015**, *6*, 1−9.

(53) Tiwari, P.; Kaur, N.; Sharma, V.; Mobin, S. M. High-Yield Graphene Produced from the Synergistic Effect of Inflated Temperature and Gelatin Offers High Stability and Cellular Compatibility. *Phys. Chem. Chem. Phys.* **2018**, *20* (30), 20096−20107.

(54) Henke, S.; Schneemann, A.; Kapoor, S.; Winter, R.; Fischer, R. A. Zinc-1,4-Benzenedicarboxylate-Bipyridine Frameworks - Linker Functionalization Impacts Network Topology during Solvothermal Synthesis. *J. Mater. Chem.* **2012**, *22* (3), 909−918.

(55) Henke, S.; Schneemann, A.; Wütscher, A.; Fischer, R. A. Directing the Breathing Behavior of Pillared-Layered Metal-Organic Frameworks via a Systematic Library of Functionalized Linkers Bearing Flexible Substituents. *J. Am. Chem. Soc.* **2012**, *134* (22), 9464−9474.

(56) Ashworth, D. J.; Cooper, A.; Trueman, M.; Al-Saedi, R. W. M.; Smith, L. D.; Meijer, A. J. H. M.; Foster, J. A. Ultrasonic Exfoliation of Hydrophobic and Hydrophilic Metal-Organic Frameworks To Form Nanosheets. *Chem. - Eur. J.* **2018**, *24* (68), 17986−17996.

(57) Coblentz Society, Inc. Evaluated Infrared Reference Spectra. In *NIST Chemistry Web Book, NIST Standard Reference Database Number 69*; Linstrom, P.J., Mallard, W.G., Eds.; National Institute of Standards and Technology: Gaithersburg MD; *20899*. DOI: 10.18434/T4D303.

(58) Li, H.; Eddaoudi, M.; Groy, T. L.; Yaghi, O. M. Establishing Microporosity in Open Metal-Organic Frameworks: Gas Sorption Isotherms for Zn(BDC) (BDC = 1,4-Benzenedicarboxylate). *J. Am. Chem. Soc.* **1998**, *120* (33), 8571−8572.

(59) Guo, Z.; Reddy, M. V.; Goh, B. M.; San, A. K. P.; Bao, Q.; Loh, K. P. Electrochemical Performance of Graphene and Copper Oxide Composites Synthesized from a Metal-Organic Framework (Cu-MOF). *RSC Adv.* **2013**, *3* (41), 19051−19056.

(60) Eddaoudi, M.; Kim, J.; Rosi, N.; Vodak, D.; Wachter, J.; O'Keeffe, M.; Yaghi, O. M. Systematic Design of Pore Size and Functionality in Isoreticular MOFs and Their Application in Methane Storage. *Science (Washington, DC, U. S.)* **2002**, *295* (5554), 469−472.

(61) Carson, C. G.; Hardcastle, K.; Schwartz, J.; Liu, X.; Hoffmann, C.; Gerhardt, R. A.; Tannenbaum, R. Synthesis and Structure Characterization of Copper Terephthalate Metal-Organic Frameworks. *Eur. J. Inorg. Chem.* **2009**, *2009* (16), 2338−2343.

(62) Carson, C. G.; Brunnello, G.; Lee, S. G.; Jang, S. S.; Gerhardt, R. A.; Tannenbaum, R. Structure Solution from Powder Diffraction of Copper 1,4- Benzenedicarboxylate. *Eur. J. Inorg. Chem.* **2014**, *2014*, 2140−2145.

(63) Thommes, M.; Kaneko, K.; Neimark, A. V.; Olivier, J. P.; Rodriguez-Reinoso, F.; Rouquerol, J.; Sing, K. S. W. Physisorption of Gases, with Special Reference to the Evaluation of Surface Area and Pore Size Distribution (IUPAC Technical Report). *Pure Appl. Chem.* **2015**, *87* (9−10), 1051−1069.

(64) Schneemann, A.; Takahashi, Y.; Rudolf, R.; Noro, S.; Fischer, R. A. Influence of Co-Adsorbates on CO 2 Induced Phase Transition in Functionalized Pillared-Layered Metal-Organic Frameworks. *J. Mater. Chem. A* **2016**, *4* (33), 12963−12972.

(65) Liscio, A.; Kouroupis-Agalou, K.; Betriu, X. D.; Kovtun, A.; et al. Evolution of the Size and Shape of 2D Nanosheets during Ultrasonic Fragmentation Evolution of the Size and Shape of 2D Nanosheets during Ultrasonic Fragmentation. *2D Mater.* **2017**, *4*, 025017.

(66) Mukhopadhyay, A.; Maka, V. K.; Savitha, G.; Moorthy, J. N. Photochromic 2D Metal-Organic Framework Nanosheets (MONs): Design, Synthesis, and Functional MON-Ormosil Composite. *Chem.* **2018**, *4* (5), 1059−1079.

(67) Lotya, M.; Rakovich, A.; Donegan, J. F.; Coleman, J. N. Measuring the Lateral Size of Liquid-Exfoliated Nanosheets with Dynamic Light Scattering. *Nanotechnology* **2013**, *24* (26), 265703.

(68) Shen, J.; He, Y.; Wu, J.; Gao, C.; Keyshar, K.; Zhang, X.; Yang, Y.; Ye, M.; Vajtai, R.; Lou, J.; et al. Liquid Phase Exfoliation of Two-Dimensional Materials by Directly Probing and Matching Surface Tension Components. *Nano Lett.* **2015**, *15* (8), 5449−5454.

(69) Hernandez, Y.; Nicolosi, V.; Lotya, M.; Blighe, F. M.; Sun, Z.; De, S.; McGovern, I. T.; Holland, B.; Byrne, M.; Gun'ko, Y. K.; et al. High-Yield Production of Graphene by Liquid-Phase Exfoliation of Graphite. *Nat. Nanotechnol.* **2008**, *3* (9), 563−568.

(70) Nečas, D.; Klapetek, P. Gwyddion: An Open-Source Software for SPM Data Analysis. *Cent. Eur. J. Phys.* **2012**, *10* (1), 181−188.

(71) Tartoni, N.; Thompson, S. P.; Tang, C. C.; Willis, B. L.; Derbyshire, G. E.; Wright, A. G.; Jaye, S. C.; Homer, J. M.; Pizzey, J. D.; Bell, A. M. T. High-Performance X-Ray Detectors for the New Powder Diffraction Beamline I11 at Diamond. *J. Synchrotron Radiat.* **2008**, *15* (1), 43−49.

(72) Thompson, S. P.; Parker, J. E.; Potter, J.; Hill, T. P.; Birt, A.; Cobb, T. M.; Yuan, F.; Tang, C. C. Beamline I11 at Diamond: A New Instrument for High Resolution Powder Diffraction. *Rev. Sci. Instrum.* **2009**, *80* (7), 075107.

(73) Thompson, S. P.; Parker, J. E.; Marchal, J.; Potter, J.; Birt, A.; Yuan, F.; Fearn, R. D.; Lennie, A. R.; Street, S. R.; Tang, C. C. Fast X-Ray Powder Diffraction on I11 at Diamond. *J. Synchrotron Radiat.* **2011**, *18* (4), 637−648.

(74) Pawley, G. S. Unit-Cell Refinement from Powder Diffraction Scans. *J. Appl. Crystallogr.* **1981**, *14* (6), 357−361.

(75) Coelho, A. A. *TOPAS Academic*, version 4.1; see http://www.topas-academic.net.

(76) Coelho, A. A.; Evans, J.; Evans, I.; Kern, A.; Parsons, S. The TOPAS Symbolic Computation System. *Powder Diffr.* **2011**, *26* (S1), S22−S25.

(77) Rietveld, H. M. A Profile Refinement Method for Nuclear and Magnetic Structures. *J. Appl. Crystallogr.* **1969**, *2* (2), 65−71.

Increasing alkyl chain length in a series of layered metal-organic frameworks aids ultrasonic exfoliation to form nanosheets

David J. Ashworth,[a] Thomas M. Roseveare,[a] Andreas Schneemann,[b] Max Flint,[a] Irene Dominguez Bernáldes,[a] Pia Vervoorts,[b] Roland A. Fischer,[b] Lee Brammer[a] and Jonathan A. Foster*[a]

a. Department of Chemistry, University of Sheffield, Brook Hill, Sheffield, S3 7HF, UK. Email: jona.foster@sheffield.ac.uk

b. Department of Chemistry, Technische Universität München, Lichtenbergstraße 4, 85748 Garching, Germany and Catalysis Research Centre, Technische Universität München, Ernst-Otto-Fischer Straße 1, 85748 Garching, Germany.

Contents

1. Dicarboxylic acid characterisation

1.1. ^{1}H NMR spectroscopy

Room temperature ^{1}H NMR spectra for the dicarboxylic acid ligand precursors (H$_2$**1**-H$_2$**4**) dissolved in d_6-DMSO were recorded on a Bruker Avance AV500US instrument operating at 400 MHz, and H$_2$**5** in CDCl$_3$ was recorded on a Bruker AVIII HD instrument operating at 400 MHz.
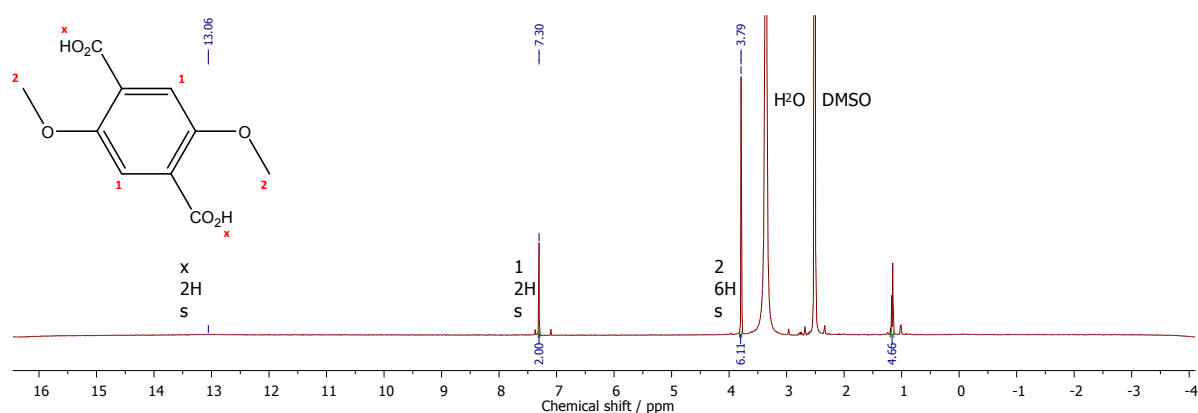
Figure S1 ^{1}H NMR spectrum of H$_2$**1**.
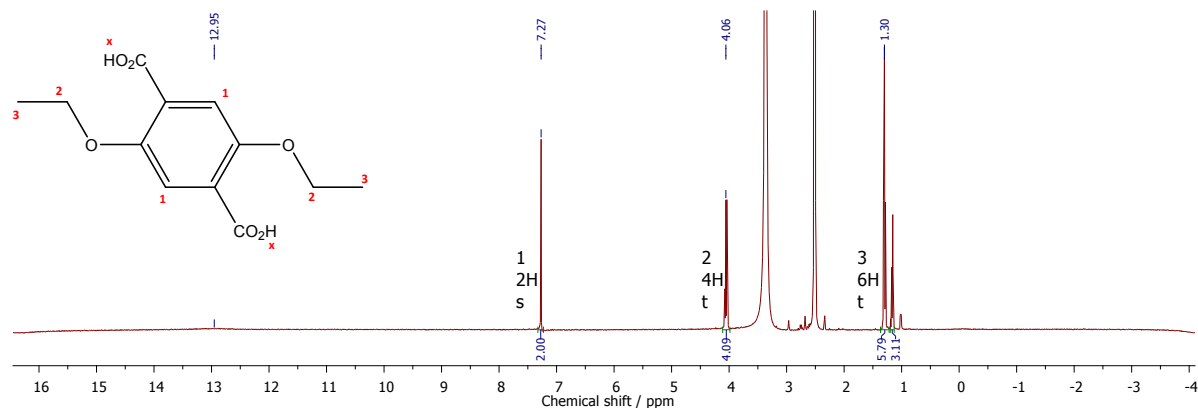
Figure S2 ^{1}H NMR spectrum of H$_2$**2**.
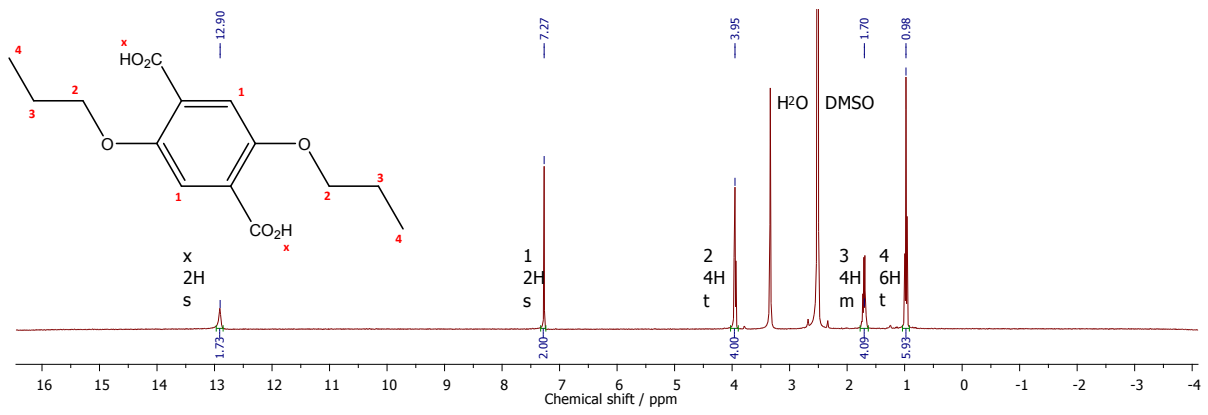
Figure S3 ^{1}H NMR spectrum of H$_2$**3**.
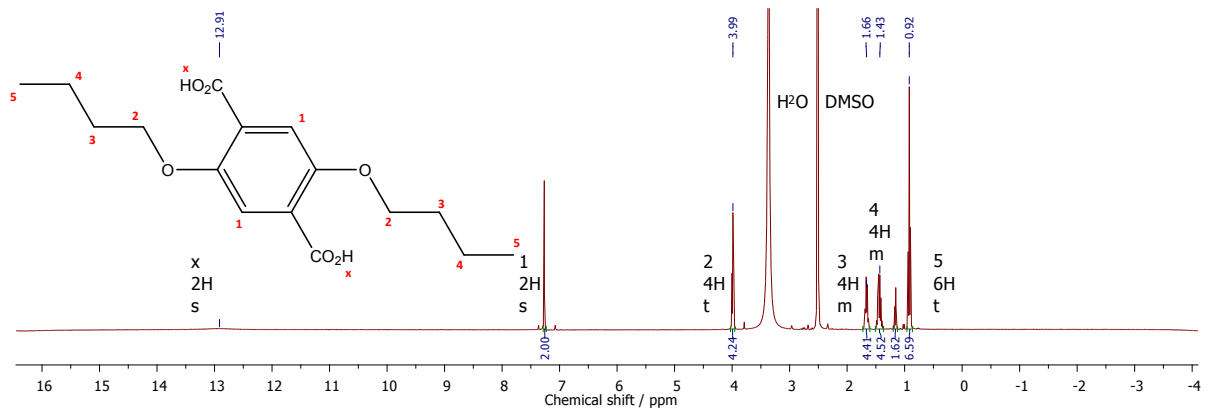
Figure S4 ^{1}H NMR spectrum of H$_2$**4**.
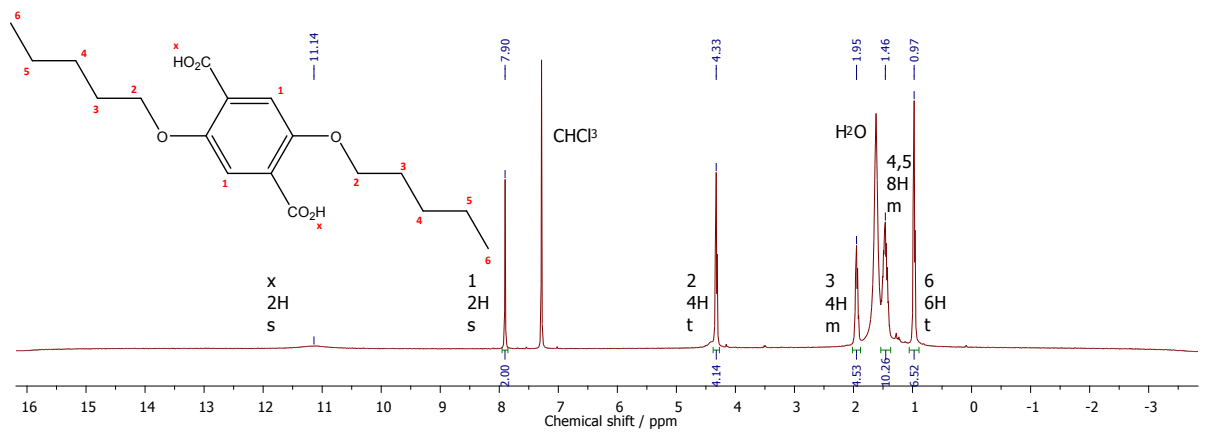
Figure S5 ^{1}H NMR spectrum of H$_2$**5**.

3

2. MOF characterisation

The products of the reactions using dicarboxylic acids H_2n (**n** = **1**-**5**) are termed Cu(**n**)(DMF). This composition is clearly established by elemental analysis and supported by PXRD for n=**3**-**5**. Elemental analysis suggests this could be a possible composition for n=**2**, however this appears mixed phase by PXRD and as such is unconfirmed. The product is designated Cu(**2**)(DMF) in the below analyses. The product of the reaction involving H_2**1** is designated Cu(**1**)(DMF), a likely product, however the composition is not clearly established from elemental analysis.

2.1. Elemental analysis

Elemental analyses were obtained on an Elementar vario MICRO cube.

Table S1 Elemental analyses of Cu(**1**-**5**)(DMF). Δ is the difference between calculated and experimental values. Calculated values are based on the structure Cu(**n**)(DMF) (**n**=**1**-**5**).

MOF	Calculated			Experimental		
	C / %	H / %	N / %	C / % (Δ)	H / % (Δ)	N / % (Δ)
Cu(**1**)(DMF)	43.28	4.19	3.88	40.69 (2.59)	4.22 (0.03)	2.90 (0.98)
Cu(**2**)(DMF)	46.33	4.93	3.60	45.91 (0.42)	5.07 (0.14)	3.58 (0.02)
Cu(**3**)(DMF)	48.98	5.56	3.36	48.99 (0.01)	5.63 (0.07)	3.30 (0.06)
Cu(**4**)(DMF)	51.29	6.12	3.15	50.72 (0.57)	6.16 (0.04)	3.13 (0.02)
Cu(**5**)(DMF)	53.32	6.61	2.85	53.10 (0.22)	6.70 (0.09)	2.95 (0.10)

2.2. FTIR spectroscopy

FTIR spectroscopy data were recorded using a Perking Elmer Spectrum One FTIR equipped with a diamond ATR accessory. Data were collected from 500-4000 cm^{-1} using a resolution of 1 cm^{-1} and 16 scans.
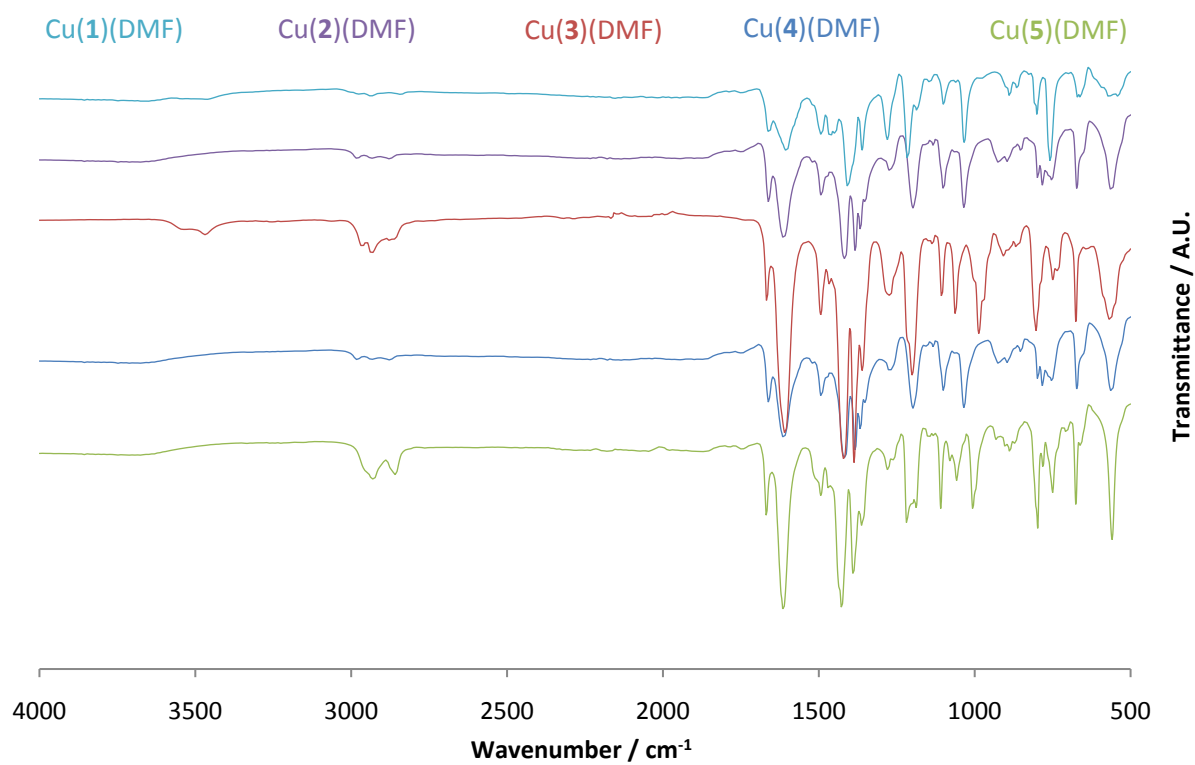
Figure S6 FTIR spectra of Cu(**1**-**5**)(DMF).

2.3. TGA

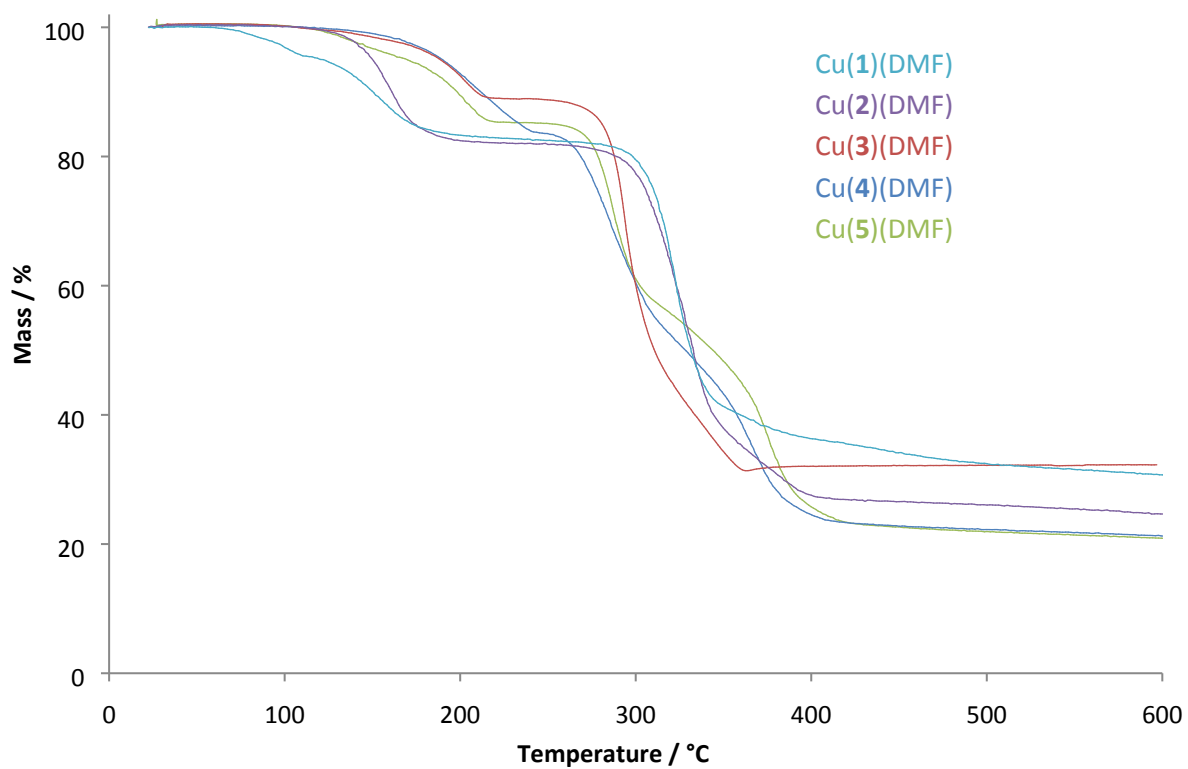Thermogravimetic analysis (TGA) was performed using a Perkin Elmer Pyris 1 TGA, from 30-600 °C at 10 °C min^{-1}, under a 20 mL min^{-1} N_2 flow.

Figure S7 TGA thermograms of Cu(**1-5**)(DMF).

Table S2 Observed mass losses through TGA of Cu(**1-5**)(DMF).

	Theoretical DMF mass / %	Mass loss in region / %			
		50-110 °C	90-240 °C	240-420 °C	30-600 °C
Cu(**1**)DMF)	20.3	4.5	15.4	47.2	69.3
Cu(**2**)DMF)	18.8	0.4	18.2	55.1	75.7
Cu(**3**)DMF)	17.5	0.6	11.4	56.9	68.0
Cu(**4**)DMF)	16.4	0.2	16.2	60.7	78.9
Cu(**5**)DMF)	15.45	0.6	15.2	61.9	79.5

6

2.4. PXRD

PXRD data were recorded on at the University of Sheffield on a Bruker D8 Advance powder X-ray diffractometer, or using synchrotron radiation at beamline I11 at Diamond Light Source.[1–3]

In-house X-ray diffraction data were collected in Bragg-Brentano geometry using a Cu Kα X-ray source (λ = 1.5406 Å) and a zero-background Si sample holder rotated at 15 rpm. The diffractometer was fitted with a focusing Göbel mirror optic and a high-resolution energy-dispersive Lynxeye XE detector. Scans were collected at room temperature in the range 4 ≤ 2θ ≤ 50 °, using a step size of 0.02 ° and step time of 1.5 s giving a total exposure time of 1 h.

Synchrotron data were collected in the range 2.1 ° ≤ 2θ ≤ 92.1 ° (λ = 0.826015(10) Å) on samples loaded into a 0.5 mm borosilicate capillary, placed in a brass sample holder and sealed with wax. Data were recorded at room temperature, while the sample was rotated, using a wide-angle PSD (position-sensitive detector)[3] which consists of 18 Mythen-2-Modules. A pair of scans was conducted at room temperature, related by a 0.25° detector offset to account for gaps between detector modules. Five such scan pairs were collected with an exposure time of 5 s and these sets were preceded and followed by a pair of 1 s scans to assess whether the sample suffered beam damage. The five scan sets were then summed to provide a final pattern for structural analysis (total beam exposure time 54 s).

Powder pattern indexing and fitting was carried out using the TOPAS program.[4,5]
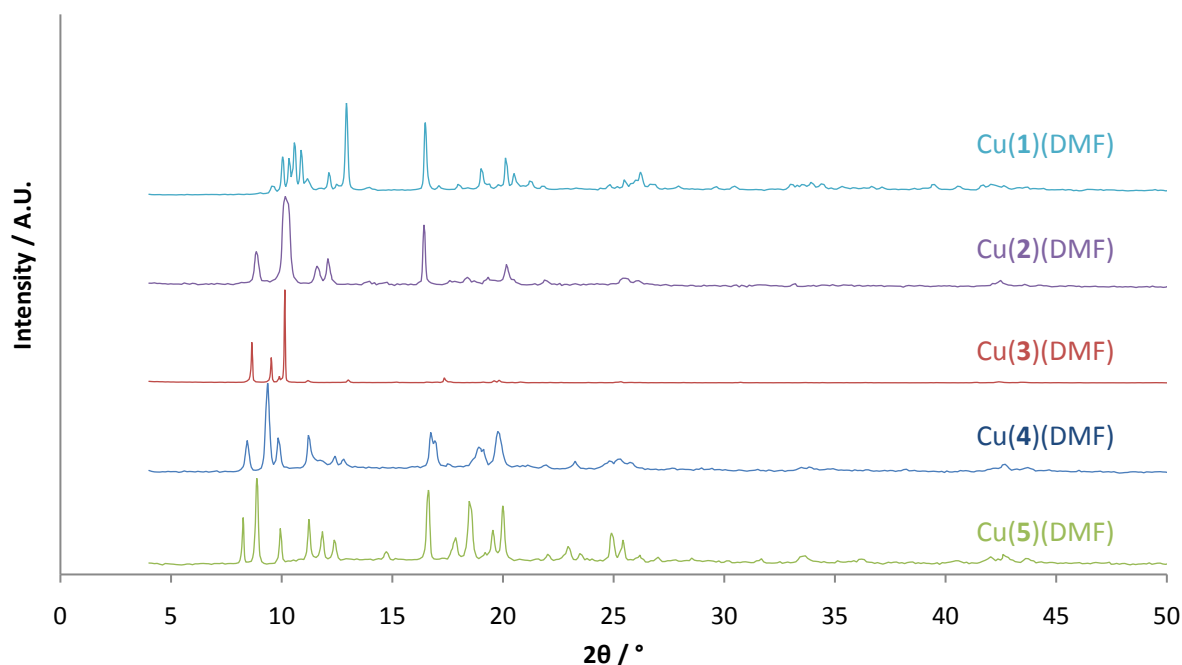
Figure S8 In-house PXRD data collected of Cu(**1-5**)(DMF) (λ = 1.5406 Å).
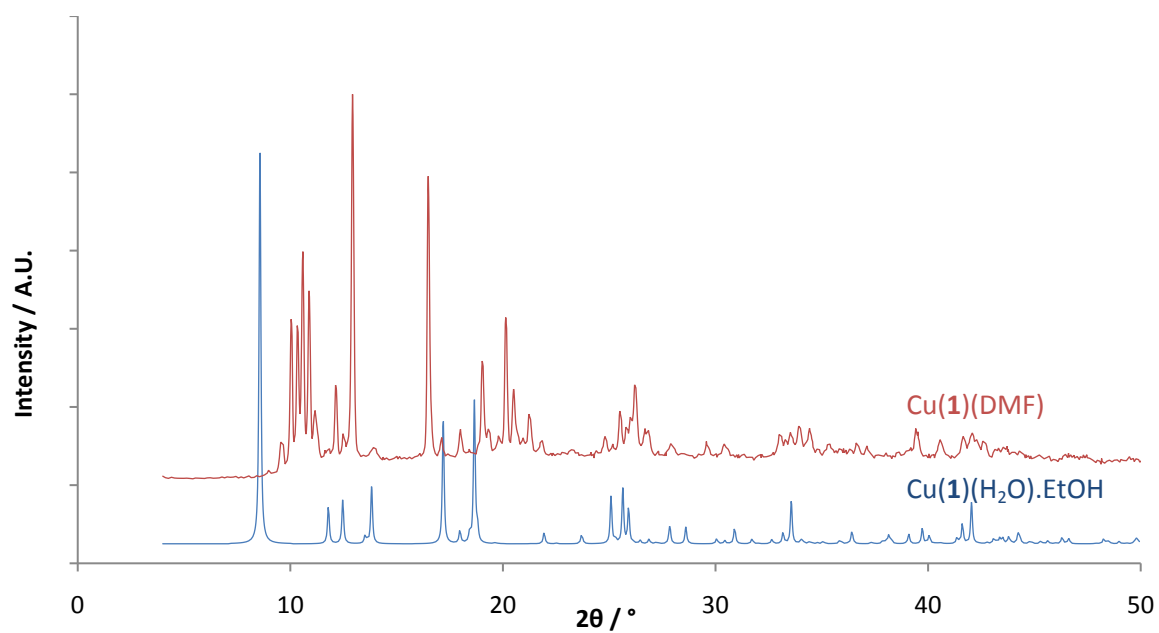
Figure S9 Comparison of experimental PXRD pattern of Cu(**1**)(DMF) (λ = 1.5406 Å) at room temperature (red) with the pattern calculated from the published crystal structure of Cu(**1**)(H$_2$O).EtOH at 100 K (blue).[6]
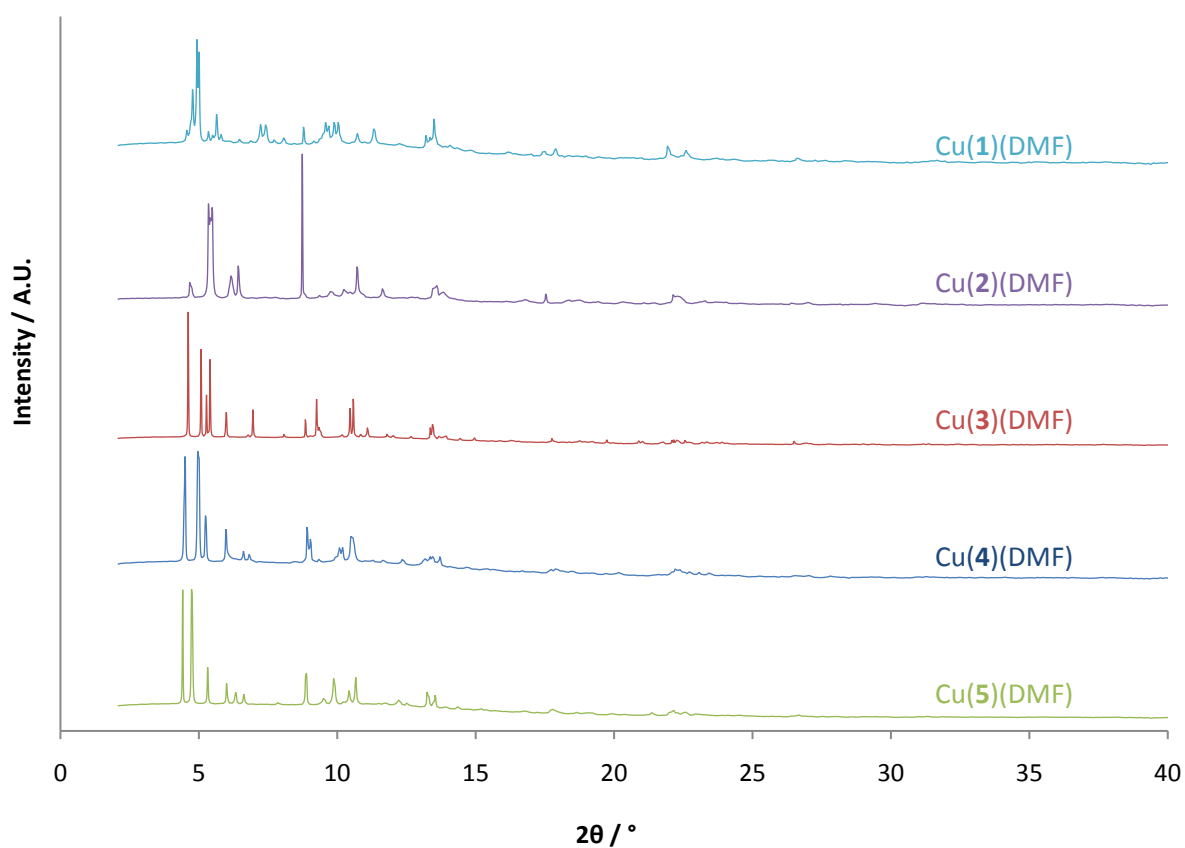

Figure S10 PXRD data of Cu(**1-5**)(DMF) collected at Diamond Light Source, beamline I11. λ = 0.826015 Å. N.B. patterns displayed here have been cut at 40 ° 2θ as there is little diffraction past this point.

2.4.1. Pawley refinement

X-Ray diffraction data were collected using synchrotron radiation (λ = 0.826015(10) Å). The patterns were indexed to give estimated unit cell parameters which were used as a starting point for Pawley refinement[7] against intensity data in the range 3 ° ≤ 2θ ≤ 40 °. Unit cell parameters and indices of fit are presented in Table S3. Least-squares parameters refined in the fits are listed in Table S4.
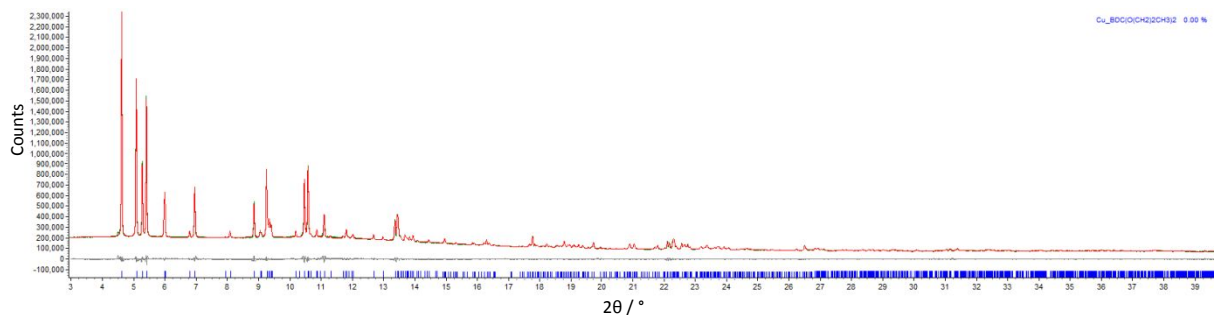
Figure S11 Pawley fit for Cu(**3**)(DMF), illustrating the observed (green) and calculated (red) diffraction patterns, with the difference plot [I_{obs}-I_{calc}] (grey) (2θ range 3.0 – 40.0 °, d_{min} = 1.21 Å). Blue tick lines denote calculated peak positions.
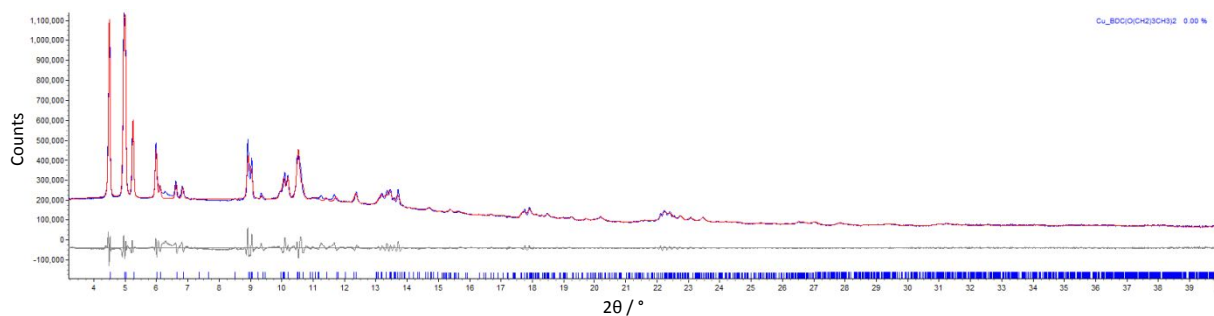
Figure S12 Pawley fit for Cu(**4**)(DMF), illustrating the observed (blue) and calculated (red) diffraction patterns, with the difference plot [I_{obs}-I_{calc}] (grey) (2θ range 3.0 – 40.0 °, d_{min} = 1.21 Å). Blue tick lines denote calculated peak positions.
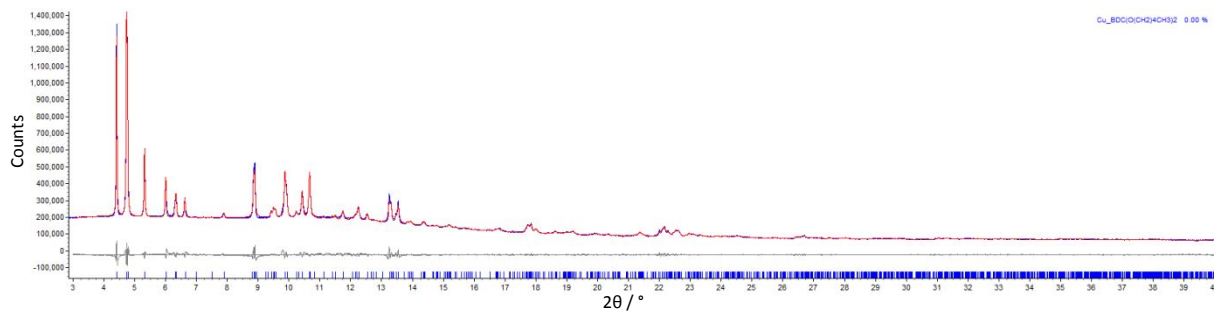
Figure S13 Pawley fit for Cu(**5**)(DMF), illustrating the observed (blue) and calculated (red) diffraction patterns, with the difference plot [I_{obs}-I_{calc}] (grey) (2θ range 3.0 – 40.0 °, d_{min} = 1.21 Å). Blue tick lines denote calculated peak positions.
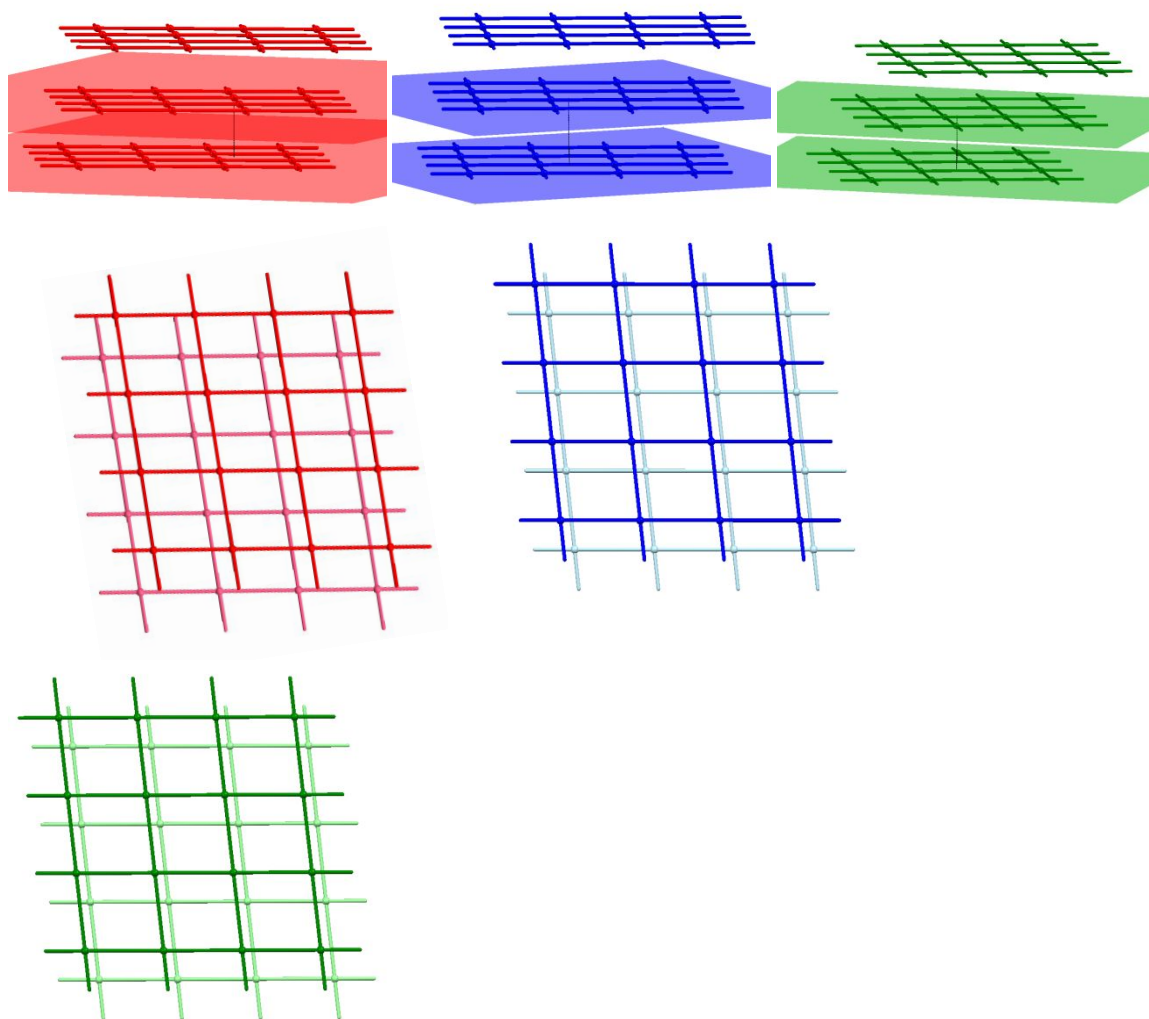
**Figure S14** (Top) Schematic of the framework topologies of Cu(**3**)(DMF) (red), Cu(**4**)(DMF) (blue) and Cu(**5**)(DMF) (green), with 2 planes indicated, between which the interlayer distance was calculated. (Bottom) View of framework topologies perpendicular to the planes indicated, in order to visualise the offset between layers.

2.4.2. Rietveld refinement

X-Ray diffraction data were collected using synchrotron radiation (λ = 0.826015(10) Å) at room temperature. A structure model for Cu(**5**)(DMF), adapted from a previously published single-crystal structure[8] was refined as a single rigid body with a common refined isotropic displacement parameter for all atoms and fitted to the PXRD pattern by Rietveld refinement[9] (Figure S15). Unit cell parameters and indices of fit are presented in Table S3. Least-squares parameters refined in the fits are listed in Table S4.
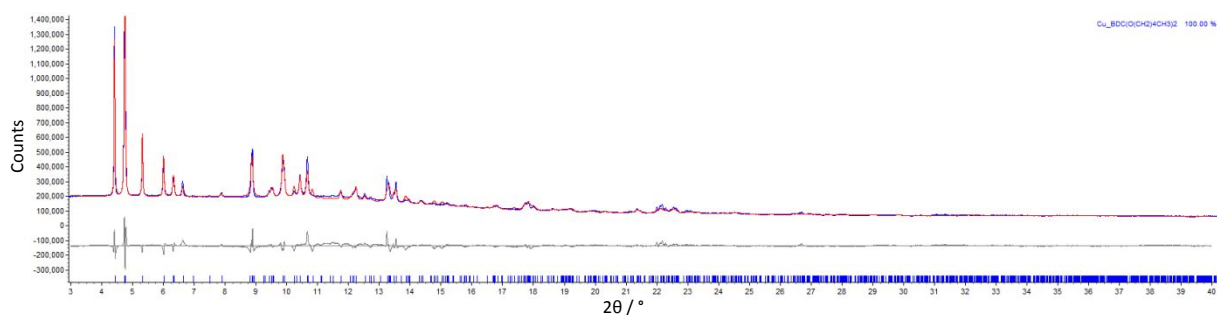
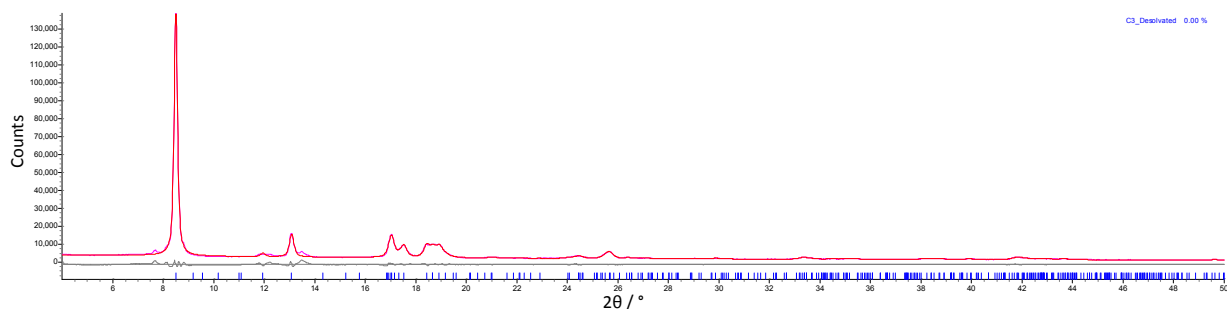**Figure S15** Rietveld fit of Cu(**5**)(DMF), illustrating the experimental (blue) and calculated (red) diffraction patterns, with the difference plot [I_{obs}-I_{calc}] (grey) (2θ range 3.0 – 40.0 °, d_{min} = 1.21 Å). Blue tick lines denote calculated peak positions.
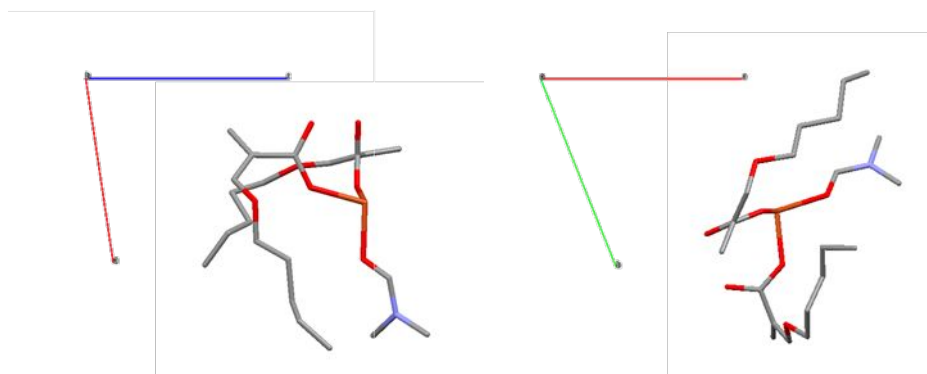
Figure S16 Asymmetric unit of the determined structure model of Cu(**5**)(DMF), viewed down the b-axis (left) and the c-axis (right).

11

2.4.3. Pawley refinement of desolvated MOFs

X-Ray diffraction data were collected for desolvated samples Cu(**3-5**) using Cu-Kα radiation (λ = 1.5406 Å). The unit cell parameters for solvated samples of Cu(**3-5**)(DMF) were used as respective starting points for Pawley refinement[7] against intensity data in the range 4.0 ° ≤ 2θ ≤ 50.0 °. Unit cell parameters and indices of fit are presented in Table S3. Least-squares parameters refined in the fits are listed in Table S4.
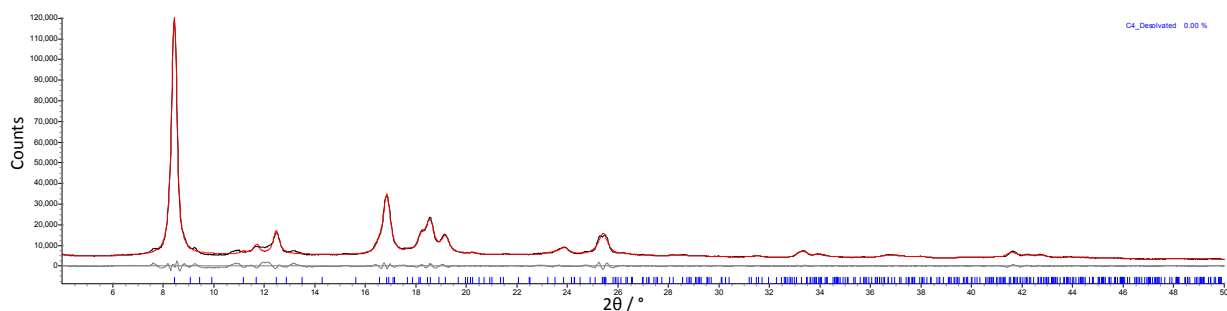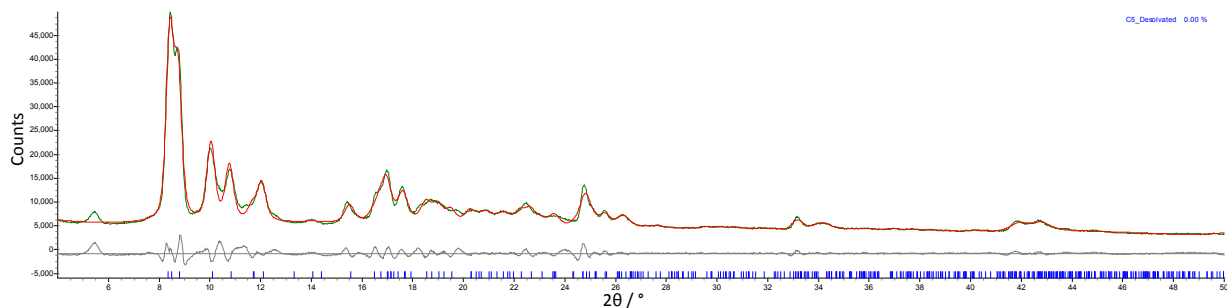

Figure S17 Pawley fit for Cu(**3**), illustrating the observed (pink) and calculated (red) diffraction patterns, with the difference plot [I_{obs}-I_{calc}] (grey) (2θ range 4.0 – 50.0 °, d_{min} = 1.82 Å). Blue tick lines denote calculated peak positions.

Figure S18 Pawley fit for Cu(**4**), illustrating the observed (black) and calculated (red) diffraction patterns, with the difference plot [I_{obs}-I_{calc}] (grey) (2θ range 4.0 – 50.0 °, d_{min} = 1.82 Å). Blue tick lines denote calculated peak positions.

Figure S19 Pawley fit for Cu(**5**), illustrating the observed (green) and calculated (red) diffraction patterns, with the difference plot [I_{obs}-I_{calc}] (grey) (2θ range 4.0 – 40.0 °, d_{min} = 1.82 Å). Blue tick lines denote calculated peak positions.
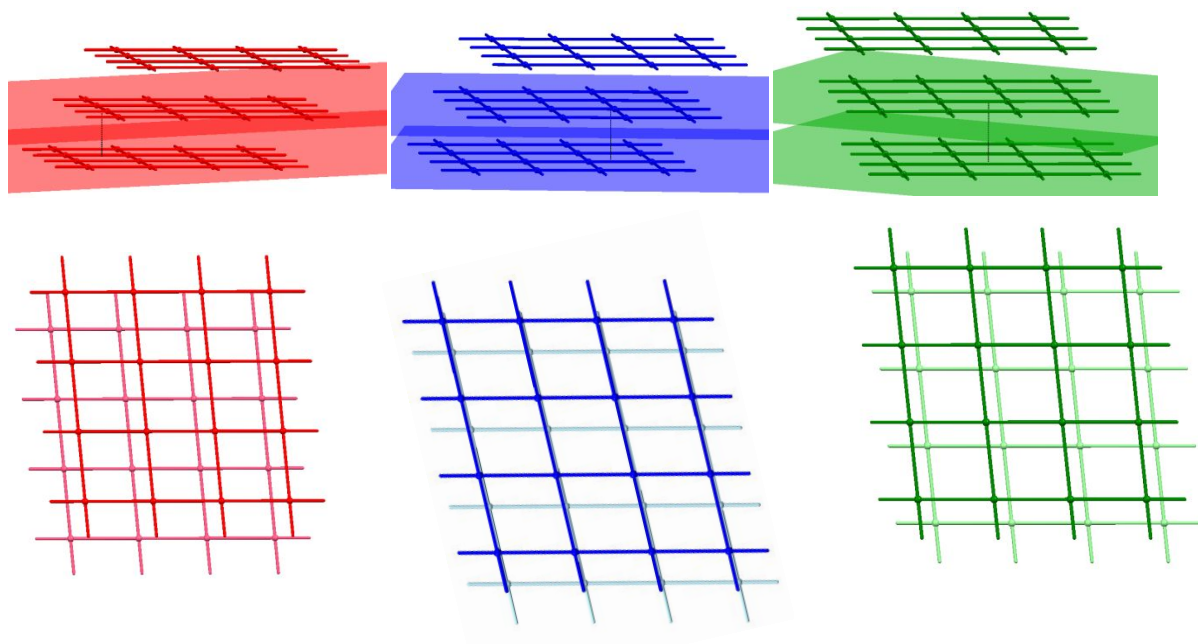
Figure S20 (Top) Schematic of the framework topologies of Cu(**3**) (red), Cu(**4**) (blue) and Cu(**5**) (green), with 2 layers shown, between which the interlayer distance was calculated. (Bottom) The framework topologies viewed perpendicular to the planes layers, in order to visualise the offset between layers.

2.4.4. MOF PXRD post-activation

Approximately 3 mg of MOFs Cu(**3-5**)(DMF) were activated in a vacuum oven at 120 °C for 2 hrs.
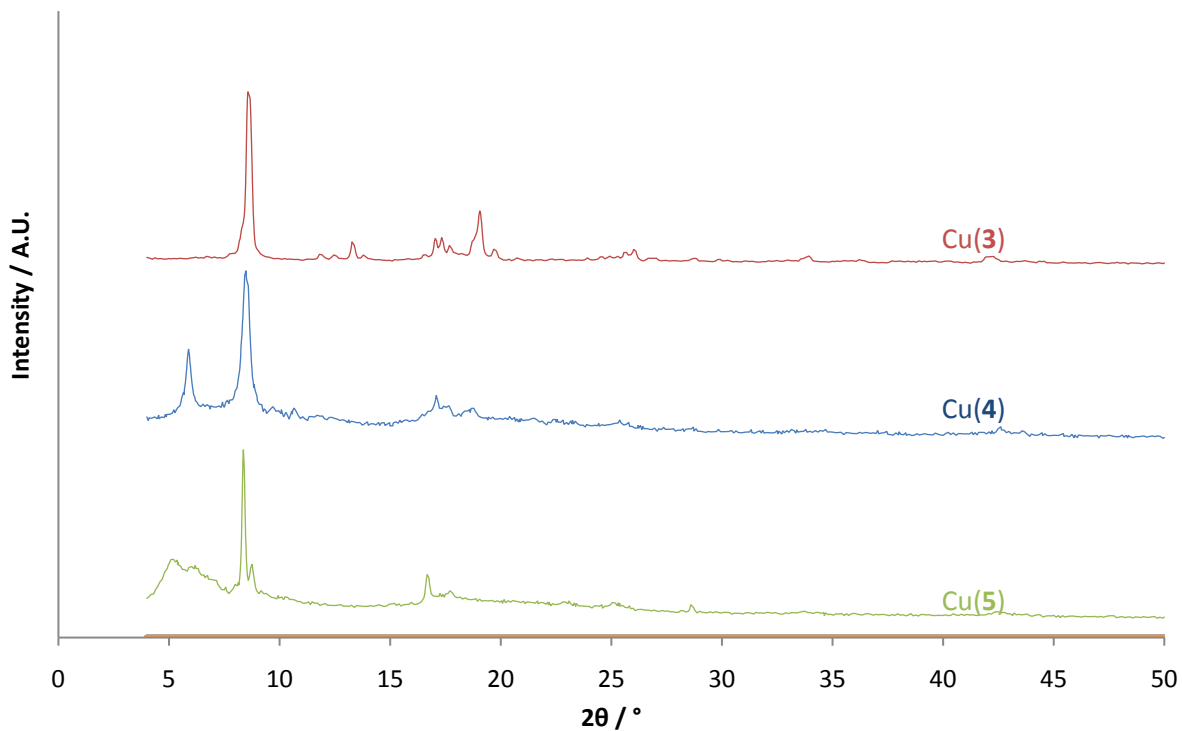

Figure S21 PXRD patterns of Cu(3-5)(DMF) after activation at 120 °C for 3 hrs (λ = 1.5406 Å).N.B. The lower temperature of 120 °C was used for these small quantities of MOF as large impurities were observed when heating these small quantities at 160 °C.

Table S3 Summary of PXRD refinement fitting data for Cu(**1**-**5**)(DMF) and Cu(**3**-**5**). Unit cell parameters *a*, *b* and *c* are in Å; α, β and γ are in degrees (°); Volume (Vol) is in Å^3.

MOF	Refinement*	SG$^+$	a	b	c	α	β	γ	Vol	R_{wp}	$R_{wp'}$
Cu(**1**)(DMF)	P	Unknown									
Cu(**2**)(DMF)	P	Unknown									
Cu(**3**)(DMF)	P	P-1	10.60167(9)	10.62440(9)	10.80847(8)	71.118(1)	79.9074(7)	61.2210(5)	1009.36(2)	0.0224	0.0894
Cu(**4**)(DMF)	P	P-1	10.6216(6)	10.8001(6)	10.9400(5)	76.008(5)	62.541(3)	81.987(6)	1080.0(1)	0.0377	0.1539
Cu(**5**)(DMF)	P	P-1	10.8443(3)	10.8050(2)	10.8648(3)	83.786(2)	79.742(3)	67.358(2)	1155.05(5)	0.0256	0.1129
Cu(**5**)(DMF)	R	P-1	10.8449(7)	10.8010(6)	10.8529(7)	83.819(6)	79.823(6)	67.438(4)	1154.4(1)	0.0517	0.2455
Cu(**3**)	P	P-1	10.807(2)	10.693(2)	10.998(3)	71.51(2)	77.35(1)	63.35(2)	1072.9(4)	0.0655	0.1278
Cu(**4**)	P	P-1	10.420(2)	10.724(2)	11.030(1)	77.27(1)	64.11(1)	82.87(1)	1081.0(4)	0.0474	0.0942
Cu(**5**)	P	P-1	10.863(3)	11.039(3)	10.867(3)	84.04(2)	76.89(2)	70.65(2)	1197.0(6)	0.0593	0.1101

* P/R indicates refinement used: Pawley (P) or Rietveld (R). $^+$ SG = space group.

Table S4 Least squares parameters used in Pawley (P) and Rietveld (R) refinements of Cu(**3**-**5**)(DMF) and Cu(**3**-**5**).

MOF	Refinement*	Total Parameters	Background	Zero Point	Peak Profile	Cell	Reflections	Thermal Displacement Parameter
Cu(**3**)(DMF)	P	1262	10	1	5	6	1240	N/A
Cu(**4**)(DMF)	P	1351	10	1	5	6	1329	N/A
Cu(**5**)(DMF)	P	1435	10	1	5	6	1413	N/A
Cu(**5**)(DMF)	R	24	10	1	5	6	N/A	1
Cu(**3**)	P	371	9	1	5	6	350	N/A
Cu(**4**)	P	398	9	1	5	6	377	N/A
Cu(**5**)	P	424	9	1	5	6	403	N/A

Table S5 Fractional coordinates of the Cu$_2$ centroids located within Cu(**3**-**5**)(DMF) and Cu(**3**-**5**).

MOF	x	y	z
Cu(**3**)(DMF)	0	0	0
Cu(**4**)(DMF)	0.5	0	0.5
Cu(**5**)(DMF)	0.5	0	0.5
Cu(**3**)	0	0	0
Cu(**4**)	0.5	0	0.5
Cu(**5**)	0.5	0	0.5

2.5. SEM

MOF samples were loaded onto carbon sticky tabs on aluminium SEM samples stubs, coated with approximately 20 nm gold using an Edwards S150B sputter coater and loaded into a TESCAN VEGA3 LMU SEM, which was operated at 15 keV and images collected at 10,000 x magnification using the secondary electron detector.
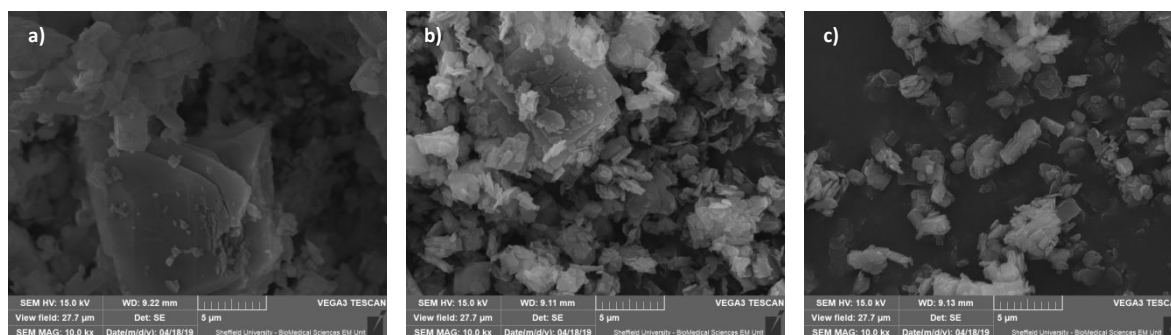

Figure S22 SEM micrograph of Cu(**3-5**)(DMF) (a-c, respectively).

2.6.MOF gas adsorption

N_2 and CO_2 adsorption isotherms were measured using a Micromeritics 3 Flex volumetric gas adsorption instrument. Prior to dosing, samples were activated on the Micromeritics Smart Vac Prep Sample preparation station at 160 °C for 10 hours, under a vaccuum pressure of approximately 10^{-3} mbar. Approximately 50 mg of solid, dried sample was used in each case. CO_2 and N_2 used had purity grades of 99.5 and 99.999 % respectively. N_2 adsorption isotherms were recorded at 77 K using a liquid nitrogen bath for cooling of the sample cell and CO_2 adsorption isotherms were conducted at 195 K using a dry ice/isopropanol slurry for cooling of the sample cell. The Brunauer-Emmett-Teller equation was used to calculate the specific surface area from adsorption data obtained at $0.05 \leq P/P_0 \leq 0.3$.
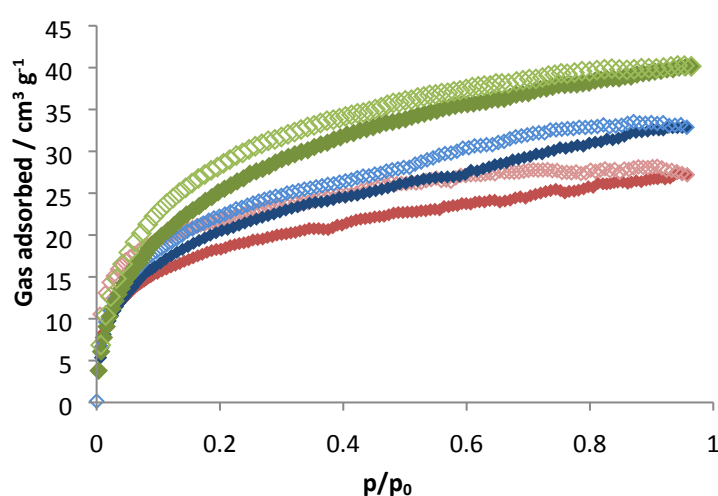
Figure S23 CO_2 isotherms for Cu(**3**)(DMF) (red), Cu(**4**)(DMF) (blue) and Cu(**5**)(DMF) (green), recorded at 195 K. Dark filled symbols indicate adsorption and lighter empty symbols indicate desorption.

Individual isotherms for Cu(**3**-**5**)(DMF)
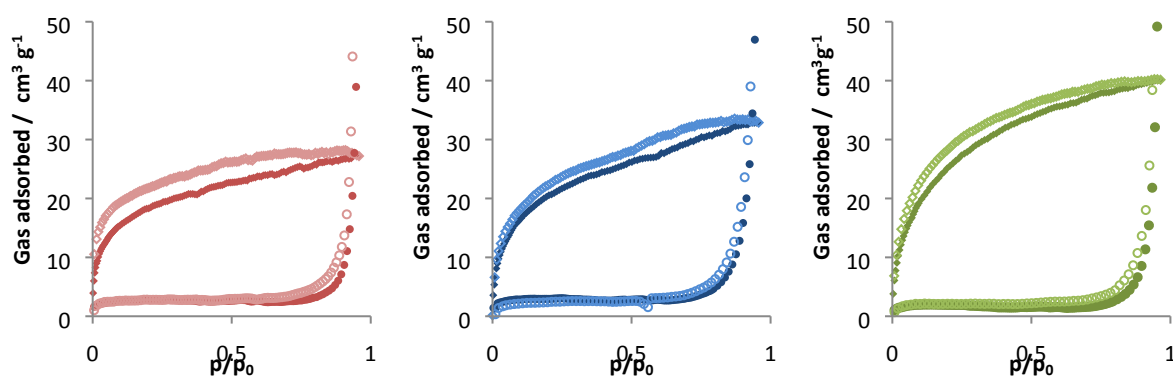

Figure S24 CO_2 (diamonds) and N_2 (circles) isotherms recorded at 77 K and 195 K respectively for Cu(**3**)(DMF) (left), Cu(**4**)(DMF) (centre) and Cu(**5**)(DMF) (right). Dark filled symbols indicate adsorption and lighter empty symbols indicate desorption.

3. Desolvated MOF characterisation

3.1. ^{1}H NMR

Solids collected from centrifugation for 1 hr at 1500 rpm were air dried at 40 °C overnight. 0.75 mL ampule of d_6-DMSO was added and 20 uL of 35 % DCl in D_2O then added, which digested the MOF. Room temperature ^{1}H NMR spectroscopy quantified the ratio of DMF to dicarboxylic acid. Under these acidic conditions, the carboxylate groups of the dicarboxylates (**3**-**5**) will deuterate/protonate. Due to rapid exchange these are not observed in the spectra. H_2O peak is shifted downfield due to presence of DCl. Spectra were recorded on a Bruker AVIIIHD instrument operating at 400 MHz.

Table S6 Anticipated DMF peaks.[10]

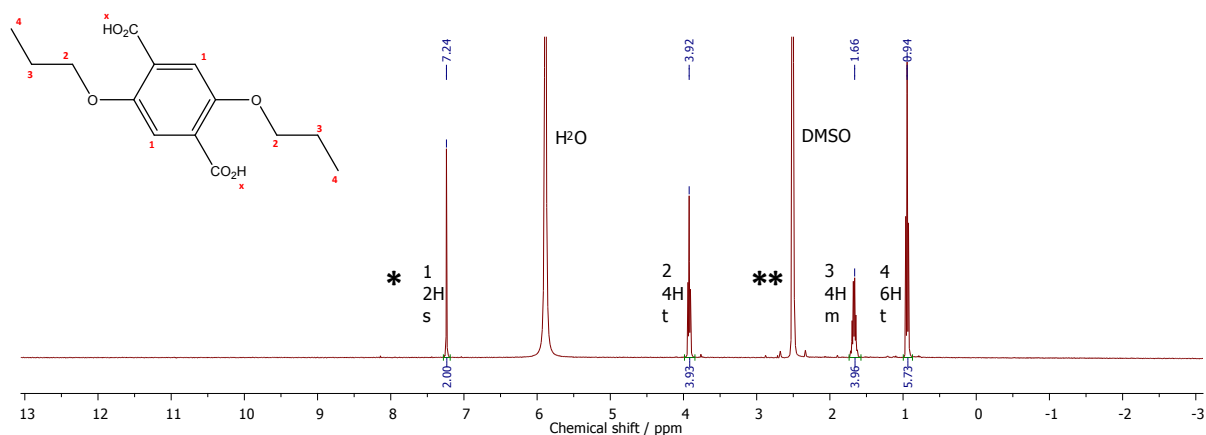| DMF proton	Multiplicity	Chemical shift / ppm	
		d_6-DMSO	D_2O
CH	s	7.95	7.92
CH_3	s	2.89	3.01
CH_3	S	2.73	2.85

Figure S25 ^{1}H-NMR spectra of digested Cu(**3**). Anticipated DMF peaks are indicated with asterisks.

18

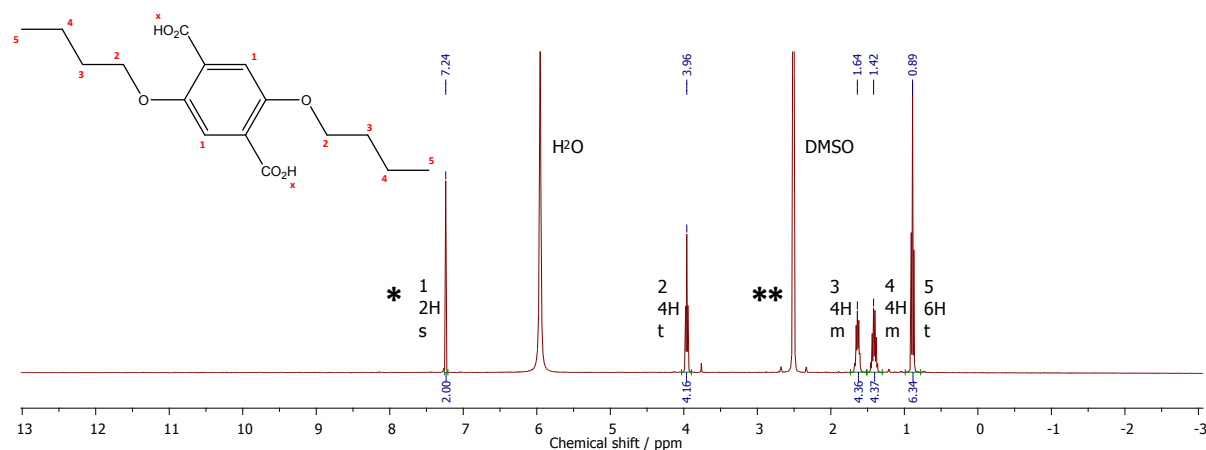**Figure S26** ^{1}H-NMR spectra of digested Cu(**4**). Anticipated DMF peaks are indicated with asterisks.

Figure S27 ^{1}H-NMR spectra of digested Cu(**5**). Anticipated DMF peaks are indicated with asterisks.
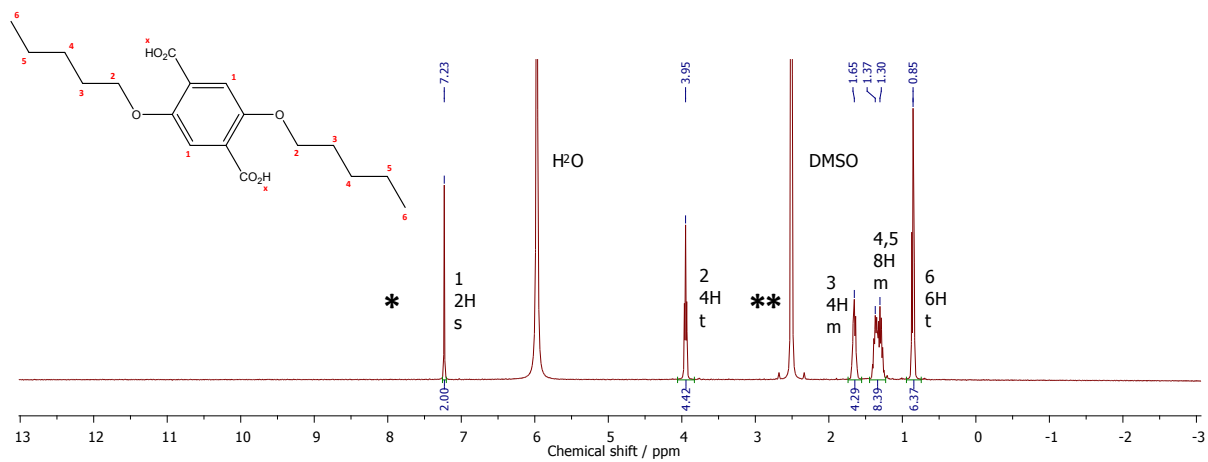
4. MON characterisation

4.1. UV-Vis spectroscopy

5 mg of MOF was sonicated in 6 mL solvent. This was then titrated into a known volume (2.5 mL or 3 mL) of solvent, and absorbance at λ_{max} was plotted against MON concentration in order to create a calibration curve by which the extinction coefficient of MONs in DMF and MeCN could be determined (Figure S28-Figure S30 and Figure S33-Figure S35).

This allowed estimations of the concentrations of unknown MON suspensions. UV-Vis spectra were recorded with a Varian Cary 50 UV spectrophotometer using a resolution of 1 nm and scan speed of 600 nm min^{-1}, controlled with Perkin Elmer Spectrum One software.
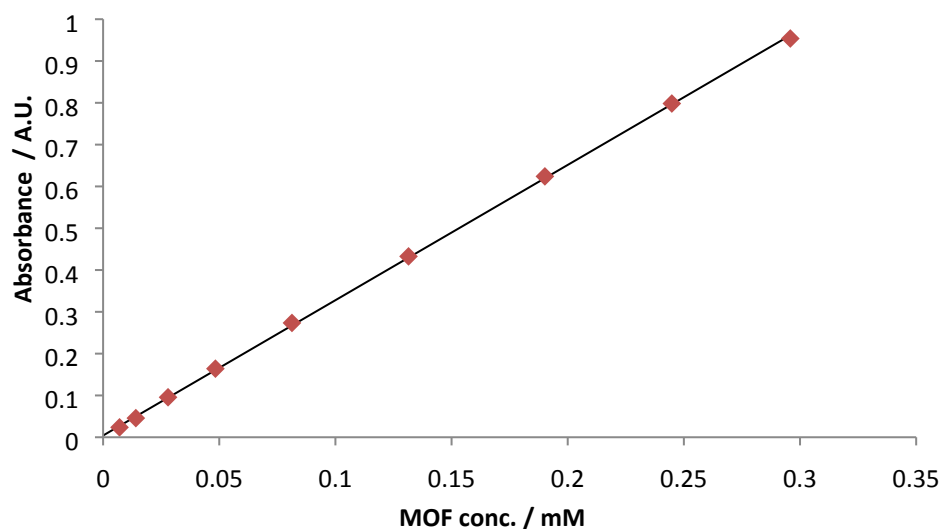

Figure S28 Absorbance of Cu(**3**)(DMF) exfoliated in DMF at λ_{max} = 327 nm at the indicated concentrations. ε = 3236 dm^3 mol^{-1} cm^{-1}.
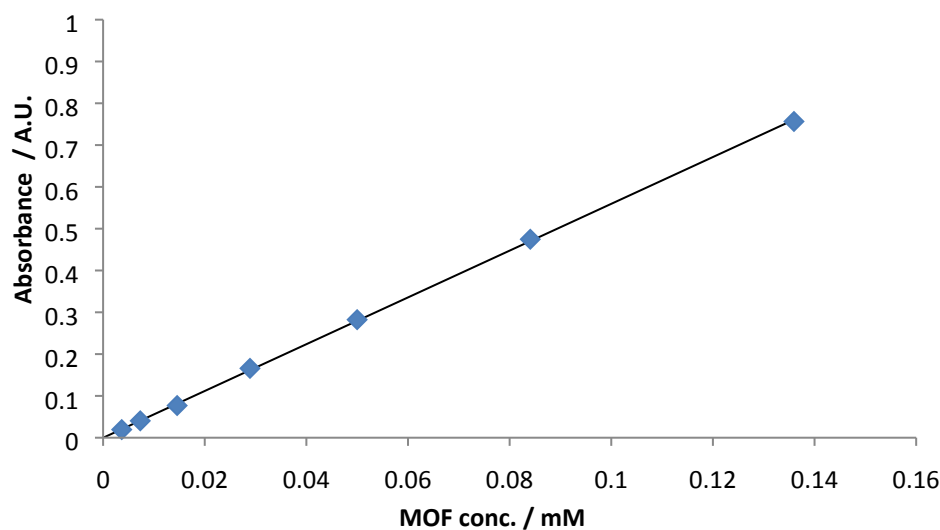
Figure S29 Absorbance of Cu(**4**)(DMF) exfoliated in DMF at λ_{max} = 303 nm at the indicated concentrations. ε = 5596 dm^3 mol^{-1} cm^{-1}.
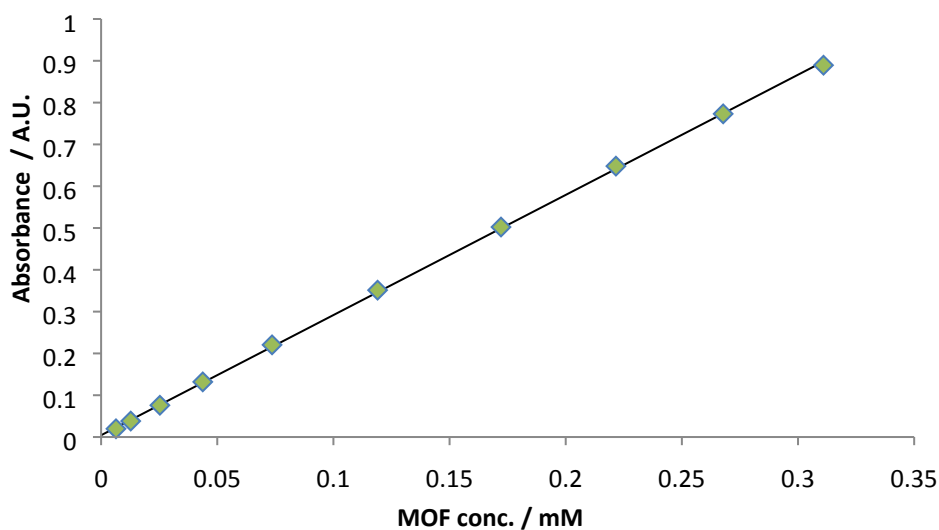

Figure S30 Absorbance of Cu(**5**)(DMF) exfoliated in DMF at λ_{max} = 304 nm at the indicated concentrations. ε = 2875 dm^3 mol^{-1} cm^{-1}.
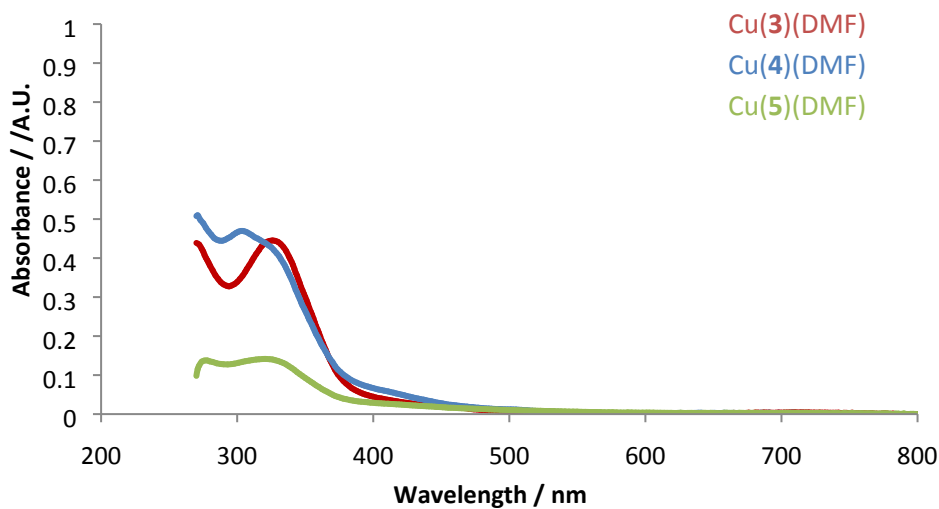

Cu(**3**)(DMF)
Cu(**4**)(DMF)
Cu(**5**)(DMF)

Figure S31 UV-Vis spectra of Cu(**3**-**5**)(DMF) exfoliated in DMF and centrifuged at 1500 rpm for 1 hr. Cu(**3**)(DMF) was diluted 1 part in 4 and Cu(**4**)(DMF) and Cu(**5**)(DMF) diluted 1 partin 6.
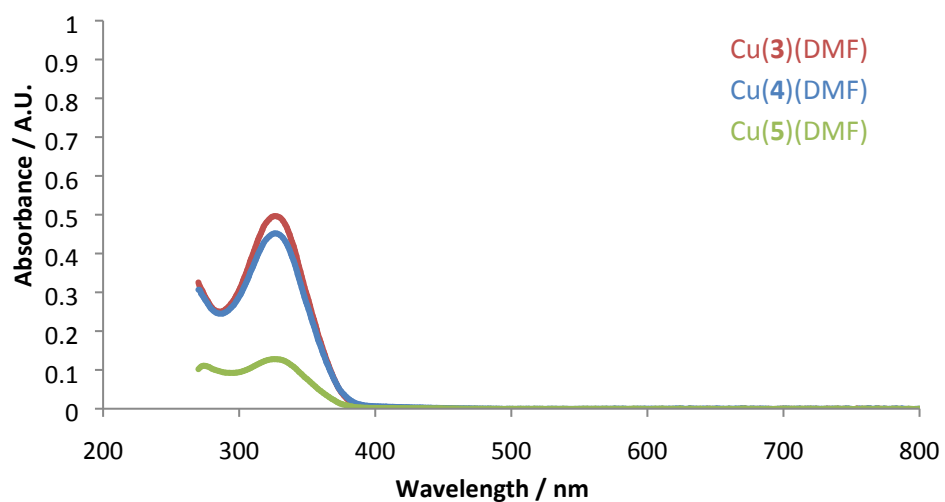
Figure S32 UV-Vis spectra of Cu(**3**-**5**)(DMF) exfoliated in DMF and centrifuged at 4500 rpm for 4.5 hr. Cu(**3**)(DMF) was diluted 1 part in 2 and Cu(**4**)(DMF) and Cu(**5**)(DMF) diluted 1 part in 3.
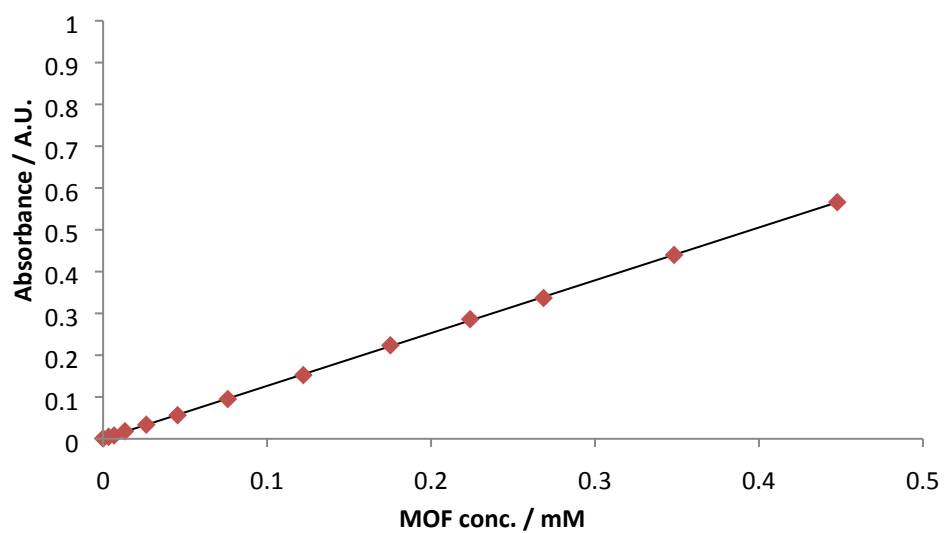

Figure S33 Absorbance of Cu(**3**)(DMF) exfoliated in MeCN at λ_{max} = 275 nm at the indicated concentrations. ε = 1263 dm^3 mol^{-1} cm^{-1}.
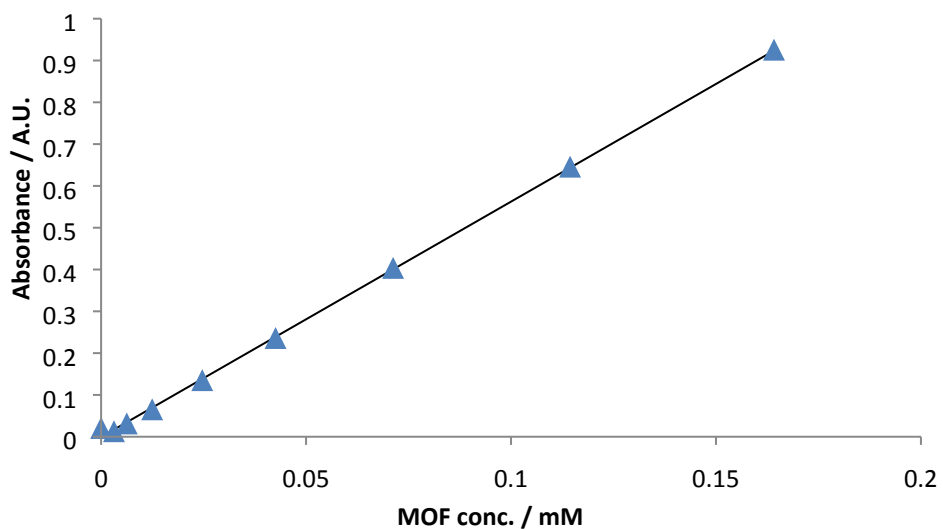
Figure S34 Absorbance of Cu(**4**)(DMF) exfoliated in MeCN at λ_{max} = 269 nm at the indicated concentrations. ε = 5630 dm^3 mol^{-1} cm^{-1}.
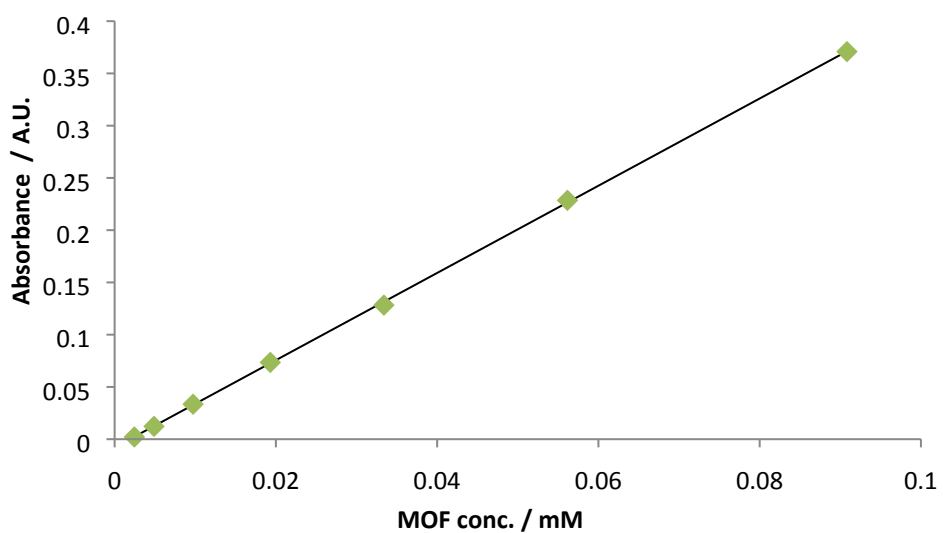

Figure S35 Absorbance of Cu(**5**)(DMF) exfoliated in MeCN at λ_{max} = 270 nm at the indicated concentrations. ε = 4173 dm^3 mol^{-1} cm^{-1}.
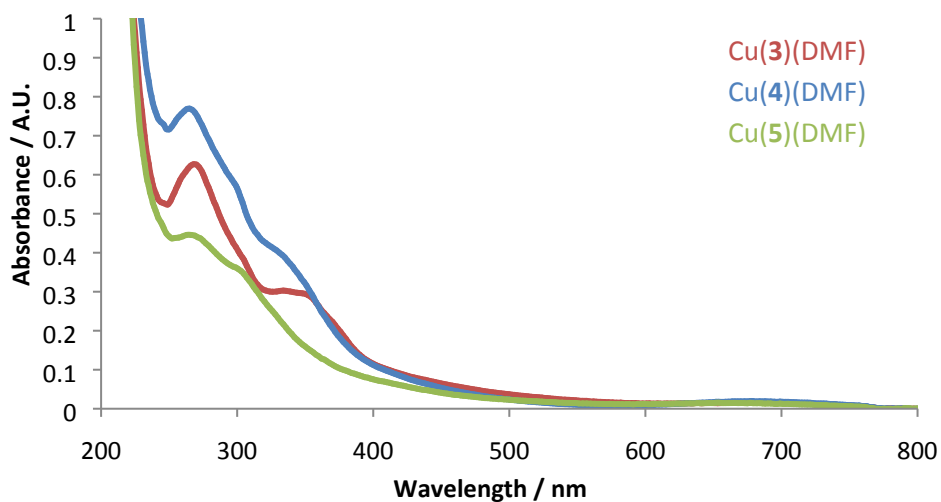
Figure S36 UV-Vis spectra of Cu(**3**-**5**)(DMF) exfoliated in MeCN and centrifuged at 1500 rpm for 1 hr. Cu(**3**)(DMF) was diluted 1 part in 2 and Cu(**4**)(DMF) and Cu(**5**)(DMF) diluted 1 part in 4.
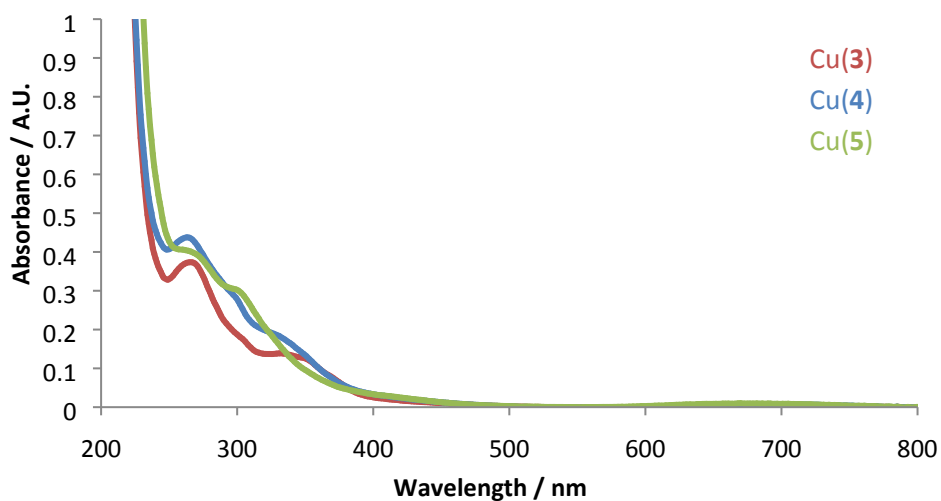

Figure S37 UV-Vis spectra of Cu(**3**-**5**)(DMF) exfoliated in MeCN and centrifuged at 4500 rpm for 4.5 hr. Cu(**4**)(DMF) and Cu(**5**)(DMF) were diluted 1 part in 2.

4.2. Atomic force microscopy

Freshly cleaved mica was loaded onto a magnetic disk for AFM analysis. This was heated to 80 °C. A 10 μL aliquot of MON suspension was dropped onto the mica substrate and air-dried at 80 °C. AFM images (Figures S33-S38) were obtained using a Bruker Multimode 5 AFM with an equipped Nokia 10x visualising lens, operating in soft tapping-mode using Bruker OTESPA-R3 cantilevers. Images were processed using standard techniques with Gwyddion software.[11] Agglomerated particles were not included within the sizing analyses if distinct particles could not be determined.

Figure S38 AFM topographical image of Cu(**3**) after exfoliation in MeCN.

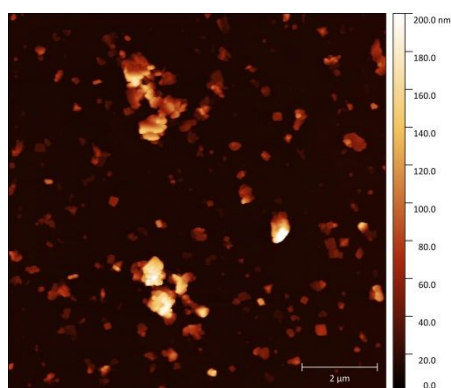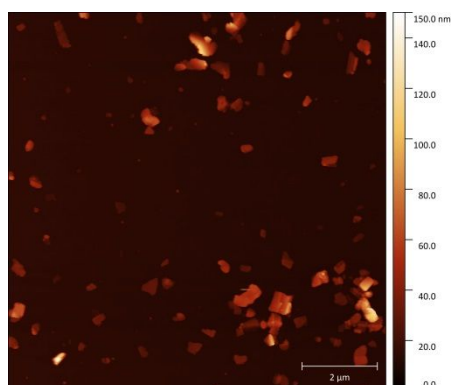**Figure S39** AFM topographical image of Cu(**4**) after exfoliation in MeCN.
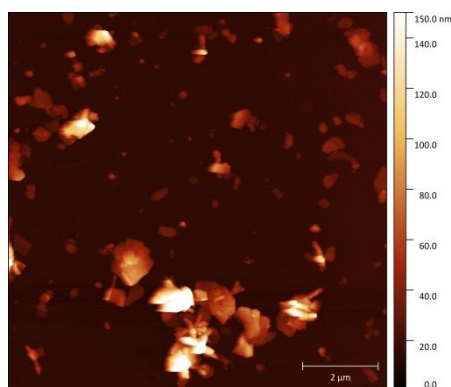

Figure S40 AFM topographical image of Cu(**5**) after exfoliation in MeCN.
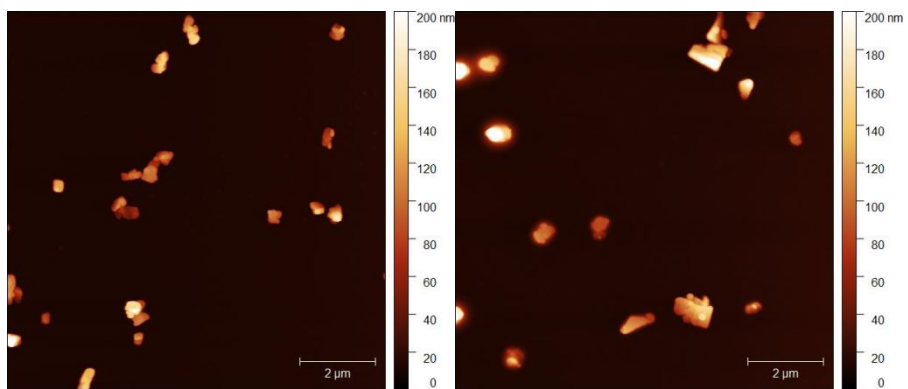
Figure S41 AFM topographical images of Cu(**3**)(DMF) after exfoliation in DMF.
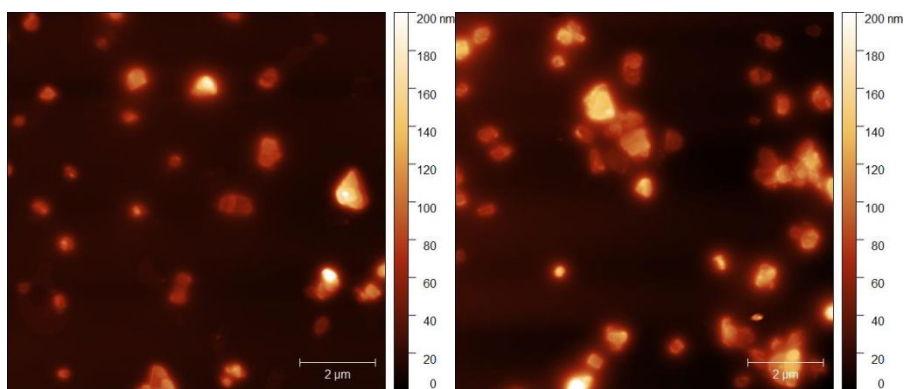
Figure S42 AFM topographical images of Cu(**4**)(DMF) after exfoliation in DMF.
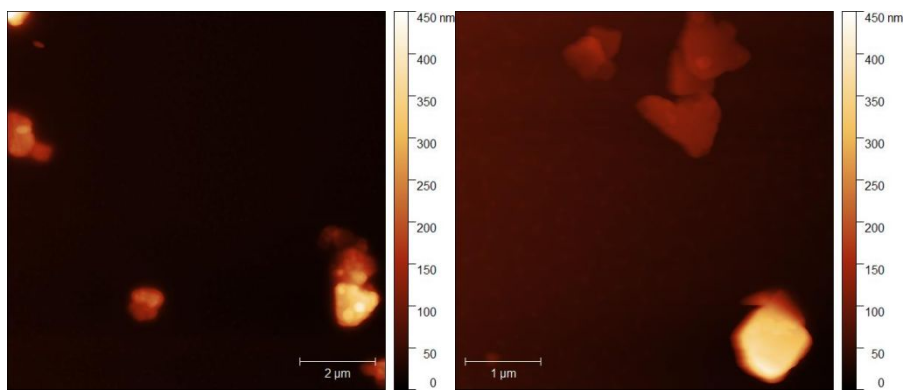
Figure S43 AFM topographical images of Cu(**5**)(DMF) after exfoliation in DMF.

4.3. DLS

DLS data were collected using a Malvern Zetasizer Nano Series particle size analyser equipped with a He- Ne laser at 633 nm, operating in backscatter mode (173 °). Data were recorded using the samples analysed by UV-Vis spectroscopy and imaged with AFM.
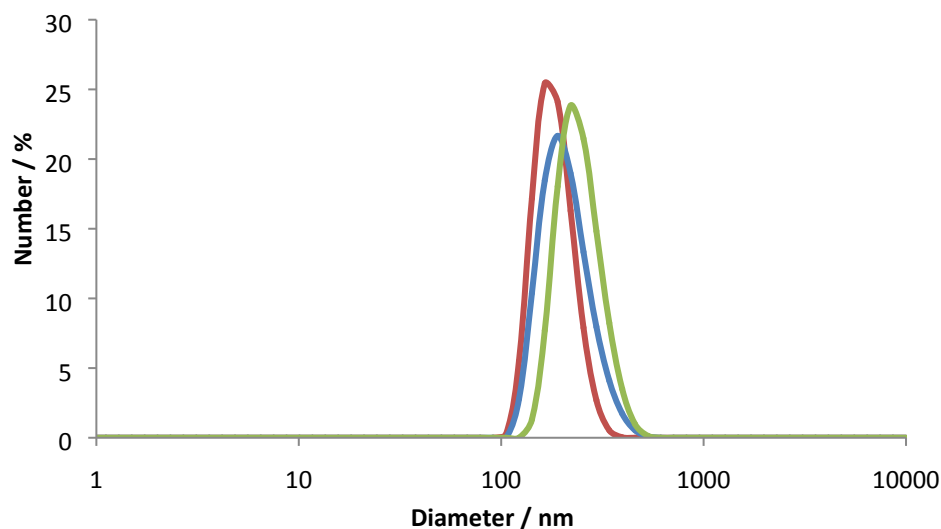
Figure S44 Number average of three repeat DLS particle size distribution collections for Cu(**3**) (red), Cu(**4**) (blue) and Cu(**5**) (green), after exfoliation in MeCN and centrifuged for 1 hr at 1500 rpm.

Table S7 DLS data: average diameter of MONs Cu(**3**-**5**) determined using Z-average, intensity average and number average, and polydispersity index (PdI)

Sample	Z-average / nm	Intensity average / nm	Number average / nm	PdI
Cu(**3**)	242	207	185	0.247
Cu(**4**)	269	316	213	0.239
Cu(**5**)	324	282	247	0.299

4.4. Statistical analysis

Size distributions of Cu(**3-5**) nanosheets were tested for statistical significance using the unpaired two-tailed t test.

Table S8 Summary of statistical size data from Cu(**3-5**) MONs observed after exfoliation of MOFs Cu(**3-5**)(DMF) in MeCN and centrifuged for 1 hr at 1500 rpm.

	n	Lateral dimensions / nm		Height / nm	
		$\bar{x}$	SD	$\bar{x}$	SD
Cu(**3**)	129	222	95	35	26
Cu(**4**)	114	275	148	22	13
Cu(**5**)	94	348	202	20	12

Table S9 Two-tailed P values resulting from the unpaired t test between the specified size populations of Samples 1 and 2.

Sample 1	Sample 2	Lateral dimensions	Height
Cu(**3**)	Cu(**4**)	0.0009	< 0.0001
Cu(**4**)	Cu(**5**)	0.0030	0.2543
Cu(**3**)	Cu(**5**)	< 0.0001	< 0.0001

4.5. Contact angles

Freshly cleaved mica was placed on the bottom of vials and Cu(**3**-**5**)(DMF) MON suspension in DMF added on top. Centrifugation deposited MONs onto the surface of the mica. The supernatant was pipetted off and the mica allowed to air dry at 40 °C, then removed from the vial and used as the substrate for contact angle analyses. 1 uL drops of solvent were used, and results are an average of three repeats.

Table S10 Contact angle of DMF and MeCN with films of MONs Cu(**3**-**5**)(DMF).

| Solvent	Contact angle / °			
	blank	Cu(**3**)(DMF)	Cu(**4**)(DMF)	Cu(**5**)(DMF)
DMF	11	0	0	0
MeCN	14	0	0	0

Complete surface wetting occurred immediately upon touching the drop of DMF or MeCN to the surface of the MON films, resulting in a contact angle of 0 °.

5. References

(1)   Tartoni, N.; Thompson, S. P.; Tang, C. C.; Willis, B. L.; Derbyshire, G. E.; Wright, A. G.; Jaye, S. C.; Homer, J. M.; Pizzey, J. D.; Bell, A. M. T. High-Performance X-Ray Detectors for the New Powder Diffraction Beamline I11 at Diamond. *J. Synchrotron Radiat.* **2008**, *15*, 43–49.

(2)   Thompson, S. P.; Parker, J. E.; Potter, J.; Hill, T. P.; Birt, A.; Cobb, T. M.; Yuan, F.; Tang, C. C. Beamline I11 at Diamond: A New Instrument for High Resolution Powder Diffraction. *Rev. Sci. Instrum.* **2009**, *80*, 1–9.

(3)   Thompson, S. P.; Parker, J. E.; Marchal, J.; Potter, J.; Birt, A.; Yuan, F.; Fearn, R. D.; Lennie, A. R.; Street, S. R.; Tang, C. C. Fast X-Ray Powder Diffraction on I11 at Diamond. *J. Synchrotron Radiat.* **2011**, *18*, 637–648.

(4)   Coelho, A. A. TOPAS Academic. *Topas Acad. Version 4.1, see http//www.topas-academic.net*.

(5)   Coelho, A. A.; Evans, J.; Evans, I.; Kern, A.; Parsons, S. The TOPAS Symbolic Computation System. *Powder Diffr.* **2011**, *26*, S22–S25.

(6)   Guo, Z.; Reddy, M. V.; Goh, B. M.; San, A. K. P.; Bao, Q.; Loh, K. P. Electrochemical Performance of Graphene and Copper Oxide Composites Synthesized from a Metal-Organic Framework (Cu-MOF). *RSC Adv.* **2013**, *3*, 19051–19056.

(7)   Pawley, G. S. Unit-Cell Refinement from Powder Diffraction Scans. *J. Appl. Crystallogr.* **1981**, *14*, 357–361.

(8)   Foster, J. A.; Henke, S.; Schneemann, A.; Fischer, R. A.; Cheetham, A. K. Liquid Exfoliation of Alkyl-Ether Functionalised Layered Metal–organic Frameworks to Nanosheets. *Chem. Commun.* **2016**, *52* , 10474–10477.

(9)   Rietveld, H. M. A Profile Refinement Method for Nuclear and Magnetic Structures. *J. Appl. Crystallogr.* **1969**, *2*, 65–71.

(10)   Gottlieb, H. E.; Kotlyar, V.; Nudelman, A. NMR Chemical Shifts of Common Laboratory Solvents as Trace Impurities. *J. Org. Chem.* **1997**, *62* , 7512–7515.

(11)   Nečas, D.; Klapetek, P. Gwyddion: An Open-Source Software for SPM Data Analysis. *Cent. Eur. J. Phys.* **2012**, *10*, 181–188.

5 ♠

Blending functionalised ligands to form multivariate metal-organic framework nanosheets (MTV-MONs) with tuneable surface chemistry

Cu(NO₃)₂·6H₂O
DMF
110 °C, 36 hrs

Sonication
Solvent

Layered MOF
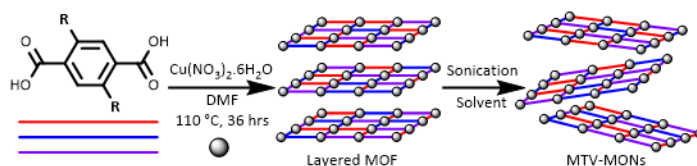
MTV-MONs

Chapter 5

Blending functionalised ligands to form multivariate metal-organic framework nanosheets (MTV-MONs) with tuneable surface chemistry

David J. Ashworth and Jonathan A. Foster

Author Contributions

David J. Ashworth	Performed all experimentation and characterisation. Drafted and redrafted the manuscript and prepared all figures.
Jonathan A. Foster	Supervised DJA and coordinated the work. Assisted in redrafting and editing the manuscript.

Blending functionalised ligands to form multivariate metal-organic framework nanosheets (MTV-MONs) with tuneable surface chemistry

David J. Ashworth[a] and Jonathan A. Foster*[a]

The properties of two-dimensional (2D) materials are dominated by the functional groups presented on their surface. Here we present a new approach to tuning the surface properties of metal-organic nanosheets (MONS) by blending functionalised ligands to produce multivariate MONs (MTV-MONs). Layered copper paddle-wheel based MOFs were synthesised incorporating two or more 2,5-difunctionalised-benzene-1,4-dicarboxylate (fu-BDC) ligands. Liquid ultrasonic exfoliation resulted in the formation of nanosheets down to monolayer thickness incorporating multiple functional moieties. Blending of ligands with relatively hydrophilic and hydrophobic functional moieties resulted in MTV-MONs which showed enhanced dispersion in both polar and apolar solvents compared to either single-ligand parent MON and intermediary binding properties. Blending of different fu-BDC ligands with different length alkoxy chains (methoxy-pentoxy) allowed incorporation of up to five different ligands within MTV-MONs and the effect on nanosheet thickness was investigated. This study demonstrates the potential of blending multiple ligands within an MTV-MON to enable fine-tuning of their structure and properties but also create new nanosheets which are more than the sum of their parts.

1. Introduction

Metal-organic framework nanosheets (MONs) are nominally two-dimensional (2D), crystalline, free standing sheets formed of metal ion or cluster nodes which are linked in two dimensions with multitopic organic ligands.[1] MONs possess many of the properties associated with 2D materials, such as nanoscopic dimensions, anisotropic morphologies and high external surface areas.[1–3] This makes them attractive candidates for a variety of sensing, catalysis, separation, composite materials and electronics applications.[1–9] The diverse chemistry and modular structure of MONs also addresses a key limitation of simple inorganic 2D materials (for example graphene, hexagonal boron nitride or transition metal oxides/chalcogenides), in that it is difficult to systematically alter the surface properties of these nanosheets without disrupting their structure or other properties.[10] For example, hydrophobic graphene can readily be oxidised to form graphene oxide, which is readily dispersible in water.[11] However, this disrupts the conjugated backbone which gives rise to the remarkable electronic and mechanical properties of graphene, whilst introduces a wide range of different chemical functionalities (hydroxyl, aldehyde, carboxylic acid) at poorly defined and difficult to control positions.[12]

The modular structure of MONs allows surface functionalisation in a systematic manner. Combining the tunability of organic ligands with the properties offered by metal atoms (*e.g.* magnetic, electronic and catalytic) places MONs at an exciting materials interface between 2D nanomaterials and metal-organic materials. MONs have been used as catalysts,[13–15] in membranes for gas separation[16–19] and within electronics,[20–23] amongst other applications. Numerous authors have developed strategies for controlling surface properties of MONs. We have recently reported covalent post-synthetic functionalisation (PSF) to introduce acidic groups to MON surfaces,[24] and dative PSF through metalation of ligands incorporated into the MON framework and coordination of ligands to labile metal sites within the framework structure have been used to introduce catalytic functionalities.[25–28]

Design of MONs according to principles of reticular chemistry[29–31] enables prediction of 2D connectivity, which has directed the synthesis of numerous MON systems. MON design has thus far utilised single ligands to build up relatively "simple" 2D structures, for example benzene-1,4-dicarboxylate (BDC) is often used as a linear linker between paddle-wheel (PW) secondary building units (SBUs).[25,32–34] We have previously used functionalised-BDC (fu-BDC) derivatives to synthesise isoreticular layered MOFs with the 2D structure of Cu-MOF-2 (*i.e.* $Cu_2(fu-BDC)_2$) and exfoliated these to tune the MON hydrophilicity,[35,36] post-synthetically modify MONs,[24] and to aid exfoliation by using different length alkoxy chains.[37]

Yaghi and coworkers combined different fu-BDC ligands within a single phase of MOF-5-type structure in 2010.[38] They combined up to eight fu-BDC ligands within the frameworks, and termed these multivariate (MTV-) MOFs. Ligand

a. *Dept. of Chemistry, The University of Sheffield, Dainton Building, Brook Hill, Sheffield, S3 7HF, UK.*
† Footnotes relating to the title and/or authors should appear here.
Electronic Supplementary Information (ESI) available: all syntheses, characterisation and analytical data. See DOI: 10.1039/x0xx00000x

combinations lead to combinations of properties that were greater than any single-ligand system, for example a tertiary blend of fu= NO_2, $(OC_3H_5)_2$ and $(OC_4H_7)_2$ exhibited up to 400 % better selectivity for CO_2 over CO compared with its best single-ligand counterpart. Numerous authors have since utilised MTV-MOFs, mainly in regard to gas adsorption,[39] but also for creating "enzyme-like" pore spaces for selective catalysis.[40]

The MTV-MOF concept has also been applied to incorporating multiple different metal ions within a single framework,[41] for example within a M_3O metalated porphyrin based MOF, where M=Mg, Mn, Co, Ni and Fe.[42] Zhuang *et al*. recently demonstrated mixed-metal MOF-74 nanosheets, however this is a non-layered framework for which they grew ultrathin layers from metal-oxide nanosheets.[43] However, to our knowledge, despite reports of several isoreticular series of MONs,[44–46] as well as MONs containing different metals in different environments (for porphyrin-based materials, several authors have demonstrated different metals in the centre of the porphyrin and within in the linking SBU)[47,48] there are no reported examples of MTV-MONs.

Mixed-ligand MTV-MONs are appealing as there are a number of possibilities that could stem from the approach. (1) Blending different ligands could allow fine-tuning of the system's properties, intermediary to that of the single-ligand analogues. (2) MTV-MONs could combine properties of single-ligand analogues to more than a sum of the parts. (3) Combinations of ligands could demonstrate new phenomena that are not associated with any of the single-ligand systems. We have previously presented isoreticular layered MOFs of the structure [Cu(fu-BDC)(DMF)]$_n$ using a number of different fu-BDC ligands: **1-5** and **5*** (Figure 1).[35–37] These MOFs have the in-plane structure of MOF-2,[49,50] where dinuclear copper PW units are linked in two dimensions through dicarboxylic acid linkers with the functional groups projecting between the layers. Through systematic studies we showed that the small changes in the length and polarity of the functional groups can have significant effect on the dimensions and concentration of the nanosheets formed.
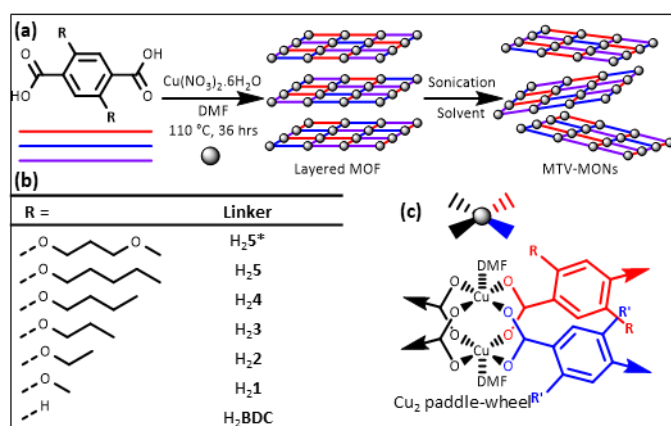

Figure 1. (a) General schematic for the synthesis of multivariate Cu(fu-BDC)(DMF) based MONs, (b) nomenclature used for diacid ligand precursors and (c) copper paddle-wheel SBU.

Here, we synthesise a new series of layered MTV-MOFs using combinations of these linkers and exfoliate them to investigate the effect of different ligand combinations on the structure and properties of the resulting nanosheets. We hypothesised that blending of ligands with different properties could produce nanosheets with intermediate properties. We also speculated that random inclusion of the ligands[51] within the 2D net could reduce interlayer interactions and so lead to higher yields and thinner nanosheets than seen in any of the parent compounds.

2. Results and discussion

2.1. Blending hydrophilic and hydrophobic linkers

Previous studies have demonstrated the exfoliation of layered frameworks [Cu(**5/5***)(DMF)]$_n$ to form MONs.[35–37] Incorporation of the 3-methoxypropoxy (**5***) or pentoxy (**5**) fu-BDC ligands instilled relatively hydrophilic or hydrophobic properties, respectively, to the MOF. Exfoliation in water or diethylether (Et_2O) produced higher concentrations of hydrophilic or hydrophobic MONs respectively, indicating that a good match of solvent and surface polarity may aid exfoliation. Acetonitrile (MeCN) was found to be a good solvent for exfoliation for these and other related Cu_2-PW based MOFs.[24]

A 50:50 mixture of H$_2$**5** and H$_2$**5*** diacids were used within a typical MOF synthesis. Copper nitrate trihydrate and diacids (totalling 110 % of copper content, i.e. a 10 % total ligand excess) were dissolved in DMF and sealed in a glass reaction vial with a Teflon-lined lid. This was heated to 110 °C for 36 hrs. The resulting microcrystalline MOF was washed and dried, yielding a blue microcrystalline powder. Further synthetic details can be found in the experimental section. This general synthetic method was used for all MOF syntheses throughout this study.

Approximately 2 mg of MOF was digested using 20 μL DCl (35 %) in D_2O in 1 mL d_6-DMSO. Liquid chromatography-mass spectrometry (LC-MS) confirmed the incorporation of both ligands within the MOF (m/z= 337.2 and 341.1 for H**5**$^-$ and H**5***$^-$ respectively) and proton-nuclear magnetic resonance (^{1}H-NMR) was used to quantify the ligand content, using the α proton environments on the chains (found **5**=53 %, **5***=47 %, ESI Figure S1). Elemental analysis was consistent with the expected [Cu(**5**)$_{0.5}$(**5***)$_{0.5}$(DMF)]$_n$ ligand:DMF ratio for the fully solvated form (ESI Table S1). Pawley refinement of the powder X-ray diffraction (PXRD) pattern indicated a structure with a unit cell very similar to that of the single-ligand MOFs (ESI Figure S1 and Table S2). This supports the formation of the anticipated layered structure of [Cu(**5***)$_{0.5}$(**5**)$_{0.5}$(DMF)]$_n$ (**5,5***-MTV-MOF). Scanning electron microscopy (SEM) revealed plate-like particle morphology, with lateral dimensions of 0.5-5 μm, and apparent thicknesses of >100 nm (Figure 2b).

5,5*-MTV-MOF was exfoliated in three different solvents: MeCN, H_2O and Et_2O. Solvent (2.4 mL) was added to a vial containing MOF powder (2 mg) and subjected to ultrasonication (12 hrs, 80 kHz) using our previously optimised protocol.[35]
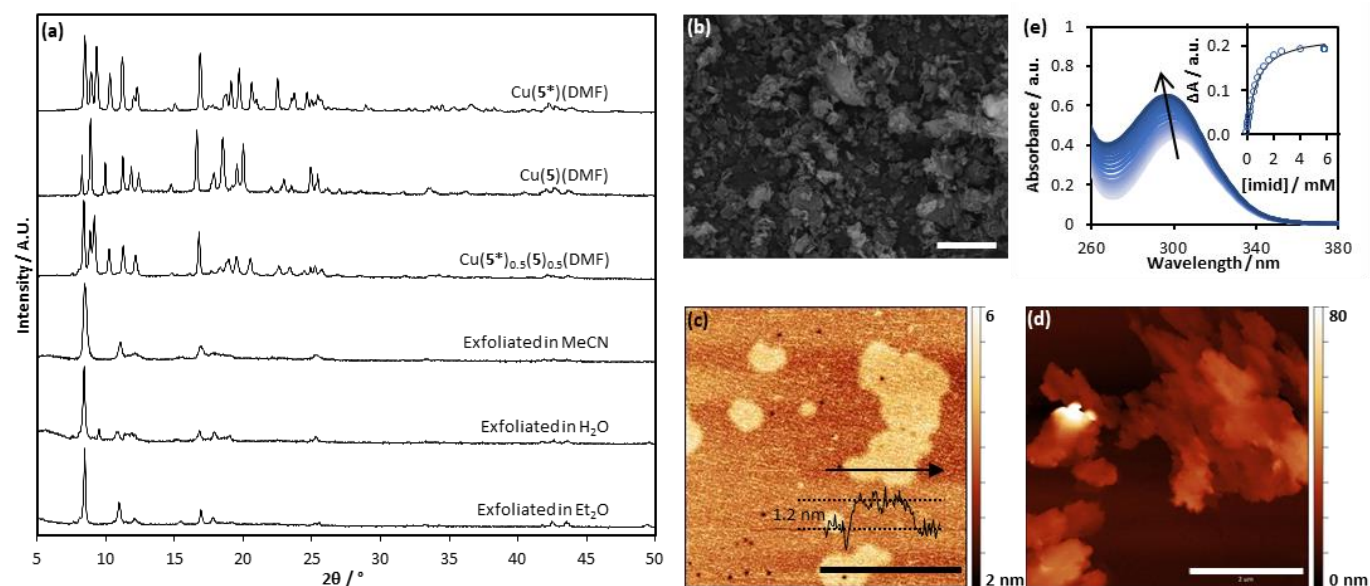
Figure 2. (a) PXRD patterns of input MOF compared to single ligand MOFs,[35] and recollected material following exfoliation in MeCN, water and Et₂O. (b) SEM micrograph of **5,5***-MTV-MOF. Scale bar is 5 µm. (c-d) AFM images of **5,5***-MTV-MOF exfoliated in Et₂O and water, respectively. Scale bars are 2 µm. (e) UV-Vis titration showing addition of imidazole solution to an aqueous MON suspension; inset is a plot of ΔA against [imidazole], fitted to a binding curve.

Centrifugation of the sonicated suspension (1 h, 1500 rpm) separated larger particles of unexfoliated material from the **5,5***-MTV-MONs which remained suspended in the supernatant, evidenced through Tyndall scattering. These sonication and centrifugation procedures are used throughout this manuscript.

To assess the structure of the materials produced, solids collected through centrifugation were air-dried and analysed using PXRD (Figure 2a). Material exfoliated in all three solvents showed PXRD patterns with peaks which corresponded to those expected for the desolvated phase (loss of DMF from the axial position of the PW) as was reported for the parent single-ligand materials. Fourier-transform infrared spectroscopy (FTIR, ESI Figure S13) and ^{1}H-NMR (ESI Figure S11) confirmed the absence of DMF in each case. Interestingly, exfoliation of **5,5***-MTV-MOFs in water produced the desolvated phase rather than the phase where water molecules replace DMF at the axial PW sites as observed in the single-ligand MOFs treated under the same conditions.[35] The MTV-MONs therefore show subtle differences in preferred structure compared to the parent MONs.

The concentration of the **5,5***-MTV-MON-containing supernatant was determined through UV-vis spectroscopy (ESI Figure S14). Calibration curves were previously prepared through titration of known MON concentration suspension into fresh solvent to calculate the extinction coefficients of the single-ligand parent MONs.[35] An average of these was taken for **5,5***-MTV-MON. This allowed calculation of unknown concentrations of suspension.

As shown in Table 1, single-ligand MONs were formed in high concentration in solvent that matches their surface chemistry and low concentration in the other, consistent with previous reports.[35] Interestingly, the **5,5***-MTV-MONs formed suspensions of higher concentration than that of either single-ligand MON in all three solvents. This is remarkable considering

the MTV-MONs only possess approximately 50 % of each surface functionality so might reasonably be expected to show intermediate preferences for solvent polarity. This therefore demonstrates the potential of combining multiple ligand functionalities to enhance the dispersion properties of MONs compared to either parent compound.

5,5*-MTV-MON suspensions were drop cast onto freshly cleaved mica substrates and were imaged using atomic force microscopy (AFM). SPIP software was used to size particles observed from exfoliation in MeCN (ESI Figure S15). Raw data from previous studies using single ligand MONs were re-sized using SPIP (ESI Figures S21-25). Average MON heights of 14±10 nm were observed for **5,5***-MTV-MONs, with average lateral dimensions 280±217 nm (n=187). This is thinner than the average heights observed for the hydrophilic **5***-MONs (35±18 nm) and similar to that of the hydrophobic **5**-MON (14±8 nm), Dynamic light scattering (DLS) showed a number average diameter of 209 nm, compared to 213 nm and 179 nm for **5**- and **5***-MONs respectively.[35]

Exfoliation in H₂O yielded much larger MONs than in MeCN with lateral dimensions in the order of 400-5000 nm (although this was challenging to accurately size by this technique), with thicknesses >5 nm (Figure 2d). MONs appeared wrinkled and folded, indicating flexibility of these sheets.[52] Exfoliation in Et₂O

Table 1. Concentrations of MONs in suspension after exfoliation in MeCN, water and diethyl ether, and binding constants for imidazole in water.

Input MOF	Concentration / mg mL⁻¹			K_a / M⁻¹
	MeCN	H₂O	Et₂O	H₂O
Cu(**5***)(DMF)	0.16	0.31	0.005	1950±140*
5,5*-MTV-MOF	0.24	0.32	0.034	1640±130
Cu(**5**)(DMF)	0.06	0.09	0.026	1370±180*

* data previously published in reference [35].
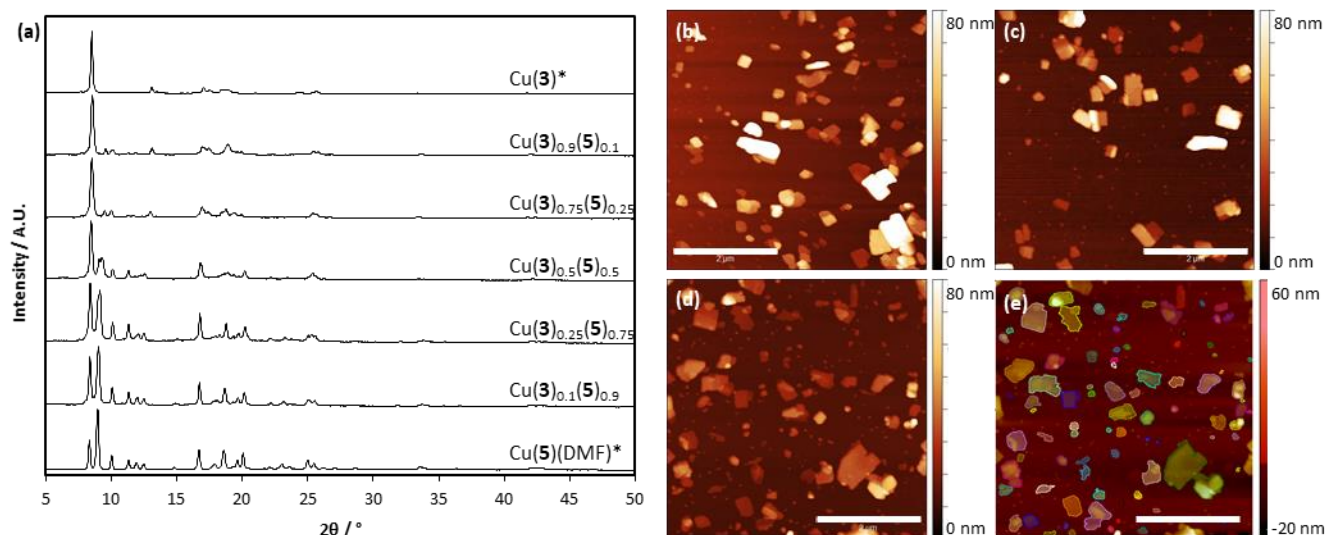
Figure 3. (a) PXRD patterns of Cu(**3**)(**5**)$_{1-x}$ MTV-MOF, where x= 0.9, 0.75, 0.5, 0.25 and 0.1. (b-d) AFM topographic images of **3,5**-MTV-MONs resulting from exfoliation of **3,5**-MTV-MOFs in MeCN, where x= 0.9, 0.5 and 0.1, respectively. (e) Example automated particle recognition using SPIP software for **3,5**-MTV-MON, where x=0.1. Scale bars in (a-e) are 2 μm.

yielded MONs of similar lateral ranges to MeCN, however ultrathin monolayer MONs were observed with thickness approximately 1.5 nm (Figure 2c). Layer thickness is 1.4 nm according to crystal structures, but this is calculated with chains fully extended, which is unlikely when at monolayer thickness.[36,37] Ultrathin monolayer MONs such as these were not previously observed through exfoliation of single-ligand MOFs in Et$_2$O.

To probe the surface chemistry further, an aqueous imidazole solution (20 mM) in MON suspension (0.18 mM) was titrated into an aqueous suspension of **5,5***-MTV-MONs (0.18 mM) and monitored using UV-Vis spectroscopy (Figure 2e and ESI Figures S18-20). The binding constant was calculated from fitting Δ(absorbance) against [imidazole] as K_a=1640±130 M^{-1}, approximately half-way (47 %) between that previously calculated for the single-ligand MONs (Table 1).[35] This demonstrates that MTV-MONs can have intermediary properties compared to single ligand parents.

2.2. Binary blending of different length alkyl chain functionalised ligands

We have previously reported an isoreticular series of layered MOFs using fu-BDC with propoxy-pentoxy alkoxy chains (ligands **3**-**5**) and showed that the longer than alkoxy chain, the greater the extent of exfoliation to MONs, with average heights found to decrease 35 > 22 > 20 nm from propoxy to pentoxy.[37] Exfoliation in MeCN resulted in loss of DMF from the axial PW sites. Pawley refinement showed that these desolvated structures maintained a similar layered form of [Cu(**x**)]$_n$ (x=**3-5**). Equivalent MOF syntheses using shorter chain methoxy/ethoxy chains did not result in the adoption of an isoreticular layered structure.

3,5-MTV-MOFs. Different ratios of H$_2$**3** and H$_2$**5** (see Figure 1) were mixed to form binary blends of **3,5**-MTV-MOFs with the target structure [Cu(**3**)$_x$(**5**)$_{1-x}$(DMF)]$_n$ (x=0.10, 0.25, 0.50, 0.75 and 0.90). MOF syntheses proceeded as described above. ^{1}H-NMR spectroscopy of digested samples indicated MTV-MOF ligand incorporation was broadly in-line with input, with the content of **3** calculated to be 0.14, 0.29, 0.52, 0.79 and 0.90, respectively (ESI Figure S4). Also evident from the ^{1}H-NMR was that DMF content was not as predicted. In general, DMF content decreased with decreasing **5** fraction (ESI Table S3). PXRD of the **3,5**-MTV-MOFs showed that with a 0.9 fraction of **5**, the structure matched closely with that of [Cu(**5**)(DMF)]$_n$, however upon decreasing the **5** content and increasing the **3**, the PXRD patterns progressed from structure similar to [Cu(**5**)(DMF)]$_n$ to a structure similar to [Cu(**3**)]$_n$ (Figure 3a). The structural transition could be due to irregular packing upon increasing **3** content within the microcrystals. As **3** is two methylene units shorter than **5**, there are fewer intralayer interactions between alkoxy chains and coordinated DMF molecules, which may favour the desolvated form upon increasing **3** content.

Liquid exfoliation of a subset of **3,5**-MTV-MOFs, where x=0.9, 0.5 or 0.1, in MeCN yielded MON suspensions. AFM particle size analysis showed the lowest average height was for x=0.1 (see Figure 3e and ESI Figures S26-28), *i.e.* the largest fraction of **5** – 11 ± 6 nm (18 ± 10 and 16 ± 11 for x=0.5 and 0.1 respectively). This fits with our previous study, where Cu(**5**) produced thinner MONs than Cu(**3**). Lateral dimensions for the three samples (x=0.9, 0.5 and 0.1) were 281±191, 333±226 and 268±198 nm, respectively.

Other binary blends of different length alkyl-chain functionalised ligands. In addition, other combinations of fu-BDC ligands were used to synthesise layered MTV-MOFs. Experimental fractions of 0.5 were used in all cases.

Table 2. Ligand inclusion and DMF content for xyz-MTV MOFs using ligands **1-5**.

xyz-MTV-MOF		**1**	**2**	**3**	**4**	**5**	DMF
3,5	Input			0.50		0.50	
	Obs			0.51		0.49	0.67
2,5	Input		0.51			0.49	
	Obs		0.63			0.37	0
2,3	Input		0.50	0.50			
	Obs		0.51	0.49			0.54
345	Input			0.34	0.33	0.33	
	Obs			0.34	0.30	0.35	0.42
2345	Input		0.25	0.25	0.25	0.25	
	Obs		0.22	0.22	0.27	0.29	0.09
12345	Input	0.11	0.22	0.22	0.22	0.23	
	Obs	0.10	0.26	0.19	0.24	0.22	0.03

Ligand content is given as a fraction. DMF content is given as a fraction relative to the total ligand content.

2,5-MTV-MOF showed 0.63 and 0.37 inclusion, respectively (see Table 2), which further indicates a possible steric effect on ligand inclusion in binary systems, and negligible DMF was observed by ^{1}H-NMR (Figure S6). PXRD indicated a structure similar to that observed for high fractions of **3** in **3,5**-MTV-MOFs, i.e. a desolvated phase (ESI Figure S5).

2,3-MTV-MOF showed near quantitative ligand inclusion of 0.51 and 0.49 respectively, and a relative DMF content of 0.54. PXRD indicated a phase similar to that of $[Cu(3)(DMF)]_n$, however there are some additional peaks that could not be accounted for by this structure. This could be indicative of a secondary desolvated phase (as only 0.54 DMF fraction was observed by NMR), or a phase relating to an unknown form of a different **2**-containing MOF (also ESI Figure S5 and 6).

Binary blended MTV-MOFs were exfoliated using ultrasonication in MeCN. Tyndall scattering was observed in the colourless supernatants following centrifugation, indicating MTV-MONs were formed in both cases. AFM of **2,5**-MTV-MONs revealed notably angular MONs with square-like morphologies, with edges up to 450 nm long. Heights ranged up to 70 nm, with a few elongated oblong particles observed up to 250 nm. Particle sizing showed an average length of 315±133 nm and height of 33±17 nm (ESI Figure S30). **2,3**-MTV-MONs were smaller laterally, typically <400 nm, and ranged up to 60 nm in height. Particle sizing showed an average length of 196 ± 87 nm and particle height of 12 ± 6 nm (ESI Figure S31). This is both the thinnest average height and narrowest distribution observed thus far for these materials. Although longer chain single-ligand MOFs previously showed improved exfoliation, the combination of a chain shorter than that previously tested may aid exfoliation due to reduced interdigitation of chains between layers, resulting in decreased interlayer interactions, and improved exfoliation.

2.3. Higher order blends of alkyl- chain functionalised ligands

In order to explore the extent to which this MTV concept can be pushed within these layered frameworks, combinations of up to five different (**1-5**) ligands were blended within MOF syntheses. These materials are referred to as **xyz**-MTV-MOFs, where **xyz** is the combination of different ligands included within the

framework. LC-MS was used to confirm the ligands' incorporation (ESI Figure S8, for example), and ligand inclusion and DMF contents were quantified through ^{1}H-NMR (ESI Figures S9-10) and are summarised in Table 2. Terminal methyl proton environments were predominantly used to assign the proportions of different ligands incorporated, however α-protons were used to assign blends incorporating **1** or **2**, as the chemical shift for each ligands' α-protons was similar. The ratio of ligand found to be included within the MOFs was broadly consistent with the input reagent ratios in all cases. Contrary to the binary blends, this suggests that the synthetic kinetics are similar for each ligand, which may be a result of more random local combinations of ligands not exhibiting as much steric pressure.

PXRD of the MTV-MOFs indicated that with the increasing number of ligands incorporated, the MOFs adopt a structure similar to that of the desolvated single-ligand MOF structure of $[Cu(3-5)]_n$ (see Figure 4). This is corroborated by the decreased DMF content of the materials (Table 2). The fact that there was still DMF observed by NMR may result from DMF that remained in the pore spaces created by inefficient packing between different length alkoxy chains between layers of the MTV-framework.

Liquid ultrasonication of the MTV-MOFs in MeCN followed by centrifugation to recollect unexfoliated material, resulted in MTV-MON suspensions. These were drop-cast onto mica for AFM analysis. Average particle heights and lateral dimensions were calculated using SPIP software and are summarised in Table 3 (ESI Figures S33-35). Notably, heights of the tertiary-quinternary blends are remarkably similar, around 20 ± 11 nm. This suggests that incorporation of increasing numbers of different ligands has no adverse effect on the structure and exfoliation potential. Average lengths sit within large size distributions, and DLS calculated the hydrodynamic diameter to be 214, 215 and 186 nm for **345**-, **2345**- and **12345**-MTV-MONs, respectively. PXRD of the recollected unexfoliated material
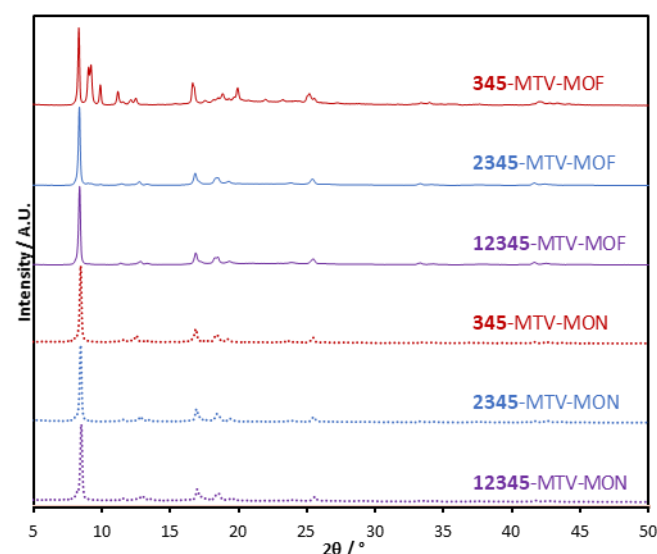

Figure 4. PXRD patterns of MTV-MOFs as synthesised, and material recollected from centrifugation following ultrasonic exfoliation (MTV-MONs).
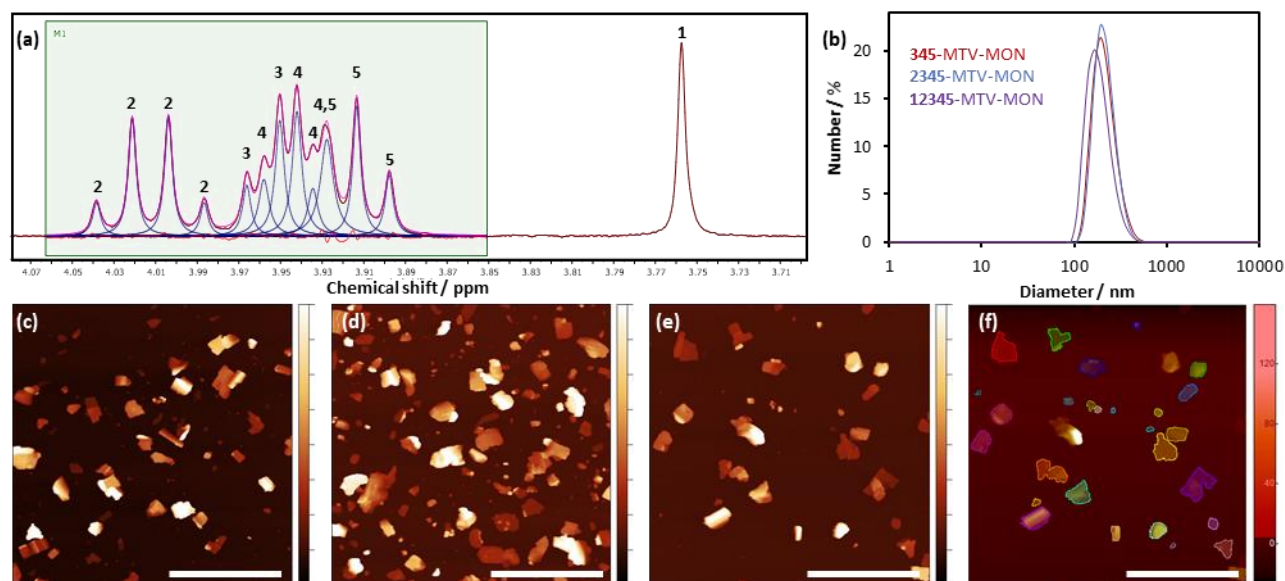
Figure 5. (a) Example deconvolution of the α-proton region for diacids H21-5 from a digested sample of **1234**5-MTV-MON. Proton contributions from the different diacids are indicated. Spectral trace is burgandy, deconvoluted peaks are blue, the fitted line is pink and the difference plot is red. (b) DLS data for MTV-MONs from exfoliation in MeCN. (c-e) AFM topographical images of **345**-, **2345**- and **12345**-MTV-MONs, respectively, from exfoliation in MeCN. Lateral scale bars are 2 µm and z-scale is 0-80 nm. (f) Automated particle recognition using SPIP software. The lateral scale bar is 2 µm.

after drying indicated that all three MTV-MONs adopted a similar phase, which matches well with the previous study on the single-ligand analogues of [Cu(**3-5**)]n,[37] therefore we suggest these MTV-MONs adopt a similar desolvated structure.

It is worth noting that previous attempts to synthesise single-ligand MOFs using ligands **1** and **2** produced mixed or unknown phases. This work suggests that incorporation of these ligands within a blended system facilitates their inclusion into a layered form. This suggests that it is possible to incorporate fractions of ligands into an expected structure that would not form that structure if included individually. MTV-MONs therefore provide a route to adding non-layer forming ligands, offering opportunities for more advanced 2D layer framework design.

Table 3. Summary of MON average particle size data.

MON	n	Length	Height	AR*	Diameter†
3	150	285±151	26±17	15±10	185[37]
4	113	305±162	17±10	20±10	213[37]
5	115	334±195	14±8	26±13	247[37]
5*	61	587±262	35±18	18±4	179[35]
5,5*-MTV-MON	187	280±217	14±10	29±29	210
3,5-MTV-MON	62	333±223	18±10	20±12	221
2,5-MTV-MON	55	315±133	33±17	11±6	197
2,3-MTV-MON	70	196±87	12±6	18±8	109
345-MTV-MON	90	319±204	20±11	18±10	214
2345-MTV-MON	173	263±201	20±10	14±10	215
12345-MTV-MON	53	294±148	21±12	18±12	186

All size values are in nm. *AR=aspect ratio, defined as length/height (calculated for each particle). †Hydrodynamic diameter according to number average DLS data.

3. Conclusions

In this study, we demonstrated the formation of MTV-MONs for the first time and studied the effect of different ligand blends on the structure and properties of the MONs produced.

A new series of layered mixed-ligand MTV-MOFs was synthesised using different combinations of six different ligands (**1-5, 5***), which incorporated ligands functionalised with alkoxy chains with different lengths and polarities.

Binary combinations of ligands were blended to form isoreticular series of MOFs with only small changes in unit cell dimensions. Ligands were generally incorporated into the MOF in the input reagent ratios, apart from **2,5**-MTV-MOF, where the shorter chain is overrepresented (63 %). We attribute this to the large difference in sterics of the two different ligands. Shorter alkyl chain lengths and higher order blends tended to result in loss of DMF leading to a common desolvated structure that has been previously characterised for single-ligand MOFs [Cu(**3-5**)]n. MTV-MOFs were formed using up to quinternary blends of ligands.

Liquid ultrasonic exfoliation of MTV-MOFs resulted in isolation of mixed-ligand MTV-MONs for the first time. Exfoliation of **5,5***-MTV-MOF in Et2O produced monolayer MONs with thickness approximately 1.2 nm, and exfoliation in water produced large MONs >5 µm laterally with approximately 5 nm height, demonstrating enhanced exfoliation compared to the parent single-ligand MOFs. Labile coordination at the axial PW sites were exploited to calculate the binding constant of imidazole from aqueous solution as K_a=1640±130 M^{-1}, roughly half-way between that of the parent single-ligand MONs. This demonstrated that chemical properties can be fine-tuned by

controlling the ratio of nanosheets. Concentrations of **5,5***-MTV-MON in suspension were found to be higher than that of the single-ligand parents in MeCN, water and Et$_2$O. This demonstrates that the MTV-MONs can have dispersion properties superior to that of the parent single ligand MONs.

A series of MTV-MOFs using ligands functionalised with varying lengths of alkyl chain were exfoliated in MeCN to see if mismatches in chain length resulted in improved exfoliation. Amongst the binary 1:1 mixtures of nanosheets, combinations of **2** and **3** produced the thinnest sheets (12±6 nm) and those with the largest mis-match in chain length, 2 and 5 produced the thickest nanosheets. A series of **3,5**-MTV-MOFs using different diacid stoichiometries additionally demonstrated that ligand ratio can be controlled by modifying the reaction stoichiometry. The average height of MTV-MONs exfoliated from tertiary-quinternary blends were remarkably similar across tertiary and higher blends, all approximately 20±11 nm. This suggests that further mismatching of different ligands does not result in improved exfoliation. In all, seven different blends of MTV-MOFs were synthesised and exfoliated to form MTV-MONs. The maximum number of ligands incorporated was five, with BDC functionalised with methoxy-pentoxy chains (*i.e.* ligands **1**-**5**). Overall, this study introduces mixed-ligand MTV-MONs as a new approach to enhancing the exfoliation of layered frameworks and tuning their properties.

As with MOFs, the multivariate approach provides a mechanism for introducing heterogenerity within MONs. We anticipate this approach will be widely applied to isoreticular series of MONs based on other SBU/ligand combinations, such as the [M(fu-benzimidazole)$_2$]$_n$[44,53] and UiO-67-type[54] series. This approach also provides distinct opportunities for improving the properties of MONs, such as through mismatching of interlayer interactions to aid exfoliation, or projecting multiple functional groups into solution to aid stability in suspension. As our study shows, combining multiple ligands can allow for fine-tuning of structure and properties. However, this approach can also lead to unexpected results where the properties are more than the sum of their parts.

4. Experimental

Materials were purchased from commercial suppliers and used without further purification.

4.1. fu-H$_2$BDC ligand precursor syntheses

fu-H$_2$BDC derivatives H$_2$(**1-5,5***) were prepared according to previously demonstrated methods.[35–37,55] Briefly, the fu-H$_2$BDC was synthesised through Williamson etherification of protected dimethyl-2,5-dihydroxybenzene-1,4-dicarboxylic acid with the corresponding fu-halide (bromide in all cases except iodide for H$_2$**1**). Deprotection in base and subsequent work-up in acid yielded the desired fu-H$_2$BDC diacid in high yields of 77-91 %.

4.2. MOF syntheses

All MOFs were synthesised on a 20-30 mg scale using a common method with mole calculations based on the anticipated structural formula [Cu(fu-BDC)(DMF)]$_n$ using a total 10% excess of ligands.[37] For example, the synthesis of 20 mg 5,5*-MTV-MOF − [Cu(**5,5***)(DMF)]$_n$ − requires 0.42 mmol copper (CuC$_{20}$H$_{29}$NO$_8$, Mr=475.00 Da). Copper nitrate trihydrate (0.42 mmol) and diacid ligand precursors H$_2$**5** (0.23 mmol) and H$_2$**5*** (0.23 mmol) were dissolved in DMF (6 mL) and sealed into a 20 mL glass reaction vial sealed with a Teflon-lined lid. This was heated at 10 C min^{-1} to 110 °C, held for 36 hrs, then cooled at 0.1 °C min^{-1} to 25 °C. The vial contents were transferred to a centrifuge tube and washed through centrifugation with DMF (3 x 5 mL) and Et$_2$O (3 x 5 mL), then transferred to a clean vial and air-dried at room temperature, yielding a blue microcrystalline powder of [Cu(**5**)$_{0.53}$(**5***)$_{0.47}$(DMF)]$_n$ (18.1 mg, 91 %). All MOF syntheses used this general synthetic method, using a total ligand excess of 10 %. For 30 mg target MOF syntheses, 9 mL DMF was used instead of 6 mL.

4.3. Liquid ultrasonic exfoliation

2 mg of MOF was suspended in 2.4 mL solvent (MeCN, water or Et$_2$O) and vortexed for 30 s then sonicated for 12 h using a Fisher brand Elmasonic P 30H ultrasonic bath operating at 80 kHz and 100 % power (320 W). Samples were rotated using an overhead stirrer to ensure even exposure and the bath was fitted with a water coil to maintain temperature at approximately 18-21 °C.[35] After sonication, samples were transferred to a centrifuge tube and centrifuged for 1 hr at 1500 rpm, which recollected unexfoliated material and yielded MON-containing supernatant.

4.4. Characterisation

Room temperature ^{1}H-NMR spectroscopy was performed with a Bruker Avance IIIHD 400 MHz spectrometer. 1H chemical shifts are reported in parts per million on the δ scale and referenced to the residual proton resonance of the solvent. Approximately 2 mg MOF was digested using 20 µL DCl (35 %) in D2O and 1 mL d_6-DMSO, resulting in solutions of diacid ligand precursors for quantification. LC-MS data were collected using an Agilent 6530 QTOF LC-MS operating in negative mode electrospray ionisation, using the samples prepared for ^{1}H-NMR. PXRD were recorded using a Bruker D8 Advance powder X-ray diffractometer equipped with a Lynxeye detector, using Cu k$_α$ radiation (λ=1.5406 Å) operating in capillary mode (MOFs) or flat-plate mode (materials recollected from centrifugation. For capillary mode, samples were ground and loaded into a 0.7 mm internal diameter borosilicate capillary. For flat plate, samples were sprinkled onto a low-background silicon plate. FTIR spectra were recorded with a PerkinElmer Spectrum One spectrometer equipped with a diamond ATR accessory. Data were collected from 500 to 4000 cm^{-1} using a resolution of 1 cm^{-1} and 8 scans. Elemental analysis was performed with an Elementar vario MICRO cube. UV-Vis spectroscopy was performed on a Cary 50 UV-Vis spectrophotometer, in the range 800-200 nm (solvent dependant) with a 1 nm resolution and 600 nm min^{-1} scan speed. Samples were prepared for SEM analysis on a carbon sticky tab loaded on an aluminium sample stub and coated with approximately 20 nm gold using an

Edwards S150B sputter coater. SEM micrographs were collected using a TESCAN VEGA3 LMU SEM instrument operating in secondary electron mode. AFM was performed with a Bruker Multimode 5 AFM operating in soft-tapping mode using Bruker OTESPA-R3 cantilevers. Samples were prepared by drop-casting 10 μL MON suspension onto freshly cleaved mica held on a magnetic sample holder which was pre-heated to just below the boiling point of the solvent. Images were processed using standard techniques within Gwyddion image processing software.[56] DLS data were collected using a Malvern Zetasizer Nano Series particle size analyzer equipped with a He–Ne laser at 633 nm, operating in backscatter mode (173°).

4.5. Particle sizing

Particle sizing was performed using SPIP software. Prior to analysis, AFM images were plane levelled, scars were removed and the background was zeroed. The particle and pore analysis tool was used to pick and size particles. The "threshold" detection method was used, which varied between images depending on how well the background had been levelled, between 2 to 6 nm. Post-processing filters for particle inclusion were used across all images: (i) minimum length of 80 nm to neglect image defects and small fragments on the sample surface; (ii) minimum height of 6 nm to avoid detecting small errors in the scan; (iii) maximum height of 150 nm to neglect large particles/ agglomerates or jumps in the probe/surface contact. Particles that lay partly on an edge of the image were not included.

Conflicts of interest

There are no conflicts to declare.

Acknowledgements

Notes and references

1   M. Zhao, Y. Huang, Y. Peng, Z. Huang, Q. Ma and H. Zhang, *Chem. Soc. Rev.*, 2018, **47**, 6267–6295.

2   D. J. Ashworth and J. A. Foster, *J. Mater. Chem. A*, 2018, **6**, 16292–16307.

3   R. Sakamoto, K. Takada, T. Pal, H. Maeda, T. Kambe and H. Nishihara, *Chem. Commun.*, 2017, **53**, 5781–5801.

4   D. Rodríguez-San-Miguel, P. Amo-Ochoa and F. Zamora, *Chem. Commun.*, 2016, **52**, 4113–4127.

5   W. Zhao, J. Peng, W. Wang, S. Liu, Q. Zhao and W. Huang, *Coord. Chem. Rev.*, 2018, **377**, 44–63.

6   M. Xu, S. S. Yang and Z.-Y. Gu, *Chem. - A Eur. J.*, 2018,

7   J. Duan, Y. Li, Y. Pan, N. Behera and W. Jin, *Coord. Chem. Rev.*, 2019, **395**, 25–45.

8   A. Dhakshinamoorthy, A. M. Asiri and H. Garcia, *Adv. Mater.*, 2019, **31**, 1900617.

9   S. Kim, H. Wang and Y. M. Lee, *Angew. Chemie Int. Ed.*, 2019, **58**, DOI:10.1002/anie.201814349.

10   R. Mas-Ballesté, C. Gómez-Navarro, J. Gómez-Herrero and F. Zamora, *Nanoscale*, 2011, **3**, 20–30.

11   S. Abdolhosseinzadeh, H. Asgharzadeh and H. S. Kim, *Sci. Rep.*, 2015, **5**, 1–7.

12   W. Gao, L. B. Alemany, L. Ci and P. M. Ajayan, *Nat. Chem.*, 2009, **1**, 403–408.

13   G. Zhan and H. C. Zeng, *Adv. Funct. Mater.*, 2016, **26**, 3268–3281.

14   Y. Huang, M. Zhao, S. Han, Z. Lai, J. Yang, C. Tan, Q. Ma, Q. Lu, J. Chen, X. Zhang, Z. Zhang, B. Li, B. Chen, Y. Zong and H. Zhang, *Adv. Mater.*, 2017, **29**, 1–5.

15   J. Huang, Y. Li, R. K. Huang, C. T. He, L. Gong, Q. Hu, L. Wang, Y. T. Xu, X. Y. Tian, S. Y. Liu, Z. M. Ye, F. Wang, D. D. Zhou, W. X. Zhang and J. P. Zhang, *Angew. Chemie - Int. Ed.*, 2018, **57**, 4632–4636.

16   Y. Peng, Y. Li, Y. Ban, H. Jin, Jiao, Wenmei, X. Liu and W. Yang, *Science*, 2014, **346**, 1356–1359.

17   Y. Peng, Y. Li, Y. Ban and W. Yang, *Angew. Chemie - Int. Ed.*, 2017, **56**, 9757–9761.

18   S. Feng, M. Bu, J. Pang, W. Fan, L. Fan, H. Zhao, G. Yang, H. Guo, G. Kong, H. Sun, Z. Kang and D. Sun, *J. Memb. Sci.*, 2020, **593**, 117404.

19   Z.-R. Tao, J.-X. Wu, Y.-J. Zhao, M. Xu, W.-Q. Tang, Q.-H. Zhang, L. Gu, D.-H. Liu and Z.-Y. Gu, *Nat. Commun.*, 2019, **10**, 1–8.

20   D. Sheberla, L. Sun, M. A. Blood-Forsythe, S. Er, C. R. Wade, C. K. Brozek, A. Aspuru-Guzik and M. Dincă, *J. Am. Chem. Soc.*, 2014, **136**, 8859–8862.

21   K. Takada, R. Sakamoto, S. T. Yi, S. Katagiri, T. Kambe and H. Nishihara, *J. Am. Chem. Soc.*, 2015, **137**, 4681–4689.

22   C. Li, X. Hu, W. Tong, W. Yan, X. Lou, M. Shen and B. Hu, *ACS Appl. Mater. Interfaces*, 2017, **9**, 29829–29838.

23   J.-X. Wu, S.-Z. Hou, X.-D. Zhang, M. Xu, H.-F. Yang, P.-S. Cao and Z.-Y. Gu, *Chem. Sci.*, 2019, **10**, 2199–2205.

24   J. Nicks, J. Zhang and J. A. Foster, *Chem. Commun.*, 2019, **55**, 8788–8791.

25   Z. Lin, N. C. Thacker, T. Sawano, T. Drake, P. Ji, G. Lan, L. Cao, S. Liu, C. Wang and W. Lin, *Chem. Sci.*, 2017, **9**, 143–151.

26   R. Xu, Z. Cai, G. Lan and W. Lin, *Inorg. Chem.*, 2018, **57**, 10489–10493.

27   G. Lan, Z. Li, S. S. Veroneau, Y.-Y. Zhu, Z. Xu, C. Wang and W. Lin, *J. Am. Chem. Soc.*, 2018, **140**, 12369–12373.

28   G. Lan, Y. Quan, M. Wang, T. Nash, E. You, Y. Song, S. S. Veroneau, X. Jiang and W. Lin, *J. Am. Chem. Soc.*, 2019, **141**, 15767–15772.

29   O. M. Yaghi, M. O'Keeffe, N. W. Ockwig, H. K. Chae, M. Eddaoudi and J. Kim, *Nature*, 2003, **423**, 705–714.

30   O. M. Yaghi, *J. Am. Chem. Soc.*, 2016, **138**, 15507–15509.

15131–15142.

31   O. M. Yaghi, *ACS Cent. Sci.*, 2019, **5**, 1295–1300.

32   Z. Q. Li, L. G. Qiu, W. Wang, T. Xu, Y. Wu and X. Jiang, *Inorg. Chem. Commun.*, 2008, **11**, 1375–1377.

33   M. Shete, P. Kumar, J. E. Bachman, X. Ma, Z. P. Smith, W. Xu, K. A. Mkhoyan, J. R. Long and M. Tsapatsis, *J. Memb. Sci.*, 2018, **549**, 312–320.

34   A. Pustovarenko, M. G. Goesten, S. Sachdeva, M. Shan, Z. Amghouz, Y. Belmabkhout, A. Dikhtiarenko, T. Rodenas, D. Keskin, I. K. Voets, B. M. Weckhuysen, M. Eddaoudi, L. C. P. M. de Smet, E. J. R. Sudhölter, F. Kapteijn, B. Seoane and J. Gascon, *Adv. Mater.*, 2018, **30**, 1707234.

35   D. J. Ashworth, A. Cooper, M. Trueman, R. W. M. Al-Saedi, S. D. Liam, A. J. Meijer and J. A. Foster, *Chem. - A Eur. J.*, 2018, **24**, 17986–17996.

36   J. A. Foster, S. Henke, A. Schneemann, R. A. Fischer and A. K. Cheetham, *Chem. Commun.*, 2016, **52**, 10474–10477.

37   D. J. Ashworth, T. M. Roseveare, A. Schneemann, M. Flint, I. Dominguez Bernáldes, P. Vervoorts, R. A. Fischer, L. Brammer and J. A. Foster, *Inorg. Chem.*, 2019, **58**, 10837–10845.

38   H. Deng, C. J. Doonan, H. Furukawa, R. B. Ferreira, J. Towne, C. B. Knobler, B. Wang and O. M. Yaghi, *Science*, 2010, **327**, 846–850.

39   A. Helal, Z. H. Yamani, K. E. Cordova and O. M. Yaghi, *Natl. Sci. Rev.*, 2017, **4**, 296–298.

40   A. M. Fracaroli, P. Siman, D. A. Nagib, M. Suzuki, H. Furukawa, F. D. Toste and O. M. Yaghi, *J. Am. Chem. Soc.*, 2016, **138**, 8352–8355.

41   B. Tu, Q. Pang, E. Ning, W. Yan, Y. Qi, D. Wu and Q. Li, *J. Am. Chem. Soc.*, 2015, **137**, 13456–13459.

42   Q. Liu, H. Cong and H. Deng, *J. Am. Chem. Soc.*, 2016, **138**, 13822–13825.

43   L. Zhuang, L. Ge, H. Liu, Z. Jiang, Y. Jia, Z. Li, D. Yang, R. K. Hocking, M. Li, L. Zhang, X. Wang, X. Yao and Z. Zhu, *Angew. Chemie Int. Ed.*, 2019, **58**, 13565–13572.

44   J. López-Cabrelles, S. Mañas-Valero, I. J. Vitórica-Yrezábal, P. J. Bereciartua, J. A. Rodríguez-Velamazán, J. C. Waerenborgh, B. J. C. Vieira, D. Davidovikj, P. G. Steeneken, H. S. J. van der Zant, G. Mínguez Espallargas and E. Coronado, *Nat. Chem.*, 2018, **10**, 1001–1007.

45   V. K. M. Au, K. Nakayashiki, H. Huang, S. Suginome, H. Sato and T. Aida, *J. Am. Chem. Soc.*, 2019, **141**, 53–57.

46   T. Rodenas, I. Luz, G. Prieto, B. Seoane, H. Miro, A. Corma, F. Kapteijn, F. X. Llabrés i Xamena and J. Gascon, *Nat. Mater.*, 2015, **14**, 48–55.

47   Y. Wang, M. Zhao, J. Ping, B. Chen, X. Cao, Y. Huang, C. Tan, Q. Ma, S. Wu, Y. Yu, Q. Lu, J. Chen, W. Zhao, Y. Ying and H. Zhang, *Adv. Mater.*, 2016, **28**, 4149–4155.

48   M. Zhao, Y. Wang, Q. Ma, Y. Huang, X. Zhang, J. Ping, Z. Zhang, Q. Lu, Y. Yu, H. Xu, Y. Zhao and H. Zhang, *Adv. Mater.*, 2015, **27**, 7372–7378.

49   H. Li, M. Eddaoudi, T. L. Groy and O. M. Yaghi, *J. Am. Chem. Soc.*, 1998, **120**, 8571–8572.

50   C. G. Carson, K. Hardcastle, J. Schwartz, X. Liu, C. Hoffmann, R. A. Gerhardt and R. Tannenbaum, *Eur. J. Inorg. Chem.*, 2009, **16**, 2338–2343.

51   X. Kong, H. Deng, F. Yan, J. Kim, J. A. Swisher, B. Smit, O. M. Yaghi and J. A. Reimer, *Science*, 2013, **341**, 882–885.

52   W. Bai, S. Li, J. Ma, W. Cao and J. Zheng, *J. Mater. Chem. A*, 2019, **7**, 9086–9098.

53   Yuan Peng, Yanshuo Li, Yujie Ban, Hua Jin, Wenmei Jiao, Xinlei Liu and Weishen Yang, *Science*, 2014, **346**, 1356–1359.

54   M. J. Cliffe, E. Castillo-Martínez, Y. Wu, J. Lee, A. C. Forse, F. C. N. Firth, P. Z. Moghadam, D. Fairen-Jimenez, M. W. Gaultois, J. A. Hill, O. V. Magdysyuk, B. Slater, A. L. Goodwin and C. P. Grey, *J. Am. Chem. Soc.*, 2017, **139**, 5397–5404.

55   J. M. Chem, S. Henke, A. Schneemann, S. Kapoor, R. A. Fischer, R. Winter and R. A. Fischer, *J. Mater. Chem.*, 2012, **22**, 909–918.

56   D. Nečas and P. Klapetek, *Cent. Eur. J. Phys.*, 2012, **10**, 181–188.

Blending functionalised ligands to form multivariate metal-organic nanosheets (MTV-MONs) with tuneable surface chemistry

David J. Ashworth[a] and Jonathan A. Foster*[a]

a. Dept. of Chemistry, The University of Sheffield, Dainton Building, Brook Hill, Sheffield, S3 7HF, UK.

Electronic Supplementary Information

Contents

1. MOF characterisation

1.1. 5,5*-MTV-MOF

Table S1. Elemental analysis of **5,5***-MTV-MOF

	Calculated / %			Observed / %		
	C	**H**	**N**	**C**	**H**	**N**
5,5*-MTV-MOF	50.57	6.15	2.95	50.80	6.19	2.64
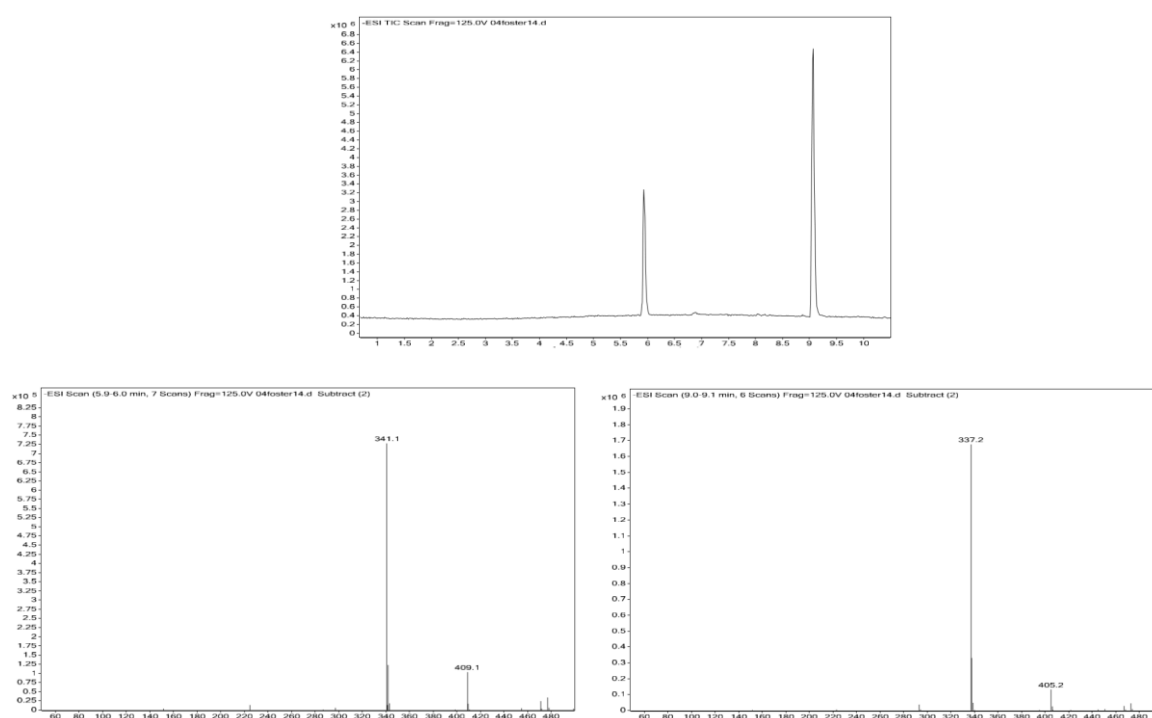
Figure S1. LC-MS data for digested **5,5***-MTV-MOF. Molecular ions for H**5***$^-$ and H**5**$^-$ appear at m/z= 341.1 and 337.2, respectively.
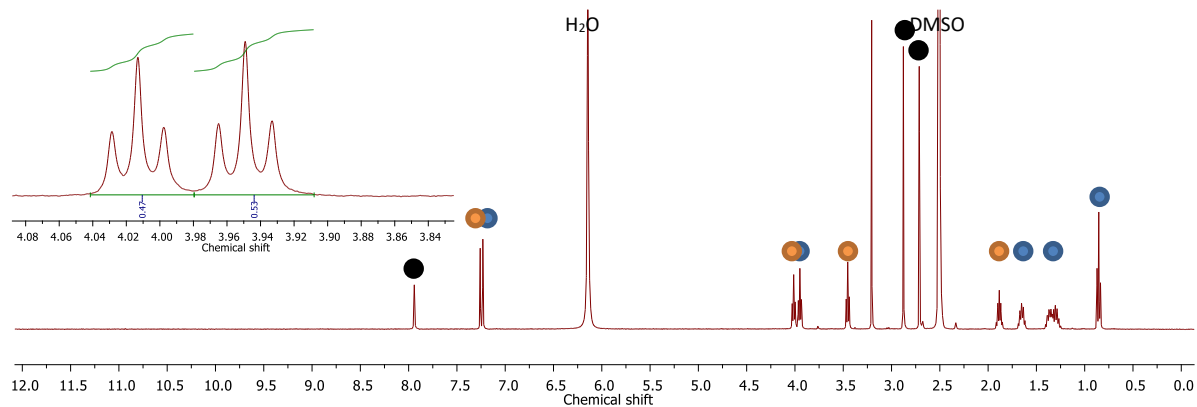
Figure S2. Room temperature ^{1}H-NMR spectra of digested **5,5***-MTV-MOF, indicating a ligand ratio of **5** : **5*** of 0.53 : 0.47. Peaks corresponding to **5** (blue), **5*** (orange), DMF (black), DMSO and H_2O are indicated.
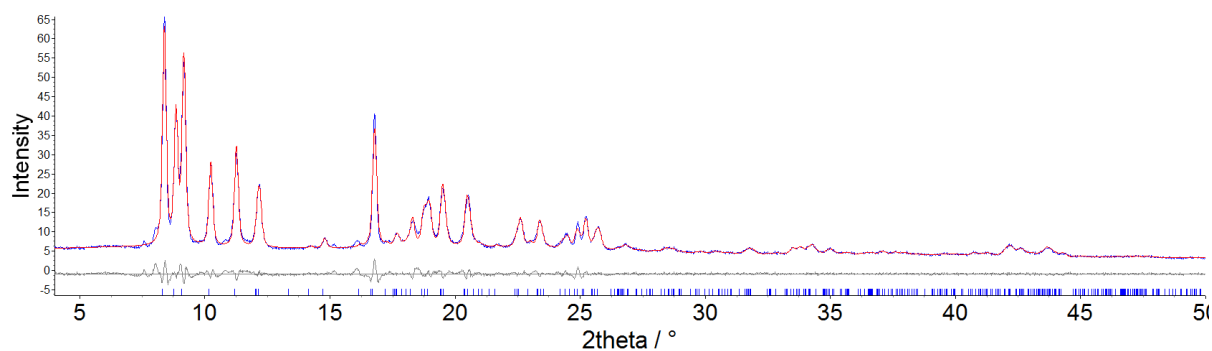
Figure S3. Pawley fits of 5,5*-MTV-MOF, illustrating the observed (blue) and calculated (red) diffraction patterns, with the difference plot [I_{obs}-I_{calc}] (grey) (2θ range 4.0 – 50.0 °, d_{min} = 1.82 Å). Blue tick lines denote calculated peak positions.

Table S2. PXRD refinement fitting data for **5,5***-MTV-MOF, compared with the previously published single-ligand MOFs structures.

MOF	Space group	a / Å	b / Å	c / Å	α / °	β / °	γ / °	Vol / Å³	R_{wp}	$R_{wp'}$
Cu(**5**)(DMF)[1]	P-1	10.845	10.801	10.853	83.82	79.82	67.44	1154.4	0.0517	0.2455
5,5*-MTV-MOF	P-1	10.597(3)	10.803(2)	10.845(3)	85.65(3)	79.00(2)	68.90(1)	1137.0(5)	4.989	11.761
Cu(**5***)(DMF)[2]	P-1	10.525	10.762	10.807	85.29	77.11	68.26	1108.4	2.898	unreported

1.2. 35-MTV-MOFs
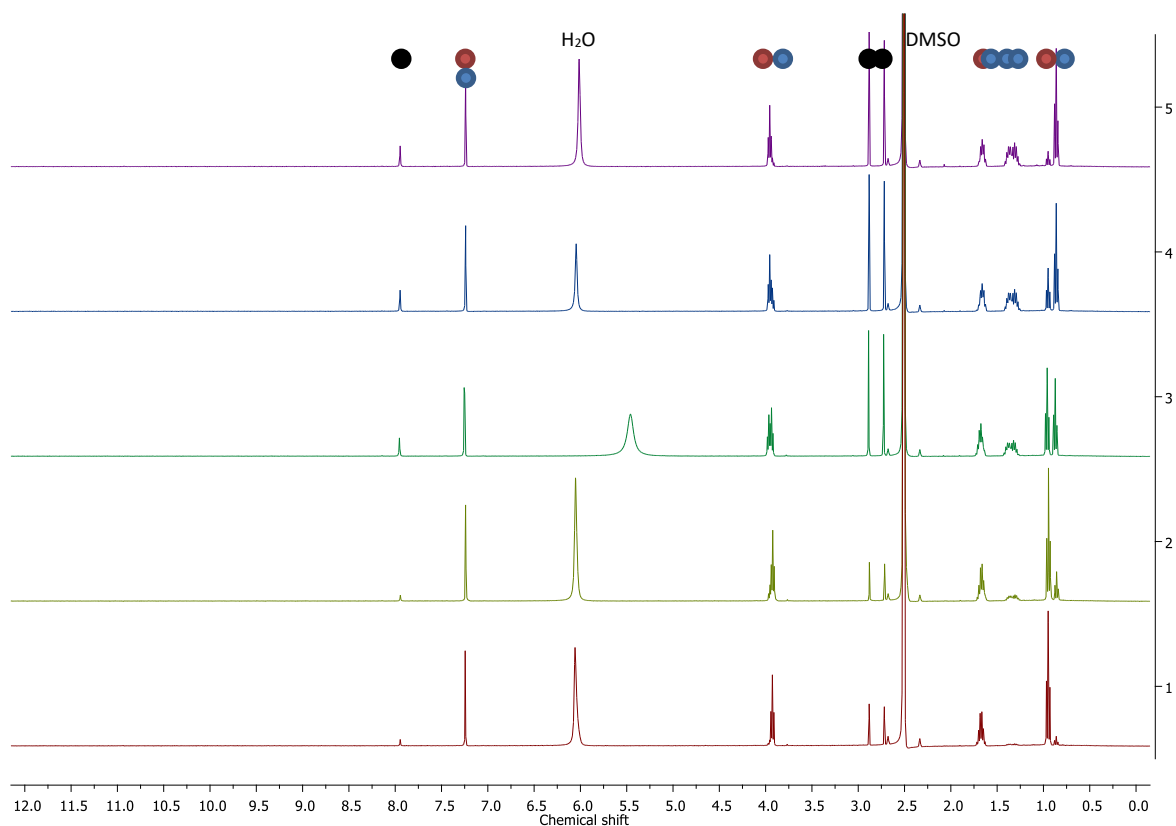
Figure S4. Room temperature 1H NMR spectra of digested **35**-MTV-MOF blends. Peaks corresponding to **3** (red circle), **5** (blue circle), DMF (black), water and DMSO are indicated. Inset, the area used for ligand quantification.

Table S3. Ligand and DMF inclusion in Cu(**3**)$_x$(**5**)$_y$ blends.

Input / %		Observed / %		
3	**5**	**3**	**5**	**DMF***
10	90	14	86	83
25	75	29	71	76
50	50	52	49	63
75	25	79	21	24
90	10	90	10	28

* DMF % is reported relative to a total ligand:DMF ratio of 1:1, i.e. for a fully solvated structure.

1.3. Other binary blends
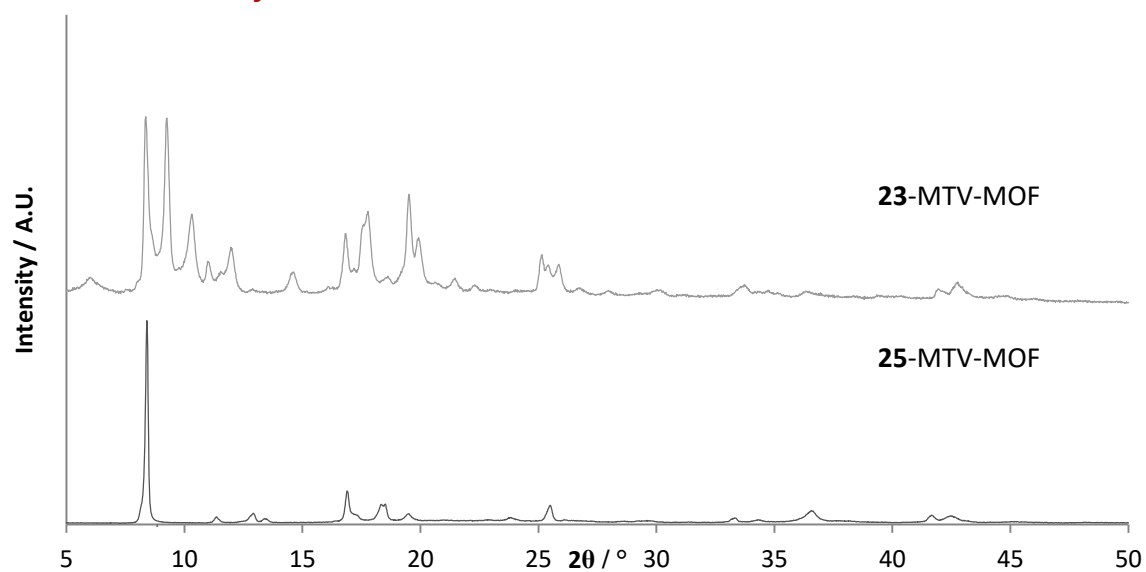
Figure S5. PXRD patterns of binary MTV-MOFs synthesised using combinations of ligands **2**, **3** and **5**.
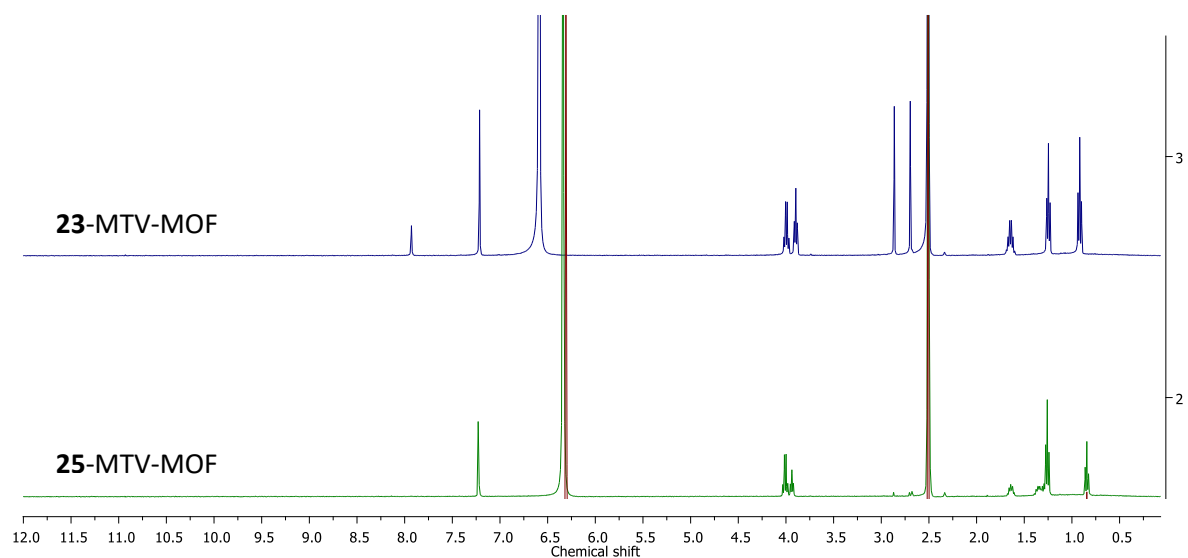
Figure S6. Room temperature ^{1}H NMR spectra of digested binary MTV-MOFs synthesised using combinations of ligands **2**, **3**, and **5**.

1.4. Tertiary and higher blends of MTV-MOFs
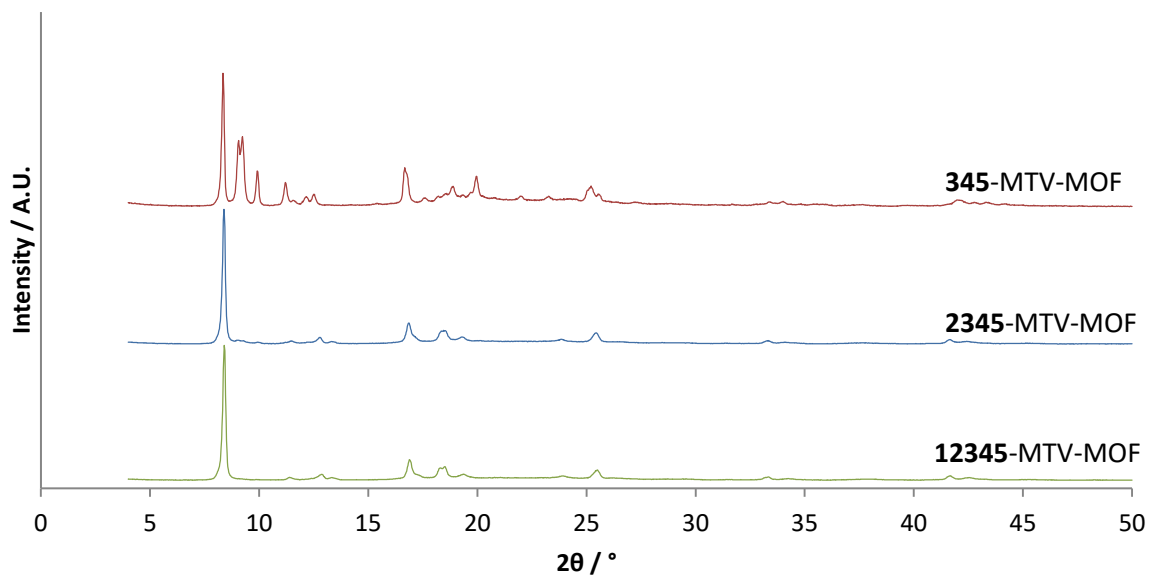
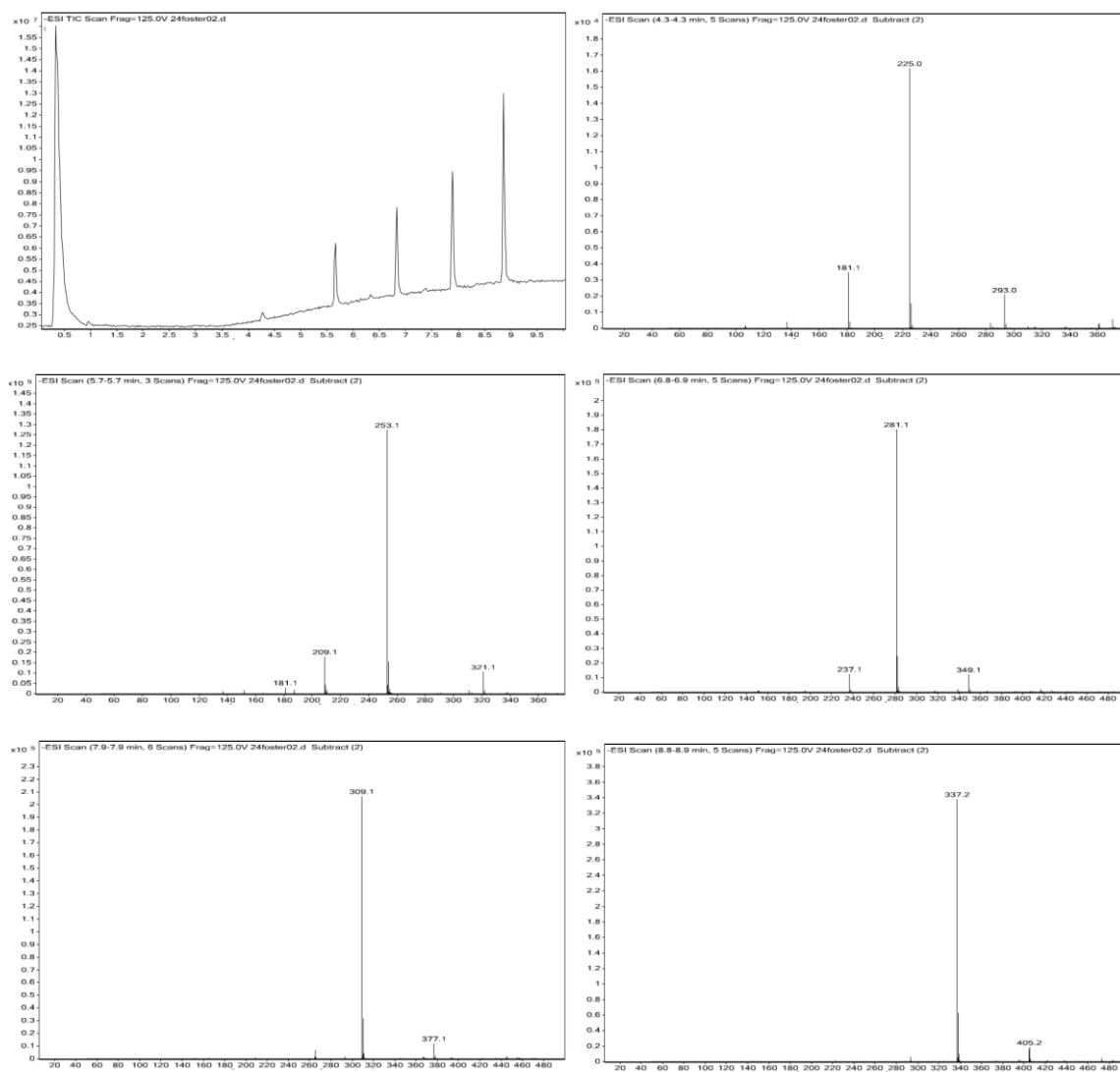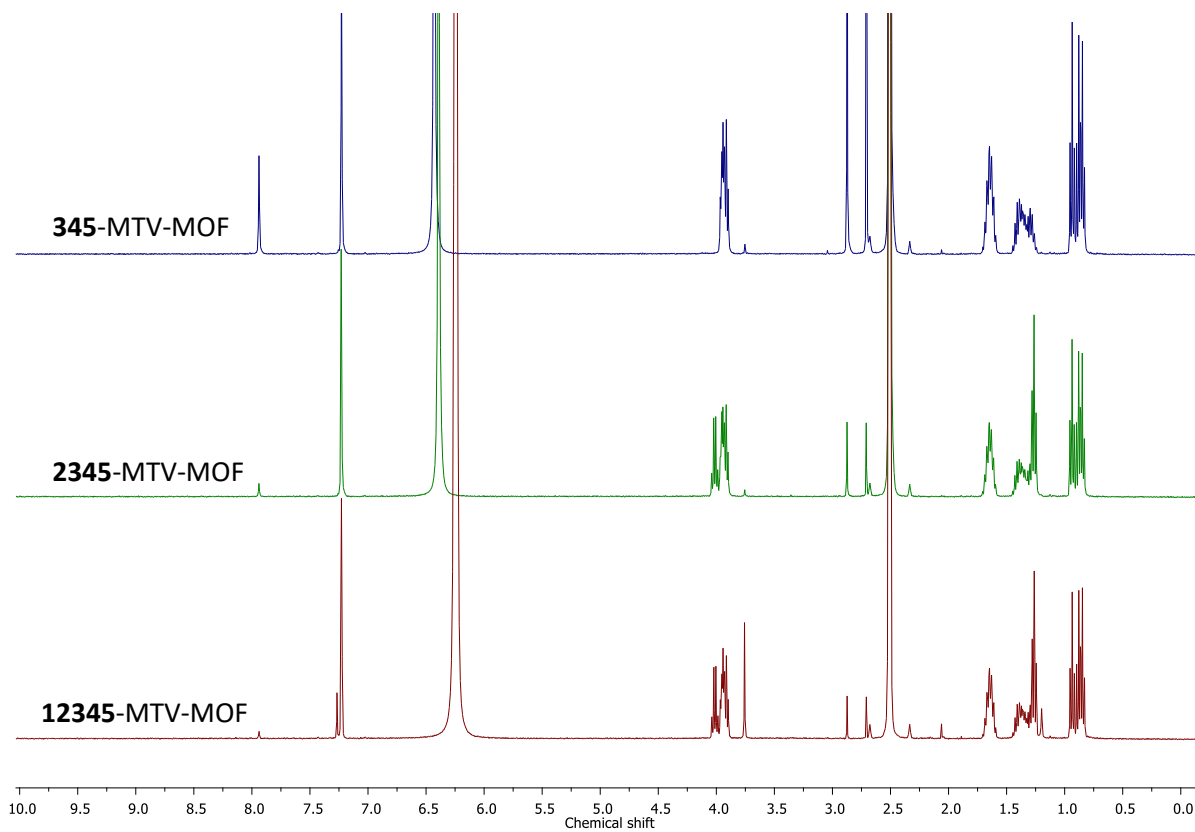**Figure S7.** PXRD patterns of MTV MOFs synthesised using combinations of ligands **1**, **2**, **3**, **4** and **5**.

Figure S8. LC-MS spectra for **12345**-MTV-MOF

Figure S9. Room temperature 1H NMR spectra of digested MTV-MOFs synthesised using combinations of ligands **1**, **2**, **3**, **4** and **5**.

Table S4. Ligand and DMF inclusion within MTV MOFs

-MTV-MOF	Input					Observed					
	1	**2**	**3**	**4**	**5**	**1**	**2**	**3**	**4**	**5**	**DMF**
345			0.33	0.33	0.34			0.26	0.36	0.37	0.76
2345		0.25	0.25	0.25	0.25		0.22	0.22	0.27	0.29	0.14
12345	0.11	0.22	0.22	0.22	0.23	0.10	0.26	0.19	0.24	0.22	0.5
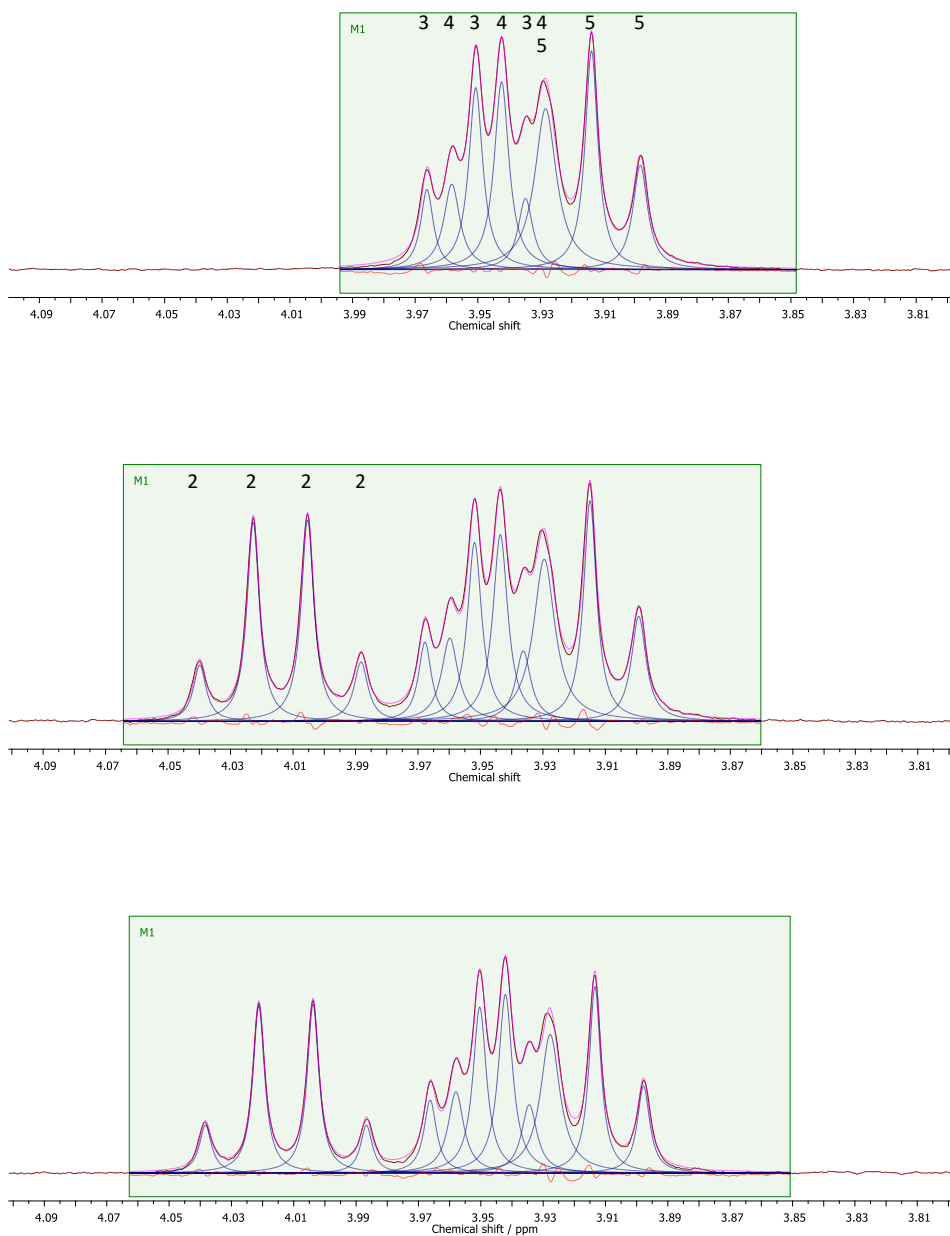
Figure S10. Peak fits used to quantify ligand inclusion in MTV-MOFs synthesised using combinations of ligands **1**, **2**, **3**, **4** and **5**, using spectra portrayed in Figure S9. Top-bottom: **345**-MTV-MOF, **2345**-MTV-MOF and **12345**-MTV-MOF.

2. MON characterisation

2.1. 5,5*-MTV-MONs

2.1.1. ^{1}H-NMR
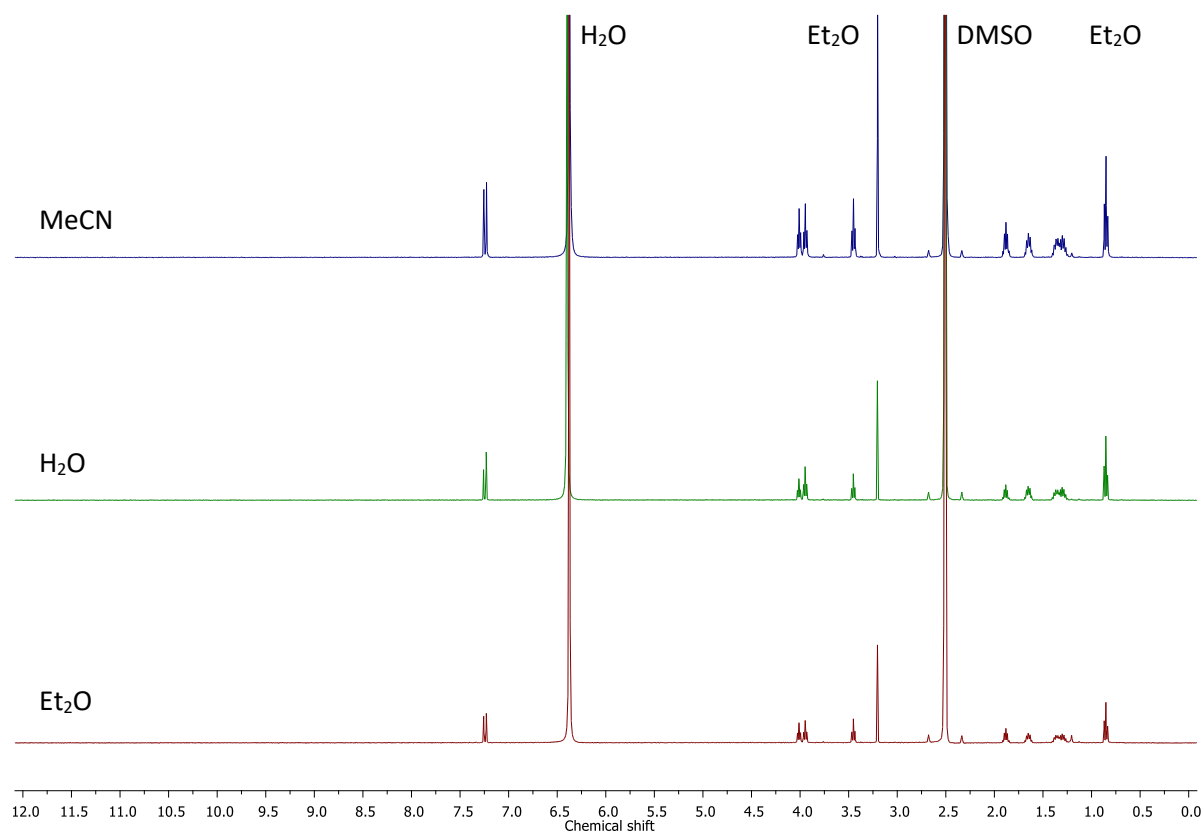
Figure S11. Room temperature 1H NMR spectra of **5,5***-MTV-MOF after exfoliation in MeCN, H_2O and Et_2O

2.1.2. PXRD
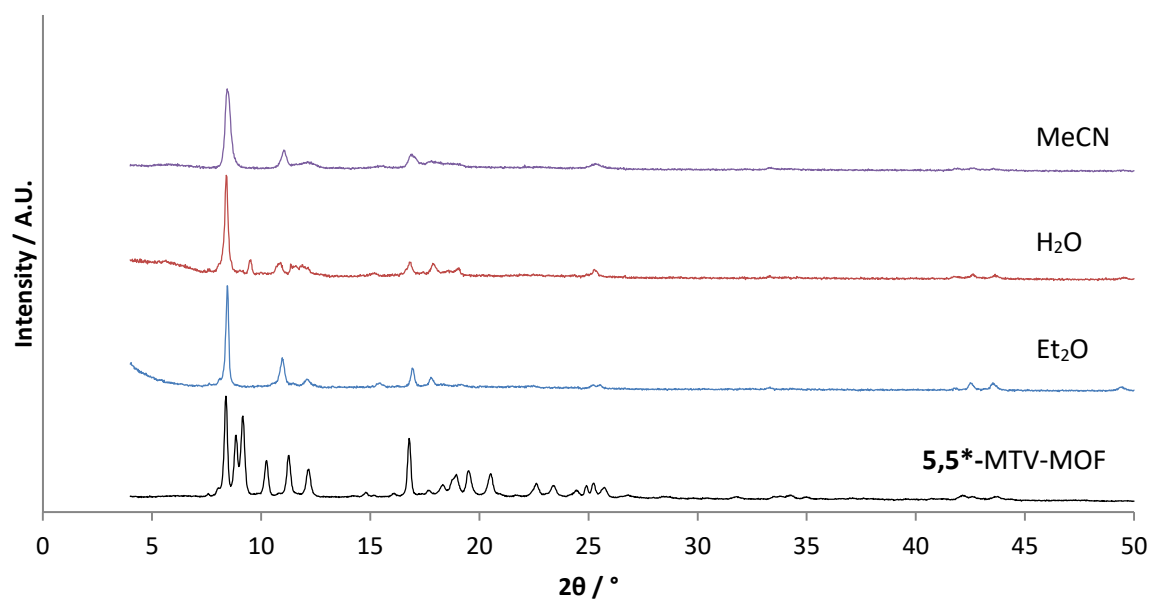
Figure S12. PXRD patterns of **5,5***-MTV-MOF after exfoliation in MeCN, H_2O and diethyl ether (Et_2O), compared to the input MOF.

2.1.3. FTIR spectroscopy
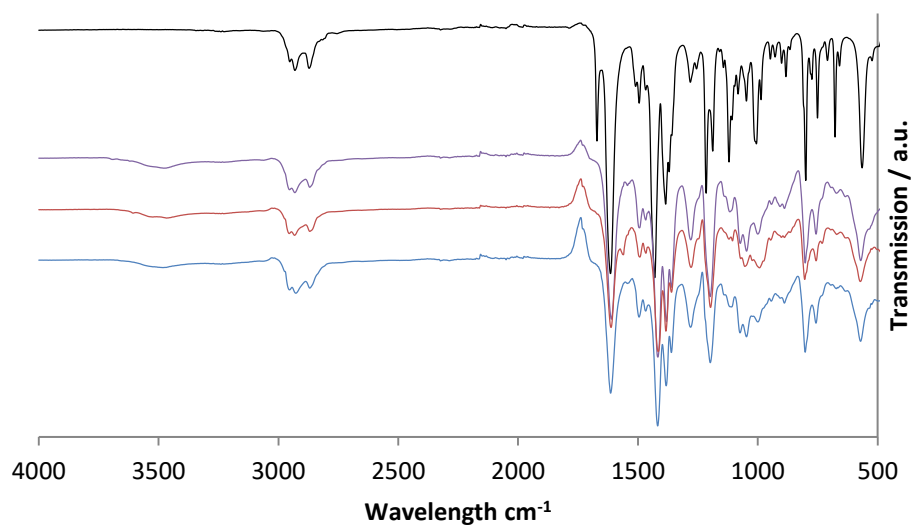
Figure S13. FTIR spectra of **5,5***-MTV-MOF (black) after exfoliation in MeCN (purple), H_2O (red) and Et_2O (blue). Note the absence of the C=O stretch at 1671 cm^{-1} in the exfoliated materials, indicating DMF loss.
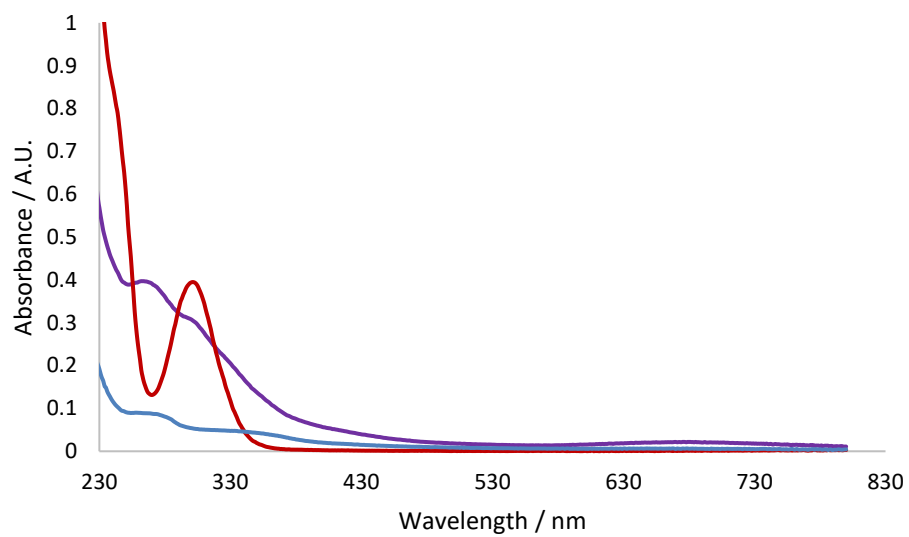
2.1.4. UV-Vis

Figure S14. UV-Vis spectra of **5,5***-MTV-MOF after exfoliation in MeCN (purple), H_2O (red) and Et_2O (blue). Dilutions used were 1 in 6, 6 and 5, respectively.
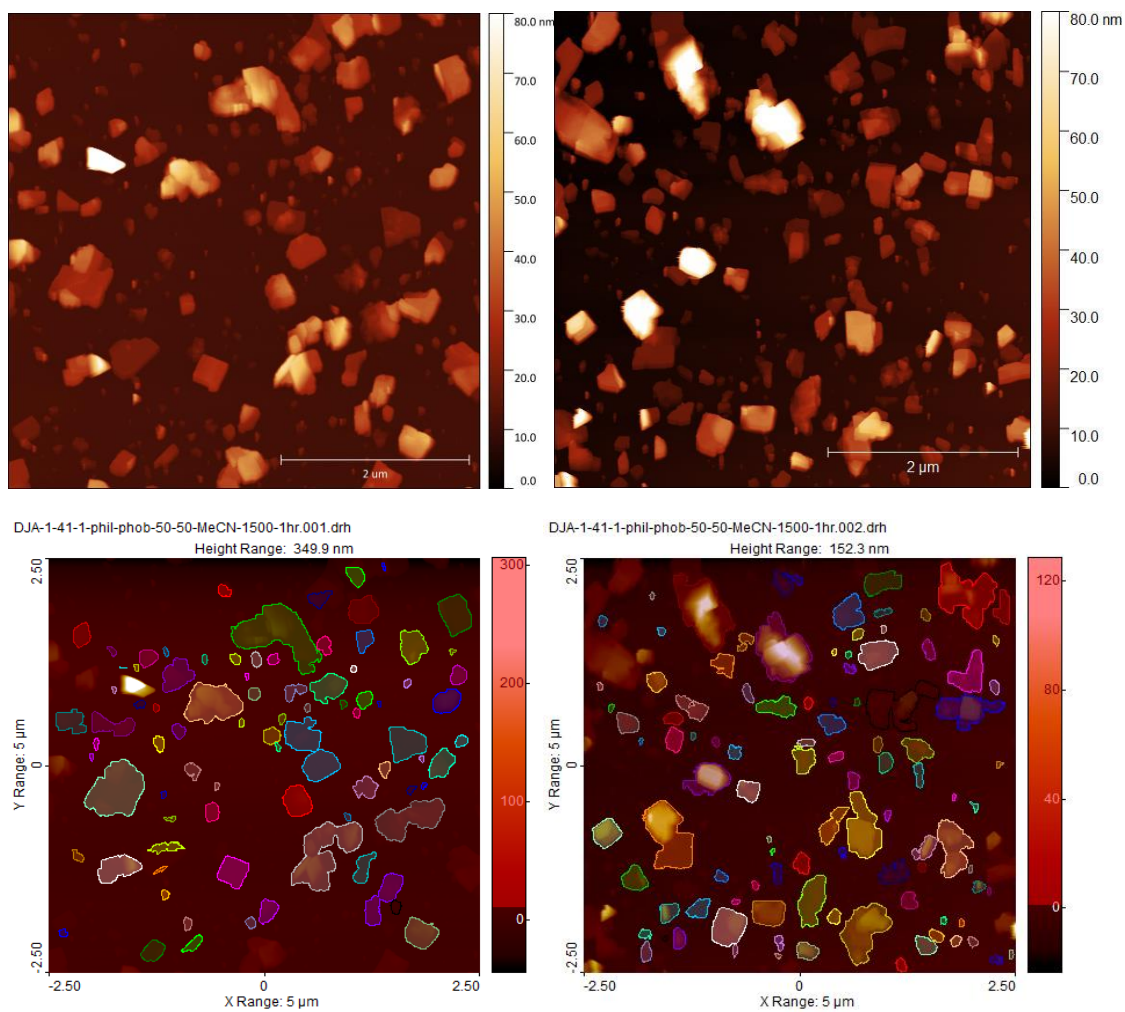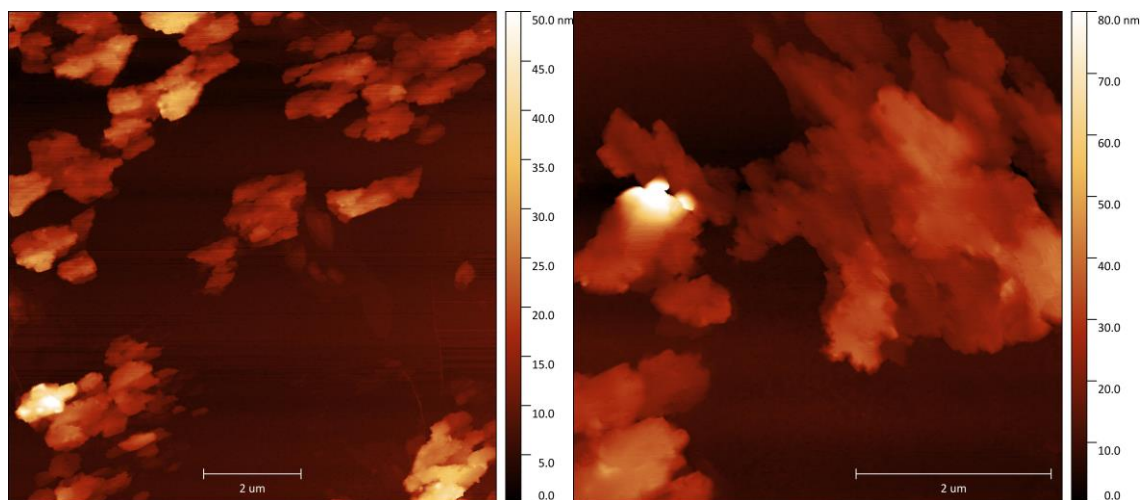
2.1.5. AFM

DJA-1-41-1-phil-phob-50-50-MeCN-1500-1hr.001.drh
Height Range: 349.9 nm

DJA-1-41-1-phil-phob-50-50-MeCN-1500-1hr.002.drh
Height Range: 152.3 nm

Figure S15. Cu(**5**)(**5***)(DMF) exfoliated in MeCN, after centrifugation at 1500 rpm for 1 hr, and automated particle identification.

Figure S16. Cu(**5**)(**5***)(DMF) exfoliated in H$_2$O, after centrifugation at 1500 rpm for 1 hr.

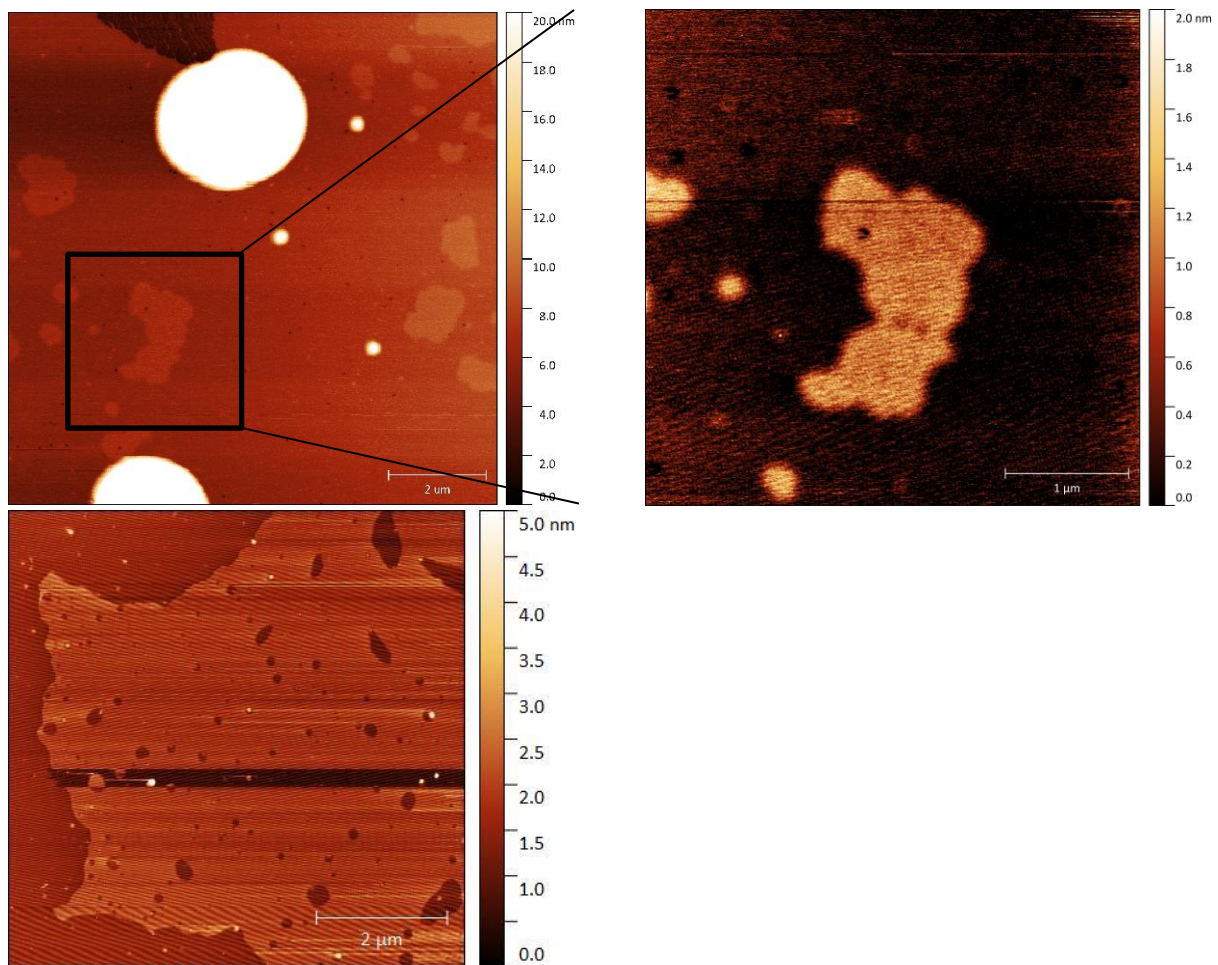**Figure S17.** Cu(**5**)(**5***)(DMF) exfoliated in diethyl ether, after centrifugation at 1500 rpm for 1 hr.
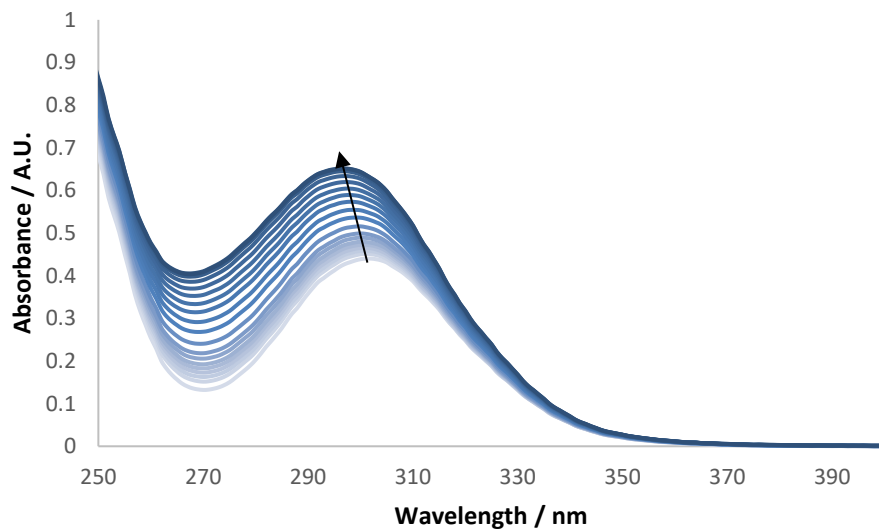
2.1.6. Imidazole binding

Figure S18. UV-Vis spectra showing the change in absorbance upon addition of aliquots of imidazole in MON suspension to a MON suspension.
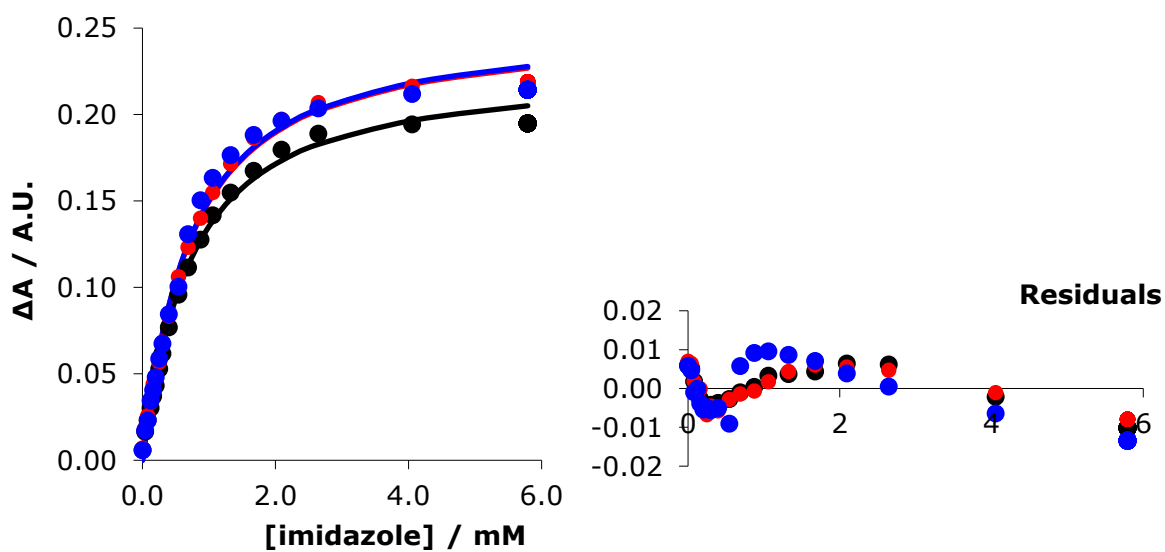

Figure S19. Change in absorbance at λ=302 nm for three repeat UV-Vis titrations of imidazole in MON suspension to MON suspension, fit to binding curves (left) , and residuals (right).
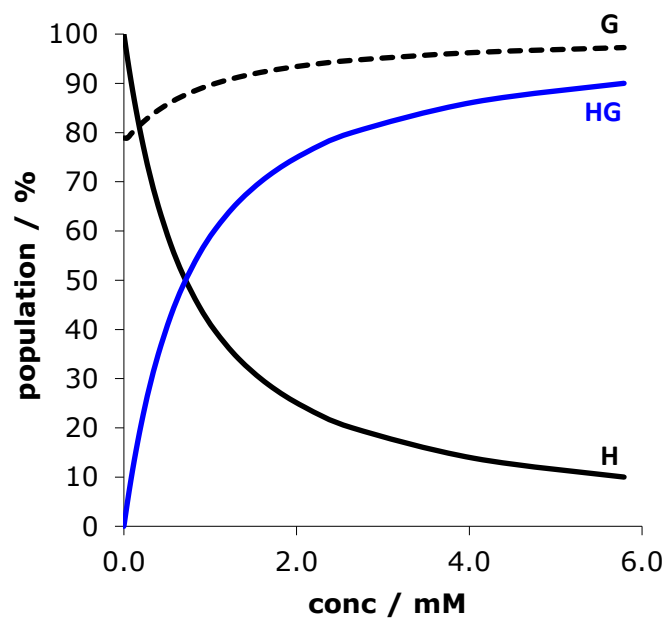
Figure S20. Speciation plot showing formation of **HG** complex upon addition of imidazole (**G**) to a suspension of Cu(**5**)$_{0.5}$(**5***)$_{0.5}$(H$_2$O) nanosheets (**H**).

2.2.Single-ligand parent MONs

Figure S21. AFM topographical images of Cu(**5***)(DMF) exfoliated in MeCN and centrifuged at 1500 rpm for 1 hr,[3] and automated particle identification.
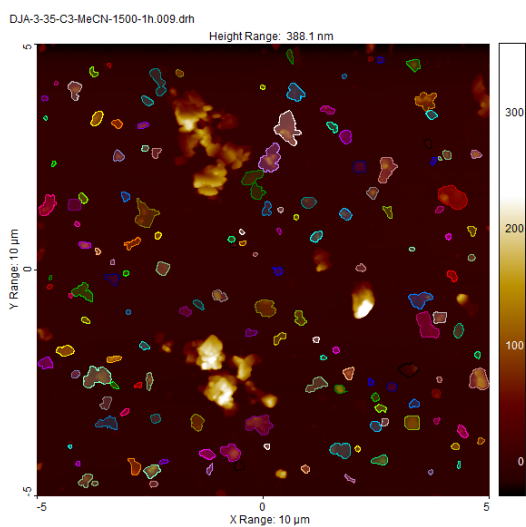
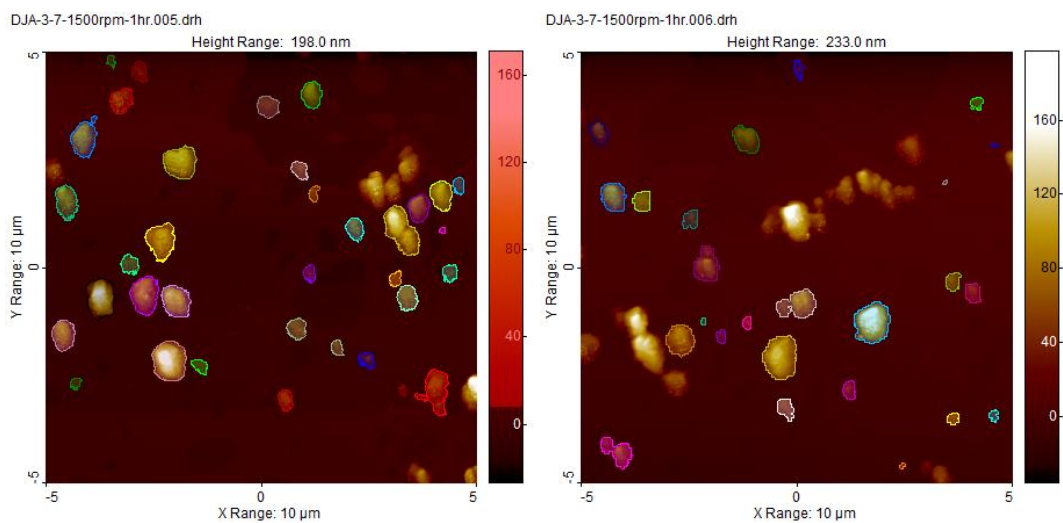**Figure S22.** AFM topographical images of Cu(**3**)(DMF) exfoliated in MeCN and centrifuged at 1500 rpm for 1 hr,[1] and automated particle identification.

DJA-3-35-C4-MeCN-1500-1h.001.drh
Height Range: 103.9 nm

DJA-3-35-C4-MeCN-1500-1h.002.drh
Height Range: 278.4 nm

Figure S23. AFM topographical images of Cu(**4**)(DMF) exfoliated in MeCN and centrifuged at 1500 rpm for 1 hr,[1] and automated particle identification.


DJA-3-24-CuB-12hr-exf-1500-1h.001.drh
Height Range: 167.8 nm

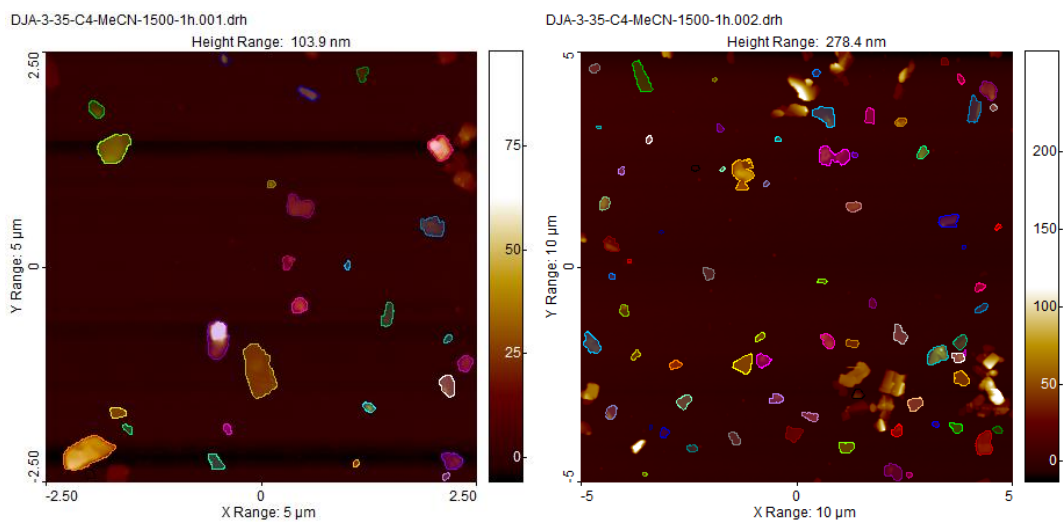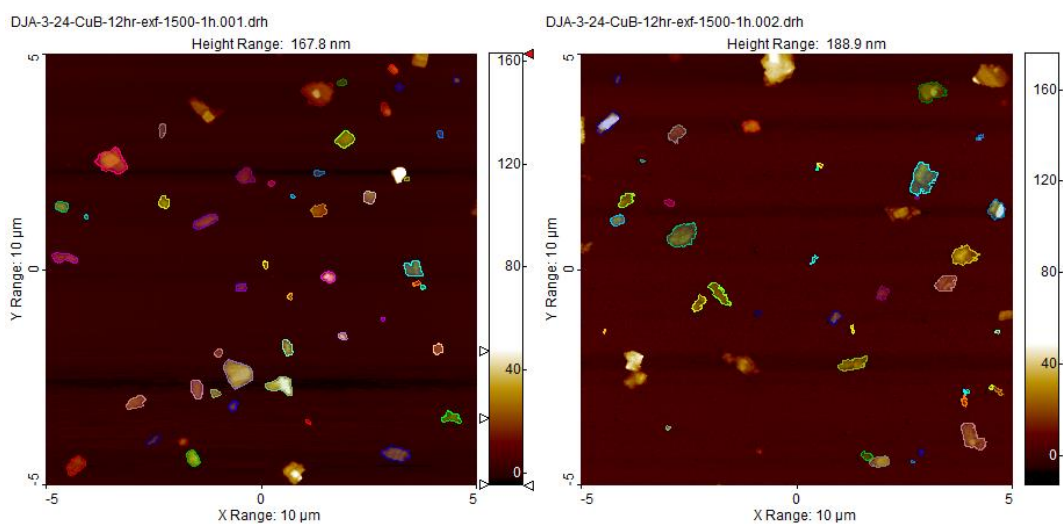DJA-3-24-CuB-12hr-exf-1500-1h.002.drh
Height Range: 188.9 nm

Figure S24. AFM topographical images of Cu(**5**)(DMF) exfoliated in MeCN and centrifuged at 1500 rpm for 1 hr,[1] and automated particle identification.

2.3. Cu(3)$_x$(5)$_y$ blends

2.3.1. PXRD
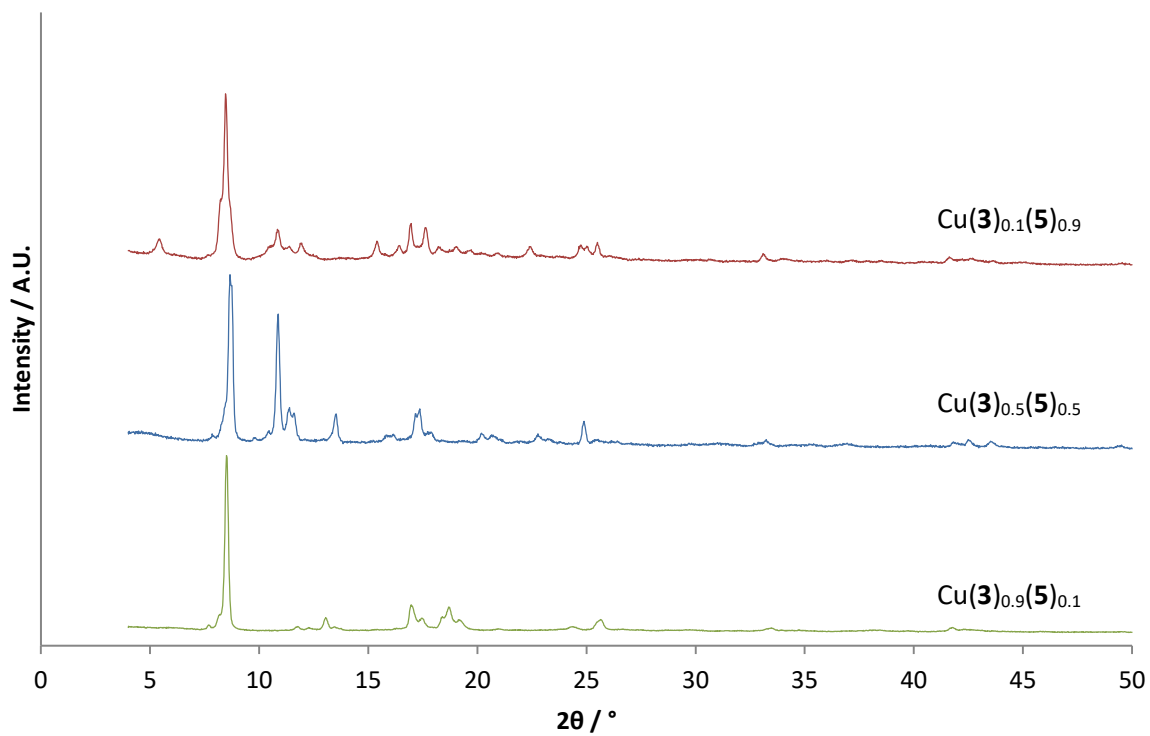
Figure S25. PXRD patterns of Cu(3)$_x$(5)$_y$ blends after exfoliation in MeCN.

2.3.2. AFM
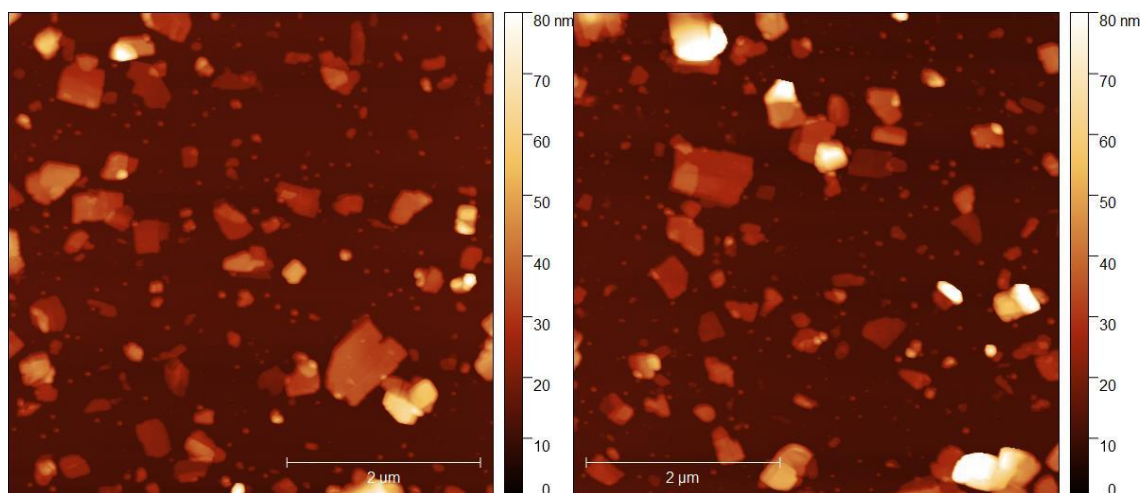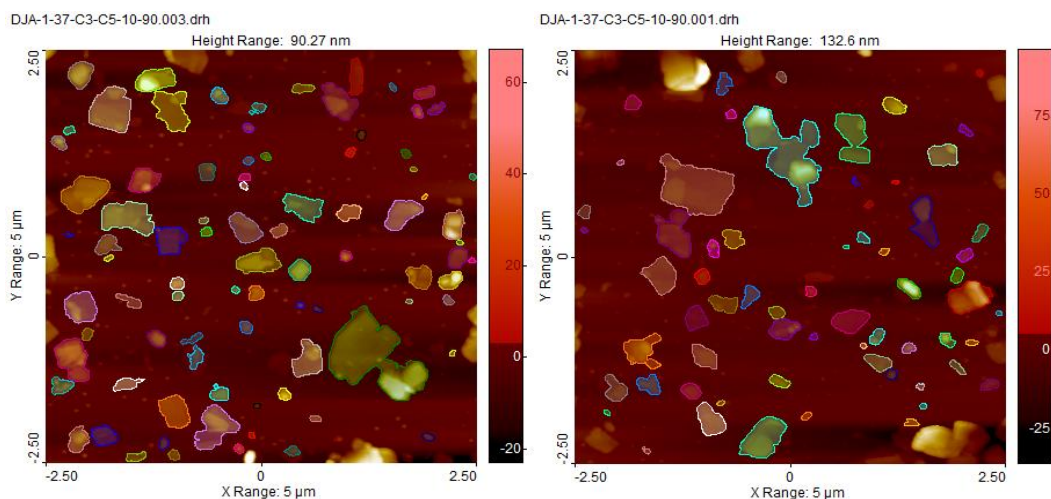
Figure S26. AFM topographical images of Cu(**3**)$_{0.1}$(**5**)$_{0.9}$ exfoliated in MeCN and centrifuged at 1500 rpm for 1 hr, and automated particle identification.

Figure S27. AFM topographical images of Cu(**3**)$_{0.5}$(**5**)$_{0.5}$ exfoliated in MeCN and centrifuged at 1500 rpm for 1 hr, and automated particle identification.

Figure S28. AFM topographical images of Cu(**3**)$_{0.9}$(**5**)$_{0.1}$-MTV-MOF exfoliated in MeCN and centrifuged at 1500 rpm for 1 hr, and automated particle identification.

2.4. Other binary blends

2.4.1. PXRD
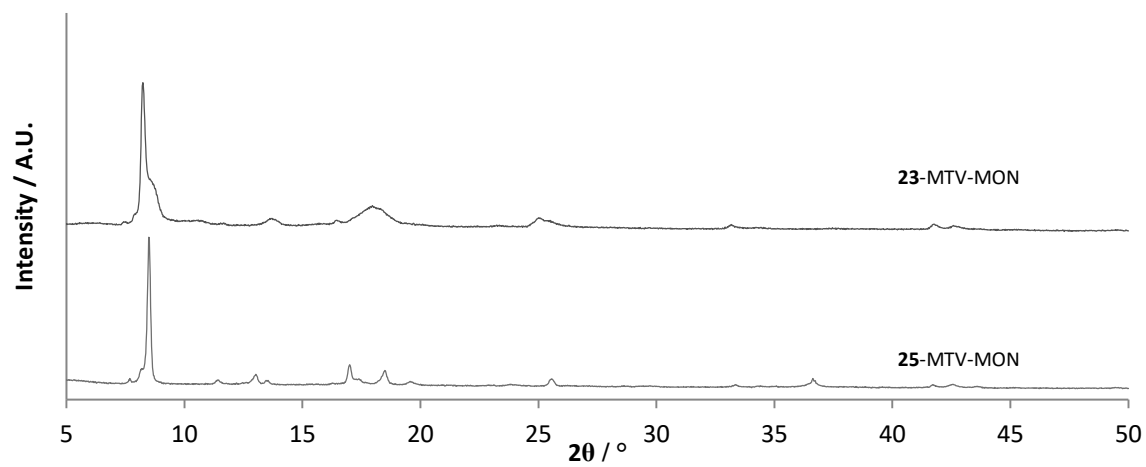
Figure S29. PXRD patterns of binary MTV-MOFs after exfoliation in MeCN.

2.4.3. AFM
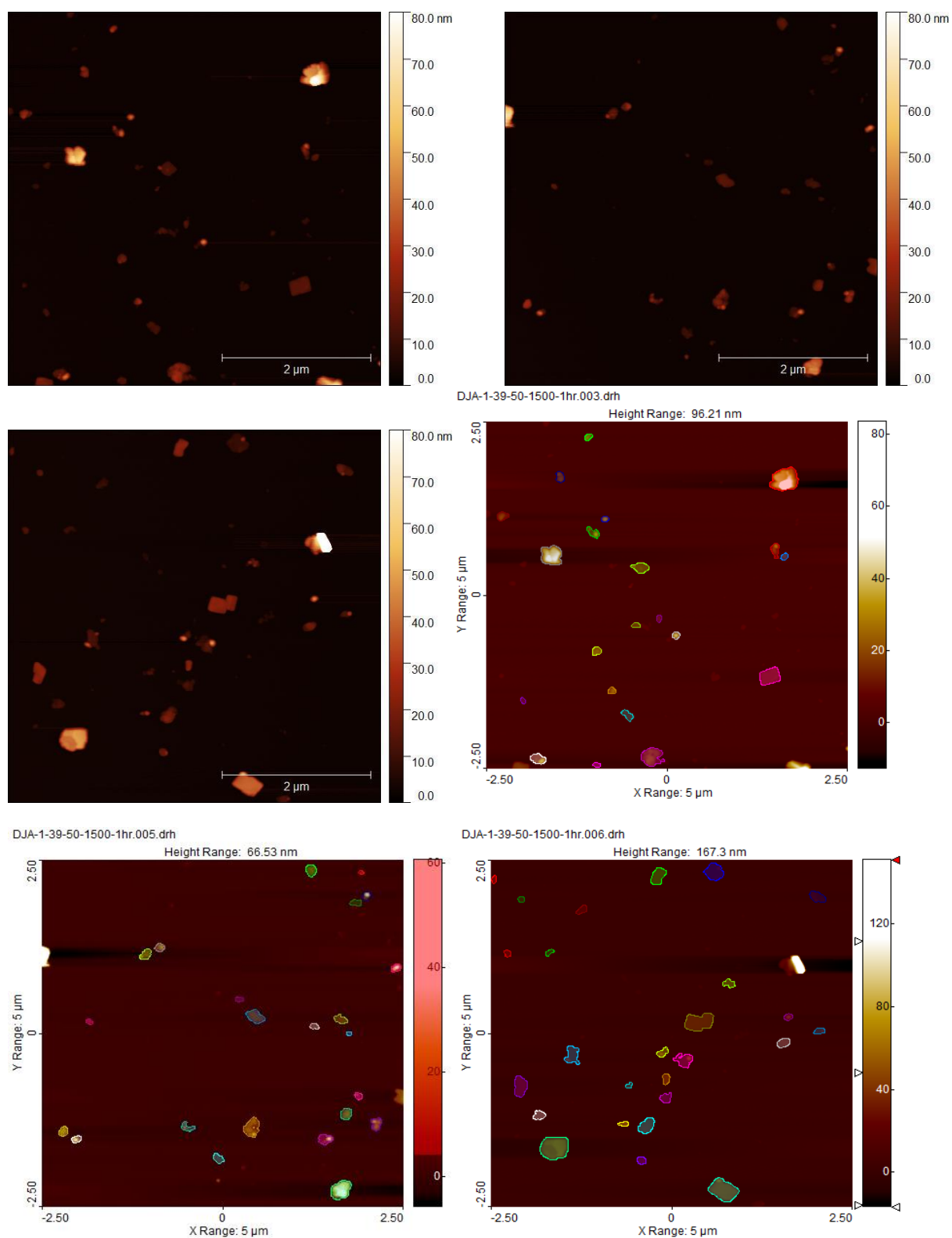
Figure S30. AFM topographical images of **23**-MTV-MOF exfoliated in MeCN and centrifuged at 1500 rpm for 1 hr, and automated particle identification.
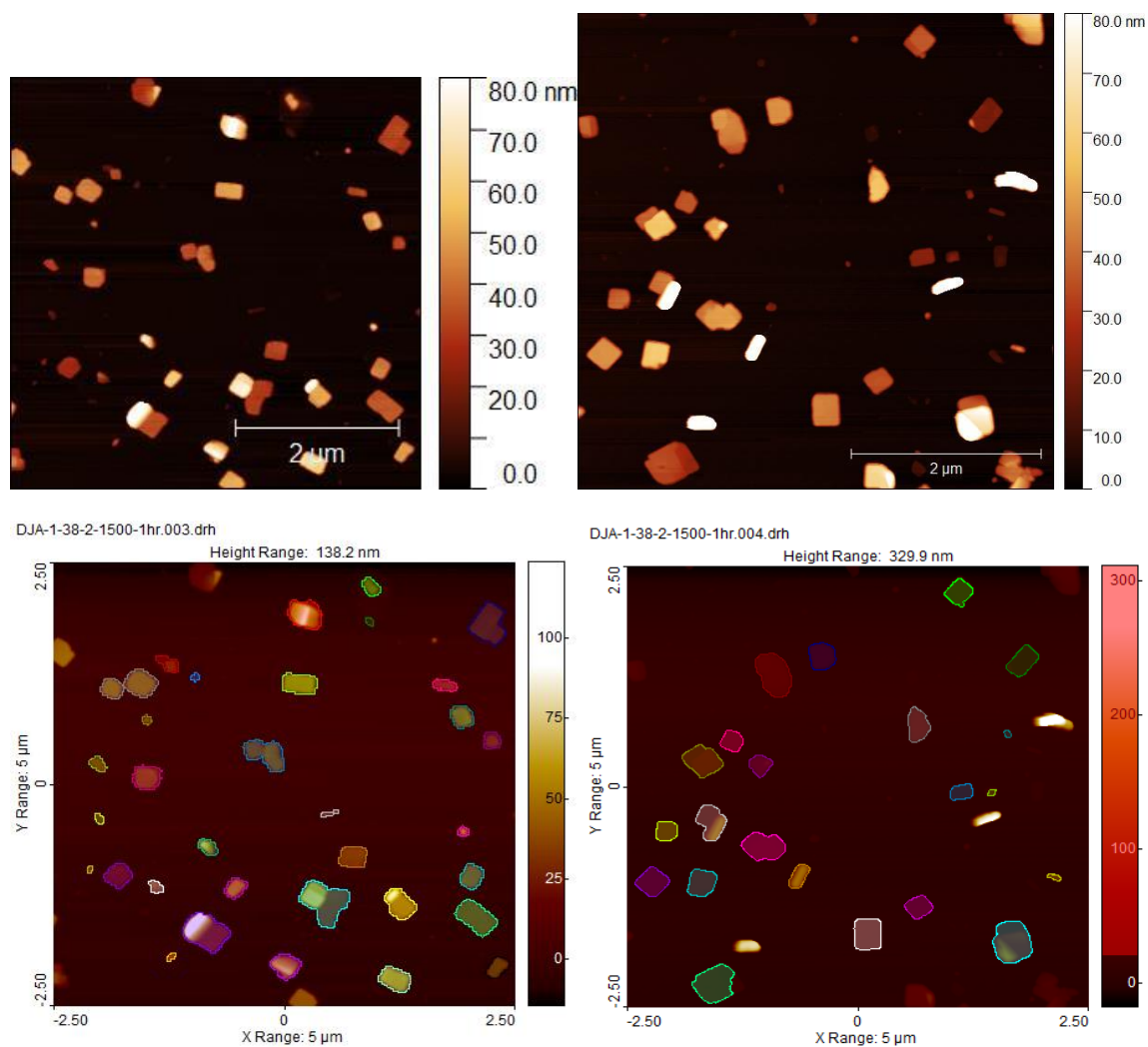
Figure S31. AFM topographical images of **25**-MTV-MOF exfoliated in MeCN and centrifuged at 1500 rpm for 1 hr, and automated particle identification.

2.5. Tertiary and higher blends of MTV-MONs

2.5.1. PXRD
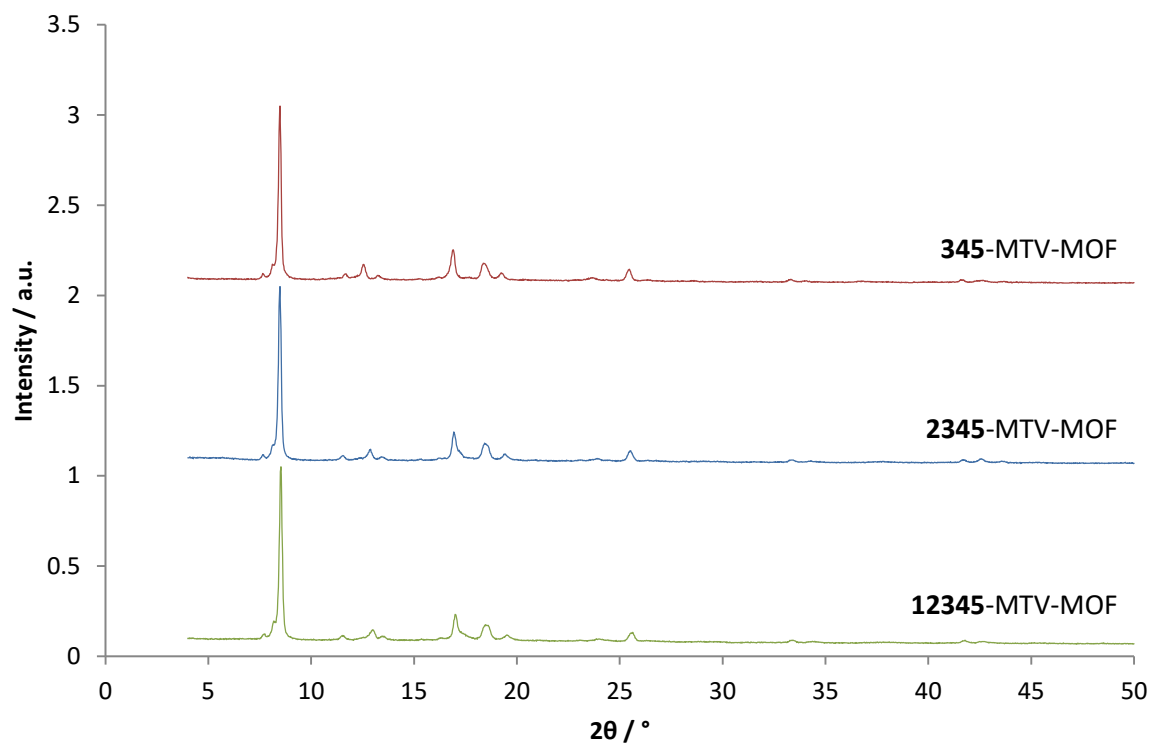
Figure S32. PXRD patterns of MTV-MOFs recollected after exfoliation in MeCN.

2.5.2. AFM

Figure S33. AFM topographical images of **345**-MTV-MOF exfoliated in MeCN and centrifuged at 1500 rpm for 1 hr, and automated particle identification.
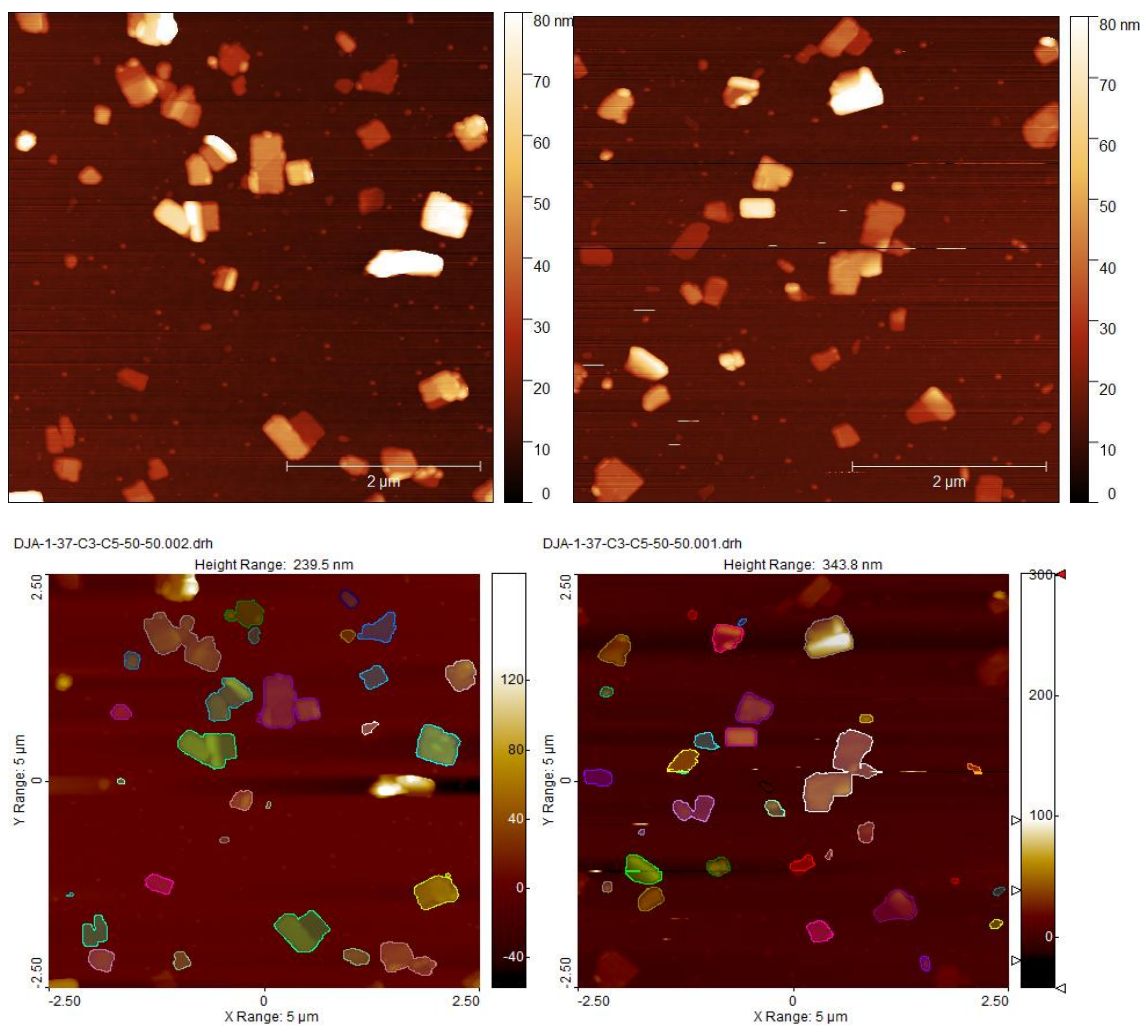
Figure S34. AFM topographical images of **2345**-MTV-MOF exfoliated in MeCN and centrifuged at 1500 rpm for 1 hr, and automated particle identification.

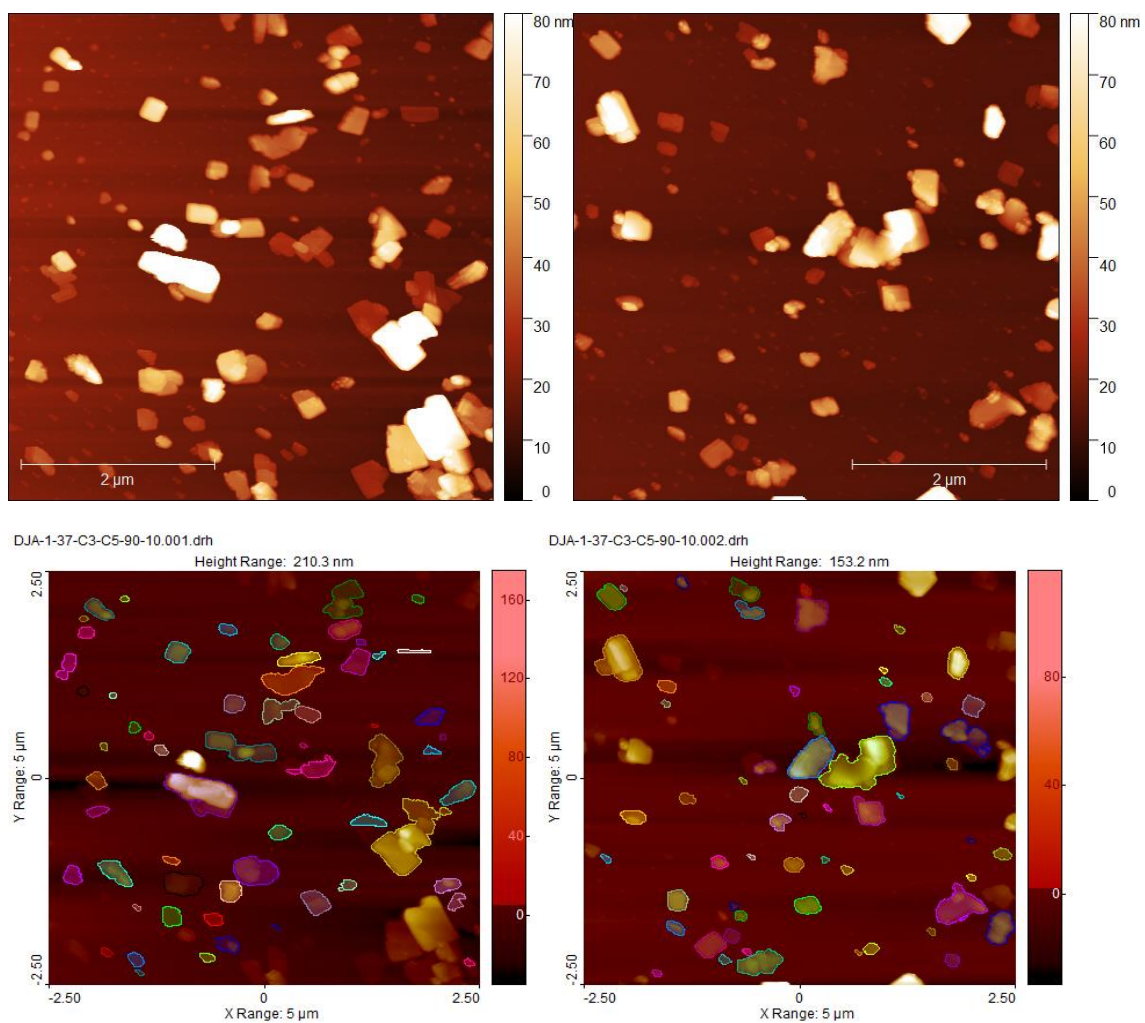**Figure S35.** AFM topographical images of **12345**-MTV-MOF exfoliated in MeCN and centrifuged at 1500 rpm for 1 hr, and automated particle identification.
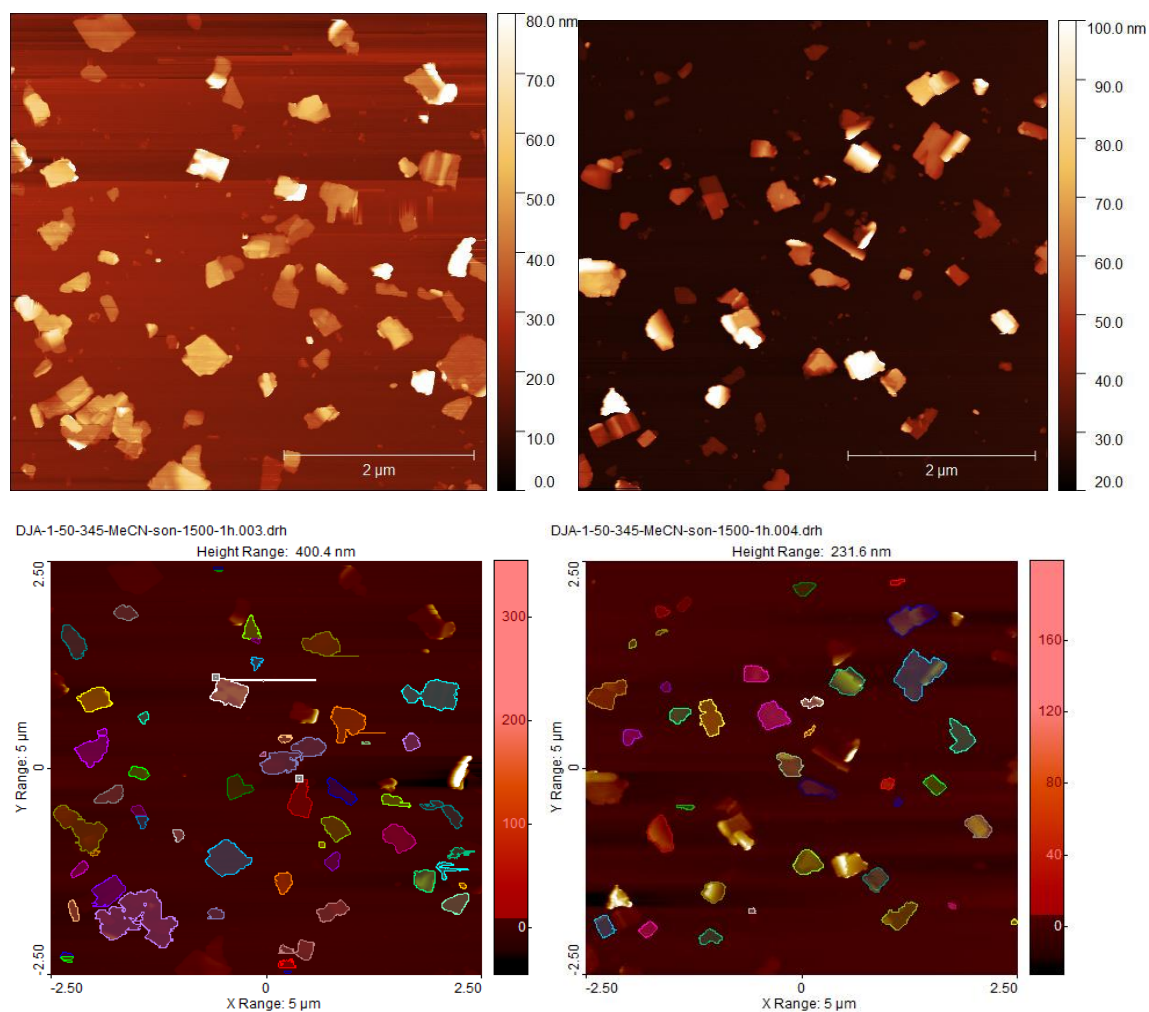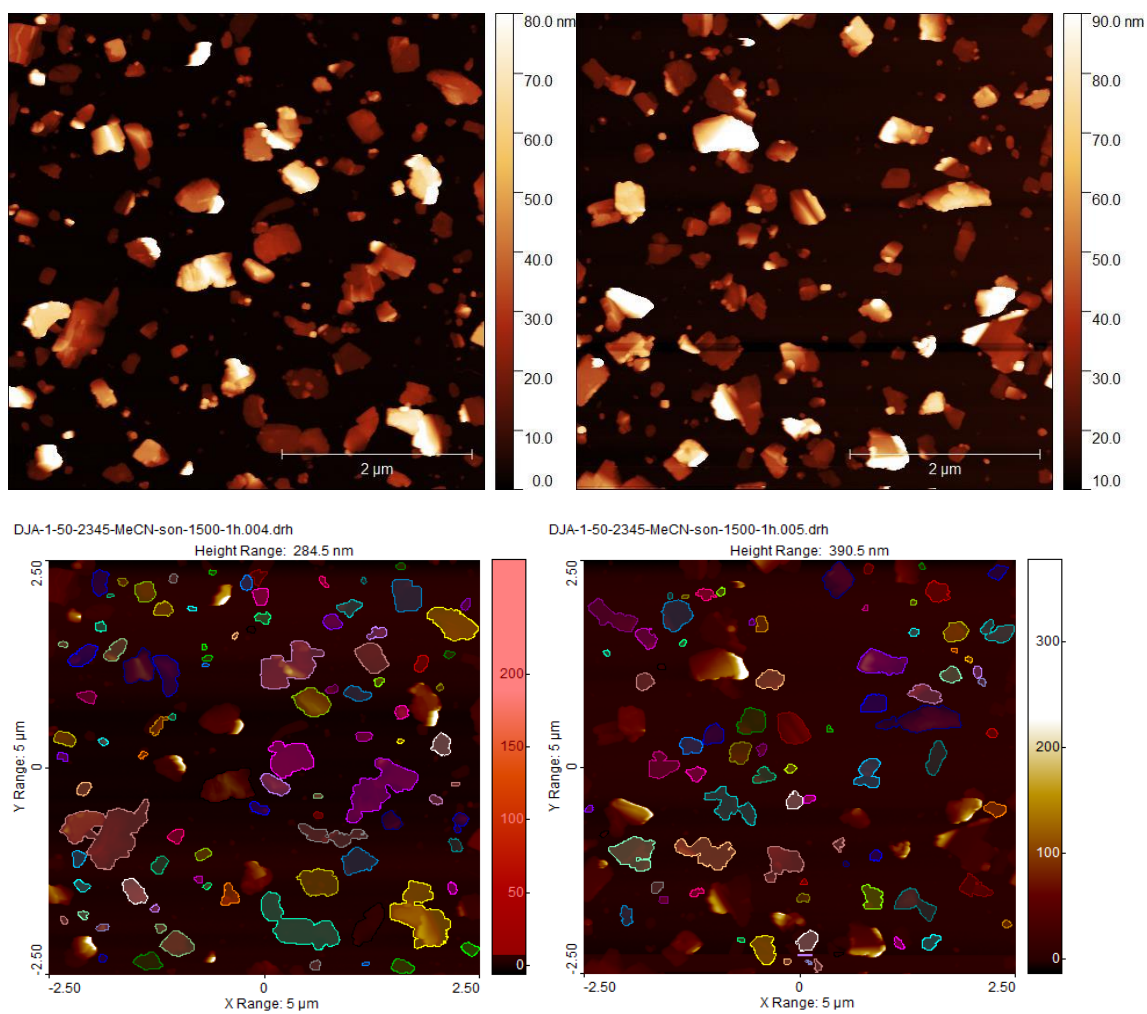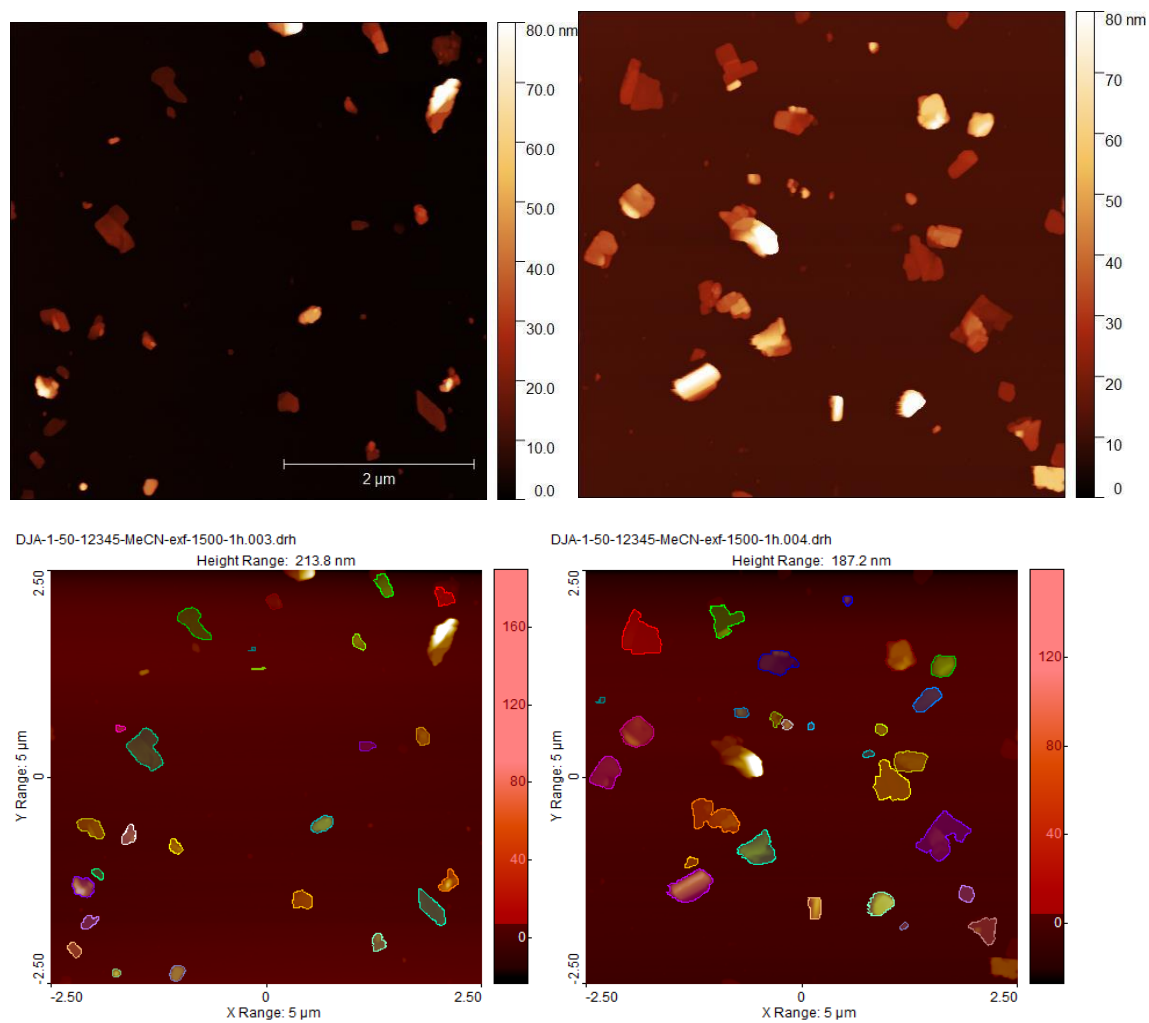
3. SPIP particle sizing

Automated particle sizing using SPIP software has both advantages and disadvantages over hand-sizing methods.[4] It is much faster, and eliminates subjective human error, particularly over height measurements where a MON may not be a single uniform height. The SPIP sizing output of "z mean" gives the average z (i.e. height) across an identified particle, which may be more informative than a single profile across a particle, as is often observed within the literature.

However, accurate sizing relies on high-quality AFM images with excellent particle/background resolution. The sample preparation is also therefore paramount, as the software cannot identify overlying particles, and instead treats these as single entities, which potentially corrupts results with erroneous measurements.

Within the manuscript, we presented size data for single ligand MOFs 3-5 and 5*. MONs were resized from raw data presented in previous studies.[1,3] A comparison of average particle size data is presented in Table S5. Generally, average lengths are larger (<20 %) when sizing with SPIP. This may result from slightly overlapping particles that can be individually sized by hand, but the software reads as single entities. Average heights are consistently lower when sized using SPIP. This is a result of the differing sizing methods: previous studies sizing the height by hand take the largest height of each particle, however SPIP parameter used was the average height of the whole particle (this is not readily available when sizing by hand). Trends for both length and height across the data series are consistent between hand sizing and SPIP, giving confidence to results.

Table S5. Average particle size data for single-ligand MONs, using SPIP automated particle sizing and hand-sizing methods

MOF	Length / nm		Height / nm	
	Hand	SPIP	Hand	SPIP
3	222±95	285±151	35±26	26±17
4	275±148	305±162	22±13	17±10
5	348±202	334±195	19±10	14±8
5*	512±234	587±262	59±234	35±18

4. References

1   D. J. Ashworth, T. M. Roseveare, A. Schneemann, M. Flint, I. Dominguez Bernáldes, P. Vervoorts, R. A. Fischer, L. Brammer and J. A. Foster, *Inorg. Chem.*, 2019, **58**, 10837–10845.

2   J. A. Foster, S. Henke, A. Schneemann, R. A. Fischer and A. K. Cheetham, *Chem. Commun.*, 2016, **52**, 10474–10477.

3   D. J. Ashworth, A. Cooper, M. Trueman, R. W. M. Al-Saedi, S. D. Liam, A. J. Meijer and J. A. Foster, *Chem. - A Eur. J.*, 2018, **24**, 17986–17996.

4   C. Backes, D. Hanlon, B. M. Szydlowska, A. Harvey, R. J. Smith, T. M. Higgins and J. N. Coleman, *J. Vis. Exp.*, 2016, **2016**, 10–13.

6

Tuning the surface chemistry of mixed-ligand multivariate metal-organic framework nanosheets (MTV-MONs)
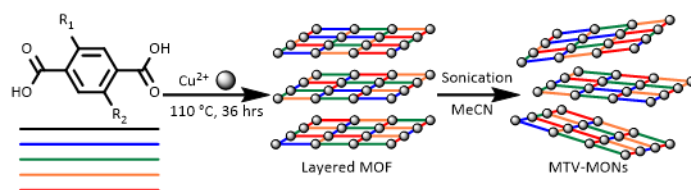
9

Chapter 6

Tuning the surface chemistry of mixed-ligand multivariate metal-organic framework nanosheets (MTV-MONs)

David J. Ashworth and Jonathan A. Foster

Author Contributions

David J. Ashworth	Performed all experimentation and characterisation. Drafted and redrafted the manuscript and prepared all figures.
Jonathan A. Foster	Supervised DJA and coordinated the work. Assisted in redrafting and editing the manuscript.

Tuning the surface chemistry of mixed ligand multivariate metal-organic framework nanosheets (MTV-MONs)

David J. Ashworth[a] and Jonathan A. Foster*[a]

Metal-organic framework nanosheets (MONs) lie at the interface between 2D materials and metal-organic materials and have shown impressive performance in applications such as gas separation, catalysis and electronics. Their modular structure means that the materials' chemistry can be altered and tuned through the use of different ligands within the framework structure. Here, we present a series of isoreticular layered metal-organic fameworks (MOFs) formed with the in-plane structure of dinuclear copper paddle-wheel secondary building units linked in two dimensions with $(H)_2$, NH_2, $(Br)_2$, $(Cl)_2$ or NO_2-functionalised benzene-1,4-dicarboxylate (fu-BDC) ligands. Liquid ultrasonic exfoliation in acetonitrile produced MONs down to monolayer thickness (0.7 nm, using $(Cl)_2$-BDC). Ultrathin MONs with height <5 nm were observed in all cases. The compatibility of ligand incorporation into the 2D layered structure was assessed through syntheses of a series of multivariate (MTV)-MOFs. Two component mixing of $(H)_2$-BDC with other fu-BDC ligands produced isoreticular MTV-MOFs, which confirmed that ligands could be blended within the framework structure, and these could be exfoliated to produce MTV-MONs. Eleven new MTV-MOFs were then synthesised using combinations of up to four different fu-BDC ligands to assess structural compatibility and ligand incorporation, and liquid ultrasonic exfoliation produced MTV-MONs in all cases. Ternary and quaternary MTV-MONs produced nanosheets with a decreased average height (down to a minimum of 7±5 nm), compared to binary blends, which we suggest results from reduced interlayer interactions due to irregular stacking of 2D layers in the layered MTV-MOF. MTV-MONs therefore demonstrate MONs as modular, tuneable 2D materials with controllable surface chemistry

1. Introduction

Two-dimensional (2D) materials have received large, sustained research attention over the last two decades thanks to their high surface area, anisotropic structure and the unique properties that arise from their nanoscopic dimensions.[1] However, simple inorganic 2D materials such as graphene, hexagonal boron nitride and dichalcogenides suffer from a shared limitation: it is generally difficult to alter the structure and surface properties of these materials. Only a limited range of functional groups can be introduced in a poorly defined way, which are often detrimental to other properties.[1]

Metal-organic materials combine the tunability of organic ligands with the unique properties (magnetic, catalytic, optical and electronic) offered by metal ions.[2,3] Metal-organic framework nanosheets (MONs) are free-standing, nominally 2D crystalline materials consisting of metal ions or clusters linker in two dimensions through coordinated multitopic organic linker ligands.[4–8] They can be synthesised through "bottom-up" methodologies, where the 2D nanosheets are crystallised directly,[9–15] or through "top-down" techniques where MONs

are isolated through exfoliation of layered metal-organic frameworks (MOFs).[16–21] MONs benefit from the vast external surface area, large aspect ratio and nanscopic dimensionality of 2D materials. However, they also share characteristics of the metal-organic materials family. In particular, they have a modular structure, which can allow substitution of different ligands in a predictable manner, while maintaining the same overall structure.

This principle of reticular chemistry[22–24] allows the design and synthesis of isoreticular series of MONs with the same in-plane structure, but with different functional groups on the layer surfaces. This has been previously exploited by Gascon and coworkers, who synthesised $[Cu(lig)(DMF)]_n$ MONs, where lig=benzene-1,4-dicarboxylate (BDC), naphthalene-1,4 or 2,6-dicarboxylate.[25] Banerjee and coworkers presented a three-member series of isoreticular MONs using benzene-1,3-dicarboxylate functionalised in the 5-position with $OMe-O^nPr$ alkoxy chains.[26] Recently, López-Cabrelles et al. demonstrated a series of isoreticular layered MOFs with the structure $[Fe(fu-BIM)_2]_n$, where fu-BIM= functionalised benzimidazole, which was functionalised in the 5-position with H, Cl, Br, CH_3, or NH_2.[27] We have also demonstrated series of isoreticular MONs using functionalised-benzene-1,4-dicarboxylate (fu-BDC) ligands difunctionalized in the 2- and 5-positions with alkoxy/alkylether chains, to aid exfoliation from MOFs to MONs.[44–46]

The preparation of isoreticular materials can introduce different properties to the different materials. An extension of

a. Department of Chemistry, the University of Sheffield, Dainton Building, Brook Hill, Sheffield, S3 7HF, UK.
* jona.foster@sheffield.ac.uk

the reticular approach, which has not yet been applied to MON design, is to blend compatible ligands together within the same MON. Such structures are known as multivariate (MTV), and this concept was initially introduced by Yaghi and coworkers, who demonstrated that up to eight different fu-BDC ligands could be incorporated within the MOF-5 structure, producing heterogenous frameworks.[28] This principle has been extensively exploited within MOF literature to enable fine-tuning of material properties.[28–32] Moreover, in some cases, combinations of different ligands resulted in MOFs that out-performed parent single-ligand MOFs, for example with increased specificity of gas adsorption,[28] and increased H_2 storage.[33] We anticipate that the unique requirements and opportunities offered by applying these principles to 2D materials will lead to interesting new insight into surface chemistry and 2D material applications.

Here, we report a series of isoreticular layered MOFs based on the structure of $[Cu(BDC)(DMF)]_n$. We use five different commercially available fu-H_2BDCs (fu=(H)$_2$, (Cl)$_2$, (Br)$_2$, and NO$_2$, see Figure 1) as ligand precursors to synthesise layered MOFs. First, we investigate the effect of the different functional groups on MONs formed following liquid ultrasonic exfoliation in acetonitrile (MeCN). We then explore the effect of 50:50 blends of (H)$_2$-BDC and other fu-BDC on the structure and properties of the resulting MONs. We then push the MTV concept to understand the effects of blending different binary, tertiary and quaternary combinations of fu-BDC ligands on the structure and properties of MTV-MOFs and subsequent exfoliation to MTV-MONs. We anticipated that different combinations of functional groups would affect the strength of interlayer and MON-solvent interactions and therefore influence the degree of exfoliation and sizes of nanosheets formed.

2. Results and discussion

$[Cu(BDC)(DMF)]_n$ is a layered MOF,[34] in which the layers consist of Cu$_2$-paddle-wheel (PW) secondary building units (SBUs) linked in two dimensions with BDC ligands, forming a 2D **sql** grid
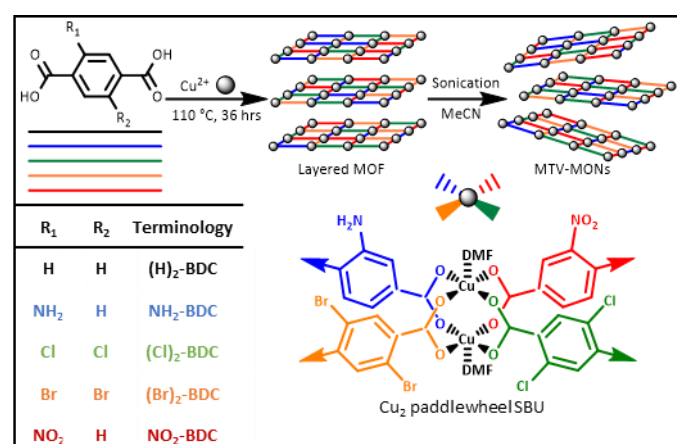

Figure 1. Schematic of MTV-MOF structure and exfoliation to MTV-MONs, with diacid ligand terminology indicated.

network.[35] DMF molecules are coordinated to the axial positions of the PW (see Figure 1), and layers stack in an offset manner, and are held together by van der Waals forces. This framework is structurally similar to MOF-2 $[Zn(BDC)(H_2O).DMF]_n$.[35,36] Related frameworks are known for NH$_2$-BDC as MOF-46 $[Zn(NH_2$-$BDC)(DMF)]_n$.[37] The layered PW-based structure is known for (Cl)$_2$-BDC, in MOF-102 $[Zn((Cl)_2$-$BDC)(DMF).H_2O_{0.75}.DMF_{1.75}]_n$,[38] where PW-fu-BDC layers have an increased layer spacing with water and DMF located in the interlayer space. Non-layered MOFs which use (Br)$_2$-BDC are known, and the monofunctionalised Br-BDC has previously been shown to form a MOF with a non-layered PW based structure.[38] To our knowledge, there are no examples of crystal structures of PW-based layered MOFs using (Br)$_2$-BDC. We are also not aware of any examples of layered PW-based structures using NO$_2$-BDC, however a variety of pillared versions are known in which the same in-plane **sql** structure is adopted.

A standard method for the syntheses of single, binary and higher order blends of MOF. Any deviations are noted in text. The method was based on the previously reported synthesis of $[Cu(BDC)(DMF)]_n$.[34] The nitrate salt was used for single-ligand MOFs (except NH$_2$-MOF) and binary (H)$_2$-fu-MTV-MOF syntheses, and the acetate salt for NH$_2$-MOF and all fu-MTV-MOFs. The copper salt and combinations of equimolar diacid ligand precursors (total copper:diacid ratio of 1:1.1) were dissolved in DMF and sealed into a reaction vial. MOF syntheses occurred at 110 °C, after which the solids were washed and dried, yielding microcrystalline MOF powders of various shades of blue-green.

A standard exfoliation protocol was used for all exfoliations. MOFs were exfoliated using liquid ultrasonic exfoliation in acetonitrile (MeCN) in an ultrasonic bath (12 hrs), followed by centrifugation at 1500 rpm for 1 hr to remove larger unexfoliated particulates. MON samples were analysed using powder X-ray diffraction (PXRD), UV-Vis spectroscopy, dynamic light scattering (DLS) and atomic force microscopy (AFM).

Single ligand MOFs are termed fu-MOFs, two-component blends of (H)$_2$-BDC and other fu-BDC MOFs are termed (H)$_2$-fu-MTV-MOFs, and MOFs synthesised using combinations of fu-BDC are termed fu-MTV-MOFs. The same reference system is used for MONs, where MON replaces MOF in the sample name (e.g. the binary (H)$_2$-NH$_2$-MTV-MOF was exfoliated to produce (H)$_2$-NH$_2$-MTV-MON).

2.1. Single-ligand fu-MOF syntheses

Five isoreticular single-ligand fu-MOFs with the in-plane structure of $[Cu(fu$-$BDC)]_n$ were synthesised using variations of reported procedures.[34,39] Copper nitrate trihydrate was used as the Cu^{2+} source, apart from for the synthesis of NH$_2$-MOF, where copper acetate monohydrate was used instead as initial synthesis using the nitrate salt formed an unidentified impurity alongside the desired phase. MOFs were characterised by powder X-ray diffraction (PXRD, Figure 2) and Pawley refinement (Table 1, ESI Figure S1 and Table S3), Fourier-transform infrared (FTIR, ESI Figure S3) spectroscopy, elemental analysis (EA, see experimental), ^{1}H NMR (of samples that had been digested

using DCl/D$_2$O, ESI Figure S4) and SEM (Figure 3). For more specific details, see experimental.

Pawley refinement of the PXRD patterns showed unit cells similar to those of related reference materials, indicating that similar structures had been adopted. FTIR confirmed DMF coordination (v C=O at lower wavenumbers than 1676 cm^{-1} of liquid phase DMF) and EA was consistent with the expected formula of [Cu(fu-BDC)(DMF)]$_n$ for (H)$_2$-MOF, NH$_2$-MOF and NO$_2$-MOF. There is a low intensity peak in the PXRD pattern of NO$_2$-MOF which we ascribe to a small amount of the desolvated phase [Cu(NO$_2$-BDC)]$_n$, as ^{1}H NMR quantified the ligand DMF ratio as 1:0.95 (see also Section 2.3.). Interestingly, ligand:DMF ratio in (Br)$_2$-MOF was 1:0.12, however the "solvated" structure was indicated by PXRD, with only a very small intensity peak around 8.4 ° 2θ indicating that there may be a small amount of a secondary phase present. We suggest that the increased sterics of the (Br)$_2$-BDC compared to BDC may prevent the known structural rearrangement upon removal of DMF from the axial PW site. However, this is not observed for the less sterically demanding (Cl)$_2$-BDC. ^{1}H-NMR quantified the ligand DMF ratio as 1:0.12, and while there is a significant amount of the "solvated" structure similar to that of MOF-46 observed by PXRD, there is also a large secondary phase, which we ascribe to the "desolvated" [Cu((Cl)$_2$-BDC)]$_n$.

SEM showed similar crystal habits across the five samples, revealing square platelet morphologies of various lengths below 20 μm (Figure 3 and ESI Figures S8-S12). Smaller crystallites <2 μm were observed for NH$_2$-MOF, possibly due to decreased solubility of the acetate salt compared to nitrate, and subsequent faster reaction kinetics.[40]

2.2. Two-component (H)$_2$-fu-MTV MOF syntheses

Equimolar amounts of (H)$_2$-BDC and each other fu-BDC were input into four MOF syntheses. Copper nitrate trihydrate was used as the Cu^{2+} source in all four cases. Various shades of blue-green microcrystalline powder were obtained (Figure 3k), yielding four (H)$_2$-fu-MTV-MOFs, where fu=NH$_2$, (Cl)$_2$, (Br)$_2$ and NO$_2$.

PXRD patterns (Figure 2) and subsequent Pawley refinement (ESI Figure S2, Table S3) of the four patterns indicated a space group of C2/m was adopted in each case. Similar unit cells were adopted across all four materials, which matched closely with that of Zn(NH$_2$-BDC)(DMF)$_n$.[41] Importantly, there was no evidence of the separate phase [Cu(BDC)(DMF)]$_n$, which gives confidence that ligands can be blended within the overall layered framework structure. This X-ray analysis cannot determine whether the materials consist of macroscopic domains of individual ligands, sequences of ligands, or random inclusion across the structure,[29] but the absence of intensity peaks corresponding to the [Cu(BDC)(DMF)]$_n$ phase gives some indication that the ligands are being successfully blended within a single phase of material.

The ratio of (H)$_2$-BDC:fu-BDC included in the framework structure differed across the series. ^{1}H NMR was used to quantify the ratio, and fu-BDC content was found to be 32, 47, 46 and 56 % for fu= NH$_2$, (Cl)$_2$, (Br)$_2$ and NO$_2$, respectively. As
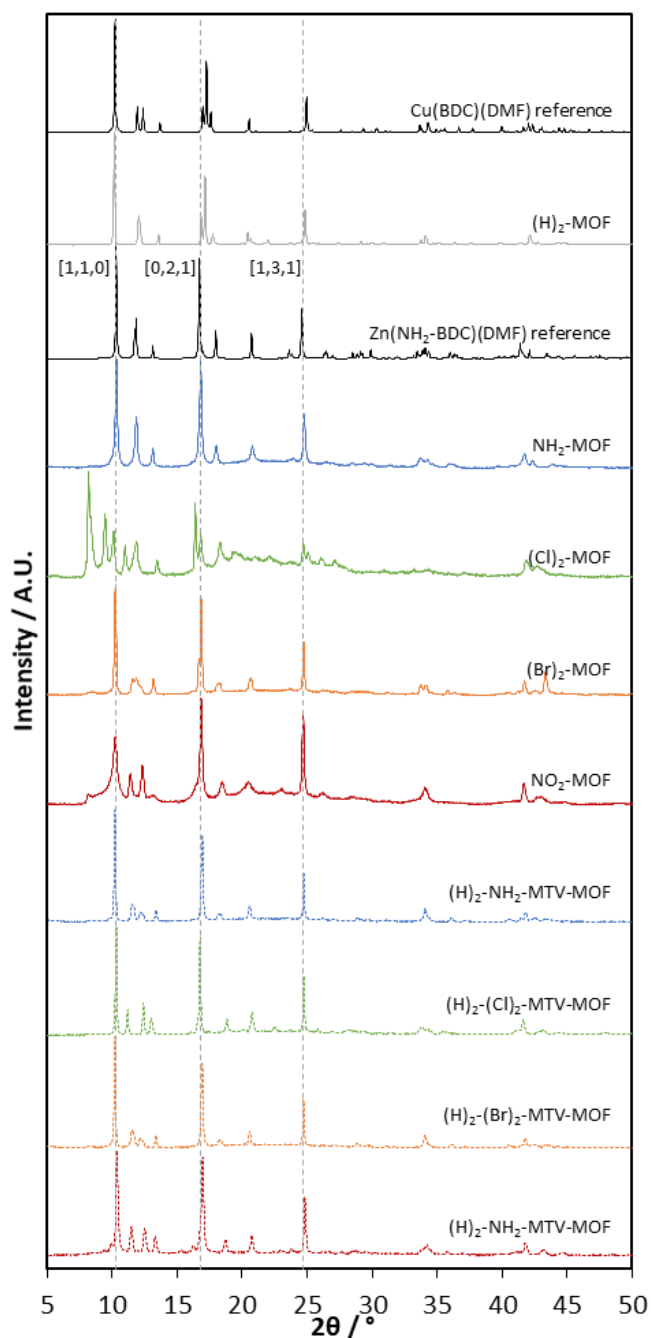
Figure 2. PXRD patterns of single-ligand fu-MOFs and two-component (H)$_2$-fu-MTV-MOFs.

the four different functional moieties have different sterics, and (Cl)$_2$ and (Br)$_2$ are difunctionalised compared to NH$_2$- and NO$_2$-BDC, it may be anticipated that sterics hold sway over ligand incorporation. It has been shown that the sterically demanding (Me)$_4$-BDC does not form a PW SBU.[38] However, the NO$_2$-moiety is the largest here, but has the highest inclusion (56 %) We suggest that this ligand inclusion is more determined by the electronics of the fu-BDC^{2-} ligand. Differences in the pk_a of the acidic protons of fu-H$_2$BDC would influence the reaction kinetics between ligand and copper^{2+} ion in the build-up of the framework. This accounts for the observed ligand inclusion here

Table 1. Unit cell parameters determined through Pawley refinements of PXRD data (298 K) for single ligand MOFs and BDC-fuBDC MTV-MOFs.

MOF	Space group	a / Å	b / Å	c / Å	β / °	Vol / Å³
Cu(BDC)(DMF) reference	C2/m	11.41	14.27	7.78	108.1	1204
(H)$_2$-MOF	C2/m	11.45	14.53	7.76	109.1	1220
Zn(NH$_2$-BDC)(DMF) – MOF-46	C2/m	11.20	15.05	8.03	111.7	1258
NH$_2$-MOF	C2/m	11.14	15.04	8.00	111.8	1245
(Cl)$_2$-MOF	-	-	-	-	-	-
(Br)$_2$-MOF	C2/m	11.17	15.20	7.96	111.2	1259
NH$_2$-MOF	C2/m	11.34	15.46	7.81	113.4	1257
(H)$_2$-NH$_2$-MTV-MOF	C2/m	11.21	15.30	7.77	111.0	1245
(H)$_2$-(Cl)$_2$-MTV-MOF	C2/m	11.22	15.77	7.85	115.0	1257
(H)$_2$-(Br)$_2$-MTV-MOF	C2/m	11.26	15.30	7.75	111.8	1240
(H)$_2$-NO$_2$-MTV-MOF	C2/m	11.29	15.54	7.80	113.7	1252

All unit cell axis lengths are rounded to two decimal places, angles to one decimal place and volume to no decimal places. For monoclinic crystal systems α=γ=90 °. More accurate values and associated errors are provided in the Supporting Information.

of electron donating NO$_2$>(Br)$_2$>(Cl)$_2$>NH$_2$ electron withdrawing.

Considering the ligand content observed in the MOF, rather than the ratio input to the reaction mixture, EA match well with the calculated for fu=NH$_2$, (Cl)$_2$ and NO$_2$. A decreased N content was observed for fu=(Br)$_2$ (2.01 % rather than 3.69 %), indicating lower than anticipated DMF inclusion. ^{1}H NMR quantified this as 0.23 of the total ligand content. Interestingly, despite this apparent difference in the level of solvation of the framework for (H)$_2$-(Br)$_2$-MTV-MOF, the PXRD indicates that the framework structure associated with the solvated phase is maintained. This, together with the PXRD of the single ligand (Br)$_2$-MOF, indicates that the inclusion of 2,5-(Br)$_2$-BDC may stabilise the structure against the known structural rearrangement of Cu(BDC)(DMF) MOF to a non-layered Cu(BDC) MOF upon desolvation.

2.3. Exfoliation of single-ligand fu-MOFs to form fu-MONs

Centrifugation of the suspensions formed from liquid ultrasonic exfoliation resulted in collection of unexfoliated bulk material as the centrifugate, leaving a MON suspension as the supernatant. Careful separation of the two components allowed separate characterisation of the recollected material, and the MONs.

PXRD of the dried solids collected through centrifugation indicated that some samples had undergone a structural change through exfoliation in MeCN (ESI Figure S15). Cu(BDC)(DMF) is known to rearrange to a non-layered [Cu(BDC)]$_n$ structure upon removal of DMF from the axial PW positions.^{34,42} DMF loss from the axial positions has been previously observed in related PW-based layered materials,$^{39,43–45}$ although does not always result in such a rearrangement. This desolvated structure of [Cu(BDC)]$_n$ is characterised by two intense diffraction peaks at 8.2 and 9.2 ° 2θ in the PXRD pattern (CCDC ref. no. 1056985),^{34,42} corresponding to the [001] and [010] reflections. Due to the different effects of the different fu-BDC ligands, an isostructural structure may not be expected for [Cu(fu-BDC], or particularly for [Cu(BDC)$_{0.5}$(fu-BDC)$_{0.5}$]$_n$ forms, but the positions of these two reflections should be fairly similar. There is no evidence of the starting phase for fu=(H)$_2$, (Cl)$_2$, (Br)$_2$ or NO$_2$. The PXRD pattern for (Cl)$_2$-MOF only has intensity peaks that are

also observed for the starting material. This indicates that the starting material was a mixed phase, and the initial "solvated" form has now transformed to the single phase observed post-exfoliation. The PXRD pattern for NO$_2$-MOF showed broad intensity peaks, which could be due to a loss of long-range order within the material, or an effect of reduced particle size. Further work is required to fully understand the differences in desolvated structures across the series.

Tyndall scattering was observed upon shining a laser through supernatant samples, indicating there were nanoparticles in suspension. UV-Vis spectroscopy was performed on all supernatant samples to confirm they contained material (ESI Figure S18). The supernatant containing NH$_2$-MON was visibly green coloured and had to be diluted 1 in 20 for UV-Vis analysis. We have previously used UV-Vis to estimate suspension concentrations by comparing unknown samples to a calibration curve. Unfortunately, this was not possible for these samples as a large amount of scattering from particles in suspension was also observed in titrations of sonicated samples, which lead to inaccurate calculations of extinction coefficients (ESI Figure S19). Samples were then analysed using dynamic light scattering (DLS) to give an indication of lateral sizes of MONs (ESI Figure S19). Although DLS produces inaccurate size measurements for 2D particles, due to the assumption of spherical particles in the Stokes-Einstein equation,^{46} measurements can be used to inform on trends and gauge approximations of particle lateral size and distribution.^{46,47} DLS analysis of (Cl)$_2$-MONs indicated a significantly larger average hydrodynamic diameter of 283 nm, where the other four samples ranged between 138-217 nm.

MON suspension was dropped onto freshly cleaved mica and dried prior to AFM analysis. Nanosheets were observed following exfoliation of all five single-ligand MOFs in MeCN (see Figure 3). Remarkably, ultrathin (<5 nm) MON were observed across all samples, however (Cl)$_2$-MON was the only sample in which monolayer sheets (0.7 nm in height; the MOF-46 crystal structure indicates 0.69 nm distance between the two axially-coordinated O atoms) were observed. As is typical for nanosheets produced by ultrasonic liquid exfoliation, a broad range of both lateral size and heights were observed. We quantified these by performing a statistical particle size analysis
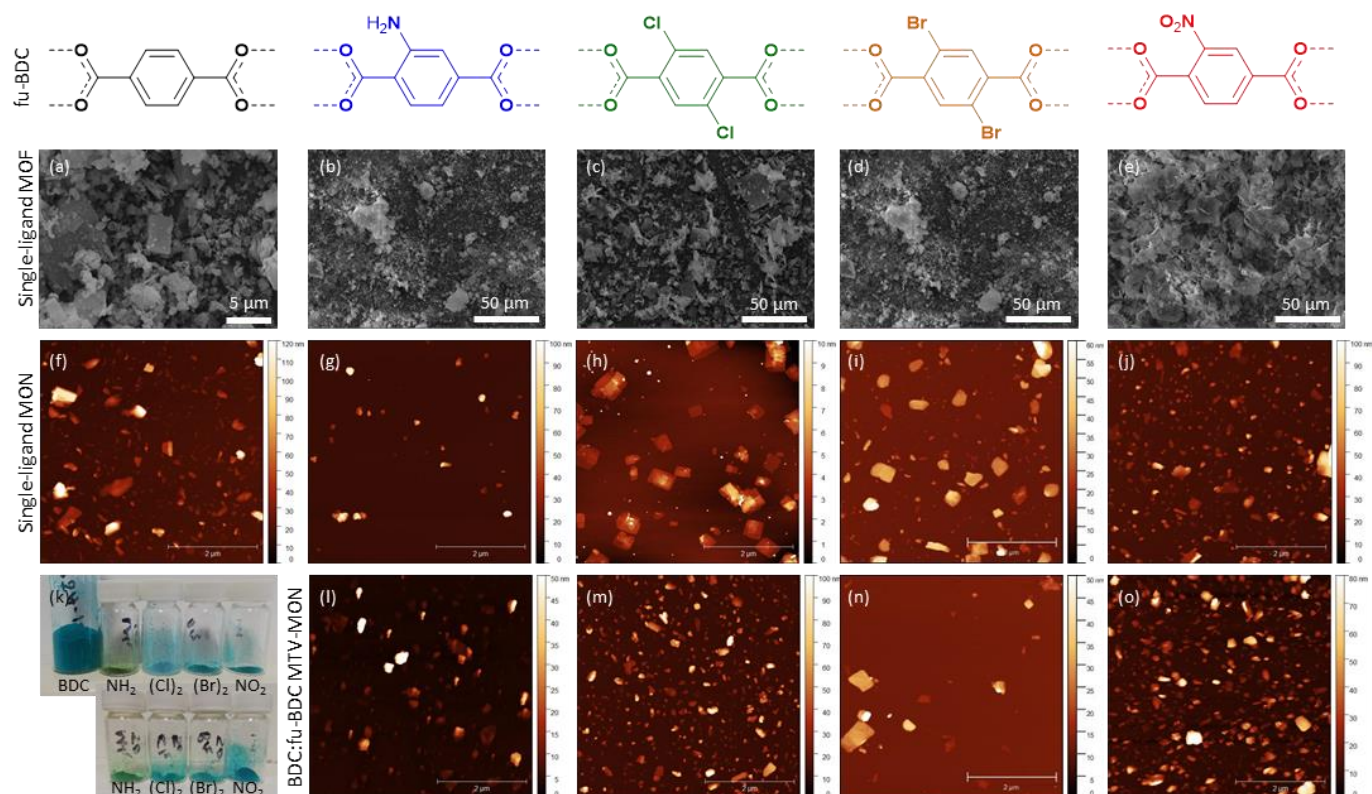
Figure 3. (a-e) SEM micrographs of single-ligand MOF powders. Topographical AFM images of single ligand (f-j) and mixed ligand $(H)_2$-fu-BDC-MTV-MOFs (l-o) after exfoliation of the MOF in MeCN and centrifugation for 1 hr at 1500 rpm. Scale bars are 2 µm in all cases. (k) Images of single ligand (top) and mixed ligand $(H)_2$-fu-BDC-MTV-MOF powders.

Table 2. Hydrodynamic diameter observed by DLS, and average particle size data of MONs imaged by AFM. and calculated using SPIP software for MONs produced through exfoliation of single- and mixed ligand MOFs in MeCN.

MONs		fu	Diameter* / nm	n	Length[†] ± SD / nm	Height[‡] ± SD / nm	Aspect ratio[§] ± SD
fu-MONs		$(H)_2$	178	375	199 ± 114	11 ± 10	23 ± 10
		NH_2	138	110	151 ± 61	18 ± 12	11 ± 5
		$(Cl)_2$	283	90	357 ± 171	3 ± 3	160 ± 82
		$(Br)_2$	176	257	232 ± 132	11 ± 6	23 ± 13
		NO_2	217	187	170 ± 89	11 ± 6	20 ± 11
$(H)_2$-fu-MTV-MONs		NH_2	164	88	221 ± 107	12 ± 15	39 ± 29
		$(Cl)_2$	133	409	175 ± 85	16 ± 10	14 ± 9
		$(Br)_2$	201	257	248 ± 159	10 ± 8	32 ± 19
		NO_2	139	344	139 ± 61	12 ± 7	20 ± 10
fu-MTV-MONs-x	1	NH_2-$(Cl)_2$	161	29	201 ± 86	23 ± 23	17 ± 11
	2	NH_2-$(Br)_2$	139	303	242 ± 131	14 ± 10	28 ± 25
	3	NH_2-NO_2	108	249	216 ± 107	20 ± 12	12 ± 5
	4	$(Cl)_2$-$(Br)_2$	131	113	236 ± 113	29 ± 15	9 ± 4
	5	$(Cl)_2$-NO_2	Conc. too low	N/A	Not enough particles observed through AFM.		
	6	$(Br)_2$-NO_2	205	N/A	Not enough particles observed through AFM.		
	7	NH_2-$(Cl)_2$-$(Br)_2$	181	94	266 ± 135	11 ± 9	32 ± 16
	8	NH_2-$(Cl)_2$-NO_2	168	100	240 ± 133	7 ± 8	53 ± 33
	9	NH_2-$(Br)_2$-NO_2	126	122	184 ± 80	10 ± 7	23 ± 12
	10	$(Cl)_2$-$(Br)_2$-NO_2	207	60	242 ± 160	7 ± 5	37 ± 17
	11	NH_2-Cl_2-Br_2-NO_2	174	122	253 ± 124	12 ± 8	25 ± 11

*Hydrodynamic diameter calculated by number averaged DLS data. n=number of particles identified by SPIP for sizing, from topographical AFM images. [†]Length was calculated as the largest lateral dimension across an identified particle. [‡]Height was calculated as the average height across the total surface of an identified particle. [§]Aspect ratio was calculated as the length divided by the height.

using the particle picking feature in SPIP software (see experimental), analysing between 90 and 375 particles. Care was taken during sample preparation to ensure that there was minimal particle overlap to ensure that the software could pick particles correctly (ESI Figures S20-S24). Average particle sizes are summarised in Table 2.

Perhaps surprisingly, this analysis revealed that despite the differences between the functional groups on the ligands the height ($\bar{x}$ ranged from 3-18 nm) and lateral dimensions ($\bar{x}$ ranged from 151-357 nm) of the MONs were broadly similar. The exceptions for height were $(Cl)_2$-MON, where the average height was 3±3 nm. This could indicate that $(Cl)_2$-MOF had the weakest interlayer interactions. NH_2-MON had the largest average height (18±12 nm), which may be a result of the stronger interlayer interaction in the MOF, as the NH_2 groups can form interlayer H-bonds, which are stronger than the van der Waals present in other MOFs. $(Cl)_2$-MON also had the largest average lateral size (357±171 nm), and the other four samples ranged 151±61 – 232±132 nm.

2.4 Exfoliation of $(H)_2$-fu-MTV-MOFs to form MTV-MONs

PXRD of recollected material post-centrifugation indicated similar structural rearrangements to the parent fu-BDC single ligand parent structures (ESI Figure S15). Interestingly, although the single ligand $(Cl)_2$-MOF underwent a complete structural transition, PXRD of the MTV-MOF indicated a significant amount of the "solvated" structure remained, with a minor but significant amount of the phase observed for $(Cl)_2$-MOF also present. Conversely, although exfoliation produced a mixed-phase for NH_2-MOF, exfoliation of $(H)_2$-NH_2-MTV-MOF revealed an absence of the initial structure, indicating a complete transtition. $(H)_2$-$(Br)_2$-MTV-MOF showed a complete transition, while $(H)_2$-NO_2-MTV-MOF showed a mixed phase.

UV-Vis again confirmed that there was material present in the supernatant, and DLS was used to indicate lateral sizes of the MTV-MONs (both ESI Figure S18), which revealed hydrodynamic diameters that ranged from 133 nm for $(H)_2$-$(Cl)_2$-MTV-MON, to 201 nm for $(H)_2$-$(Br)_2$-MTV-MON.

Samples were imaged by AFM, and particle size analysis was performed (ESI Figures S25-S29). Size data is summarised in Table 2. Average heights did not change significantly upon the addition of $(H)_2$-BDC to other fu-BDC-MOFs, other than for $(Cl)_2$-MOF. The average height increased from 3±3 nm, to 16±10 nm for $(H)_2$-$(Cl)_2$-MTV-MON. This indicates that adding $(H)_2$-BDC to $(Cl)_2$-MOF increases interlayer interactions, and prevents the facile exfoliation observed for $(Cl)_2$-MON to form ultrathin MONs. Average heights across the four MTV-MONs were broadly similar, ranging from 10±8 nm to 16±10 nm. Average lengths are broadly similar across the MTV-MON series, and are consistent with those observed for the respective single ligand MONs, other that $(H)_2$-$(Cl)_2$-MTV-MON, which also has much reduced lateral sizes, as well as height. These studies suggest that there is a delicate balance between surface chemistry and how well layered MOFs may exfoliate to form MONs, indicated by average height.

2.5. fu-MTV-MOF syntheses

Encouraged by the inclusion of different blends of $(H)_2$-BDC and other fu-BDC ligand within MTV-MOFs, we decided to explore the potential ligand inclusion of MTV-MOFs in this series. Equimolar quantities of the eleven different combinations of fu-BDC ligands (fu=NH_2, $(Cl)_2$, $(Br)_2$ and NO_2, but *not* $(H)_2$) were used within typical MOF syntheses, using copper acetate monohydrate as the Cu^{2+} source. This lead to six two-component MTV-MOFs, four three-component, and one four-component, which are termed MTV-MOF-1 to MTV-MOF-11 (see Table 3). Microcrystalline powders of various shades of blue-green were obtained (see Figure 4a). Generally, inclusion of NH_2-BDC resulted in darker greener coloured powder.

^{1}H NMR was used to quantify the ligand inclusion within the MTV-MOFs (ESI Figures S6 and S7), which can be seen in Table 3. In cases of overlapping peaks in the aromatic proton region, deconvolution techniques were used within Mestrenova software to provide more accurate integrals. Figure 4c shows an example ^{1}H NMR spectrum of digested MTV-MOF-11, with proton environments assigned for the four fu-H_2BDC components.

There were no cases of ligand exclusion within the MTV-MOFs. Broadly speaking, inclusion was as expected, with few major deviations from the input percentages of ligands. The only consistent overrepresentation of a diacid was NO_2-BDC, whose overinclusion ranges from 1-15 %. NH_2-BDC was generally slightly under included, from 0-10 % less than expected. There is not a consistent trend between Cl_2-BDC and Br_2-BDC inclusion. These results are consistent with the previous $(H)_2$-fu-MTV-MOFs. This corroborates that it is pk$_a$ of the acid (NO_2 is the most electron-withdrawing group, pulling electron density out of the ring, and therefore away from acid groups, and therefore the acidic proton is more easily lost), rather than a steric effect (NO_2 is the largest functionality) which determined reaction kinetics, and therefore relative ligand inclusion.

DMF content was also quantified using ^{1}H NMR. DMF content, relative to the total ligand content ranged from 31 % (MTV-MOF-4) to 149 % (MTV-MOF-9) (percentages based on the expected 1:1 ligand:DMF ratio), which indicated varying

Table 3. Sample reference, ligand inclusion (%) and DMF content* (%) observed through ^{1}H-NMR analysis of digested MTV-MOFs.

MTV-MOF-x	NH$_2$	(Cl)$_2$	(Br)$_2$	NO$_2$	DMF*
1	50	50	-	-	96
2	40	-	60	-	99
3	49	-	-	51	105
4	-	53	47	-	31
5	-	43	-	57	93
6	-	-	49	51	79
7	24	31	37	-	100
8	32	31	-	37	109
9	23	-	29	48	149
10	-	37	27	37	74
11	15	35	15	35	118

*DMF content as %, relative to the total ligand content, based on a 1:1 ratio.

levels of "solvation" within the structures. MTV-MOFs were analysed using PXRD to assess the effect this had on the phase of material produced, (Figure 4).

MTV-MOFs-1, 5 and 8 appear highly crystalline, and the PXRD patterns indicate they are structurally similar to MOF-46.
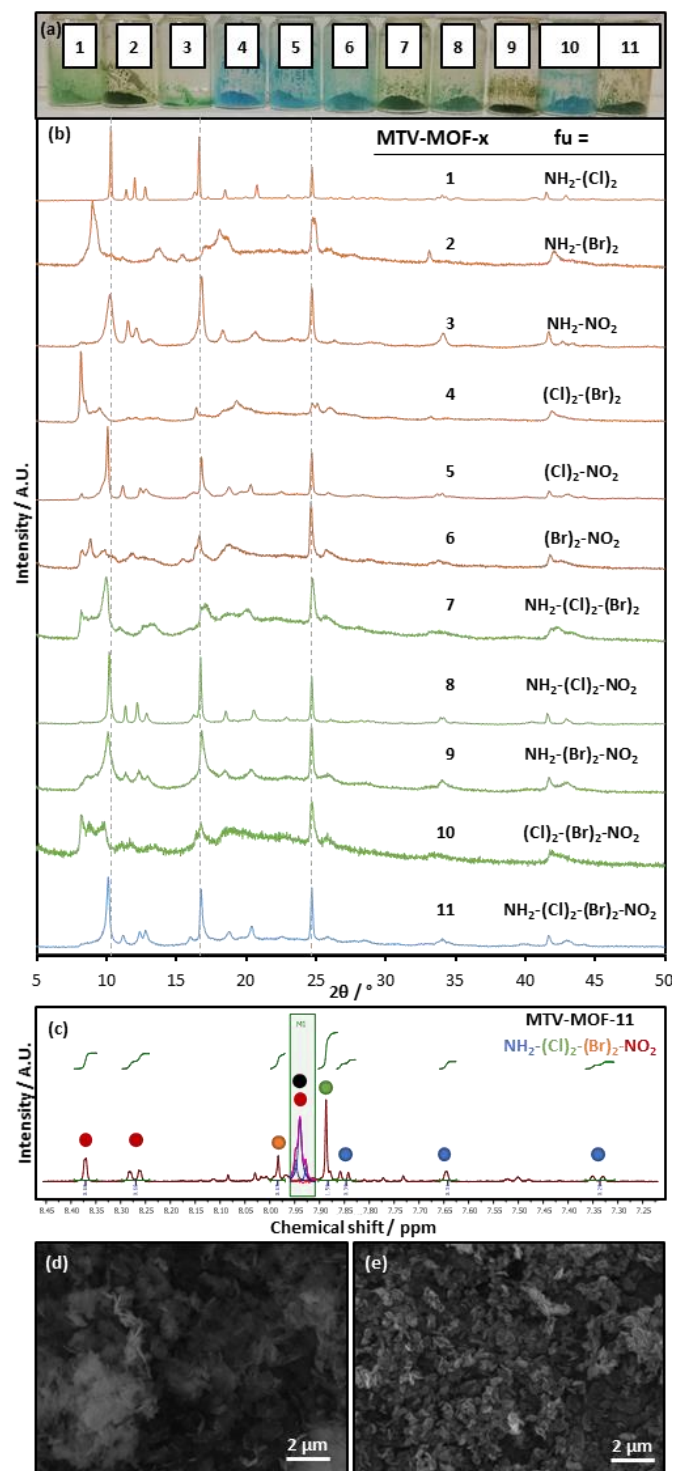

Figure 4. (a) Images of MTV-MOFs-1-11. (b) PXRD patterns of MTV-MOFs-1-11, with included fu-BDC ligands indicated. (c) Example ^1H NMR spectra for MTV-MOF-11, with proton environments assigned. Peak corresponding to DMF is indicated with a black circle. (d-e) Example SEM images of MTV-MOFs-8 and 11, respectively.

Substituting $(Br)_2$-BDC for $(Cl)_2$-BDC in each case (i.e. MTV-MOFs-2, 6 and 9) results in PXRD patterns that are less crystalline, characterised by weakly diffracting, wider peaks, and also form a mixed phase of material. This effect is also observed for other $(Br)_2$-BDC-containing MTV-MOFs-4 and 7. This was unexpected, as $(Br)_2$-MOF and $(H)_2$-$(Br)_2$-MTV-MOF had shown strongly crystalline samples which looked to adopt to the "solvated" structure similar to MOF-46. PXRD of MTV-MOF-11 indicated a structure similar to that of MOF-46. Although $(Br)_2$-BDC is included, the much smaller fraction (15 %) present than in other $(Br)_2$-BDC containing MTV MOFs may limit the effect observed in other MTV-MOFs.

We could not ascribe the observed structural effects to a single reason. NH_2 is a more electron-withdrawing group than the Br moiety, and NO_2 is more electron-donating. NO_2 is the largest moiety, however $(Cl)_2$ and $(Br)_2$ are difunctionalized. Other than $(Br)_2$-BDC, for which the incorporation in general leads to a mixed phase MOF with both the MOF-46 structure, and an additional phase that we ascribe as the desolvated [Cu(fu-BDC)] phase (characterised by the low-angle peaks around 8.2 and 8.9 ° 2θ), there is not a consistent effect observed for inclusion of a particular fu-BDC.

Irregular packing between layers as a result of different ligands stacking in different ways may lead to it being unfavourable for DMF to coordinate to the axial PW position, as there may not be stabilising van der Waals from neighbouring functionalities. It is also known that related systems in which the 2D **sql** grid network of PW-BDC, but with different fu-BDC, can result in different torsion angles of the aromatic ring away from the plane defined between two adjacent PW units and the carboxylate group. For example, $[Cu(BDC)(DMF)]_n$ has a torsion angle 25.6 °,[34] MOF-46 $[Zn(NH_2-BDC)(DMF)]_n$ has 25.2 °,[48] but MOF-102 $[Cu((Cl)_2-BDC)(DMF).H_2O_{0.5}DMF_{1.75}]_n$ has 53.4 °.[38] For MOF-102, this torsion angle and the layer packing result in larger voids between layers in the framework, in which DMF and water molecules are located. This indicates that regular layer stacking in these MTV-MOFs may be unlikely, as adjacent layers are unlikely to have the same positional ligand incorporation. Different torsion angles may result in "pockets" within the framework, which may account for observed DMF of over 100 %. Alternatively, large torsion angles would result in projection of the fu-groups into the pore space, and therefore there is not the required space for coordinated DMF to penetrate the adjacent layers (as it does for $[Cu(BDC)(DMF)]_n$[34] and $[Zn(NH_2-BDC)(DMF)]_n$),[48] promoting the desolvated structure.

As a result of using combinations of different fu-BDC ligands, there may be an array of subtle effects which influence the level of solvation of material, as well as the layer packing. The presence of high intensity peaks at 10.3, 16.6 and 24.8 ° 2θ (corresponding to the [1,1,0], [0,2,1] and [1,3,1] planes in MOF-46, respectively – all in-plane reflections) give some indication that a similar overall structure is adopted across the MTV-MOF series. This gives confidence that we have indeed formed a series of Cu_2-PW-based layered MTV-MOFs. Without more in-depth X-ray studies, it is difficult to be conclusive about the adopted structures. However, this also highlights a

characterisation limitation for these systems: irregular stacking means that there may be an absence of true long-range order in these MTV-MOFs, which was not an issue for MTV-MOF-5, as the same rigid 3D structure was maintained despite different fu-BDC inclusion.[28,29]

Further evidence of the adoption of the desired Cu(fu-BDC) structure was offered by SEM of high-component MTV-MOFs-8 and 11 (Figure 4c and d). Predominantly large agglomerates (length<80 μm) of crystallites were observed, however upon zooming into the underlying powder many small lamellar platelet-like crystallites can be observed <2 μm in length and less than 100 nm thickness, for both MTV-MOFs. This crystal habit and nanosheet morphology supports that we are indeed forming the desired layered phase. The evidence of these small lamellar MOF nanosheets gives confidence that these materials may be suited to exfoliation to produce ultrathin MONs.

2.6. Exfoliation of fu-MTV-MOFs to form MTV-MONs

Liquid ultrasonic exfoliation of MTV-MOFs-1-11 and subsequent centrifugation of the suspension resulted in recollection of unexfoliated material, leaving a suspension of MTV-MONs-1-11.

PXRD of the recollected, dried material indicated that in most cases, the original structure no longer remained post-exfolaition, and had fully transformed to a structure similar to that of $[Cu(BDC)]_n$ (ESI Figure S16). The exception to this was MTV-MOF-1, in which the structure similar to that of MOF-46 was maintained. The PXRD of MTV-MOFs-2,3,5,8,9,11 indicated a different, but consistent structure, characterised by the intense peak around 9.8 ° 2θ, whereas MTV-MOFs-4,5,6,10 formed a consistent structure characterised by the intensity peaks around 8.3 and 9.6 ° 2θ, consistent with $[Cu(BDC)]_n$.

UV-Vis spectroscopy of the MTV-MON suspensions confirmed material present in suspension. Supernatents of MTV-MONs-2,3,7,9,11 were visibly green/blue coloured (ESI Figure S17) and required dilution for UV-Vis analysis (ESI Figure S19). MTV-MONs-1,5,6 had very low absorbances, possibly indicating low concentration in suspension. The concentration of MTV-MON-5 was too low to be determined by DLS. Hydrodynamic diameters of other MTV-MOFs (see Table 2, ESI Figure S19) varied between 108 nm (MTV-MON-3, fu=NH_2-NO_2) and 207 nm (MTV-MON-10, fu=$(Cl)_2$-$(Br)_2$-NO_2).

MTV-MON suspensions were drop-cast and imaged using AFM (Figure 5) and average particle sizes were determined from sample sizes of n=29-303 (ESI Figures S29-S37). Due to the very low concentrations of MTV-MONs-5 and 6, no MONs were observed by AFM, and so these samples were excluded from the statistical analysis. Average particle sizes are summarised in Table 2.

Broadly speaking, MON morphologies were consistent across the different MTV-MON samples. MONs were remarkably square with defined corners, which was not always the case for single-ligand parents (see Figure 3f-j). Lateral sizes were relatively consistent, ranging from 184±80 nm (MTV-MON-9, fu=NH_2-$(Br)_2$-NO_2) to 266±135 nm (MTV-MON-7, fu=NH_2-$(Cl)_2$-$(Br)_2$). It is worth noting that our observations

show that blending of such different ligands does not dramatically alter the MON lateral dimensions.

MONs were observed in each sample with heights < 10 nm. Average heights varied across the series from 7±5 nm (MTV-MON-10, fu=$(Cl)_2$-$(Br)_2$-NO_2) to 29±29 nm (MTV-MON-4, fu=$(Cl)_2$-$(Br)_2$). It may have been anticipated that NH_2-BDC-containing MTV-MONs may be thicker, due to the NH_2 moiety's H-bond donating ability (all fu-groups, and DMF, are H-bond acceptors of varying strength), and therefore NH_2-BDC-
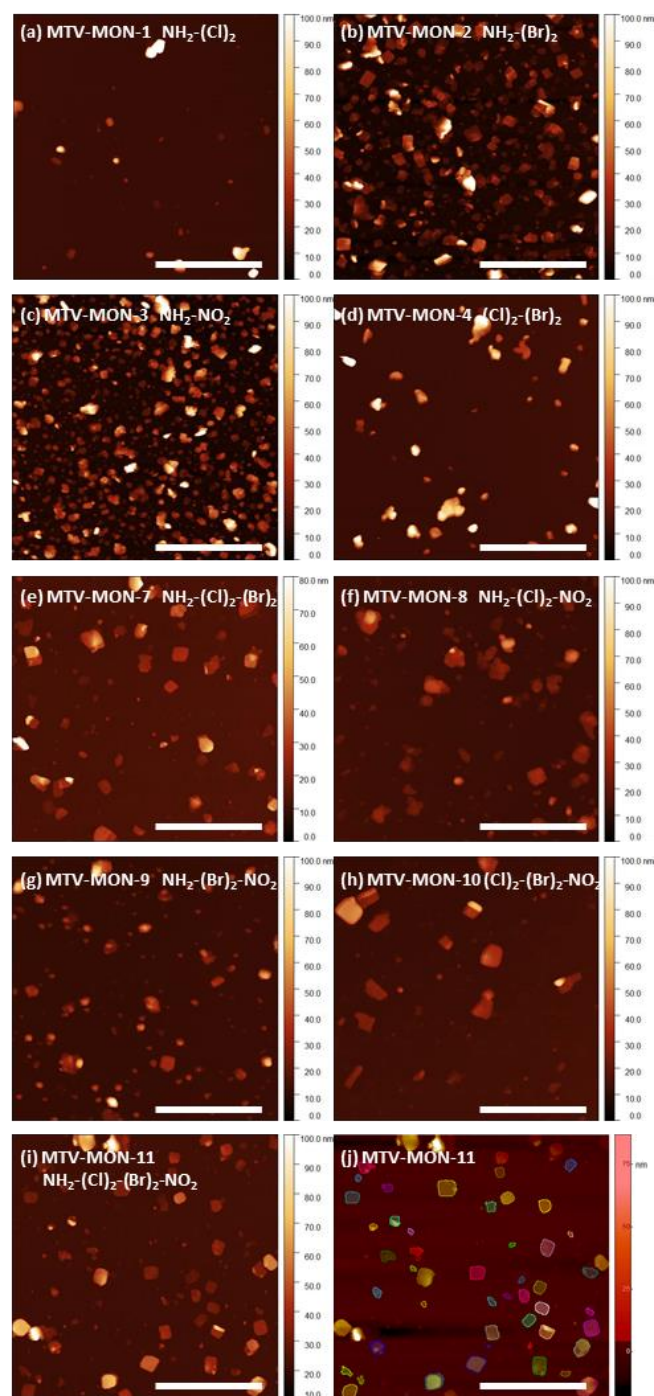

Figure 5. (a-i)Topographical AFM images of MTV-MONs-1-4 and 7-11. (j) Example of particle picking when sized using SPIP software. Lateral scale bars are 2 μm throughout.

containing MTV-MOFs may have stronger interlayer interactions. However, this is not observed here. The MON with largest average height only includes fu=(Cl)$_2$ and (Br)$_2$.

Interestingly, average particle height was lower for the higher-component ternary/quaternary blends (7±5 ≤ x̄ ≤ 12±8 nm) than binary blends (14±10 ≤ x̄ ≤ 29±29 nm). As the lateral dimensions are broadly similar across the series, this corresponded with increased aspect ratio for higher component blends (see Table 2). We suggest this could be indicative of reduced interlayer interactions in the higher component MTV-MOFs. This could be due to irregular stacking interactions between layers. Random inclusion of ligands within the framework[28,29,49] would lead to irregular packing between layers, which could result in more favourable exfoliation, leading to MONs with smaller average heights.

2.8 fu-BDC mixed ligand MON formation through bottom-up direct crystallisation

When washing single-ligand MOFs, (H)$_2$-fu-MTV-MOFs and fu-MTV-MOFs through centrifugation, the supernatant in each wash was generally colourless – a good indication that MOF particles had been collected during the centrifugation cycle (10 min at 4500 rpm). However, for MTV-MOF-3 (fu=(NH$_2$-NO$_2$) and MTV-MOF-4 (fu=(Cl)$_2$-(Br)$_2$), it was noticed that the supernatant remained slightly cloudy and green-coloured through washing with DMF. Tyndall scattering revealed that there were solid particles remaining in suspension in the supernatant following centrifugation, indicating not all crystallite particles were collected. Longer centrifugation (1 hr) did not collect these from suspension. It was hypothesised that these particles may be small crystallites, similar to those observed by SEM for MTV-MOFs-8 and 11 (Figure 4). As this had not been observed before, the supernatant of the 3rd DMF wash was retained and assessed using AFM (Figure 6).

Nanosheet crystallites were observed typically 5-20 nm in height, down to a minimum of 2 nm (just two framework layers, based on the structure of MOF-46, for which MTV-MOF-3 is structurally similar. See Figure 6), however few nanosheets with height < 5 nm were observed. Laterally, dimensions typically ranged from 100-250 nm, with the extremes observed at 80 nm and 310 nm. Particles were remarkably angular and square. Corners are clearly defined and sharp, giving insight into the crystallisation process. Direct crystallisation of MONs avoids the potential fracturing that may occur through energy-intensive

Figure 6. Topographical AFM images of MONs isolated directly from the third DMF wash of MTV-MOF-3 (fu=NH$_2$-NO$_2$).

top-down ultrasonication, resulting in MONs.

The reasons for this observation specifically for MTV-MOFs-3 and 4 are unclear, as there was no common ligand between the two MOFs. It may have been coincidental; a high concentration small particulates was indicated through the colour of the supernatant post-centrifugation, however MONs such as these may have in fact been formed through all MTV-MOF syntheses, but in lower concentrations and so had gone unnoticed and been disposed of. A further large, quantitative study on MONs resulting from direct crystallisation would be required to elucidate factors governing MON crystallisation.

Given that that formation of small MONs such as these were not anticipated through the MOF synthesis, as similar syntheses of single-ligand MOFs results in large (>25 μm^2) MOF crystallites, it seems likely that optimisation of reaction conditions such as copper salt, reagent concentration, reaction temperature and time may be able to favour the production of small MON crystallites. This would be of great interest for general MON syntheses. It is unknown whether the nature of having mixed ligands within the MOF synthesis promoted the production of MONs directly, or if this was merely coincidental. Separate crystallisation studies are required to answer this, however this preliminary work is exciting from the point of scale-up of MON synthesis. The direct crystallisation of MONs in this manner avoids added species such as polymers or surfactants,[50] as used in other bottom-up methodologies, which have been required to prevent the epitaxial growth of MONs within a crystallisation. If high quality MONs like this can be synthesised through direct methods, this paves the way for scalable processes including batch reactors and continuous flow processes for these materials.

3. Conclusions

In this study, we first synthesised an isoreticular series of 2D layered MOFs based on the in-plane **sql** grid network of MOF-2, using five different fu-BDC linkers (fu= (H)$_2$, NH$_2$, (Cl)$_2$, (Br)$_2$ and NO$_2$). Pawley refinement of PXRD patterns confirmed an isoreticular series structurally similar to MOF-46,[41] while (Cl)$_2$-MOF formed a mixed-phase material, of the anticipated structure and an additional, desolvated phase similar to that of [Cu(BDC)]$_n$.[34,42] Liquid ultrasonic exfoliation of these materials yielded MONs down to monolayer thickness in some cases, and SPIP software was used to analyse particle size. (Cl)$_2$-MOF formed the thinnest (3±3 nm) and largest (357±171 nm) MONs.

We then synthesised a series of mixed ligand MTV-MOFs using 50:50 mixtures of fu=(H)$_2$ and the other fu-BDCs. Ligand inclusion within the MTV-MOFs differed from those added to the reaction solution across the series, which we ascribe to difference in acid pk$_a$ as a result of the different functional groups. Electron withdrawing fu=NH$_2$ resulted in the lowest inclusion of fu-BDC (32 %), while electron donating fu=NO$_2$ had the highest inclusion (56 %). The series were found to be isoreticular materials, that could be fit to very similar unit cells using Pawley refinement. (H)$_2$-(Br)$_2$-MTV-MOF existed with less that quantitative DMF content (23 %) but still adopted the "solvated" framework structure, indicating that inclusion of Br$_2$-
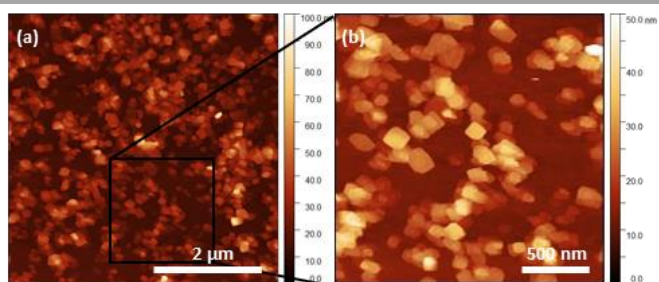
BDC stabilised the framework against rearrangement upon desolvation. Exfoliation of these MTV-MOFs produced mixed-ligand MTV-MONs for the first time.

Eleven MTV-MOFs were then synthesised using six binary combinations of fu-BDC, four ternary and one quaternary combination. MTV-MOFs were exfoliated to form MTV-MONs with average heights ranging from 7±5 to 29±29 nm. MTV-MONs with ternary and quaternary combinations formed MONs with reduced average height than binary blends. We suggest this could result from reduced interlayer interactions due to more irregular stacking of layers in the higher component layered MTV-MOFs. This series could be extended through the inclusion of other commercially available BDC derivatives, including monofunctionalised X-BDC (X=Br or Cl), $(OH)_2$-BDC,[51] and naphthalene-1,4-dicarboxylate,[52] for example.

Overall, this study introduces MTV-MONs with tuneable surface chemistry through the inclusion of multiple different ligands with different functionalities. This could be more widely applicable within the world of 2D material chemistry due to the controllability of the surface-presented functionalities. These groups could be post-synthetically functionalised to introduce a wide range of functional groups to further modify or diversify the surface chemistry. We envisage the MTV-MON approach being widely applicable across different MOF series suitable for MON production, including the UiO-67-type[53] series as well as the $[M(bim)_2]^{[27,54]}$ series.

4. Experimental

4.1. Materials

Materials were purchased from commercial suppliers and used without further purification. Copper nitrate trihydrate (SLS, 98 %), copper acetate (Alfa Aesar, 98+ %), H_2BDC (Acros, 99+ %), 2-NH_2-H_2BDC (Aldrich, 99 %), 2,5-Cl_2-H_2BDC (Fluorochem, 95 %), 2,5-Br_2H_2BDC (Fluorochem, 90 %), 2-NO_2-H_2BDC (Acros, 99+ %), DMF (Fisher, 99+ %) and MeCN (Fisher, 99.9+ %).

4.2. MOF syntheses

A general method was used for single ligand fu-MOF and $(H)_2$-fu-MTV-MOF syntheses. A target mass of fully solvated [Cu(fu-BDC)(DMF)] of either 20 or 30 mg was assigned and reagent molar quantities back-calculated, taking into account the weighted percentage of expected ligand for calculation of the molecular weight of the repeat unit. The copper salt (nitrate or acetate) was used in this molarity, and ligands were added in equal molar quantities to a total of 110 % molarity (i.e. 10 % total ligand excess). For example, for $(H)_2$-NH_2-MTV-MOF, 30 mg was targeted. Based on the formula [Cu(BDC)$_{0.5}$(NH2-BDC)$_{0.5}$(DMF)], Mr= 308.3 Da based on $CuC_{11}H_{11.5}N_{1.5}O_5$, so molar quantity = 0.097 mmol. Copper nitrate trihydrate (22.2 mg, 0.092 mmol), H2BDC (8.6 mg, 0.052 mmol) and 2-NH_2-BDC (9.3 mg, 0.051 mmol) were dissolved in 9 mL DMF and sealed into a glass reaction vial with Teflon-lined lid. This was heated at 10 °C min^{-1} to 110 C and held for 36 hrs, then cooled at 0.1 C min^{-1} to 25 C. Solids were washed through

centrifugation (4500 rpm for 10 mins) with DMF (3 x 5 mL) and diethyl ether (3 x 5 mL) and air dried at room temperature, yielding a green microcrystalline powder of [Cu(BDC)$_{0.68}$(NH$_2$-BDC)$_{0.32}$(DMF)] (26.4 mg, 93 %). Input reagent quantities and yields for other MOFs can be found in the ESI.

$(H)_2$-MOF. Pawley refinement of the powder X-ray diffraction (PXRD) pattern indicated that the material crystallised in the C2/m space group and had a similar unit cell to that calculated from the crystal structure for [Cu(BDC)(DMF)]$_n$ (CCDC ref. no. 687690).[34] FTIR indicated DMF coordination (ν C=O at 1661 cm^{-1}, shifted from 1676 cm^{-1} of liquid phase DMF) and elemental analysis (EA) was consistent with the anticipated (calc. for $C_{11}H_{11}CuNO_5$: C, 43.93; H, 3.69; N, 4.66, obs: C, 43.76; H, 3.79; N, 4.82). Square platelet crystallites with lateral dimensions <10 μm were observed using scanning electron microscopy (SEM), which stacked to form deck-of-cards-like crystallites.

NH_2-MOF. Pawley refinement of the PXRD pattern indicated that the material crystallised in the C2/m space group and had a similar unit cell to that calculated from the crystal structure for [Zn((NH$_2$)-BDC)(DMF)]$_n$ (MOF-46 – CCDC ref. no. 172613).[37] DMF coordination was evidenced by FTIR and elemental analysis was consistent with the anticipated formula of [Cu(NH$_2$-BDC)(DMF)]$_n$ (calc: C 41.84, H 3.83 N 8.87 %; obs C 41.02, H 3.97, N 8.43 %), indicating that the desired phase, isostructural to MOF-46, had been synthesised. SEM indicated platelet crystallite sizes <2 μm laterally, which formed larger agglomerates <20 μm. Platelets were smaller than those of $(H)_2$-MOF, possibly due to the increased solubility of copper acetate monohydrate compared to copper nitrate trihydrate, and subsequent faster reaction kinetics.[40]

$(Cl)_2$-MOF. PXRD indicated that a phase structurally similar to MOF-46 was formed, however there was also a second phase present. Pawley fitting of the PXRD pattern could not isolate the two phases. EA showed a much lower nitrogen content than the calculated for [Cu((Cl)$_2$-BDC(DMF)]$_n$ (calc: C 35.74, H 2.45, N 3.79 %; obs: C 32.37, H 2.33, N 0.72 %), which indicated that there may a level of "desolvation" where there is no DMF coordinated to axial PW sites, as has been observed for [Cu(BDC)(DMF)]$_n$ to form [Cu(BDC)]$_n$.[34,42] This is further evidenced upon exfoliation (see below). ^{1}H-NMR quantified the DMF content as 14 % (relative to ligand content). SEM showed that square platelet crystallites <15 μm laterally had been formed.

$(Br)_2$-MOF. Pawley refinement of the PXRD pattern indicated a unit cell similar to that of MOF-46, however EA showed a reduced N content compared to an expected repeat formula of [Cu((Br)$_2$-BDC)(DMF)] (calc: C 28.81, H 1.98, N 3.05 %; obs: C 24.92, H 0.97, N 0.30 %), and ^{1}H-NMR quantified DMF content as 12 %, compared to the ligand. The DMF C=O stretch was not observed by FTIR. Interestingly, although there is little DMF within the material, it seems that the grid structure of the solvated phase is maintained, rather than the layers slipping

upon desolvation. This could be due to the larger sterics of the dibromo groups, which may prevent changes to the grid stacking. Square platelet crystallites with edges <20 μm were observed by SEM.

NO$_2$-MOF. Pawley fitting of the PXRD pattern shows a unit cell similar to that of MOF-46. FTIR indicated DMF coordination, and EA was consistent with the formula (Cu(NO$_2$-BDC)(DMF)]$_n$ (calc: C 38.21, H 2.92, N 8.10 %, obs: C 37.38, H 2.99, N 7.74 %) There is a small intensity peak at 8.2 ° 2θ, which we ascribe to small amount of a secondary, desolvated phase (^{1}H-NMR quantified DMF content as 95 %, relative to ligand content). SEM indicated square platelet crystallites with lateral dimensions <15 μm.

(H)$_2$-fu-MTV-MOFs. Pawley refinement of the PXRD patterns indicated crystallisation in the C2/m space group, with unit cell dimensions similar to that of MOF-46 in all cases (Table 1). FTIR indicated DMF coordination in all cases (ESI Figure S3), but with a much higher transmission for (H)$_2$-(Br)$_2$-MTV-MOF, indicating a lower DMF content. ^{1}H-NMR quantified DMF content as 99, 100, 23 and 98 % for fu=NH$_2$, (Cl)$_2$, (Br)$_2$ and NO$_2$ respectively. Elemental analysis was consistent with the calculated formula of [Cu((H)$_2$-BDC)$_x$(fu-BDC)$_{1-x}$(DMF)]$_n$, taking into account observed incorporated ligand ratios, for fu=NH$_2$, (Cl)$_2$ and NO$_2$. Reduced N content in fu=(Br)$_2$ corroborated partial desolvation of the structure

Table 4. Elemental analyses of (H)$_2$-fu-MTV-MOFs, based on the anticipated structure of [Cu((H)$_2$-BDC)$_x$(fu-BDC)$_{1-x}$(DMF)]$_n$

fu	% fu	Calc / %			Obs / %		
	(1-x)	C	H	N	C	H	N
NH$_2$	32	43.24	3.73	6.05	42.07	3.74	5.31
(Cl)$_2$	47	39.95	3.08	4.32	39.94	3.20	4.05
(Br)$_2$	46	35.21	2.74	3.81	33.15	2.56	2.01
NO$_2$	56	40.53	3.23	6.70	39.98	3.24	6.72

fu-MTV-MONs. See ESI for details.

4.3. Liquid ultrasonic exfoliation

2 mg of MOF was suspended in 2.4 mL MeCN and vortexed for 30 s then sonicated for 12 h using a Fisher brand Elmasonic P 30H ultrasonic bath operating at 80 kHz and 100 % power (320 W). Samples were rotated (40 rpm) using an overhead stirrer to ensure even exposure and the bath was fitted with a water coil to maintain temperature at approximately 18-21 °C.[43] After sonication, samples were transferred to a centrifuge tube and centrifuged for 1 hr at 1500 rpm, which recollected unexfoliated material and yielded MON-containing supernatant.

4.4. Characterisation

PXRD were recorded using a Bruker D8 Advance powder X-ray diffractometer equipped with a Lynxeye detector, using Cu k$_α$ radiation (λ=1.5406 Å) operating in capillary mode (MOFs) or flat-plate mode (materials recollected from centrifugation. For capillary mode, samples were ground and loaded into a 0.7 mm

internal diameter borosilicate capillary. For flat plate, samples were sprinkled onto a low-background silicon plate. Pawley refinement[55] was performed using TOPAS software[56,57] using the unit cell parameters of [Cu(BDC)(DMF)][34] for [Cu(BDC)(DMF)] MOF, and MOF-46[37] for other single ligand MOFs and BDC:fu-BDC MTV-MOFs. FTIR spectra were recorded with a PerkinElmer Spectrum One spectrometer equipped with a diamond ATR accessory. Data were collected from 500 to 4000 cm^{-1} using a resolution of 1 cm^{-1} and 8 scans. Elemental analysis was performed with an Elementar vario MICRO cube. Room temperature ^{1}H-NMR spectroscopy was performed with a Bruker Avance IIIHD 400 MHz spectrometer. 1H chemical shifts are reported in parts per million on the δ scale and referenced to the residual proton resonance of the solvent. Approximately 2 mg MOF was digested using 21 μL DCl (35 %) in D$_2$O and 1 mL d_6-DMSO, resulting in solutions of diacid ligand precursors for quantification. Samples were prepared for SEM analysis on a carbon sticky tab loaded on an aluminium sample stub and coated with approximately 20 nm gold using an Edwards S150B sputter coater. SEM micrographs were collected using a TESCAN VEGA3 LMU SEM instrument operating in secondary electron mode. UV-Vis spectroscopy was performed on a Cary 50 UV-Vis spectrophotometer, in the range 800-230 nm (solvent dependant) with a 1 nm resolution and 600 nm min^{-1} scan speed, using polystyrene UV-Vis cuvettes. DLS data were collected using a Malvern Zetasizer Nano Series particle size analyzer equipped with a He–Ne laser at 633 nm, operating in backscatter mode (173°). AFM was performed with a Bruker Multimode 5 AFM operating in soft-tapping mode using Bruker OTESPA-R3 cantilevers. Samples were prepared by drop-casting 10 μL MON suspension onto freshly cleaved mica held on a magnetic sample holder which was pre-heated to just below the boiling point of the solvent. Images were processed using standard techniques within Gwyddion image processing software.[58]

4.5. Particle sizing

Particle sizing was performed using SPIP software. Prior to analysis, AFM images were plane levelled, scars were removed and the background was zeroed. The particle and pore analysis tool was used to pick and size particles. The "threshold" detection method was used, which varied between images depending on how well the background had been levelled, between 0.8 and 8 nm. Post-processing filters for particle inclusion were used across all images: (i) minimum length of 80 nm to neglect image defects and small fragments on the sample surface; (ii) minimum height 1 nm to avoid detecting small jumps from the scan; (iii) maximum height of 150-200 nm to neglect large particles/ agglomerates or jumps in the probe/surface contact. Particles that lay partly on an edge of the image were not included.

Conflicts of interest

There are no conflicts to declare.

Acknowledgements

References

1   R. Mas-Ballesté, C. Gómez-Navarro, J. Gómez-Herrero and F. Zamora, *Nanoscale*, 2011, **3**, 20–30.

2   S. R. Batten and N. R. Champness, *Philos. Trans. R. Soc. A Math. Phys. Eng. Sci.*, 2017, **375**, 20160032.

3   A. U. Czaja, N. Trukhan and U. Müller, *Chem. Soc. Rev.*, 2009, **38**, 1284–1293.

4   D. Rodríguez-San-Miguel, P. Amo-Ochoa and F. Zamora, *Chem. Commun.*, 2016, **52**, 4113–4127.

5   R. Sakamoto, K. Takada, T. Pal, H. Maeda, T. Kambe and H. Nishihara, *Chem. Commun.*, 2017, **53**, 5781–5801.

6   M. Zhao, Y. Huang, Y. Peng, Z. Huang, Q. Ma and H. Zhang, *Chem. Soc. Rev.*, 2018, **47**, 6267–6295.

7   M. A. Solomos, F. J. Claire and T. J. Kempa, *J. Mater. Chem. A*, 2019, **7**, 23537–23562.

8   D. J. Ashworth and J. A. Foster, *J. Mater. Chem. A*, 2018, **6**, 16292–16307.

9   T. Bauer, Z. Zheng, A. Renn, R. Enning, A. Stemmer, J. Sakamoto and A. D. Schlüter, *Angew. Chemie - Int. Ed.*, 2011, **50**, 7879–7884.

10   S. Motoyama, R. Makiura, O. Sakata and H. Kitagawa, *J. Am. Chem. Soc.*, 2011, **133**, 5640–5643.

11   T. Kambe, R. Sakamoto, K. Hoshiko, K. Takada, M. Miyachi, J. H. Ryu, S. Sasaki, J. Kim, K. Nakazato, M. Takata and H. Nishihara, *J. Am. Chem. Soc.*, 2013, **135**, 2462–2465.

12   S. C. Junggeburth, L. Diehl, S. Werner, V. Duppel, W. Sigle and B. V. Lotsch, *J. Am. Chem. Soc.*, 2013, **135**, 6157–6164.

13   T. Rodenas, I. Luz, G. Prieto, B. Seoane, H. Miro, A. Corma, F. Kapteijn, F. X. Llabrés I Xamena and J. Gascon, *Nat. Mater.*, 2015, **14**, 48–55.

14   R. Sakamoto, K. Hoshiko, Q. Liu, T. Yagi, T. Nagayama, S. Kusaka, M. Tsuchiya, Y. Kitagawa, W. Y. Wong and H. Nishihara, *Nat. Commun.*, 2015, **6**, 1–9.

15   Z. Hu, E. M. Mahdi, Y. Peng, Y. Qian, B. Zhang, N. Yan, D. Yuan, J. C. Tan and D. Zhao, *J. Mater. Chem. A*, 2017, **5**, 8954–8963.

16   P. Amo-Ochoa, L. Welte, R. González-Prieto, P. J. Sanz Miguel, C. J. Gómez-García, E. Mateo-Martí, S. Delgado, J. Gómez-Herrero and F. Zamora, *Chem. Commun.*, 2010, **46**, 3262–3264.

17   P.-Z. Li, Y. Maeda and Q. Xu, *Chem. Commun.*, 2011, **47**, 8436–8438.

18   A. Abhervé, S. Mañas-Valero, M. Clemente-León and E. Coronado, *Chem. Sci.*, 2015, **6**, 4665–4673.

19   Y. Peng, Y. Li, Y. Ban and W. Yang, *Angew. Chemie - Int. Ed.*, 2017, **56**, 9757–9761.

20   Y. Ding, Y. P. Chen, X. Zhang, L. Chen, Z. Dong, H. L. Jiang, H. Xu and H. C. Zhou, *J. Am. Chem. Soc.*, 2017, **139**, 9136–9139.

21   R. Xu, M. Jian, Q. Ji, C. Hu, C. Tang, R. Liu, X. Zhang and J. Qu, *Chem. Eng. J.*, 2020, **382**, 122658.

22   O. M. Yaghi, M. O'Keeffe, N. W. Ockwig, H. K. Chae, M. Eddaoudi and J. Kim, *Nature*, 2003, **423**, 705–714.

23   O. M. Yaghi, *J. Am. Chem. Soc.*, 2016, **138**, 15507–15509.

24   O. M. Yaghi, *ACS Cent. Sci.*, 2019, **5**, 1295–1300.

25   T. Rodenas, I. Luz, G. Prieto, B. Seoane, H. Miro, A. Corma, F. Kapteijn, F. X. Llabrés i Xamena and J. Gascon, *Nat. Mater.*, 2015, **14**, 48–55.

26   B. Garai, A. Mallick, A. Das, R. Mukherjee and R. Banerjee, *Chem. - A Eur. J.*, 2017, **23**, 7361–7366.

27   J. López-Cabrelles, S. Mañas-Valero, I. J. Vitórica-Yrezábal, P. J. Bereciartua, J. A. Rodríguez-Velamazán, J. C. Waerenborgh, B. J. C. Vieira, D. Davidovikj, P. G. Steeneken, H. S. J. van der Zant, G. Mínguez Espallargas and E. Coronado, *Nat. Chem.*, 2018, **10**, 1001–1007.

28   H. Deng, C. J. Doonan, H. Furukawa, R. B. Ferreira, J. Towne, C. B. Knobler, B. Wang and O. M. Yaghi, *Science*, 2010, **327**, 846–850.

29   X. Kong, H. Deng, F. Yan, J. Kim, J. A. Swisher, B. Smit, O. M. Yaghi and J. A. Reimer, *Science*, 2013, **341**, 882–885.

30   B. Tu, Q. Pang, E. Ning, W. Yan, Y. Qi, D. Wu and Q. Li, *J. Am. Chem. Soc.*, 2015, **137**, 13456–13459.

31   A. M. Fracaroli, P. Siman, D. A. Nagib, M. Suzuki, H. Furukawa, F. D. Toste and O. M. Yaghi, *J. Am. Chem. Soc.*, 2016, **138**, 8352–8355.

32   A. Helal, Z. H. Yamani, K. E. Cordova and O. M. Yaghi, *Natl. Sci. Rev.*, 2017, **4**, 296–298.

33   Y. B. Zhang, H. Furukawa, N. Ko, W. Nie, H. J. Park, S. Okajima, K. E. Cordova, H. Deng, J. Kim and O. M. Yaghi, *J. Am. Chem. Soc.*, 2015, **137**, 2641–2650.

34   C. G. Carson, K. Hardcastle, J. Schwartz, X. Liu, C. Hoffmann, R. A. Gerhardt and R. Tannenbaum, *Eur. J. Inorg. Chem.*, 2009, **16**, 2338–2343.

35   M. O. Keeffe, M. a Peskov, S. J. Ramsden and O. M. Yaghi, *Acc. Chem. Res.*, 2008, **41**, 1782–1789.

36   H. Li, M. Eddaoudi, T. L. Groy and O. M. Yaghi, *J. Am. Chem. Soc.*, 1998, **120**, 8571–8572.

37   M. E. Braun, C. D. Steffek, J. Kim, P. G. Rasmussen and O. M. Yaghi, *Chem. Commun.*, 2001, **2**, 2532–2533.

38   M. Eddaoudi, J. Kim, D. Vodak, A. Sudik, J. Wachter, M. O'Keeffe and O. M. Yaghi, *Proc. Natl. Acad. Sci. U. S. A.*, 2002, **99**, 4900–4904.

39   J. Nicks, J. Zhang and J. A. Foster, *Chem. Commun.*, 2019, **55**, 8788–8791.

40   M. Díaz-García, Á. Mayoral, I. Díaz and M. Sánchez-Sánchez, *Cryst. Growth Des.*, 2014, **14**, 2479–2487.

41   M. Eddaoudi, J. Kim, N. Rosi, D. Vodak, J. Wachter, M. O'Keeffe and O. M. Yaghi, *Science*, 2002, **295**, 469–472.

42   C. G. Carson, G. Brunnello, S. G. Lee, S. S. Jang, R. A. Gerhardt and R. Tannenbaum, *Eur. J. Inorg. Chem.*, 2014, 2140–2145.

43   D. J. Ashworth, A. Cooper, M. Trueman, R. W. M. Al-Saedi, S. D. Liam, A. J. Meijer and J. A. Foster, *Chem. - A Eur. J.*, 2018, **24**, 17986–17996.

44   D. J. Ashworth, T. M. Roseveare, A. Schneemann, M. Flint, I. Dominguez Bernáldes, P. Vervoorts, R. A. Fischer, L. Brammer and J. A. Foster, *Inorg. Chem.*, 2019, **58**, 10837–10845.

45   J. A. Foster, S. Henke, A. Schneemann, R. A. Fischer and A. K. Cheetham, *Chem. Commun.*, 2016, **52**, 10474–10477.

46   M. Lotya, A. Rakovich, J. F. Donegan and J. N. Coleman, *Nanotechnology*, 2013, **24**, 265703.

47   C. Backes, T. M. Higgins, A. Kelly, C. Boland, A. Harvey, D. Hanlon and J. N. Coleman, *Chem. Mater.*, 2017, **29**, 243–255.

48   M. E. Braun, C. D. Steffek, J. Kim, P. G. Rasmussen and O. M. Yaghi, *Chem. Commun.*, 2001, **2**, 2532–2533.

49   Q. Liu, H. Cong and H. Deng, *J. Am. Chem. Soc.*, 2016, **138**, 13822–13825.

50   H. N. Abdelhamid, *Nanotechnology*, 2019, **30**, 435601.

51   L. Asgharnejad, A. Abbasi, M. Najafi and J. Janczak, *J. Solid State Chem.*, 2019, **277**, 187–194.

52   P. Kanoo, K. L. Gurunatha and T. K. Maji, *J. Mater. Chem.*, 2010, **20**, 1322–1331.

53   M. J. Cliffe, E. Castillo-Martínez, Y. Wu, J. Lee, A. C. Forse, F. C. N. Firth, P. Z. Moghadam, D. Fairen-Jimenez, M. W. Gaultois, J. A. Hill, O. V. Magdysyuk, B. Slater, A. L. Goodwin and C. P. Grey, *J. Am. Chem. Soc.*, 2017, **139**, 5397–5404.

54   Y. Peng, Y. Li, Y. Ban, H. Jin, W. Jiao, X. Liu and W. Yang, *Science*, 2014, **346**, 1356–1359.

55   G. S. Pawley, *J. Appl. Crystallogr.*, 1981, **14**, 357–361.

56   A. A. Coelho, *Topas Acad. Version 4.1,see http//www.topas-academic.net*.

57   A. A. Coelho, J. Evans, I. Evans, A. Kern and S. Parsons, *Powder Diffr.*, 2011, **26**, S22–S25.

58   D. Nečas and P. Klapetek, *Cent. Eur. J. Phys.*, 2012, **10**, 181–188.

Tuning the surface chemistry of mixed ligand multivariate metal-organic framework nanosheets (MTV-MONs)

David J. Ashworth[a] and Jonathan A. Foster*[a]

a. Dept. of Chemistry, The University of Sheffield, Dainton Building, Brook Hill, Sheffield, S3 7HF, UK.

Electronic Supplementary Information

Contents

1. MOF syntheses

1.1. Single ligand MOFs and (H)$_2$-fu-MTV-MOFs

Copper salt and diacid ligand precursors were added to the reaction vial, DMF added and the vial sealed. Reagents were fully dissolved before being put in the oven for synthesis.

Table S1. Reagent masses used for MOF syntheses.

MOF	fu	Copper salt* / mg	H$_2$BDC / mg	Fu-H$_2$BDC / mg	DMF / mL	Yield** / mg
fu-MOFs	(H)$_2$	439.4	332.2		20	493.4 (90 %)
	NH$_2$*	19.4		19.4	6	26.0 (85 %)
	(Cl)$_2$	19.6		21.0	6	22.9
	(Br)$_2$	15.8		23.3	6	21.2
	NO$_2$	34.9		33.6	9	41.6 (83 %)
(H)$_2$-fu-MTV-MOFs	NH$_2$	22.2	8.6	9.3	6	26.4 (93 %)
	(Cl)$_2$	20.3	7.7	10.9	6	25.1 (89 %)
	(Br)$_2$	17.9	6.8	13.5	6	25.3
	NO$_2$	38.1	14.4	17.2	9	0.44 (86 %)

*Copper salt was copper nitrate trihydrate in all cases, other than copper acetate monohydrate for single ligand NH$_2$-BDC.

** Yields presented in brackets if phase-pure material was produced.

1.2. fu-BDC MTV MOFs

0.046 M stock solution of copper nitrate trihydrate in DMF, and 0.044 M solutions of fu-H$_2$BDC diacids in DMF were prepared. For two-component MTV-MOFs, 2.5 mL aliquots of the relevant ligands were added to reaction vials. For three-component, 1.67 mL and for four-component, 1.25 mL (in total giving 0.22 mmol ligand, 20 % total ligand excess). To this was added 4 mL copper nitrate solution (0.18 mmol). These were sealed and placed in the oven for synthesis.

Table S2. Mass yields of MTV-MOFs-1-11.

MTV-MOF-x	Yield / mg	Yield / % *
1	48.7	70
2	44.5	57
3	6.4**	10
4	55.8	67
5	50.9	71
6	57.5	71
7	40.9	53
8	47.1	68
9	43.1	57
10	53.0	67
11	43.9	58

*Yield based on the Mr of the fully desolvated form, [Cu(fu-BDC)(DMF)]$_n$. **Yield is very low as a lot of material could not be centrifuged out of DMF suspension throught the washing procedure, see in paper Section 2.8.

2. MOF characterisation

2.1. Pawley refinement
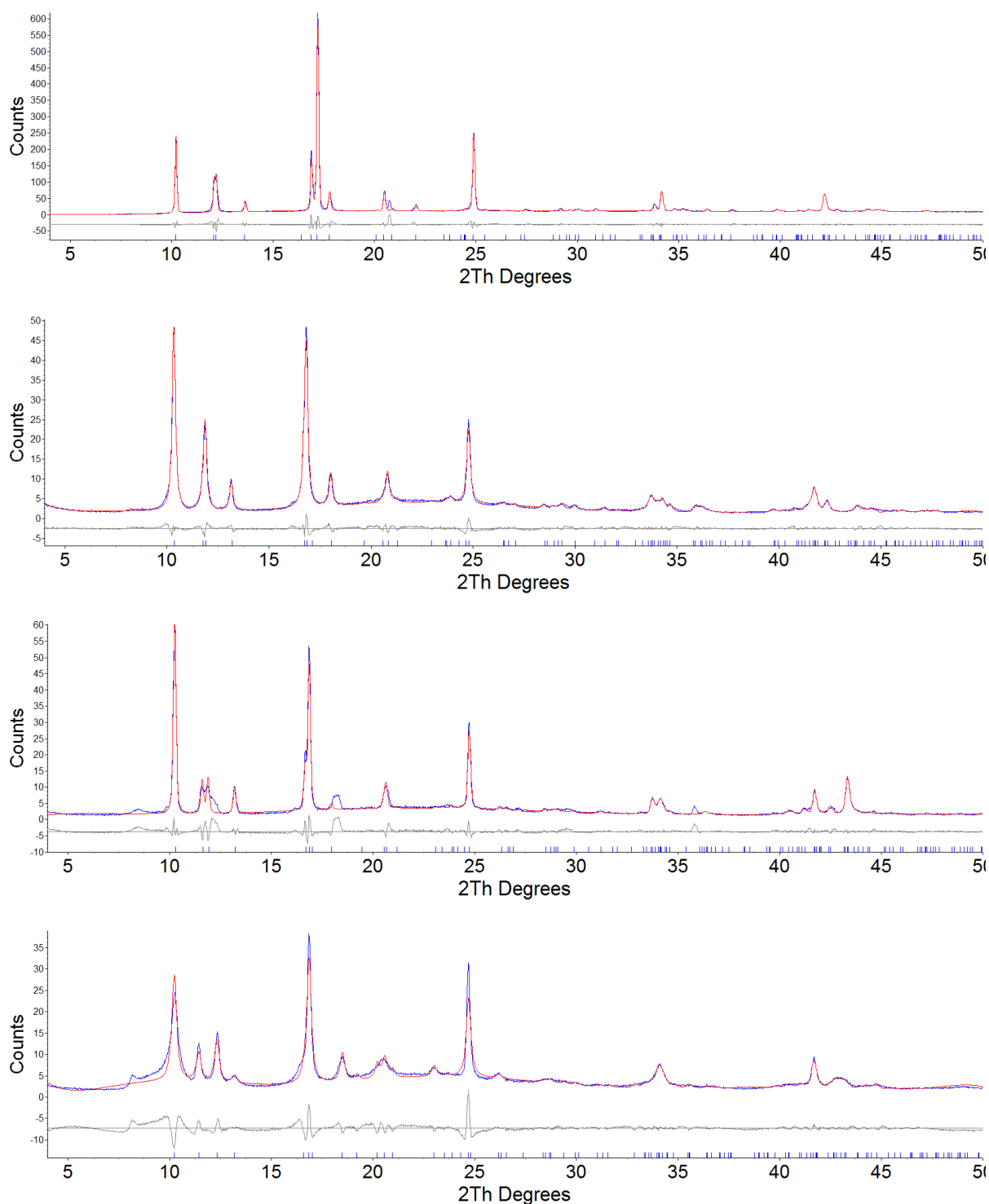
Figure S1. Pawley fits of Cu(BDC)(DMF), Cu(NH$_2$-BDC)(DMF), Cu((Br)$_2$-BDC)(DMF) and Cu(NO$_2$-BDC)(DMF) (top-bottom) illustrating the observed (blue) and calculated (red) diffraction patterns, with the difference plot [I$_{obs}$-I$_{calc}$] (grey) (2θ range 4.0 – 50.0 °, d$_{min}$ = 1.82 Å). Blue tick lines denote calculated peak positions.
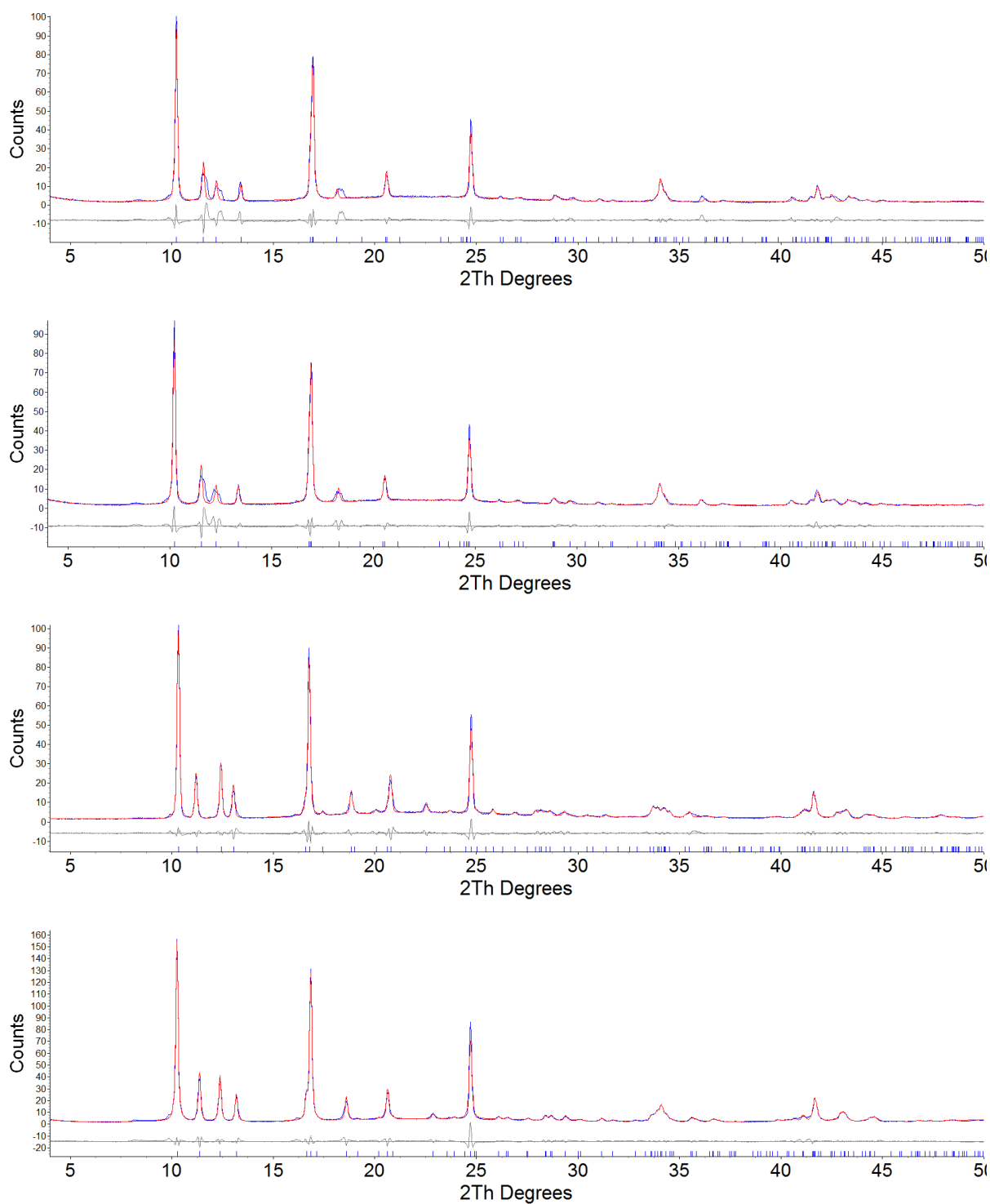
Figure S2. Pawley fits of $(H)_2$-fu-BDC MTV-MOFs, where fu=NH_2, Cl_2, Br_2 and NO_2 (top-bottom) illustrating the observed (blue) and calculated (red) diffraction patterns, with the difference plot [I_{obs}-I_{calc}] (grey) (2θ range 4.0 – 50.0 °, d_{min} = 1.82 Å). Blue tick lines denote calculated peak positions.

Table S3. Unit cell parameters for MOFs determined through Pawley refinement of the PXRD patterns.

MOF	fu	Space group	a / Å	b / Å	c / Å	β / °	Vol / Å³	R$_{wp}$	R$_{wp'}$
Single ligand fu-MOFs	(H)$_2$	C2/m	11.4492(9)	14.529(1)	7.7611(6)	109.145(5)	1219.6(2)	10.863	18.93
	NH$_2$	C2/m	11.139(1)	15.036(4)	8.004(1)	111.76(1)	1245.1(4)	6.948	13.862
	(Cl)$_2$	-							
	(Br)$_2$	C2/m	11.171(1)	15.197(4)	7.957(2)	111.22(2)	1259.1(5)	15.85	30.961
	NO$_2$	C2/m	11.338(6)	15.460(7)	7.814(4)	113.39(4)	1257(1)	13.853	30.962
(H)$_2$:fu-MTV-	NH$_2$	C2/m	11.208(1)	15.300(4)	7.766(2)	110.95(2)	1244.6(5)	16.061	29.574
	(Cl)$_2$	C2/m	11.215(1)	15.765(1)	7.8472(8)	115.002(8)	1257.4(2)	9.229	16.42
	(Br)$_2$	C2/m	11.260(2)	15.298(4)	7.752(1)	111.81(2)	1239.8(5)	14.386	24.985
	NO$_2$	C2/m	11.287(1)	15.539(1)	7.7983(8)	113.707(8)	1252.3(2)	10.077	15.928

2.2. FTIR
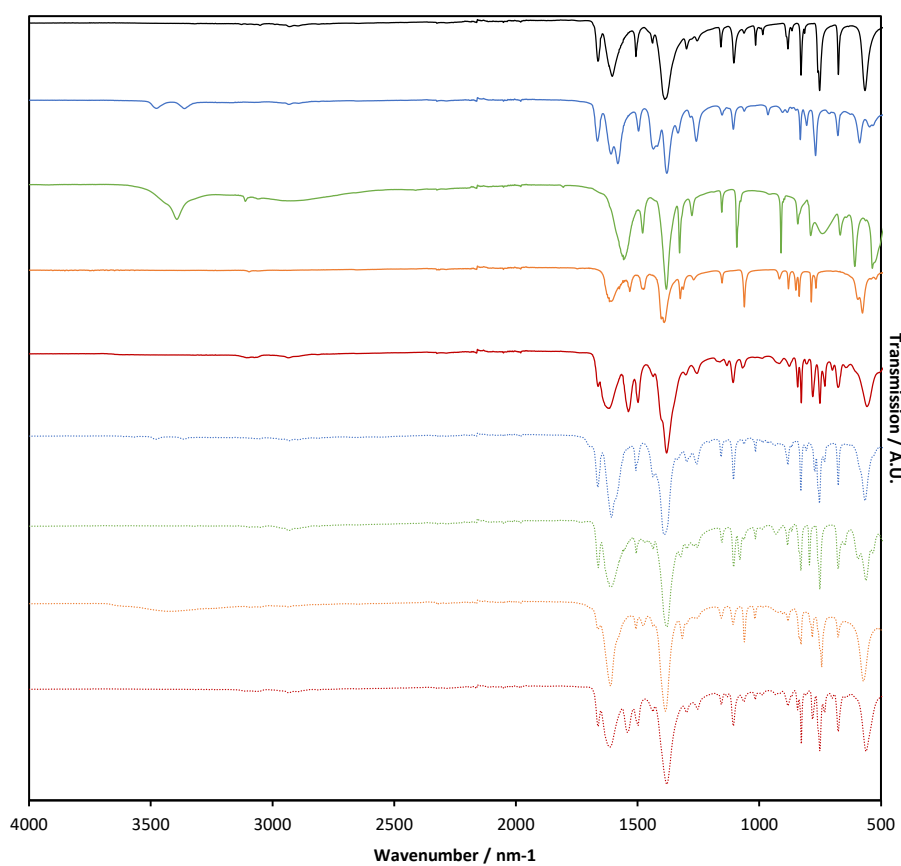
Figure S3. FTIR spectra of single ligand (solid) and (H)$_2$-fu-MTV-MOFs (dashed). Colours correspond to the used ligands: BDC=black, NH$_2$-BDC=blue, Cl$_2$-BDC=green, Br$_2$-BDC=orange and NO$_2$-BDC=red.

2.3. ^{1}H NMR

2.3.1. Single ligand fu-MOFs
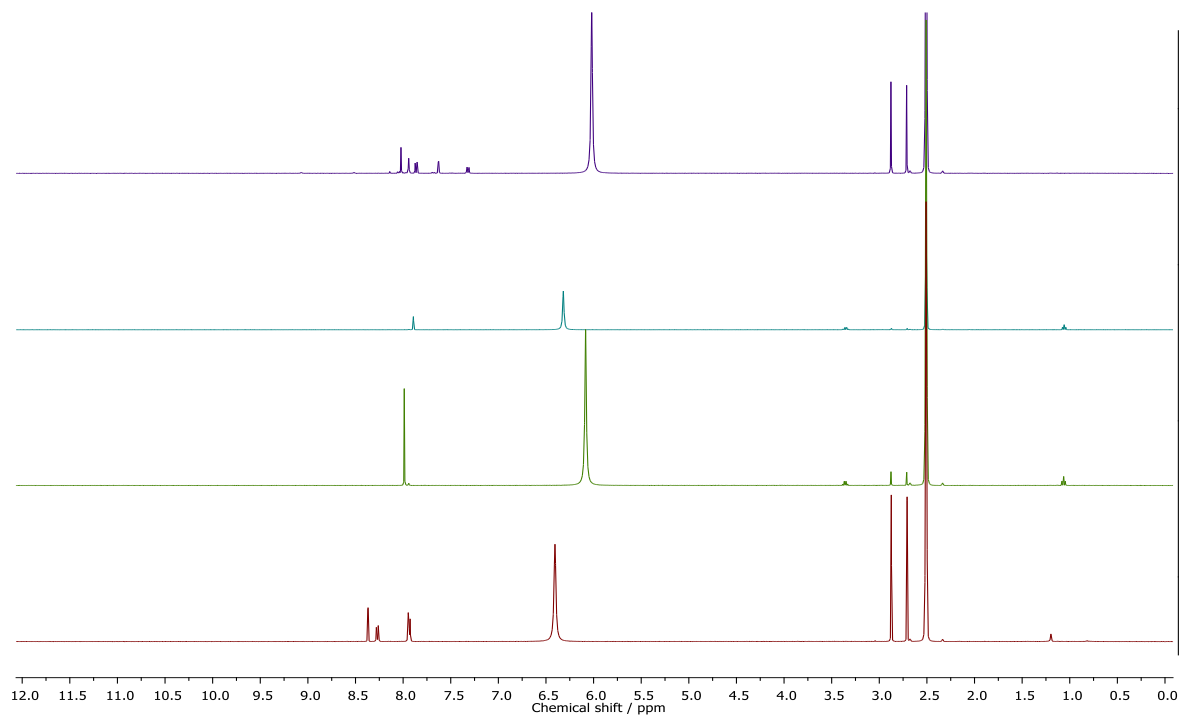
Figure S4. Room temperature ^{1}H NMR spectra of single ligand fu-MOFs. Top-bottom are fu=NH$_2$, (Cl)$_2$, (Br)$_2$ and NO$_2$, respectively.

2.3.2. Binary (H)$_2$-fu-MTV-MOFs
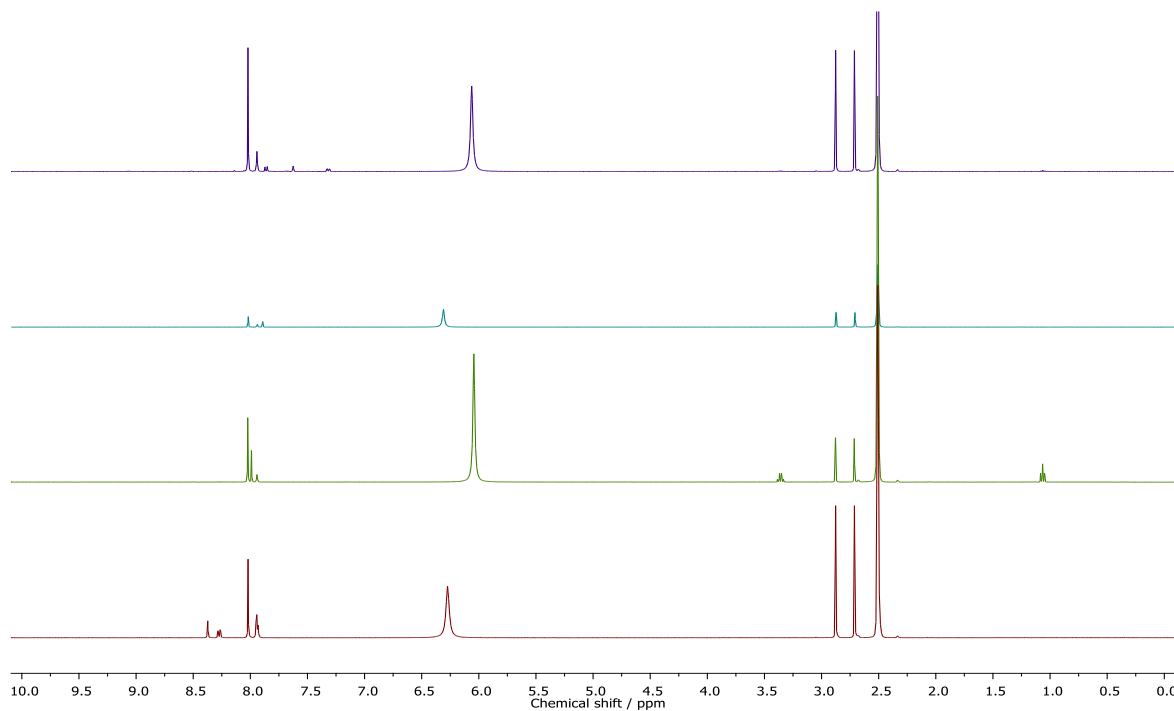
Figure S5. Room temperature ^{1}H NMR spectra of binary blended (H)$_2$-fu-MTV-MOFs. Top-bottom are fu=NH$_2$, (Cl)$_2$, (Br)$_2$ and NO$_2$, respectively.

2.3.3. Multi-ligand fu-MTV-MOFs
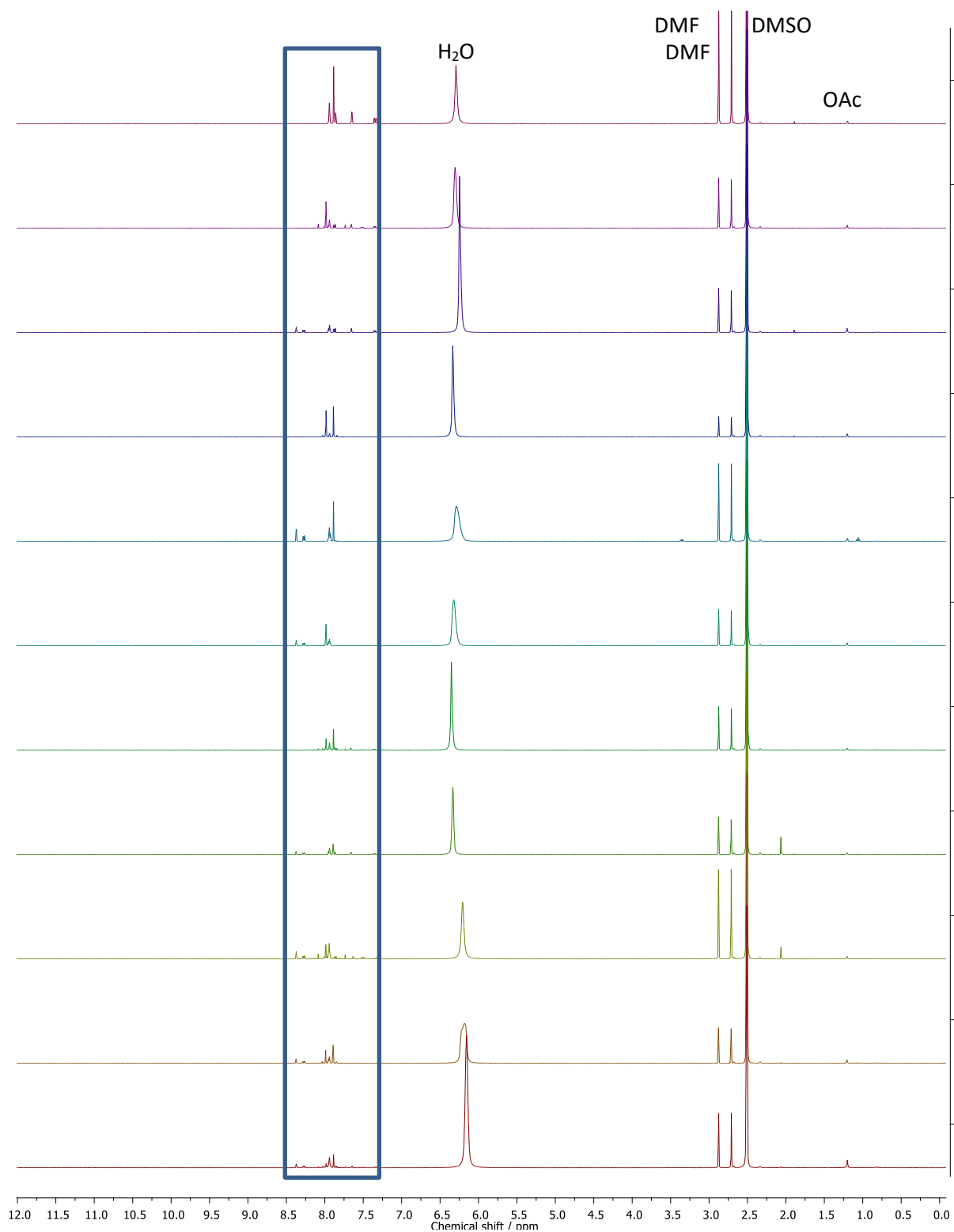
Figure S6. Room temperature ¹H NMR spectra of multi ligand fu-MTV-MOFs. Top-bottom are MTV-MOF-1-11, respectively.
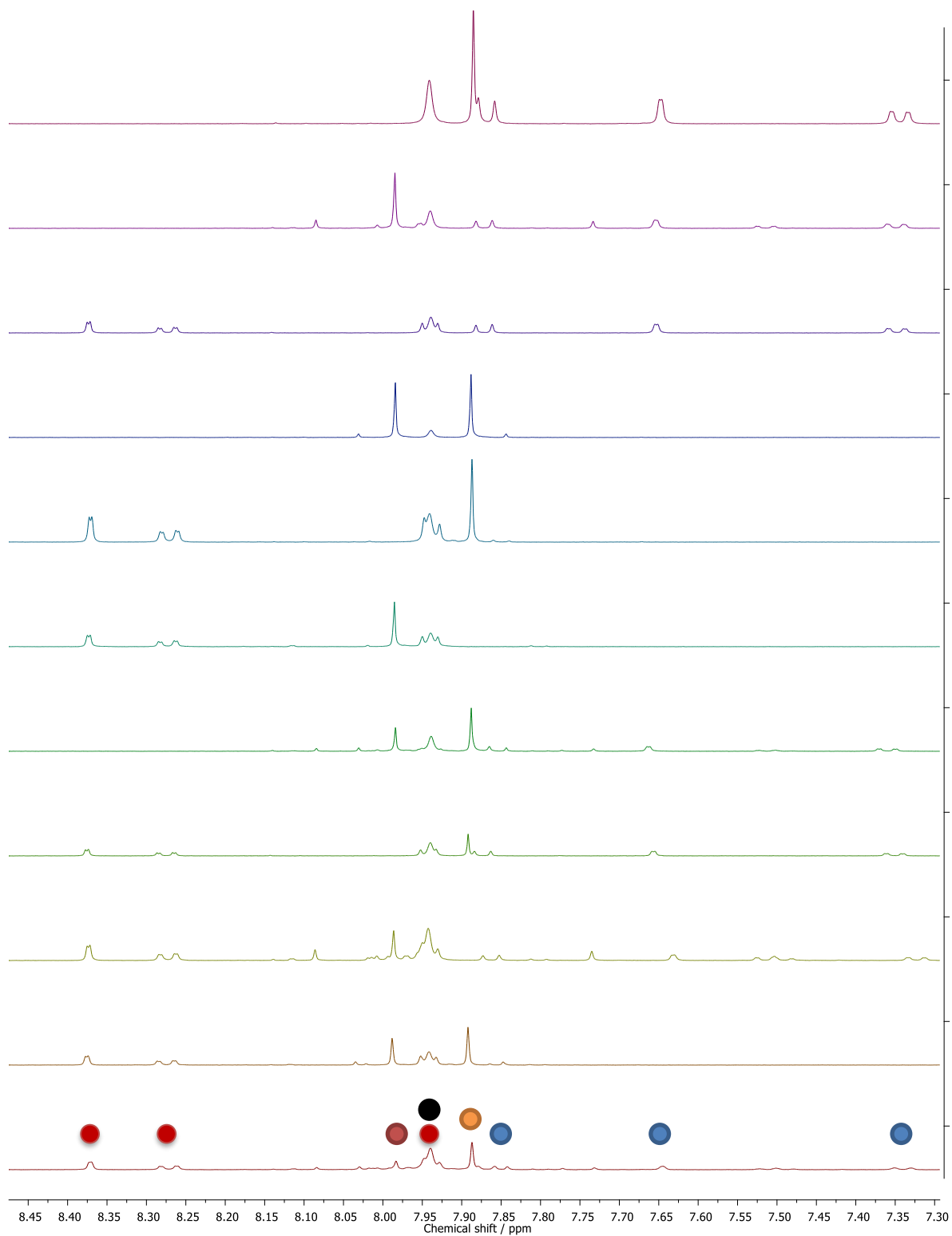
Figure S7. Room temperature ^{1}H NMR spectra of multi ligand fu-MTV-MOFs, zoomed in on 7.3-8.5 ppm. Top-bottom are MTV-MOF-1-11, respectively.

2.4.SEM
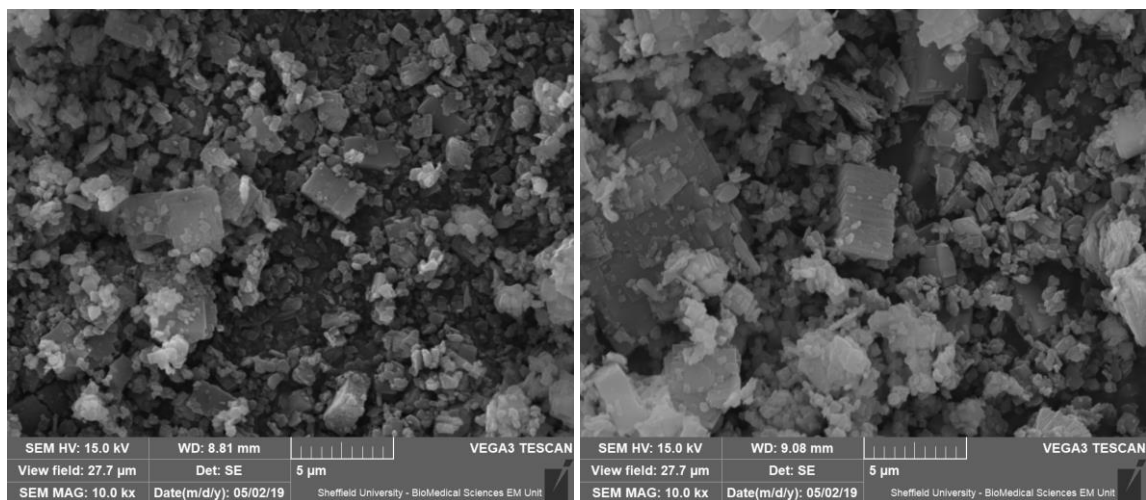
Figure S8. SEM micrographs (H)$_2$-MOF.
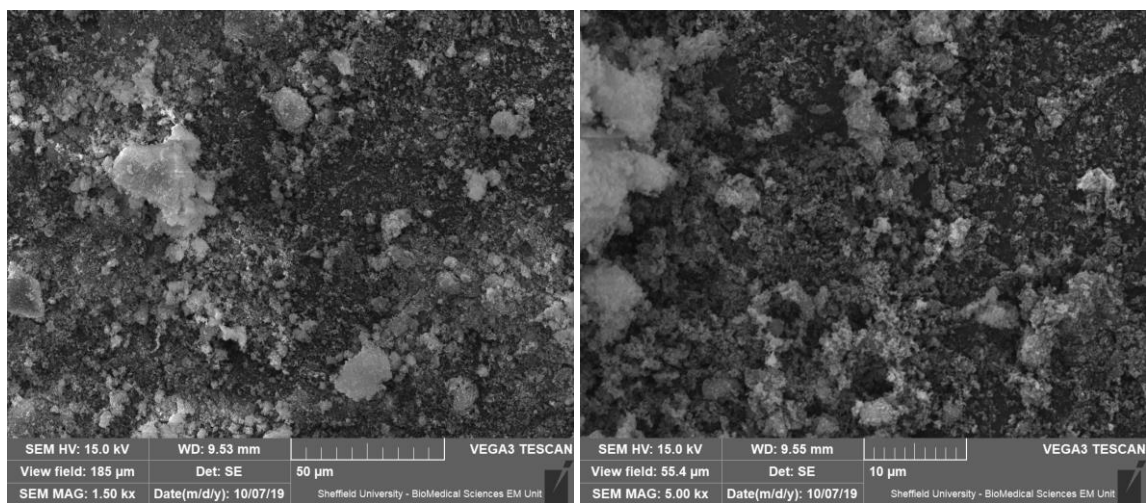
Figure S9. SEM micrographs of NH$_2$-MOF.
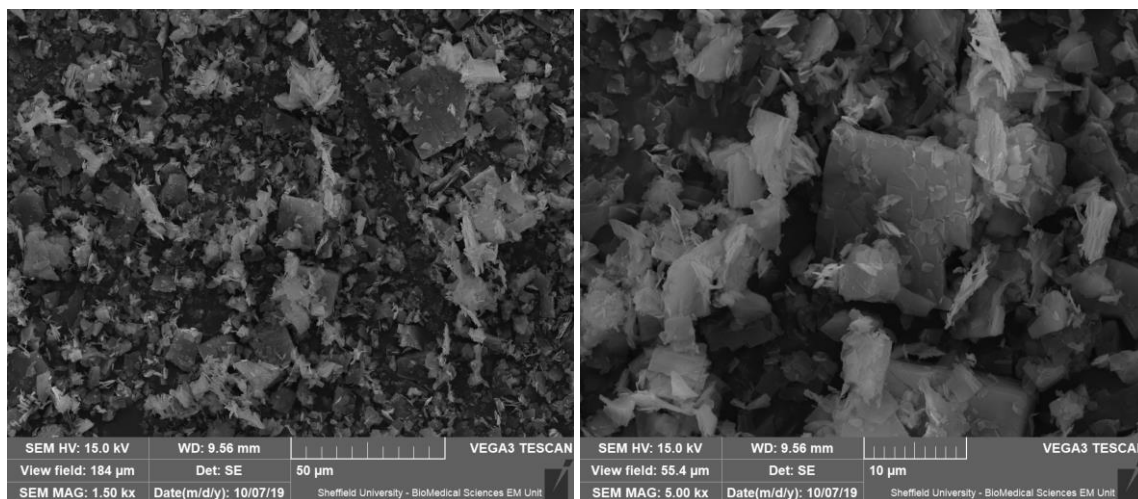
Figure S10. SEM micrographs of (Cl$_2$)-MOF.
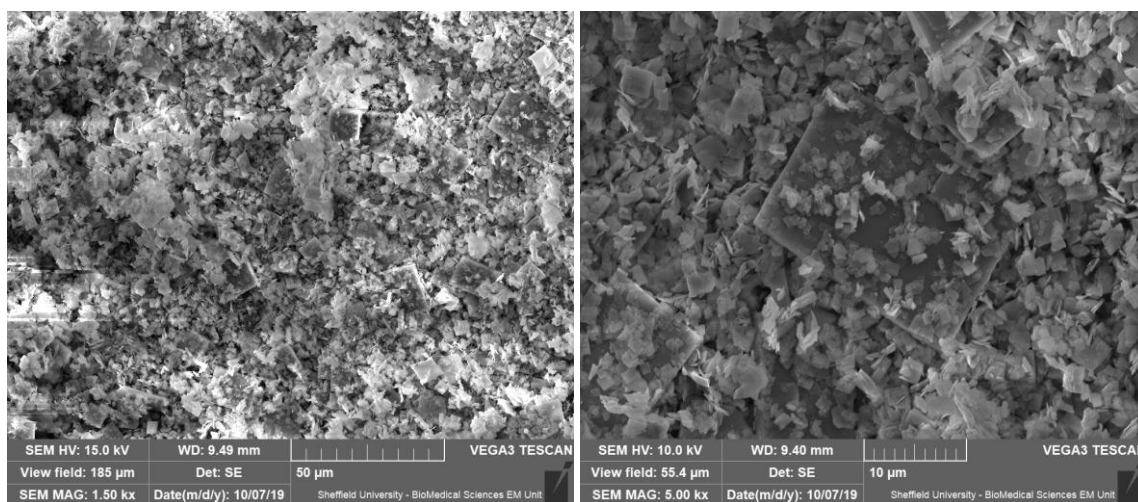
Figure S11. SEM micrographs of (Br)$_2$-MOF.
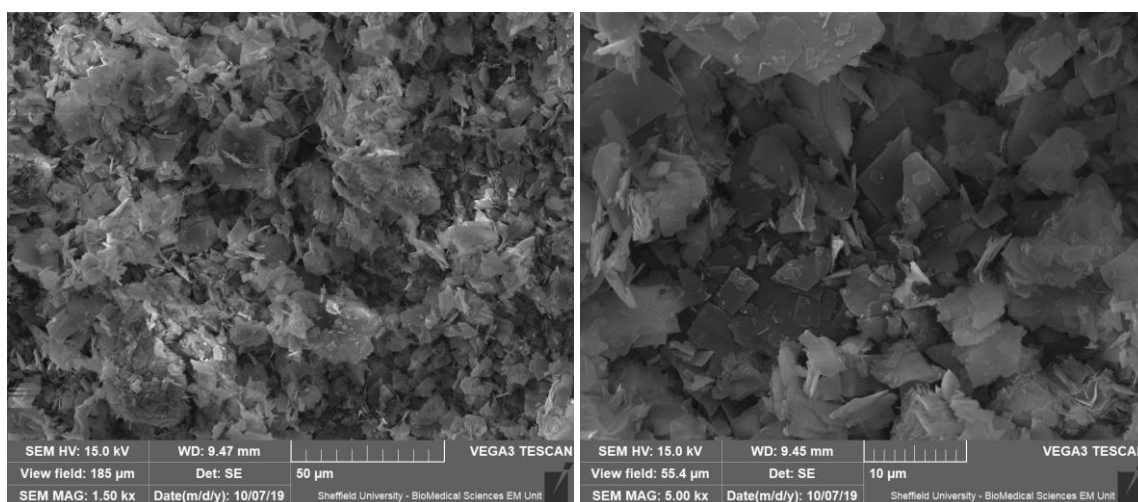
Figure S12. SEM micrographs of NO$_2$-MOF.
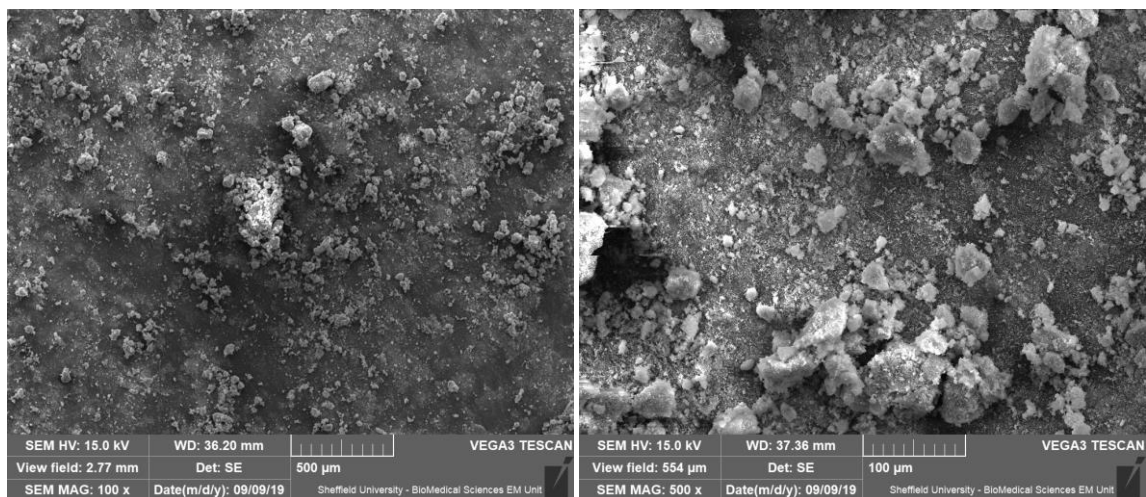
Figure S13. SEM micrographs of MTV-MOF-8.
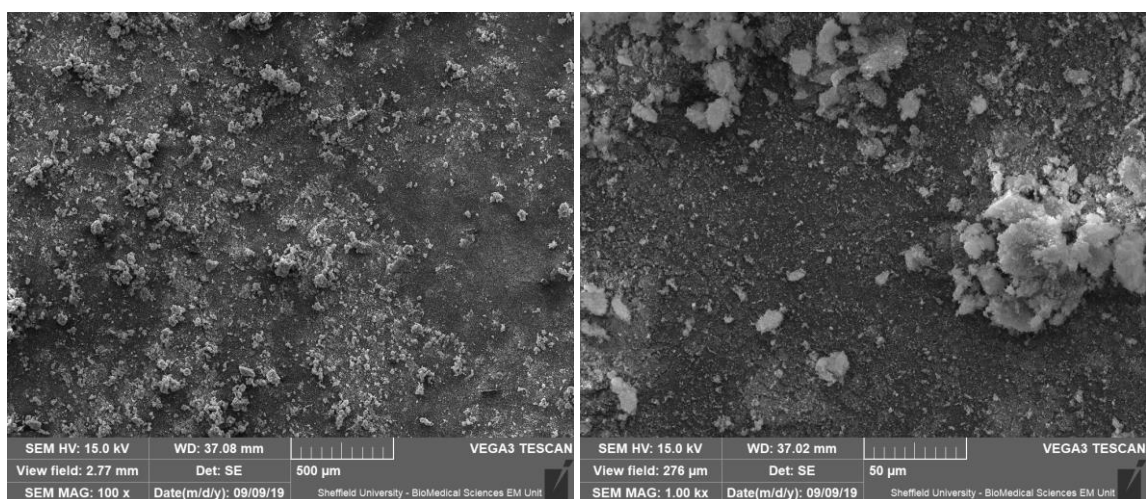
Figure S14. SEM micrographs of MTV-MOF-11

3. MON characterisation

3.1. Post-exfoliation PXRD
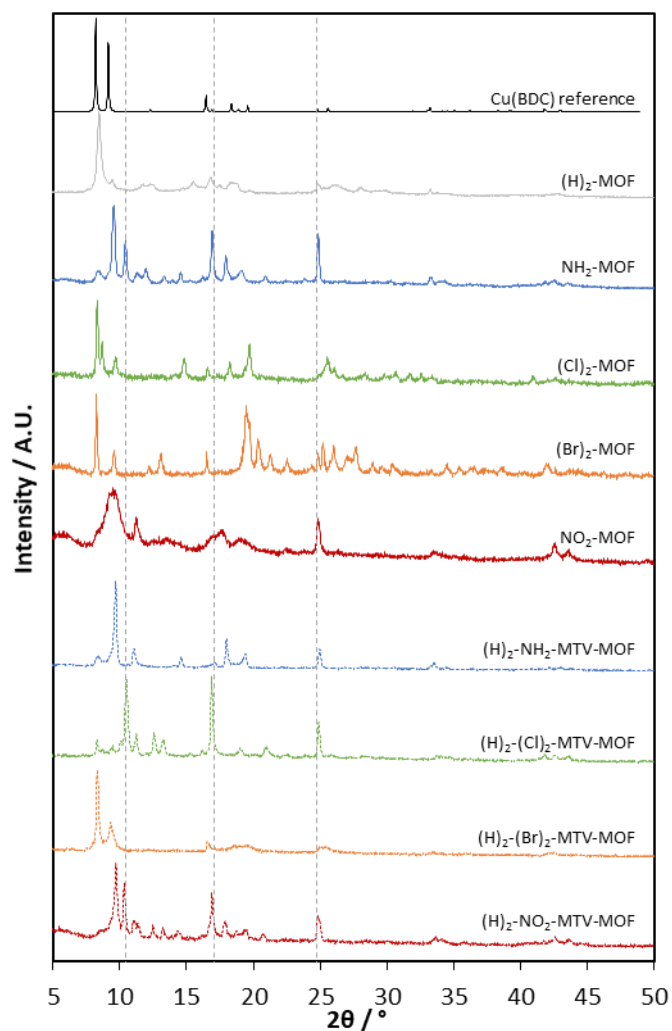
Figure S15. PXRD patterns of single ligand fu-MOFs, and two-component $(H)_2$-fu-MTV-MOFs recollected through centrifugation after liquid ultrasonic exfoliation in MeCN.
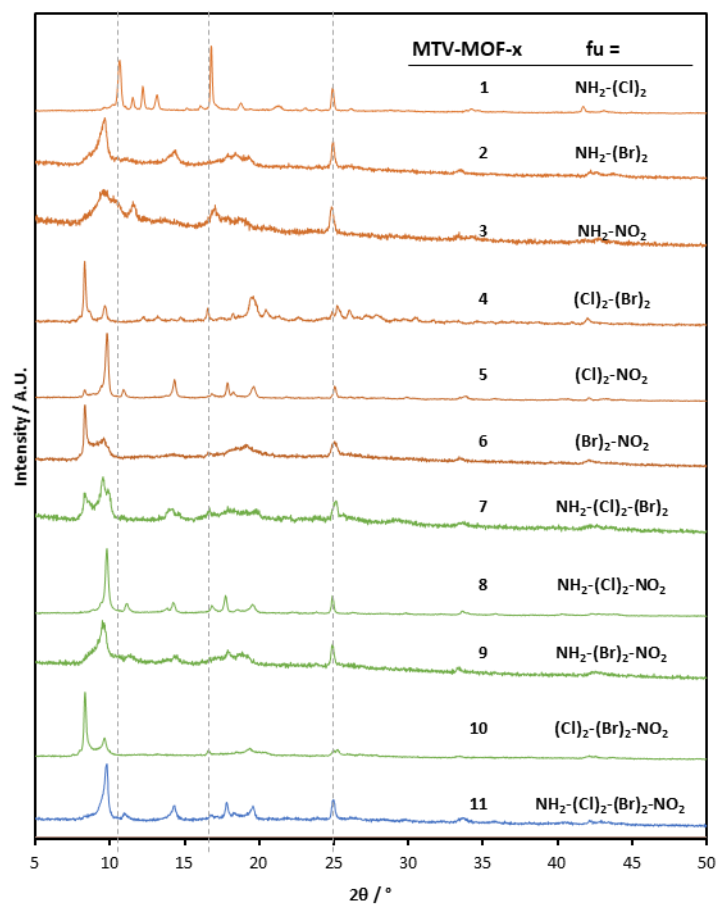
Figure S16. PXRD patterns of fu-MTV-MOFs-1-11 recollected through centrifugation after liquid ultrasonic exfoliation in MeCN, compared with the PXRD pattern predicted from the crystal structure of [Cu(BDC)]$_n$.[1]

3.2. MON suspensions

Figure S17. Coloured supernatents observed after the centrifugation of sonicated samples of MTV-MOFs-2,3,7,9,11 (left-right).
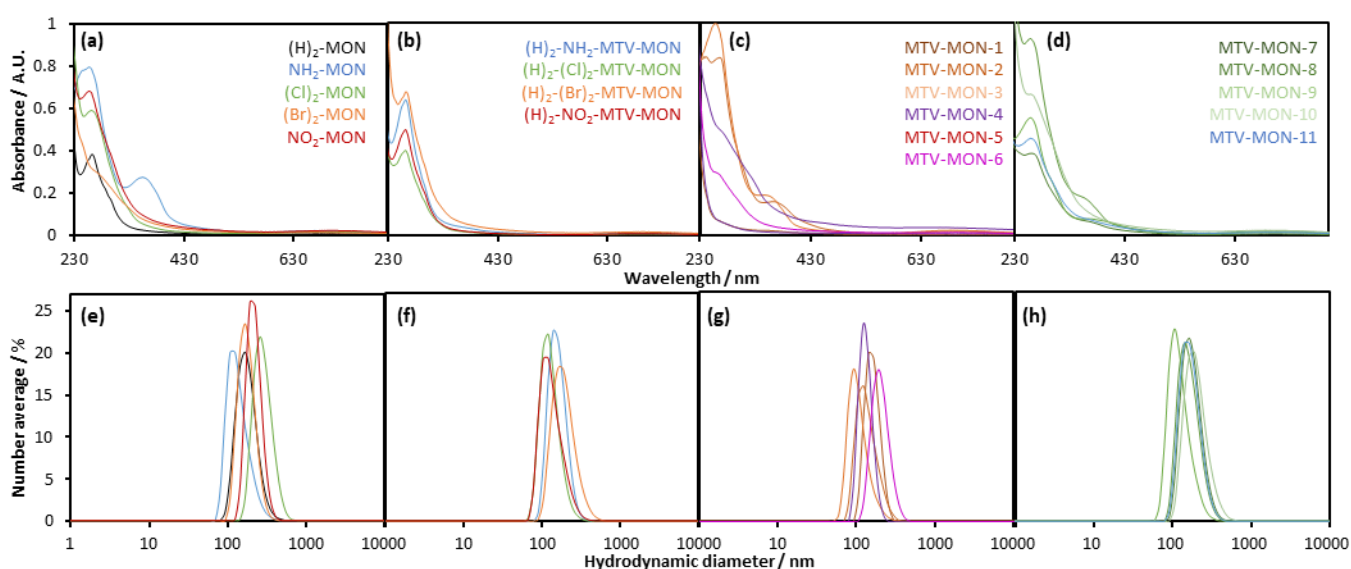
Figure S18. UV-Vis spectra (a-d) and DLS size distribution data (e-h). (H)$_2$-MON was diluted 1 in 3. NH$_2$-MON was diluted 1 in 20. (Br)$_2$-MON and (H)$_2$-(Br)$_2$-MTV-MON were analysed without dilution. All other single and two-component MONs were diluted 1 in 4. MTV-MONs-2,3,7,9 and 11 were diluted 1 in 12.5, 20, 15, 15 and 15, respectively, while other fu-MTV-MONs were analysed without dilution. DLS was performed on the same samples used for UV-Vis spectroscopy.

Prior to centrifugation of the sonicated MON suspension, ~400 μL of the suspension was removed and used to perform a titration into fresh MeCN, in order to allow calculation of the extinction coefficient. However, large amounts of background scattering from the solid particles in suspension meant this was unfortunately not possible for these materials.
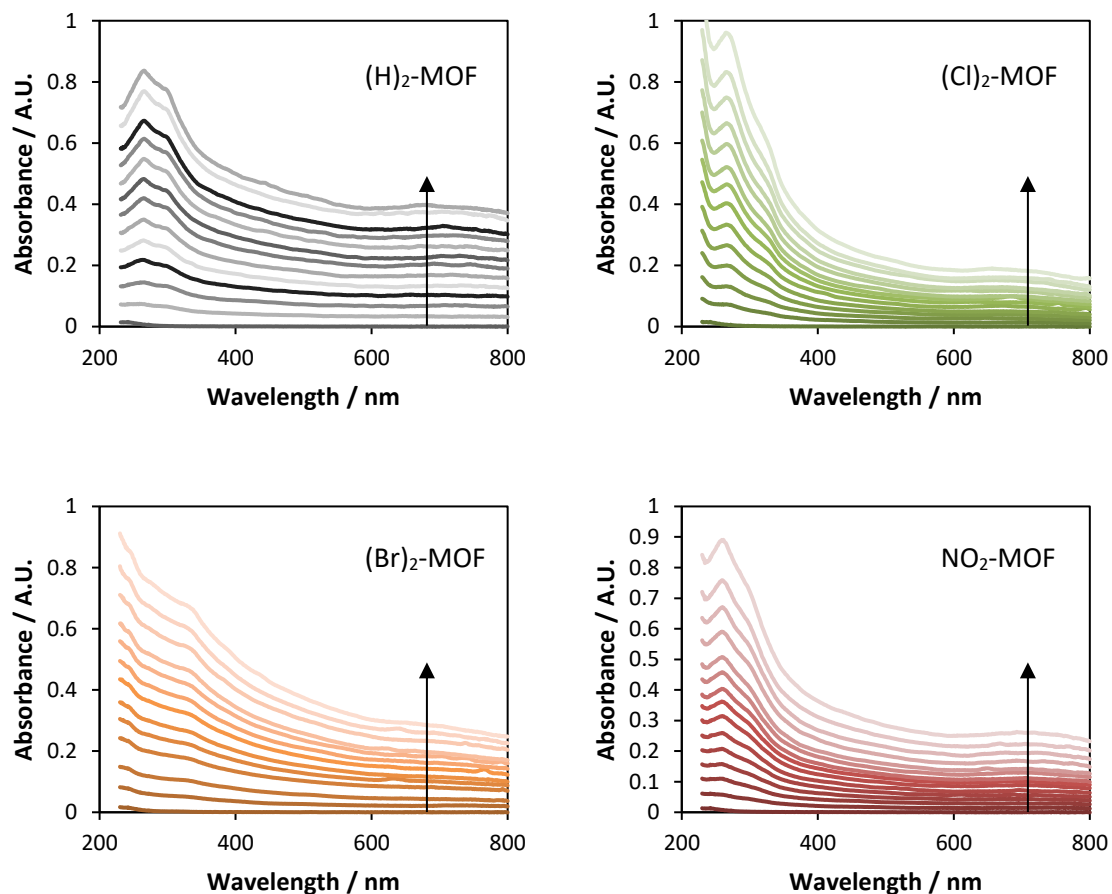
Figure S19. UV-Vis titrations of fu-MOF MeCN suspensions into MeCN.

3.3. Particle sizing

3.3.1. Single-ligand MONs
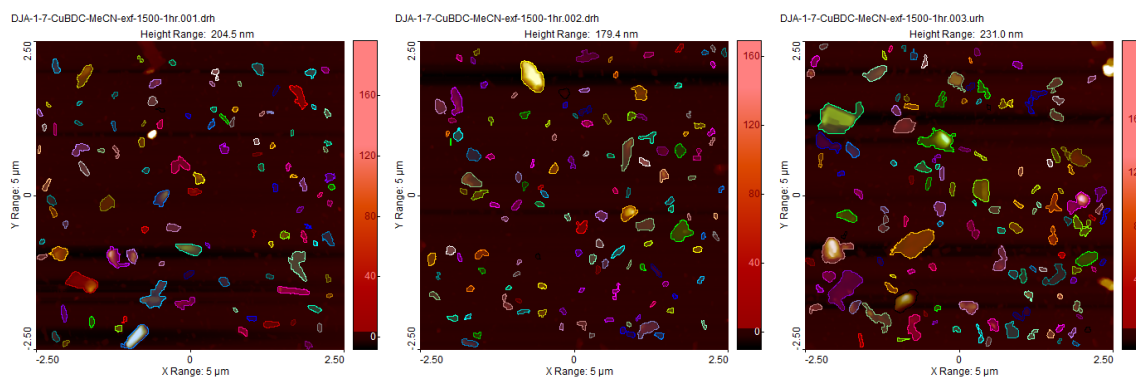
Figure S20. Particle identification for single ligand (H)$_2$-MONs.
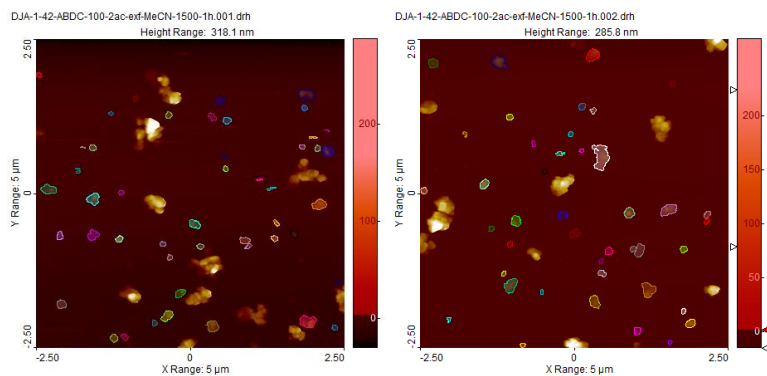
Figure S21. Particle identification for single ligand NH$_2$-MONs.
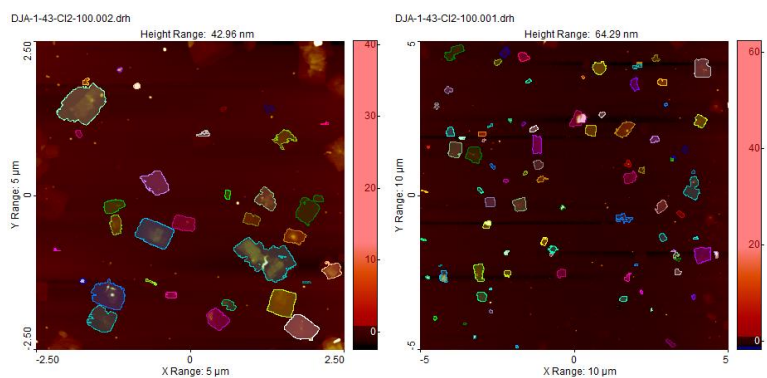
Figure S22. Particle identification for single ligand (Cl)$_2$-MONs.
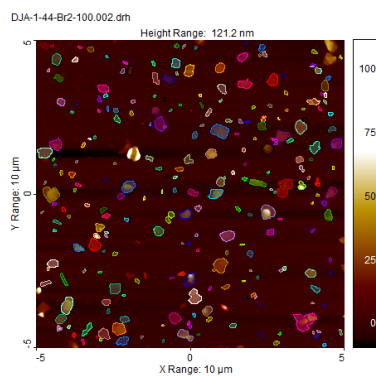
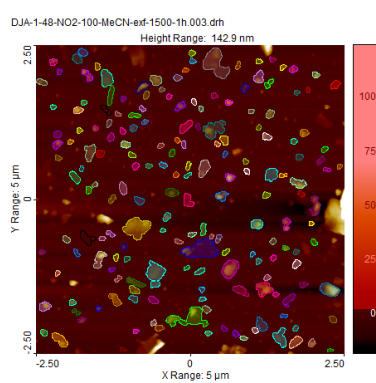**Figure S23.** Particle identification for single ligand (Br)$_2$-MONs.

Figure S24. Particle identification for single ligand NO$_2$-MONs.
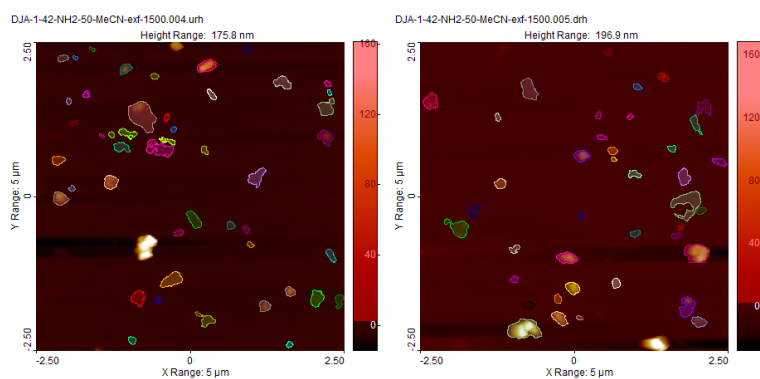
3.3.2. (H)₂-fu-MTV-MONs

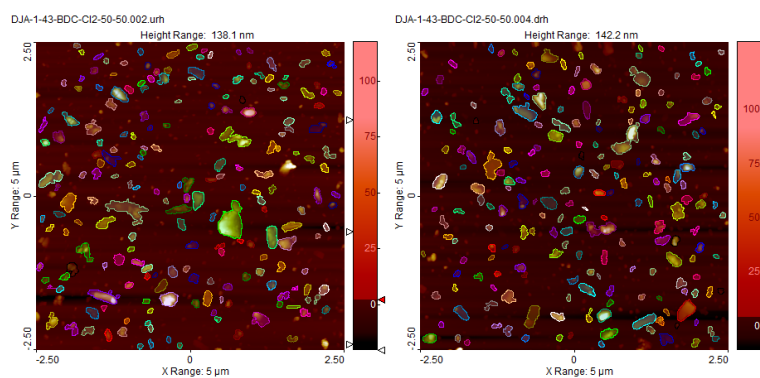**Figure S25.** Particle identification for (H)$_2$-NH$_2$-MTV-MONs.

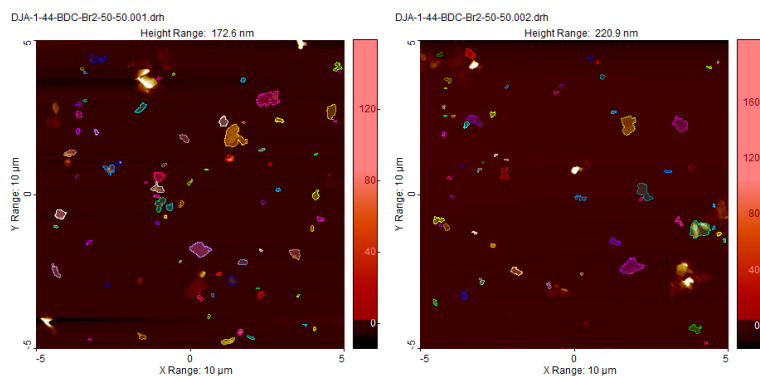**Figure S26.** Particle identification for (H)$_2$-(Cl)$_2$-MTV-MONs.

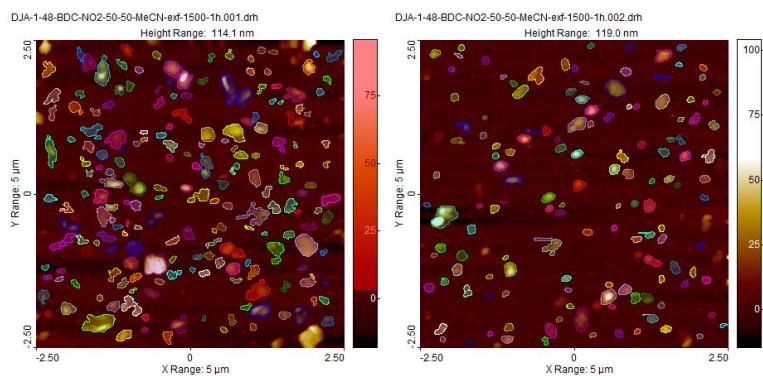**Figure S27.** Particle identification for (H)$_2$-(Br)$_2$-MTV-MONs.

Figure S28. Particle identification for (H)$_2$-NO$_2$-MTV-MONs.
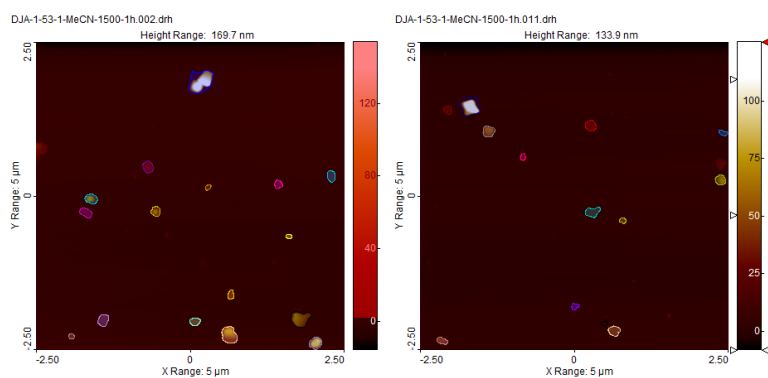
3.3.3. fu-MTV-MONs

Figure S29. Particle identification for MTV-MON-1.

Figure S30. Particle identification for MTV-MON-2.

Figure S31. Particle identification for MTV-MON-3.

Figure S32. Particle identification for MTV-MON-4.
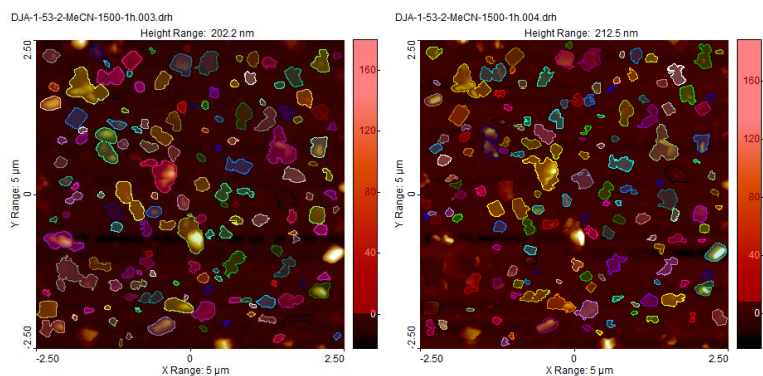

Figure S33. Particle identification for MTV-MON-7.
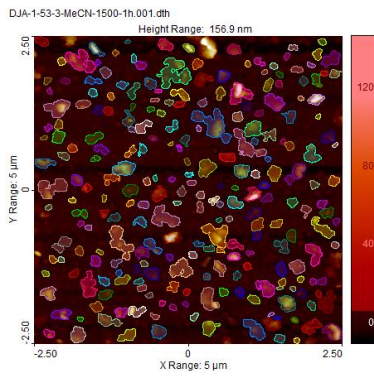
Figure S34. Particle identification for MTV-MON-8.

Figure S35. Particle identification for MTV-MON-9.

Figure S36. Particle identification for MTV-MON-10.
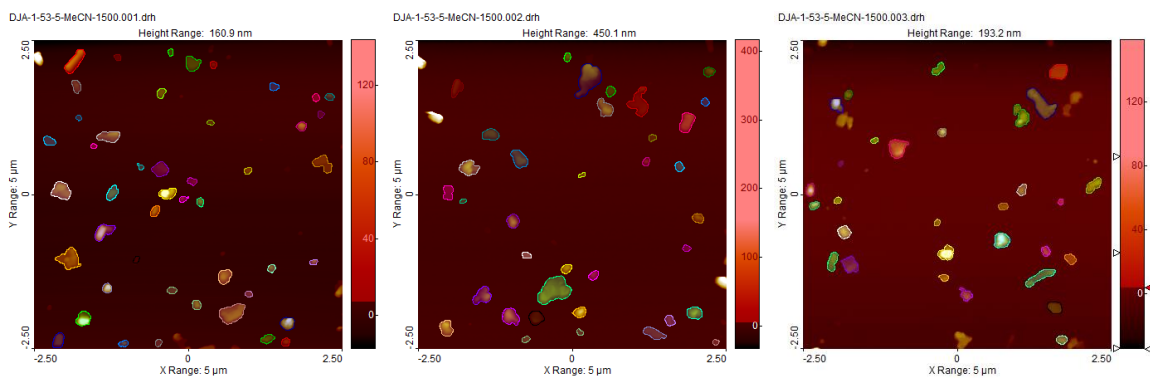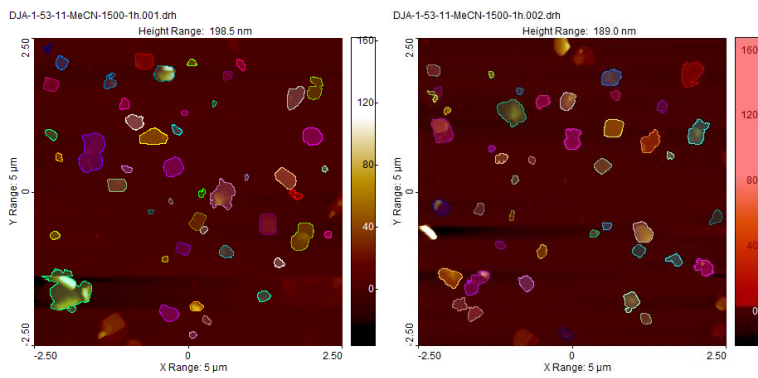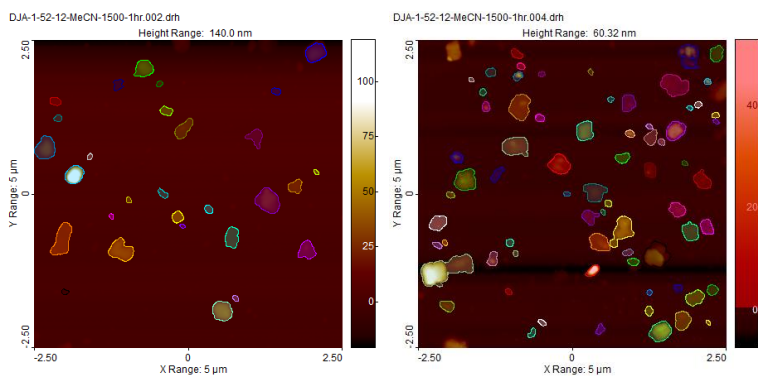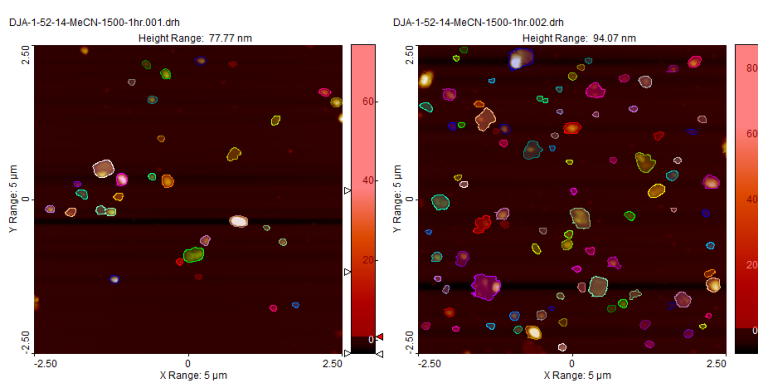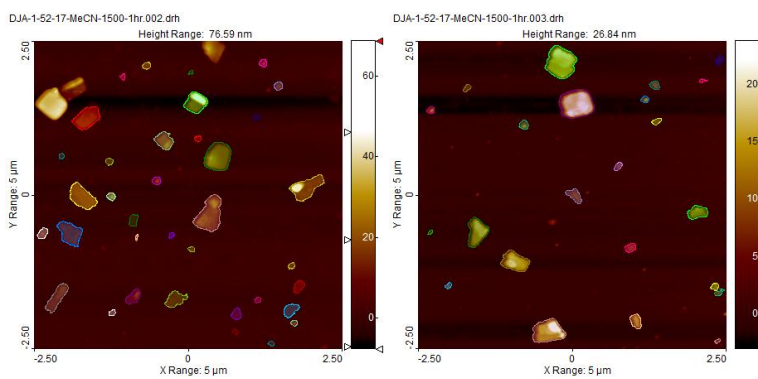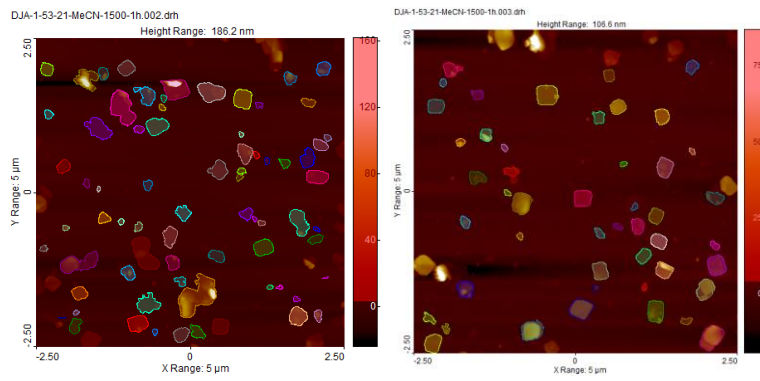
Figure S37. Particle identification for MTV-MON-11.

7 ♣

Conclusions

1 ....
2 ....
3 ....
a ....
b ....
c ....
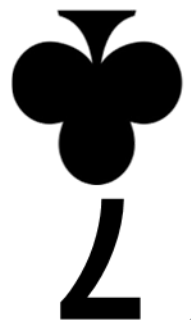
Summary

Metal-organic framework nanosheets (MONs) are rapidly carving out a niche in materials chemistry as 2D materials with controllable properties and tuneable surface chemistry. In this thesis, isoreticular series of layered paddle-wheel- (PW) based metal-organic frameworks (MOFs) which incorporated different functional groups were synthesised and exfoliated to form MONs, in order to ask a series of questions about their structure-property relationships. To achieve this, methods to characterise these complex hierarchical materials required developing. In this final chapter, I shall reflect on the progress made towards these goals.

Method development

Liquid ultrasonic exfoliation

Prior to this work, Foster *et al*. had followed an exfoliation protocol using 10 mg MOF in 10 mL solvent and subjecting this to ultrasonication for 30 mins in ice-cooled water, then centrifuging for 45 mins at 1500 rpm. A key achievement in **Chapter 3**, was optimising this protocol to enhance exfoliation and ensure consistent results in order to allow direct comparison between samples. Replacing ice-water with a cooling coil allowed a constant temperature (18-21 °C) to be maintained, enabling the exploration of longer exfoliation times (e.g. 12 hrs).[1] Early work attempting to optimise the exfoliation protocol or compare different systems was plagued by inconsistent results. This was eventually attributed to the inhomogeneity of ultrasound within the ultrasonic bath. Repeats of the same sample in a vial placed over a "hot spot" behaved very differently from those located in "dead spots". The use of an ultrasonic bath with a "sweep mode," where the frequency of ultrasound is modulated, failed to solve this problem and it was only by rotating the samples through the bath that these effects could be averaged out. Initial studies using short centrifugation times also provided inconsistent results in some solvents. Literature estimates that it can take up to 2 hrs to collect material from a 10 cm fill height.[1] Exfoliating 5 mg of MOF in 6 mL solvent gave a rough fill height of 5 cm, and therefore 1 hr centrifugation times were used. Liquid cascade centrifugation was another key innovation which provided a degree of control over MON particle size. However, there is a compromise between longer and faster centrifugation times, and the concentration of material remaining in suspension.

Factors that govern the exfoliation process are still not well understood. It is generally accepted in the literature for other nanosheets that if surface energies of layered material and solvent match, then exfoliation will proceed well.[2,3] However, due to the difficulties in characterising complex surfaces like MONs as well as the many different factors that may influence interaction with solvent (such as H-bonding ability, charge localisation, hydrophilicity, surface energy *etc*.),[4–7] it remains challenging to predict how well a given MOF will exfoliate in a given solvent. This is particularly the case for Cu_2-PW based MOFs where there is the possibility of solvent exchange at the axial coordination positions, and is likely also true for other SBUs. Acetonitrile was the solvent most-used throughout this work, initially selected in **Chapter 3** as both materials used showed reasonable concentration of MON, and accurate sizing was possible due to the minimal particle agglomeration upon drying onto a mica substrate for AFM analyses. Although this held true across other materials in **Chapters 4-6** and therefore enabled MON size comparisons between different materials, MONs with largest lateral dimensions and thinnest heights were observed in alternative solvents (H_2O or diethylether).

Ultrasonic liquid exfoliation produces MON with a large distributions of both lateral size and height. This is common of most top-down exfoliation techniques, and also true of other 2D materials.[2] Liquid cascade centrifugation was used to introduce an element of size control to isolated MONs. MONs

were only synthesised on small, usually milligram scales. The largest batch synthesis in the literature to date was 1.75 g using a bottom-up solvothermal method.[8] If MONs are to fulfil their potential within real-life applications, methods to synthesise high quality MONs on much larger scales must be realised. Bottom-up techniques such as the layering method[9] were tested for the MONs described herein, but this method is only scalable through parallel syntheses, and additionally takes a long time for a low yield of MONs. Use of additives and modulators, such as polymer surfactants, that adhere to crystal surfaces to prevent epitaxial growth and produce high quality MONs through bottom-up methods have produced larger amounts of MON, however these are often difficult to remove and therefore affect properties of the MONs. Exfoliation remains the most generalizable method for the production of MONs, however additional work should be done targeting scale-up, for example investigating the effects of concentration of MOF in suspension on the concentration and particle size of MONs formed, as well as the scalability of the MOF/solvent mixture.

Characterisation techniques

Materials characterisation of synthesised MOFs required a combination of analytical techniques to elucidate the composition and structure. These included SCXRD, PXRD (including Rietveld and Pawley refinement), FTIR spectroscopy, gas sorption, LC-MS, NMR spectroscopy and SEM. MONs are complex, hierarchical materials which require multiple levels of characterisation of the molecular, nanoscopic and macroscopic structure and properties. Characterisation of MONs additionally included UV-Vis spectroscopy, DLS, AFM and contact angle. As the first PhD student within a new research group a key part of my role was developing protocols for each method, which remain in use throughout the Foster research group.

UV-Vis was useful to indicate concentrations of MON in suspension, however it was not always possible due to the additional scattering of light from the colloidal suspensions. Sample preparation for AFM is paramount for accurate particle sizing, as sample aggregation upon drying makes it very difficult to accurately determine particle dimensions. A "hot-drop" method was developed, in which the mica substrate is pre-heated to near the boiling point of the solvent of the MON suspension. Dropping small aliquots of suspension onto the substrate minimised aggregation, due to rapid evaporation of the solvent.[1] For MON samples with low concentration, multiple aliquots could be sequentially dried on top of each other without particle aggregation.

DLS has been successfully used to size the lateral dimensions of other 2D nanosheets.[10] Regrettably, we could not find as strong a correlation between the lateral dimensions suggested by DLS (through calculation of the hydrodynamic radius of particles in suspension) and observed by AFM, however trends across series of MONs were consistent, suggesting that DLS could be used as complimentary tool. Statistical size analysis of different samples allowed quantitative size comparisons across different series to elucidate the effects of different functionalisations. AFM was found to be the most useful tool for analysis of MON particle morphology and sizing. Computerised automation of particle sizing using SPIP software was explored, however this was limited due to excessive software costs and requirement of AFM images of high resolution with exceptionally flat background. Particle overlap cannot be detected, which could result in erroneously large size measurements. MONs could be sized using the height profile function within Gwyddion software. Nanosheet sizes were mapped by drawing individual vectors for each particle. This hand-sizing remains the most accurate, although also the most time-consuming, method for determining particle size distribution.

Structure-property relationships

Prior to this work, there were no examples of studies on the systematic incorporation of functionalised ligands into layered MOF structures to affect the exfoliation to form MONs. To answer the questions posed in **Chapter 2**, series of isoreticular layered MOFs were synthesised using BDC functionalised with different groups and these were exfoliated using ultrasonication to form MONs.

In **Chapter 3**, two closely related isoreticular layered MOFs were synthesised which included relatively hydrophilic or hydrophobic functional moieties. Exfoliation in eleven solvents with widely varying properties showed that generally, higher concentrations of the more hydrophilic MONs were obtained in polar solvents, while the opposite was true for the more hydrophobic MONs. In general, the more hydrophobic system formed thinner MONs with larger aspect ratios than the hydrophilic, which was hypothesised to be due to weaker interlayer interactions in the hydrophobic system. However, concentrations of MONs formed could not be directly correlated with any single solvent parameter, and the picture was further complicated. In some solvents, the axial DMF molecules were substituted (in H_2O) or removed (in MeCN, NMP, diethylether) to form desolvated phases, which was corroborated with DFT calculations. Labile coordination at the axial PW sites was exploited for binding of small aromatic molecules. Although these MONs do function as sensors for model compounds, they are not well-designed for this purpose as the benzene ring is a poor reporter group, and the K_a of small aromatic molecules to the axial Cu site is relatively weak. Fluorescent reporter groups such as naphthalene-1,4-dicarboxylate or anthracene-9,10-dicarboxylate could be introduced to enhance sensitivity (see Figure 1). One of the opportunities of MONs is for multidentate binding, as the potential regular array of binding sites on the surface provide a platform for docking. Preliminary work has indicated that long chain diamines may bind at adjacent PW sites with K_a more than two orders of magnitude greater than the equivalent monoamine.

A three-member isoreticular series of MOFs functionalised with varying length alkoxy chains was synthesised in **Chapter 4**, which showed increasing CO_2 adsorption with increasing chain length, possibly due to increased interlayer distance. Shorter chains resulted in higher concentrations of MON in suspension, but particle size analysis showed that longer chain functionalisation resulted in thinner MONs with larger lateral dimensions and aspect ratios. Exfoliation in MeCN produced thinner MONs that in DMF which was hypothesised to be due to decreased interlayer interactions when desolvated. Although long chains may promote exfoliation in these and related systems,[11] further introduction of repelling groups (for example charged moieties) that extend between the layers, through post-synthetic modification of the MOF, may prove to be a more beneficial route to producing ultrathin MONs.[12]

Chemical functionalisation is powerful method to tailor the physical and chemical properties of 2D materials. Combinations of different surface-presented functionalities provides a route to tuneable surface chemistry in MONs. Combinations of ligands functionalised with different chains were incorporated within the same framework structure in **Chapter 5**, forming layered multivariate- (MTV) MOFs. Exfoliation produced mixed-ligand MTV-MONs for the first time. Mixed-ligand MONs had some properties that were intermediate to the parent single-ligand MONs, while concentrations of MON in suspension and sizes of MTV-MONs surpassed the parents'. MTV-MONs with combinations of up to five differently functionalised BDC ligands were demonstrated. **Chapter 6** built on this to demonstrate the applicability of this approach to another group of functionalised BDC ligands, demonstrating four BDC:fu-BDC MTV-MONs and eleven different blends of fu-BDC MTV-MONs. Blending four different fu-BDC ligands demonstrated how MON surface chemistry can be controlled and fine-tuned. Generally, higher-component blends formed thinner MONs, which was hypothesised to be a result of reduced interlayer interactions. Tuning of these systems with more strongly electron-

withdrawing/donating groups could enable fine-tuning of binding strength over a much greater range. Additional application of the MTV approach to the SBU in these systems could incorporate multiple different metals into the framework, for example zinc, manganese or heavier metals such as palladium, to impart the MONs with additional catalytic functionality. A possible progression from the mixed-ligand MTV approach would be to difunctionalise BDC with two different R groups (see Figure 1), and then incorporate these ligands with mixed functionalities into layered MOFs for exfoliation to multifunctional MONs. This could enable development of "Janus"[13] MONs, in which the individual faces possess different physical or chemical properties, or could promote bilayer MONs which could be used as artificial rigid membranes.
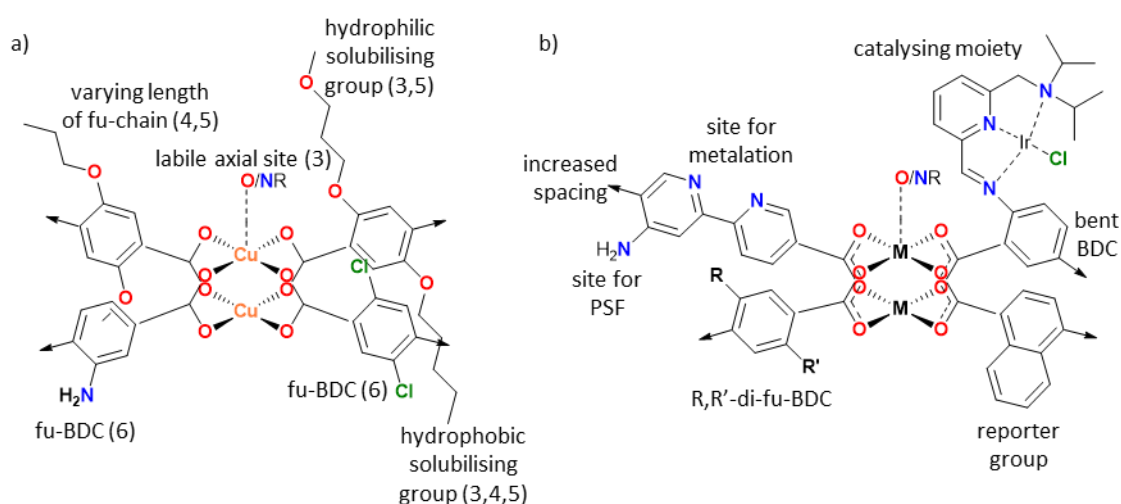

Figure 1. Opportunities for functionalisation of BDC ligands incorporated into the 2D layer structure used in this thesis (a) (with chapter in brackets) and with future potential (b).

The pre-synthetic functionalisation method used in this thesis is a useful method for decorating MOFs/MONs with functional groups, however this is not a universal method as there are limitations to the size and functionality of the groups used, as these can influence/prevent framework synthesis, or lead to structural alterations, which require extensive characterisation. Post-synthetic functionalisation (PSF) has already been demonstrated as a useful method for introducing catalytic function to MONs,[12,14–16] and this should be further utilised within MTV-MONs for complex multistep catalysis. PSF of pendent NH_2 or Br groups with functional moieties, PSF with known catalytic moieties such as Ir(L)$_3$Cl, or through metalation of 2,2'-bipyridine linkers may provide routes to new multi-functional catalysts. PSF allows a few MON systems to be developed and fully characterised, and then facilitates tuning of their surface chemistry and properties. However, PSF of materials similar to those of this thesis is complicated by the solvent exchange/coordination potential of the axial PW position. Alternative frameworks, which are coordinatively saturated by ligands intrinsic to the framework structure, avoid this issue and would simplify characterisation, however this would also mean that Lewis acid sites are not available on the framework for sensing or catalysis.

Conclusions

Outlook

Overall, this work demonstrates the utility of the top-down synthetic method of forming MONs through liquid ultrasonic exfoliation of layered MOFs. The PW SBU linked in two dimensions with BDC ligands forms a modular framework which can be functionalised through the incorporation of a variety of fu-BDC derivatives. The incorporation of different fu-BDC can result in large differences to the chemistry, structure, size and morphology of MONs formed. The MTV approach of combining different fu-BDCs provides a route to fine-tuning surface functionality. MONs therefore have significant potential to be used as two-dimensional materials with predictable, controllable surface chemistry, which can be fine-tuned towards particular properties. Tailoring the structure, and thus the properties, of MONs will remain relevant for applications such as photo and electrocatalysis, membranes for both gas separations and liquid purifications and electronics, and I look forward to continuing my research within this exciting area of materials chemistry.

References

1   C. Backes, T. M. Higgins, A. Kelly, C. Boland, A. Harvey, D. Hanlon and J. N. Coleman, *Chem. Mater.*, 2017, **29**, 243–255.

2   V. Nicolosi, M. Chhowalla, M. G. Kanatzidis, M. S. Strano and J. N. Coleman, *Science*, 2013, **340**, 1420.

3   J. N. Coleman, M. Lotya, A. O'Neill, S. D. Bergin, P. J. King, U. Khan, K. Young, A. Gaucher, S. De, R. J. Smith, I. V. Shvets, S. K. Arora, G. Stanton, H.-Y. Kim, K. Lee, G. T. Kim, G. S. Duesberg, T. Hallam, J. J. Boland, J. J. Wang, J. F. Donegan, J. C. Grunlan, G. Moriarty, A. Shmeliov, R. J. Nicholls, J. M. Perkins, E. M. Grieveson, K. Theuwissen, D. W. McComb, P. D. Nellist and V. Nicolosi, *Science*, 2011, **331**, 568–571.

4   Y. Peng, Y. Li, Y. Ban, H. Jin, W. Jiao, X. Liu and W. Yang, *Science*, 2014, **346**, 1356–1359.

5   S. C. Junggeburth, L. Diehl, S. Werner, V. Duppel, W. Sigle and B. V Lotsch, *J. Am. Chem. Soc.*, 2013, **135**, 6157–6164.

6   P. Chandrasekhar, A. Mukhopadhyay, G. Savitha and J. N. Moorthy, *J. Mater. Chem. A*, 2017, **5**, 5402–5412.

7   V. K. M. Au, K. Nakayashiki, H. Huang, S. Suginome, H. Sato and T. Aida, *J. Am. Chem. Soc.*, 2019, **141**, 53–57.

8   F. L. Li, P. Wang, X. Huang, D. J. Young, H. F. Wang, P. Braunstein and J. P. Lang, *Angew. Chemie - Int. Ed.*, 2019, **58**, 7051–7056.

9   T. Rodenas, I. Luz, G. Prieto, B. Seoane, H. Miro, A. Corma, F. Kapteijn, F. X. Llabrés i Xamena and J. Gascon, *Nat. Mater.*, 2015, **14**, 48–55.

10   M. Lotya, A. Rakovich, J. F. Donegan and J. N. Coleman, *Nanotechnology*, 2013, **24**, 265703.

11   B. Garai, A. Mallick, A. Das, R. Mukherjee and R. Banerjee, *Chem. - A Eur. J.*, 2017, **23**, 7361–7366.

12   J. Nicks, J. Zhang and J. A. Foster, *Chem. Commun.*, 2019, **55**, 8788–8791.

13   C. Casagrande and V. M., *C. R. Acad. Sci.*, 1988, **II**–**306**, 1423–1425.

14   Z. Lin, N. C. Thacker, T. Sawano, T. Drake, P. Ji, G. Lan, L. Cao, S. Liu, C. Wang and W. Lin, *Chem. Sci.*, 2017, **9**, 143–151.

15   R. Xu, Z. Cai, G. Lan and W. Lin, *Inorg. Chem.*, 2018, **57**, 10489–10493.

16   G. Lan, Z. Li, S. S. Veroneau, Y.-Y. Zhu, Z. Xu, C. Wang and W. Lin, *J. Am. Chem. Soc.*, 2018, **140**, 12369–12373.